



materials

Volume 1

Special Issue of the Manufacturing Engineering Society (MES)

Edited by

Eva M. Rubio and Ana M. Camacho

Printed Edition of the Special Issue Published in *Materials*

**Special Issue of the Manufacturing
Engineering Society (MES)**

Special Issue of the Manufacturing Engineering Society (MES)

Volume 1

Editors

Eva M. Rubio

Ana M. Camacho

MDPI • Basel • Beijing • Wuhan • Barcelona • Belgrade • Manchester • Tokyo • Cluj • Tianjin



Editors

Eva M. Rubio
Universidad Nacional de
Educación a Distancia (UNED)
Spain

Ana M. Camacho
Universidad Nacional de Educación a
Distancia (UNED)
Spain

Editorial Office

MDPI
St. Alban-Anlage 66
4052 Basel, Switzerland

This is a reprint of articles from the Special Issue published online in the open access journal *Materials* (ISSN 1996-1944) (available at: https://www.mdpi.com/journal/materials/special_issues/Manufacturing_Society).

For citation purposes, cite each article independently as indicated on the article page online and as indicated below:

LastName, A.A.; LastName, B.B.; LastName, C.C. Article Title. *Journal Name* **Year**, Article Number, Page Range.

Volume 1

ISBN 978-3-03936-742-9 (Hbk)

ISBN 978-3-03936-743-6 (PDF)

Volume 1-2

ISBN 978-3-03936-768-9 (Hbk)

ISBN 978-3-03936-769-6 (PDF)

© 2020 by the authors. Articles in this book are Open Access and distributed under the Creative Commons Attribution (CC BY) license, which allows users to download, copy and build upon published articles, as long as the author and publisher are properly credited, which ensures maximum dissemination and a wider impact of our publications.

The book as a whole is distributed by MDPI under the terms and conditions of the Creative Commons license CC BY-NC-ND.

Contents

About the Editors	ix
Eva María Rubio and Ana María Camacho Special Issue of the Manufacturing Engineering Society (MES) Reprinted from: <i>Materials</i> 2018 , <i>11</i> , 2149, doi:10.3390/ma11112149	1
Darío R. Quiñone ,David Soler-Egea, Víctor González-Pérez, Johanna Reibke, Elena Simarro-Mondejar, Ricardo Pérez-Feito, Juan A. García-Manrique, Vicente Crispín and David Moratal Open Source 3D Printed Lung Tumor Movement Simulator for Radiotherapy Quality Assurance Reprinted from: <i>Materials</i> 2018 , <i>11</i> , 1317, doi:10.3390/ma11081317	5
Ana Pilar Valerga, Moisés Batista, Jorge Salguero and Frank Girot Influence of PLA Filament Conditions on Characteristics of FDM Parts Reprinted from: <i>Materials</i> 2018 , <i>11</i> , 1322, doi:10.3390/ma11081322	17
Adrián Rodríguez-Panes, Juan Claver and Ana María Camacho The Influence of Manufacturing Parameters on the Mechanical Behaviour of PLA and ABS Pieces Manufactured by FDM: A Comparative Analysis Reprinted from: <i>Materials</i> 2018 , <i>11</i> , 1333, doi:10.3390/ma11081333	31
Mercedes Pérez, Gustavo Medina-Sánchez, Alberto García-Collado, Munish Gupta and Diego Carou Surface Quality Enhancement of Fused Deposition Modeling (FDM) Printed Samples Based on the Selection of Critical Printing Parameters Reprinted from: <i>Materials</i> 2018 , <i>11</i> , 1382, doi:10.3390/ma11081382	53
Jose Exequiel Ruiz, Magdalena Cortina, Jon Iñaki Arrizubieta and Aitzol Lamikiz Study of the Influence of Shielding Gases on Laser Metal Deposition of Inconel 718 Superalloy Reprinted from: <i>Materials</i> 2018 , <i>11</i> , 1388, doi:10.3390/ma11081388	67
Enrique Sodupe-Ortega, Andres Sanz-Garcia, Alpha Pernia-Espinoza and Carmen Escobedo-Lucea Accurate Calibration in Multi-Material 3D Bioprinting for Tissue Engineering Reprinted from: <i>Materials</i> 2018 , <i>11</i> , 1402, doi:10.3390/ma11081402	77
Francisco Cordovilla, Ángel García-Beltrán, Miguel Garzón, Diego A. Muñoz and José L. Ocaña Numerical-Experimental Study of the Consolidation Phenomenon in the Selective Laser Melting Process with a Thermo-Fluidic Coupled Model Reprinted from: <i>Materials</i> 2018 , <i>11</i> , 1414, doi:10.3390/ma11081414	97
Marc Rabionet, Emma Polonio, Antonio J. Guerra, Jessica Martin, Teresa Puig and Joaquim Ciurana Design of a Scaffold Parameter Selection System with Additive Manufacturing for a Biomedical Cell Culture Reprinted from: <i>Materials</i> 2018 , <i>11</i> , 1427, doi:10.3390/ma11081427	115

Joaquim Minguella-Canela, Sergio Morales Planas, Joan Ramon Gomà Ayats and M. Antonia de los Santos López Assessment of the Potential Economic Impact of the Use of AM Technologies in the Cost Levels of Manufacturing and Stocking of Spare Part Products Reprinted from: <i>Materials</i> 2018 , <i>11</i> , 1429, doi:10.3390/ma11081429	129
José Luis Prado-Cerqueira, Ana María Camacho, José Luis Diéguez, Álvaro Rodríguez-Prieto, Ana María Aragón, Cinta Lorenzo-Martín and Ángel Yanguas-Gil Analysis of Favorable Process Conditions for the Manufacturing of Thin-Wall Pieces of Mild Steel Obtained by Wire and Arc Additive Manufacturing (WAAM) Reprinted from: <i>Materials</i> 2018 , <i>11</i> , 1449, doi:10.3390/ma11081449	155
Kyungjin Park, Kanghyun Kim, Seung Chul Lee, Geunbae Lim and Jong Hyun Kim Fabrication of Polymer Microstructures of Various Angles via Synchrotron X-Ray Lithography Using Simple Dimensional Transformation Reprinted from: <i>Materials</i> 2018 , <i>11</i> , 1460, doi:10.3390/ma11081460	173
M. Puerto Pérez-Pérez, Emilio Gómez and Miguel A. Sebastián Delphi Prospection on Additive Manufacturing in 2030: Implications for Education and Employment in Spain Reprinted from: <i>Materials</i> 2018 , <i>11</i> , 1500, doi:10.3390/ma11091500	185
Daño R. Quiñones, Jorge Ferragud-Agulló, Ricardo Pérez-Feito, Juan A. García-Manrique, Santiago Canals and David Moratal A Tangible Educative 3D Printed Atlas of the Rat Brain Reprinted from: <i>Materials</i> 2018 , <i>11</i> , 1531, doi:10.3390/ma11091531	209
Irene Buj-Corral, Ali Bagheri and Oriol Petit-Rojo 3D Printing of Porous Scaffolds with Controlled Porosity and Pore Size Values Reprinted from: <i>Materials</i> 2018 , <i>11</i> , 1532, doi:10.3390/ma11091532	219
Jorge Salguero, Juan Manuel Vazquez-Martinez, Irene Del Sol and Moises Batista Application of Pin-On-Disc Techniques for the Study of Tribological Interferences in the Dry Machining of A92024-T3 (Al-Cu) Alloys Reprinted from: <i>Materials</i> 2018 , <i>11</i> , 1236, doi:10.3390/ma11071236	237
Yezika Sánchez Hernández, Francisco Javier Trujillo Vilches, Carolina Bermudo Gamboa and Lorenzo Sevilla Hurtado Experimental Parametric Relationships for Chip Geometry in Dry Machining of the Ti6Al4V Alloy Reprinted from: <i>Materials</i> 2018 , <i>11</i> , 1260, doi:10.3390/ma11071260	249
Álvaro Gómez-Parra, Alfredo Sanz and Antonio J. Gámez Evaluation of the Functional Performance in Turned Workpieces: Methodology and Application to UNS A92024-T3 Reprinted from: <i>Materials</i> 2018 , <i>11</i> , 1264, doi:10.3390/ma11081264	267
Severo Raul Fernandez-Vidal, Sergio Fernandez-Vidal, Moises Batista and Jorge Salguero Tool Wear Mechanism in Cutting of Stack CFRP/UNS A97075 Reprinted from: <i>Materials</i> 2018 , <i>11</i> , 1276, doi:10.3390/ma11081276	279
Álvaro Álvarez, Amaia Calleja, Mikel Arizmendi, Haizea González and Luis Norberto Lopez de Lacalle Spiral Bevel Gears Face Roughness Prediction Produced by CNC End Milling Centers Reprinted from: <i>Materials</i> 2018 , <i>11</i> , 1301, doi:10.3390/ma11081301	293

Eva María Rubio, María Villeta, José Luis Valencia and José Manuel Sáenz de Pipaón Cutting Parameter Selection for Efficient and Sustainable Repair of Holes Made in Hybrid Mg–Ti–Mg Component Stacks by Dry Drilling Operations Reprinted from: <i>Materials</i> 2018 , <i>11</i> , 1369, doi:10.3390/ma11081369	313
María Dolores Navarro-Mas, Juan Antonio García-Manrique, María Desamparados Meseguer, Isabel Ordeig and Ana Isabel Sánchez Delamination Study in Edge Trimming of Basalt Fiber Reinforced Plastics (BFRP) Reprinted from: <i>Materials</i> 2018 , <i>11</i> , 1418, doi:10.3390/ma11081418	333
Beatriz de Agustina, Marta María Marín, Roberto Teti and Eva María Rubio Analysis of Force Signals for the Estimation of Surface Roughness during Robot-Assisted Polishing Reprinted from: <i>Materials</i> 2018 , <i>11</i> , 1438, doi:10.3390/ma11081438	347
Alessandra Caggiano, Ilaria Improta and Luigi Nele Characterization of a New Dry Drill-Milling Process of Carbon Fibre Reinforced Polymer Laminates Reprinted from: <i>Materials</i> 2018 , <i>11</i> , 1470, doi:10.3390/ma11081470	355
María Jesús Martín, María José Cano, Germán Castillo, Manuel José Herrera and Francisco Martín Influence of Milling Parameters on Mechanical Properties of AA7075 Aluminum under Corrosion Conditions Reprinted from: <i>Materials</i> 2018 , <i>11</i> , 1751, doi:10.3390/ma11091751	371
Diogo F. M. Silva, Carlos M. A. Silva, Ivo M. F. Bragança, Chris V. Nielsen, Luis M. Alves and Paulo A. F. Martins On the Performance of Thin-Walled Crash Boxes Joined by Forming Reprinted from: <i>Materials</i> 2018 , <i>11</i> , 1118, doi:10.3390/ma11071118	389

About the Editors

Eva M. Rubio is a Professor at the Department of Manufacturing Engineering of the National Distance Education University (UNED, Spain). She received her MSc in Aeronautical Engineering (1997) from the Polytechnic University of Madrid and her PhD in Industrial Engineering (2002) from the National University of Distance Education (UNED). Her research activity is dedicated to the field of Manufacturing Engineering, with the following main lines of work: analysis of machining processes; analysis of metal forming processes; industrial metrology; and teaching and innovation in engineering.

Ana M. Camacho is a Professor at the Department of Manufacturing Engineering of the National Distance Education University (UNED, Spain). She received her MSc in Industrial Engineering from the University of Castilla-La Mancha (UCLM) in 2001 and her PhD in Industrial Engineering from the UNED in 2005. Her main research interest is innovation in manufacturing engineering and materials technology, especially focused on analysis of metal forming and additive manufacturing techniques through computer-aided engineering tools and experimental testing, and development of methodologies for materials selection in demanding applications.

Editorial

Special Issue of the Manufacturing Engineering Society (MES)

Eva María Rubio * and Ana María Camacho

Department of Manufacturing Engineering, Industrial Engineering School, Universidad Nacional de Educación a Distancia (UNED), St/Juan del Rosal 12, E28040 Madrid, Spain; amcamacho@ind.uned.es

* Correspondence: erubio@ind.uned.es; Tel.: +34-913-988-226

Received: 24 October 2018; Accepted: 29 October 2018; Published: 31 October 2018

Abstract: Research in the field of materials is very broad, ranging from studies on the structure and properties at the atomic or molecular level to the most complex or sophisticated applications that can be done with them, as well as studies about other aspects related to their processing, use or management. The Special Issue of the Manufacturing Engineering Society (MES), published in the Section “Manufacturing Processes and Systems” of the journal *Materials*, focuses, mainly, on the applications and key processing aspects of materials, collecting a set of 48 original papers focused on the field of manufacturing engineering and materials processing.

Keywords: additive manufacturing and 3D printing; advances and innovations in manufacturing processes; sustainable and green manufacturing; manufacturing systems: machines; equipment and tooling; metrology and quality in manufacturing; Industry 4.0; product lifecycle management (PLM) technologies; production planning; risks

The Special Issue of the Manufacturing Engineering Society (MES), published in the Section “Manufacturing Processes and Systems” of the journal *Materials*, was born as an initiative from the Manufacturing Engineering Society of Spain, with the aim to spread outstanding works in which the latest cutting-edge advances in the field of manufacturing engineering and materials processing have been presented.

This Special Issue explored the evolution of traditional manufacturing models towards the new requirements of the Manufacturing Industry 4.0; publishing, finally, 48 papers (47 research papers and one concept paper) in the main topics covered by this Special Issue, concretely in: additive manufacturing and 3D printing; advances and innovations in manufacturing processes; manufacturing systems: machines, equipment and tooling, metrology and quality in manufacturing; product lifecycle management (PLM) technologies; and manufacturing engineering and society.

Likewise, in some of them, without being the main or most outstanding subjects of the work, the following topics have been also addressed: sustainable and green manufacturing; manufacturing of new materials; manufacturing automation; design, modeling and simulation in manufacturing engineering; and production planning.

Contributions on emerging methods and technologies, such as those related to additive manufacturing and 3D printing [1–14], have been very numerous, which is not surprising as they are technologies with a lot of potential.

The number of contributions in the “advances and innovations in manufacturing processes” field has been very remarkable as well, where outstanding works have been presented in the following areas: machining [15–24], forming [25–30], moulding [31], welding [32,33], and non-traditional manufacturing processes [34–38].

No less important, as a whole, are the works on: manufacturing systems: machines, equipment and tooling [39–42], metrology and quality in manufacturing [43–45], product lifecycle management (PLM) technologies [46] and, risks, within the topic “manufacturing engineering and society” [47,48].

The Special Issue has been an excellent means of exposing some of the main current lines of research of members and collaborators of the MES, promoting the internationalization of their results and the presence of the MES itself in the international scientific-technical landscape, widely fulfilling the aims initially proposed.

It is remarkable how many readings and downloads of papers belonging to this Special Issue have been done, after only three months since the publication of the first work, showing the great interest that all these topics arouse in readers of the journal *Materials*; particularly topics related to the processing of materials.

In Memoriam

We want this Special Issue to serve as a posthumous tribute to our colleague and friend Mariano Marcos Bárcena, who participated very actively in the genesis of this thrilling project, and whose contribution to manufacturing engineering is present in this Special Issue, both explicitly, in a concrete work, and implicitly, in several papers by his research group from the University of Cadiz who have kept working on the investigation lines promoted by him.

Conflicts of Interest: The authors declare no conflict of interest.

References

1. Quiñones, D.; Soler-Egea, D.; González-Pérez, V.; Reibke, J.; Simarro-Mondejar, E.; Pérez-Feito, R.; García-Manrique, J.; Crispín, V.; Moratal, D. Open Source 3D Printed Lung Tumor Movement Simulator for Radiotherapy Quality Assurance. *Materials* **2018**, *11*, 1317. [[CrossRef](#)] [[PubMed](#)]
2. Valerga, A.; Batista, M.; Salguero, J.; Girot, F. Influence of PLA Filament Conditions on Characteristics of FDM Parts. *Materials* **2018**, *11*, 1322. [[CrossRef](#)] [[PubMed](#)]
3. Rodríguez-Panes, A.; Claver, J.; Camacho, A. The Influence of Manufacturing Parameters on the Mechanical Behaviour of PLA and ABS Pieces Manufactured by FDM: A Comparative Analysis. *Materials* **2018**, *11*, 1333. [[CrossRef](#)] [[PubMed](#)]
4. Pérez, M.; Medina-Sánchez, G.; García-Collado, A.; Gupta, M.; Carou, D. Surface Quality Enhancement of Fused Deposition Modeling (FDM) Printed Samples Based on the Selection of Critical Printing Parameters. *Materials* **2018**, *11*, 1382. [[CrossRef](#)] [[PubMed](#)]
5. Ruiz, J.; Cortina, M.; Arrizubieta, J.; Lamikiz, A. Study of the Influence of Shielding Gases on Laser Metal Deposition of Inconel 718 Superalloy. *Materials* **2018**, *11*, 1388. [[CrossRef](#)] [[PubMed](#)]
6. Sodupe-Ortega, E.; Sanz-García, A.; Pernia-Espinoza, A.; Escobedo-Lucea, C. Accurate Calibration in Multi-Material 3D Bioprinting for Tissue Engineering. *Materials* **2018**, *11*, 1402. [[CrossRef](#)] [[PubMed](#)]
7. Cordovilla, F.; García-Beltrán, Á.; Garzón, M.; Muñoz, D.; Ocaña, J. Numerical-Experimental Study of the Consolidation Phenomenon in the Selective Laser Melting Process with a Thermo-Fluidic Coupled Model. *Materials* **2018**, *11*, 1414. [[CrossRef](#)] [[PubMed](#)]
8. Rabionet, M.; Polonio, E.; Guerra, A.; Martín, J.; Puig, T.; Ciurana, J. Design of a Scaffold Parameter Selection System with Additive Manufacturing for a Biomedical Cell Culture. *Materials* **2018**, *11*, 1427. [[CrossRef](#)] [[PubMed](#)]
9. Minguella-Canela, J.; Morales Planas, S.; Gomà Ayats, J.; de los Santos López, M. Assessment of the Potential Economic Impact of the Use of AM Technologies in the Cost Levels of Manufacturing and Stocking of Spare Part Products. *Materials* **2018**, *11*, 1429. [[CrossRef](#)] [[PubMed](#)]
10. Prado-Cerqueira, J.; Camacho, A.; Diéguez, J.; Rodríguez-Prieto, Á.; Aragón, A.; Lorenzo-Martín, C.; Yanguas-Gil, Á. Analysis of Favorable Process Conditions for the Manufacturing of Thin-Wall Pieces of Mild Steel Obtained by Wire and Arc Additive Manufacturing (WAAM). *Materials* **2018**, *11*, 1449. [[CrossRef](#)] [[PubMed](#)]
11. Park, K.; Kim, K.; Lee, S.; Lim, G.; Kim, J. Fabrication of Polymer Microstructures of Various Angles via Synchrotron X-ray Lithography Using Simple Dimensional Transformation. *Materials* **2018**, *11*, 1460. [[CrossRef](#)] [[PubMed](#)]

12. Pérez-Pérez, M.; Gómez, E.; Sebastián, M. Delphi Prospection on Additive Manufacturing in 2030: Implications for Education and Employment in Spain. *Materials* **2018**, *11*, 1500. [[CrossRef](#)] [[PubMed](#)]
13. Quñones, D.; Ferragud-Agulló, J.; Pérez-Feito, R.; García-Manrique, J.; Canals, S.; Moratal, D. A Tangible Educative 3D Printed Atlas of the Rat Brain. *Materials* **2018**, *11*, 1531. [[CrossRef](#)] [[PubMed](#)]
14. Buj-Corral, I.; Bagheri, A.; Petit-Rojo, O. 3D Printing of Porous Scaffolds with Controlled Porosity and Pore Size Values. *Materials* **2018**, *11*, 1532. [[CrossRef](#)] [[PubMed](#)]
15. Salguero, J.; Vazquez-Martinez, J.; Sol, I.; Batista, M. Application of Pin-On-Disc Techniques for the Study of Tribological Interferences in the Dry Machining of A92024-T3 (Al–Cu) Alloys. *Materials* **2018**, *11*, 1236. [[CrossRef](#)] [[PubMed](#)]
16. Sánchez Hernández, Y.; Trujillo Vilches, F.; Bermudo Gamboa, C.; Sevilla Hurtado, L. Experimental Parametric Relationships for Chip Geometry in Dry Machining of the Ti6Al4V Alloy. *Materials* **2018**, *11*, 1260. [[CrossRef](#)] [[PubMed](#)]
17. Gómez-Parra, Á.; Sanz, A.; Gámez, A. Evaluation of the Functional Performance in Turned Workpieces: Methodology and Application to UNS A92024-T3. *Materials* **2018**, *11*, 1264. [[CrossRef](#)] [[PubMed](#)]
18. Fernandez-Vidal, S.; Fernandez-Vidal, S.; Batista, M.; Salguero, J. Tool Wear Mechanism in Cutting of Stack CFRP/UNS A97075. *Materials* **2018**, *11*, 1276. [[CrossRef](#)] [[PubMed](#)]
19. Álvarez, Á.; Calleja, A.; Arizmendi, M.; González, H.; Lopez de Lacalle, L. Spiral Bevel Gears Face Roughness Prediction Produced by CNC End Milling Centers. *Materials* **2018**, *11*, 1301. [[CrossRef](#)] [[PubMed](#)]
20. Rubio, E.; Villeta, M.; Valencia, J.; Sáenz de Pipaón, J. Cutting Parameter Selection for Efficient and Sustainable Repair of Holes Made in Hybrid Mg–Ti–Mg Component Stacks by Dry Drilling Operations. *Materials* **2018**, *11*, 1369. [[CrossRef](#)] [[PubMed](#)]
21. Navarro-Mas, M.; García-Manrique, J.; Meseguer, M.; Ordeig, I.; Sánchez, A. Delamination Study in Edge Trimming of Basalt Fiber Reinforced Plastics (BFRP). *Materials* **2018**, *11*, 1418. [[CrossRef](#)] [[PubMed](#)]
22. De Agustina, B.; Marín, M.; Teti, R.; Rubio, E. Analysis of Force Signals for the Estimation of Surface Roughness during Robot-Assisted Polishing. *Materials* **2018**, *11*, 1438. [[CrossRef](#)] [[PubMed](#)]
23. Caggiano, A.; Improta, I.; Nele, L. Characterization of a New Dry Drill-Milling Process of Carbon Fibre Reinforced Polymer Laminates. *Materials* **2018**, *11*, 1470. [[CrossRef](#)] [[PubMed](#)]
24. Martín, M.; Cano, M.; Castillo, G.; Herrera, M.; Martín, F. Influence of Milling Parameters on Mechanical Properties of AA7075 Aluminum under Corrosion Conditions. *Materials* **2018**, *11*, 1751. [[CrossRef](#)] [[PubMed](#)]
25. Silva, D.; Silva, C.; Bragança, I.; Nielsen, C.; Alves, L.; Martins, P. On the Performance of Thin-Walled Crash Boxes Joined by Forming. *Materials* **2018**, *11*, 1118. [[CrossRef](#)] [[PubMed](#)]
26. Han, S.; Shu, X.; Shu, C. Study on Near-Net Forming Technology for Stepped Shaft by Cross-Wedge Rolling Based on Variable Cone Angle Billets. *Materials* **2018**, *11*, 1278. [[CrossRef](#)] [[PubMed](#)]
27. Sabater, M.; Garcia-Romeu, M.; Vives-Mestres, M.; Ferrer, I.; Bagudanch, I. Process Parameter Effects on Biocompatible Thermoplastic Sheets Produced by Incremental Forming. *Materials* **2018**, *11*, 1377. [[CrossRef](#)] [[PubMed](#)]
28. Medina-Sanchez, G.; Garcia-Collado, A.; Carou, D.; Dorado-Vicente, R. Force Prediction for Incremental Forming of Polymer Sheets. *Materials* **2018**, *11*, 1597. [[CrossRef](#)] [[PubMed](#)]
29. Linke, M.; García-Manrique, J. Contribution to Reduce the Influence of the Free Sliding Edge on Compression-After-Impact Testing of Thin-Walled Undamaged Composites Plates. *Materials* **2018**, *11*, 1708. [[CrossRef](#)] [[PubMed](#)]
30. Morales-Palma, D.; Borrego, M.; Martínez-Donaire, A.; Centeno, G.; Vallellano, C.; Morales-Palma, D.; Borrego, M.; Martínez-Donaire, A.J.; Centeno, G.; Vallellano, C. Optimization of Hole-Flanging by Single Point Incremental Forming in Two Stages. *Materials* **2018**, *11*, 2029. [[CrossRef](#)] [[PubMed](#)]
31. Ferrer, I.; Vives-Mestres, M.; Manresa, A.; Garcia-Romeu, M.L. Replicability of Ultrasonic Molding for Processing Thin-Wall Polystyrene Plates with a Microchannel. *Materials* **2018**, *11*, 1320. [[CrossRef](#)] [[PubMed](#)]
32. Pradeep Kumar, J. Effect of Temperature Distribution in Ultrasonically Welded Joints of Copper Wire and Sheet Used for Electrical Contacts. *Materials* **2018**, *11*, 1010. [[CrossRef](#)] [[PubMed](#)]
33. Souto, J.; Ares, E.; Alegre, P.; Cerqueiro, J. Methodology to Reduce Distortion Using a Hybrid Thermal Welding Process. *Materials* **2018**, *11*, 1649. [[CrossRef](#)] [[PubMed](#)]
34. Sanchez, J.; Conde, A.; Arriandiaga, A.; Wang, J.; Plaza, S. Unexpected Event Prediction in Wire Electrical Discharge Machining Using Deep Learning Techniques. *Materials* **2018**, *11*, 1100. [[CrossRef](#)] [[PubMed](#)]

35. Arrizubieta, J.; Cortina, M.; Ruiz, J.; Lamikiz, A. Combination of Laser Material Deposition and Laser Surface Processes for the Holistic Manufacture of Inconel 718 Components. *Materials* **2018**, *11*, 1247. [[CrossRef](#)] [[PubMed](#)]
36. Wachulak, P.; Duda, M.; Fok, T.; Bartnik, A.; Wang, Z.; Huang, Q.; Sarzyński, A.; Jancarek, A.; Fiedorowicz, H. Single-Shot near Edge X-ray Fine Structure (NEXAFS) Spectroscopy Using a Laboratory Laser-Plasma Light Source. *Materials* **2018**, *11*, 1303. [[CrossRef](#)] [[PubMed](#)]
37. Mayuet Ares, P.; Vázquez Martínez, J.; Marcos Bárcena, M.; Gámez, A. Experimental Study of Macro and Microgeometric Defects in Drilled Carbon Fiber Reinforced Plastics by Laser Beam Machining. *Materials* **2018**, *11*, 1466. [[CrossRef](#)] [[PubMed](#)]
38. Caiazzo, F.; Alfieri, V. Simulation of Laser Heating of Aluminum and Model Validation via Two-Color Pyrometer and Shape Assessment. *Materials* **2018**, *11*, 1506. [[CrossRef](#)] [[PubMed](#)]
39. Bader, A.; Meiners, F.; Tracht, K. Accelerating High-Throughput Screening for Structural Materials with Production Management Methods. *Materials* **2018**, *11*, 1330. [[CrossRef](#)] [[PubMed](#)]
40. Gallego García, S.; García García, M. Design and Simulation of Production and Maintenance Management Applying the Viable System Model: The Case of an OEM Plant. *Materials* **2018**, *11*, 1346. [[CrossRef](#)] [[PubMed](#)]
41. Romero Subirón, F.; Rosado Castellano, P.; Bruscas Bellido, G.; Benavent Náchter, S. Feature-Based Framework for Inspection Process Planning. *Materials* **2018**, *11*, 1504. [[CrossRef](#)] [[PubMed](#)]
42. Vargas, J.; Calvo, R. Joint Optimization of Process Flow and Scheduling in Service-Oriented Manufacturing Systems. *Materials* **2018**, *11*, 1559. [[CrossRef](#)] [[PubMed](#)]
43. Brosted, F.; Zaera, A.; Padilla, E.; Cebrián, F.; Aguilar, J. In-Process Measurement for the Process Control of the Real-Time Manufacturing of Tapered Roller Bearings. *Materials* **2018**, *11*, 1371. [[CrossRef](#)] [[PubMed](#)]
44. Ontiveros, S.; Jiménez, R.; Yagüe-Fabra, J.; Torralba, M. Analysis of Surface Extraction Methods Based on Gradient Operators for Computed Tomography in Metrology Applications. *Materials* **2018**, *11*, 1461. [[CrossRef](#)] [[PubMed](#)]
45. García, J.C.; Sanz Lobera, A.; Maresca, P.; Pareja, T.F.; Wang, C. Some Considerations about the Use of Contact and Confocal Microscopy Methods in Surface Texture Measurement. *Materials* **2018**, *11*, 1484. [[CrossRef](#)] [[PubMed](#)]
46. Camarillo, A.; Ríos, J.; Althoff, K.-D. Product Lifecycle Management as Data Repository for Manufacturing Problem Solving. *Materials* **2018**, *11*, 1469. [[CrossRef](#)] [[PubMed](#)]
47. Brocal, F.; González, C.; Reniers, G.; Cozzani, V.; Sebastián, M.; Brocal, F.; González, C.; Reniers, G.; Cozzani, V.; Sebastián, M.A. Risk Management of Hazardous Materials in Manufacturing Processes: Links and Transitional Spaces between Occupational Accidents and Major Accidents. *Materials* **2018**, *11*, 1915. [[CrossRef](#)] [[PubMed](#)]
48. Van Nunen, K.; Swuste, P.; Reniers, G.; Paltrinieri, N.; Aneziris, O.; Ponnet, K. Improving Pallet Mover Safety in the Manufacturing Industry: A Bow-Tie Analysis of Accident Scenarios. *Materials* **2018**, *11*, 1955. [[CrossRef](#)] [[PubMed](#)]



© 2018 by the authors. Licensee MDPI, Basel, Switzerland. This article is an open access article distributed under the terms and conditions of the Creative Commons Attribution (CC BY) license (<http://creativecommons.org/licenses/by/4.0/>).

Article

Open Source 3D Printed Lung Tumor Movement Simulator for Radiotherapy Quality Assurance

Darío R. Quiñones ¹, David Soler-Egea ¹, Víctor González-Pérez ², Johanna Reibke ¹, Elena Simarro-Mondejar ¹, Ricardo Pérez-Feito ³, Juan A. García-Manrique ⁴, Vicente Crispín ² and David Moratal ^{1,*}

¹ Centre for Biomaterials and Tissue Engineering, Universitat Politècnica de València, 46022 Valencia, Spain; dariomrxpro2@hotmail.com (D.R.Q.); dasoeg@etsii.upv.es (D.S.-E.); johannareibke@gmail.com (J.R.); elenasimarro@gmail.com (E.S.-M.)

² Department of Radiophysics, Fundación Instituto Valenciano de Oncología, 46009 Valencia, Spain; vgonzalezper@hotmail.com (V.G.-P.); vcrispin@fivo.org (V.C.)

³ Thermodynamics Department, Universitat Politècnica de València, 46022 Valencia, Spain; riperez@upvnet.upv.es

⁴ Institute of Design for Manufacturing and Automated Production, Universitat Politècnica de València, 46022 Valencia, Spain; jugarcia@mcm.upv.es

* Correspondence: dmoratal@eln.upv.es

Received: 29 June 2018; Accepted: 26 July 2018; Published: 30 July 2018

Abstract: In OECD (Organization for Economic Co-operation and Development) countries, cancer is one of the main causes of death, lung cancer being one of the most aggressive. There are several techniques for the treatment of lung cancer, among which radiotherapy is one of the most effective and least invasive for the patient. However, it has associated difficulties due to the moving target tumor. It is possible to reduce the side effects of radiotherapy by effectively tracking a tumor and reducing target irradiation margins. This paper presents a custom electromechanical system that follows the movement of a lung tumor. For this purpose, a hysteresis loop of human lung movement during breathing was studied to obtain its characteristic movement equation. The system is controlled by an Arduino, steppers motors and a customized 3D printed mechanism to follow the characteristic human breathing, obtaining an accurate trajectory. The developed device helps the verification of individualized radiation treatment plans and permits the improvement of radiotherapy quality assurance procedures.

Keywords: respiratory movement; lung tumor; radiotherapy; arduino; cancer treatment; linear accelerator

1. Introduction

Lung cancer is the most common type of cancer in OECD (Organization for Economic Co-operation and Development) countries. It is responsible for over 1.38 million deaths annually [1]. There are currently several treatments for lung cancer, including surgery, radiotherapy, chemotherapy and palliative care. One of the most effective is radiotherapy. It is because malignant cells are eliminated via ionizing radiation and it is less invasive for the patient [2]. Nowadays, more than half of all cancer patients receive radiotherapy, either alone or in combination with surgery or chemotherapy [3]. However, radiotherapy has detrimental side effects, as healthy tissue is also affected by these usually high-dose-rate radiation beams.

Radiotherapy involves the use of controlled doses of high-intensity radiation to kill cancer cells or to reduce the size of tumors. In the case of lung cancer, radiotherapy is used as a main treatment in patients for whom surgery is impossible. It can also be applied before or after the surgery, as palliative

therapy or to relieve blocked airways. Radiotherapy is generated outside the body, in a Linear Accelerator (LINAC), and is generally used to treat non-small cell tumor.

Regarding the side effects of radiotherapy, a distinction between acute and chronic effects is made. The former are those that appear during treatment and usually disappear within a few weeks, such as fatigue and skin reactions, among others. Chronic side effects appear months or even years after treatment and may be permanent.

One of the essential parts of external radiotherapy treatment is planning [4]. Before starting treatment, it is important to calculate the dose needed, the emission angles and other parameters that will allow the patient to receive the right amount of radiation without affecting adjacent areas.

Compared to other parts of the body, the lungs are in constant motion [5,6]. According to Seppenwoolde et al. the movement of the lung in this way is largely two-dimensional and it is possible to reproduce the movement of any part of the lung when the length and capacity of the breath is known.

Previous studies have shown that a human adult breathes between 16 and 20 times per minute, which means one breath (inhalation and exhalation) every 3–3.75 s [7]. Closer inspection of the lungs shows that not all points move at the same rate and, therefore, not at the same speed [8]. Nevertheless, the general movement can be equated to a hysteresis loop [9,10], as shown in Figure 1. This is why lung tumor irradiation cannot be concentrated in a fixed tumor position at each phase of the breathing cycle, and it must be applied with small margins of the target volume to cover the tumor position during the entire respiratory cycle. To irradiate the tumor, it is necessary to follow the movement of the tumor [11] to plan the radiotherapy treatment.

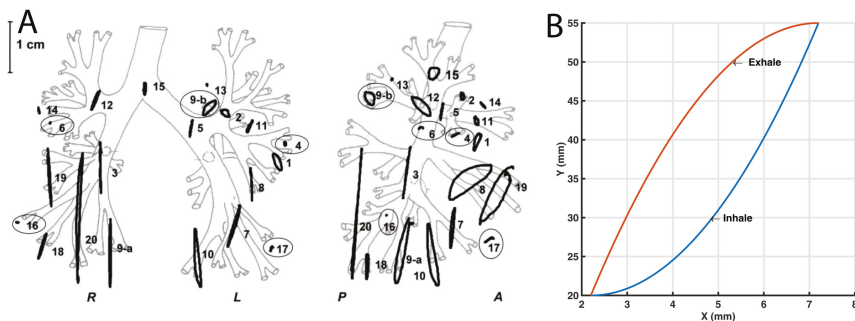


Figure 1. Hysteresis loop of lung tumors movement: (A) The orthogonal projections of the trajectories of the 21 tumors on (left) the coronal (LR-CC) and (right) the sagittal (AP-CC) plane is shown (reproduced with permission from [9]); and (B) One recreated hysteresis cycle that simulates the movement of the tumor is displayed.

Good planning will reduce the amount of radiation that healthy tissues receives, while reducing the side effects. To verify the treatment of sophisticated radiation techniques in lung cancer, a parametric simulator of the tumor movement is needed.

The imaging techniques currently available, such as the 4D Computer Tomography (4DCT), acquire images synchronized with respiratory movement [12,13]. This permits to track the tumor position in each phase of the cycle and extract a custom path from patients [14–19]. These images are taken with the patient immobilized, in the same way in which the future treatment will be applied in each of the sessions.

In this work, we present a proof of concept of a lung tumor movement simulator prototype, which considers that not every human has the same breathing characteristic curve. In addition it can be adapted to any possible specific height, width and speed of breathing movement. Although there are some commercial alternatives, they are not Open-Source. The Lung Tumor Movement Simulator was entirely created using 3D printed parts in order to achieve a customizable device that can be adapted

for specific cases. Furthermore, it was printed with an Open-Source 3D printer that makes it affordable for every research centre. With this device, individualized radiation treatment plans can be tested in advance.

2. Materials and Methods

2.1. Linear Accelerator

A Linear Accelerator (LINAC) is a device that is most commonly used to give external beam radiation therapy to patients with cancer. It supplies high-energy X-rays to the tumor region of the patient. These X-ray treatments can be designed to destroy cancer cells without affecting normal surrounding tissues.

The linear accelerator uses microwave technology to accelerate electrons and then allows these electrons to collide with a heavy metal target to produce high-energy X-rays [20]. These high energy X-rays are shaped as they exit the machine to target the tumor in the patient. The beam is shaped by a multi-leaf collimator that is incorporated into the head of the LINAC. The patient lies on a movable treatment couch and lasers are used to make sure that the patient is placed in the desired position. The ionizing beam is emitted from a part of the accelerator called a gantry, which can be rotated around the patient. Moreover, radiation can be delivered to the tumor from any angle, by rotating the gantry and by moving the treatment couch.

Because lungs are in constant motion, the tumor is constantly changing its position and this movement should be taken in account. This movement of the tumor is always studied before starting the treatment (Figure 1). To increase the LINACs accuracy and avoid irradiating healthy areas, there is a technique called tumor tracking [14] that is useful to analyze the movement of an internal lung tumor. Based on these tumor tracking studies, and to improve customized radiotherapy plan verification, the Lung Tumor Movement Simulator was created. It provides a good simulation of tumor movement and a good radiation measure because it holds a dosimeter in the Tip. In this case the Tip was designed to contain a Landauer OSL nanoDot™ (Landauer, Inc., Greenwood, IL, USA).

2.2. Electromechanical Components

To give motion to the mechanism, a pair of NEMA 17 stepper motors was used. The stepper motors have a minimum step angle of 1.8 degrees (200 steps/revolution). Each phase needs 280 mA to 7.4 V, allowing a torque of 650 g-cm (9 oz-in). To drive both stepper motors, a pair of stepper controllers DRV8825 (Texas Instruments, Dallas, TX, USA) were used, which features adjustable current limiting and six microstep resolutions (down to 1/32-step).

In cyclic or rotating movements, it is important to know the starting point of the rotation. For this reason, endstops are needed. Endstops sensors are electronic components that function as switches, sending signals when an element is placed in a certain position. There are various types such as mechanical, optical and magnetic. In the prototype two optical endstops are used because they can be activated by some element of the mechanism (Figure 2, element 3 and 9). At the same time, this type of sensor avoids the possible rebounds that may appear in mechanical sensors.

2.3. Microcontroller

The Arduino Mega 2560 (Smart Projects, Turin, Italy & SparkFun Electronics, Boulder, CO, USA) development board is a printed circuit that allows the use of a microcontroller ATMEGA2560 (Microchip Technology Inc., Chandler, AZ, USA) [21]. Arduino is commonly used in a high variety of research fields due to its versatility and low cost [22–25].

This microcontroller controls 54 digital Input/Output pins, 15 pulse width modulation pins, and 16 analog pins, and is able to automate any system. Documentation and software are open source and available at the Arduino website. The programming software is based on the C/C++ language and the power supply of this development board can be powered through USB or main supply from 5 V to 12 V.

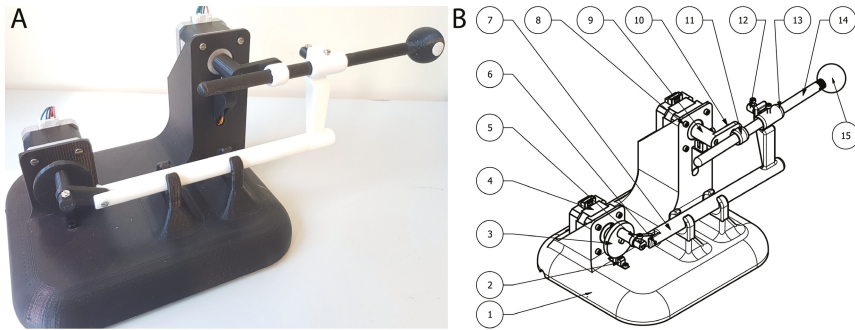


Figure 2. (A) Real Lung Tumor Movement Simulator prototype; and (B) Schematic parts of the prototype. See Table 1 for details.

Table 1. Prototype parts.

PART (Figure 2)	Description	Quantity	X (mm)	Y (mm)	Z (mm)	Weight (g)	Material
1	Base	1	209.50	180.00	145.00	550.00	PLA
2	Endstop	2	-	-	-	-	-
3	Horizontal wheel	1	45.10	40.00	51.00	9.00	PLA
4	Stepper NEMA 17	2	42.00	42.00	38.00	285.00	PLA
5	Union bar	1	15.70	36.60	4.50	3.00	PLA
6	Cylinder pin	1	2.00	3.00	30.00	2.00	Stainless Steel
7	Horizontal bar	1	200.00	26.00	85.50	28.00	PLA
8	Screw M3 x 6	15	-	-	-	5.00	Stainless Steel
9	Vertical bar	1	22.00	44.90	30.00	6.00	PLA
10	Short retainer	1	4.00	10.90	9.10	1.00	PLA
11	Stem guide	1	33.00	13.40	16.20	3.00	PLA
12	Long retainer	2	9.00	10.90	9.10	2.00	PLA
13	Stem support	1	22.00	44.90	30.00	6.00	PLA
14	Stem	1	200.10	10.00	14.90	12.00	PLA
15	Tumor sphere (Tip)	1	29.20	30.00	30.00	8.00	PLA

All of these features makes Arduino perfect for this project, but, to connect the drivers to Arduino, which control the stepper motors, an Arduino-Shield was needed. The Reprap Arduino Mega Pololu Shield (RAMPS) is a board specially designed for the use of the selected drivers. This can control up to five stepper motors and support the connection of various endstops. The RAMPS board can only be used together with an Arduino Mega 2560 board on which it is placed by inserting the male connectors of the RAMPS into female Arduino pins.

2.4. *Manufacture and Material*

The entire project was thought to be printable in any commercial or Open-Source 3D printer. A Prusa i3 MK2 with a precision of 50 microns per layer height, and a printing surface of 10,500 cm³ (25 × 21 × 20 cm or 9.84 × 8.3 × 8 in) was used to print all of the parts. The entire prototype was manufactured with poly(lactic acid) (PLA) material. This material was chosen because it achieves the specifications that are need for the prototype [26]. It is light and strong enough to enable the mechanism to function smoothly. Furthermore, it is biodegradable and environmentally friendly.

3. Results

3.1. Prototype Design

During the design of the Lung Tumor Movement Simulator (LTMS) (Figure 3), several mechanical designs were studied and proposed; in the end, a design composed of two sliders was chosen.

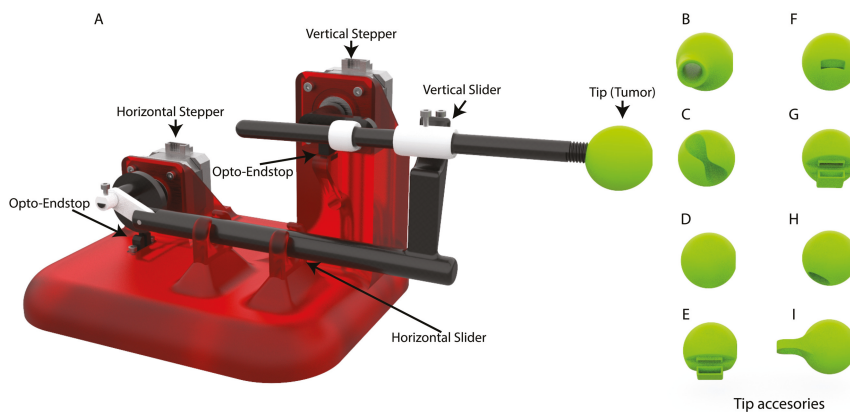


Figure 3. 3D model of the Lung Tumor Movement Simulator. Main design of the prototype A and eight tips model that were designed to give versatility to the model. Tips D–H were designed with the purpose of holding a nanoDot™ radiation dosimeter. Tips B, C and I were designed to hold a test tube with contrast fluids for other purposes.

This design is formed by two stepper motors, which move the mechanical elements (Figure 2) to achieve the desired movement. There is an upper motor, which controls the upwards and downwards motion of the Tip that simulates the tumor position. Then, there is a lower motor which controls the pushing forward and backward the Tip, which represents the targeted tumor. The entire prototype is composed of 15 different parts. Their dimensions and weights are shown in Table 1.

The biggest challenge during the design was how to achieve the synchronization of the two stepper motors in order to obtain an accurate path. This problem was overcome with the addition of two optical endstops. These endstops were placed underneath each stepper motor and a protuberance on each axis is what triggers the optic mechanism.

3.2. Movement and Path Simulation

To validate the prototype mechanism, it was necessary to evaluate the mobility of the whole system as shown in Figure 4. By using the feature of Movement Simulation from Unigraphics NX 11 (Siemens, Berlin, Germany), the Tip trajectory was simulated taking into account gravity, friction and speed limits.

During the virtual simulation, it was observed that the Tumor Movement Area, which is shown in Figure 4, was the expected area for the tumor movement cycle. Furthermore, the simulation was done with the same speed for the two stepper motors and one specific mechanical configuration; however, if the speed or the length of the mechanical transmission were modified, the height and width of the desired area would be modified.

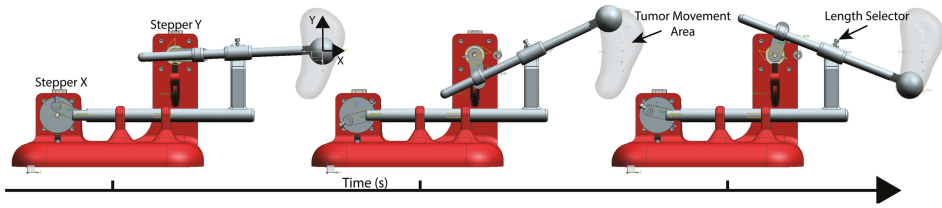


Figure 4. Virtual simulation of the desired area to cover with the LTMS in order to validate the viability of the system design.

3.3. Synchronizing the Movements

The rotation speed of the primary motor (Figure 5A), which is the operator of the horizontal movement, was fixed at a speed that depends on the respiratory frequency of the patient, so that a complete turn is made with the same duration as breathing is performed.

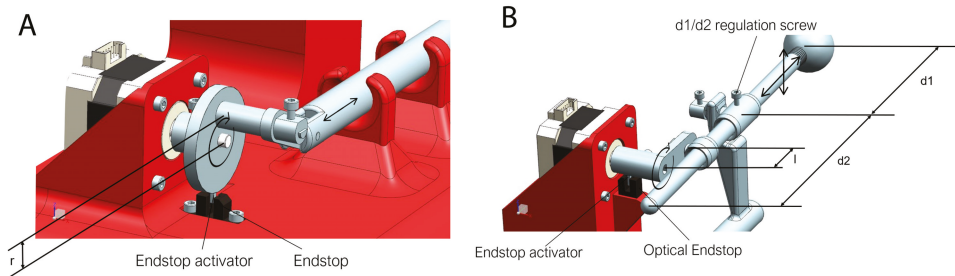


Figure 5. (A) Horizontal stepper motor; and (B) vertical stepper motor. See main text for details.

To reconstruct the hysteresis cycle, the second stepper motor (Figure 5B), which controls vertical displacement, continuously modifies the rotation speed throughout the cycle. This cycle is divided into six parts, which corresponds to a 60-degree turn of the motor. The average speed in the set of the six sections is equal to the other engine to achieve a synchronized movement and a complete turn in the same time. Therefore, the different speeds on this engine are time dependent.

The parametric variables that affects the Tip (simulated tumor) trajectory are shown in Figure 5. The simulated tumor trajectory can be adjusted in several ways:

- In width: The width can be modified by changing the distance “ r ”.
- In height: To change the height of the movement (amplitude), it is necessary only to release a little screw that is at the joint of the vertical slider (Figure 5B) and to move the rod forward or backward. This is represented by distances “ $d1$ ” and “ $d2$ ” (Equation (1)).
- In timing: In the serial console, the breathing time can be set to move at the same frequency as the patient does.

$$h = 2 \cdot \left(\frac{d1 \cdot l}{d2} \right) \quad (1)$$

As a result of changing the distances, the output path is defined by Equations (2) and (3). These equations describes the Tip trajectory during the inhalation and exhalation.

$$Y_{inhale} = \left(\left(\sqrt{\frac{h}{(2 \cdot r)^2}} \right) \cdot x \right)^2 \tag{2}$$

$$Y_{exhale} = \left(-(x - (2 \cdot r))^2 + (2 \cdot r)^2 \right) \cdot \sqrt{\frac{h}{(2 \cdot r)^2}} \tag{3}$$

3.4. Path Verification

To check the precision of the LTMS prototype, the movement was tracked (Figure 6A,B) by creating a tracking workflow with Bonsai software [27]. Bonsai is a visual programming language that allows a modular, high-performance, open-source visual programming framework for the acquisition and online processing of data streams. It permits real time data acquisition and processing among several interfaces.

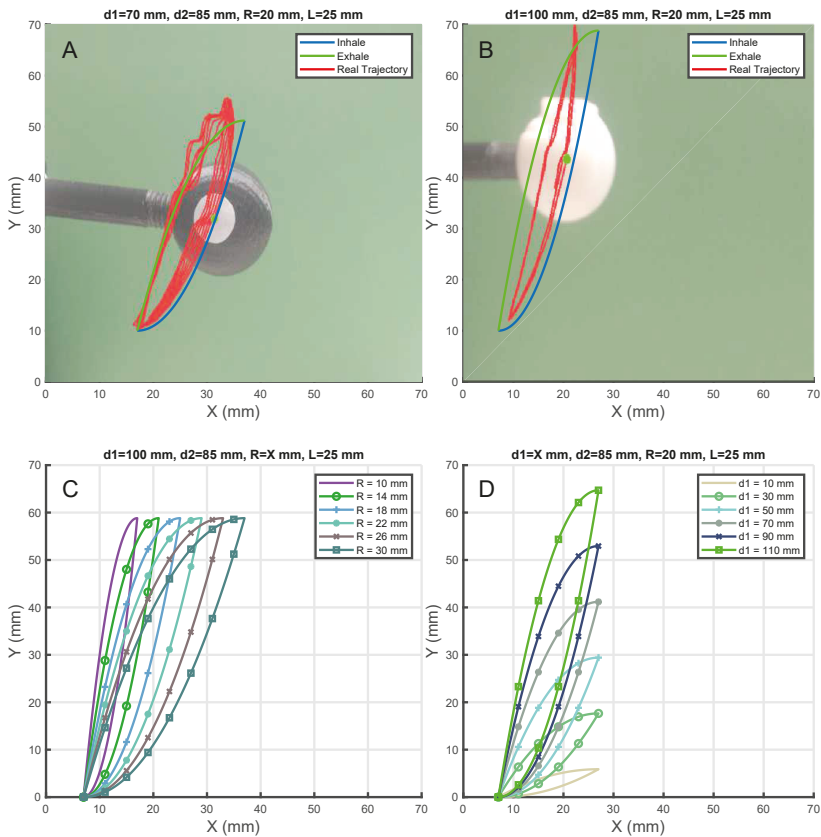


Figure 6. (A) Setup for a wider tumor trajectory is shown. (B) Setup for higher tumor trajectory is shown. (C) All possible trajectories by modifying the r parameter are displayed. (D) Possible trajectories by modifying $d1$ parameter are displayed.

A real-time data analysis was performed to constantly track the position in X and Y of the Tip, while the prototype is running the breathing cycle. In this Bonsai workflow, the camera input with the overlapped tracking were recorded, as well as the X and Y positions of the Tip plus a time-stamp.

This tracking is performed by transforming the acquired image from the camera to a Hue, Saturation, Value (HSV) image. A white sticker was attached to the Tip (sphere), which is shown in Figure 6A,B, and by means of establishing a HSV threshold it was possible to discriminate the sticker contours against the Tip (simulated tumor). Then, the largest binary region was found, which corresponded to the sticker, and the centroid of it was detected. These centroid coordinates correspond to the X and Y position of the simulated tumor.

The resulting curves of the prototype and program differ slightly from the desired hysteresis loop; even though the lower part matches well, the upper area deviates a maximum of 5 mm from the desired position, as shown in Figure 6A,B. Several tests were made with the system during 20 cycles. It deviates in the two first cycles until the synchronization process is done. After these two cycles the deviations were smaller than 1 mm in the higher setups and 4 mm in the wider setups. However, in future versions the above mentioned errors will be minimized by improving the mechanical design.

There are several combinations that could be set up with the prototype, and depending on which of the transmission components is used it is possible to achieve all of the combinations that are shown in Figure 6C,D.

The 3D Printed Lung Tumor Movement Simulator for radiotherapy quality assurance has been presented (Figure 7) to a group of expert radiation oncologists and medical physicists from the Instituto Valenciano de Oncología, Valencia, Spain.

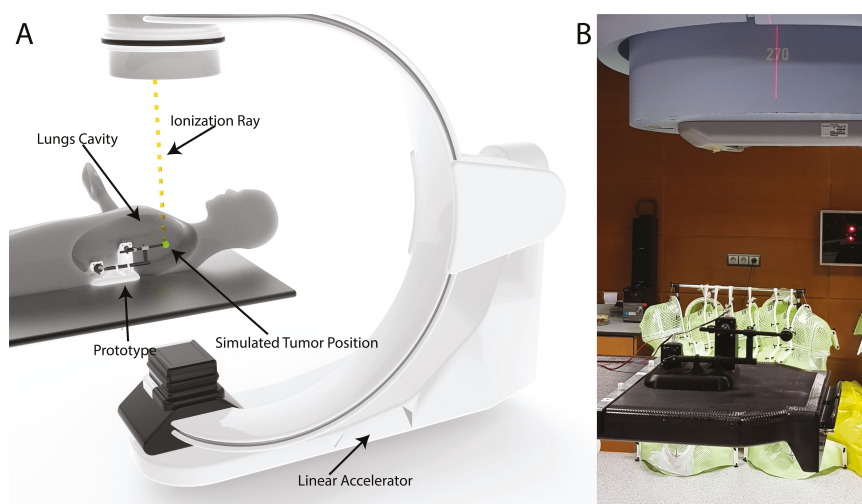


Figure 7. (A) Virtual reconstruction of the location where the prototype should be placed to simulate the tumor path is shown; and (B) the real Lung Tumor Movement Simulator placed inside a LINAC.

4. Discussion

In the radiotherapy field, movement of tumors due to the respiratory cycle makes treatment difficult and, for this reason, an area of research has focused on treatment planning [5,6,11]. There are devices that can be used to guarantee the quality and quantity of received radiation doses, which are commonly named phantoms. In this way, in the most complex cases, doctors and radiologists will perform a priori tests that ensure maximum precision before the treatment.

Although there are existing commercial devices such as QUASAR (Modus Medical Devices Inc., London, ON, Canada), Respiratory Gating Platform (Standard Imaging Inc., Middleton, WI, USA) and Dynamic Thorax Phantom (CIRS Inc., Norfolk, VA, USA), these alternatives are closed source and difficult to customize. The creation of this prototype based on 3D printing and Open-Source is intended to serve as a basis for the expansion of these devices for research purposes.

The Respiratory Motion Phantom from QUASAR is a commercial device developed by Modus QA, which, in its latest version, reproduces in two dimensions the respiratory movement of patients for use in radiotherapy [28]. It is useful for testing treatments, the correction of these tests and the commissioning of the implementation of new systems. However, this device is a licensed product that cannot be customized, and it is not accessible for researchers. The aim of this project is to pave the way for researchers to improve the treatment simulations in a cost-effective way. In addition, it facilitates the creation of parametric components, which allow the simulated tumor path to be changed. One of the strongest skills of this prototype is that all of the mechanisms are 3D printed and they can be modified as the researcher desires.

5. Conclusions

This project began with the idea of creating an Open-Source prototype that would follow the hysteresis loop of the movement of a human lung during a respiration cycle to track the movement of a tumor. We present an Open-Source Lung Tumor movement simulator, which is 3D printed for each patient and for each treatment. This prototype is completely customizable, and it paves the way for researchers, radiologists and nuclear medicine physicians to improve the radiation therapy for quality assurance procedures and outcomes.

This Lung Tumor Movement Simulator is programmable with the amplitude and frequency specific to each treatment and patient. These data are obtained thanks to the images obtained by techniques such as the 4D-CT and are translated through the serial interface that connects the computer and the hardware (drivers, motors, etc.). In the prototype, there is the possibility of introducing a dosimetric film or an ionization chamber to measure the dose of radiation absorbed. Furthermore, the Lung Tumor Movement simulator is cost-effective, because it is almost entirely 3D printed and the electronic components, as well as the motors, are not expensive.

The results of building and testing the new lung movement prototype are very promising. It has been shown that it is possible to create a simple and cost-effective machine to simulate the movement of a tumor in the lungs based on additive manufacturing. The prototype is ready to be tested and there are plans to undertake customized radiotherapy verification and research in a radiotherapy machine. In addition, all the schematics, parts and firmware are available at dmoratal.webs.upv.es/research.

Author Contributions: Conceptualization, D.R.Q., V.G.-P. and D.M.; Data curation, D.R.Q. and V.G.-P.; Formal analysis, D.R.Q., D.S.-E., V.G.-P., J.R., E.S.-M. and D.M.; Funding acquisition, J.A.G.-M. and D.M.; Investigation, D.R.Q., V.G.-P., J.A.G.-M. and D.M.; Methodology, D.R.Q., J.R., E.S.-M., R.P.-F. and J.A.G.-M.; Project administration, J.A.G.-M., V.C. and D.M.; Resources, V.G.-P., R.P.-F., J.A.G.-M., V.C. and D.M.; Software, D.R.Q., D.S.-E., J.R., E.S.-M. and R.P.-F.; Supervision, J.A.G.-M., V.C. and D.M.; Validation, D.R.Q., V.G.-P., R.P.-F. and D.M.; Visualization, D.R.Q., D.S.-E. and R.P.-F.; Writing—original draft, D.R.Q. and D.S.-E.; and Writing—review and editing, V.G.-P., R.P.-F., J.A.G.-M., V.C. and D.M.

Funding: This work was supported in part by the Spanish Ministerio de Economía y Competitividad (MINECO) and FEDER funds under grants BFU2015-64380-C2-2-R (D.M.). D.R.Q. was supported by grant “Ayudas para la formación de personal investigador (FPI)” from the Vicerrectorado de Investigación, Innovación y Transferencia of the Universitat Politècnica de València.

Conflicts of Interest: The authors declare no conflict of interest.

References

1. Fitzmaurice, C.; Dicker, D.; Pain, A. The Global Burden of Cancer 2013. *JAMA Oncol.* **2015**, *1*, 505–527, doi:10.1001/jamaoncol.2015.0735. [[CrossRef](#)] [[PubMed](#)]
2. Mountain, C.F. Revisions in the international system for staging lung cancer. *Chest* **1997**, *111*, 1710–1717. [[CrossRef](#)] [[PubMed](#)]
3. Miller, K.D.; Siegel, R.L.; Lin, C.C.; Mariotto, A.B.; Kramer, J.L.; Rowland, J.H.; Stein, K.D.; Alteri, R.; Jemal, A. Cancer treatment and survivorship statistics, 2016. *CA Cancer J. Clin.* **2016**, *66*, 271–289, doi:10.3322/caac.21349. [[CrossRef](#)] [[PubMed](#)]

4. Mayles, P.; Nahum, A. *Handbook of Radiotherapy Physics*; Taylor & Francis: London, UK, 2007; doi:10.1201/9781420012026.
5. Mageras, G.S.; Pevsner, A.; Yorke, E.D.; Rosenzweig, K.E.; Ford, E.C.; Hertanto, A.; Larson, S.M.; Lovelock, D.M.; Erdi, Y.E.; Nehmeh, S.A.; et al. Measurement of lung tumor motion using respiration-correlated CT. *Int. J. Radiat. Oncol. Biol. Phys.* **2004**, *60*, 933–941, doi:10.1016/j.ijrobp.2004.06.021. [[CrossRef](#)] [[PubMed](#)]
6. Borm, K.J.; Oechsner, M.; Wilkens, J.J.; Berndt, J.; Molls, M.; Geinitz, H.; Duma, M.N. The impact of CT window settings on the contouring of a moving target: A phantom study. *Clin. Radiol.* **2014**, *69*, e331–e336, doi:10.1016/j.crad.2014.03.006. [[CrossRef](#)] [[PubMed](#)]
7. Guyton, A.C.; Hall, J.E.; John, E.; Fernández Bernaldo de Quirós, I.; Agud Aparicio, J.L.; Alvarez Baleriola, I. *Guyton & Hall: Tratado de Fisiología Médica*, 12th ed.; Elsevier España S.A.: Madrid, Spain, 2011; p. 1112.
8. Guidi, G.; Maffei, N.; Ciarmatori, A.; Mistretta, M.G.; Gottardi, G.; Costi, T.; Vecchi, C.; Baldazzi, G. Real-time lung tumour motion modeling for adaptive radiation therapy using lego mindstorms. *J. Mech. Med. Biol.* **2015**, *15*, 1540019. [[CrossRef](#)]
9. Seppenwoolde, Y.; Shirato, H.; Kitamura, K.; Shimizu, S.; van Herk, M.; Lebesque, J.V.; Miyasaka, K. Precise and real-time measurement of 3D tumor motion in lung due to breathing and heartbeat, measured during radiotherapy. *Int. J. Radiat. Oncol. Biol. Phys.* **2002**, *53*, 822–834, doi:10.1016/S0360-3016(02)02803-1. [[CrossRef](#)]
10. Harris, R.S. Pressure-volume curves of the respiratory system. *Respir. Care* **2005**, *50*, 78–99. [[PubMed](#)]
11. Aznar, M.C.; Persson, G.F.; Kofoed, I.M.; Nygaard, D.E.; Korreman, S.S. Irregular breathing during 4DCT scanning of lung cancer patients: Is the midventilation approach robust? *Phys. Med.* **2014**, *30*, 69–75, doi:10.1016/j.ejmp.2013.03.003. [[CrossRef](#)] [[PubMed](#)]
12. Sarudis, S.; Karlsson Hauer, A.; Nyman, J.; Bäck, A. Systematic evaluation of lung tumor motion using four-dimensional computed tomography. *Acta Oncol.* **2017**, *56*, 525–530, doi:10.1080/0284186X.2016.1274049. [[CrossRef](#)] [[PubMed](#)]
13. Wang, Y.; Bao, Y.; Zhang, L.; Fan, W.; He, H.; Sun, Z.W.; Hu, X.; Huang, S.M.; Chen, M.; Deng, X.W. Assessment of respiration-induced motion and its impact on treatment outcome for lung cancer. *BioMed Res. Int.* **2013**, *2013*, 872739, doi:10.1155/2013/872739. [[CrossRef](#)] [[PubMed](#)]
14. Shimizu, S.; Shirato, H.; Ogura, S.; Akita-Dosaka, H.; Kitamura, K.; Nishioka, T.; Kagei, K.; Nishimura, M.; Miyasaka, K. Detection of lung tumor movement in real-time tumor-tracking radiotherapy. *Int. J. Radiat. Oncol. Biol. Phys.* **2001**, *51*, 304–310, doi:10.1016/S0360-3016(01)01641-8. [[CrossRef](#)]
15. Redmond, K.J.; Song, D.Y.; Fox, J.L.; Zhou, J.; Rosenzweig, C.N.; Ford, E. Respiratory Motion Changes of Lung Tumors Over the Course of Radiation Therapy Based on Respiration-Correlated Four-Dimensional Computed Tomography Scans. *Int. J. Radiat. Oncol. Biol. Phys.* **2009**, *75*, 1605–1612, doi:10.1016/j.ijrobp.2009.05.024. [[CrossRef](#)] [[PubMed](#)]
16. Harada, K.; Katoh, N.; Suzuki, R.; Ito, Y.M.; Shimizu, S.; Onimaru, R.; Inoue, T.; Miyamoto, N.; Shirato, H. Evaluation of the motion of lung tumors during stereotactic body radiation therapy (SBRT) with four-dimensional computed tomography (4DCT) using real-time tumor-tracking radiotherapy system (TRT). *Phys. Med.* **2016**, *32*, 305–311, doi:10.1016/j.ejmp.2015.10.093. [[CrossRef](#)] [[PubMed](#)]
17. Knybel, L.; Cvek, J.; Molenda, L.; Stieberova, N.; Feltl, D. Analysis of Lung Tumor Motion in a Large Sample: Patterns and Factors Influencing Precise Delineation of Internal Target Volume. *Int. J. Radiat. Oncol. Biol. Phys.* **2016**, *96*, 751–758, doi:10.1016/j.ijrobp.2016.08.008. [[CrossRef](#)] [[PubMed](#)]
18. Fassi, A.; Schaerer, J.; Fernandes, M.; Riboldi, M.; Sarrut, D.; Baroni, G. Tumor Tracking Method Based on a Deformable 4D CT Breathing Motion Model Driven by an External Surface Surrogate. *Int. J. Radiat. Oncol. Biol. Phys.* **2014**, *88*, 182–188, doi:10.1016/j.ijrobp.2013.09.026. [[CrossRef](#)] [[PubMed](#)]
19. Ruben, J.; Seeley, A.; Panettieri, V.; Ackerly, T. Variation in Lung Tumour Breathing Motion between Planning Four-dimensional Computed Tomography and Stereotactic Ablative Radiotherapy Delivery and its Dosimetric Implications: Any Role for Four-dimensional Set-up Verification? *Clin. Oncol.* **2016**, *28*, 21–27, doi:10.1016/j.clon.2015.08.010. [[CrossRef](#)] [[PubMed](#)]
20. Wangler, T.P. *RF Linear Accelerators*; Wiley-VCH Verlag GmbH & Co. KGaA: Weinheim, Germany, 2008; p. 450, doi:10.1002/9783527623426.
21. D’Ausilio, A. Arduino: A low-cost multipurpose lab equipment. *Behav. Res. Methods* **2012**, *44*, 305–313, doi:10.3758/s13428-011-0163-z. [[CrossRef](#)] [[PubMed](#)]

22. Teikari, P.; Najjar, R.P.; Malkki, H.; Knoblauch, K.; Dumortier, D.; Gronfier, C.; Cooper, H.M. An inexpensive Arduino-based LED stimulator system for vision research. *J. Neurosci. Methods* **2012**, *211*, 227–236, doi:10.1016/j.jneumeth.2012.09.012. [[CrossRef](#)] [[PubMed](#)]
23. Besson, T.; Debayle, D.; Diochot, S.; Salinas, M.; Lingueglia, E. Low cost venom extractor based on Arduino board for electrical venom extraction from arthropods and other small animals. *Toxicon* **2016**, *118*, 156–161, doi:10.1016/j.toxicon.2016.05.001. [[CrossRef](#)] [[PubMed](#)]
24. Sheinin, A.; Lavi, A.; Michaelevski, I. StimDuino: An Arduino-based electrophysiological stimulus isolator. *J. Neurosci. Methods* **2015**, *243*, 8–17, doi:10.1016/j.jneumeth.2015.01.016. [[CrossRef](#)] [[PubMed](#)]
25. Ali, A.S.; Zanzinger, Z.; Debose, D.; Stephens, B. Open Source Building Science Sensors (OSBSS): A low-cost Arduino-based platform for long-term indoor environmental data collection. *Build. Environ.* **2016**, *100*, 114–126, doi:10.1016/j.buildenv.2016.02.010. [[CrossRef](#)]
26. Mathew, A.P.; Oksman, K.; Sain, M. Mechanical properties of biodegradable composites from poly lactic acid (PLA) and microcrystalline cellulose (MCC). *J. Appl. Polym. Sci.* **2005**, *97*, 2014–2025, doi:10.1002/app.21779. [[CrossRef](#)]
27. Lopes, G.; Bonacchi, N.; Frazão, J.; Neto, J.P.; Atallah, B.V.; Soares, S.; Moreira, L.; Matias, S.; Itskov, P.M.; Correia, P.A.; et al. Bonsai: An event-based framework for processing and controlling data streams. *Front. Neuroinform.* **2015**, *9*, 7, doi:10.3389/fninf.2015.00007. [[CrossRef](#)] [[PubMed](#)]
28. Dunn, L.; Kron, T.; Johnston, P.N.; McDermott, L.N.; Taylor, M.L.; Callahan, J.; Franich, R.D. A programmable motion phantom for quality assurance of motion management in radiotherapy. *Australas. Phys. Eng. Sci. Med.* **2012**, *35*, 93–100, doi:10.1007/s13246-011-0114-0. [[CrossRef](#)] [[PubMed](#)]



© 2018 by the authors. Licensee MDPI, Basel, Switzerland. This article is an open access article distributed under the terms and conditions of the Creative Commons Attribution (CC BY) license (<http://creativecommons.org/licenses/by/4.0/>).

Article

Influence of PLA Filament Conditions on Characteristics of FDM Parts

Ana Pilar Valerga ^{1,*}, Moisés Batista ¹, Jorge Salguero ¹ and Frank Girot ^{2,3}

¹ Department of Mechanical Engineering and Industrial Design, Faculty of Engineering, University of Cadiz, Avenida de la Universidad de Cadiz, 10, Puerto Real, E-11519 Cadiz, Spain; moises.batista@uca.es (M.B.); jorge.salguero@uca.es (J.S.)

² IKERBASQUE, Basque Foundation for Science, 48013 Bilbao, Spain; frank.girot@ehu.eus

³ Faculty of Engineering, University of the Basque Country, Alameda de Urquijo s/n, 48013 Bilbao, Spain

* Correspondence: anapilar.valerga@uca.es; Tel.: +34-956-483-200

Received: 30 June 2018; Accepted: 28 July 2018; Published: 31 July 2018

Abstract: Additive manufacturing technologies play an important role in Industry 4.0. One of the most prevalent processes is fused deposition modelling (FDM) due to its versatility and low cost. However, there is still a lack of standardization of materials and procedures within this technology. This work aims to study the relationship of certain operating parameters and the conditions of poly(lactic acid) (PLA) polymer with the results of the manufactured parts in dimensional terms, surface quality, and mechanical strength. In this way, the impact of some material characteristics is analyzed, such as the pigmentation of the material and the environmental humidity where it has been stored. The manufacturing parameter that relates to these properties has been the extrusion temperature since it is the most influential in this technology. The results are quite affected especially by humidity, being a parameter little studied in the literature.

Keywords: FDM; additive manufacturing; PLA; material color; pigmentation; extrusion temperature; humidity

1. Introduction

Additive manufacturing (AM) has gained increasing acceptance because of issues such as flexibility and design benefits for high value added products. Though these benefits depend on a level of quality regarding material, geometry, and surface finish where significant challenges still remain [1]. However, these technologies already allow the manufacture of a wide range of prototypes as well as functional components with complex and customized geometries, being able to obtain products assembled in a single step and lighten weights through a topology optimization process [2].

Additive manufacturing is at the heart of strategic discussions by the European Factories of the Future Research Association (EFFRA) because of its capabilities in personalized parts, high manufacturing flexibility, and resource efficiency [3].

For this reason, development of this type of technology has experienced a great increase since it was introduced in the market, leading to a set of manufacturing process families that are alternative to subtractive manufacturing or formative manufacturing. However, the need to convert the model into Standard Triangle Language or STL format (mesh of triangles) and the subsequent slicing to obtain the G-code, simplifies the geometry losing resolution in most cases, especially for circular or small parts. This causes improbable geometric deviations, as well as a characteristic roughness associated with layer stacking. Additionally, there is still a lack of information, communication, standardization, and consequent development of these processes [4–6].

One of the most widespread processes, due to its versatility and low cost, is fused deposition modelling (FDM) [7,8]. Fused deposition modelling grows almost 20% in profit each year in industries

such as automotive or aeronautics [9]. This method generally uses thermoplastic polymers. Despite being one of the most used AM processes, it is not completely industrialized yet. This is due to the large number of parameters that govern the process, as well as the lack of standardization, studies, and communication [9].

Fused deposition modelling is a process that selectively dispenses a thermoplastic polymer through a nozzle. There are specific challenges for this and other additive manufacturing processes, among which are the lack of standardization adapted to each technology and surface quality. In addition, the European Union wants to allow only the consumption of recyclable plastics and eliminate residues of this type of material. For this reason, poly(lactic acid) (PLA) can replace other more used materials, like acrylonitrile butadiene styrene (ABS). Poly(lactic acid) is a natural polymer, derived from renewable sources such as starch, a large carbohydrate that plants synthesize during photosynthesis.

Poly(lactic acid) has played a central role in the replacement of fossil-based polymers for certain applications by being a completely aliphatic polymer.

Furthermore, PLA is a more printable material and has mechanical properties significantly higher than most other plastics except some kinds of polycarbonate, nylon, and composite blends [10,11]. However, this plastic is little studied in relation to the FDM process, despite its great potential because it is renewable, compostable, and biocompatible [12–14].

Even though, there are studies that indicate that the working temperature is one of the most important parameters to obtain good quality and accuracy of the PLA parts, by way of other materials [2,15]. Another characteristic barely evaluated is the influence of different pigmentations, whose properties established by the manufacturer are the same regardless of color. This characteristic influences some aspects of the parts according to previous investigations [16].

Likewise, this material is sensitive to humidity, so that environmental conditions may be important in PLA manufacturing. This means that the place where PLA is manufactured has a significant impact on the results, unless the methods are standardized.

Given the importance of the lack of standardization and the influence of the parameters of the material, this paper aims to study some of the final characteristics of the parts obtained with FDM. PLA is used, a biostable material, to take into account the environmental component. In addition, it seeks to increase the component of sustainability without using adhesives for the printing platform, as well as reducing the cost of energy without using heating on the platform. Therefore, the object of this work is the study of the relation of certain studied parameters and environmental non studied parameters with the final quality of the manufactured parts. In this way, the behavior of PLA is analyzed when strategic aspects, such as the environmental humidity of the place where it is stored, the working temperature, and the pigmentation of the material have been modified.

2. Materials and Methods

A methodology for studying some manufacturing features is proposed relying on two different tests in order to obtain results that diminish the defects or improve the final characteristics of the manufactured parts by FDM.

These two tests have two types of test pieces: hexahedral specimens (30 mm cube) and monolayer specimens. Each trial follows a process divided into three stages, as shown in Figure 1. Hexahedral samples were created in order to measure dimensional deviations more easily and reliably, while monolayers were manufactured for mechanical tests.

On the one hand, hexahedral samples' infill was 100% rectilinear, 0° raster orientation, with 3 top and bottom layers.

On the other hand, S-H. Anh et al. [17] have analyzed different possible trajectories for the manufacture of monolayer specimens. Other more recent authors as C. Wendt et al. [6] determined a specific geometry for monolayer samples' dimensions and trajectories suitable for conducting studies with tensile tests. These dimensions and trajectories are reflected in Figure 2.

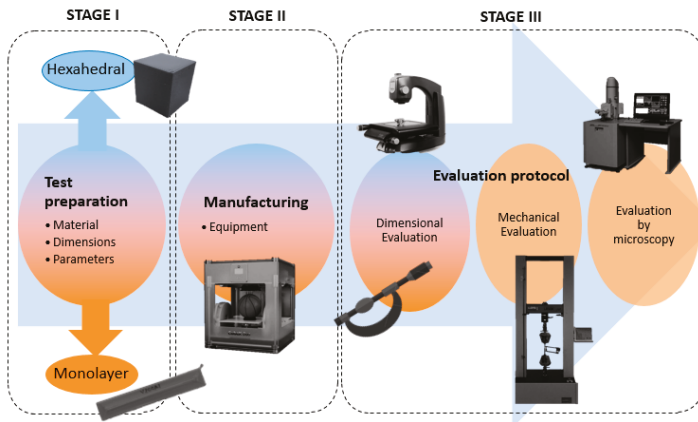


Figure 1. Flow chart of the experimental Procedure.

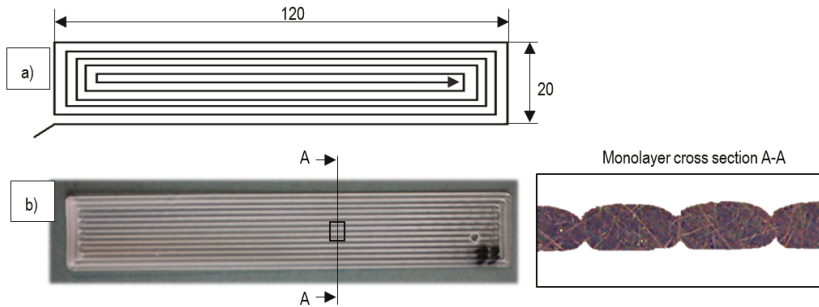


Figure 2. (a) Dimensions and trajectories used for monolayer samples [6]; (b) monolayer cross-sectional mesostructure.

Poly (lactic acid), from the same manufacturer BQ, has been used to manufacture the specimens. This material, has properties poorly defined by the manufacturer, Table 1. Specifications include only a few specific ranges. In addition, the manufacturer gives the same characteristics regardless of the selected color, and in this case, nothing is recommended about material storage. However, more adjusted ranges about the characteristics of this material have been obtained in previous studies. Nevertheless, the literature consulted shows different values depending on the manufacturer of the material, and its pigmentation is usually not referred to.

Table 1. Characteristics of the poly(lactic acid) (PLA) according to the manufacturer.

Property	Value
Tensile Strength	16–114 MPa
Elongation at Break	0.5–430%
Modulus of Elasticity	0.230–13.8 GPa
Melting Point	120–170 °C
Working Temperature	180–200 °C
Softening Point	45–120 °C

CubeX[®] Duo was used to manufacture all the samples, highlighting 0.25 mm layer thickness, 30 mm/s feed rate, and an acceleration of 1500 mm/s² as constant parameters. A 1.75 mm filament

diameter was printed with a 0.5 mm nozzle size. In addition, 0.5 mm of retraction at 15 mm/s speed was used after ending a path. The print speed was low because no adhesives or heated platform were used. These conditions were also chosen on the basis of previous studies [18]. The study variables of this work are reflected in the Table 2. The Gcode was obtained with the software KISSlicer (1.6.3 version, Trimaker, Buenos Aires, Argentina).

Table 2. Variables used in the manufacturing of hexahedron and monolayer samples.

Property	Extrusion Temperature (°C)	Relative Humidity (%)	Pigmentation
Hexahedral	180, 190, 200, 220, 240 °C	-	Pink, Green, Grey, Transparent
Monolayer	200, 220, 240 °C	16, 50, 98%	Pink, Green, Grey, Transparent

The pigmentation of the filament is an influential factor. For this reason, four different colors (pink, grey, green-transparent, and transparent) have been selected in order to determine if this pigmentation modifies the final properties of the parts. Cubes were manufactured in a temperature range between 180 and 240 °C, but for the monolayer specimens, it was between 200 and 240 °C, due to their difficulty of adhesion to the build platform, owing to the non-use of adhesives and a larger fixing surface than in manufacturing of the cubes (warping).

In relation to the cubic samples, the influence of this pigmentation and the extrusion temperature in the dimensional tolerances and surface quality of the parts were studied. The hexahedral geometry was chosen, since it has all its edges and faces equal, leaving the specimen with a single nominal dimension, which facilitates its analysis.

In order to study the influence of the relative humidity on the results of the monolayer samples, three extreme relative humidity values were used: dry, which corresponds with a relative humidity of 16%; environmental humidity, which corresponds with a relative humidity of 50%; and humid environment, which corresponds with a relative humidity of 98%. This humidity control was achieved by ARL-0680 ESPEC climatic chamber (ESPEC, Osaka, Japan). The temperature of the chamber remained constant at 25 °C. The material was stored in the climate chamber under the conditions defined during a week prior to the manufacturing. Additionally, cubes were manufactured only with material which was stocked in environmental humidity.

Both types of test specimens were subjected to a dimensional evaluation, as well as to an evaluation of the surface quality in terms of roughness average (Ra). The dimensional study was done in terms of deviations from the nominal value (Δd) of each of the main dimensions, where:

$$\Delta d = \bar{X}(\Delta x + \Delta y + \Delta z) \quad (1)$$

The difference between the two tests is that for the hexahedral specimens, the evaluation procedure collected data that was later analyzed.

Additionally, deposited cross-sections of filaments extruded at different temperatures were analyzed to establish the correlation between dimensional deviation and working temperature.

Conversely, the dimensional evaluation of the monolayer specimens serves as the basis for the evaluation of the mechanical properties of the material. These dimensional deviations were characterized using Optical Measures 3D Techniques, concretely Tesa Visio 300 (Tesa SE, Norderstedt, Germany) was used. Also, a contact profilometer, Mahr Perthometer PGK 120 (Mahr GmbH, Göttingen, Germany), was used for microgeometric characterization.

The universal testing machine Shimadzu® AG-X (Shimadzu, Kyoto, Japan) was used for mechanical tests. These tensile tests were executed with a continuous testing velocity of 1 mm/s as recommended in standardization for molding and extrusion plastics [19]. These tests were carried out under conditions of temperature and humidity similar to those of service parts (25 °C and 50%).

Finally, all of the specimens were analyzed before and after the mechanical tests mentioned, to assess by means of stereoscopic optical microscopy (SOM) and scanning electron microscopy (SEM)

and support the study of the fracture type that appears in these samples according to their characteristic pigmentations and storage conditions. The equipment used for the application of SOM was Nikon® SMZ800 (Nikon, Chiyoda, Japan), and the EDAX EDS System (Mahwah, NJ, USA) was the equipment used for SEM.

3. Results and Discussion

The low homogeneity of the material was verified due to the uncontrolled and arbitrary appearance of the defects typical of this technology. Dissimilar results have been obtained for the same material, under the same starting conditions and with the same path and parameters, which means a low repeatability of the process. This low repetitiveness is associated with the appearance of defects related to the FDM process. Some of them occur frequently and their type and severity are varied. The most outstanding defects analyzed by other authors are: bubbles, cracks, warping, contamination, discolorations, and incorrect binding [6,7].

In spite of this, these can be rectified by modifying some manufacturing parameters. The most complex to solve is the low compaction due to air occlusion (bubbles) or insufficient overlap between filaments that cause cavities.

The appearance of the bubbles will condition the results of both surface quality and tensile strength. The manifestation of this defect, which at lower temperatures is almost non-existent, is due to the fact that at high temperatures the material reaches the extruder nozzle practically liquid. According to other authors, this is due to the fact that at higher temperatures the viscosity decreases [6,7,16]. The PLA, by the time it slides through the nozzle, produces friction with the walls which in turn generates turbulence contributing to the air intake. This results in more bubbles, and therefore in a greater dimensional deviation (Δd), roughness (R_a) and a lower tensile strength.

Moreover, by modifying only the extrusion temperature, the deposited section changes not only the dimensions of the specimen but also causes air bubbles between layers. The dimensional values in height (h) and width (l) of extruded filaments deposited at different temperatures are shown in Figure 3. The total Δd can be related to the deviations observed in the section of the filament, since in the final length of the deposited filament (3rd dimension), minor deviations related to the kinematics of the machine have been observed exclusively.

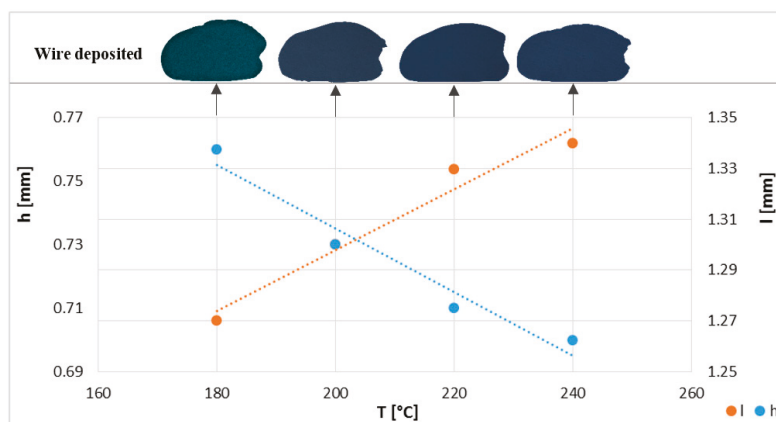


Figure 3. Wire cross-section dimensions of fused deposition modelling (FDM) filament extruded and deposited at different temperatures.

The dimensional determination of the hexahedral specimens was carried out. Figure 4 shows the dimensional deviations (Δd) of the hexahedrons. In both, as the extrusion temperature (T) increases,

the pieces also increase in XY dimensions, moving away from the nominal size of 30 mm. On the contrary, the height in the cubes tends to decrease as the manufacturing temperature increases. This is because at higher temperatures the material becomes more fluid, and therefore expands freely by decreasing the measurement on the z-axis.

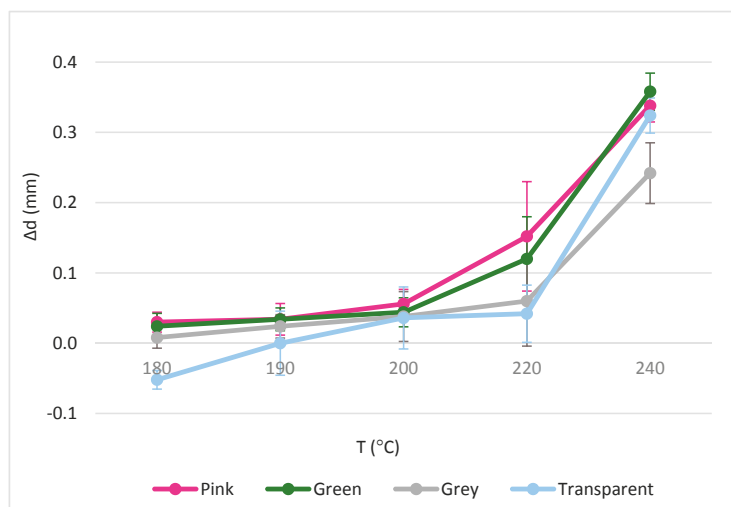


Figure 4. Dimensional deviations in relation to the used temperatures and pigments.

The different pigments follow the same trend. Even so, some of them differ from the nominal dimension more than others, even having conformed to the same temperature. This proves that the pigmentation has a direct relation with the properties of the parts. Curiously, the lightest colors among those studied, transparent and grey, were kept closer to the nominal measurement than the more intense colors. This preliminary study of the pigments coincides with Aydemir et al. [16].

Moreover, the dimensional deviations were affected by the temperature. Normally, positive deviations are obtained in xy and which increase when the temperature rises, while the layer height decreases, and therefore the height of the complete solid. According to other authors, the material is more fluid and can expand freely in the xy plane [18].

Other material whose pigmentation also lets the light pass is the green test sample. However, this sample behaves very differently than the transparent specimen, so it can be deduced that the green pigment has a very unequal influence on the material even though it has given them the property of being translucent. Surely, if the translucent green material is compared with its opaque counterpart, it would be seen that translucent green behaves much better against dimensional tolerances than opaque [16]. But if compared to other materials with other pigments, whether opaque, translucent or transparent, this color produces parts of worse dimensional quality.

This agrees with other authors who assert that the wettability or the ability to adhere and spread on the surface of a solid is more pronounced in materials with translucent or transparent pigmentation [16]. This favors that the translucent materials stay closer to the nominal measures, because of their ability to adhere to the already solidified layers, reducing the appearance of imperfections. The latter reaffirms the need to standardize each material to be used industrially to avoid that something that is marketed as a material are actually different materials with wide range of properties.

With all this, the dimensional deviations always have little dispersion which are easily solved by redesigning the specimens by establishing a mathematical relationship of the results, or by undergoing

a finishing process. However, the mechanical properties do not provide themselves equally to such an advantage.

Nevertheless, surface quality is a major constraint in this manufacturing process [5]. The temperature in the range recommended by the manufacturer apparently does not affect the mechanical properties. Conversely, some pigments can be used in a wider temperature range, as shown in Figure 5. Transparent PLA is usually the material with the lowest value of roughness related to other materials. This is because its viscosity is much greater, adapting the conditions to the formation of a smoother and homogeneous surface, which, according to other authors [16], is caused by its lack of pigment.

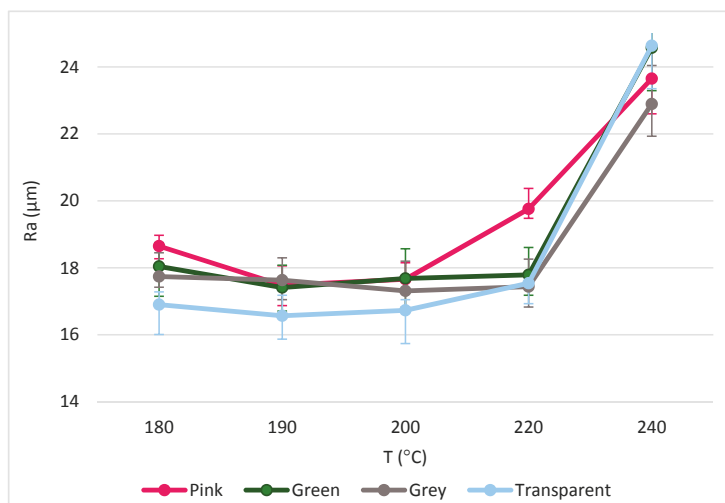


Figure 5. Evolution of roughness average (Ra) as a function of temperature and different pigments.

Even so, the obtained values of roughness are too high for the vast majority of applications, so that, for implantation in some industries, it would be necessary to use post-processing processes that improve this characteristic of the parts.



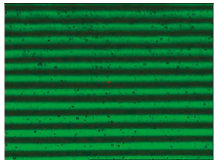
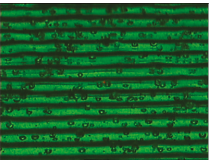

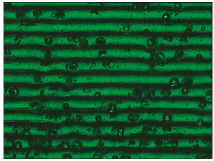
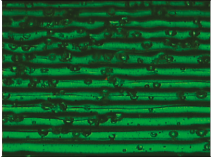
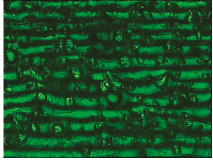
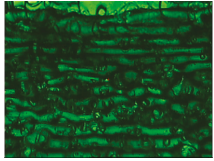
The accumulation of defects favored the propagation of cracks in the mechanical tests. It also prevented the test pieces from reaching their elastic limit. This accumulation of defects, mainly bubbles, was aggravated by a higher relative humidity of the environment where the material was stored. Table 3 shows that the storage conditions of the material are even more important than temperature or pigmentation, and it is not often a subject of study [7].

Furthermore, there were some intervals of stresses and deformations of the PLA, regardless of what were their initial conditions, considering between 350 and 900 N the maximum force that it can withstand and between 1 and 4 mm its maximum elongation for all the tests.

Accordingly, the stress–strain curves of the specimens behaved in very similar way. The plastic zone was practically negligible, and the reason why a fragile breakage was predicted. However, since the beginning of the test, small premature fissures occurred throughout the whole piece that made the process irreversible.

In addition, some samples had not been adjusted correctly to the jaws. These measures were rejected in data analyses and corroborated the need to standardize or improve the current standard of the tensile test analysis process for this particular manufacturing process.

Table 3. Influence of storage conditions and operating temperature on the surface finish.

	200 °C	220 °C	240 °C
16%			
50%			
98%			

In relation to the crack of the samples, this occurred abruptly without strain hardening, indicating that the failure was probably due to the discontinuity in the material and not because it exceeded its limit.

Furthermore, comparing the data obtained by families of specimens (Figure 6), it can be seen that specimens whose material was stored in an atmosphere with low relative humidity resisted higher tensile forces. The equations that define the four regression planes corresponding to the tensile strength (T_{max}) as a function of the used interval of humidity (H) and temperature (T) coincide with (2–5), (2-grey, 3-pink, 4-transparent, 5-green).

$$T_{max}(T, H) = 3.191 + 0.188x - 0.048y \quad (2)$$

$$T_{max}(T, H) = 3.098 + 0.187x - 0.011y \quad (3)$$

$$T_{max}(T, H) = 3.196 + 0.181x - 0.048y \quad (4)$$

$$T_{max}(T, H) = 3.603 + 0.185x - 0.171y \quad (5)$$

In addition, lower temperature usually created stronger specimens, even if the initial conditions of the material were varied. This is the opposite of what happens with geometric deviations.

If the pigment was prioritized on the mechanical properties of the specimens, it should be noted that those more translucent colors, such as green and transparent, resisted less tensile strength than those characterized by their brightness and opacity.

As in the dimensional and surface quality evaluation, the pigment that gave the worst mechanical properties to the PLA was green again. It is obvious that the pigment seriously modifies the properties of the polymer, making it unsuitable for some applications. However, this should be further explored.

It can be seen that the relative humidity was the most relevant variable studied. This feature is almost never studied in the literature [19]. Specimens whose material was stored in an atmosphere with low relative humidity resisted higher tensile forces. This was due to the degradation that the material undergoes by the action of water. Also, the high temperatures in the nozzle caused water

boiling and this transforms into part bubbles. The accumulation of bubbles favored the propagation of cracks in the mechanical tests.

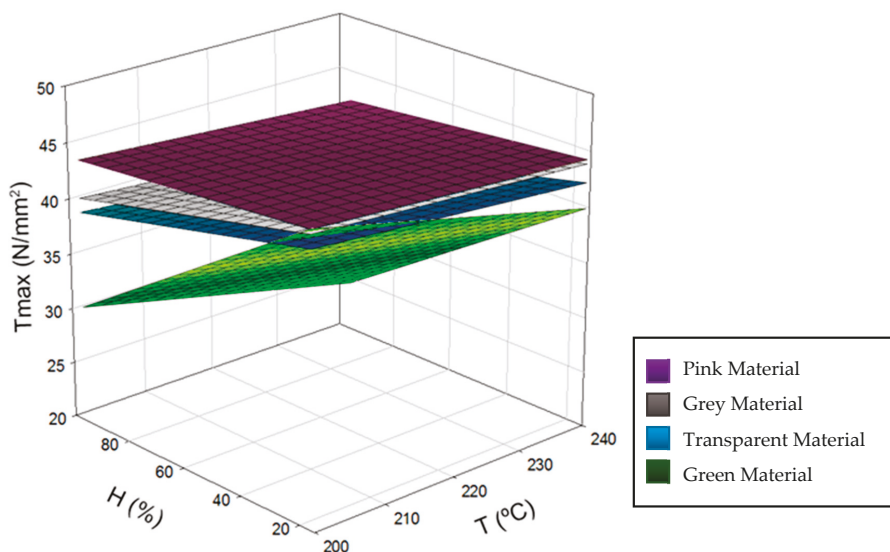


Figure 6. Plot of tensile strength (T_{max}) trends as function of variable temperature (T) and relative humidity (H).

Furthermore, if the elongation of the samples was analyzed, it was observed that the samples made with dry material had less elongation than environmental ones, as shown in Table 4. This resulted in less tenacity or in a more fragile fracture as seen in Table 5.

However, although the transparent color was one of the least resistant, its elongation was greater for the same increase in charge. Thus the absence of pigment returns to the PLA more plastic and malleable, making it able to modify its molecular structure to relieve the internal tensions.

Table 4. Elongation of the samples according to their storage conditions.

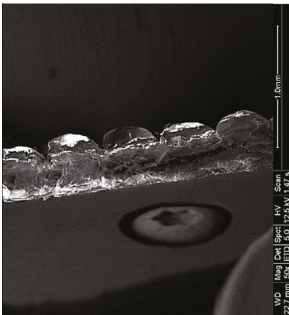

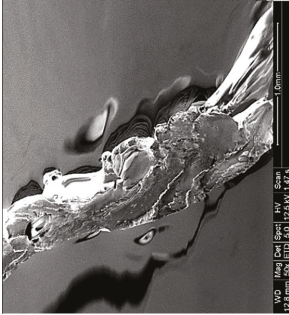



	16%	50%	98%
Transparent	2.215	3.295	2.015
Pink	2.312	2.478	2.186
Grey	2.417	2.588	1.972
Green	2.417	2.200	1.760

On the other hand, the specimens that were in the dry state, had a very similar value independently of the color and the temperature. In this way, to store the PLA correctly in a cold and dry environment to preserve its mechanical resistance, instead makes it more fragile.

In general, PLA fractures are fragile, an assertion that was true for all specimens tested. However, the breakage varied considerably according to the conditions of the material.

Different sections of specimens made at 220 °C can be seen in Table 5. Although they were manufactured with different initial conditions in the material, it can be seen the discontinuities produced by the degradation of the material or by the appearance of defects linked to humidity.

Table 5. SEM section of monolayer specimens subjected to tensile tests.

16%	50%	98%
		
		

Material separation, which normally implies severing bonds on the atomic level, is called chain scission. A factor that aids chain scission in PLA is that molecules are not stressed uniformly, because it is an amorphous polymer.

The specimens formed with a material preserved in atmosphere with low relative humidity break through several zones at the same time, so that most of the specimens explode when subjected to the tensile test. This was because the characteristic bubbles were almost non-existent, but the ones that appeared were located in very specific areas, so that the cracks began at the same time in very distributed points. This was due to certain chain segments carrying a disproportionate amount of load when stress was applied, which can be sufficient to exceed the bond strength. The fractures followed a practically straight line, making a clean fracture without detaching small fragments of PLA.

On the other hand, the specimens made with the material stored under environmental conditions, usually broke by a single place, characterized by an uneven fracture. This was because the fissure was propagated by the defects that the material had spread throughout its entire section. Contrary to what happens in dry specimens, small chips of material were released all over the contour of the fracture.

Finally, the specimens made with the material preserved in an atmosphere with high relative humidity had a fracture very similar to the environmental specimens, but this crack was much more pronounced. Therefore, the bubbles had a larger size and they were many more per unit area. In addition, in this case, the crack was no longer always performed by a single place, but several may have appeared along the length of the specimen.

It seems that the oxygen of the water, far from disappearing with increasing temperature of the material, remained in its microstructure causing serious defects that would preclude its use in most industries. In this case, it seems that fracture occurred by chain disentanglement, where molecules separated from one another intact. By increasing the amount of bubbles and subjecting the sample to traction, this defect lengthens until reaching the next closest. This causes that in the breakage there is no distinction between the filaments. In addition, flow lines were observed for the more ductile rupture than in the other cases.

Once again, it is clear the influence of humidity in PLA and the importance of good stocking prior to its manufacture, independently of the parameters chosen for it.

4. Conclusions

Additive manufacturing technologies are a new step in the technological revolution towards a 4.0 industry that generates associated services with high added value. This means that there is a need for improvement of these technologies in order to be able to implement them widely in the industry.

One of the necessary steps is the standardization and improvement of the existing regulations as far as materials, processes, and evaluations are concerned. To this end, a methodology was developed to carry out the study of certain characteristics of the material in the results of manufactured parts using FDM technology.

The constant demand for material in this manufacturing process has led to the increase of filament manufacturers, as well as their pigmentation in the market. In this sense, the precise nature of the material will depend on each manufacturer, being unknown, since there are no standards in this regard. For this reason, in each existing study in relation to FDM, the manufacturer is particularized, without specifying in most cases the material color.

In order to approximate this study to the actual industrial context, in this case different specimens have been made from the same base material, from the same manufacturer, stored in different atmospheres, with different pigmentation, and they are extruded at different extrusion temperatures. These three features or characteristics have been related to the results of the parts in terms of dimensional deviations, surface quality, and tensile strength.

On the one hand, it is verified that the materials without pigmentation generally obtain dimensional values closer to the nominal ones. This agrees with studies conducted by other authors that use different manufacturers of filament. In addition, by increasing the extrusion

temperature, the material becomes more fluid, which causes an increase in its fluidity and consequently larger dimensional deviations. However, at higher temperatures, up to a maximum of 220 °C, better mechanical strength is achieved.

On the other hand, the lack of pigmentation translates as a greater viscosity of the material, which brings better surface quality to the parts. However, the surface quality of the parts obtained by this technology is often insufficient for most industries, so it would be necessary to develop a post-processing stage.

Finally, PLA is a polymer highly influenced by the environmental conditions in which it is stored. This means that the relative humidity where the material is prior to its manufacture changes its structure. In dry atmospheric conditions, the PLA becomes stronger but less tenacious. A more fragile break is observed, the drier the storage environment.

However, the breakage occurs due to the appearance of defects and not the limit of the material. For this reason, it is essential to achieve a control of the large number of parameters that govern the process, starting with new proposals for standardization of both the material, composition, and storage, as well as the procedures for manufacturing and analyzing the parts.

Author Contributions: A.P.V. and M.B. conceived and designed the experiments; A.P.V. and M.B. performed the experiments; A.P.V., M.B., J.S. and F.G. analyzed the data; A.P.V. wrote the paper; M.B., J.S. and F.G. reviewed the work.

Funding: This research was funded by the Spanish Government via the Ministry of Economy, Industry and Competitiveness, the European Union (FEDER/FSE), and the Andalusian Government (PAIDI), project MINERVA.

Acknowledgments: The authors acknowledge the financial support for the work. A special mention for a passionate engineer with a tireless capacity for work, whose academic contributions have left a legacy and shown us the way forward due to his determination to continue progressing and developing not just engineering professionals, but good people overall. His great research contributions and his memory are a stimulus for us to try to be at his level, day by day, without disappointing him. Mariano Marcos-Barcelona, in memoriam.

Conflicts of Interest: The authors declare no conflict of interest.

References

1. Muthu, M.M.; Savalani, S.S. *Handbook of Sustainability in Additive Manufacturing*; Springer: Berlin/Heidelberg, Germany, 2016.
2. Chacon, J.M.; Caminero, M.A.; Garcia-Plaza, E.; Nunez, P.J. Additive manufacturing of PLA structures using fused deposition modelling: Effect of process parameters on mechanical properties and their optimal selection. *Mater. Des.* **2017**, *124*, 143–157. [CrossRef]
3. EFFRA Factories 4.0 and Beyond. Recommendations for the work Programme 18-19-20 of the FoF PPP under Horizon 2020. 2016. Available online: <https://www.effra.eu/factories-future-roadmap> (accessed on 21 June 2018).
4. Vallés, J.L. *Additive Manufacturing in FP7 and Horizon 2020*; Report from EC Workshop on Additive Manufacturing; European Commission: Bruselas, Belgium, 2014. [CrossRef]
5. Nuñez, P.J.; Rivas, A.; García-Plaza, E.; Beamud, E.; Sanz-Lobera, A. Dimensional and Surface Texture Characterization in Fused Deposition Modelling (FDM) with ABS plus. *Procedia Eng.* **2015**, *132*, 856–863. [CrossRef]
6. Wendt, C.; Fernández-Vidal, S.R.; Gómez-Parra, Á.; Batista, M.; Marcos, M. Processing and Quality Evaluation of Additive Manufacturing Monolayer Specimens. *Adv. Mater. Sci. Eng.* **2016**. [CrossRef]
7. Turner, B.N.; Strong, R. A review of melt extrusion additive manufacturing processes: Process design and modelling. *Rapid Prototyp. J.* **2014**, *20*, 192–204. [CrossRef]
8. Yang, C.; Tian, X.; Li, D.; Cao, Y.; Zhao, F.; Shi, C. Influence of thermal processing conditions in 3D printing on the crystallinity and mechanical properties of PEEK material. *J. Mater. Process. Technol.* **2017**, *248*, 1–7. [CrossRef]
9. Patel, J.; Patel, R.; Patel, S. A Review on Optimization of Process Parameter of Fused Deposition Modeling for Better Dimensional Accuracy. *Int. J. Eng. Dev. Res.* **2014**, *2*, 1620–1624.

10. Tymrak, B.M.; Kreiger, M.; Pearce, J.M. Mechanical properties of components fabricated with open-source 3-D printers under realistic environmental conditions. *Mater. Des.* **2014**, *58*, 242–246. [[CrossRef](#)]
11. Lanzotti, A.; Grasso, M.; Staiano, G.; Martorelli, M. The impact of process parameters on mechanical properties of parts fabricated in PLA with an open-source 3-D printer. *Rapid Prototyp. J.* **2015**, *21*, 604–617. [[CrossRef](#)]
12. Mathew, A.P.; Oksman, K.; Sain, M. Mechanical properties of biodegradable composites from poly lactic acid (PLA) and microcrystalline cellulose (MCC). *J. Appl. Polym. Sci.* **2005**, *97*, 2014–2025. [[CrossRef](#)]
13. Farah, S.; Anderson, D.G.; Langer, R. Physical and mechanical properties of PLA, and their functions in widespread applications—A comprehensive review. *Adv. Drug Deliv. Rev.* **2016**, *107*, 367–392. [[CrossRef](#)] [[PubMed](#)]
14. Messimer, S.L.; Patterson, A.E.; Muna, N.; Deshpande, A.P.; Rocha Pereira, T. Characterization and Processing Behavior of Heated Aluminum-Polycarbonate Composite Build Plates for the FDM Additive Manufacturing Process. *J. Manuf. Mater. Process.* **2018**, *2*, 12. [[CrossRef](#)]
15. Vijay, P.; Danaiah, P.; Rajesh, K.V.D. Critical Parameters Effecting the Rapid Prototyping Surface Finish. *J. Mech. Eng. Autom.* **2012**, *1*, 17–20. [[CrossRef](#)]
16. Aydemir, A.C.; Yenidoğan, S.; Karademi, R.A. Effects of Color Mixing Components on Offset Ink and Printing Process. *Mater. Manuf. Process.* **2017**, *32*, 1310–1315. [[CrossRef](#)]
17. Valerga, A.P.; Batista, M.; Fernandez, S.R.; Gomez-Parra, A.; Marcos, M. Preliminary Study of the Influence of Manufacturing Parameters in Fused Deposition Modeling. In Proceedings of the 26th DAAAM International Symposium on Intelligent Manufacturing and Automation, Zadar, Croatia, 21–24 October 2016; pp. 1004–1008. [[CrossRef](#)]
18. International Organization for Standardization. *Plastics—Determination of Tensile Properties*; ISO 527-1:2012; International Organization for Standardization: Geneva, Switzerland, 2012.
19. Nidagundi, V.B.; Keshavamurthy, R.; Prakash, C.P.S. Studies on Parametric Optimization for Fused Deposition Modelling Process. *Mater. Today Proc.* **2015**, *2*, 1691–1699. [[CrossRef](#)]



© 2018 by the authors. Licensee MDPI, Basel, Switzerland. This article is an open access article distributed under the terms and conditions of the Creative Commons Attribution (CC BY) license (<http://creativecommons.org/licenses/by/4.0/>).

Article

The Influence of Manufacturing Parameters on the Mechanical Behaviour of PLA and ABS Pieces Manufactured by FDM: A Comparative Analysis

Adrián Rodríguez-Panes, Juan Claver and Ana María Camacho *

Department of Manufacturing Engineering, Universidad Nacional de Educación a Distancia (UNED), Madrid 28040, Spain; adrian.rodriguez@invi.uned.es (A.R.-P.); jclaver@ind.uned.es (J.C.)

* Correspondence: amcamacho@ind.uned.es; Tel.: +34-913-988-660

Received: 2 July 2018; Accepted: 30 July 2018; Published: 1 August 2018

Abstract: This paper presents a comparative study of the tensile mechanical behaviour of pieces produced using the Fused Deposition Modelling (FDM) additive manufacturing technique with respect to the two types of thermoplastic material most widely used in this technique: polylactide (PLA) and acrylonitrile butadiene styrene (ABS). The aim of this study is to compare the effect of layer height, infill density, and layer orientation on the mechanical performance of PLA and ABS test specimens. The variables under study here are tensile yield stress, tensile strength, nominal strain at break, and modulus of elasticity. The results obtained with ABS show a lower variability than those obtained with PLA. In general, the infill percentage is the manufacturing parameter of greatest influence on the results, although the effect is more noticeable in PLA than in ABS. The test specimens manufactured using PLA perform more rigidly and they are found to have greater tensile strength than ABS. The bond between layers in PLA turns out to be extremely strong and is, therefore, highly suitable for use in additive technologies. The methodology proposed is a reference of interest in studies involving the determination of mechanical properties of polymer materials manufactured using these technologies.

Keywords: additive manufacturing; FDM; polylactide (PLA); acrylonitrile butadiene styrene (ABS); tensile behaviour; layer height; infill density; layer orientation

1. Introduction

Additive manufacturing (AM) encompasses numerous technologies that allow for the construction of three-dimensional parts by superimposing layers of material. These techniques have undergone great development in recent years. The most widespread group of these is Material Extrusion manufacturing. These processes have the great advantage of low equipment and material costs, ease of use in laboratories and domestic environments, and the versatility to manufacture all kinds of shapes with a wide range of materials, mainly plastics, in a short time. Additive manufacturing enables the obtaining of extremely complex geometries in a single process, also with regard to interior cavities, thus providing great freedom during the design stage [1]. On the other hand, the development of new technologies and commercially available equipment for additive manufacturing using different materials, such as metals [2] and composites, brings the pieces obtained ever closer to the optimum values, not only with respect to performance in service, but also with respect to dimensional and geometrical precision [3]. Furthermore, this type of processes also provides advantages and new challenges [4] from the point of view of sustainability [5,6] and design optimisation [7,8]. Additive manufacturing is constantly developing and talk is already afoot regarding advanced concepts such as 4D printing, reflected by Momeni et al. in their 2017 review [9]. Its use is also being extended to

applications in medicine [10] and even within the area of university teaching, as shown in studies such as that carried out by Garcia-Domínguez et al. [11].

The origin of the concept goes back to the 1980s with “Stereolithography” [12] and a whole host of new techniques have been developed since then, as explained by Gibson et al. in their book released in 2015 [13]. One of the categories or typologies acknowledged both in works undertaken by diverse authors [12] and in the recent ISO 17296-2:2015 standard on Additive Manufacturing [14] is Material Extrusion (Figure 1). This category encompasses processes in which the material, usually thermoplastic, is selectively applied using a nozzle to form each layer. The most important commercial process is known as Fused Deposition Modelling (FDM), which was patented by the founder of Stratasys over 20 years ago. Another similar process, but one that is not subject to this patent, is Fused Filament Fabrication (FFF).

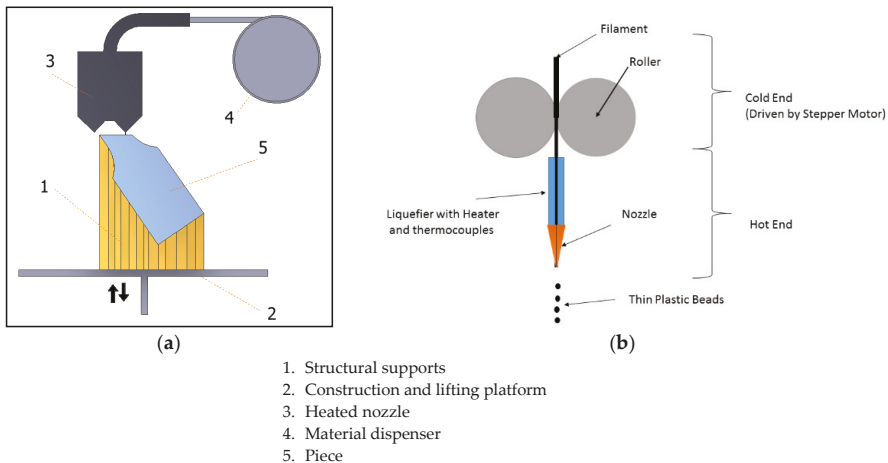


Figure 1. (a) A sketch of the material extrusion process; (b) An extruder sketch in an FDM/FFF (Fused Deposition Modelling/ Fused Filament Fabrication) process.

When compared with conventional manufacturing processes, one of the main problems to be tackled is that the traditional test procedures cannot always be applied to additive manufacturing processes. As opposed to the traditional processing of polymers, layer-based production generates parts with anisotropic properties and residual stresses. For this reason, standardised methods are required that enable the linking of the properties of the material, the manufacturing parameters and the design of the piece, which represents a major challenge. Given the emerging nature of some of the technologies and their rapid development, the literature available in this area is not very extensive. However, a number of works have recently been published devoted to the mechanical characterisation of parts produced using FDM, such as that of Goh et al. [15], on reinforced thermoplastics; that of Domingo et al. [16], on using polycarbonate as the material; that of Mohamed et al. [17], where the effect of the process conditions on the temperature-dependent dynamic mechanical properties of processed PC-ABS (polycarbonate-acrylonitrile butadiene styrene) parts by FDM was analysed; that of Tymrak et al. [18], focusing on ABS and PLA (polylactide); and that of Chacón et al. [19], which concentrates on studying the influence of the manufacturing parameters on the mechanical properties of PLA parts, all of which show the interest of the scientific community to increase the knowledge about this subject.

Standard ISO17296-3 [20] covers the main surface, geometrical and mechanically requirements depending on the material (metal, plastic, or ceramic) and on the criticality ratings of the parts (highly engineered parts, functional parts that are not safety critical and prototype pieces). It also indicates the standards to be used to determine the principal quality characteristics and the corresponding

test standards, not only for the starting material, but also for the pieces produced. In this respect, the most appropriate test standard is indicated for determining the mechanical requirements of the plastic pieces produced using additive manufacturing, with ISO 527-2 [21] being specified for the tensile strength. It sets forth the tensile test conditions for rigid and semi-rigid extruded plastics, which is the closest example to the pieces that form the objective of this study. For its part, standard ISO/ASTM 52921-13 [22] specifies the nomenclature and terms associated with coordinate systems and testing methodologies for additive manufacturing. Additionally, on the other hand, standard ASTM D638-14 [23] establishes a test method for determining the tensile properties of reinforced and unreinforced plastics. The problem with all of these guidelines is that they refer to test procedures that still do not include specific considerations for AM. This lack of specific regulation with respect to additive manufacturing represents a serious problem as it makes it difficult to establish valid comparisons between machines, materials, and models that make it possible to predict the properties of the final pieces and establish design guidelines.

In this respect, Forster [24] collates the existing procedures for the testing of polymers and analyses their viability for additive manufacturing processes. The aforementioned standards ISO 527 [21] and ASTM D638-14 [23] can be consulted for the profiling of tensile properties. These standards are recognised as being valid for additive manufacturing processes, although amendments might be required with respect to the post-processing of the test specimens in order to meet the demands of the standard (surface finish or dimensional requirements) or their applicability might be limited as they do not meet the material isotropy requirements [25]. Although the methods for isotropic materials can be applied, this would lead to the results obtained being more uncertain and it will not be possible to equate the properties obtained for the material with those of the specific piece.

As claimed by Tymrak et al. [18], in order for FDM printed parts to be useful for engineering applications, the mechanical properties of parts produced by this technique must be known. Forster identifies a number of geometrical variables of the deposition of material with an influence on the mechanical properties of the piece, such as raster angle, the height and width of the layer, the space between extruded filaments, the combination of variables (space between extruded filaments, layer width and height or deposition velocity) that might increase the overlap between filaments, or the orientation of the piece during manufacture (which can affect the transfer of load between filaments and layer interfaces).

There are previous studies that have analysed the influence of some of these parameters for certain materials. Many of these focus on the influence of raster angle [26], a parameter of the process that significantly affects the anisotropy and strength of the pieces. According to the study undertaken by Rodríguez et al. [27], this parameter causes variations in Young's modulus between 11% and 37%. The majority of these works show that the parts are stronger when the lines are oriented in the load direction for tensile tests [28–30], mixed angles for flexion [28,31], and orthogonal to the yield load [32]. The higher the raster angle, the lower the tensile properties of the material [27,28], with these reaching a minimum of around 50° [33].

The mechanical strength of a piece produced using AM is always lower than that of the original material or that of injection moulded pieces [34]. However, 80% of an injection moulded piece's strength can be achieved by orienting the lines in the direction of the load [35]. Fernández-Vicente et al. [36] carried out a study that analyses the influence of the pattern and infill percentage, with the conclusion being that the influence of the different print patterns produces a variation of at least 5% in the maximum tensile strength, meaning that the performance is similar. On the other hand, the density of the infill is a decisive factor in tensile strength; the combination of a rectilinear pattern and a 100% infill provides the greatest tensile strength with a value of 36.4 MPa and a difference of less than 1% with respect to the filament (ABS).

Regarding the influence of the space between filaments, the presence of cavities and sharp corners increases the stress within the piece, which may cause failure [21]. In general, minimising the space between the filaments increases the contact area between them and lead to a stronger fusion interface. The material extrusion processes depend on the temperature gradients between contiguous

filaments as these enable the thermoplastic polymers to form a solid fusion interface. Different studies set out to establish manufacturing guidelines related to the deposition speed and temperature and the temperature of the chamber which enable the production of stronger joints and, consequently, improved mechanical properties [32,37]. These type of studies enables the manufacturing parameters, the design of the parts and the final properties to be linked. Narrowing the width of the lines extruded reduces the residual stress in the filament and can increase the diffusion length. However, this would require more passes to create the piece, which increases the residual stress caused by the contraction of the polymer during cooling and, furthermore, the successive changes of nozzle speed have negative consequences in the diffusion [28].

With respect to manufacturing direction, Riddick et al. [29] combined orientations xz , yz , and xy with various raster angles (0° , $0^\circ/90^\circ$, and 90°) and found that orientation xz had the highest modulus of elasticity, ($E = 2.67$ GPa) and the greatest tensile strength (15.26 MPa). Other authors have verified that the strength is increased by maximising the alignment of the layers in the load direction [31].

On the other hand, the manufacture of pieces using FDM/FFF processes is subject to numerous variables dependent upon thermophysical and/or chemical phenomena that are going to result in pieces with different characteristics depending on the method used along with the parameters of the process. One of these important phenomena is the inter-molecular diffusion between layers and/or dissimilar materials that influences the interfacial bonding strength, as explained in the work by Yin et al. [38] where inter-molecular diffusion theory based on heat transfer is developed and the influence of processing parameters on bonding strength has been investigated. A significant improvement in layer adhesion and a more isotropic part was obtained by Levenhagen and Dadmun [39] by developing a process in which bimodal blends of the same polymer with different molecular weight were used. Another interesting approach is the one presented by Ravi et al. [40], consisting of the development of a pre-deposition heating method to heat the region of an existing layer before the new layer is deposited; thus, the temperature at the inter-layer interface increases, improving the interpenetrating diffusion, leading to a better bond strength. Particularly for polymer-fibre composites but not limited to, other aspects including void formation, blockage due to filler inclusion and/or poor adhesion of fibres and matrix must be addressed in the close future, as stated by Parandoush and Lin in their work from 2017 [41]. The complexity of these processes due to the high number of parameters involved and their interdependencies requires multidisciplinary research [42]. Something that further complicates the analysis of the mechanical performance of these pieces is that they are normally fragile and fracture easily due to interlaminar failure caused by manufacturing defects that are difficult to control [15]. The nature of these phenomena is very complex, as they are also affected by the influence of related environmental and process conditions; for example, if the process is performed within a controlled atmosphere, the existence (or the lack thereof) of a heated bed and/or the heat transmission process affects the thermal gradients of the workpiece, particularly between layers.

Our study is focused on analysing more global trends for a wide range of parameters, including the most used values in the practice, independently of the equipment. The main interest of these parameters is that they can be accurately defined as they are strictly “manufacturing parameters” and they can be reproduced in all the FDM equipment independently of the technology used so that they can be reproducible for third parts in different application fields.

This paper sets out to establish a relationship between the manufacturing parameters and the mechanical properties of the piece by using the test procedures set forth in the existing standards on plastics for the polymer materials most used in FDM techniques: acrylonitrile styrene butadiene (ABS) and polylactide (PLA). These, together with nylon, polyethylene (PET, PETG), polycarbonate (PC), and thermoplastic elastomers (TPE) are commonly used for prototyping design and the creation of low-performance parts. This comparative study will enable us to know more about the mechanical performance of ABS and PLA pieces manufactured using FDM in terms of the main manufacturing parameters: the influence of layer height, the percentage of infill and the orientation of the object during manufacture.

2. Materials and Methods

2.1. Materials and Equipment

This paper analyses the mechanical performance of pieces manufactured using PLA and ABS, the most commonly used materials in material extrusion 3D printing technologies. PLA is a biodegradable polymer derived from lactic acid. The main advantage of this material is how easy it is to use in 3D printing and the good results it delivers. It requires a lower extrusion temperature than ABS, it does not suffer significant distortions during printing and it adheres well to the platform, which means it does not require a heated base. Neither does it give off a bad smell or toxic vapours during printing. It must not be used for parts that have to withstand high temperatures because PLA tends to warp at over 60 °C. ABS is a thermoplastic that is extremely resistant to impact, abrasion, and chemical elements. In 3D printing, it is the most used material after PLA. Its good mechanical properties, resistance to temperature, low price, moderate flexibility, long service life and range of melting temperatures make this material an excellent option for manufacturing all manner of parts using FDM technologies, above all, parts that have to withstand cyclical loads and temperature changes. However, it is not suitable for all applications as it presents problems of contraction and warping during printing, tends to peel away from the platform, and tends to give off toxic gases. Table 1 shows the data provided by the manufacturer for the filaments of the two materials used. As can be seen, PLA is more rigid and has a greater tensile strength while ABS is more ductile. However, the impact strength of ABS is far greater (320 J/m against 220 J/m (Notched Izod Impact)), one of the main properties that differentiates it from other plastics.

Table 1. The mechanical tensile properties of the filaments employed according to the manufacturer.

Material (Manufacturer)	Colour	Tensile Strength (MPa)	Nominal Strain at Break (%)	Modulus of Elasticity (GPa)	Density (g/cm ³)
PLA (BQ)	Yellow	51	6	3.5	1.25
ABS (PrintedDreams)	Blue	41–45	20	2.1	1.05

The additive manufacturing equipment to be used is the Prusa I3 Aluminium printer (Prague, Czech Republic) (Figure 2a), which employs FFF technology. The Cura software (Ultimaker, Geldermalsen, the Netherlands) is used to export the three-dimensional models of the samples to G-code. The main technical characteristics of the FDM printer are defined in Table 2. The tests are carried out using a HOYTOM HM-D 100 kN model universal testing machine (Leioa, Spain) (Figure 2b).

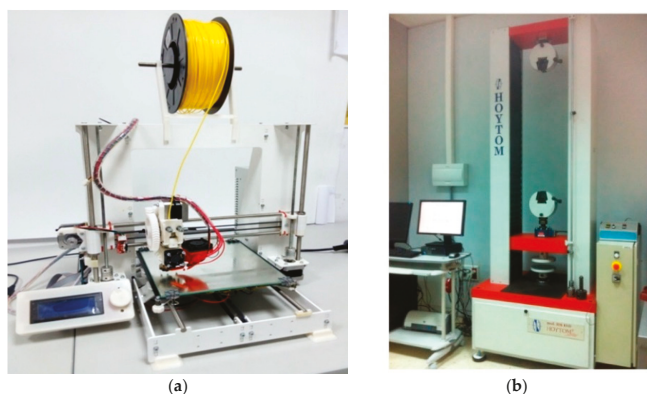


Figure 2. The equipment: (a) a Prusa i3 printer; (b) a HOYTOM HM-D 100kN Universal testing machine.

Table 2. The technical characteristics of the FDM equipment.

Characteristic	Value
Maximum printing volume (mm ³)	215 (x) × 210 (y) × 180 (z)
Firmware	Marlin
Nozzle diameter (mm)	0.4
Resolution (mm)	0.1
Maximum printing velocity (mm/s)	80
Maximum displacement velocity (mm/s)	120

2.2. Mechanical Properties of FDM Filaments

Mechanical tests were carried out on filaments of the two materials in their raw state to compare the data with those obtained by the manufacturer. Two filaments of every material (ABS 1, ABS 2, PLA 1, and PLA 2) were tested by the authors (Figure 3) and the average values of the main mechanical parameters (tensile strength, nominal strain at break, modulus of elasticity) were compared with those provided by the manufacturer (Table 1) and presented in Table 3; in this case, the manufacturers did not specify how these properties were determined, but standardized specimens of thermoplastic materials for tensile testing are traditionally manufactured by injection moulding or machined. In this work, we want to check how accurate the results from those obtained by the manufacturer by traditional processes by applying tensile tests directly to filaments as they are the starting material for an FDM process. There are no specific standards for this kind of testing due to the novelty of the FDM technique, where pieces are obtained after depositing the filament during a layer by layer operation. The filaments are provided as solid wires of diameter 1.75 mm in coils and the tests were carried out directly by applying tensile forces to filaments of 165 mm in length.

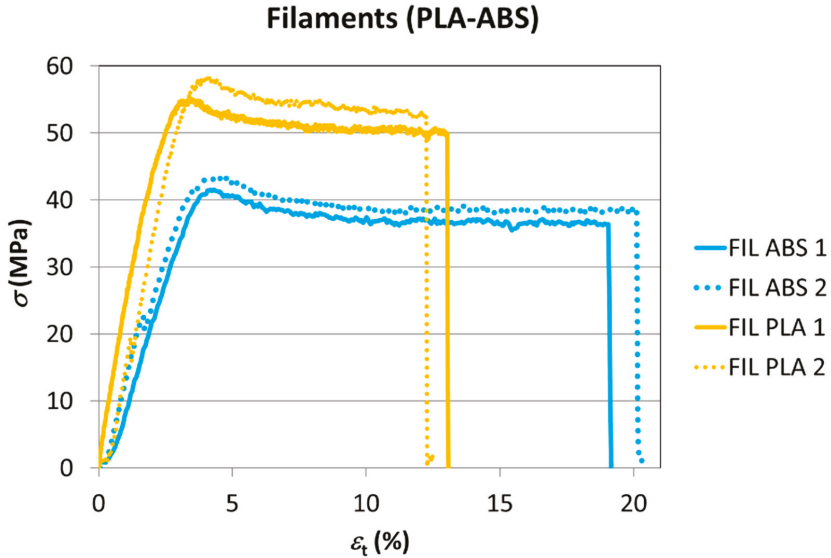


Figure 3. The tensile tests of the filaments.

The mechanical properties derived from the tests are shown in Table 3.

Table 3. The comparison of mechanical properties (laboratory vs. manufacturer).

Material	Average Tensile Strength (MPa)	Manufacturer Tensile Strength (MPa)	Difference (%)	Average Nominal Strain at Break (%)	Manufacturer Nominal Strain at Break (%)	Difference (%)	Average Modulus of Elasticity (GPa)	Manufacturer Modulus of Elasticity (MPa)	Difference (%)
PLA	55.80	51.0	+9.4	12.75	6	+112.5	1.94	3.5	-44.6
ABS	42.35	42.5	-0.4	19.58	20	-2.1	1.49	2.1	-29.0

As it can be seen, the data obtained for the ABS and the PLA from tensile tests of the filaments are only qualitatively congruent with those provided by the manufacturer; the data that show a higher degree of coincidence are those associated with mechanical tensile strength, particularly results for ABS, that present a very similar value (0.4%); significant differences are found for the other two parameters recorded (nominal strain at break and modulus of elasticity), especially in the case of the material PLA, where differences of 112.5% and 44.6% have been obtained, respectively. This can be due to differences between the procedures followed, as explained before; however, the tensile strengths seem to have a better coincidence among results.

2.3. Design of Manufacturing Parameters and Case Studies

The mechanical characteristics of the pieces produced using AM are very much dependent upon the manufacturing parameters. Figure 4 includes a diagram of the most relevant of those parameters.

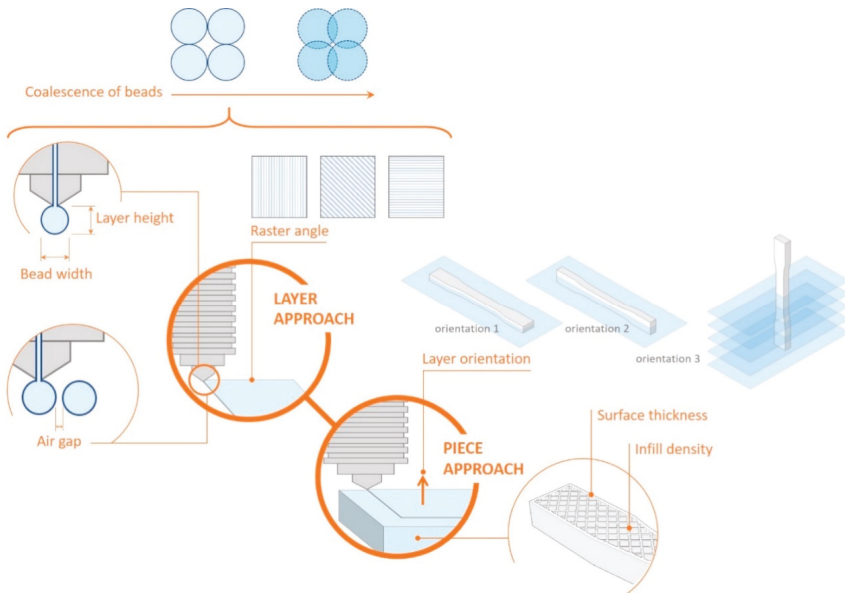


Figure 4. The geometrical parameters with a direct influence on the mechanical properties of pieces manufactured using FDM.

This paper will study the influence of layer height, the percentage of infill, and construction orientation of the test specimen on the mechanical tensile properties of the two materials as these are the three most influential parameters. One of the main objectives is to check how much the mechanical performance improves when the percentage of the infill is increased, which is why two values (20% and 50%) have been included in the study. By considering one or the other infill value, the volume ratio of material changes due to the variation of the infill density which applies different sizes of cell patterns.

On the other hand, the thickness of the piece's shell remains constant, with a value of 0.8 mm. Layer height is a parameter that influences manufacturing time; the precision of details and the finish are significantly improved by using finer layers. However, this study sets out to also analyse the influence of this parameter on mechanical strength. To do so, two layer heights, 0.1 mm and 0.2 mm, will be used. Finally, a comparison will be made to discover how much the mechanical strength varies with respect to the orientation of the piece during its construction. This is a fundamental factor due to the anisotropy conferred upon the piece by the layering manufacturing process. Both in the case of using orientation 1 and in that of using orientation 2, the layers are parallel to the stress, but the orientation of the infill raster varies with respect to the tensile force. Furthermore, in this case, it is necessary to use supports, and this causes a certain degree of roughness on the overhanging surface when removing them, but the results are acceptable for test purposes. In the case of orientation 3, layering in a direction perpendicular to the stress should result in a reduction of mechanical strength. A summary of the parameters whose influence on mechanical performance is going to be analysed is presented in Table 4.

Table 4. The definition of case studies for a layer width of 0.4 mm, a printing velocity of 60 mm/min (30 mm/min on wall and bases), a line-type wall pattern, and infill patterns of 45° and 135°.

Case	Layer Height (mm)	Infill (%)	Manufacturing Orientation
Case 1 (Reference)	0.1	20	Orientation 1
Case 2	0.2	20	
Case 3	0.1	50	
Case 4	0.1	20	Orientation 2
Case 5	0.1	20	Orientation 3

Finally, the rest of the parameters are specifically defined for each material in Table 5.

Table 5. The remaining manufacturing parameters specified for each material.

Material	Fusor Temp. (°C)	Base Temp. (°C)	Wall Vel./Infill (mm/s)	Layer Width (mm)	Adhesion Plat.	Vent. Layer	Dist./Vel. Retraction (mm/mm/s)	Wall/Infill Pattern and Angle (°)
ABS	235	80	60/30	0.4	YES (8 mm)	100%	6/25	Lines/grid (45, 135)
PLA	200	50			NO			

2.4. Experimental Procedure and Geometrical Dimensions of Test Specimens

The test procedure that is going to be followed is explained in a previous work [43] and uses the type I general usage test specimen as per ASTM 638-14 [23] (Figure 5, above), as explained in detail in that study. It also includes the principal difficulties encountered during the testing of plastic material specimens obtained using FDM and the fact that the test specimen breaks prematurely due to the concentration of stresses, which have also been reported by other authors, such as Wendt et al. [44]. The ASTM 638-14 standard, indicated by Dizon et al. [45], is the most used for this type of mechanical characterisation. The specimen is fixed by the clamps, aligning its longitudinal axis with the axis of the test machine. The wedges should be tightened enough to avoid the specimen to slide without causing it to collapse. The HOWIN software is used to control the test, to set the input parameters and to gather the values obtained. The speed of the test should be 5 mm/min according to the ASTM D638-14 standard (the minimum value of those established in the standard that causes the break between 0.5–5 min).

According to the ASTM 638-14 standard, the nominal tensile stresses must be used, that is, the tensile load carried by the test specimen at any given moment per unit area of the minimum original cross section. Since this standard is used for determining the tensile properties of solid plastics obtained for traditional processes, the minimum original cross section is computed by multiplying the thickness of the sample and the width of the narrow section.

Two identical test specimens of each type are going to be manufactured and, in the event of the results varying significantly, a third test shall be carried out. The elongations will refer to the variation of the distance between grips and not to the variation of the benchmark length measured using an extensometer, indicated in standard ISO 527-1:2012 [46], which recommends the use of the nominal distortion when extensometers are not used. Finally, a velocity of 5 mm/min is going to be set in accordance with that established in the ASTM standard, so that the rupture occurs between 0.5 and 5 mins. Figure 5 shows examples of the PLA and ABS test specimens used in the tests arranged by case.

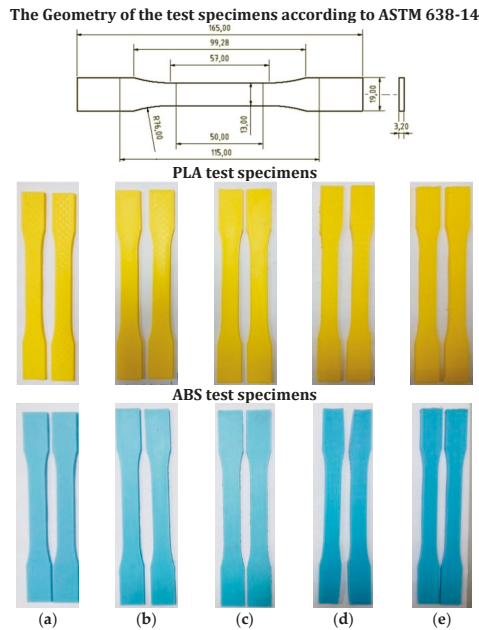


Figure 5. The test specimens manufactured using PLA and ABS. (a) Case 1; (b) Case 2; (c) Case 3; (d) Case 4; (e) Case 5.

The variables to be studied are tensile yield stress (R_p), mechanical tensile strength (R_m), nominal strain at break (ϵ_t), and the modulus of elasticity (E_t).

3. Results

3.1. Mechanical Behaviour of the PLA Parts

Figure 6 shows the PLA test specimens after the test, with a specimen of each type being included. Although all of them fracture in the narrow area, it can be seen that some do so outside the limits of the benchmark length. This is one of the difficulties experienced during the laboratory tests described in a previous study [35].

In the first two cases, a rupture with an irregular breakage line can be observed. This is due to the layers being oriented in the direction of the stress and the raster angle of the infill being 45°. In the third case (50% infill), the test specimen behaves almost as though it were solid, as can be observed in its transversal cross-section. In the fourth case (orientation 2), the line of fracture occurs along a line perpendicular to the stress and located at a point where the infill joins with the walls. In the last case (orientation 3), the fracture occurs as a result of the layers separating because they were built up perpendicular to the stress due to the construction orientation.

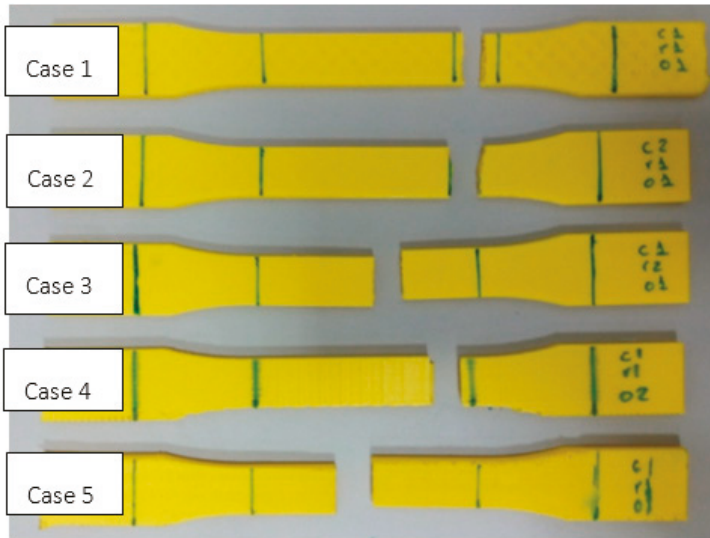


Figure 6. The PLA test specimens tested (one of each type).

The graphs in Figure 7 show the test results for the different parameters. To help analyse these data more clearly, a graph is provided showing the test data for each type of test specimen grouped together along with the properties of the filament (Figure 7f). In each case, the results showing the intermediate values of each series have been chosen.

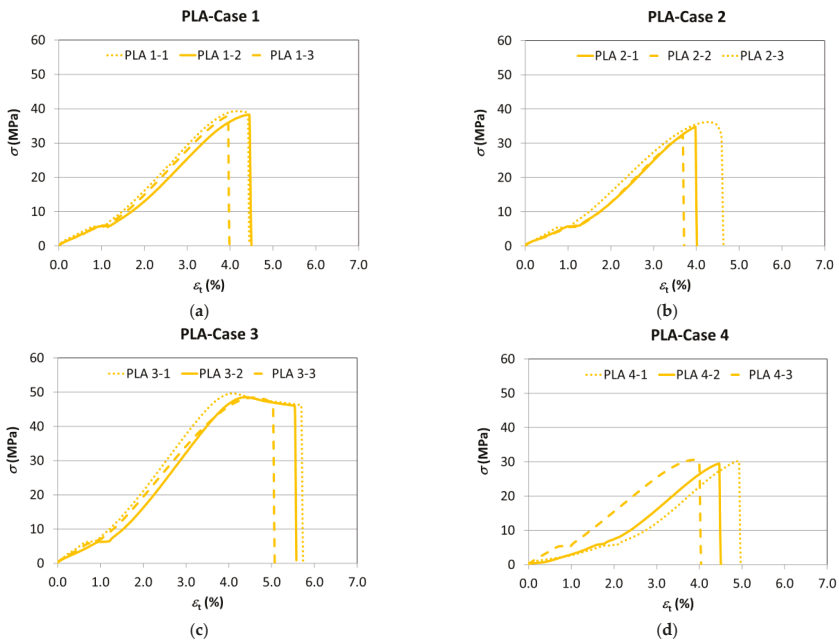


Figure 7. Cont.

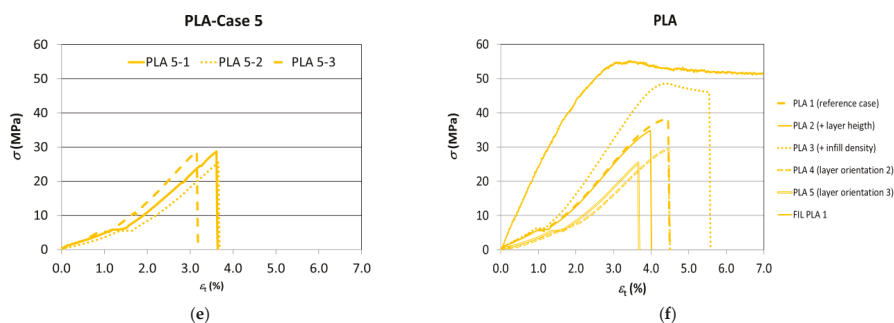


Figure 7. The stress–strain curves (PLA). (a) Case 1; (b) Case 2; (c) Case 3; (d) Case 4; (e) Case 5; (f) the comparison of the results with the intermediate values of each series of test specimens.

The corresponding mechanical properties of the PLA test specimens have been calculated based on the information gathered during the tests. The data corresponding to the yield stress, tensile strength, nominal strain at break, and the modulus of elasticity are shown in Table 6.

Table 6. The mechanical properties of PLA test specimens and the variation with respect to the benchmark case (Case 1).

Case	E_t (GPa)		ϵ_t (%)		R_p (MPa)		R_m (MPa)	
	Mean	(St. Dev.)	Mean	(St. Dev.)	Mean	(St. Dev.)	Mean	(St. Dev.)
Case 1	1.000	(0.02)	4.20	(0.30)	38.43	(0.68)	38.47	(0.74)
Case 2	0.987	(0.03)	≈	4.07 (0.50)	≈	33.13 (1.19)	–	34.37 (2.08)
Case 3	1.343	(0.08)	++	5.47 (0.32)	++	46.53 (2.27)	++	48.87 (0.64)
Case 4	0.760	(0.11)	–	4.70 (0.72)	+	29.03 (0.70)	--	30.10 (0.56)
Case 5	0.735	(0.02)	–	3.77 (0.21)	--	27.63 (1.85)	--	27.63 (1.85)

≈ (similar to the benchmark case), + (higher than the benchmark case), ++ (much higher than the benchmark case), – (lower than the benchmark case), -- (much lower than the benchmark case).

Firstly, by comparing the results with respect to the benchmark case (Case 1), it is found that, indeed, the variation of the manufacturing parameters causes a variation in the tensile behaviour of the PLA test specimen, with its general performance being on the fragile side compared with that of the filament, which presents a high degree of ductility.

The slope of the elastic area (and, consequently, Young’s modulus) remains practically unmodified by the change in layer height (Case 2), while it clearly diminishes when the manufacturing orientation is modified (Cases 4 and 5), and rises on the infill percentage being increased (Case 3).

The nominal strain at break (and, therefore, the ductility) clearly increases in those cases with a higher infill percentage (Case 3) and also with orientation 2 (Case 4), while it is reduced with manufacturing orientation 3 (Case 5) and remains more or less invariable with the increase of layer height (Case 2).

In all the cases, Young’s modulus and the nominal strain at break are lower than in the filament.

The mechanical strength rises with the increase of infill percentage (Case 3) with respect to the initial conditions (Case 1). Meanwhile, a reduction thereof is observed in the cases of increased layer height (Case 2) and variation of the construction orientation (Cases 4 and 5), with this reduction being especially noteworthy in the case of orientation 3 (Case 5), as was to be expected.

Finally, the yield stress presents a performance similar to the tensile strength, bearing in mind that they practically coincide in many cases given the generally fragile performance of the PLA test specimens.

Considering mechanical strength to be the parameter of greatest interest due to its greater repeatability across laboratories and to its importance as a mechanical property from the design and functionality point of view for certain applications, Table 7 shows the percentage variation of the average mechanical strength in terms of the parameters used and the variation with respect to the material of the filament (data provided by the manufacturer).

Table 7. The comparison of the mechanical properties of PLA test specimens with those of the filament.

Case	Mean R_m (MPa)	Difference to Case 1 (Benchmark)	Difference to Filament
Case 1	38.47	—	−25%
Case 2	34.37	−11%	−33%
Case 3	48.87	+27%	−4%
Case 4	30.10	−22%	−41%
Case 5	27.63	−28%	−46%

These data reveal that increasing the infill up to 50% (Case 3) greatly improves the mechanical strength (27%) as this makes the part more solid and reduces the number of cavities (its weight increases by 16%). The increase of layer height (Case 2) causes the maximum tensile strength to fall by 11%. Although this effect is less pronounced than that of varying the infill and the manufacturing orientation, it can be seen that finer layers lead to better results as far as both the finish and mechanical properties are concerned. With respect to the manufacturing orientations, orientation 2 (Case 4), with the layers in a direction parallel to the stress, but perpendicular to those of orientation 1, reduces the mechanical tensile strength by 22% (Figure 8a). On observing the fractured part (Figure 8b), it can be seen that this behaviour might be due to the different orientation of the infill with respect to the direction of the stress, which is what causes the part to rupture at the point where the infill joins the wall.

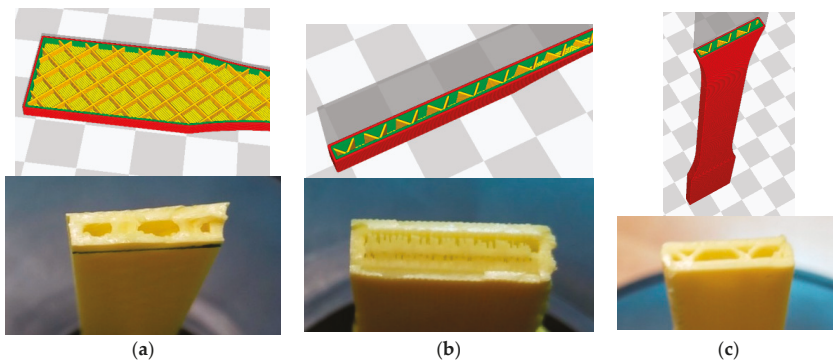


Figure 8. The detail of the infill and fracture surface in terms of orientation. (a) Orientation 1; (b) Orientation 2; (c) Orientation 3.

In the case of orientation 3 (Case 5), the overlap of layers perpendicular to the direction of the tensile stress causes the tensile strength to fall by 28%. This reduction of strength caused by varying the manufacturing orientation is due to the anisotropy of the pieces manufactured in the layers. In Case 5, this orientation causes the stress to revert to the interface between the layers, namely the weakest area of the pieces produced using additive manufacturing (Figure 8c).

In the table, it can also be seen that with the best of the combinations of parameters (Case 3) it is possible to achieve a strength that is only 4% less than that specified for the filament by the manufacturer.

3.2. Mechanical Behaviour of the ABS Pieces

Figure 9 shows the ABS test specimens after the test, with a specimen of each type being included. It can be observed that all the test specimens rupture where they are narrowest (some of them outside the benchmark length) except the one manufactured with orientation 3 (layers perpendicular to the stress), which ruptured with an extremely low stress due to a separation of layers in the area of the agreed radius.

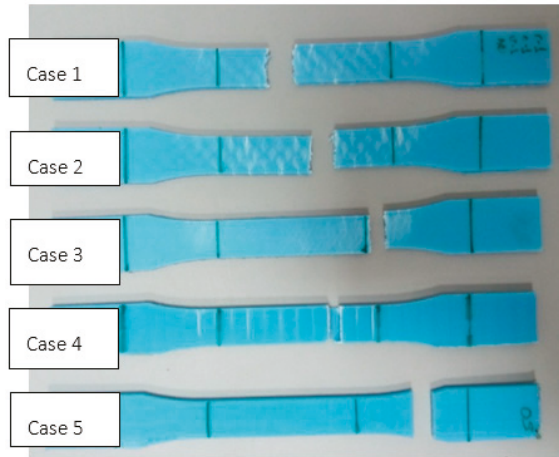


Figure 9. The ABS test specimens tested (one of each type).

In Cases 1 and 2, a rupture with a jagged line can be observed. This is due to the layers being oriented in the direction of the stress and the raster angle of the infill being 45° (Figure 10a). In Case 3, given that it has 50% of infill, the test specimen is almost solid, which is why the distortion is more uniform (Figure 10b). In Case 4, the fracture occurs along lines perpendicular due to the stress and located at the points where the infill joins the walls (Figure 10c). In Case 5, the fracture occurs at low distortions as a result of the separation of layers because, due to the construction orientation these build up perpendicular to the stress, which causes the test specimen to break prematurely as the interface between the layers in this material is extremely weak (Figure 10d).

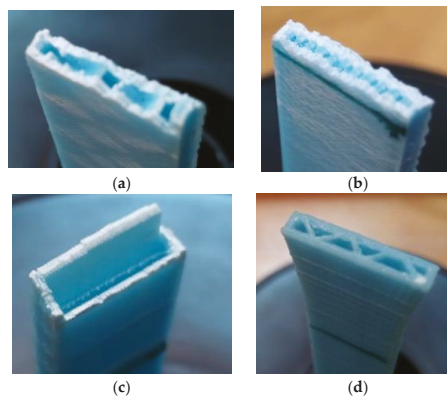


Figure 10. The fracture cross-section. (a) Case 1; (b) Case 3; (c) Case 4; (d) Case 5.

The graphs of Figure 11 show the results of the tests with the different parameters for the test specimens manufactured using ABS, where a lower variability in the results than in the case of the PLA test specimens can be observed.

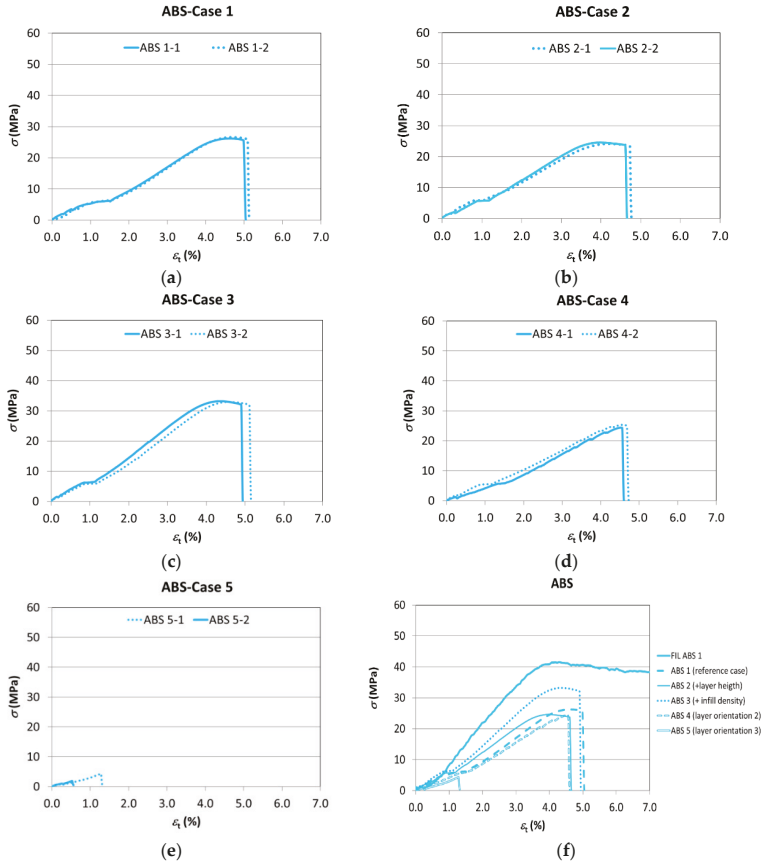


Figure 11. The stress–strain curves (ABS). (a) Case 1; (b) Case 2; (c) Case 3; (d) Case 4; (e) Case 5; (f) The comparison of the results with the intermediate values of each series of test specimens.

The data corresponding to the yield stress, tensile strength, nominal strain at break, and modulus of elasticity are shown in Table 8.

Table 8. The mechanical properties of the ABS test specimens and variation with respect to the benchmark case (Case 1).

Case	E_t (GPa)		ϵ_t (%)		R_p (MPa)		R_m (MPa)					
	Mean	(St. Dev.)	Mean	(St. Dev.)	Mean	(St. Dev.)	Mean	(St. Dev.)				
Case 1	0.650	(0.01)	5.10	(0.00)	25.60	(0.00)	26.40	(0.28)				
Case 2	0.732	(0.02)	+	4.75	(0.07)	–	23.45	(0.35)	–	24.40	(0.28)	–
Case 3	0.943	(0.11)	++	5.15	(0.21)	≈	31.95	(0.07)	++	33.05	(0.21)	++
Case 4	0.600	(0.03)	≈	4.80	(0.00)	≈	23.60	(1.27)	–	24.85	(0.64)	–
Case 5	–		–	0.75	(0.35)	--	3.15	(1.77)	--	3.15	(1.77)	--

≈ (similar to the benchmark case), + (higher than the benchmark case), ++ (much higher than the benchmark case), – (lower than the benchmark case), -- (much lower than the benchmark case).

It can be seen how the change of manufacturing parameters also causes a variation in the tensile performance of the ABS test specimens.

The slope of the elastic area (stiffness) remains almost the same when orientation 2 is used (Case 4), while said incline (and, therefore, Young’s modulus) increases significantly with an infill of 50% (Case 3), and less noticeably with an increase in layer height (Case 2). As regards orientation 3 (Case 5), the test specimen breaks so quickly that it is hardly possible to draw conclusions as to its tensile performance except for the fact that its deformation capacity is practically nil.

The nominal strain at break is slightly affected by layer height (Case 2), nor by the change to orientation 2 (Case 4) or by the increased percentage of infill (Case 3). However, the strain at the break diminishes significantly with respect to Case 1 when orientation 3 is used (Case 5).

In all the cases, Young’s modulus and strain at break are lower than in the filament, as would occur in the case of PLA.

On the other hand, with the exception of the cases of vertical orientation (Case 5) and the increase of the infill (Case 3), the differences with regards to mechanical strength are not too pronounced in all the other cases. Both the use of thicker layers (Case 2) and the change of the layer orientation to keep them parallel to the stress (Case 4) reduce the maximum strength, but only slightly. Increasing the infill to 50% (Case 3), with the resulting 18.5% rise in weight, causes the tensile strength to increase by 25.19%, while orienting the layers perpendicularly to the stress (Case 5) causes the premature rupture of the test specimen with a strength reduction of 88.07% (Table 9). Another interesting fact shown by the table is that with the different combinations of parameters, the best results that can be obtained are 22% worse than those of the filament.

Table 9. The comparison of the mechanical properties of ABS test specimens with those of the filament.

Case (ABS)	Mean R_m (MPa)	Difference to Case 1 (Benchmark)	Difference to Filament
Case 1	26.40	—	−38%
Case 2	24.40	−7.57%	−43%
Case 3	33.05	+25.19%	−22%
Case 4	24.85	−5.87%	−42%
Case 5	3.15	−88.07%	−93%

The change of infill results in a more solid test specimen and a reduction of cavities, once again result in an increase of mechanical strength. As regards layer orientation, if this is perpendicular to the stress, it causes the strain to revert to the interface between layers, namely the weakest area in the pieces obtained using additive manufacturing and especially in the case of ABS. The weakness of this interface can be seen in the graph, which shows that the piece breaks under a far lower strain than the pieces manufactured using other orientations due to layer separation.

3.3. Comparative Analysis

In the stress-strain graph of Figure 12, the tensile performance of both materials is shown together to facilitate the comparative analysis.

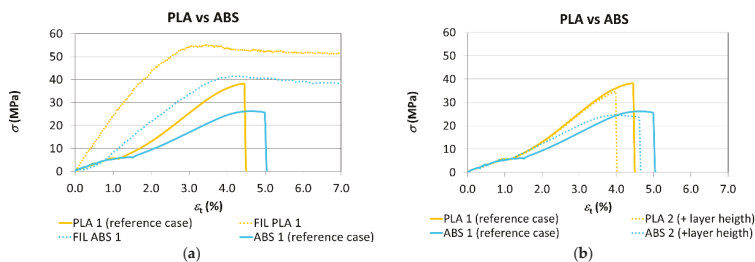


Figure 12. Cont.

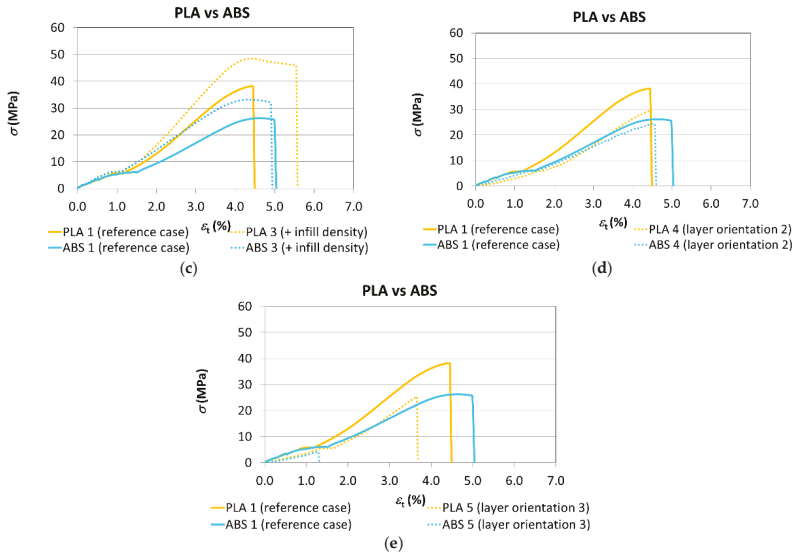


Figure 12. The comparison of the stress–strain curves for both materials. (a) Filaments vs. Reference case, (b) Reference case vs. + layer height, (c) Reference case vs. + infill density, (d) Reference case vs. layer orientation 2, (e) Reference case vs. layer orientation 3.

The variability of the results can be compared for both materials through Tables 6 and 8 through the standard deviation. The variability of the modulus of elasticity is very similar for PLA and ABS, although, in general, it can be stated that results with ABS showed a lower variability than in the case of PLA. To help quantify the effect of the manufacturing parameters, Figure 13 shows the data corresponding to the modulus of elasticity, nominal strain at break, yield stress, and tensile strength obtained following the tests for the 5 cases analysed.

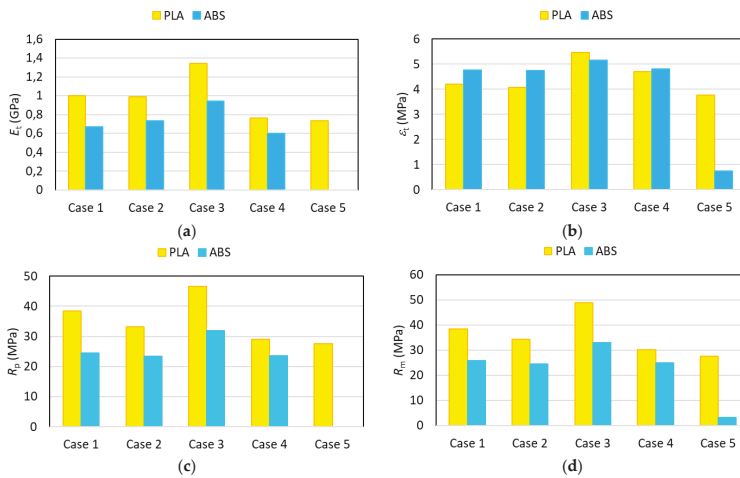


Figure 13. The comparison of mechanical properties for PLA and ABS. (a) Modulus of elasticity; (b) Nominal strain at break; (c) Yield stress; (d) Tensile strength.

Both figures show that the test specimens manufactured using PLA generally present a more rigid performance associated with the higher values of Young's modulus found, in line with the values obtained for the filament. The influence of the manufacturing parameters presents a similar trend for both materials.

As far as the strain at break values obtained are concerned, it can be said that there is no clear trend given that, for example, in Cases 1 and 2, a greater ductility is obtained for ABS, while in Cases 3 and 5 the PLA's ductility is clearly higher, with very similar values being obtained for both materials in Case 4.

On the other hand, in light of the values obtained, the pieces manufactured using PLA have a greater tensile strength than their ABS counterparts, just as would occur with the filament. Furthermore, the change of parameters has less of an influence on mechanical strength in the case of ABS, with the exception being Case 5, where the reduction of mechanical strength is more significant. Figure 13d shows that PLA undergoes more significant reductions of maximum strength than ABS when layer height is increased (Case 2) and transversal orientation is used (Case 4). Under all circumstances, the infill percentage (Case 3) is the factor with the greatest influence on the results. The performance of the tensile yield stress is identical to that of the maximum strength.

Finally, the differences with respect to the starting material and the decrease of mechanical strength in the case of orienting the layers perpendicular to the stress (Case 5) are less in the PLA, which would appear to indicate a significantly stronger bond of the layers in this material (Table 10).

Table 10. The comparison of mechanical strength with the benchmark case and the filament.

Material	Case 1	Case 2	Case 3	Case 4	Case 5
PLA	38.47	34.37	48.87	30.10	27.63
Difference to Case 1	—	−11%	+27%	−22%	−28%
Difference to filament	−25%	−33%	−4%	−41%	−46%
ABS	26.40	24.40	33.05	24.85	3.15
Difference to Case 1	—	−8%	+25%	−6%	−88%
Difference to filament	−38%	−43%	−22%	−42%	−93%

Based on this data, it can be observed that increasing the infill up to 50% (Case 3) causes a marked increase in mechanical strength, with this being of a similar magnitude in both materials (27% PLA + 16% weight and 25% ABS + 18% weight). This is because the piece is more solid and has fewer cavities.

As has already been explained, the layer height effect (Case 2) is more significant with PLA as it causes an 11% reduction in tensile strength, whereas in the case of ABS this is only 8%. It can thus be seen that finer layers lead to better results not only where the finish is concerned, but also in mechanical properties, although the effect is more noticeable in the PLA than in the ABS.

As far as the manufacturing orientations are concerned, orienting the layers in the direction parallel to the stress, but perpendicular to Case 1 (Case 4), greatly reduces tensile strength in PLA, (−22%) while its effect is not remarkable in ABS (−6%).

In the case of vertical orientation (Case 5), the overlapping of layers perpendicular to the direction of the tensile force reduces tensile strength by 28% in PLA, a much lower figure than in the case of ABS, which fractures prematurely (with an 88% reduction of maximum strength) due to its weak bond between layers.

The variations with respect to the filament lead to the conclusion that the material which undergoes a lower reduction of its mechanical properties during the additive manufacturing process is PLA (a mere 25% as against the 38% of ABS under benchmark conditions), which would appear to indicate the bond it achieves between layers is better than that of ABS, thus, making it an ideal thermoplastic for use in FFF/FDM technologies.

Finally, in Table 10 it can be observed that with the best combination of parameters it is possible to achieve a strength of only 4% less than that specified by the manufacturer for the PLA material, namely,

figures that are far better than those returned by ABS (−22%). This indicates that the bond between layers in this material is far better than in ABS, at least with the manufacturing parameters used in this study, and that with an optimum combination of parameters (a 100% infill, the alignment of layers in the direction of the stress, a layer height of 0.1 mm, and optimum raster and pattern, temperature and velocity parameters), it could be possible to achieve strength results very similar to those of the starting filament or injection or compression moulded pieces.

4. Conclusions and Future Work

This work has studied the influence of the principal manufacturing parameters of an FDM process on the mechanical properties of the two thermoplastic materials most widely used in this type of additive technique: ABS and PLA. These parameters are infill percentage, layer height and manufacturing orientation. The results with ABS show a lower variability than in the case of PLA.

Generally speaking, the pieces manufactured with PLA behave more rigidly than in the case of ABS, just as with the starting material, with the influence of the manufacturing parameters being very similar for both materials. However, there is no clear trend regarding the influence of the manufacturing parameters on the strain at fracture values obtained, unlike the starting material, where the ABS showed a higher degree of ductility than the PLA.

Regarding ABS, the mechanical strength results barely vary with respect to layer height (the maximum strength only falls by 7.57% when the layer height is increased from 0.1 to 0.2 mm) and when using another orientation in which the layers remain parallel to the stress (a reduction of tensile strength by an average of 5.87%). However, increasing the infill up to 50% (with an 18.5% weight increase) causes the tensile strength to rise by 25.19% given that the test specimen is more solid and the cavities are smaller. On the other hand, the vertical orientation of the layers perpendicular to the stress causes the premature rupture of the test specimen with a strength reduction of 88.07%. This is due to the strain reverting to the interface between layers, namely, the weakest area in the pieces obtained using additive manufacturing, especially in the case of ABS.

Another interesting point to emerge from this study is that, with the different combinations of parameters chosen, the best results that can be obtained are 22% worse than those of the starting material. This, combined with the lack of strength of the test specimens whose layers are oriented perpendicularly to the stress, confirms that the ABS pieces manufactured using this technology and these parameters show an extremely weak bond compared with the strength of the material.

In the case of PLA, the increased layer height causes the tensile strength to diminish by 11%, which is notably greater than in the case of ABS, which is why it can be concluded that finer layers lead to better results not only where finish is concerned, but also in mechanical properties, although the effect is more noticeable in the PLA than in the ABS. On the other hand, it can be seen that increasing the infill up to 50% (with a 16% rise in weight), greatly improves mechanical strength (27%), which is very similar to that of ABS (25.19%).

With respect to the manufacturing orientations of the layers in a direction parallel to the stress, but perpendicular to those of the initial orientation, the tensile strength is reduced by 22%, far and above that of ABS (5.87%). This behaviour can be attributed to the different orientation of the infill with respect to the direction of the stress, which is what causes the part to fracture at the point where the infill joins the wall.

The orientation with the overlapping of layers perpendicular to the tensile force reduces maximum tensile strength by 28%, a much lower figure than in the case of ABS, which fractured prematurely (with an 88.07% reduction of the maximum strength) due to its weak bond between layers.

Regarding PLA it can be concluded that, with the best of the combinations of parameters a strength of only 4% less than that specified by the manufacturer for the material can be achieved, which is far better than that returned by the ABS (−22%). This indicates that the bond between layers in this material turns out to be extremely strong and is, therefore, highly suitable for use in additive

technologies given that with an optimum combination of parameters it is possible to achieve strength results very similar to those provided by injection or compression moulded pieces.

In general, the infill percentage is the factor of greatest influence in the results. The performance of the yield stress is identical to that of the maximum strength.

The methodology proposed is a reference of interest in studies involving the determination of mechanical properties of polymer materials manufactured using these technologies. Specifically speaking, these results can be extremely useful for the selection of suitable materials and parameters in FDM design and manufacturing processes.

The inclusion of other factors of interest such as the direction of the raster and manufacturing speed, as well as the influence of the interaction of these factors on the results, is proposed as a line of work for the future. Additionally, the influence of other advanced parameters that are closely related to more specific thermophysical and/or chemical phenomena (the local temperature of the filament during deposition, the molecular diffusion at the polymer interface, and the deposition pressure/force, among others) will be also addressed in future studies; this kind of analysis will require specialised equipment in most of the cases due to its complex nature.

Author Contributions: Conceptualization, J.C. and A.M.C. Funding acquisition, J.C. and A.M.C.; Investigation, A.R.-P. and J.C.; Supervision, A.M.C.; Writing—Original draft, A.R.-P.; Writing—Review & editing, A.M.C.

Funding: The APC was funded by the Annual Grants Call of the E.T.S.I.I. of UNED through the projects of reference [2018-ICF04] and [2018-ICF10].

Acknowledgments: This work has been developed within the framework of the project DPI2016-81943-REDT of the Ministry of Economy, Industry and Competitiveness. The authors also want to acknowledge Miguel Ángel Sebastián for his valuable comments and support in the experimental tests developed in this work. The authors would like to take this opportunity to thank also the Research Group of the UNED “Industrial Production and Manufacturing Engineering (IPME)”.

Conflicts of Interest: The authors declare no conflict of interest. The funders had no role in the design of the study; in the collection, analyses, or interpretation of data; in the writing of the manuscript, and in the decision to publish the results.

References

1. Snyder, T.J.; Andrews, M.; Weislogel, M.; Moeck, P.; Stone-Sundberg, J.; Birkes, D.; Hoffert, M.P.; Lindeman, A.; Morrill, J.; Fercak, O.; et al. 3D Systems’ Technology Overview and New Applications in Manufacturing, Engineering, Science, and Education. *3D Print. Addit. Manuf.* **2014**, *1*, 169–176. [[CrossRef](#)] [[PubMed](#)]
2. Xiong, J.; Li, Y.; Li, R.; Yin, Z. Influences of process parameters on surface roughness of multi-layer single-pass thin-walled parts in GMAW-based additive manufacturing. *J. Mater. Process. Technol.* **2018**, *252*, 128–136. [[CrossRef](#)]
3. Everton, S.K.; Hirsch, M.; Stravroulakis, P.; Leach, R.K.; Clare, A.T. Review of in-situ process monitoring and in-situ metrology for metal additive manufacturing. *Mater. Des.* **2016**, *95*, 431–445. [[CrossRef](#)]
4. Tofail, S.A.M.; Koumoulos, E.P.; Bandyopadhyay, A.; Bose, S.; O’Donoghue, L.; Charitidis, C. Additive manufacturing: Scientific and technological challenges, market uptake and opportunities. *Mater. Today* **2017**, *21*, 22–37. [[CrossRef](#)]
5. Ford, S.; Despeisse, M. Additive manufacturing and sustainability: An exploratory study of the advantages and challenges. *J. Clean. Prod.* **2016**, *137*, 1573–1587. [[CrossRef](#)]
6. Rejeski, D.; Zhao, F.; Huang, Y. Research needs and recommendations on environmental implications of additive manufacturing. *Addit. Manuf.* **2018**, *19*, 21–28. [[CrossRef](#)]
7. García-Domínguez, A.; Claver, J.; Sebastián, M.A. Propuestas para la optimización de piezas para fabricación aditiva. *Dyna* **2018**, *93*, 293–300. [[CrossRef](#)]
8. García-Domínguez, A.; Claver, J.; Sebastián, M.A. Methodology for the optimization of work pieces for additive manufacturing by 3D printing. *Procedia Manuf.* **2017**, *13*, 910–915. [[CrossRef](#)]
9. Momeni, F.; Liu, X.; Ni, J. A review of 4D printing. *Mater. Des.* **2017**, *122*, 42–79. [[CrossRef](#)]
10. Zhao, F.; Li, D.; Jin, Z. Preliminary Investigation of Poly-Ether-Ether-Ketone Based on Fused Deposition Modeling for Medical Applications. *Materials* **2018**, *11*, 288. [[CrossRef](#)] [[PubMed](#)]

11. García-Domínguez, A.; Claver, J.; Camacho, A.M.; Sebastián, M.A. Valuation of Strategies for the Incorporation of 3D Printing Contents in the Teaching of Subjects Linked to Productive Processes from Different Approaches. In *Materials Science Forum*; Trans Tech Publications: Zurich, Switzerland, 2017; Volume 903, ISBN 9783035711820.
12. Hull, C. Apparatus for Production of Three-Dimensional Objects by Stereolithography. U.S. Patent 4,575,330, 8 August 1984.
13. Gibson, I.; Rosen, B.; Stucker, D. *Additive Manufacturing Technologies*; Springer: New York, NY, USA, 2015.
14. ISO 17296-2:2015. *Additive Manufacturing—General Principles—Part 2: Overview of Process Categories and Feedstock*; International Organization for Standardization: Geneva, Switzerland, 2015.
15. Goh, G.D.; Dikshit, V.; Nagalingam, A.P.; Goh, G.L.; Agarwala, S.; Sing, S.L.; Wei, J.; Yeong, W.Y. Characterization of mechanical properties and fracture mode of additively manufactured carbon fiber and glass fiber reinforced thermoplastics. *Mater. Des.* **2018**, *137*, 79–89. [[CrossRef](#)]
16. Domingo-Espin, M.; Puigoriol-Forcada, J.M.; Garcia-Granada, A.A.; Llumà, J.; Borros, S.; Reyes, G. Mechanical property characterization and simulation of fused deposition modeling Polycarbonate parts. *Mater. Des.* **2015**, *83*, 670–677. [[CrossRef](#)]
17. Mohamed, O.; Masood, S.; Bhowmik, J. Analytical Modelling and Optimization of the Temperature-Dependent Dynamic Mechanical Properties of Fused Deposition Fabricated Parts Made of PC-ABS. *Materials* **2016**, *9*, 895. [[CrossRef](#)] [[PubMed](#)]
18. Tymrak, B.M.; Kreiger, M.; Pearce, J.M. Mechanical properties of components fabricated with open-source 3-D printers under realistic environmental conditions. *Mater. Des.* **2014**, *58*, 242–246. [[CrossRef](#)]
19. Chacón, J.M.; Caminero, M.A.; García-Plaza, E.; Núñez, P.J. Additive manufacturing of PLA structures using fused deposition modelling: Effect of process parameters on mechanical properties and their optimal selection. *Mater. Des.* **2017**, *124*, 143–157. [[CrossRef](#)]
20. ISO 17296-3:2014. *Additive Manufacturing—General Principles. Part 3: Main Characteristics and Corresponding Test Methods*; International Organization for Standardization: Geneva, Switzerland, 2014.
21. ISO 527-2:2012. *Plastics—Determination of Tensile Properties—Part 2: Test Conditions for Moulding and Extrusion Plastics*; International Organization for Standardization: Geneva, Switzerland, 2012.
22. ISO/ASTM 52921:2013. *Standard Terminology for Additive Manufacturing—Coordinate Systems and Test Methodologies*; International Organization for Standardization: Geneva, Switzerland, 2013.
23. ASTM D638-14: 2014. *Standard Test Method for Tensile Properties of Plastics*; ASTM International: West Conshohocken, PA, USA, 2014.
24. Forster, A.M. *Materials Testing Standards for Additive Manufacturing of Polymer Materials: State of the Art and Standards Applicability*; US Department of Commerce, National Institute of Standards and Technology: Gaithersburg, MD, USA, 2015. [[CrossRef](#)]
25. Casavola, C.; Cazzato, A.; Moramarco, V.; Pappalettere, C. Orthotropic mechanical properties of fused deposition modelling parts described by classical laminate theory. *Mater. Des.* **2016**, *90*, 453–458. [[CrossRef](#)]
26. Wu, W.; Geng, P.; Li, G.; Zhao, D.; Zhang, H.; Zhao, J. Influence of Layer Thickness and Raster Angle on the Mechanical Properties of 3D-Printed PEEK and a Comparative Mechanical Study between PEEK and ABS. *Materials* **2015**, *8*, 5834–5846. [[CrossRef](#)] [[PubMed](#)]
27. Rodriguez, J.F.; Thomas, J.P.; Renaud, J.E. Mechanical behavior of acrylonitrile butadiene styrene (ABS) fused deposition materials. Experimental investigation. *Rapid Prototyp. J.* **2006**, *7*, 148–158. [[CrossRef](#)]
28. Ahn, S.; Montero, M.; Odell, D.; Roundy, S.; Wright, P. Anisotropic material properties of fused deposition modeling ABS. *Rapid Prototyp. J.* **2002**, *8*, 248–257. [[CrossRef](#)]
29. Riddick, J.; Hall, A.; Haile, M.; Wahlde, R.; Cole, D.; Biggs, S. Effect of manufacturing parameters on failure in Acrylonitrile-Butadiene-Styrene fabricated by fused deposition modeling. In Proceedings of the 53rd AIAA/ASME/ASCE/AHS/ASC Structures, Structural Dynamics and Materials Conference, Honolulu, HI, USA, 23–26 April 2012; pp. 1–8.
30. Hill, N.; Haghi, M. Deposition direction-dependent failure criteria for fused deposition modeling polycarbonate. *Rapid Prototyp. J.* **2014**, *20*, 221–227. [[CrossRef](#)]
31. Bellini, A.; Selcuk, G. Mechanical characterization of parts fabricated using fused deposition modeling. *Rapid Prototyp. J.* **2003**, *9*, 252–264. [[CrossRef](#)]
32. Sood, A.K.; Ohdar, R.K.; Mahapatra, S.S. Parametric appraisal of mechanical property of fused deposition modelling processed parts. *Mater. Des.* **2010**, *31*, 287–295. [[CrossRef](#)]

33. Huang, B.; Singamneni, S. Raster angle mechanics in fused deposition modelling. *J. Compos. Mater.* **2015**, *49*, 363–383. [[CrossRef](#)]
34. Dawoud, M.; Taha, I.; Ebeid, S.J. Mechanical behaviour of ABS: An experimental study using FDM and injection moulding techniques. *J. Manuf. Process.* **2016**, *21*, 39–45. [[CrossRef](#)]
35. Masood, S.H.; Mau, K.; Song, W. Tensile properties of processed fdm polycarbonate material. In *Materials Science Forum*; Trans Tech Publications: Zurich, Switzerland, 2010; pp. 2556–2559.
36. Fernandez-Vicente, M.; Calle, W.; Ferrándiz, S.; Conejero, A. Effect of infill parameters on tensile mechanical behavior in desktop 3D printing. *3D Print. Addit. Manuf.* **2016**, *3*, 183–192. [[CrossRef](#)]
37. Sood, A.K.; Ohdar, R.K.; Mahapatra, S.S. Experimental investigation and empirical modelling of FDM process for compressive strength improvement. *J. Adv. Res.* **2012**, *3*, 81–90. [[CrossRef](#)]
38. Yin, J.; Lu, C.; Fu, J.; Huang, Y.; Zheng, Y. Interfacial bonding during multi-material fused deposition modeling (FDM) process due to inter-molecular diffusion. *Mater. Des.* **2018**, *150*, 104–112. [[CrossRef](#)]
39. Levenhagen, N.P.; Dadmun, M.D. Interlayer diffusion of surface segregating additives to improve the isotropy of fused deposition modeling products. *Polymer* **2018**. in Press. [[CrossRef](#)]
40. Ravi, A.K.; Deshpande, A.; Hsu, K.H. An in-process laser localized pre-deposition heating approach to inter-layer bond strengthening in extrusion based polymer additive manufacturing. *J. Manuf. Process.* **2016**, *24*, 179–185. [[CrossRef](#)]
41. Parandoush, P.; Lin, D. A review on additive manufacturing of polymer-fiber composites. *Compos. Struct.* **2017**, *182*, 36–53. [[CrossRef](#)]
42. Bose, S.; Ke, D.; Sahasrabudhe, H.; Bandyopadhyay, A. Additive manufacturing of biomaterials. *Prog. Mater. Sci.* **2018**, *93*, 45–111. [[CrossRef](#)]
43. Rodríguez-Panes, A.; Claver, J.; Camacho, A.M.; Sebastián, M.Á. Análisis normativo y evaluación geométrica de probetas para la caracterización mecánica de piezas obtenidas por fabricación aditiva mediante FDM. In *Actas del XXII Congreso Nacional de Ingeniería Mecánica*; CNIM: Madrid, Spain, 2018; pp. 1–11.
44. Wendt, C.; Batista, M.; Moreno, E.; Valerga, A.P.; Fernández-Vidal, S.R.; Droste, O.; Marcos, M. Preliminary Design and Analysis of Tensile Test Samples Developed by Additive Manufacturing. *Procedia Eng.* **2015**, *132*, 132–139. [[CrossRef](#)]
45. Dizon, J.R.C.; Espera, A.H.; Chen, Q.; Advincula, R.C. Mechanical characterization of 3D-printed polymers. *Addit. Manuf.* **2018**, *20*, 44–67. [[CrossRef](#)]
46. ISO 527-1:2012. *Plastics—Determination of Tensile Properties—Part 1: General Principles*; International Organization for Standardization: Geneva, Switzerland, 2012.



© 2018 by the authors. Licensee MDPI, Basel, Switzerland. This article is an open access article distributed under the terms and conditions of the Creative Commons Attribution (CC BY) license (<http://creativecommons.org/licenses/by/4.0/>).

Article

Surface Quality Enhancement of Fused Deposition Modeling (FDM) Printed Samples Based on the Selection of Critical Printing Parameters

Mercedes Pérez ¹, Gustavo Medina-Sánchez ¹, Alberto García-Collado ¹, Munish Gupta ² and Diego Carou ^{1,3,*}

¹ Department of Mechanical and Mining Engineering, University of Jaén, EPS de Jaén, Campus LasLagunillas, 23071 Jaén, Spain; mpj00011@red.ujaen.es (M.P.); gmedina@ujaen.es (G.M.-S.); acollado@ujaen.es (A.G.-C.)

² Mechanical Engineering Department, National Institute of Technology, Hamirpur, H.P. 177005, India; munishguptanit@gmail.com

³ Centre for Mechanical Technology and Automation (TEMA), University of Aveiro, Campus Santiago, 3810-193 Aveiro, Portugal

* Correspondence: dcarou@ujaen.es; Tel.: +34-953-211-712; Fax: +34-953-212-420

Received: 29 June 2018; Accepted: 6 August 2018; Published: 8 August 2018

Abstract: The present paper shows an experimental study on additive manufacturing for obtaining samples of polylactic acid (PLA). The process used for manufacturing these samples was fused deposition modeling (FDM). Little attention to the surface quality obtained in additive manufacturing processes has been paid by the research community. So, this paper aims at filling this gap. The goal of the study is the recognition of critical factors in FDM processes for reducing surface roughness. Two different types of experiments were carried out to analyze five printing parameters. The results were analyzed by means of Analysis of Variance, graphical methods, and non-parametric tests using Spearman's ρ and Kendall's τ correlation coefficients. The results showed how layer height and wall thickness are the most important factors for controlling surface roughness, while printing path, printing speed, and temperature showed no clear influence on surface roughness.

Keywords: 3D printing; additive manufacturing; ANOVA; correlation coefficients; fused deposition modeling; non-parametric tests; surface roughness

1. Introduction

1.1. Additive Manufacturing

Currently, the manufacturing industry is a sector highly globalized with a constant need for productivity gains and innovation. In this regard, additive manufacturing (AM) is considered to be one of the latest manufacturing revolutions and a future leading edge technology [1]. Additive manufacturing is entering the market to meet the demand of custom parts of complex geometry and reduce investment in tooling. Nowadays, this manufacturing process is still considered as a promising technology and is studied extensively in order to assess its viability in commercial applications such as electronics (resistors and sensors), optical (antennas), medical (artificial hip joints, bone structures, and tissue scaffolds), automotive, communication, and aerospace industries (engines, turbines, and thermal insulation coatings) [2]. Despite the great improvements that have been made in recent years, additive manufacturing still has some limitations. For instance, Orpalo and Piegl [3] identified ten challenges that should be conveniently studied and solved in coming years, such as shape optimization, design for 3D printing, or pre- and post-processing.

Additive manufacturing is characterized by the manufacture of pieces from a CAD model through the accumulation and joining of layers for obtaining the desired physical model. Recently,

ASTM International defined a body of terms for additive manufacturing [4]. The different types of processes can be classified depending on [5]: (a) raw material (liquid, powder or solid); and (b) the kind of physical joint between the material. Currently, there are available several processes such as Stereolithography (SLA) [6], Selective Laser Sintering/Melting (SLS/SLM) [7], Laminated Object Manufacturing (LOM) [8], and Fused Deposition Modeling (FDM) [9,10].

The selection of the additive manufacturing process must take into account the pros and cons of each of the technologies. For instance, the FDM process is simple, which makes it a suitable candidate for being chosen by general users. Its main advantages are [10–13]: low machinery cost, no expensive tooling is necessary, broad range of materials, high durability of the components, acceptable dimensional accuracy, and not being time consuming. But, the process also has some disadvantages, such as low mechanical strength, difficulty to obtain thin walls, and poor surface quality. Polymers are widely used as the main base material in FDM processes. Typical materials include PLA [14] and ABS [15], but composite materials are also being adopted for manufacturing complex components. For instance, Fe-nylon6 composite wires were compared to ABS solutions, concluding that the composite materials are highly wear resistant [16]. Polypropylene reinforced with glass-fiber was studied, showing adequate mechanical properties for small series of parts [17].

Although FDM processes have significant industrial value for manufacturing complex components, there is a need to carry out proper research focused on prominent aspects such as surface roughness and performance optimization. The performance of the manufactured parts depends upon a large number of process factors, such as the type of material and process parameters, so it is quite difficult to obtain an ideal FDM process that fulfils all the requirements, particularly producing products of high surface quality.

1.2. Surface Quality in FDM Processes

In additive manufacturing, in general, pre-processing and post-processing activities should be carried out [3]. However, the quality of the parts is not adequate when compared to other mature manufacturing processes, such as machining. One of the main problems for obtaining good surface quality in additive manufacturing is the staircase effect. According to Strano et al. [18], usually manual post-processing operations are needed for obtaining adequate surface roughness because complex geometries compromise the advantages of additive manufacturing. Pandey et al. [19] analyzed the staircase effect that generates “chordal error” between an original surface of a CAD model and the corresponding triangle in the tessellated model. The authors concluded that the tessellation and slicing during the manufacturing process are two sources of surface inaccuracies that must be taken into account.

Various studies have been specifically carried out on FDM process parameters, discussing their effect on outputs, such as mechanical properties, and surface topography and quality [20–22]. For instance, Altan et al. [14] studied the effect of process parameters on surface roughness and the tensile strength on polylactic acid (PLA) samples. The samples were fabricated as per the ASTM standards and a Taguchi L16 experimental design, using three parameters: layer thickness, deposition head velocity, and nozzle temperature. The authors concluded that the layer thickness and deposition head velocity are dominant factors on surface roughness.

Campbell et al. [23] investigated surface roughness for different materials. The authors found that, in the case of ABS material, when using layer thickness of 0.253 mm, the surface roughness values for FDM processes ranged between 9 μm and 40 μm . Recently, Akande et al. [24] analyzed the optimal process parameters for obtaining good surface finish and dimensional accuracy. The authors employed a layer height of 0.25 and 0.5 mm, varying the filling density and speed of deposition, identifying that the surface roughness for PLA material ranged between 2.46 μm and 22.48 μm . Altan et al. [14] used layer thickness between 0.1 mm and 0.4 mm to create PLA samples using a FDM process. The surface roughness obtained varied within the range of 9.102 to 10.275 μm .

From previous scientific records, it has been identified that the performance of the FDM process extensively depends upon its process parameters and their levels. However, the number of publications dealing with the identification of critical factors and the optimization of the manufacturing process depending on adequate selection of factors and levels is still limited, particularly when it comes to surface roughness.

The optimization of the process parameters used for printing is an adequate strategy for improving part performance in terms of surface finish. So, the present paper addresses the study of surface roughness for FDM pieces, which has not been studied in detail in the literature. The paper shows an experimental study on fused deposition modeling, analyzing the quality of the parts after varying a set of printing parameters: layer height, wall thickness, printing speed, temperature, and printing path using both statistical and graphical methods.

2. Materials and Methods

2.1. Materials

The 3D printer used was a WITBOX printer (Figure 1) by BQ manufacturer (Madrid, Spain) using FDM technology. It is equipped with 0.4 mm diameter nozzle and glass cold base, A4-size (297 × 210 mm). The recommended printing speed is 50 mm/s and the maximum is 80 mm/s. The own-design extruder has a blower for cooling printed objects. The software used and recommended by the WITBOX printer manufacturer is Ultimaker Cura Software 3.2.1., which allows using STL and G-Code standards.

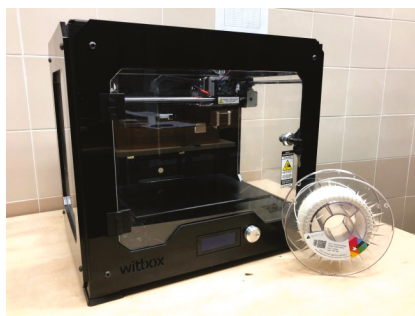


Figure 1. WITBOX printer and PLA filament.

Polylactic acid (PLA) (Smart Materials 3D, Alcalá la Real, Spain) has been used as base material (Table 1). The company that provided the material was Smart Materials 3D. It does not incorporate recycled or recovered material. It is fully stabilized and it has a diameter of 1.75 mm with a variability of ± 0.03 mm in diameter. Besides, no warping is expected.

Table 1. Material properties.

Chemical Name	Composition	Density (g/cm ³)	Printing Temperature (°C)	Diameter (mm)
Polylactic Acid	PLA (Polylactide Resin) 99% CAS: 9051-89-2	1.24	220 ± 20	1.75 ± 0.03

Surface roughness was measured using a handheld Mitutoyo Surftest SJ-210 (Mitutoyo, Kawasaki, Japan) profilometer (Figure 2a) with sampling length of 2.5 mm and measuring speed of 0.5 mm/s. With this technology, cylindrical samples such as those shown in Figure 2b were measured.



Figure 2. (a) Surface roughness measurement setup (b) Printed samples for experiment 1.

2.2. Experimental Plan

In additive manufacturing, there are several factors that could influence surface roughness, such as [25–28]:

- Material extrusion: temperature, viscosity, density, type of material, and mechanical properties.
- Chamber: temperature, pressure, vibrations, position of the platform, position of the extruder, system coordinates, and heat evacuation.
- Extruder: speed, angle of inclination, diameter of extrusion, vibration, and acceleration.
- Deposition characteristics: building direction, wall thickness, layer height, orientation, external geometry, and speed.

Due to the high number of factors, a selection of factors to carry out a more economical and practical study was made. The experimental investigation was divided into two stages. The first stage was designed as a screening stage [29] to identify the most critical printing factors for surface roughness. The second stage was performed in order to increase the knowledge of the printing factors based on the results of the first stage.

All printed samples had dimensions of 30 mm in diameter and 40 mm in height. The first analysis was done to study the influence of layer height, wall thickness, printing speed, and temperature (material). These factors were varied using two levels: minimum and maximum. So, eight tests were performed by means of a fractional factorial design of four factors with two levels. Fractional factorial designs allow carrying out experimental studies with limited number of experiments and, thus, reducing cost and time.

For layer height, values of 0.15 and 0.25 mm were chosen. The first one is the minimum recommended by the predefined options of the Cura software. The second one is a higher value, which was selected expecting an increase in surface roughness as it was identified in the literature. For printing speed, a value of 40 mm/s was selected; a speed lower than that recommended by the printer manufacturer, and a value of 80 mm/s, the maximum recommended. For temperature, a maximum value lower than the one recommended by the PLA filament manufacturer (240 °C) was selected, i.e., 225 °C and, as minimum value, 195 °C was selected that lies slightly below the minimum recommended (200 °C). Finally, values of 1 and 3 mm were selected for wall thickness, considering that wall thickness should be higher than two times the size of the nozzle extruder (0.4 mm), according to Noorani [30]. The experimental factors, along their symbols, units, and levels are listed in Table 2.

Factors and levels for experiment 1 allow generating an experimental plan to carry out experiment 1, as shown in Table 3. The experimental plan was made in a random order to guarantee that the observations or errors are independently distributed random variables [29].

Table 2. Experimental factors for experiment 1.

Factor	Symbol	Units	Levels
Layer height	LH	mm	0.15, 0.25
Printing speed	PS	mm/s	40, 80
Temperature	T	°C	195, 225
Wall thickness	WT	mm	1, 3

Table 3. Experimental plan for experiment 1.

Test	LH (mm)	PS (mm/s)	T (°C)	WT (mm)
1	0.25	40	195	3
2	0.15	40	225	3
3	0.15	80	195	3
4	0.25	80	195	1
5	0.15	40	195	1
6	0.25	80	225	3
7	0.15	80	225	1
8	0.25	40	225	1

The second analysis was done to specifically study the influence of wall thickness and its relation to the printing path: zig-zag, concentric, and grid. These tests were performed using the parameters used in the first stage to obtain one of the best surface roughness, so the lowest layer height was chosen (0.15 mm), but it was decided to also have a reduced printing time (estimated printing time of 47 min), so the printing speed of 80 mm/s was selected. Moreover, temperature of 225 °C was chosen. So, two factors were analyzed in this stage, using three levels for printing strategy and five for wall thickness. For printing path, concentric, zig-zag, and grid were selected. The experimental factors, along with their symbols, units, and levels are listed in Table 4.

Table 4. Experimental factors for experiment 2.

Factor	Symbol	Units	Levels
Layer height	LH	mm	0.15
Printing speed	PS	mm/s	80
Temperature	T	°C	225
Printing path	PP	-	Concentric, zig-zag, grid
Wall thickness	WT	mm	0.50, 0.75, 1.00, 1.25, 1.50

The experiment was done using a full factorial design and the experimental tests were performed in a random order as shown in Table 5.

Table 5. Experimental plan for experiment 2.

Test	LH (mm)	PS (mm/s)	T (°C)	PP	WT (mm)
1	0.15	80	225	Zig-zag	0.5
2	0.15	80	225	Grid	0.75
3	0.15	80	225	Zig-zag	1.5
4	0.15	80	225	Concentric	0.75
5	0.15	80	225	Concentric	1
6	0.15	80	225	Zig-zag	1
7	0.15	80	225	Grid	0.5
8	0.15	80	225	Concentric	1.5
9	0.15	80	225	Zig-zag	0.75
10	0.15	80	225	Concentric	1.25
11	0.15	80	225	Grid	1
12	0.15	80	225	Grid	1.5
13	0.15	80	225	Concentric	0.5
14	0.15	80	225	Zig-zag	1.25
15	0.15	80	225	Grid	1.25

2.3. Surface Roughness Evaluation

Surface roughness was evaluated in terms of the arithmetic average of the roughness profile (R_a). Six surface roughness measurements were taken in each sample. The samples were divided into two sections: bottom (printing start) and top (printing end) sections. In addition, three generatrices were drawn on the surface. No measurement was done in the section where the zipper effect generated by the layer change can be seen. The measurements of R_{a1} , R_{a2} , and R_{a3} were taken at the top in the generatrices in a clockwise direction. The measurements of R_{a4} , R_{a5} , and R_{a6} were taken at the bottom in the generatrices in a counter clockwise direction (Figure 3). Therefore, 48 and 90 measurements were obtained for experiment 1 and 2, respectively. Finally, with the six surface roughness measurements, the average roughness was calculated for each sample.

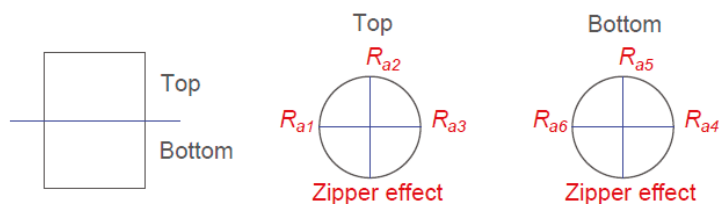


Figure 3. Details of the measurement procedure.

3. Results and Discussion

3.1. Surface Roughness Results

The surface roughness results obtained, their mean values and standard deviation (SD), in terms of R_a , are listed in Tables 6 and 7 for experiment 1 and 2, respectively.

Table 6. Experimental surface roughness results for experiment 1.

Test	R_{a1} (μm)	R_{a2} (μm)	R_{a3} (μm)	R_{a4} (μm)	R_{a5} (μm)	R_{a6} (μm)	R_a (μm)	SD (μm)
1	26.045	20.202	23.188	23.284	19.558	24.358	22.773	2.474
2	20.473	20.497	20.565	17.776	18.318	22.525	20.026	1.728
3	17.937	18.46	21.145	17.205	18.182	21.051	18.997	1.680
4	19.756	17.258	21.908	18.732	19.511	20.347	19.585	1.559
5	16.066	15.252	15.338	14.842	15.239	15.524	15.377	0.405
6	25.138	24.092	25.052	19.995	20.064	22.725	22.844	2.348
7	18.252	16.929	17.705	14.073	15.709	16.697	16.561	1.499
8	23.226	23.809	23.547	21.582	19.814	22.063	22.340	1.512

Table 7. Experimental surface roughness results for experiment 2.

Test	R_{a1} (μm)	R_{a2} (μm)	R_{a3} (μm)	R_{a4} (μm)	R_{a5} (μm)	R_{a6} (μm)	R_a (μm)	SD (μm)
1	12.761	14.304	13.034	12.87	16.46	12.586	13.669	1.499
2	15.695	16.514	13.67	15.371	16.64	16.431	15.720	1.123
3	19.471	21.602	22.279	19.625	20.775	20.536	20.715	1.096
4	16.733	18.797	14.103	13.592	17.96	14.047	15.872	2.250
5	16.108	16.705	15.439	15.04	15.91	13.965	15.528	0.955
6	16.082	18.292	16.925	14.068	14.827	14.734	15.821	1.590
7	11.591	13.259	14.995	11.947	19.792	14.446	14.338	2.987
8	18.971	19.016	20.688	19.352	20.013	18.499	19.423	0.797
9	16.789	16.559	16.638	14.482	16.302	15.181	15.992	0.939
10	16.39	17.199	19.007	16.626	18.918	16.354	17.416	1.236
11	17.142	14.435	14.746	16.892	17.001	16.796	16.169	1.232
12	16.283	16.893	18.545	16.305	17.521	17.145	17.115	0.849
13	10.698	12.158	12.455	11.721	18.122	11.319	12.746	2.706
14	18.357	19.093	19.091	17.274	20.99	17.999	18.801	1.275
15	18.175	18.1	20.777	16.035	15.569	16.799	17.576	1.891

From the tables, it is possible to see how the values of surface roughness are high compared to other conventional manufacturing processes, such as machining. In all cases, the values are higher than 12 μm . Moreover, the results present high variability depending on the measuring point for all the tests. This variability makes it difficult to obtain conclusions on surface roughness depending on the measuring location (bottom and top). No clear trends can be found depending on the location. The standard deviation calculated for all tests show clearly this performance. It is important to see how the ranges obtained for the mean values are also high. So, for experiment 1, the values varied between 15.377 μm and 22.844 μm and, for experiment 2, they varied between 12.746 μm and 20.715 μm . Mean values for experiment 1 and experiment 2 were 19.813 and 16.460 μm , respectively. These results are used for selecting a layer height of 0.15 mm for experiment 2, expecting that the surface roughness in experiment 2 would be similar to that obtained in experiment 1.

3.2. Identification of Critical Factors

Statistical methods are adequate tools for identifying influential factors in datasets such as those obtained for surface roughness. Thus, Analysis of Variance (ANOVA) is performed for both experiment 1 and 2. The results are listed in Tables 8 and 9 for experiment 1 and 2, respectively.

Table 8. Analysis of variance for experiment 1.

Source of Variation	Df	Sum sq	Mean sq	F Value	Pr (>F)
LH	1	34.366	34.366	41.3466	0.007625
PS	1	0.799	0.799	0.9619	0.399039
T	1	3.174	3.174	3.8186	0.145684
WT	1	14.518	14.518	17.4669	0.024956
Residuals	3	2.494	0.831		
Total	7	55.351			

Table 9. Analysis of variance for experiment 2.

Source of Variation	Df	Sum sq	Mean sq	F Value	Pr (>F)
PP	2	2.184	1.0918	1.2238	0.3438
WT	4	54.192	13.5480	15.1850	8.139×10^{-4}
Residuals	8	7.138	0.8922		
Total	14	63.514			

The normality of the residuals is checked using the Shapiro–Wilk test. Normality is verified by the calculated statistics and p -values: 0.86373 (W statistic) and 0.1308 (p -value), and 0.95369 (W statistic), and 0.5844 (p -value) for experiment 1 and 2, respectively. In both cases, the p -values are lower than the statistic, so no departure from normality was identified.

Considering that p -values lower than 0.05 are related to influential sources of variation, from Table 8, it is possible to recognize that layer height and wall thickness are influential factors on surface roughness. In particular, layer height has the lowest value. In addition, printing speed and temperature can be considered as nonsignificant factors for surface roughness. When analyzing the results listed in Table 9, only wall thickness is a significant source of variation, with printing path being nonsignificant.

3.3. Correlations between Surface Roughness and the Analyzed Factors

In the previous section, the influential factors on surface roughness: layer height and wall thickness in experiment 1, and wall thickness in experiment 2, were identified. To evaluate the influence of these factors on surface roughness, graphical methods for identifying trends and additional statistical analysis for checking correlations were used. Based on the ANOVA results, the results of

experiment 1 are plotted in Figure 4. In the figure, the tests are grouped by layer height. In the figure, it is possible to see clearly how the surface roughness obtained for the layer height of 0.15 mm is lower than the one obtained for the layer height of 0.25 mm. This result agrees well with the conventional knowledge on surface roughness obtained in additive manufacturing processes [18,31]. Moreover, it is possible to see how the lowest surface roughness was obtained for the tests that used the lowest layer height and wall thickness (e_5 and e_7).

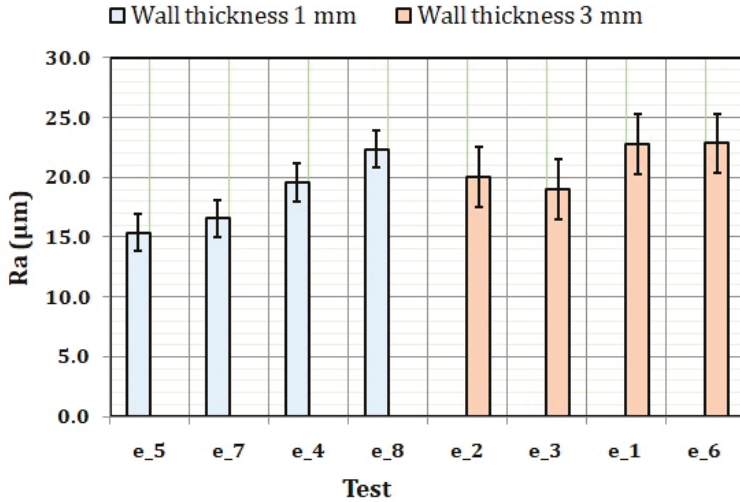


Figure 4. Surface roughness results of experiment 1 grouped by layer height.

When grouping the results by wall thickness and plotting them, it is possible to appreciate how wall thickness has a clear influence on surface roughness. Again, obviously, the results for the wall thickness of 1 mm and layer height of 0.15 mm (e_5 and e_7) are those that produced the lowest surface roughness.

Similar results to those obtained in Figure 5 were obtained when grouping the results of experiment 2 by wall thickness. In this case, the influence of the printing path (strategy) is negligible. In general, an increasing trend can be seen when wall thickness is increased, as seen in Figure 6. According to our best knowledge, the influence of wall thickness on surface roughness has not been previously studied in detail in the literature. In addition, a clear relation was not found between printing path strategy and wall thickness, though this relation should be studied in detail for lower values of wall thickness.

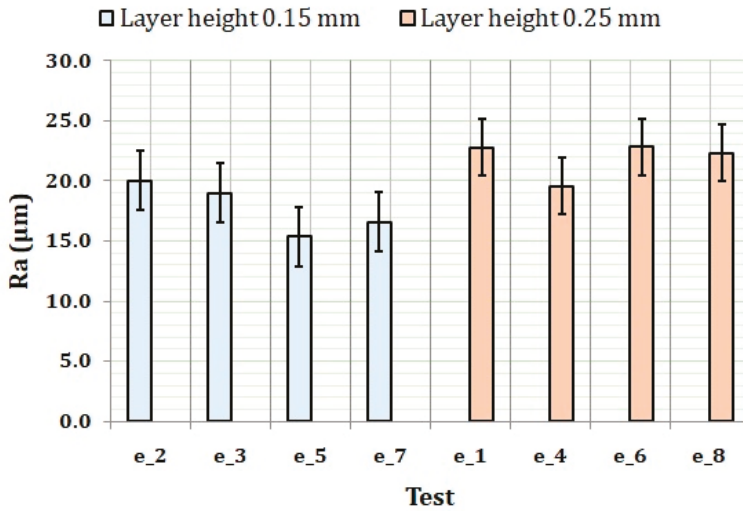


Figure 5. Surface roughness results of experiment 1 grouped by wall thickness.

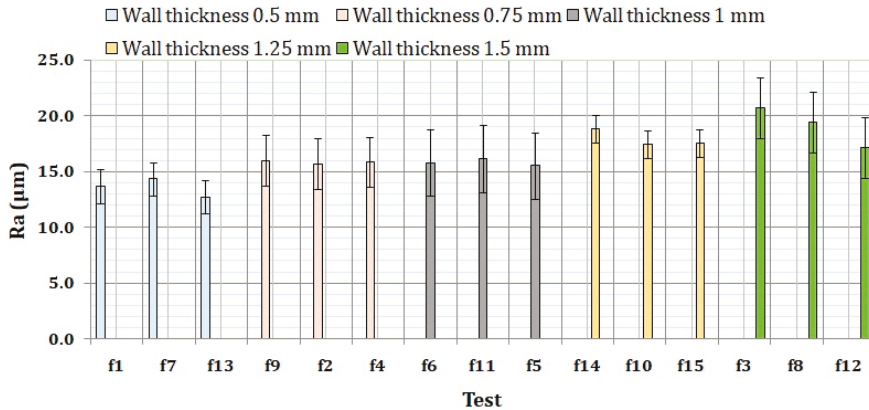


Figure 6. Surface roughness results of experiment 2 grouped by wall thickness.

From the previous results, it is clear that both layer height and wall thickness have an important influence on surface roughness. However, the influence of the printing speed and temperature is not clear in the figures, as it was identified using the ANOVA results.

In order to confirm the influence of the different factors on surface roughness, an analysis based on the use of non-parametric tests was carried out. In this sense, Spearman’s ρ and Kendall’s τ correlation coefficients are calculated as done by Carou et al. [32]. These two tests are useful to identify monotonic relationships, being resistant to the effect of outliers [33]. Moreover, it is important to note that these tests do not assume a specific parametric model or specific distributions for the data [34]. The two coefficients can be calculated using Equations (1) and (2) for the Spearman’s ρ and Kendall’s τ , respectively [33,34].

$$\rho = \frac{\sum_{i=1}^n (R_{Xi} - R_{Yi})^2 - n(n + 1)^2 / 2}{n(n^2 - 1) / 2} \tag{1}$$

$$\tau = \frac{P - M}{n(n-1)/2} \quad (2)$$

n is the number of pairs (x_i, y_i) ; R_{xi} and R_{yi} the ranks of x and y , respectively; and P and M , the numbers of pluses and minuses, respectively. R Software was used for calculating the coefficients for the different factors: layer height, printing path, printing speed, temperature, and wall thickness versus surface roughness based on the results listed in Tables 6 and 7. The results obtained are shown in Table 8. The correlation coefficients can vary from -1 (perfect negative association) to $+1$ (perfect positive association). When there is no correlation, the coefficient gets a value of 0 [33]. In the table, the correlation coefficients are listed along with their p -values.

In Table 10, similarly to the ANOVA results, it is possible to see how only layer height and wall thickness resulted as significant factors when computing the coefficients. Therefore, it is possible to state that no clear relation exists between surface roughness and printing path, printing speed, and temperature. Besides, the calculated coefficients for these relations are close to 0 (in all cases, lower than 0.3273268).

Table 10. Correlation coefficients for experiment 1 and 2 versus the analyzed factors.

	Experiment 1		Experiment 2	
	Spearman's ρ - p -value	Kendall's τ - p -value	Spearman's ρ - p -value	Kendall's τ - p -value
Layer height	0.7637626 0.0274 *	0.6614378 0.04331 *	-	-
Printing speed	-0.1091089 0.797	-0.09449112 0.7728	-	-
Temperature	0.3273268 0.4287	0.2834734 0.3865	-	-
Wall thickness	0.5455447 0.1619	0.4724556 0.1489	0.8946933 6.729×10^{-6} *	0.7612299 0.0001789 *
Printing path	-	-	0.1322876 0.6384	0.1014185 0.6345

Note: * significant factor considering p -value < 0.05 .

Regarding layer height and wall thickness, the coefficients have positive values. So, when increasing these two factors, higher values of surface roughness are expected. Although their values are not very close to $+1$, they show a monotonic correlation with values ranging from 0.47 to 0.90 for both Spearman's ρ and Kendall's τ coefficients. The results show small differences between the values obtained for these two coefficients. However, a bigger difference was found when comparing the results of experiment 1 and 2. In this case, it should be noted that only 8 experiments were carried out in experiment 1, while 15 experiments were carried out in experiment 2. So, the dataset of experiment 2 should be considered as more reliable for identifying monotonic relations. In fact, the calculated coefficients for experiment 2 show a clear correlation between surface roughness and wall thickness with p -value below 0.05 and values for the correlation coefficients very close to $+1$, while the p -value in the case of experiment 1 was not below 0.05.

Finally, from the graphical analysis and the statistical analysis using ANOVA and non-parametric tests, a general recommendation can be drawn. So, it is highlighted that when surface roughness is a critical requirement in additive manufacturing, particularly using FDM processes, layer height and wall thickness should be fixed at lower values. It seems clear that layer height should be as low as possible to minimize the staircase effect. However, further research should be carried out for wall thickness to understand whether it is possible to reduce its value to a minimum or not, considering issues such as the size of the nozzle extruder and even printing path strategies that could have a negative impact when the wall thickness is too small.

4. Conclusions and Future Work

The present study shows an experimental investigation on surface roughness obtained in additive manufacturing processes. Fused Deposition Modeling (FDM) technology was specifically analyzed when manufacturing PLA samples. Several manufacturing parameters (layer height, printing path, printing speed, temperature, and wall thickness) were varied and the results analyzed by means of graphical and statistical analysis. The main conclusions of the investigation include the following:

- The quality of the manufactured parts depends greatly on the selection of the printing parameters. In particular, previous results that indicate that the layer height is a critical factor were validated using Analysis of Variance. But, in addition, it was found that wall thickness has an important influence on the results, which was given less attention by researchers.
- Some parameters seem to have no clear influence on the results, specifically, printing path, printing speed, and temperature. However, it should be noted that only three printing strategies were analyzed in the present study: grid, concentric, and zig-zag.
- By using Spearman's ρ and Kendall's τ correlation coefficients, the influence of layer height and wall thickness on the results was verified, especially, for experiment 2, obtaining correlation coefficients very close to +1 with p -values lower than 0.05.
- The effect of the layer height and wall thickness on surface roughness is to worsen the quality of the surface when one of these parameters is increased or when both are increased.
- As criteria for improving surface quality in FDM manufacturing processes, it is recommended to use reduced values of layer height, diminishing the importance of the staircase effect and also wall thickness that is generally selected based on the size of the nozzle extruder.

The results obtained in the present preliminary study will help establish new lines for future work. For instance, the influence of the material on the results should be considered; particularly the influence of the material (PLA) provided by different manufacturers should be conveniently analyzed. The use of larger datasets and higher ranges for the critical factors for verifying the results would be recommended in new experimental studies. Finally, a comprehensive analysis of the influence of wall thickness should be carried out.

Author Contributions: Conceptualization, M.P., G.M.-S. and D.C.; Data curation, M.P. and D.C.; Formal analysis, M.P. and D.C.; Investigation, M.P., A.G.-C., M.G. and D.C.; Methodology, M.P., G.M.-S. and D.C.; Project administration, M.P., G.M.-S. and D.C.; Resources, M.P., G.M.-S., A.G.-C. and D.C.; Software, M.P., G.M.-S. and D.C.; Supervision, D.C.; Validation, D.C.; Visualization, M.P., M.G. and D.C.; Writing—original draft, M.P., G.M.-S., A.G.-C., M.G. and D.C.; Writing—review & editing, M.P. and D.C.

Funding: This research received no external funding

Acknowledgments: The authors would like to thank the support given by the Mechanical and Energy Engineering (TEP250) research group of the University of Jaén.

Conflicts of Interest: The authors declare no conflict of interest.

References

1. Hopkinson, N.; Hague, R.; Dickens, P. *Rapid Manufacturing: An Industrial Revolution for the Digital Age*; John Wiley & Sons: Hoboken, NJ, USA, 2006; ISBN 9780470032862.
2. Sugavaneswaran, M.; Arumaikkannu, G. Modelling for randomly oriented multi material additive manufacturing component and its fabrication. *Mater. Des.* **2014**, *54*, 779–785. [[CrossRef](#)]
3. Oropallo, W.; Piegl, L.A. Ten challenges in 3D printing. *Eng. Comput.* **2015**, *32*, 135–148. [[CrossRef](#)]
4. ASTM International. *Standard Terminology for Additive Manufacturing Technologies*; ASTM International: West Conshohocken, PA, USA, 2012.
5. Chua, C.K.; Chou, S.M.; Wong, T.S. A study of the state-of-the-art rapid prototyping technologies. *Int. J. Adv. Manuf. Technol.* **1998**, *14*, 146–152. [[CrossRef](#)]
6. Jacobs, P.F. *Rapid Prototyping & Manufacturing: Fundamentals of Stereolithography*; Society of Manufacturing Engineers: Dearborn, MI, USA, 1992; ISBN 9780872634251.

7. Yang, J.; Ouyang, H.; Wang, Y. Direct metal laser fabrication: Machine development and experimental work. *Int. J. Adv. Manuf. Technol.* **2009**, *46*, 1133–1143. [[CrossRef](#)]
8. Mueller, B.; Kochan, D. Laminated object manufacturing for rapid tooling and patternmaking in foundry industry. *Comput. Ind.* **1999**, *39*, 47–53. [[CrossRef](#)]
9. Hutmacher, D.W.; Schantz, T.; Zein, I.; Ng, K.W.; Teoh, S.H.; Tan, K.C. Mechanical properties and cell cultural response of polycaprolactone scaffolds designed and fabricated via fused deposition modeling. *J. Biomed. Mater. Res.* **2001**, *55*, 203–216. [[CrossRef](#)]
10. Yan, X.; Gu, P. A review of rapid prototyping technologies and systems. *Comput. Aided Des. Appl.* **1996**, *28*, 307–318. [[CrossRef](#)]
11. Griffiths, C.A.; Howarth, J.; De Almeida-Rowbotham, G.; Rees, A. A design of experiments approach to optimise tensile and notched bending properties of fused deposition modelling parts. *Proc. Inst. Mech. Eng. Pt. B J. Eng. Manuf.* **2016**, *230*, 1502–1512. [[CrossRef](#)]
12. Raju, M.; Gupta, M.K.; Bhanot, N.; Sharma, V.S. A hybrid PSO–BFO evolutionary algorithm for optimization of fused deposition modelling process parameters. *J. Intell. Manuf.* **2018**. [[CrossRef](#)]
13. Winder, J.; Bibb, R. Medical rapid prototyping technologies: State of the art and current limitations for application in oral and maxillofacial surgery. *J. Oral Maxillofac. Surg.* **2005**, *63*, 1006–1015. [[CrossRef](#)] [[PubMed](#)]
14. Altan, M.; Eryildiz, M.; Gumus, B.; Kahraman, Y. Effects of process parameters on the quality of PLA products fabricated by fused deposition modeling (FDM): Surface roughness and tensile strength. *Mater. Test.* **2018**, *60*, 471–477. [[CrossRef](#)]
15. Mahmood, S.; Qureshi, A.J.; Talamona, D. Taguchi based process optimization for dimension and tolerance control for fused deposition modelling. *Addit. Manuf.* **2018**, *21*, 183–190. [[CrossRef](#)]
16. Garg, H.; Singh, R. Tribological Properties of Fe–Nylon6 Composite Parts Prepared Using Fused Deposition Modelling. *Trans. Indian Inst. Met.* **2016**, *70*, 1241–1244. [[CrossRef](#)]
17. Carneiro, O.S.; Silva, A.F.; Gomes, R. Fused deposition modeling with polypropylene. *Mater. Des.* **2015**, *83*, 768–776. [[CrossRef](#)]
18. Strano, G.; Hao, L.; Everson, R.M.; Evans, K.E. Surface roughness analysis, modelling and prediction in selective laser melting. *J. Mater. Process. Technol.* **2013**, *213*, 589–597. [[CrossRef](#)]
19. Pandey, P.M.; Reddy, V.; Dhande, S.G. Slicing procedures in layered manufacturing: A review. *Rapid Prototyp. J.* **2003**, *9*, 274–288. [[CrossRef](#)]
20. Adel, M.; Abdelaal, O.; Gad, A.; Nasr, A.B.; Khalil, A. Polishing of fused deposition modeling products by hot air jet: Evaluation of surface roughness. *J. Mater. Process. Technol.* **2018**, *251*, 73–82. [[CrossRef](#)]
21. Boschetto, A.; Bottini, L.; Veniali, F. Finishing of Fused Deposition Modeling parts by CNC machining. *Robot. Comput. Integr. Manuf.* **2016**, *41*, 92–101. [[CrossRef](#)]
22. Jin, Y.; Wan, Y.; Zhang, B.; Liu, Z. Modeling of the chemical finishing process for polylactic acid parts in fused deposition modeling and investigation of its tensile properties. *J. Mater. Process. Technol.* **2017**, *240*, 233–239. [[CrossRef](#)]
23. Campbell, R.I.; Martorelli, M.; Lee, H.S. Surface roughness visualisation for rapid prototyping models. *Comput. Aided Des. Appl.* **2002**, *34*, 717–725. [[CrossRef](#)]
24. Akande, S.O. Dimensional Accuracy and Surface Finish Optimization of Fused Deposition Modelling Parts using Desirability Function Analysis. *Int. J. Eng. Res. Appl.* **2015**. [[CrossRef](#)]
25. Bourell, D.; Kruth, J.P.; Leu, M.; Levy, G.; Rosen, D.; Beese, A.M.; Clare, A. Materials for additive manufacturing. *CIRP Ann.* **2017**, *66*, 659–681. [[CrossRef](#)]
26. Hällgren, S.; Pejryd, L.; Ekengren, J. Additive Manufacturing and High Speed Machining -cost Comparison of short Lead Time Manufacturing Methods. *Procedia CIRP* **2016**, *50*, 384–389. [[CrossRef](#)]
27. Umaras, E.; Tsuzuki, M.S.G. Additive Manufacturing—Considerations on Geometric Accuracy and Factors of Influence. *IFAC-Pap. OnLine* **2017**, *50*, 14940–14945. [[CrossRef](#)]
28. Bikas, H.; Stavropoulos, P.; Chryssolouris, G. Additive manufacturing methods and modelling approaches: A critical review. *Int. J. Adv. Manuf. Technol.* **2015**, *83*, 389–405. [[CrossRef](#)]
29. Montgomery, D.C. *Design and Analysis of Experiments*; John Wiley & Sons: Hoboken, NJ, USA, 2017; ISBN 9781119113478.
30. Noorani, R. *3D Printing: Technology, Applications, and Selection*; CRC Press: Boca Raton, FL, USA, 2017; ISBN 9781351651547.

31. Kumbhar, N.N.; Mulay, A.V. Post Processing Methods used to Improve Surface Finish of Products which are Manufactured by Additive Manufacturing Technologies: A Review. *J. Inst. Eng. (India) Ser. C* **2018**, *99*, 481–487. [[CrossRef](#)]
32. Carou, D.; Rubio, E.M.; Lauro, C.H.; Davim, J.P. Experimental investigation on finish intermittent turning of UNS M11917 magnesium alloy under dry machining. *Int. J. Adv. Manuf. Technol.* **2014**, *75*, 1417–1429. [[CrossRef](#)]
33. Gotway, C.A.; Helsel, D.R.; Hirsch, R.M. Statistical Methods in Water Resources. *Technometrics* **1994**, *36*, 323. [[CrossRef](#)]
34. Bodenhofer, U.; Krone, M.; Klawonn, F. Testing noisy numerical data for monotonic association. *Inf. Sci.* **2013**, *245*, 21–37. [[CrossRef](#)]



© 2018 by the authors. Licensee MDPI, Basel, Switzerland. This article is an open access article distributed under the terms and conditions of the Creative Commons Attribution (CC BY) license (<http://creativecommons.org/licenses/by/4.0/>).

Article

Study of the Influence of Shielding Gases on Laser Metal Deposition of Inconel 718 Superalloy

Jose Exequiel Ruiz *, Magdalena Cortina, Jon Iñaki Arrizubieta and Aitzol Lamikiz

Department of Mechanical Engineering, University of the Basque Country, Plaza Torres Quevedo 1, 48013 Bilbao, Spain; magdalena.cortina@ehu.eus (M.C.); joninaki.arrizubieta@ehu.eus (J.I.A.); aitzol.lamikiz@ehu.eus (A.L.)

* Correspondence: joseexequiel.ruiz@ehu.eus; Tel.: +34-946-017-347

Received: 28 June 2018; Accepted: 6 August 2018; Published: 9 August 2018

Abstract: The use of the Laser Metal Deposition (LMD) technology as a manufacturing and repairing technique in industrial sectors like the die and mold and aerospace is increasing within the last decades. Research carried out in the field of LMD process situates argon as the most usual inert gas, followed by nitrogen. Some leading companies have started to use helium and argon as carrier and shielding gas, respectively. There is therefore a pressing need to know how the use of different gases may affect the LMD process due there being a lack of knowledge with regard to gas mixtures. The aim of the present work is to evaluate the influence of a mixture of argon and helium on the LMD process by analyzing single tracks of deposited material. For this purpose, special attention is paid to the melt pool temperature, as well as to the characterization of the deposited clads. The increment of helium concentration in the gases of the LMD processes based on argon will have three effects. The first one is a slight reduction of the height of the clads. Second, an increase of the temperature of the melt pool. Last, smaller wet angles are obtained for higher helium concentrations.

Keywords: LMD; laser metal deposition; shielding gas; argon; helium; additive manufacturing; Inconel 718; melt pool temperature

1. Introduction

Laser Metal Deposition (LMD) is an Additive Manufacturing (AM) technology that consists on the deposition of material layers that are melted by a laser source. This process belongs to the Directed Energy Deposition (DED) technology group and enables working with a very wide range of metal materials. The filler material to be deposited is usually supplied in the form of powder and is conducted through a nozzle into the melt pool, which has been created on a substrate surface by a laser beam. In this process, the powder is melted and deposited by creating a new layer of material. Subsequent layers generate geometries, enabling the addition of features to existing parts or the manufacturing of new ones [1].

The entire process is carried out employing two different gas flows: a shielding gas, whose function is the generation of a protective atmosphere so that oxidation reactions are avoided, and a carrier gas that is used to transport the powder through the entire circuit and nozzle to the melt pool. The use of these two different gas flows has direct consequences on the process. Firstly, similar to other welding processes, the shielding gas is necessary to protect the deposited material from oxidation [2]. It represents the largest gas flow used and it has a direct impact on the quality of the deposited material, mainly in the porosity generation, but this phenomenon can be easily avoided by parameters modification [3,4]. Secondly, the carrier gas drags the powder from the powder feeder to the nozzle and into the melt pool. This gas flow accelerates and injects the powder particles at the nozzle exit. The interaction of both, carrier and shielding gas, with the powder and the atmosphere determines the powder distribution in the focal point of the nozzle. This powder distribution is a key factor for the LMD process efficiency [5,6].

Bibliography of LMD process situates argon as the most common gas (both for protective and drag gas), followed by nitrogen. This is due to the fact that nitrogen is mostly unreactive and more economical than argon, but does not always protect the process from chemical reactions, since nitrogen reacts with Ti, Nb, and V [7].

The use of the LMD technology as a manufacturing and repairing technique in industrial fields, like the die and mold and aerospace industry, is increasing within the last years. In these industrial sectors, the process is specially focused on different steel alloys, nickel superalloys [8,9] and titanium alloys. Steels are usually alloyed with vanadium, nickel superalloys, like Inconel 718 or Inconel 625, have titanium and niobium in its chemical composition and one of most typical titanium alloys is Ti6Al4V, which contains both titanium and vanadium. Thus, in these cases nitrogen should not be used as shielding or dragging gas on LMD process.

There are many similarities between the LMD process and Laser Beam Welding in terms of shielding gases. In fact, both use the same heat source and materials must be protected from chemical reactions with a shielding gas. Different research work carried out in the field of Laser Beam Welding states that the use of argon with high densities of energy can lead to plasma formation due to the lower ionization energy of argon compared to other gases, like helium [10]. This plasma formation creates a shield that blocks the laser beam [11], thus reducing the energy that finally reaches the workpiece. On the one hand, the depth of the welds using an argon-helium mixture is comparable to those that are achieved with a pure argon flow. On the other hand, the width is bigger when the argon-helium mixture is used [10].

As previously mentioned, argon and not nitrogen is usually employed for LMD. In fact, machine tool builders working with LMD process, like DMG MORI (DGM MORI, Bielefeld, Germany), Trumpf (TRUMPF GmbH + Co., KG, Ditzingen, Germany), or MAZAK (Yamazaki Mazak Corporation, Oguchi, Japan), among others, usually recommend the use of argon despite its high price in order to avoid the risk of unwanted reactions in the process. However, some of these leading companies have started to use helium and argon as carrier and shielding gas, respectively. This is due to a fluid dynamical issue: helium's density is lower than argon's, so when the helium flow crosses the argon one, turbulences are reduced, and a more stable gas flow is achieved at the substrate. This phenomenon helps to improve the powder concentration and protective gas concentration at the melt-pool, hence simplifying the nozzle design.

Therefore, there is a necessity to know how the use of different gases may affect the LMD process. From the literature review, it is noted that some research has been realized focusing on the use of argon or nitrogen individually, with the argon case the most documented. However, there is a lack of information about the influence that helium or gas mixtures may have on the LMD process.

The aim of the present work is to evaluate the effect of a mixture of argon and helium on the LMD process by analyzing single tracks of Ni based alloy Inconel 718. The height, width, and depth of the clads, along with the temperature of the process, are measured for the different gas mixtures employed.

2. Materials and Methods

The selected material for this work is a nickel-based superalloy, Inconel 718. This material is commonly used in the aerospace industry for turbine and other structures where temperatures can be higher than 600 °C. It is probably one of the most typical materials used in LMD process. Thus, substrate material is an Inconel 718 alloy and powder material is an Oerlikon MetcoClad 718 (Oerlikon, Freienbach, Switzerland), which has been used as the filler material. Both share the same chemical composition within certain compositional limits, as shown in Tables 1 and 2. Powder particle size distribution is shown in Table 3, in order to enable other fellow researchers to replicate the same tests.

Table 1. Chemical composition (wt %) of the Inconel 718 substrate [12].

Ni	Cr	Cb + Ta (Nb + Ta)	Cb (Nb)	Mo	Ti	Al	Co	Mn
52.50	18.40	5.08	5.08	3.04	1.03	0.54	0.33	0.24
Si	C	Cu	B	Ta	P	S	Fe	
0.11	0.052	0.05	0.005	<0.05	0.006	<0.002	BAL	

Table 2. Chemical composition (wt %) of the MetcoClad 718 powder [13].

Cr	Mo	Nb	Fe	Ti	Si	Mn	C	B	Ni
19.00	3.00	5.00	18.00	1.00	0.20	0.08	0.05	0.005	BAL

Table 3. Particle size, which follows a Rosin-Rammler distribution.

Minimum Size (μm)	Mean Size (μm)	Maximum Size (μm)	Spread Parameter	Number of Diameters
50	90	135	4.2	10

All of the tests that are described within this work were carried out on a laser processing cell, Kondia Aktinos 500 (Kondia, Elgoibar, Spain), rebuilt from a conventional milling center. It has three linear plus two rotary axes for a total of five-axis cinematics, and a work volume of $700 \times 360 \times 380 \text{ mm}^3$. The laser source is a Rofin FL010 (ROFIN-SINAR, Bergkirchen, Germany), a Yb:YAG fiber laser of 1 kW of maximum power and 1070 nm wavelength. An optical multi-mode fiber is used to guide the laser beam to the processing cell and an optical lens focuses it at 200 mm, thus creating a circular spot of 1.6 mm of diameter, approximately. In addition, the powder feeder employed is a Sulzer Metco Twin 10-C (Oerlikon Metco, Pfäffikon, Switzerland), which can be used with argon, nitrogen, and other gases, like helium. The powder is injected by means of a self-developed coaxial nozzle EHU/Coax 2015 (UPV/EHU, Bilbao, Spain) [5].

The gases that were used during the experimental tests, supplied by Praxair (Praxair, Inc., Danbury, USA), are (1) Argon, with a purity of 99.998%, (2) Helistar 25, whose composition is argon 75% and helium 25%, and (3) Helistar 50, which is a half argon and half helium mixture [14–16]. The same gases were supplied both as shielding and as carrier gas, in order to avoid mixing and knowing the precise composition.

Two different experiments were designed. One was intended to measure the melt pool temperature and its cooling time. The second one aimed to characterize the deposited tracks by measuring their height, width, dilution depth, and wet angle, along with the temperature of the process. The temperature was measured by means of a digital two-color pyrometer with an IGAR 12-LO (LumaSense Technologies, Inc., Santa Clara, CA, USA) optic fiber [17], which was focused on the same point as the laser beam. The use of this kind of technique instead of a standard one-color pyrometer is because the measurement of a two-color pyrometer is independent of the emissivity in a wide range of temperature and it is unaffected by fume or powder in this case.

2.1. Melt Pool Temperature Measurement and Cooling Time

The tests were realized on a 10 mm thickness substrate in order to avoid considerable thermal affection. Previously, the test specimens were cleaned and prepared so that a homogeneous surface was attained. The k-factor (also known as emissivity slope) of the two-color pyrometer was calibrated with a similar substrate of equal dimensions and characteristics heated in a furnace (Helmut ROHDE GmbH, Prutting, Germany) up to 1423 K and then measured with a thermocouple type K. The laser was set at the focal distance of the nozzle with the dragging and shielding gas flows on, while a laser power of 250 W was used to heat the surface for 1 s, so that the melting point was reached.

Once the laser power was off, the measurement of the temperature continued until the pyrometer stopped registering any signal intensity from the substrate. The time between measurements was set to 16 ms, as it showed stability and compromise with immediate measurements. The three different gases (Argon, Helistar 25 and Helistar 50) were tested with four repetitions of the measurement for each of them. The Figure 1 shows the experimental setup.

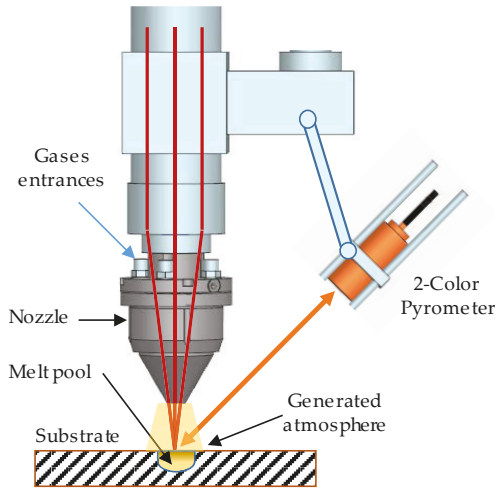


Figure 1. Experimental setup.

2.2. Laser Metal Deposition Experiments

The same substrate preparation for these experiments were carried out. For the data record and subsequent analysis, three tracks were deposited with pure argon, so that they could be used as the reference tracks. The process parameters were also set with reference values, in order to test the different gases with the same conditions. The parameters were selected from previous works in order to avoid cracks and porosity, and they are shown in Table 4.

Table 4. Laser Metal Deposition (LMD) experiments process parameters.

Reference	Power (W)	Feed Rate (mm·min ⁻¹)	Spot Diameter (mm)	Powder Mass Flow (g·min ⁻¹)	Shielding Gas Flow (L·min ⁻¹)	Dragging Gas Flow (L·min ⁻¹)
[1]	400	500	1.6	8.0	12.0	4.5
[2]	600	500	1.6	8.0	12.0	4.5
[3]	800	500	1.6	8.0	12.0	4.5

Once the reference tests were carried out, the same process parameters were used for testing the two gas mixtures, Helistar 25 and Helistar 50, with 25% and 50% of helium concentration, respectively. The measurement of the temperature was taken by following the laser spot, so that the pyrometer was always coincident with the melt pool. Once the experimental tests were finished, the different tracks were cut in a wet abrasive cut-off machine with a corundum cut-off wheel bonded with rubber and then etched with Kalling’s reagent 2. The cross sections were analyzed by means of a confocal microscope Leica DCM 3D (Leica Microsystems GmbH, Wetzlar, Germany). For the cross section characterization, four main parameters were measured (See Figure 2), including height, width, depth of dilution, and wet angle [18,19].

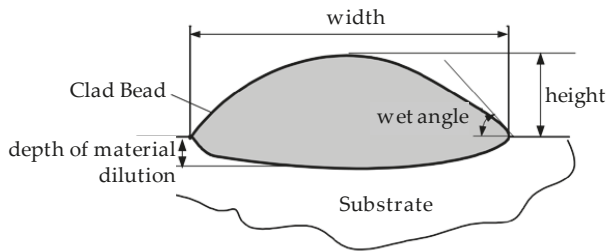


Figure 2. Clad cross section parameters.

3. Results

3.1. Analysis of the Melt Pool Temperature and Cooling Time

A preliminary analysis of the temperature indicates that measurements taken before the first 500 ms are very unstable. This is due to the different phenomena occurred during the rapid rise of the temperature that mislead the pyrometer sensor. For this reason, the time while the laser was radiating the substrate was set to one second. The results show the same order of magnitude of temperature for the three studied gases.

Figure 3 shows the measurement results. The pyrometer has a minimum temperature range of 823 K on display, and a maximum of 2773 K, and it was calibrated before the experiments.

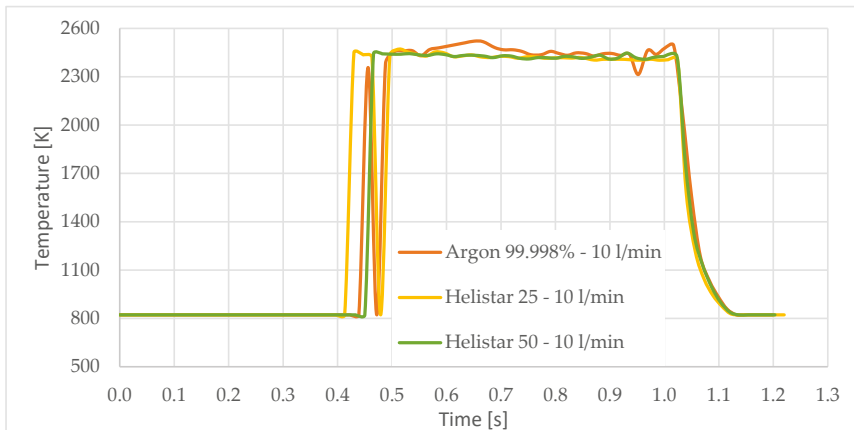


Figure 3. Temperature [K] vs. time [s].

In all cases, temperature reaches a mean value of approximately 2420 K at the time of 1 s, and it takes approximately 130 ms (131 ms for Argon 99.998%, 130 ms for Helistar 25, and 138 ms for Helistar 50) from that point to reach a temperature below 823 K approximately. These results imply that, when working with low laser power (such as 250 W), there is no significant difference between the mixtures that were studied.

3.2. Analysis of the Laser Metal Deposition Experiments

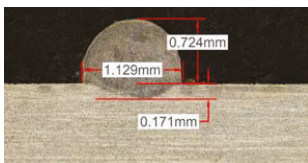
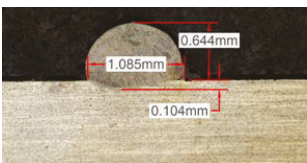
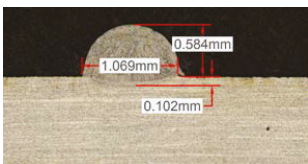
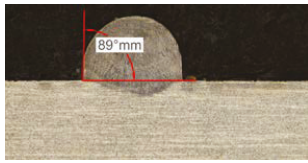
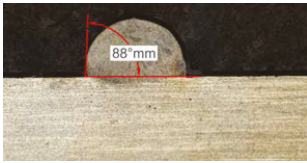
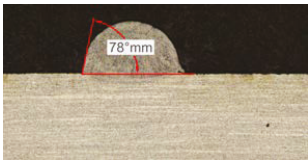
Along these tests, the influence of different gas mixtures on the LMD process was analyzed for three different laser powers: 400, 600, and 800 W. The following figures illustrate the experimental tests and the

resulting tracks for the different gas mixture. The morphology of the clads is represented and measured, followed by a table with average values of each of the three repetitions of the experimental tests.

3.2.1. Experimental Tests with 400 W

Table 5 shows that, for the same energy density value, width, dilution depth and height of the track decrease as the concentration of helium grows. The results show very similar height, width, and dilution in all cases. Wet angle presents also differences between the tests, but the main variation is for the Helistar 50.

Table 5. Measurements for different gases at 400 W.

Argon 99.998%	Ar 75% He 25%	Ar 50% He 50%
		
		

Regarding the wet angles, the optimal values should not exceed 65°. In this case, the parameter combination of 400 W laser power and selected powder mass flow is not adequate to obtain optimum wet angles.

Due to possible variations in the measurements of the clads, the experimental tests were repeated three times. Average values of the measurements are presented in Table 6 with average absolute deviation around the mean (MAD) value in brackets.

Table 6. Summary of results for experimental tests at 400 W. (absolute deviation around the mean (MAD) in brackets).

Gas Mixture	Height (mm)	Width (mm)	Depth (mm)	Wet Angle (°)
Argon 99.998%	0.69 (0.040)	1.15 (0.018)	0.16 (0.013)	89 (1.0)
Ar 75% He 25%	0.63 (0.020)	1.10 (0.014)	0.13 (0.023)	88 (1.5)
Ar 50% He 50%	0.60 (0.029)	1.06 (0.009)	0.10 (0.009)	78 (1.0)

3.2.2. Experimental Tests at 600 W

Continuing with the same methodology, tests with a laser power of 600 W are presented in Table 7. There are significant increments in width due to the higher power, but not in height, which mainly depend on the powder mass flow. For this laser power, the width of the different clads hardly varies among gas mixtures as well as the depth of material dilution. However, the variation of the height as a result of the use of different gases is more significant, and, again, a greater variation is observed for the highest helium concentration tests (Helistar 50).

Table 7. Measurements for different gases at 600 W.

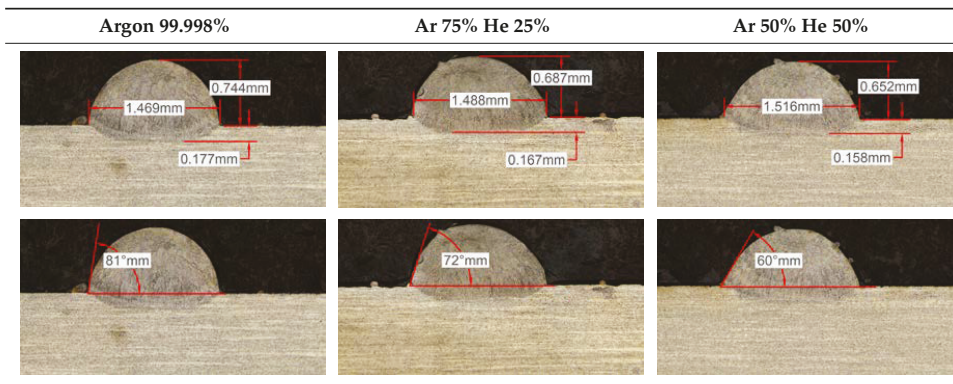


Table 7 shows also a reduction of wet angles of the clads due to the higher laser power. However, significant differences of wet angle are observed for clads made with each gas mixture. The higher the helium concentration, the smaller the wet angle of the clad.

Again, a repetition of the tests was made in order to consider the possible variations. The results with average values are presented in Table 8. As it can be observed, height, width, and dilution depth values are practically constant, regardless of the gas composition. However, the wet angles vary considerably for the different gas mixtures.

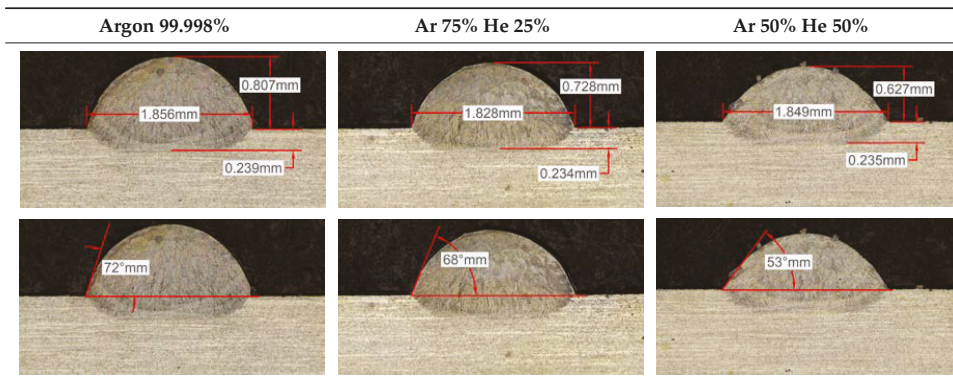
Table 8. Summary of results for experimental tests at 600 W.

Gas Mixture	Height (mm)	Width (mm)	Depth (mm)	Wet Angle (°)
Argon 99.998%	0.75 (0.009)	1.48 (0.015)	0.18 (0.004)	81 (1.2)
Ar 75% He 25%	0.70 (0.016)	1.49 (0.009)	0.17 (0.008)	73 (1.0)
Ar 50% He 50%	0.66 (0.009)	1.51 (0.010)	0.15 (0.009)	60 (0.8)

3.2.3. Experimental Tests at 800 W

Tests results for 800 W laser power are shown in Table 9. Because of power increment, the width and dilution are higher than those obtained in the 400 W and 600 W tests.

Table 9. Measurements for different gases at 800 W.



Similarly to the previous experiments, the highest variation between the clads is in height, whereas the dilution depth and width remain almost invariable.

Because of a higher laser power, the wet angle is smaller than previous tests with lower laser power. In addition, the wet angle changes for different gas compositions, as it can be observed in Table 9. The wet angle reduction is the most significant variation when using different gases, while the rest of measurements present similar values.

The experimental tests once again are repeated to obtain more information and to analyze the possible variation on the geometry of the clad. Table 10 shows these results as mean values of the measurements. As it was stated before, the more significant effect of the different gases use is the wet angle variation, and this variation is more considerable for higher helium concentrations.

Table 10. Summary of results for experimental tests at 800 W.

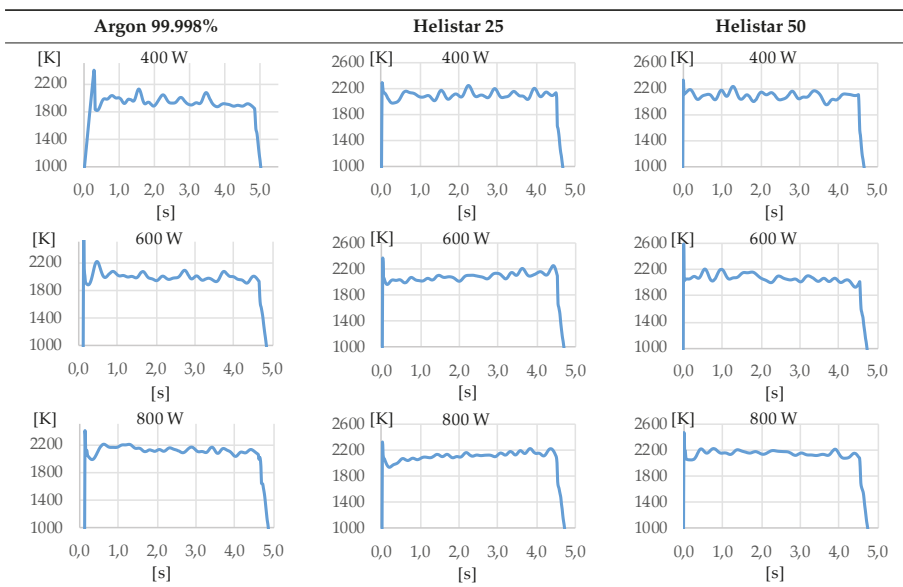
Gas Mixture	Height (mm)	Width (mm)	Depth (mm)	Wet Angle (°)
Argon 99.998%	0.79 (0.014)	1.87 (0.013)	0.25 (0.010)	73 (1.0)
Ar 75% He 25%	0.73 (0.009)	1.82 (0.015)	0.26 (0.008)	67 (1.2)
Ar 50% He 50%	0.65 (0.020)	1.84 (0.010)	0.23 (0.006)	53 (0.8)

3.2.4. Temperature Analysis

In addition to the geometry analysis, the temperature of the process was registered via pyrometry and Table 11 shows the outputs of these measurements.

In all cases, the utilization of helium in the process results in higher temperature. When pure argon was used, mean temperatures of 1938 K, 1991 K, and 2121 K were reached for laser powers of 400 W, 600 W, and 800 W, respectively. Meanwhile, when Helistar 25 (Ar 75% and He 25%) and Helistar 50 (Ar 50% and He 50%) was employed, temperatures with average values of 2093 K and 2097 K were measured, respectively, at 400 W. However, increasing the amount of helium in the mixture did not result in a higher temperature.

Table 11. Summary of results for experimental tests at 400 W, 600 W, and 800 W.



4. Discussion

As it has been observed in the previous tests, the helium content of the gas affects the geometry of the deposited clad. The comparison between the tests that were realized with argon and those with Helistar 50, shows height value differences of 70 μm , 90 μm , and 140 μm for laser power values of 400 W, 600 W, and 800 W, respectively. These height variations are slightly lower when Helistar 25 is used. With regard to width and depth values, the differences do not exceed 30 μm for dilution depth and 50 μm for width, and no clear tendency is appreciated. Moreover, the wet angle seems to have a correlation with the helium concentration of the gas, changing the shape of the clad geometry by smoothing the slope. The wet angle decreases when the helium proportion is increased and variation values up to 21 degrees are registered.

The melt pool temperature variation is other factor, which is strongly influenced by the gas mixture. With argon, variations of almost 200 K were registered from a 400 W to 800 W laser power. However, the same differences of laser power do not show significant variations of the temperature when gases with presence of helium are used, merely of 20 K approximately.

As Andreas Patschger and Rolf Wester et al. state [6,7], the ionization energy of the gas is important due to the formation of plasma in the laser beam way. In this case, argon is more susceptible of forming ionized gas because of its lower ionization energy value, which is near to the 64% of the helium's one. In addition, the heat conductivity of these two gases are very different, being helium's ($0.151 \text{ W}\cdot\text{m}^{-1}\cdot\text{K}^{-1}$) near 40 times higher than argon's thermal conductivity ($0.018 \text{ W}\cdot\text{m}^{-1}\cdot\text{K}^{-1}$).

Plasma works as an isolation for the laser beam and higher heat conductivities allow for the heat that is radiated to be fed back to the process. The variation of the temperature for the different gases can be explained with these two phenomena. For a high energy density process, the use of argon contributes to plasma formation, and thus, the isolation of part of the energy provided by the laser. On the other hand, helium is able to work with higher energy densities without promoting plasma formation and contributing to feeding back heat to the process due to its greater thermal conductivity.

5. Conclusions

The present work studies the influence of the gas composition on the LMD process. Three different gas compositions have been tested: Ar 99.99%, Ar 75%-He 25%, and Ar 50%-He 50%. Up to 150 microns, differences in height are observed between Ar 99.99% and Ar 50%-He 50% concentration gases. The higher the helium presence in the mixture, the smaller the height of the clad. The rest of the geometry characteristics remain virtually stable with a variation of less than 60 microns for extreme cases.

The most significant variation on the shape of clads is the wet angle. This parameter varies within a wide range with the helium concentration, decreasing its value while the presence of this gas goes in augment. Variations of 10 to 20 degrees are observed between the use of pure argon and a mixture with 50% of helium. In addition, the temperature of the melt pool is also influenced by the presence of helium when it is combined with high energy densities.

Conclusions of the present research work can be summarized in the following way:

1. Helium and argon process gases have different effects on LMD. Its influence is not negligible and must be taken into account.
2. The increment of helium concentration in the gases of the LMD processes based on argon will have three effects. The first one is a slight reduction of the height of the clads. Second, an increase of the temperature of the melt pool. Last, smaller wet angles are obtained for higher helium concentrations.
3. However, some variations can be neglected due to its small values, like width and dilution depth, since helium concentration seems to have no special influence on these parameters.

Author Contributions: J.I.A. and J.E. conceived and designed the experiments; M.C. and J.E.R. performed the experiments and analyzed the data, helped by J.I.A.; A.L. supervised the whole research work; J.E.R., M.C. and A.L. wrote the paper.

Funding: This research received no external funding.

Acknowledgments: This work was supported by the DPI 2016-79889-R INTEGRAddi Project and the POCTEFA 90/15 Transfron3D Project. Special thanks are addressed to Praxair (Praxair, Inc., Barakaldo 48903, Spain) for their technical and supply supports in this work.

Conflicts of Interest: The authors declare no conflict of interest.

References

1. Gibson, I.; Rosen, D.; Stucker, B. Directed Energy Deposition Processes. In *Additive Manufacturing Technologies*, 2nd ed.; Springer: New York, NY, USA, 2015; pp. 245–268. ISBN 978-1-4939-2112-6.
2. Cortina, M.; Arrizubieta, J.I.; Ruiz, J.E.; Lamikiz, A.; Ukar, E. Design and manufacturing of a protective nozzle for highly reactive materials processing via Laser Material Deposition. *Procedia CIRP* **2018**, *68*, 387–392. [[CrossRef](#)]
3. Li, P.; Yang, T.; Li, S.; Liu, D.; Hu, Q.; Xiong, W.; Zeng, X. Direct laser fabrication of nickel alloy samples. *Int. J. Mach. Tools Manuf.* **2015**, *45*, 1288–1294. [[CrossRef](#)]
4. Kumar, L.J.; Nair, C.K. Laser metal deposition repair applications for Inconel 718 alloy. *Mater. Today Proc.* **2017**, *4*, 11068–11077. [[CrossRef](#)]
5. Gasser, A. Laser Metal Deposition. In *Tailored Light 2*, 1st ed.; Poprawe, P., Ed.; Springer: Berlin/Heidelberg, Germany, 2011; pp. 15–40. ISBN 978-3-642-01236-5.
6. Arrizubieta, J.I.; Taberner, I.; Ruiz, J.E.; Lamikiz, A.; Martínez, S.; Ukar, E. Continuous coaxial nozzle design for LMD based on numerical simulation. *Phys. Procedia* **2014**, *56*, 429–438. [[CrossRef](#)]
7. Elmer, J.W.; Vaja, J.; Carlton, H.D.; Pong, R. The Effect of Ar and N₂ Shielding Gas on Laser Weld Porosity in Steel, Stainless Steels, and Nickel. *Weld. J.* **2015**, *94*, 313s–325s.
8. Petrat, T.; Graf, B.; Gumenyuk, A.; Rethmeier, M. Laser Metal Deposition as repair technology for a gas turbine burner made of Inconel 718. *Phys. Procedia* **2016**, *83*, 761–768. [[CrossRef](#)]
9. Raymond, C.B.; Randy, P.S. Additively Manufactured Inconel Alloy 718. In Proceedings of the 7th Symposium on Superalloy 718 and Derivatives, Pittsburgh, PA, USA, 10–13 October 2010. [[CrossRef](#)]
10. Patschgera, A.; Sahibb, C.; Bergmann, J.P.; Basticka, A. Process Optimization through Adaptation of Shielding Gas Selection and Feeding during Laser Beam Welding. *Phys. Procedia* **2011**, *12*, 46–55. [[CrossRef](#)]
11. Wester, R. Absorption of Laser Radiation. In *Tailored Light 2*, 1st ed.; Poprawe, P., Ed.; Springer: Berlin/Heidelberg, Germany, 2011; pp. 216–224. ISBN 978-3-642-01236-5.
12. Haynes International. *Haynes(R) 718 Alloy Plate Test Certificate*; Haynes International: Kokomo, IN, USA, 2018.
13. Oerlikon Metco. *MetcoClad 718 Material Product Data Sheet*; Oerlikon Metco: Pfäffikon, Switzerland, 2018.
14. Praxair, Inc. *Praxair Argon Product Data Sheet*; Praxair, Inc.: Danbury, CT, USA, 2018.
15. Praxair, Inc. *Praxair Helistar 25 Product Data Sheet*; Praxair, Inc.: Danbury, CT, USA, 2018.
16. Praxair, Inc. *Praxair Helistar 50 Product Data Sheet*; Praxair, Inc.: Danbury, CT, USA, 2018.
17. LumaSense Technologies, Inc. *IMPAC Pyrometer IGAR 12-LO MB 25 Product Data Sheet*; LumaSense Technologies, Inc.: Santa Clara, CA, USA, 2018.
18. Toyserkani, E.; Khajepour, A.; Corbin, S. *Laser Cladding*, 1st ed.; CRC Press LLC: Boca Raton, FL, USA, 2005; pp. 11–50. ISBN 0-8493-2172-7.
19. Bennett, J.; Wolff, S.; Hyatt, G.; Ehmann, K.; Cao, J. Thermal effect on clad dimension for laser deposited Inconel 718. *J. Manuf. Process.* **2017**, *28*, 550–557. [[CrossRef](#)]



© 2018 by the authors. Licensee MDPI, Basel, Switzerland. This article is an open access article distributed under the terms and conditions of the Creative Commons Attribution (CC BY) license (<http://creativecommons.org/licenses/by/4.0/>).

Article

Accurate Calibration in Multi-Material 3D Bioprinting for Tissue Engineering

Enrique Sodupe-Ortega ¹, Andres Sanz-Garcia ^{2,*}, Alpha Pernia-Espinoza ¹
and Carmen Escobedo-Lucea ^{2,*}

¹ EDMANS Group, Department of Mechanical Engineering, University of La Rioja, San José de Calasanz 31, Edificio Departamental, 26004 Logroño, Spain; enrique.sodupeo@unirioja.es (E.S.-O.); alpha.pernia@unirioja.es (A.P.-E.)

² Division of Pharmaceutical Biosciences, University of Helsinki, Viikinkaari 5 E, P.O. Box 56, 00014 Helsinki, Finland

* Correspondence: andres.sanz-garcia@helsinki.fi (A.S.-G.); carmen.escobedo-lucea@helsinki.fi (C.E.-L.); Tel.: +358-294-159-326 (A.S.-G.); +358-294-159-329 (C.E.-L.)

Received: 9 July 2018; Accepted: 7 August 2018; Published: 10 August 2018

Abstract: Most of the studies in three-dimensional (3D) bioprinting have been traditionally based on printing a single bioink. Addressing the complexity of organ and tissue engineering, however, will require combining multiple building and sacrificial biomaterials and several cells types in a single biofabrication session. This is a significant challenge, and, to tackle that, we must focus on the complex relationships between the printing parameters and the print resolution. In this paper, we study the influence of the main parameters driven multi-material 3D bioprinting and we present a method to calibrate these systems and control the print resolution accurately. Firstly, poloxamer hydrogels were extruded using a desktop 3D printer modified to incorporate four microextrusion-based bioprinting (MEBB) printheads. The printed hydrogels provided us the particular range of printing parameters (mainly printing pressure, deposition speed, and nozzle z-offset) to assure the correct calibration of the multi-material 3D bioprinter. Using the printheads, we demonstrated the excellent performance of the calibrated system extruding different fluorescent bioinks. Representative multi-material structures were printed in both poloxamer and cell-laden gelatin-alginate bioinks in a single session corroborating the capabilities of our system and the calibration method. Cell viability was not significantly affected by any of the changes proposed. We conclude that our proposal has enormous potential to help with advancing in the creation of complex 3D constructs and vascular networks for tissue engineering.

Keywords: additive manufacturing; synthetic polymer; bioprinting; multi-material microextrusion; bioink

1. Introduction

The rise of three-dimensional (3D) printing in the last three decades has permitted the arrival of a new manufacturing technology called 3D bioprinting for organ and tissue engineering (TE) [1–4]. This technology aims to deposit multiple biomaterials, growth factors, and living cells with precise control over their compositions, spatial distribution and architecture [5]. Since the appearance of the first bioprinting studies in 2003 introduced by Wilson and Boland [6], the field has experienced a growing interest by the scientific community in the last decade. The rapid increase in the number of related publications provides evidence of this tendency (Figure 1).

Today, allograft organ transplantation is still the only therapy effective against organ failures, but relatively simple implantable tissue constructs have been printed and successfully transplanted into animal models [7]. These works bring great hope for those patients who are looking for alternatives

to the organ transplantation methods. Looking forward, the challenge remains of how to reproduce the complex cellular organization and micro-environment of an entire solid organ. This is still well beyond the capabilities of currently available bioprinting technologies [8].

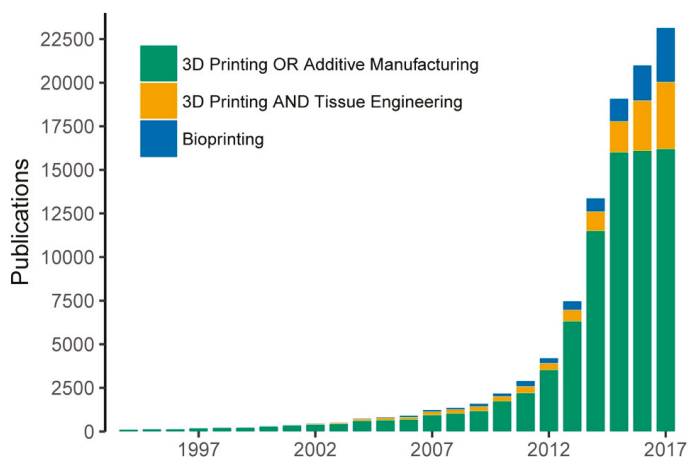


Figure 1. Evolution of bioprinting and 3D printing publications measured by the number of Google Scholar hits. The keywords utilized for the searching included: “3D printing” OR “additive manufacturing”, “3D printing” and “tissue engineering” and “bioprinting”.

Three main bioprinting technologies have been developed: inkjet-, laser- and microextrusion-based bioprinting (MEBB) systems. Each of them has been utilized in several biological applications, offering different features in terms of cell viability, deposition speed, print resolution, scalability, cost or materials compatibility [9]. MEBB is the most extended technology because of its versatility and fast deposition of a wide range of bioinks, which enables the rapid generation of large-scale constructs [10–12]. Although excessive printing pressures could reduce cell viability, it is an excellent method for depositing high cell densities in several candidate bioinks [13]. The bioinks can be defined as formulation of biomaterials, biological molecules and cells processed using bioprinting technologies [14,15]. Most of the studies in 3D bioprinting have traditionally been limited to the use of one or two bioinks at one time, which is perhaps an oversimplification that limits the structural, material and biological potential of this technology [16].

Employing multiple building and sacrificial biomaterials and cells types in a single biofabrication session seems to be the right way of addressing the complexity of organ engineering and producing outstanding advances in the field [17–19]. Multi-material bioprinters have recently been developed by several research groups [7,11,12,20–22]. These bioprinting systems normally incorporate up to three or four printheads to perform multi-material extrusion like the open-source solution utilized by the authors in this study. To the best of our knowledge, advances in multi-material bioprinting will enable researchers to integrate intricate perfusable channels inside of complex shape constructs, and create constructs with several different cell densities, among other advantages. A more detailed study in multi-material bioprinting [8], using stem-cell-laden bioinks, alongside a network of reinforcing poly(ϵ -caprolactone) (PCL), led to the biofabrication of so-called developmentally inspired templates of bone tissue microfibers.

All of this cannot be accomplished without answering fundamental questions such as the ideal properties of the bioinks and the relationships between the bioprinting process parameters and the print resolution and fidelity [13]. In the case of MEBB, some previous research studies have correlated bioprinting parameters and printed outcomes. Wang et al. showed that optimized printing parameters

such as bioink concentration, nozzle speed and extrusion rate produced poly(lactic-co-glycolic acid) (PLGA) scaffolds [23]. Mixtures of Gel-Alg were investigated by He and his coworkers to find the optimal values of air pressure, feed rate, and layer height to assure proper printing quality [13]. Suntonnonnd et al. used poloxamers to develop a mathematical model to correlate print resolution with process parameters [24]. Similarly, a prediction model was obtained by Trachtenberg et al. to determine the suitability of poly-propylene fumarate for MEBB [25] while Ting et al. examined the effect of PLGA composition and printing parameter on print resolution [26]. However, today, there is no a definite method to calibrate multi-material 3D bioprinters as well as to determine their final print resolution. Understanding how parameters such as printing speed and nozzle height affect the print resolution is vital not only for the shape of the printed constructs but also for their mechanical properties. When encapsulating cells, selecting the optimal printing parameters will reduce the adverse effect of the viscoelastic stresses on the cell viability [27,28].

In this paper, we advance in the development of the multi-material 3D bioprinting by proposing a method that analyzes the influence of the main printing parameters and accurately controls the print resolution. We anticipate that a significant increase on printing speed and quality of the constructs using the multi-material bioprinter is due to the use of an automatic calibration system. Poloxamer 407 (P407) hydrogels with different fluorescent inks were printed into different complex constructs for finding the optimal printing parameters. This allowed us to emulate the bioprinting of four materials, but, at the same time, also remove other secondary factors such as excessive swelling or temperature dependence. The proposed method was also tested printing a mixture of gelatin-alginate (Gel-Alg), a more cell-friendly bioink. Cell-laden Gel-Alg and P407-based bioinks were printed in a single session. After printing, cell viability of stem cells embedded in the Gel-Alg was analyzed to verify the effects of the calibration. The results demonstrated that our proposal has huge potential to help in creating large multi-material 3D constructs and potential vascular networks for tissue engineering.

2. Materials and Methods

2.1. Bioprinting System Incorporating Four Printheads

The experiments were performed using a desktop open-source 3D printer Witbox 2 (BQ, Madrid, Spain) modified for extruding hydrogels at 24 °C (Figure 2a). The mechanical resolution of the 3D printer is up to 20 µm according to the manufacturer's specifications. The Witbox 2 movements follow a Cartesian dimensional coordinate system, in which the printheads are moving across the xy horizontal plane while the printing platform only moves vertically (z -axis). The Witbox 2 was modified by substituting the standard fused deposition modeling nozzle in the x -carriage for four pneumatic-based MEBB printheads (Figure 2b,c). The four printheads' movements are controlled using open-source Rumba electronics (Reprap Universal Mega Board with Allegro driver; RepRapDiscount, Hong Kong, China).

The printing pressure of the four printheads can be independently adjusted using individual air pressure regulators (ARP20K-N01BG-1Z; SMC, Tokyo, Japan). Hydrogel deposition in each printhead is controlled by opening and closing the solenoid valve (VT307-6DZ1-01F-Q; SMC, Tokyo, Japan) connected to the metal-oxide-semiconductor field-effect transistor (MOSFET) terminals of the Rumba controller board.

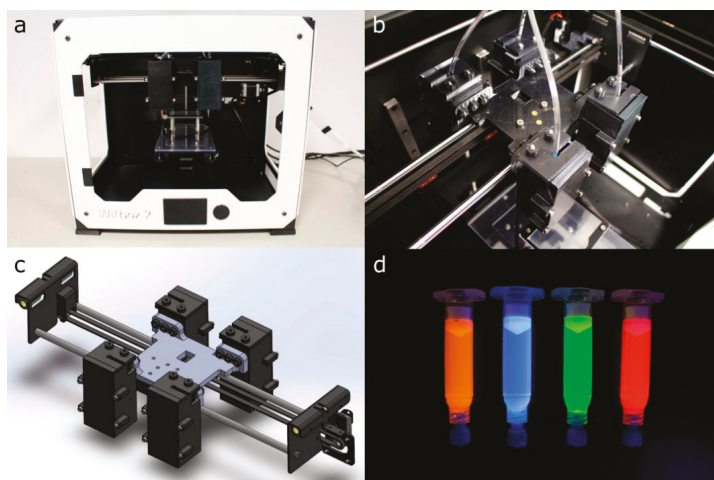


Figure 2. (a,b) general and detailed view of the modified Witbox 2 3D printer with four bioprinting printheads; (c) 3D CAD design of the 3D printer x-carriage; (d) 5 mL syringe barrels loaded with dyed P407 hydrogels.

2.2. G-Code Generation and Printing Software

The software employed to control the modified bioprinter and the bioprinting process was comprised of several tools. First of all, a modification of Marlin firmware (v1.1) was loaded into the 3D printer main board [29]. The modified firmware allowed us to manage and coordinate all the activities of the 3D printer, including the movement of the four printheads and the deposition of the bioinks.

A computer-aided design (CAD) software (SolidWorks; Dassault Systems, v2016) was utilized to create the 3D models for bioprinting and generate the final stereolithography (STL) files. The open-source slicing software Slic3r (v1.2.9) [30] was utilized for G-code generation. Slic3r is mainly utilized in FDM and therefore it is not designed to operate pneumatic printheads. For that reason, custom post-processing Perl scripts were required to transform the original G-Code to the particular characteristics of the multi-material 3D bioprinter used. The four printheads moved according to G-code instructions, depositing biomaterials where they were initially programmed. Finally, the G-code was sent to the bioprinter using Repetier-Host (v1.6.2) software [31], which was also in charge of monitoring the bioprinting process.

2.3. Multi-Material Bioprinting Procedure and Calibration

Figure 3 describes the procedure to prepare a 3D model for the multi-material bioprinting process. This procedure starts opening the STL files containing the original geometry with the slicing software. In case a multi-material printing process is desired, several STL files should be generated, each of them assigned to the particular printhead that will print that part of the geometry. The assigning operation is performed in Slic3r using the “Settings” button. Each STL file will be displayed in a list on the left-hand side of the window and assigned to a specific printhead (Figure 4a).

When several printheads are assigned, the 3D model visualization will appear with a different color for each printhead (Figure 4). If only one printhead is utilized, a single STL will be required. Once the printing settings are introduced (deposition speed, infill pattern, number of perimeters, etc.), the G-code is generated and sent to the 3D printer through the Repetier-Host.

xy offsets of the 3D printer utilized were configured according to Figure 5a. When using multiple printheads, the original offset coordinates of the first printhead (P1) are set to zero ($x = 0, y = 0$). Then, the xy offset coordinates of every additional printhead must be determined with respect to

the coordinates of P1. Every offset must be entered in the slicing software to compensate for the misalignments between the printheads. Depending on the particular printer used and the configuration of its printheads, the values of the offset coordinates can be very different.

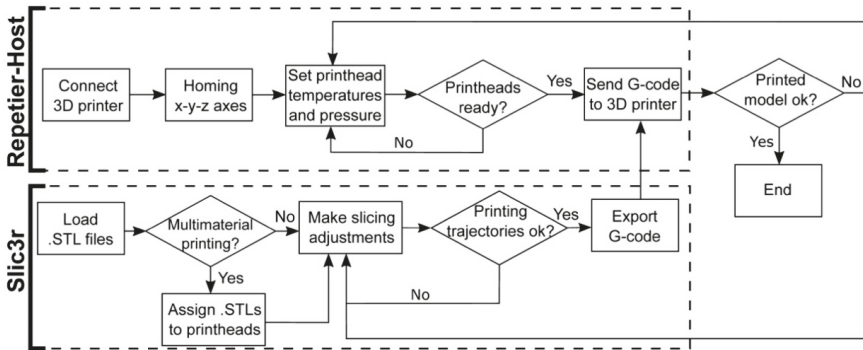


Figure 3. Flowchart of the procedure for the G-code generation and the interaction with the 3D bioprinter interface.

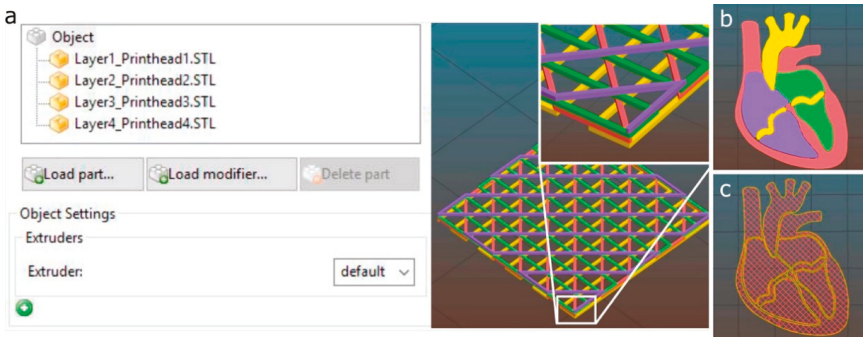


Figure 4. Multi-material printheads assignment using Slic3r software. (a) porous structure with four layers stacked, each one assigned to a different printhead; (b) 3D model of a heart section composed of four parts; (c) printhead trajectories calculated by the slicing software using a porous infill.

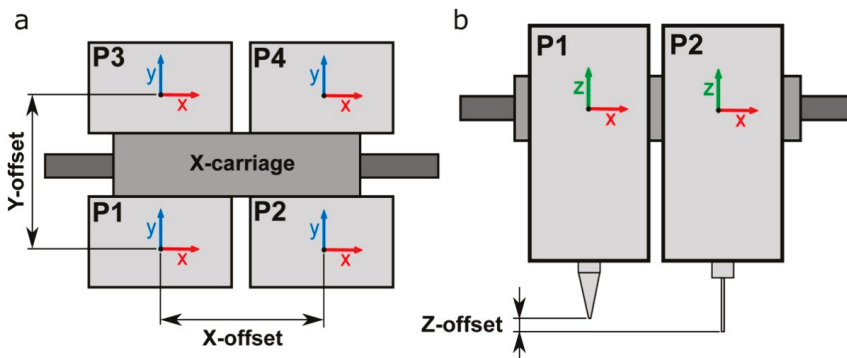


Figure 5. Schematic representation of the (a) *xy*-offsets and the (b) *z*-offset of four printheads P1/P4.

z-offset between various printheads also represents a crucial point for multi-material calibration (Figure 5b). A z-homing push button was installed in the 3D multi-material bioprinter to perform the automatic calibration of the z-offsets. This configuration allows us to use nozzles of different types and heights. In addition, this automatic system reduces drastically the time required to start the printing process because there is no necessity to perform any manual adjustment and the whole calibration process is done at once.

2.4. Hydrogel Preparation

Poloxamer 407 (P407, Pluronic® F127; Sigma-Aldrich, Madrid, Spain) was prepared at 40 wt % by weighing the quantity of polymer required and mixing in cold Milli-Q water at 4 °C. P407 powder was added gradually to MilliQ water to facilitate the dilution and stirred vigorously for 3 h using a magnetic stirrer at 4 °C. Once the solution was homogenized, it was centrifuged and stored overnight at 4 °C to remove air bubbles. P407 prepared solutions were always stored at 4 °C until further use.

Gelatin from porcine skin (G1890; Sigma-Aldrich) and sodium alginate from brown algae (A0682; Sigma-Aldrich) were dissolved in phosphate buffered saline (PBS) without salts at 10 wt % and 4 wt % respectively. A solution of 5%Gel-2%Alg was prepared by blending. The pH of the solution was adjusted to 7.2–7.4. Solutions were mixed using vortex and centrifuged at 1000 rpm for 1 min to remove air bubbles.

Four different fluorescent dyes (see clear differences in fluorescence under UV light at the Figure 2d) were utilized to improve the visualization of P407 and Gel-Alg (except in the case of using cells to avoid cytotoxicity) bioinks: orange (1:100; IFWB-33; Risk Reactor, Santa Ana, USA), clear blue (1:500; IFWB-C0; Risk Reactor), yellow-green (1:1000; IFWB-C8; Risk Reactor) and red (1:1000; IFWB-C7; Risk Reactor).

2.5. Cell Isolation and Culture

Human adipose derived mesenchymal stem cells (hASCs) were isolated from lipoaspirates of young healthy donors undergoing aesthetic surgery (from 18 to 35 years-old), following written informed consent and Research Ethical Board approval by Clinica Isabel Moreno and Hospital General Foundation, Valencia, Spain. Donors were previously screened for Human Immunodeficiency Virus (HIV), hepatitis C and other infectious diseases. hASCs were expanded following the protocol described by Escobedo-Lucea et al. [32] and harvested with Tryple® (Invitrogen, Carlsbad, NM, USA) at 85% confluence.

2.6. Bioprinting Cell-Laden Constructs Using Gel-Alg Blends

hASCs were mixed with the bioink (cell density of 10^6 cells/mL) by gentle pipetting to create a homogeneous suspension that was transferred into a 5 mL Luer-lock syringe (Nordson EFD, Alfafar, Spain) and closed with a piston (SmoothFlow; Nordson EFD). Extrusion was performed under controlled air pressure. The cell-laden bioinks were deposited into class slides through a 25G tapered nozzle (Nordson EFD) at a printing speed of 15 mm s^{-1} . The 3D-printed constructs were finally crosslinked in 3 wt % calcium chloride (CaCl_2 ; Wako, Tokyo, Japan) for 6 min and then washed three times with phosphate buffer (PBS) and replaced with growth medium, Dulbecco's modified Eagle's medium (DMEM, Invitrogen) supplemented with 6% human serum.

2.7. Cell Viability Assay

Cell viability in the printed constructs was assessed by live/dead assay (R37601; Life Technologies, Carlsbad, NM, USA) according to manufacturer's instructions. Briefly, after printing, and crosslinking, samples were washed three times with PBS, stained with live green (A) (Calcium-AM; $0.5 \mu\text{L/mL}$) and dead red (B) (ethidium homodimer; $2 \mu\text{L/mL}$), and incubated for 15 min at RT. Fluorescence images of printed samples were captured 1 h and 24 h after deposition under confocal microscope

(Olympus FV1200, Olympus, Tokyo, Japan). Data are representative of the printed samples of four layers stacked images.

2.8. Calibration Models for the Multi-Material Bioprinting Process

Two main calibration models were proposed to adjust the four printheads' xy positions with respect to each other and define the optimal printing pressure. These models aim to determine the printability and final print resolution in multi-material bioprinting systems. The proposed calibration 3D models were designed using the CAD modeling software SolidWorks (Dassault Systems, v2016), and exported as STL files. A detailed description and justification of the calibration models are given in the following paragraphs:

- xy -offset pattern (calibration model 1): straight lines were printed in the x and y directions using two different printheads (Figure 6a). xy offsets of the four printheads were calculated with regard to the first printhead (P1). For that reason, half of the straight lines were printed using P1 and the other half were printed using a different printhead (P2, P3 or P4).
- Zigzag path (calibration model 2): a continuous zigzag was printed using each printhead in order to determine the correct printing pressure and speed (Figure 6b). An increasing distance of 20 μm was separated between all of the lines (Δd) with a separation between lines ranging from 200 μm to 500 μm . The optimal printing pressure was determined when all the printed lines did not overlap and were printed forming continuous strands.

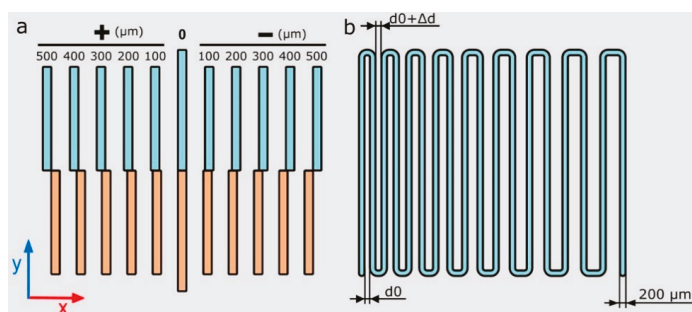


Figure 6. Schematic illustration of the calibration models xy -offset pattern (a) and printing pressure dependent zigzag path (b) where the distance $d_0 = 200 \mu\text{m}$, and the variation $\Delta d = 20 \mu\text{m}$.

Both calibration models were printed using 40 wt % P407 on $50 \times 75 \times 1 \text{ mm}$ glass slides (Corning Inc., New York, NY, USA). The P407 was loaded into 3 mL and 5 mL syringe barrels (Nordson EFD) at $4 \text{ }^\circ\text{C}$ and extruded at $24 \text{ }^\circ\text{C}$. xy -offset calibration model was printed using tapered nozzles with three different inner diameters: 200 μm (27G; Nordson EFD), 250 μm (25G; Nordson EFD) and 330 μm (23G; Nordson EFD). The calibration model 2 was printed in a range of pressures from 12 psi to 20 psi and speed from 5 mm s^{-1} to 25 mm s^{-1} using a 27G tapered nozzle.

2.9. Printing Performance Metrics

Printing accuracy was assessed utilizing the measurement of specific distances in printed calibration models using ImageJ (NIH, Bethesda, MD, USA) [33]. Printed models were photographed right after the printing process to prevent drying of the samples and potential deformations.

All of the micro-photographs of samples and additional videos of the printing process were taken using a digital single-lens reflex (DSLR) camera (EOS 700D; Canon, Tokyo, Japan), placed on a firm tripod and under controlled lighting conditions. Images of printed samples' heights were taken using a USB microscope camera (KKmoon 500 \times ; Digital microscope, Shenzhen, China).

3. Results and Discussion

3.1. Efficient Calibration for Multi-Material Bioprinting

Bioink P407 was used in the 3D bioprinter calibration, and the evaluation of the printing process. This bioink was selected because of its stable nature, exceptional printability, adequate viscosity, and low swelling [22,34]. Note that the P407 allows for evaluating the capabilities of any bioprinter minimizing the influence of material properties and other secondary factors involved. All of the properties mentioned facilitated the creation of complex architectures and their subsequent evaluation.

First, calibration model 1 was printed to perform a quick visual calibration of the xy offsets in the four printheads utilized (Figure 7a–d). Calibration errors or deviations in both x and y axes were measured simultaneously using the printed strand patterns of both axes (Figure 7c). After printing, the patterns allowed the alignment of the printheads P2, P3, and P4 with respect to P1. We considered either positive or negative misalignments in a range between 100 μm and 500 μm . For instance, Figure 7b,d show clear x -axis misalignments of +200 μm and $-500 \mu\text{m}$, respectively. Once the deviations are visually identified, the correction values can be introduced in the slicing software, and the new G-code will correct the position of the printhead nozzles.

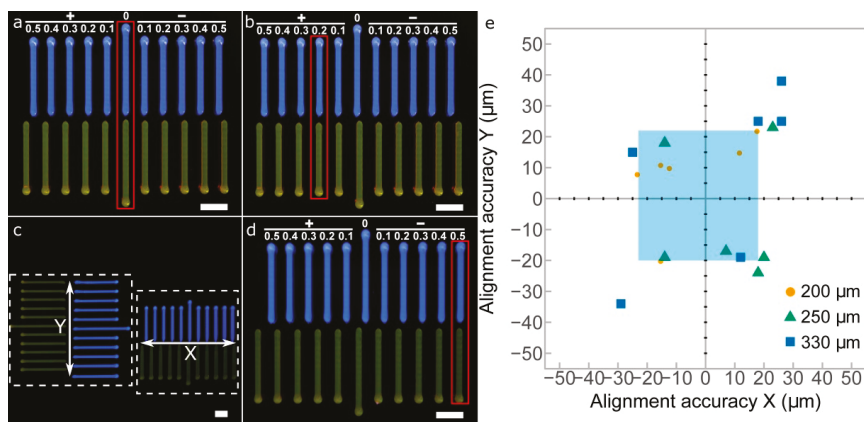


Figure 7. Images of the printed xy -offset pattern calibration model between P1 and P2. (a) perfect alignment between P1 and P2; (b) +200 μm x -offset of P2 respect P1; (c) overall picture of x and y calibration models printed at the same time; (d) $-500 \mu\text{m}$ x -offset of P2 respect P1; (e) alignment accuracy in x and y axes measured for three different nozzle sizes (200 μm , 250 μm , and 330 μm); scale bars: 2 mm.

The results of the xy alignment for three different nozzles are shown in Figure 7e. The increase of the nozzle diameter produced a decrease in the alignment accuracies of both directions. These results can be explained by the much thicker printed lines produced when using bigger nozzles. The same observations, the smaller the nozzle diameter, the higher the line with resolution, were reported by Suntornnond et al. evaluating pluronic F127 [24]. Therefore, it is preferable to perform the 3D printer calibration with the smaller nozzle available. The light blue area indicates the limits for the 200 μm nozzle in the x and y directions, which obtained the best results of the three nozzles. The maximum alignment errors obtained for this nozzle were in a range from $-23 \mu\text{m}$ to $18 \mu\text{m}$ in the x direction and from $-20 \mu\text{m}$ to $22 \mu\text{m}$ in the y direction. These values are sufficiently low and guarantee that the alignment accuracy is at least of a similar order of magnitude to the mechanical resolution of the 3D printer (20 μm).

The layer-by-layer approach characteristic of additive manufacturing (AM) makes the thickness of the printed layers become the primary factor defining the print resolution along the z-axis. When the nozzle is too far from the platform, the printed layers will not adhere to the surface, creating discontinuous strands, and the next layer will not be deposited adequately (Figure 8a). On the other hand, if the tip is too close to the platform, it might lead to a clogging of the nozzle or a discontinuous printing. In some research works, the 3D models are sliced into layers with a slicing height equal to 70% or 80% of the inner needle diameter [26,35]. A lower layer height will result in fewer errors between the layers, but longer printing times. Herein, we found that using a slicing height equal to the nozzle diameter was beneficial when determining the effective deposition rate. Therefore, establishing the right distance between the nozzle and the printing bed for the first layer is of vital importance for avoiding further deposition problems.

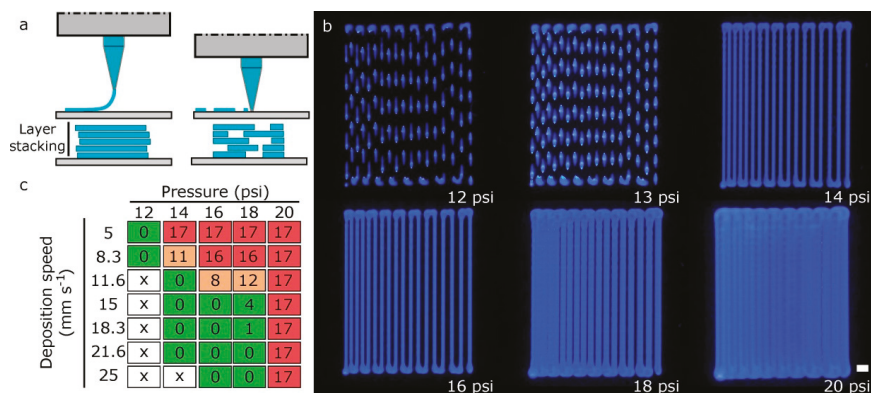


Figure 8. (a) scheme of the possible defects in the first layer calibration: nozzle too far from printing platform and nozzle too close to printing platform; (b) images of the zigzag path calibration models printed at a deposition speed of 15 mm s^{-1} for various printing pressures; scale bar: 1 mm; (c) quantification of the number of filled spaces between strands in the calibration model 2 varying printing pressure and deposition speed (green: good; orange: normal; red: bad; x: discontinuous printing).

The second calibration model or zigzag-path model was useful for determining the printing pressure needed to produce strands of the desired diameter. The variation of the printing pressure in Figure 8b for a fixed deposition speed of 15 mm s^{-1} produced strand widths of different dimensions. As expected, an excessive printing pressure and a low deposition speed produced dramatically wider strands that can eventually overlap (Figure 8c).

3.2. Print Resolution in Multi-Material Bioprinting

Extruded hydrogels usually result in spreading or diffusion from the initial shape as a consequence of standing their weight and their slow gelation rates [13]. In addition, the printed strands are never cylindrical, even if we use hollow cylinder-shaped nozzles. For these reasons, we decided to evaluate the print resolution of printed P407 filaments by two dimensions: width and height. We measured these two variables (Figure 9a,b) for different values of printing pressure and deposition speed to identify the optimal printing setup.

We observe that pressure and speed are strongly correlated while working at intermediate pressures (14–20 psi). However, the pressure is probably a more critical factor than deposition speed, especially for the height of the filaments printed (Figure 9a). This is consistent with previous studies on shear thinning hydrogels as the one performed by Trachtenberg et al. printing poly(propylene fumarate) (PPF) [25]. They determined that fiber height and width decreased with increasing deposition

speed and decreasing pressure. In addition, they also showed the higher effect of pressure with respect to speed and that the interaction of both factors (pressure and speed) is of great importance.

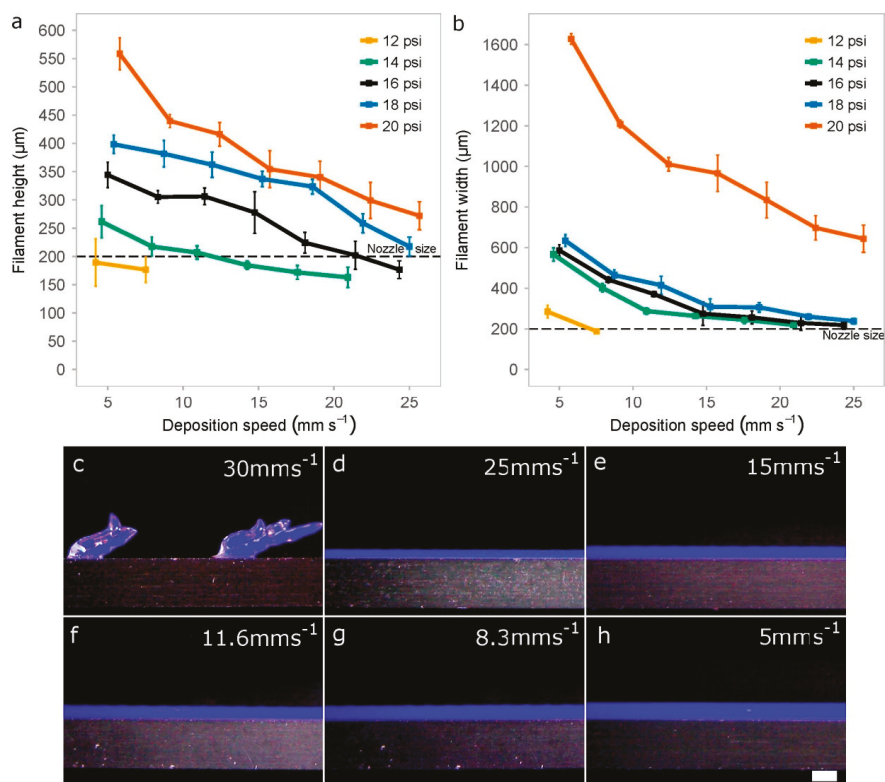


Figure 9. Impact of the printing pressure and deposition speed when creating rectilinear filaments. Quantification of the height (a) and width (b) of the printed filaments using 40 wt % P407 and a 27G tapered nozzle. Data represents the mean and standard deviation of six different samples ($n = 6$); (c–h) Representative photographs of different filaments printed at a constant pressure of 16 psi on a cover glass while reducing the deposition speed from 30 mm s^{-1} to 5 mm s^{-1} ; scale bar: 500 μm .

When printing at very low pressures (12 psi), there was a limitation in the deposition speed (around 8 mm s^{-1}) for creating continuous filaments, much lower value than the 25 mm s^{-1} achieved at the pressure of 16 psi. Discontinuous strands were usually generated when printing at higher deposition speed (Figure 9c).

In general, strand width should be almost always greater than height when keeping constant the value of the thickness layer (200 μm) because the nozzle tends to flatten the printed samples. We hypothesized that optimal printing configuration would be that the filaments show similar height and width values with a low swelling ratio. Figure 9a,b demonstrated that these conditions were achieved for printing pressures of 16 psi and 18 psi, and deposition speeds of around 21 mm s^{-1} and 25 mm s^{-1} , respectively. Using these parameters and 27G nozzles, the height and width of the strands were very similar: (i) for 16psi was around 202 μm and 230 μm ; and (ii) for 18 psi, the height–width values were 219 μm and 238 μm , respectively. Finally, we would like to highlight that very high pressure (20 psi) was a synonym of nonlinear response with too much bioink deposition and diffusion.

3.3. Multi-Material Bioprinting of Complex Scaffolds and 3D Constructs

After the four printheads were calibrated in x , y , and z axes and the appropriate setup was found, representative complex structures were printed to demonstrate the goodness of our proposed method. Different bioinks were printed per each layer to study the accumulated misalignments that produce heterogeneous patterns in the lattice scaffolds, and consequently the further reduction of the porosity.

Firstly, porous lattice structures composed of one bioink per layer were printed using two printheads (two fluorescent bioinks). The lattice structures were printed using infill percentages ranging from 10% to 35%. Low and medium infill percentages produced homogeneous patterns across the xy plane (Figure 10a–d) because of the successful calibration method. Nevertheless, the higher the infill percentage, the less homogeneous the pattern is. In that case (Figure 10e,f), there was a difference between the theoretical pore area designed and the total pore area printed. The printed pore area was smaller than the theoretical one, similar to what He et al. reported [13].

After printing the first layer, the second layer became a weight load to the first layer at the intersection. In addition, and as explained by [13], the radial diffusion of the upper hydrogel layer on the lower one at the intersections produced a radial narrowing of the pore. As a result, we obtained more rectangular-shaped pores than squared ones. These observations were more evident when the infill density was between 25% and 35% (Figure 10d–f). The limiting higher infill percentage seems to be 30%, with only a few overlapping areas observed. Therefore, we demonstrated that conducting an accurate calibration process is a guarantee of the integrity of the structures created layer-by-layer.

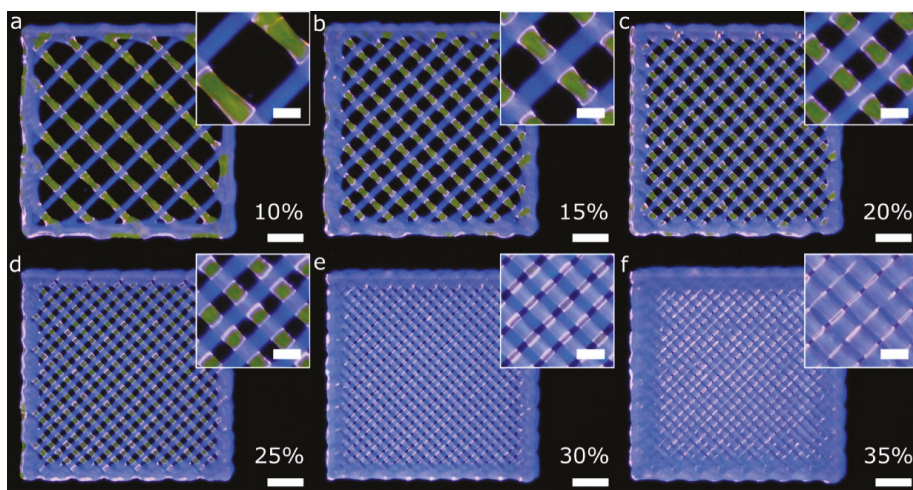


Figure 10. General and detailed views of porous lattice structures printed with two bioinks and two printheads. Each bioink was used in a different layer. The G-code was generated using the slicing software with the infill percentages: 10% (a), 15% (b), 20% (c), 25% (d), 30% (e) and 35% (f). The printing pressure and speed utilized in all the cases were 16 psi and 15 mm s^{-1} , respectively; scale bars: 2 mm (general views) and $500 \mu\text{m}$ (detailed views).

More complex lattice structures with fluorescent bioinks were printed using the four printheads mounted in the bioprinter. Diagonal and rectilinear patterns (Figure 11a–d) were stacked successfully into two different multi-material scaffolds (Figure 11g,k). The step by step stacking of the layers is depicted in Figure 11e–g,i–k. As in the previous scaffolds, the fidelity at the central part of the structures was better than that at the edges. The lack of accuracy near the edges was due to the accumulation of material in the region where the lines change their angles, similar to the mistakes reported by He et al. for single material extrusion [13]. Looking at the intersection point of the diagonal

structure (Figure 11h), we observed that the printheads in charge of dispensing blue and red hydrogels were slightly deviated in the $+x$ coordinate (according to Figure 7b). This effect was probably the leading cause of the small dissimilarities in shape observed at the empty triangular areas. These differences were consistent with the geometry tolerances of the structures due to the alignment errors in the x -direction reported in the previous sections. In summary, both multi-material structures were printed successfully due to the automatic calibration system used.

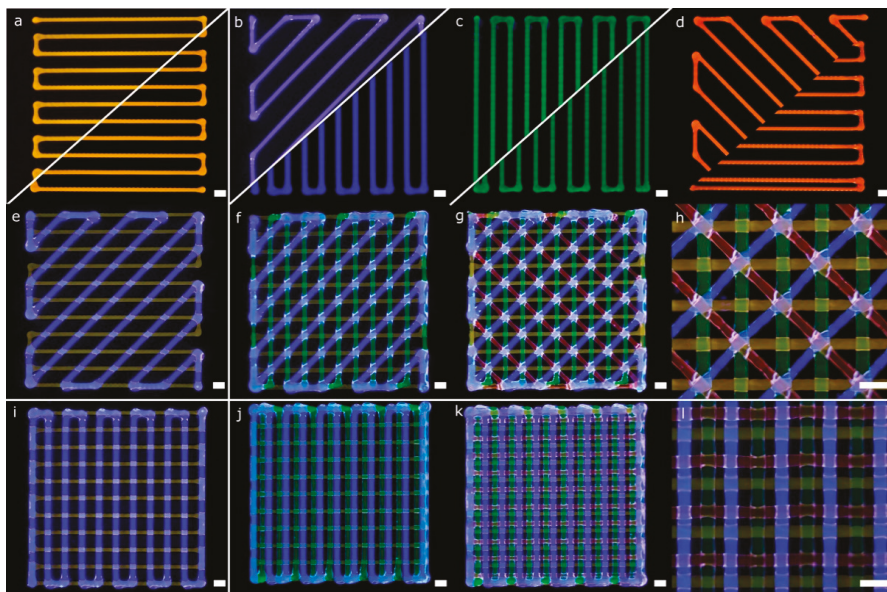


Figure 11. Pictures of a complex porous structures printed using four printheads with parallel and diagonal rectilinear patterns. Each fluorescent bioink was deposited in a different layer (a–d) with a total of four layers stacked (e–g,i–k). Detailed view of the diagonal (h) and perpendicular lattice structures (l); scale bars: 1 mm.

Regarding the rectilinear scaffold, the structure was created without overlapping areas (Figure 11i). The diffusion of the upper layer toward the lower one was due to the gravity being more evident than in the previous structure (Figure 11l). This effect is mainly related to the higher infill density (or smaller pore area). Through the successful printing of these two complex scaffolds, the proposed calibration methodology for multi-material bioprinting was verified. We believe that this approach will allow precise control of the deposition of various hydrogels and cell types for the fabrication of more biomimetic tissue structures.

Another CAD computer model (Figure 12a), which entails greater complexity compared to the previous structures (Figures 10 and 11), and thereby more calibration requirements, was printed using four fluorescent bioinks (Figure 12b). The model is a lattice structure formed by parallel rectilinear strands, each one with its particular bioink color (Figure 12c). We checked the existence of overlaps or empty spaces between the strands as a sign of an erroneous calibration across the xy axes. The overlaps with excessive material accumulated tended to break the continuity of the strands of the next layer (Figure 12e), whereas the errors in the calibration process produced distinct gaps between the parallel strands (see the blue filament in Figure 12d). On the other hand, if the xy offsets of the four printheads were correctly determined, the strands were printed without being merged as shown in Figure 12f. Note that the slicing of the 3D models took into account the swelling ratio of the hydrogel P407

(Figure 12a). This ratio was estimated at 100 μm per strand. Therefore, the initial diameter in the computing model needed to be 200 μm to obtain printed strands of 300 μm without overlapping. We conclude that the structures printed are an excellent example of correct calibration cases.

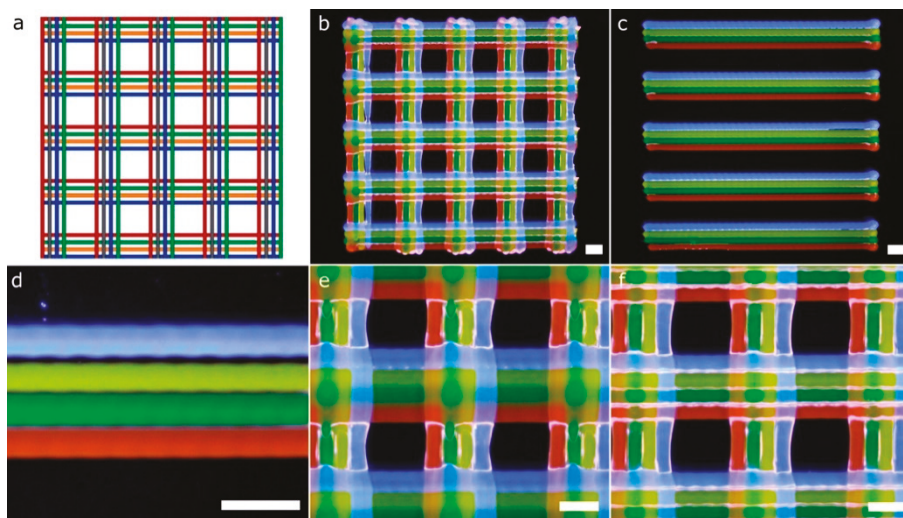


Figure 12. Pictures of a complex porous structure printed using four printheads and rectilinear patterns. The four printheads deposited dyed P407 in the same layer with a total of two layers stacked. General view of the CAD design (a) and printed porous structure (b); (c) general view of the first layer; (d) detailed view of printhead misalignments on the y -axis; (e) detailed view of strands diffusion in the second layer; (f) detailed view of the porous structure printed correctly. Scale bars: 1 mm.

Kang et al. [7] proved the immense potential of these kinds of lattice constructs (Figure 12b) to produce mandible bone and ear-shaped cartilage using cell-laden bioinks side-by-side with PCL to ensure the mechanical strength of the printed constructs. In this paper, we followed a similar approach regarding the MEBB system with four printheads but avoiding the proprietary nature of their multi-material bioprinter. Similar geometries with several bioinks printed right next to the other using parallel rectilinear strands (Figure 12c) but not in a lattice construct were fabricated by Lui et al. [12]. However, their approach incorporates an array of bioink reservoirs routed to a single printhead instead of our multiple and separate printheads. An advantage of the Lui et al. system is that it can eject the bioinks in individually or simultaneously, but it is limited to the use of a single nozzle, which restricts the ability to print hydrogels with very different viscosities. Other multi-material bioprinters such as the 3D-Bioplotter (EnvisionTEC, Gladbeck, Germany) incorporates a mechanism designed to exchange the printheads, which gives flexibility but increases the cost and complexity. Multiple bioinks can be printed in the same 3D model, but increasing the total printing time significantly. Although commercially available 3D bioprinters from EnvisionTEC and RegenHU can assure mechanical resolutions up to 1 μm and 5 μm , respectively, we demonstrated that our system with limited mechanical precision also produced complex structures with enough accuracy for tissue engineering applications [16,25,26,35,36].

Another CAD model to show the potential of a well-calibrated multi-material 3D bioprinter for generating complex structures is depicted in Figure 13. The model represents a human heart section where each of the parts consisted of a single perimeter and a porous infill at 15% printed in two layers. All of the printing trajectories, either for the perimeter or the porous infill (Figure 4b,c), were generated automatically by the slicing software, which greatly facilitated the printing process. We proceed with

the following printing sequence: orange (P1), blue (P2), green (P3) and red (P4), but this ordering can be easily changed.

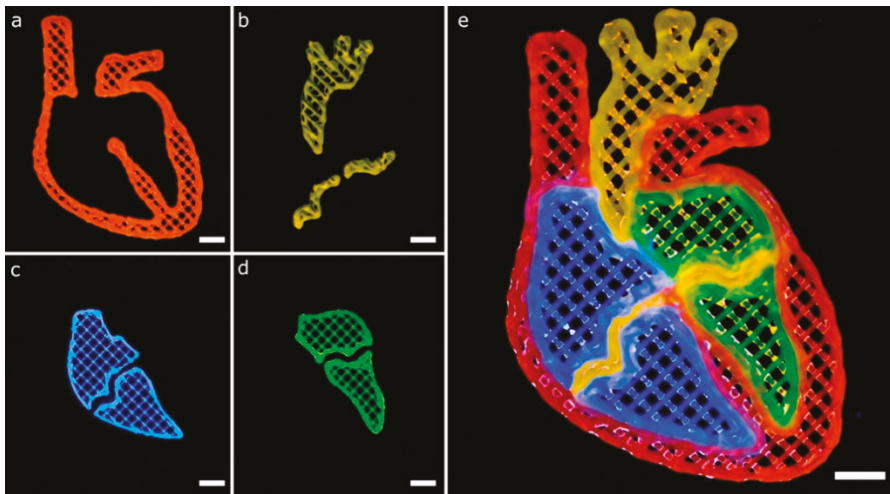


Figure 13. Complex multi-material printing of model that represents a human heart section. The model is composed of heterogeneous bioinks to demonstrate the multi-material capabilities of our system. (a–d) printing of the main parts of the heart section separately; (e) combination of the multiple parts using the four bioinks in a complex structure; scale bars: 5 mm.

The CAD model of the heart section has curvilinear geometries that create complex trajectories than previous models (Figure 12) based on straight lines. These geometries increased the number of print errors detected. For instance, blue (Figure 13c) and green (Figure 13d) bioinks overlaid the thin middle sections of the heart printed of orange bioink (Figure 13b). Better calibration procedures might avoid these defects by incorporating the effect of the bioink swelling during CAD models generation. Liu et al. printed a very similar geometry of the human heart section using their multi-material platform described before [12]. We obtained similar results with our constructs showing good demarcation among adjacent materials.

Cell-laden Gel-Alg and P407 bioinks were printed in a single session creating multi-material constructs (Figure 14). Gel-Alg represents a more challenging material regarding printability when compared to P407. Consequently, the printed strands were not straight and the openings were irregular, reducing the pore area (Figure 14a). Other authors also reported complications when printing Gel-Alg mixes. Paxton et al. attributed the weak printability to the lower yield stress point of Gel-Alg blends [35]. Despite this, we were capable of calibrating the bioprinter and obtaining the proper printing parameters to create complex constructs from the CAD models in a single multi-material session (Figure 14b–d). High cell viability in the bioprinted Gel-Alg constructs (Figure 15a) was also ensured at 1 h and 24 h post-printing (Figure 15b,c). These observations demonstrated that our calibration method using P407 was helpful in adjusting some printing parameters to specific values that did not reduce cell viability after bioprinting cells with another hydrogel, Gel-Alg blends.

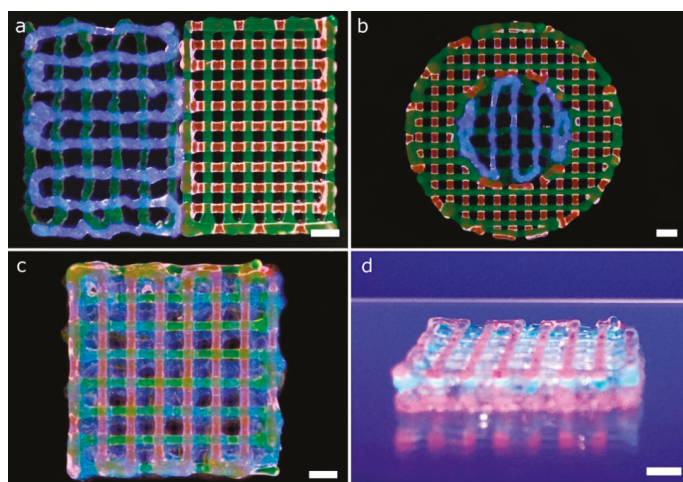


Figure 14. Complex multi-material structures printed. Gel-Alg and P407 bioinks were printed using 25G and 27G tapered nozzles, respectively. (a) general view of a 2-layer porous lattice structures printed with Gel-Alg (left, green for printhead 1 and blue for printhead 2) and P407 (right, green for printhead 3 and red for printhead 4) bioinks; (b) general view of circular lattice structure with the inner circle printed in Gel-Alg (green for printhead 1 and blue for printhead 2), and the outer circle printed in P407 (green for printhead 3 and red for printhead 4); general (c) and side view (d) of an 8-layer porous lattice with alternating layers of Gel-Alg and P407. Sequence of colors: Gel-Alg (orange), Gel-Alg (blue), P407 (green) and P407 (red); scale bars: 2 mm.

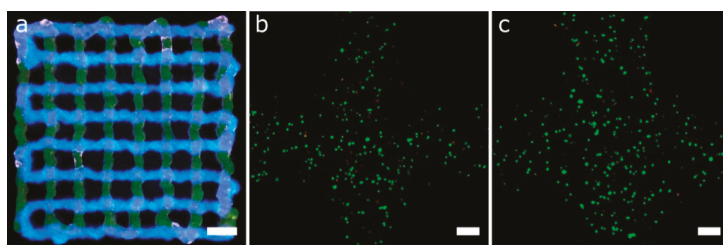


Figure 15. (a) general view of 2-layer porous lattice structure printed with Gel-Alg bioinks and two printheads. Each bioink was utilized for a different layer using a 25 G nozzle (scale bar: 2 mm). (b,c) Representative confocal images of cell viability assay of printed hASCs using the same Gel-Alg mixture and printing parameters than that of (a) but without fluorescence inks at 1 h (b) and 24 h (c) post-printing (scale bars: 200 μm).

3.4. Multi-Material Printing of Complex 3D Vascular Networks

Several tests were performed to produce pillars (vertical strands) and hanging bridges between them using P407, similar to the fugitive structures printed by Kolesky et al. that mimic vascular networks [22]. It should be pointed out that the constructs presented in this section were printed using only 40wt % P407 hydrogels colored with different dyes. This does not diminish the widespread of the solution proposed for multi-material bioprinting. Pillars were printed moving the printhead on the z-axis and keeping constant the xy -coordinates. When printing one pillar, and prior to the printhead movement in the z-direction, the tip of the nozzle was placed at 200 μm from the glass slide and the solenoid valve was opened a waiting time of 500 ms. Within this time, the P407 started to

flow and permitted to deposit an excess of material in the base of the pillar, in order to give it more stability (Figure 16d). If no waiting time was utilized, a weaker pillar base was produced, decreasing the structure stability. Once the nozzle extruded the pillar moving to the desired height, an additional waiting time of 1 s was considered to allow the column to stabilize. After that, the nozzle was raised at a fast speed (25 mm s^{-1}), a distance 2 mm higher than the pillar height to improve its verticality. There was a limit in the column heights that could be achieved without losing verticality.

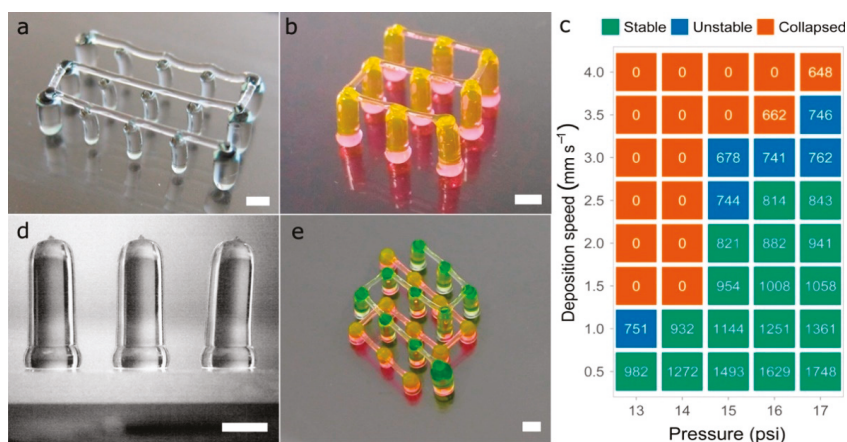


Figure 16. (a,b) complex vascular 3D networks printed in P407; (c) evaluation of the stability of 3D printed vertical pillars for a fixed height of 8 mm. Printing pressure ranging from 13 psi to 17 psi and deposition speeds ranging from 0.5 mm s^{-1} to 4 mm s^{-1} . The data inside the figure represents the mean of pillars diameter (in μm) of six different samples ($n = 6$); (d) side view of 3D printed 4 mm height pillars; (e) vascular structure printed at two different heights (2 mm and 5 mm) with interconnected bridges; scale bars: 1 mm.

Different printing pressures (13 psi to 17 psi) and deposition speeds (0.5 mm s^{-1} to 4 mm s^{-1}) were tested, producing pillars with different diameters and stability (Figure 16c). A constant pillar height of 8 mm was set for all the vertical pillars printed with a 27G nozzle. As expected, the lower the speed and the higher the pressure, the larger the diameter of the pillars extruded. Regardless of the pressure and the speed utilized, pillars with diameters above $814 \mu\text{m}$ always remained stable while pillars with diameters between $678 \mu\text{m}$ and $762 \mu\text{m}$ tended to bend slightly losing their verticality. Above these diameters, pillars collapsed utterly touching the glass slide.

Regarding the hanging bridges between the pillars, the deposition speed on the xy -plane and the distance between pillars have a direct influence on the straightness of the bridge (Figure 16a). To generate continuous straight strands (Figure 16b,e), pillars were spaced up to 4 mm while the deposition speed was set at 7.5 mm s^{-1} . When faster deposition speeds were utilized for the bridges, the pillars tended to collapse by the impact of the deposited strands. In general, the samples printed demonstrated excellent results for maximum heights of 8 mm to 10 mm.

If different materials or even the same material but in different concentrations are used to print this type of vascular 3D networks, it would be first necessary to evaluate the stability of the vertical pillars for different process parameters, as shown in this section (Figure 16c). Then, the next step would be to find the optimal deposition speed for the hanging bridges. These types of constructs were tested by Ribeiro et al. [36] printing poloxamer-poly(ethylene glycol) (PEG) blends at different concentrations (poloxamer/PEG: 30%, 29/1%, 28/2%, 27/3%, 26/4% and 20%). They found that higher concentration of P047 led to a decrease in bridge sagging, which coincides with our observations at higher concentrations of poloxamer.

We agree with He et al. [13] that the ideal multi-material 3D bioprinter for tissue engineering applications should be high throughput, ease of use, with excellent print resolution, and capability of dispensing multiple bioinks with different viscosities. Even if some of the commercially available bioprinters incorporate all these specifications, the authors would like to stand up for the open-source bioprinters. This equipment can provide all discussed advantages plus avoiding the proprietary nature of the commercial ones. Indeed, our open-source 3D printing platform was capable of achieving high accuracy and cell viability in multi-material bioprinting with a relatively lower cost than other commercial units.

3.5. Limitations of the Calibration Method in the Multi-Material Bioprinting Proposed

From a mechanical perspective, the calibration of the four printheads depends on the P1 printhead stability, and errors on the P1 are propagated to the other printheads. Similarly, a proper leveling of the printing platform is essential for a successful calibration of the z-offset, which becomes even more significant when printing large 3D models. Another limitation of our calibration method is the intrinsic *xy*-offset tolerance that depends on the predefined separation of the printed lines of the pattern proposed called calibration model 1. We assume that our results could dramatically change when printing with very different nozzle diameters or even depending on the material when swelling after printing and the strands' straightness are not the ideal ones. Moreover, different human errors could cause incorrect choices in the visual identification of the best-aligned pair of strands. Potential users must consider all the tolerances and mistakes mentioned when determining the final print accuracy of their equipment. Concerning the structures printed, critical locations such as sharp corners still need more effort to identify the proper changes in the printing pressure and deposition speed to avoid an excessive accumulation of materials in those areas.

4. Conclusions

The use of multiple cell types and biomaterials is essential to recapitulate the architecture, mechanical strength, and complexity of human tissues. In 3D bioprinting, maintaining the print resolution along the layer-by-layer manufacturing process offers greater stability when creating thick self-supporting tissue constructs. We presented a non-expensive and useful calibration method applicable to multi-material 3D bioprinting. The particular multi-material 3D bioprinter herein used was a desktop 3D printer modified to incorporate four independent MEBB printheads.

The base bioink employed for calibration due to its remarkable stability was P407 hydrogel mixed with four fluorescent dyes. Our calibration procedure is exportable to any bioprinting system, but it is strongly recommended to use an automatic *z* offset system to reduce the configuration time drastically. Parameters such as the printing pressure, deposition speed, nozzle height, and nozzle diameter were evaluated from the experimental results to obtain the optimal printing conditions.

Multi-material constructs were printed in different combinations of P407 and Gel-Alg bioinks. In addition, complex multi-material 3D models and intricate vascular networks were created assessing the final accuracy and printing precision of the bioprinting platform. Cell viability after printing cell-laden Gel-Alg bioinks was also verified with successful results. Future works will explore the creation of more complex tissue constructs with different biomaterials and cell types. Other technologies such as drop-on-demand bioprinting could also benefit from the method proposed. Future works could consider the use of different bioprinting technologies to demonstrate the potential and universality of the proposed multi-material calibration method.

Author Contributions: Conceptualization, A.S.-G. and E.S.-O.; Funding acquisition, C.E.-L.; Investigation, E.S.-O.; Supervision, A.P.-E. and C.E.-L.; Writing—Original draft, E.S.-O. and A.S.-G.; Writing—Review and editing, A.P.-E. and C.E.-L.

Funding: This research was funded by the FPI-CAR-2014 granted by the Government of La Rioja (Spain), research funding No. 266486, 273689 and 273689 (FINSKIN), and mobility grants No. 276371 (VATURP), No. 286793

(VASC BIOEXP), 286788 and 278153 by the Academy of Finland (Finland). “Instituto de Estudios Riojanos” (Spain) and APPI17/04 from University of La Rioja also funded parts of this research.

Acknowledgments: The authors would like to thank to BQ (Mundo Reader S.L.) for their collaboration in the study.

Conflicts of Interest: The authors declare no conflict of interest. The funders had no role in the design of the study; in the collection, analyses, or interpretation of data; in the writing of the manuscript, and in the decision to publish the results.

References

1. Khademhosseini, A.; Langer, R. A decade of progress in tissue engineering. *Nat. Protocols* **2016**, *11*, 1775. [[CrossRef](#)] [[PubMed](#)]
2. Lee, W.; Debasitis, J.C.; Lee, V.K.; Lee, J.-H.; Fischer, K.; Edminster, K.; Park, J.-K.; Yoo, S.-S. Multi-layered culture of human skin fibroblasts and keratinocytes through three-dimensional freeform fabrication. *Biomaterials* **2009**, *30*, 1587–1595. [[CrossRef](#)] [[PubMed](#)]
3. Zhao, X.; Liu, L.; Wang, J.; Xu, Y.; Zhang, W.; Khang, G.; Wang, X. In vitro vascularization of a combined system based on a 3D printing technique. *J. Tissue Eng. Regen. Med.* **2016**, *10*, 833–842. [[CrossRef](#)] [[PubMed](#)]
4. Wang, X.; Yan, Y.; Zhang, R. Rapid prototyping as a tool for manufacturing bioartificial livers. *Trends Biotechnol.* **2007**, *25*, 505–513. [[CrossRef](#)] [[PubMed](#)]
5. Zhang, Y.S.; Yue, K.; Aleman, J.; Mollazadeh-Moghaddam, K.; Bakht, S.M.; Yang, J.; Jia, W.; Dell’Erba, V.; Assawes, P.; Shin, S.R.; et al. 3D Bioprinting for Tissue and Organ Fabrication. *Ann. Biomed. Eng.* **2017**, *45*, 148–163. [[CrossRef](#)] [[PubMed](#)]
6. Wilson, W.C.; Boland, T. Cell and organ printing 1: Protein and cell printers. *Anat. Rec. Part A Discov. Mol. Cell. Evol. Biol.* **2003**, *272*, 491–496. [[CrossRef](#)] [[PubMed](#)]
7. Kang, H.-W.; Lee, S.J.; Ko, I.K.; Kengla, C.; Yoo, J.J.; Atala, A. A 3D bioprinting system to produce human-scale tissue constructs with structural integrity. *Nat. Biotechnol.* **2016**, *34*, 312. [[CrossRef](#)] [[PubMed](#)]
8. Daly Andrew, C.; Cunniffe Gráinne, M.; Sathy Binulal, N.; Jeon, O.; Alsberg, E.; Kelly Daniel, J. 3D Bioprinting of Developmentally Inspired Templates for Whole Bone Organ Engineering. *Adv. Healthcare Mater.* **2016**, *5*, 2353–2362. [[CrossRef](#)] [[PubMed](#)]
9. Ozbolat, I.T.; Moncal, K.K.; Gudapati, H. Evaluation of bioprinter technologies. *Addit. Manuf.* **2017**, *13*, 179–200. [[CrossRef](#)]
10. Ning, L.; Chen, X. A brief review of extrusion-based tissue scaffold bio-printing. *Biotechnol. J.* **2017**, *12*, 1600671. [[CrossRef](#)] [[PubMed](#)]
11. Ozbolat, I.T.; Hospodiuk, M. Current advances and future perspectives in extrusion-based bioprinting. *Biomaterials* **2016**, *76*, 321–343. [[CrossRef](#)] [[PubMed](#)]
12. Liu, W.; Zhang Yu, S.; Heinrich Marcel, A.; De Ferrari, F.; Jang Hae, L.; Bakht Syeda, M.; Alvarez Mario, M.; Yang, J.; Li, Y.-C.; Trujillo-de Santiago, G.; et al. Rapid Continuous Multimaterial Extrusion Bioprinting. *Adv. Mater.* **2016**, *29*, 1604630. [[CrossRef](#)] [[PubMed](#)]
13. He, Y.; Yang, F.; Zhao, H.; Gao, Q.; Xia, B.; Fu, J. Research on the printability of hydrogels in 3D bioprinting. *Sci. Rep.* **2016**, *6*, 29977. [[CrossRef](#)] [[PubMed](#)]
14. Moroni, L.; Boland, T.; Burdick, J.A.; De Maria, C.; Derby, B.; Forgacs, G.; Groll, J.; Li, Q.; Malda, J.; Mironov, V.A.; et al. Biofabrication: A Guide to Technology and Terminology. *Trends Biotechnol.* **2018**, *36*, 384–402. [[CrossRef](#)] [[PubMed](#)]
15. Lei, M.; Wang, X. Biodegradable Polymers and Stem Cells for Bioprinting. *Molecules* **2016**, *21*, 539. [[CrossRef](#)] [[PubMed](#)]
16. Wang, X.; Ao, Q.; Tian, X.; Fan, J.; Tong, H.; Hou, W.; Bai, S. Gelatin-Based Hydrogels for Organ 3D Bioprinting. *Polymers* **2017**, *9*, 401. [[CrossRef](#)]
17. Jetze, V.; Benjamin, P.; Thijs, J.B.; Jelle, B.; Wouter, J.A.D.; Ferry, P.W.M.; Jos, M. Biofabrication of multi-material anatomically shaped tissue constructs. *Biofabrication* **2013**, *5*, 035007.
18. Xu, M.; Wang, X.; Yan, Y.; Yao, R.; Ge, Y. An cell-assembly derived physiological 3D model of the metabolic syndrome, based on adipose-derived stromal cells and a gelatin/alginate/fibrinogen matrix. *Biomaterials* **2010**, *31*, 3868–3877. [[CrossRef](#)] [[PubMed](#)]

19. Kai, H.; Xiaohong, W. Rapid prototyping of tubular polyurethane and cell/hydrogel constructs. *J. Bioact. Compat. Polym.* **2011**, *26*, 363–374. [[CrossRef](#)]
20. Jin-Hyung, S.; Jung-Seob, L.; Jong Young, K.; Dong-Woo, C. Bioprinting of a mechanically enhanced three-dimensional dual cell-laden construct for osteochondral tissue engineering using a multi-head tissue/organ building system. *J. Micromech. Microeng.* **2012**, *22*, 085014.
21. Rocca, M.; Fragasso, A.; Liu, W.; Heinrich, M.A.; Zhang, Y.S. Embedded Multimaterial Extrusion Bioprinting. *SLAS Technol. Transl. Life Sci. Innov.* **2017**, *23*, 154–163. [[CrossRef](#)] [[PubMed](#)]
22. Kolesky, D.B.; Homan, K.A.; Skylar-Scott, M.A.; Lewis, J.A. Three-dimensional bioprinting of thick vascularized tissues. *Proc. Natl. Acad. Sci. USA* **2016**, *113*, 3179–3184. [[CrossRef](#)] [[PubMed](#)]
23. Wang, X.; Rijff, B.L.; Khang, G. A building-block approach to 3D printing a multichannel, organ-regenerative scaffold. *J. Tissue Eng. Regen. Med.* **2017**, *11*, 1403–1411. [[CrossRef](#)] [[PubMed](#)]
24. Suntornnond, R.; Tan, E.Y.S.; An, J.; Chua, C.K. A Mathematical Model on the Resolution of Extrusion Bioprinting for the Development of New Bioinks. *Materials* **2016**, *9*, 756. [[CrossRef](#)] [[PubMed](#)]
25. Trachtenberg, J.E.; Placone, J.K.; Smith, B.T.; Piard, C.M.; Santoro, M.; Scott, D.W.; Fisher, J.P.; Mikos, A.G. Extrusion-Based 3D Printing of Poly(propylene fumarate) in a Full-Factorial Design. *ACS Biomater. Sci. Eng.* **2016**, *2*, 1771–1780. [[CrossRef](#)]
26. Ting, G.; Timothy, R.H.; Casey, G.L.; Feng, G.; Ankit, G.; Jordan, E.T.; Antonios, G.M.; John, P.F. 3D printing PLGA: A quantitative examination of the effects of polymer composition and printing parameters on print resolution. *Biofabrication* **2017**, *9*, 024101.
27. Teng, G.; Gregory, J.G.; Joshua, S.C.; Anil Kumar, P.R.; Young-Joon, S.; Anthony, A.; James, J.Y.; Sang Jin, L. Optimization of gelatin–alginate composite bioink printability using rheological parameters: A systematic approach. *Biofabrication* **2018**, *10*, 034106.
28. Wang, X.; He, K.; Zhang, W. Optimizing the fabrication processes for manufacturing a hybrid hierarchical polyurethane–cell/hydrogel construct. *J. Bioact. Compat. Polym.* **2013**, *28*, 303–319. [[CrossRef](#)]
29. Sodupe-Ortega, E. Modification of Marlin Firmware. Available online: https://github.com/ensod/Marlin_4printheads (accessed on 1 July 2018).
30. Ranellucci, A. Slic3r G-Code Generator for 3D Printers. Available online: <http://slic3r.org> (accessed on 1 July 2018).
31. Littwin, M. Repetier. Available online: <https://www.repetier.com> (accessed on 1 July 2018).
32. Escobedo-Lucea, C.; Bellver, C.; Gandia, C.; Sanz-Garcia, A.; Esteban, F.J.; Mirabet, V.; Forte, G.; Moreno, I.; Lezameta, M.; Ayuso-Sacido, A.; et al. A Xenogeneic-Free Protocol for Isolation and Expansion of Human Adipose Stem Cells for Clinical Uses. *PLoS ONE* **2013**, *8*, e67870. [[CrossRef](#)] [[PubMed](#)]
33. Rasband, W.S. ImageJ. Available online: <http://rsb.info.nih.gov/ij/index.html> (accessed on 10 August 2018).
34. Chang Carlos, C.; Boland Eugene, D.; Williams Stuart, K.; Hoying James, B. Direct-write bioprinting three-dimensional biohybrid systems for future regenerative therapies. *J. Biomed. Mater. Res. Part B Appl. Biomater.* **2011**, *98*, 160–170. [[CrossRef](#)] [[PubMed](#)]
35. Paxton, N.; Smolan, W.; Bock, T.; Melchels, F.; Groll, J.; Jungst, T. Proposal to assess printability of bioinks for extrusion-based bioprinting and evaluation of rheological properties governing bioprintability. *Biofabrication* **2017**, *9*, 044107. [[CrossRef](#)] [[PubMed](#)]
36. Ribeiro, A.; Blokzijl, M.M.; Levato, R.; Visser, C.W.; Castilho, M.; Hennink, W.E.; Vermonden, T.; Malda, J. Assessing bioink shape fidelity to aid material development in 3D bioprinting. *Biofabrication* **2017**, *10*, 014102. [[CrossRef](#)] [[PubMed](#)]



© 2018 by the authors. Licensee MDPI, Basel, Switzerland. This article is an open access article distributed under the terms and conditions of the Creative Commons Attribution (CC BY) license (<http://creativecommons.org/licenses/by/4.0/>).

Article

Numerical-Experimental Study of the Consolidation Phenomenon in the Selective Laser Melting Process with a Thermo-Fluidic Coupled Model

Francisco Cordovilla ^{1,*}, Ángel García-Beltrán ¹, Miguel Garzón ², Diego A. Muñoz ³ and José L. Ocaña ¹

¹ UPM Laser Centre, E.T.S. Ingenieros Industriales, Universidad Politécnica de Madrid, C/José Gutiérrez Abascal 2., 28006 Madrid, Spain; agarcia@etsii.upm.es (A.G.-B.); jlocana@etsii.upm.es (J.L.O.)

² PM-Tec Engineering S.A.S., Portos Sabana 80, Bodega 78, Cota, Cundinamarca 250017, Colombia; mgarzon@pm-tec.co

³ Optimización Matemática de Procesos ÓPTIMO, Centro de Ciencia Básica, Universidad Pontificia Bolivariana, Circular 1, 70-01, Medellín 050031, Colombia; amunoz@pm-tec.co

* Correspondence: francisco.cordovilla.baro@upm.es; Tel.: +34-65-518-4271

Received: 4 July 2018; Accepted: 9 August 2018; Published: 12 August 2018

Abstract: One of the main limiting factors for a widespread industrial use of the Selective Laser Melting Process is its lack of productivity, which restricts the use of this technology just for high added-value components. Typically, the thickness of the metallic powder that is used lies on the scale of micrometers. The use of a layer up to one millimeter would be necessarily associated to a dramatic increase of productivity. Nevertheless, when the layer thickness increases, the complexity of consolidation phenomena makes the process difficult to be governed. The present work proposes a 3D finite element thermo-coupled model to study the evolution from the metallic powder to the final consolidated material, analyzing specifically the movements and loads of the melt pool, and defining the behavior of some critical thermophysical properties as a function of temperature and the phase of the material. This model uses advanced numerical tools such as the Arbitrary Lagrangean–Eulerian formulation and the Automatic Remeshing technique. A series of experiments have been carried out, using a high thickness powder layer, allowing for a deeper understanding of the consolidation phenomena and providing a reference to compare the results of the numerical calculations.

Keywords: Selective Laser Melting; thermo fluidic; phase change; consolidation; Arbitrary Lagrangean–Eulerian Method; metallic powder

1. Introduction

In the Selective Laser Melting Process (SLM), the objective, in an industrial context, is to manufacture continuous solid components layer by layer. It uses a laser beam to consolidate the metallic powder at each of the steps in the growth of the workpiece [1]. The layer-by-layer philosophy of production theoretically eliminates the geometrical complexity of the part as a restriction for the manufacturing process. This circumstance provides the additive manufacturing technologies with large advantages to face geometrically complicated designs and a high flexible demand, in comparison with conventional techniques [2].

As is well known, productivity is one of the main limiting factors for a wide use of the additive manufacturing technologies [3], restricting their industrial application to only high added value parts, such as aeronautical parts [4] or medical implants [5].

The use of high thickness powder layers in the SLM process can contribute to improve productivity by reducing the number of steps for a given height of the desired component. There are multiple

works, of theoretical or experimental nature, where the thickness of the powder layer and the diameter of the laser beam lies on the microscale. In reference [6], a layer of 30 μm is used to carry out an experimental parametrization of the process. Reference [7] calculates the evolution of the temperature during the SLM process considering a beam diameter of several tens of microns. If the thickness of the layer is turned into a scale ranging from several hundred microns up to 1 mm, and, the laser beam is adjusted to a diameter of several mm, the productivity of the process necessarily experiences a dramatic increase.

Although the relation between the size of the powder layer and the beam diameter with the productivity is extremely clear, there is neither significant research nor industrial usage of large beams and thicknesses for the SLM process. It can be associated with the more complex behavior of the melt pool, when a larger amount of material is involved, which makes the process more difficult to be governed.

Although most of the relevant phenomena in the consolidation of the material are present with small bed thicknesses, such as limited diffusivity associated to poor particle contact, phase changes, and, for the liquid metal, gradients of surface tension associated with Marangoni convection, or even recoil pressure; in the case of large thicknesses these factors strongly influence the size and shape of the melt pool leading to a relatively high degree of curvature of the geometry of the consolidated material.

There are different approaches to study the consolidation of the material during the SLM process. The work of [8], highlights very important aspects of the consolidation, such as the evolution of the material throughout several phases, powder, liquid and solid. The relevance of considering the evolution of the melt pool, with explicit use of the fluidic properties of the liquid metal, such as dynamic viscosity or surface tension, is emphasized. However, the use of a discrete particle model forces the representation of the domain to be at the scale of the metallic particles (several microns) and makes it difficult, from a computational point of view, to project the behavior of the melt pool on the final dimension of the consolidated material in a real process.

A totally different approach is carried out on the models based on the activation of layers of finite elements when they are reached by the laser beam, reproducing in this way the manufacturing of the part layer by laser [9]. These models depart from the final design of the part that is going to be manufactured, study the evolution of the temperature, and, in some cases, estimate the residual stresses in the bulk of consolidated material. No analysis of the phase change or the melt pool is performed. While this approach can provide interesting results, at little computational cost, associated to processes with a very low layer thickness, where the movements of the melt pool are very small, in the case of normal or high thickness of the powder bed, the simulation cannot depart from the final design of the part since, in these cases, the final shape of the consolidated material cannot be predicted with only thermal or mechanical stress considerations. For instance, in reference [10], it can be seen that the initial powder has given rise, as a consequence of the SLM process, to a drop-like profile in the cross section of the consolidated material. It can only be due to the surface tension when the metal was in liquid state.

The present work proposes the use of a coupled thermo-fluidic model in the frame of a moving mesh, in combination with experimental test of the process with a powder bed of 1 mm thickness. When a large thickness of the powder bed is considered, there is such an amount of liquid metal submitted to the effect of the surface tension that the differences between the original flat domain representing the powder bed and the arising droplet forces the domain not only to move but also to recursively experience re-meshing. The droplet formation process happens in a time scale of milliseconds. The model considers the evolution of the material during the different phases, powder, liquid and solid, associating some critical thermo-physical properties, such as thermal conductivity, dynamic viscosity or surface tension, with the temperature and the phase of the material, making specific considerations to describe phase change. The concatenation of the thermo-fluidic properties to describe two different phase changes, powder to liquid and liquid to solid, must be adapted to the characteristics of each process in particular. Sigmoid functions are proposed to describe the evolution

of the thermo-physical properties during the different states of the matter. The use of this explicit formulation for the phase change introduces an innovative way of dealing with it, which does not have high computational requirements. The application of the finite element method on domains representing the powder bed and the substrate, makes the study of the consolidation happen at a scale where the final macroscopic dimensions of the material can be predicted, thus favoring, in this way, its application to real industrial situations. The so-called Arbitrary Lagrangean–Eulerian formulation [11] is used to allow the movement of the mesh to be performed, which, along with some specific numerical tools, like Automatic Remeshing techniques, enables the movements of the melt pool to be fully represented. A series of experimental tests was carried out using a 1 mm thickness powder bed. These tests were used, in the first place, to understand some critical aspects associated to the use of large thicknesses. Finally, theoretical and experimental cross sections were compared, showing a good degree of agreement.

2. Materials and Methods

The AISI 316L has been chosen as working material. This election has its basis on the wide use of this kind of steel in those fields where the additive manufacturing technologies have the maximum potential of application [12]. The AISI 316 steel offers high mechanical resistance, good corrosion behavior, and, of interest for medical applications, good biocompatibility properties [13]. The combination of these characteristics of the material with the capability of additive manufacturing to manufacture very complex geometries, made to measure in some cases, make of high interest the use of powders of AISI 316L and understanding its behavior in the selective laser melting process.

The commercial powder METCO MetcoClad™ 316L-SI has been used to carry out the real tests. The dominating spherical shape of its particles and its granulometric size distribution, facilitate the development of theoretical hypotheses to adjust the thermo-physical properties in the modelling. Table 1 shows the main characteristics of the commercial powder used.

Table 1. Composition and particle size distribution of the MetcoClad™ 316L-SI powder.

Composition (%wt)	Fe	Ni	Cr	Mo	Si	Mn	C	Others
	Balance	12.0	17.0	2.5	2.3	1.0	0.03	≤0.05
Particles size (µm)	Nominal Range 44–106		–	(%) > 106 5	44 < (%) < 106 90		(%) < 44 5	

2.1. Constitutive Equations and Its Implications on the Modeling

2.1.1. Absorption Coefficient of the Metal Powder

When the laser beam hits the metallic powder, part of the electromagnetic radiation is absorbed leading to an elevation of the temperature in the interaction area. During the time in which the powder is heated but not having experienced melting yet, that part of the radiation that is reflected from a given particle may impact on one of the surrounding ones, which, in turn, will behave in the same way absorbing part of the radiation and reflecting the remaining. The repetition of this process among adjacent particles (see Figure 1) leads to a higher overall absorption coefficient, especially, if compared with the situation of a laser beam irradiating a flat surface where the reflected radiation escapes from the material.

The total absorption, A_T , can be characterized by the addition of the radiation absorbed by each particle A_i plus the effect of the reflected radiation on each particle, when it impacts on the surrounding ones, as the product of the reflection coefficient of the first one R_i by the respective absorption coefficient corresponding to the particle which receives this reflection A_{i+1} . According to the Fresnel Equations from the electromagnetic theory [14], the absorption coefficient of radiation when it impacts on the surface of a conductive media depends on the kind of polarization of the radiation, its wavelength, the

optical properties of the material (complex refractive index) and the angle of incidence between the propagation direction of the radiation and the normal vector of the irradiated surface, θ . While most of the indicated variables can be fixed for a given process configuration, and the complex refractive index of the material for the process wavelength can be taken from [15], the incidence angle of the laser radiation on each particle is a random variable, whose value can vary between 0 and $\pi/2$ rad. Since there is no reason to consider any value of the defined range as the most likely, this uncertainty can be solved by taking the average absorption coefficient from all the values of the range, $A(\theta_{\pi/2}^0)$. In this way $A_{i+1} = A_i = A(\theta_{\pi/2}^0)$. Additionally, not all radiation reflected from a given particle is trapped by the surrounding ones, and it can be released definitely from the bulk of powder. This phenomenon can be described by a coefficient to retain radiation within the bulk of powder, η , which can be related with the thickness of it, h . Like this, the multiple reflection process can be described mathematically by a series, as Equation (1):

$$A_T = A(\theta_{\pi/2}^0) + \eta(h)R(\theta_{\pi/2}^0)A(\theta_{\pi/2}^0) + \eta(h)^2R^2(\theta_{\pi/2}^0)A(\theta_{\pi/2}^0) + \eta(h)^3R^3(\theta_{\pi/2}^0)A(\theta_{\pi/2}^0) + \dots \quad (1)$$

Equation (1) corresponds to a convergent series that can be expressed by a general term as Equation (2):

$$A_T = \frac{A(\theta_{\pi/2}^0)}{1 - \eta(h)R(\theta_{\pi/2}^0)} \quad (2)$$

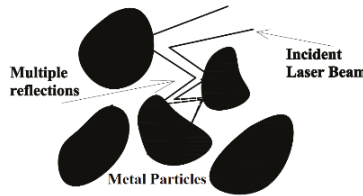


Figure 1. Illustration of the way in which the radiation reflected from a given particle may impact on the surrounding ones, in a multiple reflection process, resulting in a high absorption of the radiation supplied by the laser beam.

2.1.2. Thermo-Fluidic Coupling

Once the energy from the laser source has been absorbed by the powder, its temperature quickly increases. At the beginning, the short contact surface of the particles limits thermal diffusivity and the melting of the powder occurs just in the proximities of the laser-powder interaction zone. Once the liquid has been formed, the heat diffusion and wettability conditions improve, and the melt pool spreads beyond the limits of the interaction area [16]. The first phase change that takes places happens, therefore, for that part of the powder that becomes liquid, and the subsequent phase change will happen with the solidification of that liquid to form a consolidated solid. Both transitions, powder to liquid and liquid to solid, are driven by the thermal cycle imposed by the scanning of the laser source (fast heating and fast cooling respectively), although, each of them takes places under specific circumstances. The material which experiences melting during the heating stage evolves from being disaggregated particles with very low cohesion force among them and no continuous surface (each particle has its own one), to a continuous medium where exists friction among molecules characterized by the dynamic viscosity of the liquid metal, and, at the surface, cohesive forces associated to the surface tension of the liquid. The shape of the melt pool is configured, therefore, by the combined effect of the own weight of the melt pool (hydrostatic pressure), the influence of dynamic viscosity and surface tension. This combination of loads leads, as will be seen with the experimental and numerical results, to a geometry of the melt pool tending to acquire drop shape.

The solidification of the liquid, during the cooling stage, takes place by the increase of the cohesive forces among molecules of the material during the consolidation phenomena. In this way, the shape acquired by the melt pool tends to be maintained despite the disappearing of the effect of the balance between the surface tension and the hydrostatic pressure.

Figure 2 schematically represents the traversing of the laser beam across a given section for different temperatures, T , in order to illustrate the preceding ideas. The final height of the consolidated material, as well as its drop shape are the consequence of several physics phenomena. In the first place, the poor thermal conductivity of the powder makes the energy supplied by the laser beam concentrate intensely around the laser-powder interaction area. It makes that in that region the melting point is exceeded, not only by the powder and substrate which are strictly under the laser beam, but also by the powder around it. It makes that, in the end, the volume submitted to melting is larger than just the volume of powder strictly under the laser beam. Once the volume of heated powder becomes liquid, its surface tension forces it to evolve form a volume with the shape of a rectangle in the powder to a taller drop of liquid metal, whose height is dependent mainly of the time that the material evolves in liquid state. Additionally, given the low amount of energy needed to melt isolated particles, those of them around the melt pool are wetted by it and consequently melted, being incorporated into the melt pool, contributing significantly to the amount of liquid material. The concentration of energy under the laser-powder interaction area must also allow for melting the substrate to ensure a proper adhesion of the consolidated material to it. If the melting of the substrate does not happen, the melt pool does not penetrate it, and, although a consolidated ribbon might be formed, it is not welded to the substrate. During the melting of the powder, the air contained initially in the pours is released, making the density of the domains increase. Again, during the cooling of the material some effect of shrinkage happens, which is also reflected in the evolution of density. This effect during cooling is also considered in Figure 2.

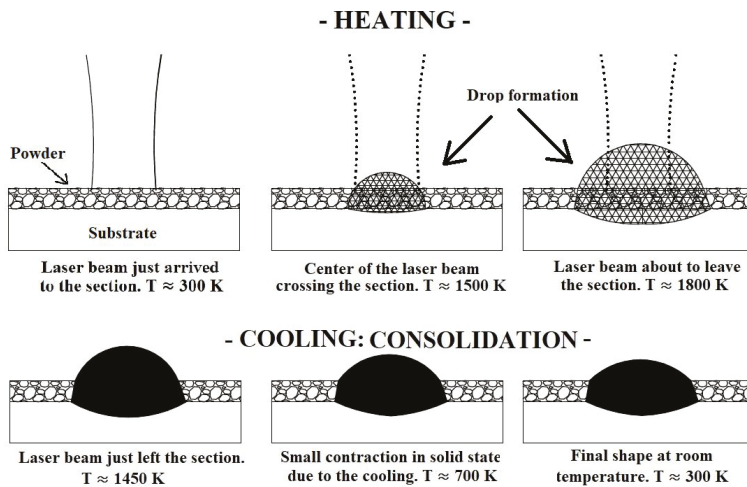


Figure 2. Illustrative representation of the consolidation of the material during the traversing of a given cross section by the laser beam.

The thermal part of the calculations is governed by the heat conduction equation in a fluidic media, Equation (3);

$$\rho C_p \frac{\partial T}{\partial t} + \rho C_p \mathbf{u} \cdot \nabla T = \nabla(\kappa \nabla T) + Q. \quad (3)$$

In Equation (3) the term Q represents any volumetric energy exchange that takes places in the studied bulk material. In this context, the latent heat of the phase changes and the metallurgical transformations are the inputs for that term. Equation (4) introduces the laser source as a surface boundary condition:

$$-\mathbf{n} \cdot (-\kappa \nabla T) = Q_b \tag{4}$$

In Equation (4) Q_b represents the irradiance of the laser beam.

The fluidic evolution of the melt pool, when the material is in liquid state, is governed by the Navier–Stokes equation, as Equation (5) indicates:

$$\rho \frac{\partial \mathbf{u}}{\partial t} = \nabla[-pI + \mu \nabla \mathbf{u} + \mu(\nabla \mathbf{u})^T] + \rho g z \tag{5}$$

In Equation (5), the last term, $\rho g z$, includes the weight of the liquid as a load in the balance of forces. ρ is the density of the material, g is the gravity constant and z is the height under the surface of the fluid. The tangential force at the surface of the fluid F_t because of the surface tension σ is described by Equation (6):

$$-\nabla \sigma + \sigma(\nabla \cdot \mathbf{n}) - p_{ext} \mathbf{n} = \mathbf{n} \cdot \mathbf{F}_t. \tag{6}$$

In Equation (6) the term p_{ext} includes the effect of the external pressure (the atmospheric pressure at room temperature) on the surface of the fluid.

Figure 3 shows a flux diagram of the thermo-fluidic coupling. It happens, therefore, due to the phase and temperature dependence of some critical properties of the matter, such as dynamic viscosity, μ , surface tension, σ , and density, ρ . The specific capability, C_p , and thermal conductivity, κ , which are associated exclusively with the thermal balance, also show phase and temperature dependence. For numerical purposes, a variable to identify the phase of the matter is defined, Ψ (Phase Variable), its value is set to 1 if the material has exceeded the melting point, and 0, if it has never happened up to the analyzed instant.

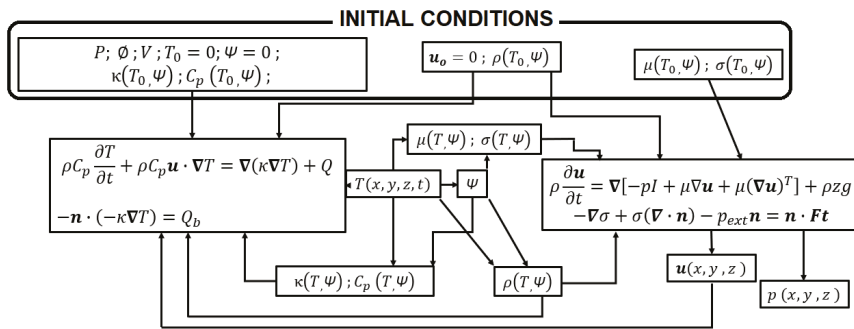


Figure 3. Flux diagram of the constitutive equations, boundary conditions and initial conditions of the thermo-fluidic coupling.

Figure 3 shows the coupling between the thermal calculations associated to the heat conduction equation and the laser beam irradiance Q_b as a surface boundary condition (block to the left) with the fluidic calculations by means of the Navier–Stokes equations submitted to surface tension, σ , and the external pressure, P_{ext} , at the boundaries of the domain (block to the right) [17]. The top block in Figure 3 contains the initial conditions with the process parameters included. Some of them, such as the power of the laser P , the beam diameter \emptyset (a Gaussian beam is considered), the scanning speed of the laser V , the heat capability C_p and thermal conductivity κ are associated with the thermal calculations. Other properties, such as dynamic viscosity μ and surface tension σ , participate only in the fluidic

calculations. In the case of density of the material, ρ , it influences the thermal balance since thermal diffusivity χ is obtained by Equation (7):

$$\chi = \frac{\kappa}{\rho C_p} \quad (7)$$

and density also appears in the Navier–Stokes Equation. The velocity field of the domain, \mathbf{u} , represents the three spatial components of the speed of any point of the domain. At the beginning it is set to zero, since there is no movement of the particles in the bulk of powder. On the one hand, the motion of the fluid affects the thermal balance; on the other hand, it is the main output of the fluidic calculations. It allows for determining the movement of the fluid, and therefore, the evolution of its geometry. At the first step of calculation, the properties of the material derive from the initial temperature, T_0 , and initial phase, $\Psi = 0$, since the material has not experienced melting yet. The effective thermo-fluidic coupling is driven, as is implicit in Figure 3, by the thermal cycle, and therefore, by the heat calculations. Once the initial step has been taken, the rising of the temperature determines the turning of the affected points as $\Psi = 1$ (the material has molten in these points). The temperature and phase dependence of dynamic viscosity and surface tension regulate, in turn, the flowing of it, associated to the heating, and, at the same time, the evolution of density, from the low apparent density of the powder to the higher density of the fluid, is able to represent the releasing of the interstitial air of the powder, and the appearance of the liquid as a continuum medium.

During the cooling stage, the use of phase-dependent thermo-fluidic properties, along with the phase variable, Ψ , determines if the material must cool, either, as unmolten powder or as a rigid solid.

The theoretical basis for the consolidation of the material has been established: the driving force to turn the powder into liquid is the thermal cycle associated with thermo-fluidic properties dependent on the temperature and the phase of the matter. This dependence also determines the phenomena during cooling, giving rise to a rigid solid in those regions where the melting point has been exceeded. In this context two, challenges arise for the modelling work. From a physics point of view, the behavior of the thermo-fluidic properties must be adjusted considering the requirements of temperature and phase dependence. From the numerical point of view, the distinction between molten and unmolten region by means of a discrete variable, Ψ , has to be implemented on the frame of a moving mesh, capable of representing the movement of the melt pool.

2.1.3. Numerical Tools to Carry Out the Thermo-Fluidic Coupling

The main goal of the thermo-fluidic approach is the calculation of the shape acquired by the liquid material under the effect of the surface tension, gradient of the surface tension, the hydrostatic pressure, the variations of dynamic viscosity and density, as well as maintaining that complex shape during the solidification of the material. It has some important implications for the numerical calculations.

Figure 2 in the previous section illustrates the cross section of a drop formation during the scanning of the laser beam. It can be seen that, starting from a flat contour representing the powder bed, the domain has to evolve to a convex contour several times higher than the original thickness of the powder bed.

The Arbitrary Lagrangean–Eulerian formulation of the Finite Element Method [11] is able to deal with the movement of the mesh and can be used to adapt it to the deformation imposed by the fluidic loads. The basis of this numerical methodology lies in the use of different coordinate systems to have a reference of the movement of the mesh. While the Eulerian part of the calculation uses a fixed reference system, the Lagrangean part uses a reference system associated with the points of the material which moves with them.

Nevertheless, the motion capability of the nodes of the mesh is not enough to represent high complex geometries. The movement of the nodes of a given element with different directions may lead to it having a high level of distortion.

According to the general theory of the Finite Element Method [18], a high degree of distortion of the elements negatively affects the accuracy of the calculations and may lead to the impossibility of

performing the convergence of the solution. It happens due to the fact that the values of the analyzed function are calculated, in the interior of each element, by interpolating the values of the nodes. If the aspect ratio of the element is too high, the result of that interpolation is wrong.

The use of the Automatic Remeshing technique allows the problem of the distortion of the elements to be managed. It is a feature directly available in the software used for the simulations; COMSOL Multiphysics™. In this way, the distortion is calculated internally by the program as a positive dimensionless number for each element. The value of this number for an undistorted element is 0. It can rise and, even descend, following the geometrical evolution of the element. When the distortion of any element reaches a critical value, the calculations are stopped, and a new mesh is built on the basis of the deformed geometry at the current simulation step. Figure 4 illustrates the simulation of the formation of a drop as a consequence of the melting of the powder. The initial mesh (left) resembles the flatness of the bed of powder. From that moment the simulation proceeds and the droplet appears progressively (center). At a given instant the distortion reaches the maximum permitted value. In that instant the numerical calculation stops, and a new mesh is automatically built by the program (right), if not exactly equal to the deformed geometry, optimized according to the algorithms of the program, and the initial user-defined mesh size.

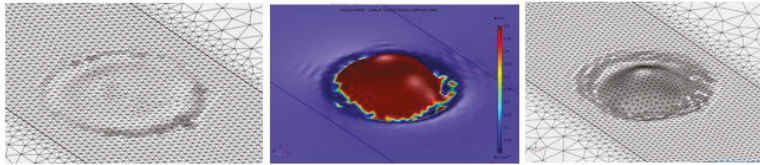


Figure 4. Process of an Automatic Remeshing. Departing from the initial mesh (left), the drop formation starts (center), and, when a high value of distortion in any element is reached, a new mesh is built, based on the deformed geometry (right).

The maximum value of the distortion at which a new mesh has to be done is user-defined. The procedure to adjust this value starts by attempting to carry out the simulation without limiting the distortion of the elements. The simulation finds problems in making the solution converge with a value of distortion about 20, and the calculations can no longer carry on. From this evidence it may be thought that by limiting the distortion to a very low value the convergence of the solution is guaranteed. Nevertheless, low values of distortion, such as 1–2, may be quickly reached and forced to stop and resume the simulation very frequently, with the associated wastes of time and memory. Considering the aforementioned restrictions, a maximum value of 5 has been used as a criterion to proceed with the automatic remeshing.

2.2. Thermo-Physical Properties for the Thermo-Fluidic Coupling

Thermal conductivity shows a high phase-dependent behavior. [19] highlights the influence of the limited contact surface among the particles or the powder bed as a limiting factor for the heat to diffuse. In the work referred to, where the AISI 316L steel is considered, the thermal conductivity of the powder at room temperature is significantly shorter than the conductivity of the same material in solid state. The present work proposes the use of different temperature functions depending on the absolute maximum temperature reached for each region of the domain. If a given region has reached, at any time, a temperature corresponding to a melting condition, its phase variable is set to, $\Psi = 1$. It determines that its cooling happens by a function different from the one during the heating, which, instead of returning to the initial conductivity of the powder, evolves along the conductivity corresponding to the cooling of the solid, considering, even, the different solid state metallurgical phases, if it is the case. Figure 5 shows the temperature and phase dependence of thermal conductivity.

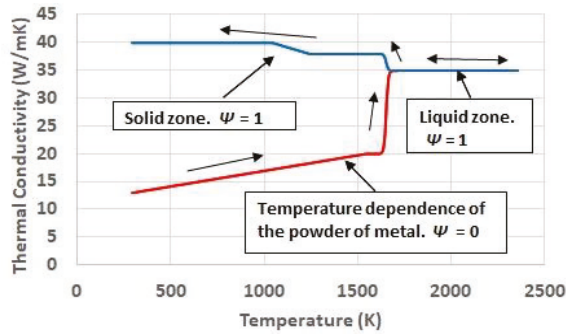


Figure 5. Temperature and phase dependence of thermal conductivity.

An important feature of the proposed behavior is the transition between either, powder to liquid or liquid to solid. It considers conditions far from the thermodynamic equilibrium associated to the high speed of the heating induced by the laser in the material, and the subsequent cooling, which is something considered in some references for the case of high power laser treatments [20]. In this way, the change of state, instead of being quasi-instantaneous, as for a situation of equilibrium, takes place along a temperature interval following a sigmoid behavior. It is reflected on the thermo-physical properties.

Density, considering the same hypotheses as for thermal conductivity, shows an intuitive behavior. It evolves from the apparent density corresponding to the powder of metal, to the density corresponding to the metal liquid. During the cooling, those regions which have molten, use the evolution of density with temperature corresponding to a solid. Figure 6 illustrates the phase and temperature dependence of density.

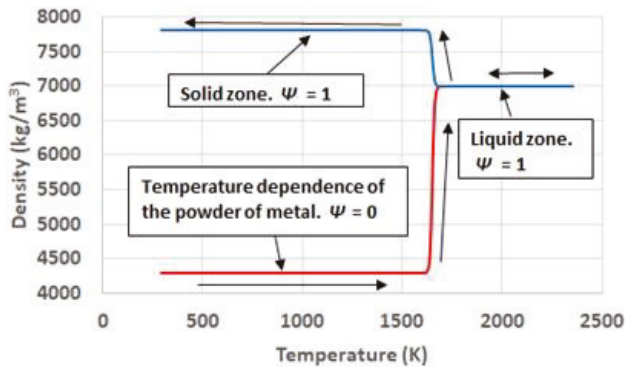


Figure 6. Temperature and phase dependence of density.

Dynamic viscosity plays a crucial role in the evolution of the shape of the material treated. The value of the dynamic viscosity of a liquid steel can be found in [16]. It can be maintained constant along the liquid state. Dynamic viscosity can also be used to emulate the behavior of a solid during the cooling of the material. By associating the dynamic viscosity at room temperature with a value high enough, the shape acquired by the melt pool during the time that the material is in liquid state, can be maintained when it cools. This methodology is proposed by [21] for the keyhole welding process, where a value of 100 Pa·s is considered to be enough to reproduce the behavior of the solid metal. The value of dynamic viscosity to represent the behavior of the powder of metal is the variable surrounded

by a higher level of uncertainty. In this work it has been estimated by considering the size and the dimensions of the droplet formed. The formation of it takes place in a volume where the droplet is surrounded by powder. Several experiments have been carried out by using a powder bed with a relatively high thickness of 1 mm. The objective of using such a large layer lies in investigating whether a big volume of powder tends to limit somehow the capability of the melt pool to acquire a free shape. If this is not the case, it can be concluded that powder presents no significant wear for the development of the melt pool, and, therefore, its dynamic viscosity is negligible. The fundamentals of this analysis lie in the comparison of it with the re-melting test where a laser beam is applied on a solid metallic plate [22]. When this is done, despite the material reaching the liquid state, no droplet formation happens. It can be associated with the limitations that the solid metal surrounding the melt pool imposes on the free movement of it.

Figure 7 contains the image of the cross section of several ribbons obtained after the scanning of the laser beam on a powder layer of 1 mm. In all the cases the power of the laser beam was 4000 W and the scanning speed of 400 mm/s, 600 mm/s and 800 mm/s.

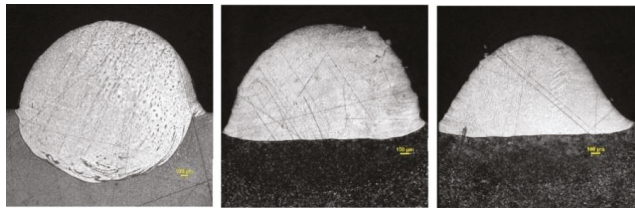


Figure 7. Cross sections of the consolidated material made with a layer of 1 mm of powder with 4000 W, 400 mm/s (left), 600 mm/s (center) and 800 mm/s (right).

From the results in Figure 8 it can be assumed that the powder around the melt pool, despite having a high thickness, it has not prevented the liquid material from adopting the corresponding drop shape. Consequently, the dynamic viscosity of the metallic powder is considered negligible in comparison with the value of the liquid. Figure 8 contains the proposed phase and temperature functions for dynamic viscosity.

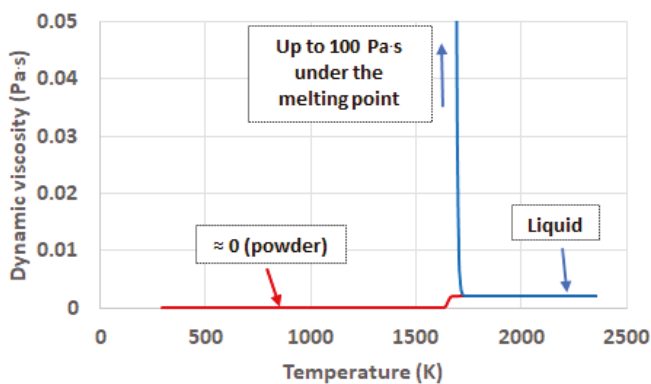


Figure 8. Phase and temperature dependency of dynamic viscosity.

Finally, the surface tension is the last variable that is introduced as critical for the definition of the shape of the melt pool. In the liquid state it shows dependence with temperature as line function with negative slope. The particular value for the working material is reported by [8]. The consideration

of this dependence with temperature in the liquid state plays a crucial role in the definition of the melt pool shape, since it is related to the so-called Marangoni Convection. Under the influence of this phenomenon, the liquid metal flows from the regions with low surface tension to the regions where the surface tension is higher. In the case of the metal powder, since there is no continuous surface, it can be considered that the surface tension shows a negligible value. For the case of the solid metal the attribution of a value for the surface tension makes no sense. The material is going to be frozen under the effect of a high value of dynamic viscosity and no tangential effects on its surfaces can affect the shape of it.

Conclusively, the important aspects of the surface tension are the transition of the material from powder to liquid, and the temperature dependence of it in the liquid state. Figure 9 shows the phase and temperature evolution of the surface tension. Reference [23] highlights the influence of the surface tension in the Selective Laser Melting Process by the effect of the capillarity force on the melt pool.

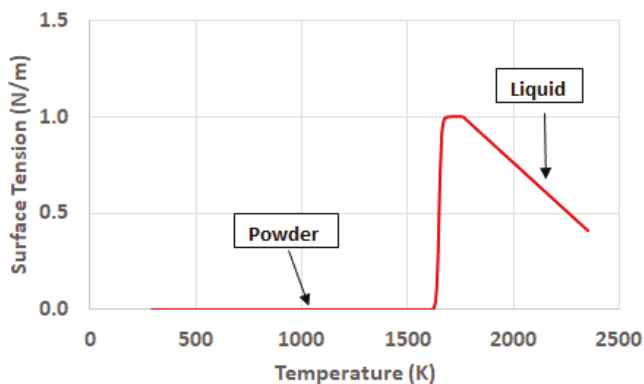


Figure 9. Phase and temperature dependency of the surface tension.

2.3. Typical Output from the Simulation Process

As a result of the modeling process, involving the thermofluidic coupling and the phase and temperature dependency of the thermo-physical properties, the development of a consolidated ribbon is obtained. Figure 10 presents the consolidated ribbon obtained during the interaction time of the laser beam, τ ($\tau = \varnothing/V$) for a process speed of 600 mm/min and a beam power of 1800 W with a beam diameter of 3 mm. The simulation during the interaction time allows for representing the effect of the full traversing of the laser beam for a given point and analyzing the characteristic dimensions of it, within manageable computation times. The model is also prepared to take into account the recoil pressure [24], although, provisionally it has not been considered for the proposed tests, given the relatively moderated heating conditions and the large amount of material involved.

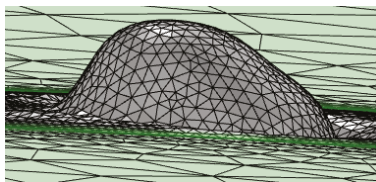


Figure 10. Ribbon formed during the interaction time of the laser beam.

Figure 11 shows the way in which the results of the simulation are exploited, by comparing the height and width of the cross section predicted by the simulation with the experimental ones.

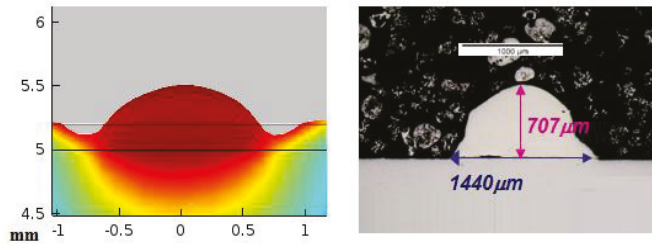


Figure 11. Theoretical (left) and experimental (right) cross sections.

The next section carries out some representative comparisons between theoretical and experimental results for some tests carried out with typical sets of process parameters.

3. Results

The main goal of the proposed model is the prediction of the shape and dimensions of the cross section of the consolidated material. The progress of the process, in terms of the advance in the direction in which the part is being grown, is determined by the final height of the cross section. In addition, the heat conduction conditions for the consolidation process of the successive layers depend on the geometry of the previously consolidated material, which configures the paths for the diffusion of the heat.

All the tests were made on a substrate layer of 1000 μm , with a gaussian laser beam with a diameter of 3 mm. The laser equipment was a fiber IPG laser with 6 kW of maximum output power releasing radiation with a wavelength of 900 nm.

Three different tests have been carried out. The corresponding conditions of power and scanning speed are shown in Table 2.

Table 2. Conditions of the tests to compare the theoretical with the experimental results.

Test Number	Laser Power (W)	Scanning Speed (mm/min)
1	1000	400
2	2000	600
3	3000	800

Figure 12 shows the cross section predicted by simulation (left) and the real result obtained in the experimental test number 1 (right). It can be seen that the theoretical calculation has been capable of predicting the height of the consolidated material, as well as the general shape of the area. In both the theoretical and the experimental cross section, the maximum height of the consolidated material, from the reference line of the substrate, lies around 1400 μm (note that the cross section displayed from the theoretical results starts at the level of the substrate, while in the experimental case the dilution under the substrate is shown). In the same way, the width of the cross section at the level of the line of the substrate is of about 2800 μm . The biggest discrepancies between the theoretical and the experimental cross sections appear at the sides of it, at the level of the substrate. It may be associated to dynamic viscosity attributed to the solid in the numerical simulation which predicts a slightly higher level of consistence for the consolidated material than in reality. No contrast of the amount of dilution of the consolidated material into the substrate is highlighted in the numerical simulation, which must be predicted by means of metallurgical consideration from the thermal cycle and will be considered in future developments of the model.

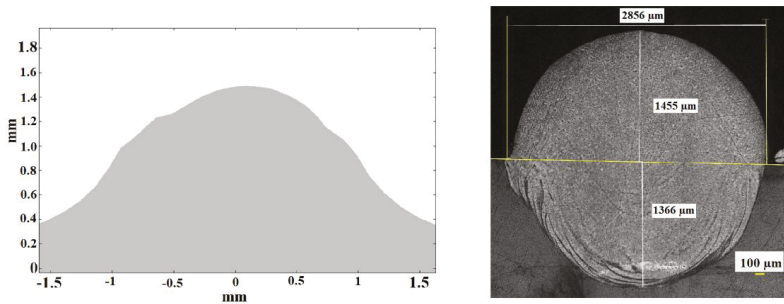


Figure 12. Theoretical (left) and experimental (right) cross sections corresponding to test 1. Note that in the case of the experimental one the dilution under the substrate is shown while the theoretical one represents exclusively the external part of the consolidated material, from the top of the substrate.

Figure 13 shows the theoretical (left) and experimental (right) cross sections corresponding to test 2.

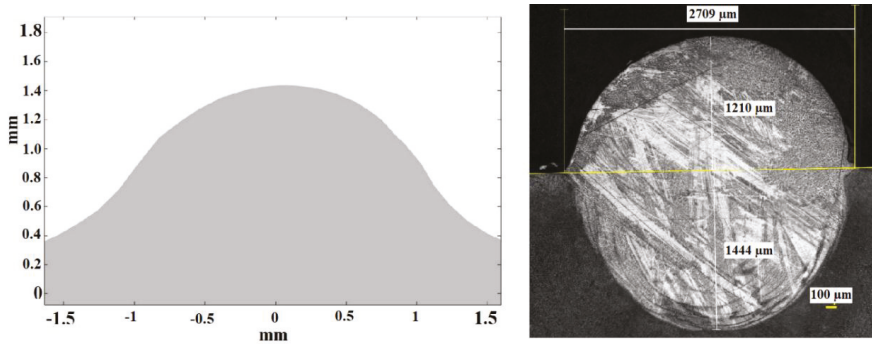


Figure 13. Theoretical (left) and experimental (right) cross sections corresponding to test 2.

In Figure 13 it can be seen again, from the cross section of the experimental test, that the high thickness of the layer of metallic powder has given rise to a high dilution of the consolidated material into the substrate. Considering the dimensions of the external part of it, the simulation has been capable of predicting its maximum height and width.

Figure 14 represents the theoretical (left) and experimental (right) results for test 3. Once again, the general external dimensions predicted by the simulation match with an acceptable level of accuracy the dimensions of the experimental cross section. In this case, the use of the highest scanning speed has led to a shorter height of the consolidated material.

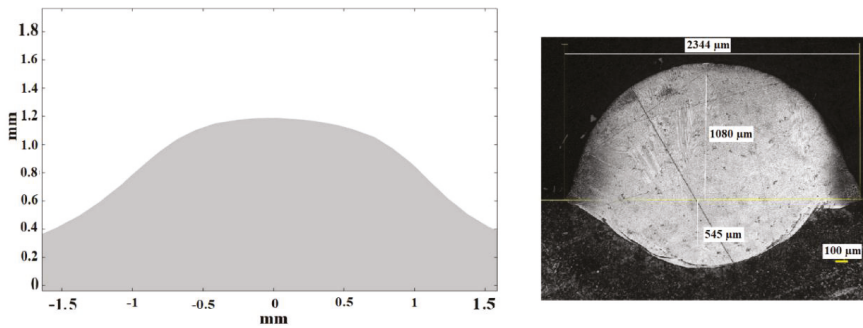


Figure 14. Theoretical (left) and experimental (right) cross sections corresponding to test 3.

4. Discussion

The use of temperature and phase-dependent thermo-physical properties has allowed an accurate prediction of the dimensions of the cross section. While the influence of the exclusively thermal properties, such as the thermal conductivity, cannot be directly analyzed; the proposed modelling for the surface tension and the dynamic viscosity is accurate enough to make the output of the simulation approach the experimental results.

From the experimental-theoretical comparison some ideas can be extracted. While the general dimensions of the cross sections can be satisfactorily predicted by the theoretical calculations in terms of height and width, the shape of it, at the level of the contact with the substrate is affected, in the theoretical calculations, by some effect of adhesion that makes the transition from the consolidated material to the substrate smoother than in the real case. It may be associated with the theoretical evolution of the dynamic viscosity which, when it is representing the behavior of the solid, tends to slightly overestimate the adhesion phenomena. Both, numerical calculations and experimental tests highlight the influence of the large thickness of the powder bed in the transformation experienced by the material, evolving from a flat layer of powder to a taller ribbon whose cross section has the shape of a drop. In other papers where a much shorter layer of thickness is considered, this evolution of the material during the drop formation is less evident. Reference [25] is capable of estimating the shape of the melt pool in the SLM process of nanocomposites just by means of thermal calculation. It is possible due to the subtle motion of the liquid metal derived from the small thickness of the powder bed. References [26–28] present different SLM process with applications in various fields. The powder bed is not larger than 50 μm in any of the cases. The comparison of the melt pool in the figures of that papers with Figures 12–14 of the present study highlights the influence of the thickness of the powder bed in the shape and size of the consolidated material, justifying the use of a thermo-fluidic approach.

From a strictly experimental point of view, the use of a high thickness powder layer is associated to a high degree of dilution of the consolidated material into the substrate. It can be related with the greater amount of material which is melted because of the large thickness of the layer and the size and big power of the laser beam. The inclusion of metallurgical considerations in new versions of the model will focus on calculating the magnitude of the dilution. The aggressiveness of the process parameters used in the present study in comparison with studies with a shorter powder layer can be checked considering the process parameters in the tests of references [29,30].

The relation of the process parameters from the experimental tests with the dimensions of the melt pool, as a function of the thermo-fluidic properties of the material, provides a deep understanding of the physics involved in the consolidation process. In test 1, despite having a relatively low value of laser power, 1000 W, the large interaction time associated to the relatively low process speed, 400 mm/min, has permitted an efficient absorption of the energy to be achieved. In Section 2.1.1 the high efficiency of the powder to absorb radiation was shown. Additionally, in Section 2.2, the poor thermal conductivity

of the powder was indicated; it favors the concentration of the heat around the laser-powder interaction area. The combination of a large interaction time with an efficient absorption and concentration of the laser power has led to a melt pool of relatively large dimensions. The hypothesis of considering the powder around the melt pool as a fluid with very low friction (very low dynamic viscosity), can be accepted from the result of this test: the spherical shape of the cross section indicates that the melt pool has not found appreciable resistance to move under the effect of surface tension. No signs of porous in the cross section, which suggests that the density of the material has evolved from the value corresponding to the powder to the value of the solid during the consolidation process.

Test 2 presents a more aggressive combination of process parameters than test 1. The higher level of power, 2000 W, has allowed a larger amount of energy to traverse the powder to the substrate, which, in combination with an intermediate level of process speed, 600 mm/min, has favored a deeper penetration of the melt pool into the substrate. Once again, the low friction of the powder around the melt pool has allowed the external part of it acquire spherical shape. The high degree of symmetry of this contour reinforces the idea of the very limited restriction of the powder to the movement of the melt pool, as considered in the thermo-fluidic coupled model.

In the case of test 3, the use of the most aggressive combination of process parameters highlights the importance of the dynamic effects during the consolidation phenomenon. Despite having the largest level of power, 3000 W, the shorter interaction time has limited both the process of drop formation and the penetration of the melt pool into the substrate. The shape of the external part of the melt pool presents a profile which is not as close to a sphere as the profile of the previous tests: the limited interaction time has led to the cooling of the material before it has been capable of finishing its evolution to a spherical profile. In addition, the heating and cooling processes, happening more quickly than in the previous tests, limits the time of the molecules of the material to move from their equilibrium positions, restricting any diffusion process which might occur as a consequence of the thermal cycle.

The numerical aspects of the theoretical model have allowed the convergence of the calculations to be achieved. The mesh deformed under the effect of the loads affecting the fluid, and automatically re-meshed when the distortion of the elements reached the user-defined maximum permitted value.

5. Conclusions

The thermo-fluidic coupling has been revealed as a valid tool to evaluate the behavior of the material in its evolution from powder to liquid and from liquid to solid. The dimensions of the cross section predicted by the simulations matched the experimental results with an acceptable level of accuracy. It reinforces the idea of phase and temperature-dependent thermo-physical properties to understand the behavior of the material during the different stages that it experiences in the Selective Laser Melting Process.

The use of the finite element method in combination with advanced numerical tools has allowed realistic domains with large dimensions to be used, thus favoring, in this way, the study or real processes at an industrial scale, surpassing the capabilities of conventional models with domains at the microscale level.

The governability of the process with a large thickness powder bed has been revealed to be possible, since the simulations have been capable of estimating the dimensions of the cross section resulting from a particular combination of process parameters. Specific consideration about the amount of dilution associated with large powder beds are necessary. Future works dealing with metallurgical aspects of the process will be carried out.

Author Contributions: F.C.: He was the main developer of the thermo-fluidic model and postulated the temperature and phase dependency of the thermo-fluidic properties. He also adjusted the use of the advanced numerical tools such as the Arbitrary Lagrangean-Eulerian Method and the Automatic Re-meshing. Á.G.-B.: He assisted in the development of the model in all the different stages of the process. M.G.: He contributed with the firsts version of developments of the model and provided fundamental assistance during all the stages. D.A.M.: He contributed with the firsts version of developments of the model and provided fundamental assistance during

all the stages. J.L.O.: He participated and led in all the stages in the development of the present work. He provided fundamental knowledge for the theoretical model as well as for the interpretation of the experimental results.

Funding: This research was funded by the Spanish Centre for the Development of Industrial Technology (CDTI) in the frame of the CIEN-FRACTAL project with grant number MQM-2010290.

Acknowledgments: The Authors wish to acknowledge the assistance of Piera Alvarez and María Ángeles Montealegre from Ikerdune A.I.E. (Etxe-Tar group) who helped during the preparation and analysis of the experimental tests.

Conflicts of Interest: The authors declare no conflict of interest.

References

1. Yap, C.Y.; Chua, C.K.; Dong, Z.L.; Liu, Z.H.; Zhang, D.Q.; Loh, L.E.; Sing, S.L. Review of selective laser melting: Materials and applications. *Appl. Phys. Rev.* **2015**, *2*, 041101. [[CrossRef](#)]
2. Busachi, A.; Erkoyuncu, J.; Colegrove, P.; Martina, F.; Watts, C.; Drake, R. A review of additive manufacturing technology and cost estimation techniques for the defence sector. *CIRP J. Manuf. Sci. Technol.* **2017**, *19*, 117–128. [[CrossRef](#)]
3. Gusarov, A.V.; Grigoriev, S.N.; Volosova, M.A.; Melnik, Y.A.; Laskin, A.; Kotoban, D.V.; Okunkova, A.A. On productivity of laser additive manufacturing. *J. Mater. Process. Technol.* **2018**, *261*, 213–232. [[CrossRef](#)]
4. Chen, Y.; Zhang, K.; Huang, J.; Hosseini, S.R.E.; Li, Z. Characterization of heat affected zone liquation cracking in laser additive manufacturing of Inconel 718. *Mater. Des.* **2016**, *90*, 586–594. [[CrossRef](#)]
5. Trevisan, F.; Calignano, F.; Aversa, A.; Marchese, G.; Lombardi, M.; Biamino, S.; Manfredi, D. Additive manufacturing of titanium alloys in the biomedical field: Processes, properties and applications. *J. Appl. Biomater. Funct. Mater.* **2018**, *16*, 57–67. [[CrossRef](#)] [[PubMed](#)]
6. Mercelis, P.; Kruth, J.P. Residual stresses in selective laser sintering and selective laser melting. *Rapid Prototyp. J.* **2006**, *12*, 254–265. [[CrossRef](#)]
7. Buchbinder, D.; Schleifenbaum, H.B.; Heidrich, S.; Meiners, W.; Bültmann, J. High power selective laser melting (HP SLM) of aluminum parts. *Phys. Procedia* **2011**, *12*, 271–278. [[CrossRef](#)]
8. Khairallah, S.A.; Anderson, A. Mesoscopic simulation model of selective laser melting of stainless steel powder. *J. Mater. Process. Technol.* **2014**, *214*, 2627–2636. [[CrossRef](#)]
9. Loh, L.E.; Chua, C.K.; Yeong, W.Y.; Song, J.; Mapar, M.; Sing, S.L.; Zhang, D.Q. Numerical investigation and an effective modelling on the Selective Laser Melting (SLM) process with aluminium alloy 6061. *Int. J. Heat Mass Transfer.* **2015**, *80*, 288–300. [[CrossRef](#)]
10. Yadroitsev, I.; Gusarov, A.; Yadroitsava, I.; Smurov, I. Single track formation in selective laser melting of metal powders. *J. Mater. Process. Technol.* **2010**, *210*, 1624–1631. [[CrossRef](#)]
11. Benson, D.J. An efficient, accurate, simple ALE method for nonlinear finite element programs. *Comput. Meth. Appl. Mech. Eng.* **1989**, *72*, 305–350. [[CrossRef](#)]
12. Guo, P.; Zou, B.; Huang, C.; Gao, H. Study on microstructure, mechanical properties and machinability of efficiently additive manufactured AISI 316L stainless steel by high-power direct laser deposition. *J. Mater. Process. Technol.* **2017**, *240*, 12–22. [[CrossRef](#)]
13. Geringer, J.; Atmani, F.; Forest, B. Friction–corrosion of AISI 316L/bone cement and AISI 316L/PMMA contacts: Ionic strength effect on tribological behaviour. *Wear* **2009**, *267*, 763–769. [[CrossRef](#)]
14. Reitz, J.R.; Milford, F.J.; Christy, R.W. *Foundations of Electromagnetic Theory*, 4th ed.; Addison-Wesley Publishing Company: Reading, MA, USA, 2008; Volume 630, pp. 200–400, ISBN 0321581741.
15. Prokhorov, A.M. *Laser Heating of Metals: 0*; CRC Press: Boca Raton, FL, USA, 1990; Volume 233, ISBN 9781351082396.
16. Zhou, J.; Tsai, H.L.; Wang, P.C. Transport phenomena and keyhole dynamics during pulsed laser welding. *J. Heat Transf.* **2006**, *128*, 680–690. [[CrossRef](#)]
17. Jacqmin, D. Calculation of two-phase Navier–Stokes flows using phase-field modeling. *J. Comput. Phys.* **1999**, *155*, 96–127. [[CrossRef](#)]
18. Johnson, A.A.; Tezduyar, T.E. Mesh update strategies in parallel finite element computations of flow problems with moving boundaries and interfaces. *Comput. Meth. Appl. Mech. Eng.* **1994**, *119*, 73–94. [[CrossRef](#)]

19. Khairallah, S.A.; Anderson, A.T.; Rubenchik, A.; King, W.E. Laser powder-bed fusion additive manufacturing: Physics of complex melt flow and formation mechanisms of pores, spatter, and denudation zones. *Acta Mater.* **2016**, *108*, 36–45. [CrossRef]
20. Mioković, T.; Schulze, V.; Vöhringer, O.; Löhe, D. Prediction of phase transformations during laser surface hardening of AISI 4140 including the effects of inhomogeneous austenite formation. *Mater. Sci. Eng. A* **2006**, *435*, 547–555. [CrossRef]
21. Bruyere, V.; Touvre, C.; Namy, P. Comparison between Phase Field and ALE methods to model the keyhole digging during spot laser welding. In Proceedings of the 2013 COMSOL Conference 2013, Rotterdam, The Netherlands, 23–25 October 2013.
22. Tur, A.; Cordovilla, F.; García-Beltrán, Á.; Ocaña, J.L. Minimization of the thermal material effects on pulsed dynamic laser welding. *J. Mater. Process. Technol.* **2017**, *246*, 13–21. [CrossRef]
23. Khorasani, A.M.; Gibson, I.; Ghaderi, A.R. Rheological characterization of process parameters influence on surface quality of Ti-6Al-4V parts manufactured by selective laser melting. *Int. J. Adv. Manuf. Technol.* **2018**, *97*, 3761–3775. [CrossRef]
24. Wu, Y.C.; San, C.H.; Chang, C.H.; Lin, H.J.; Marwan, R.; Baba, S.; Hwang, W.S. Numerical modeling of melt-pool behavior in selective laser melting with random powder distribution and experimental validation. *J. Mater. Process. Technol.* **2018**, *254*, 72–78. [CrossRef]
25. AlMangour, B.; Grzesiak, D.; Cheng, J.; Ertas, Y. Thermal behavior of the molten pool, microstructural evolution, and tribological performance during selective laser melting of TiC/316L stainless steel nanocomposites: Experimental and simulation methods. *J. Mater. Process. Technol.* **2018**, *257*, 288–301. [CrossRef]
26. Mazur, M.; Brincat, P.; Leary, M.; Brandt, M. Numerical and experimental evaluation of a conformally cooled H13 steel injection mould manufactured with selective laser melting. *Int. J. Adv. Manuf. Technol.* **2017**, *93*, 881–900. [CrossRef]
27. Lopez-Botello, O.; Martinez-Hernandez, U.; Ramirez, J.; Pinna, C.; Mumtaz, K. Two-dimensional simulation of grain structure growth within selective laser melted AA-2024. *Mater. Des.* **2017**, *113*, 369–376. [CrossRef]
28. Teng, C.; Gong, H.; Szabo, A.; Dilip, J.J.S.; Ashby, K.; Zhang, S.; Stucker, B. Simulating melt pool shape and lack of fusion porosity for selective laser melting of cobalt chromium components. *J. Manuf. Sci. Eng.* **2017**, *139*, 011009. [CrossRef]
29. Delgado, J.; Ciurana, J.; Rodriguez, C.A. Influence of process parameters on part quality and mechanical properties for DMLS and SLM with iron-based materials. *Int. J. Adv. Manuf. Technol.* **2012**, *60*, 601–610. [CrossRef]
30. Yadroitsev, I.; Yadroitsava, I.; Bertrand, P.; Smurov, I. Factor analysis of selective laser melting process parameters and geometrical characteristics of synthesized single tracks. *Rapid Prototyp. J.* **2012**, *18*, 201–208. [CrossRef]



© 2018 by the authors. Licensee MDPI, Basel, Switzerland. This article is an open access article distributed under the terms and conditions of the Creative Commons Attribution (CC BY) license (<http://creativecommons.org/licenses/by/4.0/>).

Article

Design of a Scaffold Parameter Selection System with Additive Manufacturing for a Biomedical Cell Culture

Marc Rabionet ^{1,2}, Emma Polonio ^{1,2}, Antonio J. Guerra ², Jessica Martin ¹, Teresa Puig ^{1,*} and Joaquim Ciurana ^{2,*}

¹ Oncology Unit (TargetsLab), Department of Medical Sciences, Faculty of Medicine, University of Girona, Emili Grahit 77, 17003 Girona, Spain; m.rabionet@udg.edu (M.R.); emma.polonio@udg.edu (E.P.); jessica.martin@udg.edu (J.M.)

² Department of Mechanical Engineering and Industrial Construction, University of Girona, Maria Aurèlia Capmany 61, 17003 Girona, Spain; antonio.guerra@udg.edu

* Correspondence: teresa.puig@udg.edu (T.P.); quim.ciurana@udg.edu (J.C.)

Received: 10 July 2018; Accepted: 10 August 2018; Published: 14 August 2018

Abstract: Open-source 3D printers mean objects can be quickly and efficiently produced. However, design and fabrication parameters need to be optimized to set up the correct printing procedure; a procedure in which the characteristics of the printing materials selected for use can also influence the process. This work focuses on optimizing the printing process of the open-source 3D extruder machine RepRap, which is used to manufacture poly(ϵ -caprolactone) (PCL) scaffolds for cell culture applications. PCL is a biocompatible polymer that is free of toxic dye and has been used to fabricate scaffolds, i.e., solid structures suitable for 3D cancer cell cultures. Scaffold cell culture has been described as enhancing cancer stem cell (CSC) populations related to tumor chemoresistance and/or their recurrence after chemotherapy. A RepRap BCN3D+ printer and 3 mm PCL wire were used to fabricate circular scaffolds. Design and fabrication parameters were first determined with SolidWorks and Slic3r software and subsequently optimized following a novel sequential flowchart. In the flowchart described here, the parameters were gradually optimized step by step, by taking several measurable variables of the resulting scaffolds into consideration to guarantee high-quality printing. Three deposition angles (45° , 60° and 90°) were fabricated and tested. MCF-7 breast carcinoma cells and NIH/3T3 murine fibroblasts were used to assess scaffold adequacy for 3D cell cultures. The 60° scaffolds were found to be suitable for the purpose. Therefore, PCL scaffolds fabricated via the flowchart optimization with a RepRap 3D printer could be used for 3D cell cultures and may boost CSCs to study new therapeutic treatments for this malignant population. Moreover, the flowchart defined here could represent a standard procedure for non-engineers (i.e., mainly physicians) when manufacturing new culture systems is required.

Keywords: scaffold; PCL; RepRap; fused filament fabrication; three-dimensional; cell culture

1. Introduction

Scaffolds are solid structures usually made of a polymeric material that is used for a wide range of applications. They provide a necessary support for three-dimensional (3D) cell growth, thanks to their biocompatibility and biodegradability [1], and are extremely useful in *in vitro* 3D cell cultures. Traditional cell culture is applied to two-dimensional (2D) models on flat surfaces, but this methodology is not representative of the cells' physiological environment and usually confers them with less malignancy. The literature has reported that 3D cell culture with scaffolds can increase the cancer stem cell (CSC) population [2–4]. CSCs correspond to a small population within the tumor

which is resistant to chemotherapy and capable of dividing to form the tumor again after treatment (this is known as recurrence or metastasis) [5,6]. Since this malignant subpopulation represents a small percentage within the tumor, the population expansion and enrichment described would help in their study and promote further development of therapeutic strategies.

Additive manufacturing (AM) technologies have arisen as a novel set of tools with which to fabricate scaffolds [5,7]. In particular, 3D printers based on fused filament fabrication (FFF) technology are one of the most accessible and simplest options [8]. They are open-source, low-cost machines which usually use thermoplastic materials [9,10] and can easily be modified to improve the quality of the printed 3D products [11]. A variety of biocompatible polymers can be used for scaffold production with FFF. Poly-L-lactic acid (PLA) is a biodegradable thermoplastic aliphatic polyester that has great potential in clinics thanks to its biocompatibility and restorability. Consequently, it is widely used in tissue engineering [12]. Poly(ϵ -caprolactone) (PCL; Figure 1) is also a biodegradable polyester proven to be biocompatible and toxic-dye-free, but it has a slower degradation rate and different mechanical and physical features. For instance, PCL has a lower melting point (60 °C), reflecting its lower hydrogen bonding and polarity which determine its chemical and molecular behavior. Moreover, PCL does not have any isomers so there are no variances in the melting temperature and biological degradation. Due to these characteristics, its use in tissue engineering, drug delivery, and cell cultures is increasing [2,3,6,13,14]. PCL can be also used as copolymers, such as PCL-collagen and PCL-gelatin, and in combination with other polymers, for example PLA or PEG [13,15].

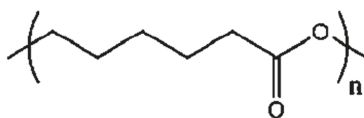


Figure 1. Poly(ϵ -caprolactone) chemical structure.

As scaffold production with 3D printers is a new area, greater effort should be made to determine the optimal parameters for the process [1,6,9]. The processing parameters in question are closely related to the properties of the polymer chosen and the subsequent application intended for the scaffold(s). First, the design parameters determine the architecture of the scaffold and can comprise the filament diameter, the distance between filaments, and the deposition angle [16]. They can also be modified depending on the desired design and application of the scaffold. Second, fabrication parameters control the printing process. These parameters include the extruder and bed temperature, deposition velocity, and layer height, and are closely linked to the material of the polymer and the environment [9,17].

When scaffolds are produced for tissue engineering or regenerative medicine, controlling features, such as pore size, pore shape, or mechanical strength, is mandatory [9,18]. Although there are some studies into the 3D printing of scaffolds based on fused deposition modeling (FDM) [19,20] very few analyze the effects the architecture of the scaffold may have on cell proliferation, and none develop schematic procedures or methods aimed at retaining any knowledge gained. Grémare et al., [21] studied the physicochemical and biological properties of PLA scaffolds produced by 3D printing (FFF). The authors studied four different square pore sizes (0, 150, 200, and 250 μ m). Results showed that scaffold pore size had negligible effects on their mechanical properties. After three and seven days of human bone marrow stromal cell (HBMSC) culture being applied, the scaffolds exhibited excellent viability and homogeneous distribution regardless of the pore size. Hutmancher et al. [22] studied the mechanical and cell culture response of PCL scaffolds using $61 \pm 1\%$ porosity and two matrix architectures. Results showed that five-angle scaffolds had significantly lower stiffness under compression loading than those with a three-angle pattern. Data also revealed that in terms of cell proliferation, while a scaffold with a 0/60/120° lay-down pattern had a higher proliferation rate in the first 2 weeks, the scaffolds with a 0/72/144/36/108° lay-down overtook the three-angle matrix

architecture in Weeks 3 and 4. Recently, Rabionet et al. [23] analyzed the effects of tubular scaffold architecture on cell proliferation for vascular applications. Results showed the strong influence the 3D process parameters have on the scaffold architecture and, subsequently, cell proliferation. Narrow pores produced lower cell proliferation due to the lower oxygen and nutrient exchange.

As the literature has reported, cell proliferation onto a scaffold depends on the material, the architecture, and cell kinetics. Whenever physicians need to work with cells, they require the best scaffolding features to obtain ideal cell culture results. In fact, the main problem was that scaffolds did not provide the same results for different lines of cells when the cells are cultured. When working with cells, physicians have different purposes and goals. For instance, they may want to enrich or treat the cells or to determine the impact a drug is having/has had on the cells. While identical scaffold features do not provide the same results, the cell line does. In fact, each cell line works better with different scaffold features. For this reason, this work aims to optimize the design features and the selection of the manufacturing process parameters when the open-source 3D extruder machine RepRap is utilized. This methodology focuses on manufacturing PCL scaffolds suitable for 3D cancer cell cultures and CSCs expansion as a first step before expanding to other cell lines. Both design and fabrication parameters have been optimized by following a specific flowchart step by step, and checking a measurable variable. In addition, preliminary *in vitro* experiments were performed to study the impact the scaffold design and fabrication have on the efficiency physicians require from the 3D cell culture and the scaffolds produced. Therefore, a sample application for the mass production of PCL scaffolds using a low-cost machine could be used to improve cancer stem cell research. The flowchart developed here provides a novel methodology to adjust process parameters to print micrometric scaffolds suitable for three-dimensional cell culture because, as is demonstrated, each cell line required different scaffold features. Hence, an optimization diagram could represent a common procedure which could be used by non-engineering professionals when a 3D cell culture protocol has to be established *de novo*. Physicians working with 3D cell cultures usually need some kind of rules or guidelines to follow to set up the cell culture. This paper's contribution is the methodology required to set up the 3D printing technology for a new line of cell culture by first defining the design characteristics and then the parameter selection for the manufacturing process. This paper does not contribute to the knowledge about PCLs or the 3D printing machine itself, but instead provides a methodology for physicians. The contribution is the method and steps to follow when scaffolds need to be manufactured for a new cell line.

2. Experimental Setup

2.1. Material

A 3 mm poly(ϵ -caprolactone) (PCL) wire (Perstorp, Malmö, Sweden) with a density of 1145 Kg/m³ and a molecular weight of 80,000 g/mol, was used to fabricate circular scaffolds 19 mm in diameter (Corning Life Sciences, New York, NY, USA). PCL is a biodegradable polyester with a low melting point (60 °C) and a glass transition of about –60 °C.

2.2. Three-Dimensional Printer Machine

An open-source and modular RepRap BCN 3D+ printer (CIM, Barcelona, Spain) was used to produce three-dimensional scaffolds (Figure 2). This printer was selected because of its capacity to allow a user to optimize its parameters as they see fit. It uses fused filament fabrication (FFF). First, the filament was unwound from a roll of wire and supplied to the extruder. Then, the material was extruded through the nozzle using different temperatures depending on the value being tested. Finally, the printed filament was deposited onto a heated platform (also known as a bed).

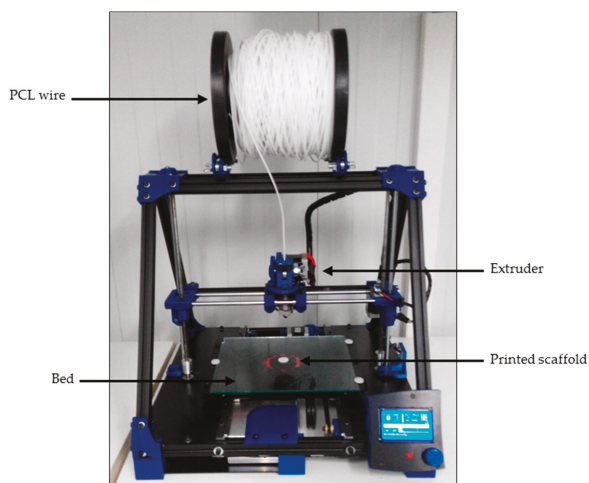


Figure 2. RepRap BCN 3D+ printer with a 3 mm PCL wire.

2.3. Scaffold Design and Additive Manufacturing

SolidWorks (Waltham, Massachusetts, Estats Units) was the computer-aided design (CAD) software chosen for the scaffolds' design. The stereolithography (STL) file formats the designs that were transferred to the computer-aided manufacturing (CAM) software Slic3r to establish the fabrication parameters. This software, while maintaining the SolidWorks design, generated G-code files which can control and regulate the machine to obtain the correctly-printed scaffolds. Scaffold design features were selected based on other research work focused on tissue engineering which had similar goals to this work, i.e., cell enrichment or treatment, or drug delivery applicability. The features are described in Table 1. Previous screening experiments were carried out to adjust the range of the scaffold design features.

Table 1. Process parameters used for PCL scaffold printing.

	Parameters	Tested Values	Measurable Variable
Fabrication parameters	Extruder temperature	65, 70, 75, 80, 85, and 90 °C	Printed filament diameter
	Bed temperature	25, 30, 33, 35, and 37 °C	1-Material adhesion (Y/N)
	Deposition velocity	10, 20, and 30 mm/s	2-First layer height
	Layer height	0.28 and 0.3 mm	Printed filament diameter Printing quality (absence of blobs)
Design parameters	Filament diameter	0.175, 0.3, and 0.5 mm	1-Adhesion of contiguous filaments (Y/N)
	Distance between filaments	0.5, 0.7, and 1 mm	2-Printed filament diameter
	Deposition angle	90°, 45°, and 60°	1-Real distance between filaments 2-Smallest pore option Pore angles

2.4. Process Parameter Optimization

The fabrication parameters and design feature values used for the experimental setup are shown in Table 1. A wide range of characteristics and parameter values were selected from the literature as the screening values with which to start. A wide range of processing parameters were selected based on the research work focused on tissue engineering with similar goals to ours, i.e., the enrichment or treatment of cells of the applicability for drug delivery. Thus, previous screening experiments

were carried out to adjust the range of the processing parameters for the scaffolds. By following a sequential flowchart (Figure 3), the optimal tested value to be selected for each parameter was determined. Optimization was first performed using a generic geometrical form. A fixed circular scaffold design was used as the control pattern: 0.4 mm in diameter and layer height extruded filament, 1 mm distance between filaments, 90° deposition angle, 19 mm in diameter scaffold, and eight scaffold layers. As optimization progressed, design feature values were replaced by the optimal ones, resulting in a final scaffold design suitable for three-dimensional cancer cell culture. Furthermore, the cancer cell culture is now more like real physiological conditions, including an enrichment of the CSCs' subpopulation. Each step on the flowchart presented in Figure 3 included parameter testing and a physical scaffold variable measurement to assess the quality of the printing. Thus, optimal parameter values were sequentially determined and considering the final application as the optimal function to be reached. Physical variables, such as printed filament diameter, first layer height, and real distance between filaments, were measured using an inverted optical microscope (Nikon, Tokyo, Japan). Printed structures, as well as a nanometric ruler, were placed on the stage. Binomial variables (material adhesion, adhesion of contiguous filaments, printing quality such as the absence of blobs etc.) were assessed by sight. Finally, the cell efficiency of the different deposition angles was evaluated through a three-dimensional breast cancer cell culture to validate the parameters selected. Breast CSCs were used because their expansion would represent a new opportunity to develop new treatments against cancer stem features related to cancer relapse and metastasis.

2.5. Cell Line

MCF-7 breast carcinoma cells (ATCC® HTB-22™) and NIH/3T3 murine fibroblasts cell lines (ATCC® CRL-1658™) were obtained from the American Type Culture Collection (ATCC, Rockville, MD, USA). MCF-7 and NIH/3T3 cells were cultured in DMEM (Dulbecco's Modified Eagle's Medium) (Gibco, Waltham, MA, USA) supplemented with 10% fetal bovine serum, 1% L-glutamine (which means 2 mM L-glutamine), 1% sodium pyruvate (which means 1 mM sodium pyruvate), 50 U/mL penicillin and 50 µg/mL streptomycin (HyClone, Logan, UT, USA). Cells were maintained at 37 °C and in a 5% CO₂ atmosphere.

2.6. Scaffold Sterilization

Scaffolds were sterilized following a previously-described methodology [2,24]. Meshes were submerged in a 70% ethanol/water solution overnight, washed with PBS (Gibco, Waltham, MA, USA), and finally exposed to UV light for 30 min. Only the top side was irradiated because PCL has a semi-transparent behavior when exposed to UV wavelengths [25]. This sterilization method was followed to avoid any changes in the stents' final properties [18].

2.7. Three-Dimensional Cell Culture in Scaffolds

Scaffolds were designed by considering their subsequent use in regular 12-well cell culture microplates. First, cells were detached from the original cell culture microplate and counted using the trypan blue dye method. As viable cells possess an intact membrane, trypan blue cannot penetrate them, but as dead cells have an altered membrane the dye can penetrate them. Therefore, trypan blue was added in a cell sample and cell viability was counted using a Neubauer Chamber (Mariesfeld-Superior, Lauda-Königshofen, Germany) and an inverted optical microscope. A total of 100,000 cells (MCF-7) or 40,000 (NIH/3T3) in 250 µL cell suspension were placed onto the center of the scaffolds' surface to allow cell attachment. After 3 h of incubation, 1.5 mL of fresh medium was added to cover the scaffold and the cells were incubated for 72 h. Then, the scaffold was placed in a new well to quantify only the cells attached. It was washed with PBS and 1 mL of trypsin was added. After incubation, 2.5 mL of fresh medium was added, and the cell suspension was collected and centrifuged at 1500 rpm for 5 min. Finally, the supernatant was discarded, and the cells were re-suspended and counted.

2.8. Statistical Analysis

Results were collected from at least six independent experiments. All data are expressed as mean ± standard error (SE). Data were analyzed by Student's *t* test.

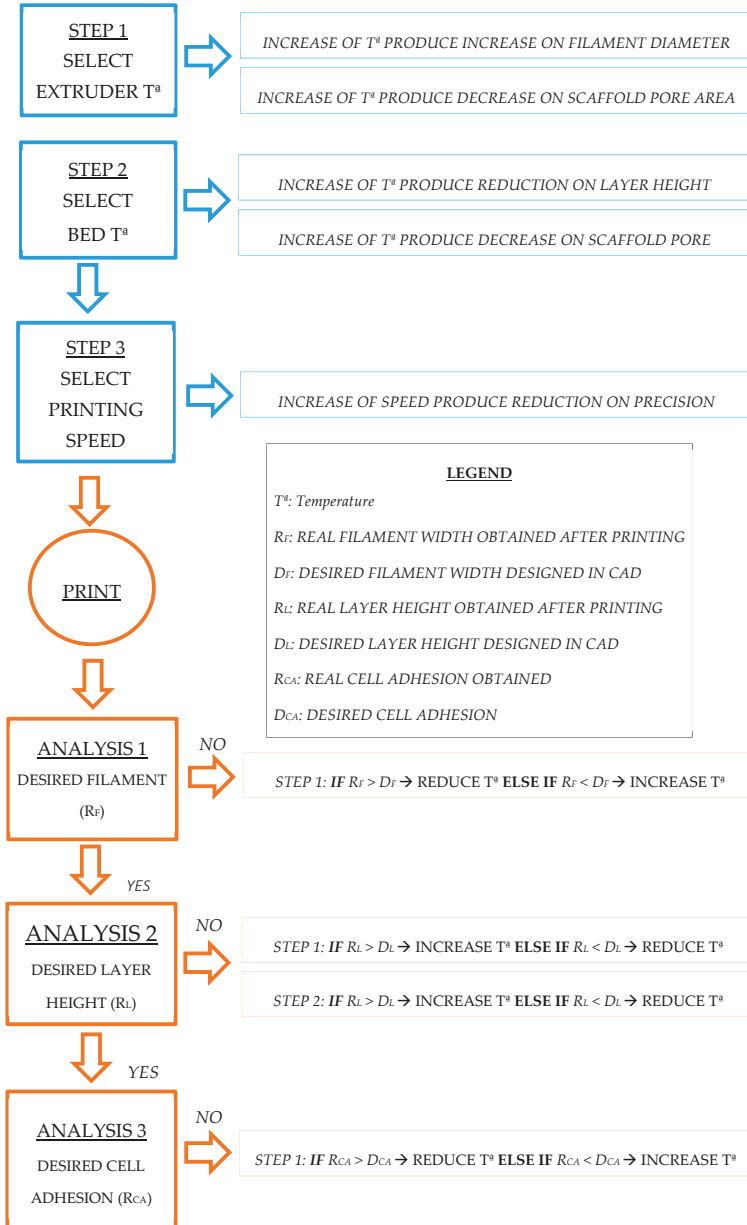


Figure 3. Flowchart of process parameter optimization. Every parameter consists of the values tested and, on the right, the corresponding measurable variable for new cell cultures. Fabrication parameters are in the left column and design parameters in the right.

3. Results: Scaffolds Production

Following the method developed, experimental work was first carried out to find the best way to produce scaffolds which can sustain cell cultures. Sequential work was done to set scaffold design features and manufacturing process parameters.

3.1. Optimization of Process Parameters

Processing parameters were optimized to achieve high quality scaffold printing for cell culture application. Thus, different physical scaffold variables were measured to ensure the correct fit between the computer design and the printed scaffold. The processing parameters included both fabrication and design parameters as shown in the “Experimental Setup” section (Table 1). Processing parameters were chosen according to the literature and the state-of-art [9,11,16,17]. However, the process optimization methodology explained here, based on a sequential flowchart (Figure 3), is both innovative and unique.

Experiments were initially carried out with a generic scaffold design (see Section 2.4 “Methods”) to set the fabrication parameters and then adjusted to the design parameters required to produce the scaffolds.

Fabrication parameters (extruder and bed temperature, deposition velocity, and layer height) were introduced with Slic3r software. These parameters are related to the characteristics of the polymeric material (mainly PCL) and the printing process. However, different values were tested for the parameters (by checking the measurable variable mentioned in Table 1) in order to meet scaffold manufacturing requirements.

Once the polymeric material and its fabrication parameters had been characterized and set, design features were subsequently established using the SolidWorks 3D software. Parameters, such as filament diameter, distance between filaments, and deposition angle, were tested. These are related to the three-dimensional design of the scaffold and the effect they have on the cancer cell culture.

First, to determine the optimal fabrication parameters, a fixed scaffold design was established as a control pattern: 90° deposition angle, 0.4 mm in diameter filament and 1 mm distance between filaments. This enabled us to do printings with the same design, but different fabrication parameters, to find the optimal ones. Later, as the design parameters were optimized, they were replaced.

Following the flowchart defined in Figure 3, all the parameters were characterized and selected sequentially to obtain the appropriate setup for producing 3D-printed scaffolds. The optimization of each process parameter is described in the following sections.

3.2. Extruder Temperature

Poly(ϵ -caprolactone) was chosen as the polymer to work with because of its compatibility with cell cultures. PCL has a low melting point (60 °C). To achieve enough malleability and considering there is some heat dissipation, higher temperatures were also tested to find the optimal value (Table 1). A fixed scaffold design described in the Methods section was printed. Then, *the printed filament diameter* was measured as a physical variable. Low extruder temperatures (65–80 °C) could not melt the material enough, thus the amount of the extruded material was low. As a consequence, the printed filament diameter was smaller than the one designed (0.4 mm). High temperatures (90 °C) melt the polymer excessively and also increase the diameter of the filament due to flattening and some blobs being produced. Therefore, the optimal extruder temperature was established at 85 °C. The printed filament diameter was 0.39 ± 0.05 mm.

3.3. Bed Temperature

To set the optimal bed temperature, a generic geometrical scaffold design was printed, and two different measurable variables were evaluated. Material adhesion was assessed as a binomial variable (yes/no), firstly testing the lowest temperature (25 °C, Table 1). If the printed material had not adhered enough to the surface (no), another printing was performed, this time with a higher bed

temperature. Once the material had adhered to the surface (yes), the first layer height was then measured. Bed temperatures ranging from 25 to 33 °C gave a non-adherent first layer scaffold. In addition, much higher temperatures (37 °C) melt the material excessively, flattening the filament and decreasing the height of the first layer (lower than the 0.4 mm designed one). A 35 °C bed temperature was considered optimal as this allowed first layer adhesion and the filaments were not flattened. Their first layer height was 0.37 ± 0.07 mm.

3.4. Deposition Velocity

The goal with this parameter was to find a high deposition velocity without forgetting the quality of the printed scaffold. The printed filament diameter was chosen as the tangible variable with which to analyze the impact this parameter has on the scaffold. The optimal deposition velocity was established as being 10 mm/s. The filament diameter was 0.42 ± 0.05 mm. When the speed was faster (20 and 30 mm/s) the material did not have enough time to deposit itself on the surface, resulting in smaller filament diameter or sometimes even discontinuous filament production.

3.5. Filament Diameter

At this point, the diameter of the printed filament deposited on the collector was analyzed. Extrusion and deposition velocity can exert a direct influence on fiber morphology. Therefore, once the manufacturing velocity had been fixed, the diameter of the extruded filament was evaluated next. Three different design filament diameters were tested: 0.175, 0.3, and 0.5 mm. To ensure the filaments remained tangent along the vertical axis, the printer's layer height was adjusted to each design filament diameter. Diameters that were too large caused the adhesion of two contiguous filaments, favored by their proximity and elevated temperature. For this reason, the first variable studied was the possible adhesion of contiguous filaments, such as a binomial variable (yes/no). Thus, only the values that did not cause the adhesion of two filaments in the same layer were selected to continue the analysis (0.175 and 0.3 mm). The second measured variable was the printed filament diameter. A design diameter of 0.175 mm caused erratic printing because the amount of material was too low to form a linear filament. The final value tested, 0.3 mm, was found to be optimal as it gave a printed filament diameter of 0.31 ± 0.02 mm. The established filament diameter value also determined the thickness of each layer. The scaffolds were manufactured with eight layers, so the final thickness of the scaffolds was 2.4 mm.

3.6. Layer Height

Layer height is defined as the distance between two connected layers along the Z axis. Since all layers are designed and printed on top of each other, this parameter was determined by the printed filament diameter. For this reason, the filament diameter, although being a design parameter, was established before finishing, optimizing the fabrication parameters (Figure 3). In some cases, the deposited material tends to flatten out and so the printed height is lower. At that point, two different values were analyzed: 0.3 mm (the whole filament diameter) and 0.28 mm (because of a certain flattening) and the quality of the printing recorded (absence of blobs). In this case, 0.3 mm was found to be the optimal layer height for our design as flattening, due to high temperatures, did not occur. When evaluating smaller established heights, the printing process produced blobs.

The absence of filament flattening may be attributed to the relatively low extruder temperature used, (85 °C, see Section 2.1) which can be considered low compared with other biocompatible polymers used in 3D printing, such as PLA [9,12].

3.7. Distance between Filaments

This is a key parameter because it affects the pore size of the scaffold [9]. This design parameter consists of the shortest distance between the axis of two filaments located within the same layer. We were interested in achieving small pore sizes, thus, we focused on the testing small distances (0.5,

0.7, 1 mm). Nevertheless, small distances between filaments may be problematic if two contiguous filaments join. For this reason, the real distance between filaments was measured to take into account whether this value matched that of the one expected (designed).

Distances of 0.7 and 1 mm gave no filament joining, so real distances were higher than 0. Within these values, the smallest value was chosen (0.7 mm). Taking into account this parameter and the optimal filament diameter previously established, the distance between the outer parts of two contiguous filaments was, consequently, 0.4 mm (Figure 4).

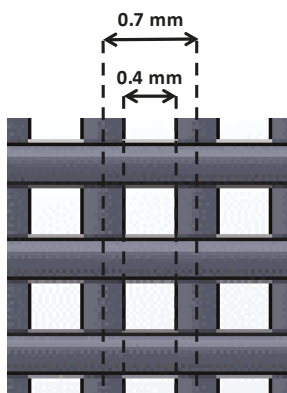


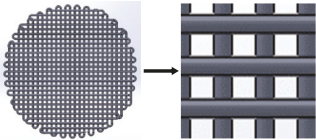
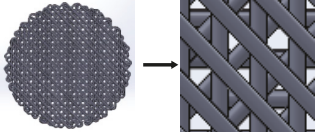
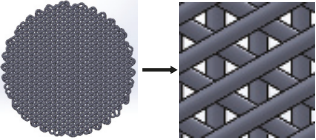
Figure 4. Distances between two contiguous filaments. Axis (0.7 mm) and outer distance (0.4 mm) are represented. Filament diameter was fixed at 0.3 mm.

3.8. Deposition Angle

Once all previous parameters were optimized, three different scaffolds with different deposition angles were designed and manufactured, thus obtaining different pore characteristics, which may influence cell attachment and growth (Table 2). As high-quality printings for all three designs were achieved, it was agreed to test the adequacy for 3D cell culture with all three designs.

An MCF-7 breast carcinoma cell line was used to preliminarily evaluate scaffold ability in terms of three-dimensional cell culture. MCF-7 cells were seeded onto scaffolds and cultivated for 72 h. Then, attached cells were trypsinized and counted. No cells were counted on the 90° scaffolds. Under an optical microscope, no cells were observed on the filament, but rather attached at the bottom of the microplate well (Figure 5a), which is in agreement with cell counting. Scaffolds of 45° showed a subtle cell adhesion of $3.52 \pm 1.16\%$ when compared with the 2D control. We subsequently tested 60° scaffolds, which showed an increased cell adhesion of $26.50 \pm 10.98\%$. In both cases, cells were previously observed at the well bottom and attached to the scaffold filaments, with the last ones are indicated by white arrows (Figure 5b,c, respectively).

Table 2. Scaffold designs with different deposition angles: 90°, 45°, and 60°.

Deposition Angles	Pore Shape	Area	Plan View
90°	Square	0.16 mm ²	
45°	Six variable forms (triangles and irregular polygons)	1.98 × 10 ⁻⁴ to 0.13 mm ²	
60°	Equilateral triangle	0.1256 mm ²	

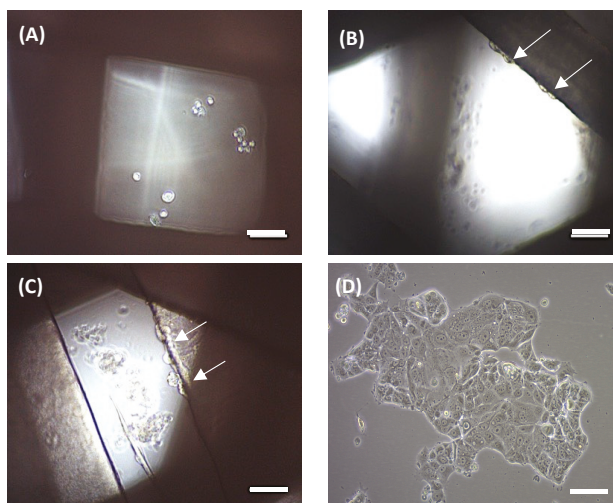


Figure 5. Optical microscope images of MCF-7 cells seeded on the scaffolds. In 90° scaffolds, cells were attached at the bottom of the well (A). In 45° and 60° scaffolds, cells were attached both on the scaffold and at the well (B,C, respectively). (D) MCF-7 cells in 2D culture. White arrows on the images indicate cells adhered to PCL filaments. Scale bars represent 100 μ m.

Then, scaffolds were also evaluated through fibroblast cell cultures. Murine NIH/3T3 fibroblasts were seeded onto the three designs during 72 h and cell proliferation was assessed. In this case, fibroblasts adhered to all three scaffold models (Figure 6), with the highest cell proliferation value being found on the 90° design ($56.30 \pm 5.03\%$ compared to the 2D control). The other two architectures exhibited slightly smaller values. For instance, 60° scaffolds presented a $49.52 \pm 5.62\%$ cell growth and 45° models, $39.11 \pm 8.12\%$, compared to the monolayer culture.

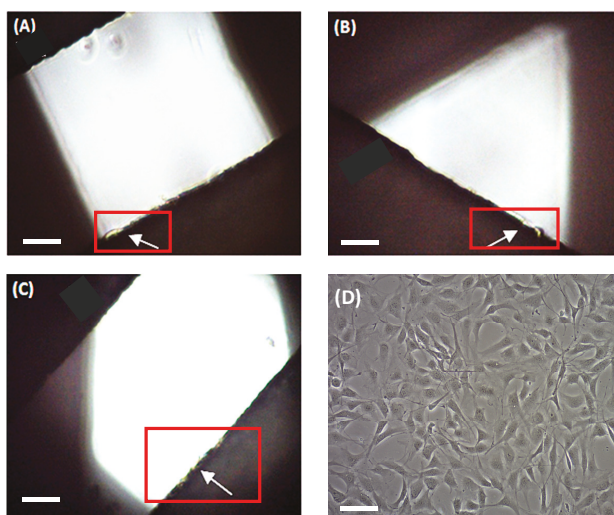


Figure 6. Optical microscope images of NIH/3T3 cells seeded on the scaffolds. Cells were attached on scaffolds of 90° (A), 60° (B), and 45° (C). (D) NIH/3T3 cells in a 2D culture. White arrows on the images indicate cells adhered to PCL filaments. Scale bars represent 100 μ m.

3.9. Optimal Process Parameters Values

After the optimization experiments and basic cell culture tests had been completed, the optimal processing parameters for PCL scaffold printing were established (see Table 3) once the methodology had been applied to set each optimal parameter for cell cultures and for future experiments with CSCs culture enrichment using PCL scaffolds.

Table 3. Optimal processing parameter values to be used for PCL scaffold printing.

Title	Parameters	Optimal Values
Manufacturing parameters	Extruder temperature	85 °C
	Bed temperature	35 °C
	Deposition velocity	10 mm/s
	Layer height	0.3 mm
Design parameters	Filament diameter	0.3 mm
	Distance between filaments	0.7 mm
	Deposition angle	60° (MCF-7 breast cancer cells) 90° (NIH/3T3 murine fibroblasts)

4. Discussion

In this work, a methodology to optimize the processing parameters for PCL scaffold production using a RepRap 3D printer has been developed. By using an optimization flowchart, PCL scaffolds suitable for cell culture were manufactured (Figure 3). The optimal processing parameters determined are closely related to those defined in other studies using the same technology and material. Domingos et al., (2013) set up an 80 °C printing temperature, 10 mm/s velocity, an approximately 0.3 mm filament diameter and a layer height of 0.28 mm [15]. A previous study by the same research group used an extrusion temperature of 70 °C and a speed of 8 mm/s [1]. These small variations support the idea of using a single, common methodology (Figure 3) to optimize the processing parameters. Compared with previous work in the literature, the flowchart provided here makes it

easier to adjust scaffold design features and processing parameters according to cell line characteristics. Several case studies were run to validate the flowchart depicted in Figure 3. Results show how cell culture is improved by using scaffolds which allow cell cultures to be created in 3D conditions and optimized based on the cells' features. In addition, process parameters were also evaluated using cell culture experiments. All scaffold culture experiments presented sterility resulting from the sterilization procedure described here. Both 60° and 45° scaffolds showed adequate design parameters for the MCF-7 cell cultures. In particular, the 60° scaffold design displayed the highest percentage of cell attachment, and exhibited good biocompatibility for the MCF-7 breast cancer cells. In contrast, the NIH/3T3 fibroblast cells presented a more homogeneous growth along the three scaffold designs. However, the 90° scaffold showed the highest cell proliferation value. Therefore, different kinds of cells may prefer different scaffold architectures, further demonstrating the need of a common procedure to find the optimal values. Moreover, a tumor and a non-tumor cell line were tested, showing the flexibility of the flowchart described here.

Three-dimensional cell culture on scaffolds may also be improved by other fabrication-independent parameters such as polarity of cell culture plates, culture media and time [26], as well as different cell culture types, including a dynamic model [27]. This optimization will be the focus of further studies as we attempt to improve cell attachment percentages. Furthermore, CSC population enrichment by cell culture on scaffolds will be evaluated using different approaches.

To date, most of the work related to scaffold production focuses on optimizing design features and forgets about improving fabrication parameters [1,9,16]. In this work, a flowchart to optimize the parameters of the whole process has been proposed (Figure 3) to help with their selection. In addition, this methodology may be further used to set up scaffold manufacturing (both the design features and the fabrication parameters) when using a RepRap 3D printer or any other AM technologies and/or materials.

5. Conclusions

In this work, the design features and fabrication parameters of scaffolds and the RepRap 3D printer were optimized to produce PCL scaffolds suitable for three-dimensional cell cultures. The optimization was performed following a detailed and unidirectional flowchart, thus providing some procedural guidelines with great potential for other popular manufacturing technologies and materials. The contribution of this paper is for scaffolds made with PCL materials. However, this experiment was only carried out to validate the methodology developed as a valuable method for future cell cultures. Often, physicians work with 2D cell cultures, but, as seen here, 3D cell cultures appear to be good method of improving cell culture enrichment. Furthermore, as the design features and manufacturing parameters need to be set for the different cell lines used each time, this methodology will help physicians and other operators to do just that.

Moreover, the scaffolds produced were proven to allow cell attachment and cell growth. The 60° scaffold design mainly worked for the MCF-7 cells and the 90° for the NIH/3T3 fibroblasts. Three-dimensional cell cultures with PCL scaffolds fabricated with a 3D printer offer both researchers and clinics a set of novel applications for the future. The flowchart developed represents a new tool with which to quickly manufacture scaffolds for a wide range of applications, including cell cultures and tissue engineering. For instance, the use of 3D cell cultures can boost CSC populations to study new therapeutic treatment.

Author Contributions: Conceptualization, J.C. and T.P.; Methodology, J.C.; Validation, A.J.G. and M.R.; Formal Analysis, M.R., J.M. and E.P.; Writing-Original Draft Preparation, J.C.; Writing-Review & Editing, M.R., E.P. and A.J.G.; Supervision, T.P. and J.C.

Funding: This research was funded by Spanish Grants: Fundación Ramón Areces, Instituto de Salud Carlos III (PI1400329) and Ministerio de Economía y Competitividad (DPI2016-77156-R), and through the support of the Catalan Government (2014SGR00868) and the University of Girona (MPCUdG2016/036).

Conflicts of Interest: The authors declare no conflicts of interest. The sponsors had no role in the design of the study, in the collection, analyses, or interpretation of data, in the writing of the manuscript, or in the decision to publish the results.

References

1. Domingos, M.; Dinucci, D.; Cometa, S.; Alderighi, M.; Bártolo, P.J.; Chiellini, F. Polycaprolactone Scaffolds Fabricated via Bioextrusion for Tissue Engineering Applications. *Int. J. Biomater.* **2009**, *2009*, 23964. [[CrossRef](#)] [[PubMed](#)]
2. Feng, S.; Duan, X.; Lo, P.-K.; Liu, S.; Liu, X.; Chen, H.; Wang, Q. Expansion of breast cancer stem cells with fibrous scaffolds. *Integr. Biol.* **2013**, *5*, 768–777. [[CrossRef](#)] [[PubMed](#)]
3. Sims-Mourtada, J.; Niamat, R.A.; Samuel, S.; Eskridge, C.; Kmiec, E.B. Enrichment of breast cancer stem-like cells by growth on electrospun polycaprolactone-chitosan nanofiber scaffolds. *Int. J. Nanomed.* **2014**, *9*, 995–1003. [[CrossRef](#)] [[PubMed](#)]
4. Saha, S.; Duan, X.; Wu, L.; Lo, P.-K.; Chen, H.; Wang, Q. Electrospun fibrous scaffolds promote breast cancer cell alignment and epithelial-mesenchymal transition. *Langmuir* **2012**, *28*, 2028–2034. [[CrossRef](#)] [[PubMed](#)]
5. Khalil, S.; Sun, W. Bioprinting endothelial cells with alginate for 3D tissue constructs. *J. Biomech. Eng.* **2009**, *131*, 111002. [[CrossRef](#)] [[PubMed](#)]
6. Gu, G.X.; Su, L.; Sharma, S.; Voros, J.L.; Qin, Z.; Buehler, M.J. Three-Dimensional-Printing of Bio-Inspired Composites. *J. Biomech. Eng.* **2016**, *138*, 021006. [[CrossRef](#)] [[PubMed](#)]
7. Giró-Perafita, A.; Rabionet, M.; Puig, T.; Ciurana, J. Optimization of Poli(ϵ -caprolactone) scaffolds suitable for 3D cancer cell culture. *Procedia CIRP* **2016**, *49*, 61–66.
8. De Ciurana, J.; Serenó, L.; Vallès, È. Selecting process parameters in RepRap additive manufacturing system for PLA scaffolds manufacture. *Procedia CIRP* **2013**, *5*, 152–157. [[CrossRef](#)]
9. Milionis, A.; Noyes, C.; Loth, E.; Bayer, I.S.; Lichtenberger, A.W.; Stathopoulos, V.N.; Vourdas, N. Water-Repellent Approaches for 3-D Printed Internal Passages. *Mater. Manuf. Process.* **2016**, *31*, 1162–1170. [[CrossRef](#)]
10. Mohamed, O.A.; Masood, S.H.; Bhowmik, J.L. Experimental Investigations of Process Parameters Influence on Rheological Behavior and Dynamic Mechanical Properties of FDM Manufactured Parts. *Mater. Manuf. Process.* **2016**, *31*, 1983–1991. [[CrossRef](#)]
11. Gupta, B.; Revagade, N.; Hilborn, J. Poly(lactic acid) fiber: An overview. *Prog. Polym. Sci.* **2007**, *32*, 455–482. [[CrossRef](#)]
12. Duling, R.R.; Dupaix, R.B.; Katsube, N.; Lannutti, J. Mechanical characterization of electrospun polycaprolactone (PCL): A potential scaffold for tissue engineering. *J. Biomech. Eng.* **2008**, *130*, 011006. [[CrossRef](#)] [[PubMed](#)]
13. Baker, B.M.; Nerurkar, N.L.; Burdick, J.A.; Elliott, D.M.; Mauck, R.L. Fabrication and modeling of dynamic multipolymer nanofibrous scaffolds. *J. Biomech. Eng.* **2009**, *131*, 101012. [[CrossRef](#)] [[PubMed](#)]
14. Lange, B.I.; Brendel, T.; Hüttmann, G. Temperature dependence of light absorption in water at holmium and thulium laser wavelengths. *Appl. Opt.* **2002**, *41*, 5797–5803. [[CrossRef](#)] [[PubMed](#)]
15. Domingos, M.; Intranuovo, F.; Russo, T.; De Santis, R.; Gloria, A.; Ambrosio, L.; Ciurana, J.; Bartolo, P. The first systematic analysis of 3D rapid prototyped poly(ϵ -caprolactone) scaffolds manufactured through BioCell printing: the effect of pore size and geometry on compressive mechanical behaviour and in vitro hMSC viability. *Biofabrication* **2013**, *5*, 045004. [[CrossRef](#)] [[PubMed](#)]
16. Bartolo, P.; Domingos, M.; Gloria, A.; Ciurana, J. BioCell Printing: Integrated automated assembly system for tissue engineering constructs. *CIRP Ann-Manuf. Technol.* **2011**, *60*, 271–274. [[CrossRef](#)]
17. Sultana, N.; Mokhtar, M.; Hassan, M.I.; Jin, R.M.; Roozbahani, F.; Khan, T.H. Chitosan-Based Nanocomposite Scaffolds for Tissue Engineering Applications. *Mater. Manuf. Process.* **2015**, *30*, 273–278. [[CrossRef](#)]
18. Zein, I.; Huttmacher, D.W.; Tan, K.C.; Teoh, S.H. Fused deposition modeling of novel scaffold architectures for tissue engineering applications. *Biomaterials* **2002**, *23*, 1169–1185. [[CrossRef](#)]
19. Hsu, S.-H.; Yen, H.-J.; Tseng, C.-S.; Cheng, C.-S.; Tsai, C.-L. Evaluation of the growth of chondrocytes and osteoblasts seeded into precision scaffolds fabricated by fused deposition manufacturing. *J. Biomed. Mater. Res.* **2007**, *80*, 519–527. [[CrossRef](#)] [[PubMed](#)]

20. Yen, H.-J.; Tseng, C.-S.; Hsu, S.-H.; Tsai, C.-L. Evaluation of chondrocyte growth in the highly porous scaffolds made by fused deposition manufacturing (FDM) filled with type II collagen. *Biomed. Microdevices* **2009**, *11*, 615–624. [[CrossRef](#)] [[PubMed](#)]
21. Grémare, A.; Guduric, V.; Bareille, R.; Heroguez, V.; Latour, S.; L'heureux, N.; Fricain, J.C.; Catros, S.; Nihouannen, D.L. Characterization of printed PLA scaffolds for bone tissue engineering. *J. Biomed. Mater. Res. Part A* **2018**, *106*, 887–894. [[CrossRef](#)] [[PubMed](#)]
22. Hutmacher, D.W.; Schantz, T.; Zein, I.; Ng, K.W.; Teoh, S.H.; Tan, K.C. Mechanical properties and cell cultural response of polycaprolactone scaffolds designed and fabricated via fused deposition modeling. *J. Biomed. Mater. Res.* **2001**, *55*, 203–216. [[CrossRef](#)]
23. Rabionet, M.; Guerra, A.J.; Puig, T.; Ciurana, J. 3D-printed Tubular Scaffolds for Vascular Tissue Engineering. *Procedia CIRP* **2018**, *68*, 352–357. [[CrossRef](#)]
24. Rabionet, M.; Yeste, M.; Puig, T.; Ciurana, J. Electrospinning PCL Scaffolds Manufacture for Three-Dimensional Breast Cancer Cell Culture. *Polymers* **2017**, *9*, 328. [[CrossRef](#)]
25. Guerra, A.J.; Cano, P.; Rabionet, M.; Puig, T.; Ciurana, J. Effects of different sterilization processes on the properties of a novel 3D-printed polycaprolactone stent. *Polym. Adv. Technol.* **2018**, *29*, 2327–2335. [[CrossRef](#)]
26. Chen, M.; Michaud, H.; Bhowmick, S. Controlled Vacuum Seeding as a Means of Generating Uniform Cellular Distribution in Electrospun Polycaprolactone (PCL) Scaffolds. *J. Biomech. Eng.* **2009**, *131*, 1–8. [[CrossRef](#)] [[PubMed](#)]
27. Ferlin, K.M.; Prendergast, M.E.; Miller, M.L.; Nguyen, B.N.B.; Kaplan, D.S.; Fisher, J.P. Development of a Dynamic Stem Cell Culture Platform for Mesenchymal Stem Cell Adhesion and Evaluation. *Mol. Pharm.* **2014**, *11*, 2172–2181. [[CrossRef](#)] [[PubMed](#)]



© 2018 by the authors. Licensee MDPI, Basel, Switzerland. This article is an open access article distributed under the terms and conditions of the Creative Commons Attribution (CC BY) license (<http://creativecommons.org/licenses/by/4.0/>).

Article

Assessment of the Potential Economic Impact of the Use of AM Technologies in the Cost Levels of Manufacturing and Stocking of Spare Part Products

Joaquim Minguella-Canela ^{1,*}, Sergio Morales Planas ², Joan Ramon Gomà Ayats ¹ and M. Antonia de los Santos López ³

¹ BarcelonaTECH, Centre CIM/Departament d'Enginyeria Mecànica, Universitat Politècnica de Catalunya, Av. Diagonal, 647, 08028 Barcelona, Spain; joan.goma@upc.edu

² Fluidra S.A., C/Ametllers, 6, 08213 Polinyà, Barcelona, Spain; smorales@fluidra.com

³ Departament d'Enginyeria Mecànica, Universitat Politècnica de Catalunya, Av. Diagonal, 647, 08028 Barcelona, Spain; tania.santos@upc.edu

* Correspondence: joaquim.minguella@upc.edu; Tel.: +34-93-405-4285

Received: 30 June 2018; Accepted: 9 August 2018; Published: 14 August 2018

Abstract: Additive manufacturing (AM) technologies are appropriate manufacturing technologies to produce low rotation products of high added value. Products in the spare parts business usually have discontinuous demand levels of reduced numbers of parts. Indeed, spare parts inventories handle myriad of products that require big immobilized investments while having an intrinsic risk of no-use (for example due to obsolescence or spoilage). Based on these issues, the present work analyses the fundamental cost factors in a real case study of a company dedicated to the supply of spare parts for fluid conduction systems. Real inventory data is assessed to determine the product taxonomy and its associated costs. A representative product of the stock is analyzed in detail on original manufacturing costs, in AM costs and then redesigned with topological optimization to reduce the AM cost levels (via design for additive manufacturing). A general equation for cost assessment is formulated. Given the specific data collected from the company, the parameters in this general equation are calculated. Finally, the general equation and the product cost reduction achieved are used to explore the potential economic impact of the use of AM technologies in the cost levels of manufacturing and stocking of spare part products.

Keywords: additive manufacturing; design; topological optimization; cost; stock; spare parts; free-form filament fabrication (FFF)

1. Introduction

1.1. AM as an Enhancer of Potential Cost Reductions in the Context of Companies with Large Inventories

Companies providing supplies of spare parts are usually obliged to hold large sets of stocks. These inventory parts cause many issues to the companies, in the form of costs, warehouse space and logistic implications. Additive manufacturing (AM) technologies are perceived as a very powerful tool to address mass product customization, delocalized production and short series manufacturing, by maneuvering in relatively low levels of cost and short delivery periods for short series of products. This means that AM technologies could change the way that the companies supplying spare parts organize their business.

However, there is a lack of detailed studies on how the AM technologies impact the cost levels of inventories held by companies. The common case studies focus on the improvement and switch in production methods for very specific selected parts that, of course, yield major potential results. However in effect, all these studies lack of contextualization on the form of the relevance of those

case studies for the overall results in the company. Issues such as (i) the representativeness of the modified parts of the overall set of products, (ii) the cost impact of the part once sold in the overall of the company performance or (iii) the importance of the part studied in the business area of the company are usually not analyzed in detail. This means that the results cannot be extrapolated from the engineering case to the business case or, in the cases it be done, that normally the extrapolation is of relatively low economic impact.

Therefore, the present work addresses the whole matter, providing an engineering case study of a relevant part applied to a relevant business area. This article assesses the technical feasibility of implementing AM technologies in the manufacturing of spare parts. In particular, the assessment is applied to a case that it is representative of the taxonomy of a relevant company for spare parts providing in the fluid conduction systems sector. It undertakes the AM production process for the initial (conventional) design and evaluates the cost levels in comparison with the conventional manufacturing technologies. Furthermore, it performs a redesign of the case study part by means of topological optimization, validating the results both by means of computer aided and physical material testing methods.

Moreover, the study case contains the study of the context characteristics and consequences of the engineering case. It enunciates a frame for cost modelling that can be extended to other companies for further comparison and analysis, it analyzes the cost factors for the parts in the inventory and it finally produces an estimation of the possible impact of the utilization of AM over the cost levels of manufacturing and stocking of spare part products.

This work does not address the design of a new inventory policy in the sense of the number of units to be held. Instead, the present work analyses the possible cost reduction while maintaining the same quantities of stock parts. In this manner, the purpose of the present study is to quantify, the potential impact of the application of AM technologies to the supply inventory parts in a relevant context in a realistic manner (not optimistic or pessimistic). The significance of the work relates to the fact that this refers to a real engineering case study with relevant data, that could be used in future references for benchmarking the state of the art as the frame and methodology can be replicable with different products and technologies.

1.2. Research Background and Motivations

1.2.1. Additive Manufacturing: Production and Design

AM technologies, also commonly referred as 3D printing technologies, comprise numerous different techniques concerned with the materialization of three-dimensional digital models as physical objects, without the need of molds or special tooling. All these techniques have a process in common—that the material is added and consolidated layer by layer, which is the reason why many authors refer to them as additive layered manufacturing technologies. This specific manner of construction consolidation yields a specific directional material behavior effect in the direction in which the layers are added (usually taken as 'z' direction, and so named as 'z-effect'), thus making the parts to adopt an anisotropic behavior being usually the 'z' direction the one yielding the least traction capabilities compared to the other directions 'x' and 'y'.

AM technologies can certainly be classified by two different criteria, i.e., depending on the physical solution in the systems for (i) material incorporation and for (ii) energy incorporation. Usual material incorporation procedures include feeding the raw material from a point (0d), from a line (1d), of an entire layer (2d) or in a bed (3d). Usual energy incorporation procedures include applying it to the raw material in a single point (0d), within a line (1d) or within a plane (2d). Very recent approaches in holographic patterning is opening new possibilities for the application in (3d) [1]. The classification in the AM systems is crucial as it determines the materials that can be processed, the characteristics of the parts that can be obtained and the cost levels of each specific technology.

Generally speaking, AM technologies make possible to manufacture functional parts with complex design geometries, offering the possibility to optimize the mechanical properties of a part while minimizing the weight and so the energy required in their manufacturing [2]. To this regard, the topological optimization techniques deal with the material distribution within a part domain, where material density can be increased or reduced therefore changing the rigidity of each specific domain [3], and even materializing a continuous density graduation.

One particular set of AM technologies that has widespread since the expiration of many patent protections (during 2005–2010) is the fused filament fabrication technologies (FFF). In FFF, the material is incorporated in the part from an extrusion head, being this an application of both (i) and (ii) as a point (0d). FFF processing has relatively low-cost levels of hardware and materials, as well as a huge list of possible materials to be processed [4]. During the last years, industry and academia have researched and developed solutions that cover industrial needs and that are capable to address market niches, and so its use has spread and the penetration in working environments has deepened. These facts position very well the FFF technologies to be utilized as means for production in short runs of delocalized production.

The mechanical properties of the parts manufactured via FFF depend on different parameters such as the internal structure, the orientation in the construction platform and the generation of printing paths [5]. Because of its nature, parts manufactured by FFF technologies have an intrinsic danger of delamination between construction levels, which mean that the construction direction must consider the different working modes that the part will have. Because of the so-called z-effect, introduced above, FFF technologies are far from achieving isotropic parts and its mechanical properties differ from the different construction planes [6]. In the literature, this has been extensively assessed and quantified, especially in computer aided engineering and under static loading conditions. Furthermore, some studies have been conducted to assess the behavior of printed parts under dynamical loads; yielding results more adjusted to the real physical performance of the parts [7].

Moreover, the transition of conventional manufacturing technologies to AM procedures imply many added challenges in the fields of design and materials use for each specific AM technology [8]. Again, there is a very important need for the topological optimization of the parts, which is key for decreasing the costs of the parts, the environmental impact as well as the material usage. This optimization process must be addressed during the design stages of the parts. It requires a detailed study of the working conditions considered for the part and it is normally undertaken by setting an objective function with the constraints of: Material properties, geometrical characteristics, design domain, loads, and supports. The optimization itself is performed by means of computing, iterating solutions between different models. However, it is necessary to allow some human design input to conduct certain aspects of optimization, which is the reason why it is so needed to have tools that allow to ease the free-form design [9]. The overall result of the design for additive manufacturing (DfAM) methods are three-dimensional models redesigned, normally with complex structures and capable to be manufactured by a specific AM technology.

Quantifying the impact of the possible substitution of a conventional manufacturing technology for an AM technology is an open technological challenge that needs to involve both technical knowledge (product optimization) and economic analysis (costing policies). The recent times have been of a high increase in the sales of desktop manufacturing systems—the units believed to be already sold in 2017 nearly double the figures of two years earlier, reaching over 528,952 units worldwide [10], so technologies such as FFF are now more available than ever to industrial companies. Now the challenge is to explore up to which point the current technology can reach relevant product materialization.

1.2.2. Cost Modelling of Additive Manufacturing Technologies

The manufacturing costs levels of manufacturing AM technologies can be characterized relating it to three different factors: (i) Part weight, (ii) part dimensions, and (iii) construction time.

Part weight (i) is a common improvement claim for AM from conventional manufacturing technologies. This is because AM technologies only consolidate the material that would be a slice of the product. The material not used can be reutilized, thus saving raw material. However, the reality is that the material consumption to be accounted is higher in some AM methods. For example, in bed technologies, such as selective laser sintering (SLS) there are limits on the number of recirculation's of material in the bed, so further material consumption must be considered. Furthermore, some deposition technologies, such as FFF, require printing supports (normally in the form of a honeycomb) to manufacture some of the parts, that will also be a scrap material rate.

Concerning (ii) and (iii), some industrialists prefer to treat them autonomously and some combine them in the elaboration of product's quotations. The reason is that the main factor for the cost in the volume of the part is the 'z' direction of the part when set in the machine for 3D printing. Moving the 3D printer head in the 'X'-'Y' plane can be very fast, but the maximum amount of time is spent when moving head and bed relatively over the 'Z' direction. Some authors have studied in detail the consolidation parameters, for example in selective laser melting [11], at all levels: Track, layer, and 3D object. The so-called 'hierarchical approach' facilitates the obtention of high-quality high-density parts. In this context, some industrialists prefer having construction time (iii) as a separate cost factor to integrate better the setting-up and post-production costs while others handle them in combination to have easier cost models.

With this rationale it is clear to see that, in AM technologies, complexity does not affect the final manufacturing cost of the part. Because of this, it is significant to undertake DfAM analysis before performing the manufacturing process, so to minimize the manufacturing cost levels.

In previous works of the authors [12], the costs configuration of the AM production technologies has been formulated in function of: Machinery costs, materials costs, energy consumption costs and labor costs. Implicit in these terms there are the factors of mass, 'z' dimension and construction times. Some other costs models [13] differentiate the well-structured direct production costs (labour, materials, equipment, etc.) from the ill-structured production costs (construction failures, transportation, inventory, etc.).

Having revised all this, in the present study, the Hopkinson and Dickens method [14] has been selected as the reference framework for manufacturing costs calculation. This method calculates the costs by splitting assumes that the energy consumption costs of the machines are negligible (assuming less than 1% of the final cost). Furthermore, the present work tries to broaden the work scope to the costs of manufacturing plus the costs caused by its stockage. Concerning this, some authors have prepared product lifecycle models for the spare parts sector [15], as it keeps being an active working topic.

1.2.3. Cost Modelling and Issues of Holding Stock Parts

The evaluation of the inventory cost is a field widely addressed in the literature because of its many implications in the product supply chain. The economic order quantity (EOQ) is the more extended model used by the authors [16]. EOQ is a model that addresses how much product to order, taking into consideration the ordering costs and the holding costs. The ordering costs include some cost elements such as labor and other indirect office costs that enable to process the order. The holding cost includes the costs of storage, insurance, spoilage and others. The cost of capital is usually considered in the holding cost calculation [17] although some authors advocate for maintaining it as a separate cost factor.

Traditionally in the EOQ model, the holding costs are modeled in function of the average number of units per order. This term represents the stock cost [18,19]. Some authors introduce variations in this model, while others [20] consider two parts of a holding cost; i.e., one depending on the average number of units per order and another one depending of sudden increases in cost such as renting or renovating a warehouse for keeping extra units of product.

The inventory policies for controlling and maintaining optimal inventory levels study the balance between expenditure in ordering costs and in holding costs. This is the reason why it is necessary to develop and select the most effective inventory model yielding the optimum inventory framework minimizing its cost. Some authors [21] have assessed different models, such as lot for lot, EOQ, period order quantity (POQ), least unit cost, least total cost, least period cost, and the Wagner-Whitin model. After the assessment, this last model yielded the best results for the least total annual inventory cost.

In the frame of EOQ theory a cost model with arbitrary function is also developed [22]. In this case, the time-depending holding cost is introduced, in order to take into account the higher money effort for keeping fresh some perishable goods. Some other authors develop more complicated frameworks [23], incorporating the demand modelling as distribution functions [24], addressing the shortage implications in the ordering [25] and solving optimization problems using metaheuristics [18], genetic algorithms and multicriteria analysis [26].

Based on the literature review, there is a clear industrial need to be addressed in the present work, concerning the usual industrial parameters for decision taking; namely: Costs of labor, regional costs, and the time dimension. In the models reviewed, labor and regional costs are normally merged into the holding costs calculation. Therefore, there is a need to separate the accountability of such costs to compare the product costs when locating the supply chain in different geographical facilities.

1.2.4. Case Studies and Implementation of AM Technologies to Industry Parts

Case study research (CSR) is a very suitable methodology for undertaking assessments in both the fields of engineering technology and production administration, which has been gaining importance over many different disciplines during the last years [27]. Compared to pure experimentation, which is probably the most common engineering approach, CSR can handle with the propositions on 'how' and 'why' of contemporary data without having to control behavioral events [28].

The study cases of application of AM technologies to product manufacturing in the recent literature have commonly addressed metal AM applications, and are characteristics of the companies that manufacture and sell AM equipment [29]. Some pure research experimentation approaches are capable of assessing in more detail the conditions and optimal parameters for parts obtention [30]. However, these very comprehensive studies focus on the technical product optimization that can be achieved, and do not assess whether the products improved have a defining impact on the company which produces them at its overall level. The reality is that, at the present time, most of the products optimized in such case studies are parts that are only product prototypes that are not in the main product core range of the firms. Alternatively, in some cases that the products are in the core activities of the companies, some parts fail to be economically relevant in the broader perspective.

The case study formulations can be prepared in single-case designs or multiple-case designs [28]. The results obtained in the engineering case are extrapolated and the impact is evaluated at the company level. Due to the nature of the case study, there has been a very comprehensive process to select the unit of analysis to make sure that the results can be extrapolated to the effect in the size of a company.

2. Materials and Methods

The presented case study methodology is grounded in the real circumstances of *Unistral Recambios*, a company that belongs to the *Fluidra* group, which accounted for a total price list cost of spare parts held in the inventory books over 15 M€ in 2017 (considered the year of the study). In such example, the large volume of references does not allow to treat all the cases one by one. In the present work, the decision taken has been to formulate a case study with a holistic (single unit of analysis) single-case design. The results obtained in the engineering case are extrapolated and the impact is evaluated at the company level.

Due to the nature of the case study, there has been a very comprehensive process to select the unit of analysis to make sure that the results can be extrapolated to the effect in the size of a company. This selection of the unit of analysis (segmentation and taxonomy) has been conducted in the phase of Study definition. In parallel to the study definition, there has been constructed the framework construction for costs evaluation.

The core of the study development has been performed in the engineering case, assessing a product relevant from the global set. The final phase is the analysis of the Impact of the optimization level achieved and the discussion of the possible extrapolation to the potential impact in both company and sector levels. From these, further achievable impact could be explored by the extension of the analysis to other product fractions and/or with the introduction of changes in the inventory policies of the company.

The overall flow diagram of the methodology undertaken in the study is presented in Figure 1.

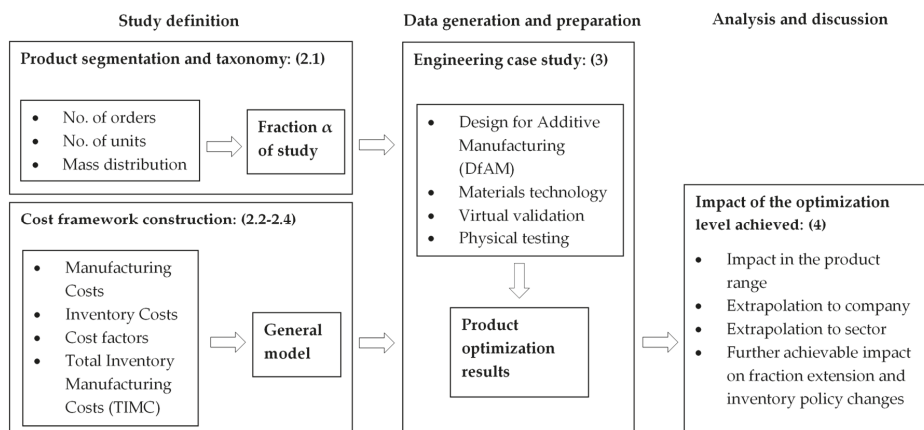


Figure 1. Flow diagram of the present study methodology.

2.1. Inventory Case Study: Spare Parts for Fluid Conduction Systems

In a first exploratory analysis of the data obtained from enterprise resources planning software (ERP) utilized by the company. There are 9072 references which can be object of study, and that can be categorized as follows:

- Kits: Sets of different parts; which can be composed, for example, of a plastic part, a sealing gasket, and screws.
- Plastics: Plastic parts mainly manufacturing by injection molding, blowing or machining processes.
- Chemicals: Chemical substances such as chlorine, acids, and bases.
- Electrical: Including motors, electrical cables, and connectors, among others.
- Mechanical: Standard mechanical elements such as screws, mechanical seals, washers, etc.
- Elastomers: Comprising elements based on elastomeric materials, mainly sealing gaskets, and membranes.
- Filtration: Including filter beds, membranes, and filter cartridges.
- Measurement: Including sensors and devices for temperature measuring, alkalinity, and active oxygen, among others.
- Others: Including items purchased by external suppliers or standard plastic elements, such as junction boxes.

From this product aggregation, the category of 'Plastics' account for 2735 product references, that represent a 30.3% of the total number of articles considered. These are the specific targeted parts

focused in the present study, as most of them could in fact be manufactured by plastic AM technologies, despite being originally designed to be manufactured by other means.

In these selected plastic product references, the next step in the methodology consists on evaluating the relative demand and rotation of each product reference. Therefore, the study analyses both the distribution of the orders and the average lot size of each of them.

Firstly, it has been studied the number of orders received for each of the references. For this reason, a Pareto-type analysis has been made showing the distribution of the number of orders of each product or reference within the category 'Plastics' (see Figure 2). During the study year, the 2735 product references were called in a total of 99,009 independent orders.

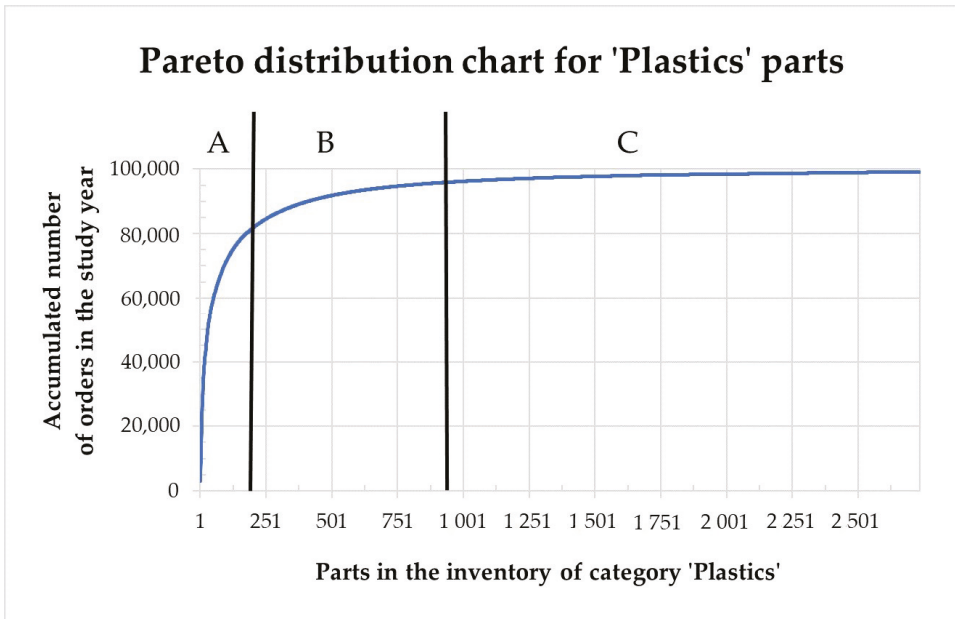


Figure 2. Pareto distribution A-B-C of the orders received for all references within the category 'Plastics'. Elaborated by the authors from *Unistral Recambios* data.

The Pareto analysis divides the orders received in the category 'Plastics' within three population levels 'A', 'B' and 'C'. The 'A' sector comprises the products that represent the 80% of orders expressed in number of units. The 'B' sector comprises the products that represent a supplementary 15% of the orders and, finally, the 'C' sector includes the products that represent the 5% of the remaining orders. The specific data for this analysis is shown in Table 1. In this table it is also shown the maximum, average and minimum numbers of orders for the references classified in each sector. As a preliminary conclusion, the 166 references categorized in Sector A have continuous levels of demand, which can continue to be produced by conventional manufacturing means that lead to economies of scale. On the contrary, the references in the sectors B and C are potentially good candidates to be analyzed in the present study as they add up total of 2569 part references (93.9% of the products in the 'Plastics' category) with discontinuous levels of demand (29.9 orders/year in average for Sector B and 2.4 orders/year in average for sector C).

Table 1. Pareto distribution A-B-C of all references. Elaborated by the authors from thanks to the data facilitated by *Unistral Recambios* data.

References and Orders in eEach Pareto Sector	Sector A	Sector B	Sector C
Total number of references in the sector	166	513	2056
Maximum number of orders for a part in the sector	3078	80	9
Average number of orders for a part in the sector	477.5	29.9	2.4
Minimum number of orders for a part in the sector	80	10	0

Secondly, it is important to quantify the real rotation of the products; i.e., how many of each of the parts are ordered in their (possible) different orders. As stated earlier, these figures can be obtained by analyzing the average number of parts served in each of the orders for every part. Concerning to this, Figure 3 depicts the actual rotation of the products.

Figure 3 shows a very clear distribution for a company dedicated to the spare parts supply. In effect, the quantity of parts ordered in average in an independent order is relatively small. This fact, combined with what was demonstrated in Figure 2, shows how most of the parts receive relatively low numbers of orders containing relatively low numbers of units of products in each order. Only few products receive recurrent large orders. In fact, the plastic parts that do have large recurring orders are commonly small plastic bags and small foam spacers with manufacturing costs that normally fall below 0.0002 €/unit, having a limited impact in the inventory costs. Furthermore, some 142 product references accounted for zero orders in the study year.

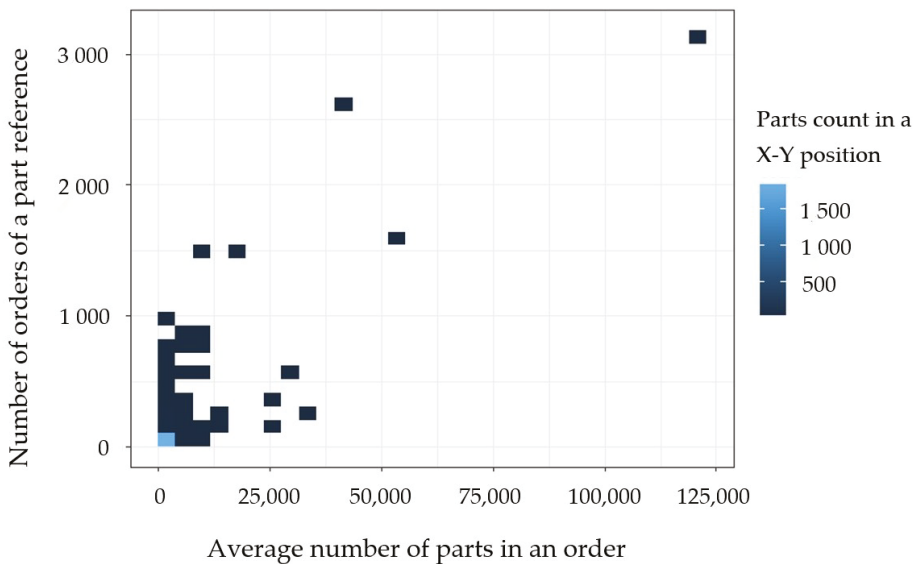


Figure 3. 3D quantification of the rotation of the products. For each part, a plot in X and Y is configured with the number of orders received and the average number of units sold in each order within the categories ‘Plastics’. Elaborated by the authors from *Unistral Recambios* data.

More specific information on the distribution of the number of units in an independent order can be found in Table 2. In particular, having an average number of units in an order of 78.9 parts, in fact 75% of the orders are of 15 parts or less. Therefore, in this sector, the real industrial interest for manufacturing solutions is to respond to the orders of small batches of products.

Table 2. Distribution of the number of units demanded in each independent order.

Total Number of Orders	Max. no. of Units in an Order	Average no. of Units in an Order	Min. no. of Units in an Order	Max. no. of Units in an Order on Percentile 25	Max. no. of Units in an Order on Percentile 50	Max. no. of Units in an Order on Percentile 75
99,009	118,893	78.9	1	1	4	15

From the mass distribution perspective of the analyzed parts, it can be produced an analogous study which is shown in Table 3. For the 2735 references analyzed in the ‘Plastics’ category, some weighty parts increase the overall average weight of a part to 2.179 kg. However, 75% of the references weight are of 1.005 kg or less. Clearly, the majority of the parts within the category have small masses.

Table 3. Distribution of the mass in the product references.

Total Number of References	Max. Part Weight (kg)	Av. Part weight (kg)	Min. Part Weight (kg)	Part Weight on Percentile 25	Part Weight on Percentile 50	Part Weight on Percentile 75
2735	25	2.179	1.0×10^{-12}	0.252	0.655	1.005

As a summary, the taxonomy analysis undertaken in the present exploration yields that the prototype part in the ‘Plastics’ category, for this company in this sector:

1. Received 80 or less orders in the study year, so it has a discontinuous level of demand (receives less than five orders per week),
2. The ordered quantities were very low. Being conservative, most products demand fall below 2400 of total units in the period (which would imply, for example, 80 independent orders of 30 parts of the same product), so do not justify manufacturing in long runs, and
3. The mass of each part is below 1 kg of weight, so it is sensible to be manufactured by means of AM technologies.

Therefore, the case study will focus on the parts that fulfil these conditions and will be referred as the fraction ‘ α ’ of the inventory.

2.2. Total Inventory Manufacturing Costs

In order to quantify the costs in its context, it can be formalized the total inventory manufacturing cost (TIMC), which can be calculated by making the addition for all parts in the inventory of its number and manufacturing cost, as formalized in Equation (1):

$$TIMC = \sum_{i=1}^{i=n} \sum_{j=1}^{j=m} (Q_i^j \cdot C_{MANi}^j), \tag{1}$$

where:

- (TIMC) is the global aggregate total inventory manufacturing cost
- (i) is a part in the inventory
- (j) is an order manufactured and hold in the inventory
- (Q_i^j) is the number of repetitions of product ‘i’ in the order ‘j’
- (C_{MANi}^j) is the manufacturing cost of product ‘i’ in the order ‘j’

In particular, $TIMC_\alpha$ can be used to refer the Total Inventory Manufacturing Cost (TIMC) of a subset of products ‘ α ’, in particular those belonging to the filtering undertaken with the ‘Plastics’ category.

2.3. Costing Model for Injection Molding Parts

In the present study, the calculation of the costs for manufacturing a part utilizing injection molding technologies is performed as indicated in Equation (2):

$$C_{IM} = C_E + C_{TOL} + C_L + C_{MAT}, \quad (2)$$

where:

- (C_E) is the equipment cost per part, calculated as a ratio of the utilization time of the equipment for the manufacturing of a part, considering the equipment depreciation, the energy average consumption and the maintenance associated
- (C_{TOL}) is the tooling cost per part, calculated as a division of the total tooling costs by the total number of parts manufactured
- (C_L) is the labor cost per part, calculated as a multiplication of the time dedicated by a worker to a part by the labor hourly cost
- (C_{MAT}) is the material cost per part, calculated as a multiplication of the product mass by the material cost per weight unit

In this costing model, C_E and C_L are function of the processing time required, and C_{MAT} is function of the material weight utilized.

2.4. Costing Model for Additive Manufactured Parts via Fused Filament Fabrication

In the present study, the calculation of the costs for manufacturing a part utilizing AM technologies is performed as indicated in Equation (3):

$$C_{AM} = C_E + C_L + C_{MAT}, \quad (3)$$

where:

- (C_E) is the equipment cost per part, calculated as a ratio of the utilization time of the equipment for the manufacturing of a part, considering the equipment depreciation and the maintenance associated cost. In AM, the product physical dimensions (volume) affects the processing time; so, it is implicit in this cost factor. The energy average consumption is neglected following the model in Section 2.
- (C_L) is the labor cost per part, calculated as a multiplication of the time dedicated by a worker to a part by the labor hourly cost
- (C_{MAT}) is the material cost per part, calculated as a multiplication of the product mass by the material cost per weight unit

In this costing model, again, C_E and C_L are function of the processing time required, and C_{MAT} is function of the material weight utilized.

2.5. Costing Model for Parts in Stock

In the present study, the calculation of the costs generated for a stocked part is make as indicated in Equation (4):

$$C_S = C_{MAN} + C_{TRA} + C_H + C_{MGT}, \quad (4)$$

where:

- (C_{MAN}) is the cost of manufacturing of a part, calculated as in previous sections, depending on the manufacturing technology utilized
- (C_{TRA}) is the cost of the transportation incurred when moving the part from the production unit to the warehousing facility

- (C_H) is the cost of holding stocked the part, considering the physical space cost in the warehouse and other derived costs such as the insurance cost for the part
- (C_{MGT}) is the cost of managing the stocked part, considering the labor in warehousing and surveillance and other derived costs such as the software license costs for the part

In this costing model, C_{MAN} , C_{TRA} , C_H and C_{MGT} are function of the processing time required, of the material weight and of the physical dimensions of the part. For this reason, Cs can be expressed as shown in Equation (5):

$$Cs = (K_{MAN}^t \cdot t_{MAN} + K_{MAN}^m \cdot m + K_{MAN}^v \cdot v) + (K_{TRA}^t \cdot t_{TRA} + K_{TRA}^m \cdot m + K_{TRA}^v \cdot v) + (K_H^t \cdot t_H + K_H^m \cdot m + K_H^v \cdot v) + (K_{MGT}^t \cdot t_{MGT} + K_{MGT}^m \cdot m + K_{MGT}^v \cdot v) \tag{5}$$

where:

- (K_i) are the constants associated to the different cost factors
- (t_i) are the processing times for each part of the process (manufacturing, transportation, holding and management)
- (v) is the envelope volume for a part, calculated by multiplying the maximum dimensions in the three cartesian directions (X·Y·Z).

This cost modelling framework is interesting for global companies as it enables a comparison of different manufacturing and inventory costs incurred in different locations, as far as the labor costs, the land costs and the logistic chains are quantified; as well as the processing times required, material weight and physical dimensions of the parts.

If a designer can reduce the mass and the manufacturing processing times of a product, without modifying any of the rest of factors, the variation of Cs for a single part in the stock can be calculated as shown in Equation (6):

$$\Delta Cs = (K_{MAN}^t \cdot \Delta t_{MAN} + K_{MAN}^m \cdot \Delta m + K_{TRA}^m \cdot \Delta m + K_H^m \cdot \Delta m + K_{MGT}^m \cdot \Delta m), \tag{6}$$

where:

$$\Delta t_{MAN} = t_{MAN}^{Conventional\ process} + t_{MAN}^{DfAM\ process}, \tag{7}$$

$$\Delta m = m^{Conventional\ product} + m^{DfAM\ product}, \tag{8}$$

Or, grouping the terms of Equation (7), as shown in Equation (10):

$$\Delta Cs = (K_{MAN}^t \cdot \Delta t_{MAN} + K_{MAN}^m \cdot \Delta m) + (K_{TRA}^m + K_H^m + K_{MGT}^m) \cdot \Delta m \tag{9}$$

Which, in the aggregation of all the changes in Cs for all the parts in the stock, can be calculated as expressed in Equation (11):

$$\sum_{i=1}^{i=n} \Delta Cs_i = \sum_{i=1}^{i=n} \Delta C_{MAN_i} + \sum_{i=1}^{i=n} (K_{TRA}^m + K_H^m + K_{MGT}^m) \cdot \Delta m_i. \tag{10}$$

Or, in terms of the TIMC, as expressed in Equation (12):

$$\sum_{i=1}^{i=n} \Delta Cs_i = (TIMC_{\alpha}^{Conv. proc.} \cdot \delta) + (K_{TRA}^m + K_H^m + K_{MGT}^m) \cdot m_{total\ \alpha}^{Conv. proc.} \cdot \gamma. \tag{11}$$

where:

- (α) is the target group for the switch to AM processes; i.e., ‘Plastics’
- (δ) is the average cost reduction in manufacturing of the parts achieved for the target group (α)
- ($m_{total\ \alpha}^{Conv. proc.}$) is the original total mass of the target group for the switch to AM processes; i.e., ‘Plastics’
- (γ) is the average mass reduction in the parts achieved for the target group (α)

3. Results

The product object of the case study in the present work is a real case articulated in the fluid handling industry. To be consistent in the analysis and following to the product segmentation undertaken in Section 2.1, it has been chosen a relatively common product (weighting less than 1 kg), demanded on a relatively low number of orders (less than 42 orders) and in relatively short series (less than 2400 units per order in average). The product is redesigned, and the costs are assessed in the conventional manufacturing process and in an AM technology (FFF) both for the original part design and for its redesign. The reduction in the manufacturing costs are then used to infer the reduction of overall inventory costs that could be achieved through the introduction of AM.

3.1. Case Study (Spare Part for Fluid Handling): Product Definition

3.1.1. Product Specifications

The overall product is a flow regulation system for fluids (an automatic valve), which contain many different parts. A pneumatic piston acts on the actuator (green) which is connected to the membrane (black) by means of a metal insert in form of a pin. The support (red) is responsible for aligning the actuator with the membrane so that it can restrict the flow and separate the pneumatic system from the hydraulic system. Finally, the body of the valve (dark gray) is responsible for the conduction of the fluid (see Figure 4). The system is fixed with stainless steel screws that go through all the parts until reaching the pneumatic piston.

In this case, the part to be studied is the support of the automatic valve. The need is to manufacture 2000 units of supports to fully supply the customer.

The technical specifications of the support require the use of materials with good mechanical and thermal properties. For this reason, technical polyamide (PA666) also used in the automotive industry, is the material selected for manufacturing the part. It is a strong, ductile and easy to print material. The filament for the present study (*Novamid*[®] ID1070), was supplied by *Nexeo Solutions*, suppliers of the material used.

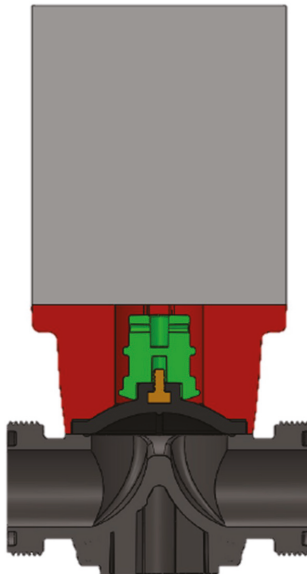


Figure 4. Automatic valve section, in red the part to be redesigned and assessed (support).

3.1.2. Original Product Costs (Molding)

The case study for this inventory part starts with the costs assessment considering that this part was originally designed to be manufactured by injection molding technologies. All the economic treatment is handled in Euros as the company in the case study has its headquarters in the Barcelona region (Spain).

As it can be seen in Table 4, the cost analysis reaches a minimum total cost per part of 1.71 €, in the case of a total production volume of 275,940 parts per year over a 10 years' production period. In the case of manufacturing only the 2000 units to supply the demand in the considered order, the total cost per part is of 21.61 €.

Table 4. Injection molding costs assessment for the original product at a maximum production rates and at an order level of 2000 units.

Injection Molding Manufacturing Cost Per Part		
Operation data		
Production rate per hour (h^{-1})	35	35
Hours per year in operation (h)	7884	7884
Production volume total (per year)	275,940	2000
Cost of Equipment		
Machine and ancillary equipment (€)	400,000	400,000
Equipment depreciation cost per year (€)	40,000	40,000
Machine maintenance cost per year (€)	8000	8000
Total machine cost per year (€)	48,000	48,000
Total machine cost during the time of operation (€)	48,000	347.9
(C_E) Machine cost per part (€)	0.17	0.17
Cost of Tooling		
Mold cost (€)	40,000	40,000
(C_T) Mold cost per part (€)	0.14	20
Cost of Labor		
Machine operator cost per hour (€)	17	17
Post-processing time per part (min)	0.5	0.5
(C_L) Labor cost per part (€)	0.14	0.14
Cost of Material		
Material per part (kg)	0.862	0.862
Build material cost per kg (€)	1.5	1.5
(C_{MAT}) Material cost per part (€)	1.293	1.293
(C_{IM}) Total cost per part (€)	1.75	21.61

3.1.3. Original Product Costs (AM)

As a starting point approximation, the 3D printing costs of the case study part (support) are analyzed without carrying out any type of structural redesign. The printer used for the present study is an FFF machine from the manufacturer "BCN3D" (Sigma model) that has the impact on the cost of the part accounted in Table 5. With this calculation method, the total cost per part when manufactured via AM technologies is of 40.06 € with independency of the number of units to be manufactured.

Table 5. Additive manufacturing (AM) costs assessment for the original product.

Additive Manufacturing Cost Per Part (Original Design)	
Operation data	
Number of parts manufactured per platform	2
Platform build time (h)	143
Hours per year in operation (h)	7884
Production volume total (per year)	110
Cost of Equipment	
Machine and ancillary equipment (€)	2100
Equipment depreciation cost per year (€)	262.5
Machine maintenance cost per year (€)	100
Total machine cost per year (€)	362.5
(C_E) Machine cost per part (€)	3.29
Cost of Labor	
Machine operator cost per hour (€)	17
Set-up time to control machine (min)	5
Post-processing time per part (min)	3
(C_L) Labor cost per part (€)	1.13
Cost of Material	
Material per part (kg)	0.862
Build material cost per kg (€)	41.35
(C_{MAT}) Material cost per part (€)	35.64
(C_{AM}) Total cost per part (€)	40.06

The operation data presented in Table 5 has been calculated with the BCN3D CURA software, including the number of parts per platform in the present case-2-, and the platform build time—143 h. CURA also calculates the amount of material used in the construction, given a determined level of infill; which in the present case accounts for 862 g per part.

The relevant printing parameters utilized by the BCN3D CURA software (Version 2.0, BCN3D Technologies, Barcelona, Spain) to calculate the cited output, which will be needed for the cost calculations are the following:

- Nozzle diameter: 0.4 mm
- Diameter of the filament: 2.85 mm
- Print speed: 80 mm/s
- Layer height: 0.1 mm
- Wall thickness: 0.8 mm
- Platform adhesion: Brim
- Extrusion temperature: 230 °C
- Temperature of the hot bed: 100 °C

BCN3D CURA software graphical interface is capable of representing the parts in 3D located in the construction platform as they will be obtained once the parts manufacturing is completed. For the manufacturing of the case study part, it is chosen to place the parts laying on its bigger flat surface. The BCN3D CURA graphical simulation is shown in Figure 5.

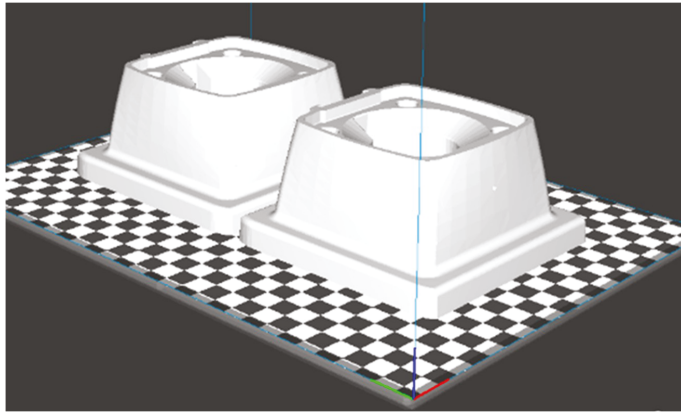


Figure 5. BCN3D CURA software platform simulation the case study part (support) in the original design model.

3.2. Case Study (*Spare Part for Fluid Handling*): Product Redesign and Virtual Validation

3.2.1. Preliminary Infill Study

As a starting point in the product redesign it is interesting to evaluate the effect of the reduction of the infill percentage of the part. Providing that the external features of the case study part remain the same, the same model can be printed with a different internal structure (filler or infill). The infill modification as a percentage is a very powerful approach, due to its easiness, to reduce the amount of material needed while maintaining the necessary stress resistance of the parts. In many cases, the filling of the part does not need to be 75% to 100%. A 25% fill can also provide enough strength and saves time and print material.

Also, in FFF, very solid parts can yield to warping and deformations due to the cooling process of the part. This deformation or warping can be reduced either through good adhesion to the construction platform or also through the printing configuration. In particular, it can be significantly reduced if a less dense structure is used.

One of the best approaches for tuning the infill level is to test it live by printing a part. Figure 6 shows a couple of 3D printed repetitions of the case study part. The part in the left was manufactured with an infill level of 25%, while the one in the right was manufactured with an infill level of 75%. Only with this infill percentage reduction, a significant change in the shape of the part the material is reached. In particular, for the printed tests, the shape distortion is reduced between 5 and 7 mm in the four lower edges of the part. Furthermore, a significant cost reduction is observed as the printing time is reduced by a 30%.

These exploratory results can be utilized as preliminary quantitative figures for a starting point of the specific product improvement. Based on these, the product redesign, in form of DfAM, should be explored in detail undertaking the complete topological optimization and analysis.

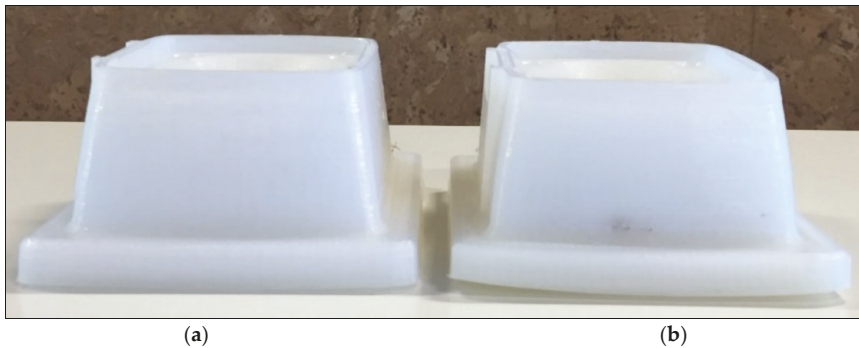


Figure 6. Case study printed parts: (a) Support manufactured with an infill percentage of 25%; (b) support manufactured with an infill percentage of 75%.

3.2.2. Product Redesign and Virtual Validation

The computer aided design (CAE) analysis starts with the definition of the constraints imposed by the components in the context of the system. As such, the first element to be considered for the simulation is the gold membrane that exerts a pressure on the surroundings of the housing of the support (see Figure 7a). The central part of the membrane also exerts pressure, but only when there is water pressure inside, for this reason it is presented in the study of loads. The material of the membrane is EPDM rubber (ethylene propylene diene monomer rubber), a rubber derivative with 6 mm thickness and a modulus of elasticity of 10 MPa.

The support object of the case study in the simulation is shown in Figure 7a represented in blue color. However, for the redesign and simulation means, the support is divided into two domains. The outer shell or skin, for aesthetic reasons, should remain as it is in the original design, but the interior of the support can be modified. Therefore, as presented in Figure 7b the part is divided into the design domain (interior, in red) and the non-design domain (housing or skin, in blue) with a thickness of 2 mm.

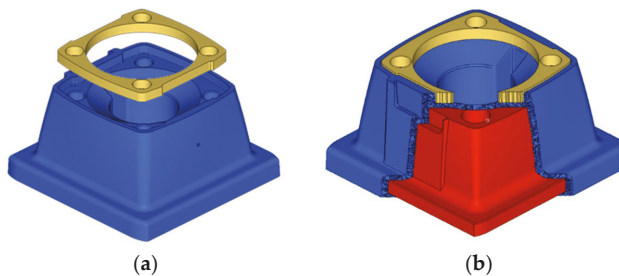


Figure 7. Case study part: Support (in blue) and membrane (in gold). (a) Support and membrane; (b) design domain (red) and non-design domain (blue).

Secondly, the study of the supporting surfaces of the part is addressed. The biggest surface of part is in direct contact with the base of the metallic piston and therefore, there must be included a surface restriction (see Figure 8a). As for the screws, which joins the body with the piston, it restricts movement in the X, Y and Z directions (see Figure 8b). In the center of the part there is a through housing where the rod and the actuator pass through the support until they encounter the membrane. The loads on the sides of the housing are not considered in this case study, assuming the actuator next to the stem will not contact with the walls around it.

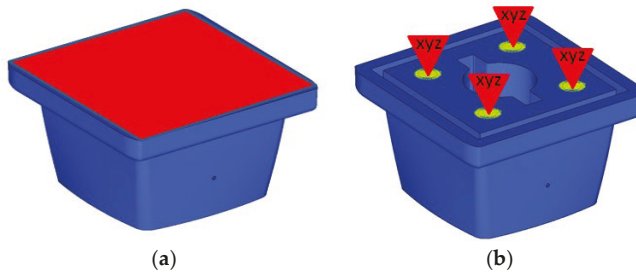


Figure 8. Case study part (support, in blue) and membrane (in yellow): (a) Surface (red) including a restriction; and (b) four screw fasteners support (yellow), which are the points at where the model does not allow any physical displacement over any of the cartesian directions (X-Y-Z).

The third step is to identify the loads in the model and two extreme conditions have been defined: Valve totally open, and valve totally closed. In the first condition, the pneumatic actuator is resting, and the membrane passes the flow through the interior of the body at a nominal pressure of 10 bar (PN10). In this case, the pressure acts on both sides of the support (see Figure 9a). In the second condition, the pneumatic actuator applies force on the membrane stepping on the body and preventing the passage of the flow inside. In this case, the pressure acts only on one of the faces (See Figure 9b).

The body and the support are assembled by means of screws with a tightening of 6 Nm, in both cases a pressure of 1 MPa of compression has been applied on the membrane that corresponds to a deformation of 0.6 mm in its dimensions. The *Novamid® ID1070* material (which is the filament used in the manufacturing of the present case study) was characterized for the two most common printing patterns (0-90 and 45-45) for the X-Y printing plane (see Table 6).

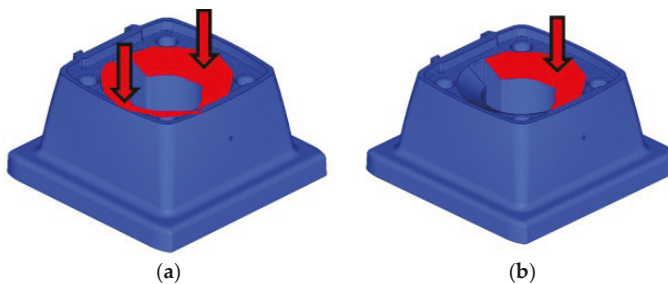


Figure 9. Case study part (support, in blue) with load in the conditions of: (a) Valve totally open; and (b) valve totally closed.

Table 6. Mechanical properties of *Novamid® ID1070*.

Parameters		E [MPa]	ϵ [%]	σ [MPa]
0-90	X-Y	1,714 ± 103.83	7.21 ± 2.97	44.85 ± 2.62
45-45	X-Y	2,124 ± 80.05	14.89 ± 6.97	50.14 ± 1.86

From this material characterization, the virtual testing has been executed assuming a linear simulation and utilizing the least favorable values for the material properties that are presented in Table 7 (X-Y print at 0-90). A safety factor of 30 has been considered in the voltage factor for the simulation.

Table 7. Mechanical properties imposed in the virtual testing conditions.

Parameters		E (MPa)	σ (MPa)
0–90	X–Y	1600	42

Once the model is ready, the first simulation run is used to evaluate the behavior of the initial totally solid (100% level of infill) model of the part. With the simulation results it is possible to quantify to the material deformation (as presented in Figure 10a) as well as the Von Mises stress values (as presented in Figure 10b), providing detailed information on the different model areas.

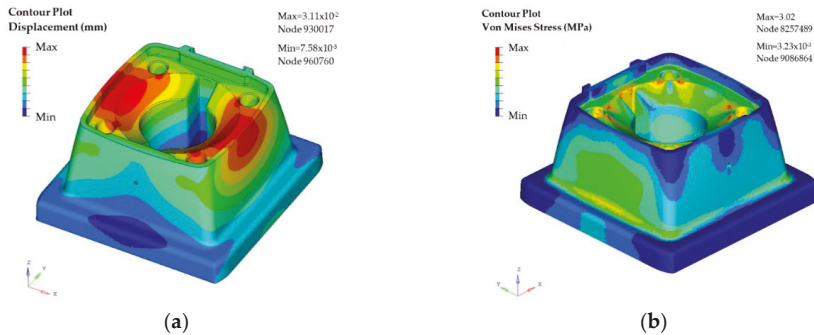


Figure 10. Case study part (support): (a) Displacements of the material for the solid model; and (b) Von Mises stress for the solid model.

In particular, the maximum displacement results are 0.031 mm obtained at the top of two of the sides of the part. The maximum stress of Von Mises is estimated around fixations with a value of 3.02 MPa (see Figures 10b and 11a).

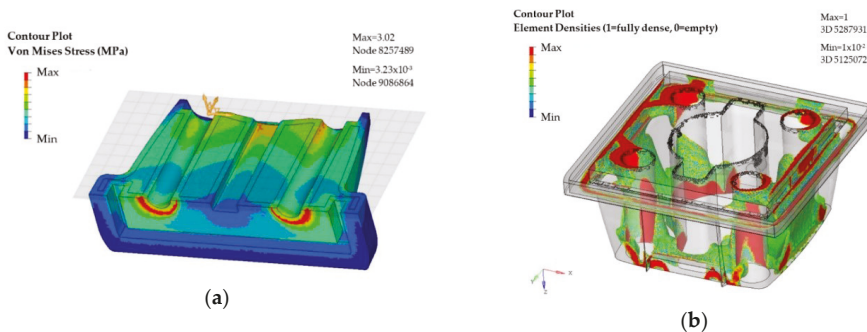


Figure 11. Case study part (support): (a) Von Mises stress focused on fixations; and (b) results of topological optimization.

These values obtained in the simulation indicate that the model is oversized and that there is room for material optimization. In this case, the objective of the topological assessment is to propose material to remove in those points where the interaction of the loads is low, and/or no displacements occur. In this manner, the objective function is set to maximize the rigidity of the model, taking into account the restrictions and supports. The results of the topological optimization are presented in Figure 11b.

The results obtained in the analysis indicate the areas where it is necessary to have a greater density of material so that the part is functional according the specified mechanical requirements. Due to

the asymmetry in the load results, the proposed design in this case is not completely symmetrical. However, to make sure that the part would meet the solicitations in any of the possible mounting dispositions, the denser side has been mirrored to the opposite side of the initial plane of symmetry of the part. Once the redesigned model is completed, a new simulation is run to evaluate the level of displacements and stress. The results are presented in Figure 12a,b.

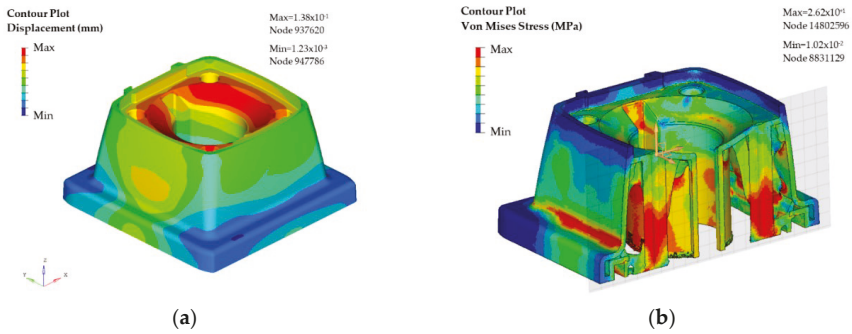


Figure 12. CAE of the case study part (support): (a) Displacement results in the optimized design, and (b) Von Mises stress result in the optimized design.

In the redesigned product, the maximum displacements meet are of 0.138 mm, which are considered acceptable within the normal operation limits. Furthermore, the maximum stress (mostly due to compression efforts) is of 26.2 MPa, falling on the safe operating area.

3.2.3. Manufacturing Specifications for the Product Redesign

To achieve the desired dimensions in the printed part, thermal contractions must be considered. For this, it is necessary to over-scale the three-dimensional model, increasing the volume in a proportion of a certain value. This value is dependent on the printing conditions, but in general, for *Novamid® ID1070 1.02*, a 2% of increase in dimensions can be used. In this way, it is possible to correct the deformation contraction effect by ensuring the correct dimensions after printing (see Figure 13).

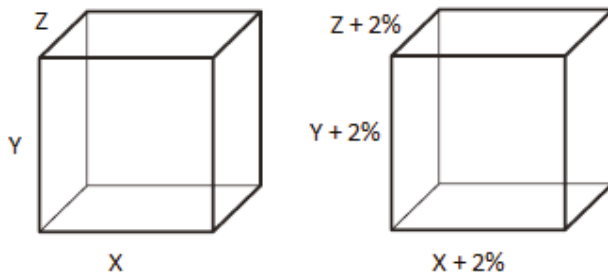


Figure 13. Original model (left). Corrected model (right).

Novamid® ID1070 is printable with FFF machines whose extrusion nozzle head with temperature ranges between 220–245 °C. The most usual printing temperature is 230 °C, achieving the homogeneous melting of the material at temperatures above 225 °C. The optimum mechanical properties are observed at temperatures between 225–245 °C.

The *Novamid® ID series* is a range of high performance filaments for extreme resistance and ductility. These properties are closely related to the level of crystallization of the material. In order to

achieve performance similar to the standard injection molding of PA6, the high level of crystallinity in the material has been maintained. Because of this increased crystallinity, using the optimum printing conditions is necessary.

To print the new models, it was used with the BCN3D Technologies Sigma 3D with the same printing values for the parameters of nozzle diameter, filament diameter, print speed, layer height, extrusion temperature and temperature of the hot bed than in the initial printing. The infill parameters are set at 100% in this new trial of manufacturing. The reason is that once the part has undergone the topological optimization, the material allocation needs to match the computer aided design.

Concerning the adhesion of the printing part to the construction plate, the accumulation of stresses due to contractions during printing can cause the separation of the printing substrate. To this regard, adhesion can be increased by chemical bonding or mechanical bonding. To achieve a correct adhesion in the hot bed, an adhesive promoter (*Dimafix*[®]) was used, also adding an edge to increase the contact surface.

3.2.4. Physical Functional Validation of the Redesigned Printed Part

After the virtual Computer aided engineering testing, the printed parts have been functionally validated in a specific test bench at the company *Fluidra*.

The test bench consists on a small circuit composed by a compressor that introduces pressurized atmospheric air into an accumulator that is presented in Figure 14. A pressure regulator set at 10 bar allows the air flow through a normally closed solenoid, which commands the piston that lifts the membrane. As presented previously in Section 3.1.1, the movement of the membrane (opening and closing) allows and stops the flow of liquid through the main body of the valve. Therefore, the support analyzed in the present case study is mounted between the piston and the main body of the valve. The solenoid valve is controlled by a square signal, with short cycles of five seconds with voltage and five seconds without voltage. According to the established protocol, the study part (support) must meet the same minimum operating life as the minimum membrane life, which is set at 5000 cycles.

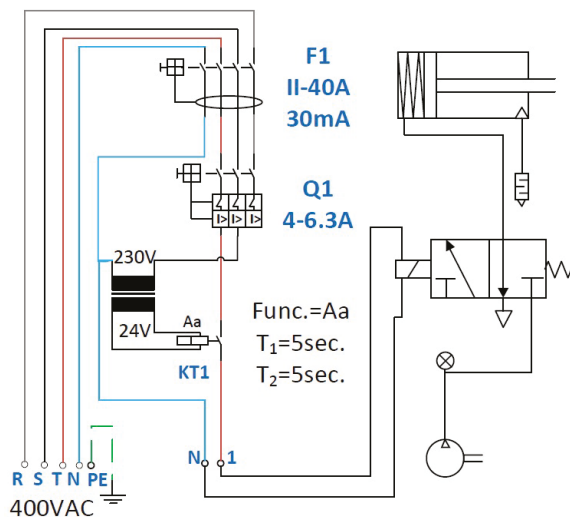


Figure 14. Schematics of the testing set for the pneumatic valve according to the protocol at the *Fluidra* group. Contains the solenoid valve, the piston and the compressor.

For the validation of the present study, three printed samples were tested during 5500 cycles to check the resistance of the support in accelerated operation. All three sample parts were able to be

mounted correctly, fitting in size and not having dimensional or tolerance problems. Furthermore, the three parts worked correctly showing no damage or defect in their geometry. The physical bench set is depicted in Figure 15.

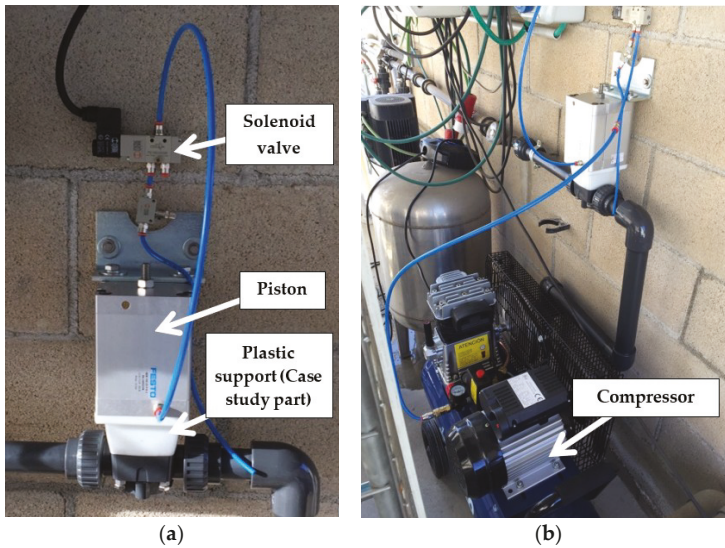


Figure 15. Physical testing of the printed part. It can be seen how the command circuit is mounted on a main fluid circuit. (a) Detailed view of the support mounted under the pneumatic piston. On top, the solenoid valve. (b) General overview of the fluid testing set, containing the compressor, valves, piston and the case study support.

4. Discussion

4.1. Cost Comparison between Additive Manufacturing Designs and Other Relevant Manufacturing Approaches

A cost study has been carried out another time with the new design to compare the results with the original design and the cost of manufacturing it by plastic injection (see Table 8).

Table 8. AM costs assessment for the redesigned product.

Additive Manufacturing Cost Per Part (Original and Redesigned Parts)		
Operation data		
Number of parts manufactured per platform	2	2
Platform build time (h)	143	84
Hours per year in operation (h)	7884	7884
Production volume total (per year)	110	188
Cost of Equipment		
Machine and ancillary equipment (€)	2100	2100
Equipment depreciation cost per year (€)	262.5	262.5
Machine maintenance cost per year (€)	100	100
Total machine cost per year (€)	362.5	362.5
(C_E) Machine cost per part (€)	3.29	1.93

Table 8. Cont.

Cost of Labor		
Machine operator cost per hour (€)	17	17
Set-up time to control machine (min)	5	5
Post-processing time per part (min)	3	3
(C_L) Labor cost per part (€)	1.13	1.13
Cost of Material		
Material per part (kg)	0.862	0.237
Build material cost per kg (€)	41.35	41.35
(C_{MAT}) Material cost per part (€)	35.64	9.8
(C_{AM}) Total cost per part (€)	40.06	12.86

If both designs are compared in terms of manufacturing times, a significant reduction can be observed and consequently production increases by a 41.4% per year. In addition, the reduction of the material used decreases by 72.5% compared to the original design. These factors directly impact part cost, decreasing up to 67.9%. Again, this cost is independent of the number of units manufactured. As seen before, injection molding reaches figures much lower of cost per part, providing that the number units to be manufactured is very high.

Figure 16 summarizes the cost levels of the three production strategies. Given the order level of 2000 units, the AM redesigned geometry is the production strategy that delivers the minimum manufacturing cost (12.86 € per part). The cutting production volumes between the different production strategies yield the different decision points. In the original AM design, AM production was the best preferred option for orders of 1045 parts or below, at a cost of 40.06 € per part. Otherwise, Injection molding would be the best desired strategy. In the part redesigned for AM, AM production is the best preferred option for orders of 3605 parts or below. For larger order figures, injection molding remains as the best production strategy.

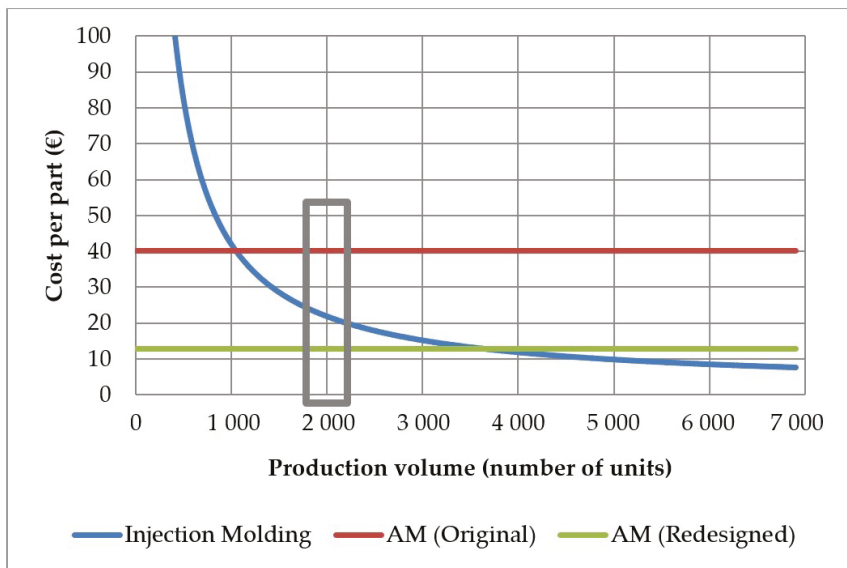


Figure 16. Graphical comparison of the levels of manufacturing costs of the injection molding and AM strategies.

Figure 16 is thus the synthesis of the levels of cost for the current state of the art in AM and molding technologies. Providing that AM cheaper materials and faster AM machines can be developed, the horizontal cost lines for AM are expected to keep decreasing over time.

At the present time, the inventory taxonomy described in Section 2 shows that for inventory parts, normal ordering levels are very low. It has been found that it is very unlikely to require more than 2400 repetitions of a part in a year. Therefore, the zone of interest of the graph is below 2400 product units. From this selection, Figure 16 shows that substitution of manufacturing technologies—from conventional to AM—has economic sense only if DfAM is undertaken.

4.2. Potential Impact in the Inventory Cost

Following to the product filtering conducted in Section 2.1, the figures of the overall inventory parts considered in the present study yield a $TIMC_{\alpha}^{Conv. proc.}$ calculated as formalised in Equation (1) of 1,350,670 €.

Then, in the case study, it has been possible to achieve a reduction in manufacturing costs per part of a 67.9% (δ) thanks to a reduction in the material utilised of an 72.5% in mass (γ) and a reduction on the processing time of manufacturing of a 41.4%. These percentages of reduction are aligned with the company previous experience and, according to the industrialists, can be considered a realistic average reference (not too optimistic or pessimistic).

Furthermore, given the company’s data, it is possible to calculate the factors ‘K’ needed in Equation (6) to calculate de change in costs (ΔC_s) of the products analysed. The values of the cited constants can be found in Table 9.

Table 9. (Ki) constants associated to the different cost factors, calculated for the 2017 inventory figures at Unistral Recambios.

(Ki) Constants	Values	Units
K_{MAN}^t	0.4504	€/h
K_{MAN}^m	1	€/kg
K_{TRA}^m	0.0333	€/kg
K_H^m	0.0556	€/kg
K_{MGT}^m	0.0222	€/kg

With these figures and considering that the original total mass of the target group for the switch to AM processes; i.e., fraction ‘ α ’ of the ‘Plastics’ category ($m_{total \alpha}^{Conv. proc.}$) is of 220,514 kg, the potential impact to the inventory associated costs can be found by utilizing Equation (12) as follows:

$$\sum_{i=1}^{i=n} \Delta C_{s_i} = TIMC_{\alpha}^{Conv. proc.} \cdot (-0.679) + (0.0333 + 0.0556 + 0.0222) \cdot m_{total \alpha}^{Conv. proc.} \cdot (-0.725) = -934,868.56, \tag{12}$$

The overall reduction in costs is huge for the fraction ‘ α ’ of the product category of ‘Plastics’. Indeed, it represents a reduction of a 69.22% of its Cs. Knowing that the entire TIMC of all the product categories ascended to 6,861,642 €, the possible cost reduction associated to the stocks change in manufacturing of fraction ‘ α ’ of 934,868.59 €, represents a 13.62% decrease in the inventory costs. This data yields a brief estimator of what can be feasible to achieve when switching from conventional manufacturing to AM technologies in the sector of the spare parts for fluid conduction systems.

4.3. Considerations on Further Achievable Impact in the Inventory Cost

As some considerations on the study and its hypotheses, it is important to mention that the present work completes a case study calculating a feasible cost reduction of a part—considered representative of the group, to estimate the impact that this exercise could have when extended to a relevant share of its product range (fraction ‘ α ’). This estimation is performed on the context of

switching from conventional manufacturing technologies— injection molding in the part analyzed—to AM technologies. Therefore, the study might be extended by selecting other parts in the inventory manufactured with different conventional technologies and so applying the methodology to yield additional cost reductions.

Also, the application of AM technologies could help achieving shorter delivery times; which could be incorporated in the study to quantify more precisely the cost reduction effects. So far, the implications that this would effectively have in the supply chain is out of the scope of the present study. Furthermore, as the batch size can be reduced to any figure, once switching to AM processes, the company might choose to modify the stocks level of the subset of products, this bringing further implications on possible savings. Moreover, some further plastic parts could be identified and redesigned from the category 'Kits', that could yield additional cost reductions on the overall stock cost.

These considerations on side-effects have not been analyzed in the present study to maintain a conservative savings quantity estimation. Future research may target the study of different inventory policies for the parts of the company, starting from the costing models formulated in the present article.

5. Conclusions

The present study articulates and utilizes a methodology and a cost frame for assessing the potential impact of a switch in the production technologies from conventional strategies to AM strategies. The methodology consists on a taxonomy product analysis, the engineering case study analysis, the discussion of the results and the extrapolation of the findings to the potential impact in the company overall.

The taxonomy analysis is undertaken in detail to (i) select a relevant product for the case study analysis, as well as to (ii) quantify the hierarchical and economic parts catalog of the company. The engineering case study analysis covers the analysis of the product manufacturing both in the conventional process and in the AM process. The latter is evaluated in the manufacturing of the original design and of a specific product redesign implementing DfAM techniques. Being a single-case design with a single unit of analysis, the engineering case study has been screened to make sure of its validity and reliability in the context of a real engineering case from a company.

The cost frame articulated formalizes a method for calculating the impact of a product modification based on the TIMC and of several factors affecting the inventory costs, which are divided into manufacturing costs, transportation costs, holding costs, and management costs. The factors affecting the costs are dependent on basic cost generators; namely: Processing time, material weight, and material dimensions.

The engineering case study part selected is a support for an automatic valve that it is required in a volume of 2000 parts. Following the taxonomy analysis performed, it is considered a representative part of the inventory in terms of weight and demand. The original design, weighting 0.862 kg has been assessed in its costs of manufacturing. Then, topological optimization has been undertaken reaching a weight of 0.237 kg without modifying the external shape. The DfAM has been validated experimentally both in virtual and physical conditions. This enormous reduction in mass has led to cost reductions in terms of material and processing times. The estimation within the category analyzed yields that a cost reduction of 69.22% of the manufacturing costs of 'Plastics' parts could be achieved. When considering this impact in the company overall, it is found that a reduction of 13.69% of inventory costs could be feasible to obtain.

The methodology and the cost frame in the article are applied to a company dedicated to the provision of spare parts for fluid conduction systems. However, both methodology and cost frame could be applied to any other industrial company. The specific figure of the reduction of a 13.62% in the inventory costs can be extrapolated to other companies operating in similar contexts. In addition, analogous analysis could be done assessing different product fractions to incorporate AM technologies

to other product categories. For example, it could be used in the category of ‘Kits’ for AM plastic technologies or in other categories for example with metal technologies.

Concerning the cost frame, the factors affecting the inventory costs have been specifically split into the presented division to ease the treatment of the effect of costs of the use of materials, technology, regional locations and human factor. Therefore, the same kind of study that has served to evaluate a topological optimization that has led to savings in different cost factors (volume and weight), could be undertaken with the same cost frame model for a change on the regional change in location affecting the product value chain from manufacturing to inventory.

Author Contributions: Conceptualization, J.M.-C. and J.R.G.A.; Methodology, J.M.-C., J.R.G.A. and S.M.P.; Software, S.M.P.; Validation, J.R.G.A. and M.A.d.I.S.L.; Formal Analysis, J.M.-C., S.M.P. and M.A.d.I.S.L.; Investigation, J.M.-C., S.M.P. and M.A.d.I.S.L.; Resources, S.M.P.; Data Curation, J.M.-C. and S.M.P.; Writing-Original Draft Preparation, J.M.-C., S.M.P. and M.A.d.I.S.L.; Writing-Review & Editing, J.M.-C.; Visualization, J.M.-C. and S.M.P.; Supervision, J.M.-C. and J.R.G.A.; Project Administration, J.M.-C. and S.M.P.; Funding Acquisition, J.M.-C. and M.A.d.I.S.L.

Funding: This research was cofounded by the “Agència de Gestió d’Ajuts Universitaris i de Recerca” (AGAUR) of the “Generalitat de Catalunya”, under the schema “Programa de Doctorats Industrials”, with grant number 2015DI 29.

Acknowledgments: For the present study, the authors want to acknowledge the manufacturer *Nexeo Solutions Spain SL*, suppliers of the filament used in the physical tests (*Novamid® ID1070*), for the material and its characterization information. Also, the authors want to thank the partner company *Krotwaar CAE* for the execution of the finite element calculations.

Conflicts of Interest: The authors declare no conflict of interest.

References

1. Shusteff, M.; Browar, A.E.M.; Kelly, B.E.; Henriksson, J.; Weisgraber, T.H.; Panas, R.M.; Fang, N.X.; Spadaccini, C.M. One-step volumetric additive manufacturing of complex polymer structures. *Sci. Adv.* **2017**, *3*. [[CrossRef](#)] [[PubMed](#)]
2. Rezaie, R.; Badrossamay, M.; Ghaie, A.; Moosavi, H. Topology Optimization for Fused Deposition Modeling Process. *Procedia CIRP* **2013**, *6*, 521–526. [[CrossRef](#)]
3. De AmorimAlmeida, H.; da Silva Bártolo, P.J. Virtual topological optimisation of scaffolds for rapid prototyping. *Med. Eng. Phys.* **2010**, *32*, 775–782. [[CrossRef](#)]
4. Carneiro, O.S.; Silva, A.F.; Gomes, R. Fused deposition modeling with polypropylene. *Mater. Des.* **2015**, *83*, 768–776. [[CrossRef](#)]
5. Bagsik, A.; Schöppner, V. Mechanical properties of fused deposition modeling parts manufactured with Ultem*9085. In Proceedings of the 69th Annual Technical Conference of the Society of Plastics Engineers, Boston, MA, USA, 1–5 May 2011; Volume 2, pp. 1294–1298.
6. Domingo-Espin, M.; Puigoriol-Forcada, J.M.; Garcia-Granada, A.A.; Llumà, J.; Borros, S.; Reyes, G. Mechanical property characterization and simulation of fused deposition modeling Polycarbonate parts. *Mater. Des.* **2015**, *83*, 670–677. [[CrossRef](#)]
7. Domingo-Espin, M.; Borros, S.; Agullo, N.; Garcia-Granada, A.-A.; Reyes, G. Influence of Building Parameters on the Dynamic Mechanical Properties of Polycarbonate Fused Deposition Modeling Parts. *3D Print. Addit. Manuf.* **2014**, *1*, 70–77. [[CrossRef](#)]
8. Ligon, S.C.; Liska, R.; Stampfl, J.; Gurr, M.; Mülhaupt, R. Polymers for 3D Printing and Customized Additive Manufacturing. *Chem. Rev.* **2017**, *117*, 10212–10290. [[CrossRef](#)] [[PubMed](#)]
9. Thompson, M.K.; Moroni, G.; Vaneker, T.; Fadeld, G.; Campbell, R.I.; Gibson, I.; Bernard, A.; Schulz, J.; Graf, P.; Ahuja, B.; et al. Design for Additive Manufacturing: Trends, opportunities, considerations, and constraints. *CIRP Ann. Manuf. Technol.* **2016**, *65*, 737–760. [[CrossRef](#)]
10. Wohlers, T. *Wohlers Report 2018*; Wohlers Associates, Inc.: Fort Collins, CO, USA, 2018; p. 344. ISBN 978-0-9913332-4-0.
11. Yadroitsev, I.; Krakhmalev, P.; Yadroitsava, I. Hierarchical design principles of selective laser melting for high quality metallic objects. *J. Addit. Manuf.* **2015**, *1*, 45–56. [[CrossRef](#)]

12. Minguella-Canela, J.; Muguruza, A.; Lumbierres, D.R.; Heredia, F.-J.; Gimeno, R.; Guo, P.; Hamilton, M.; Shastry, K.; Webb, S. Comparison of production strategies and degree of postponement when incorporating additive manufacturing to product supply chains. *Procedia Manuf.* **2017**, *13*, 754–761. [[CrossRef](#)]
13. Thomas, D.S.; Gilbert, S.W. *Costs and Cost Effectiveness of Additive Manufacturing: A Literature Review and Discussion*; NIST Special Publication 1176; NIST: Gaithersburg, MD, USA, 2014.
14. Hopkinson, N.; Dicknes, P. Analysis of rapid manufacturing—Using layer manufacturing processes for production. *Proc. Inst. Mech. Eng. Part C J. Mech. Eng. Sci.* **2003**, *217*, 31–39. [[CrossRef](#)]
15. Khajavi, S.H.; Partanen, J.; Holmström, J. Additive Manufacturing in the Spare Parts Supply Chain. *Comput. Ind.* **2014**, *65*, 50–63. [[CrossRef](#)]
16. Alfares, H.K. Production-inventory system with finite production rate, stock-dependent demand, and variable holding cost. *RAIRO Rech. Opér.* **2014**, *48*, 135–150. [[CrossRef](#)]
17. Berling, P. The capital cost of holding inventory with stochastically mean-reverting purchase price. *Eur. J. Oper. Res.* **2008**, *186*, 620–636. [[CrossRef](#)]
18. Al Masud, M.A.; Paul, S.K.; Azeem, A. Optimisation of a production inventory model with reliability considerations. *Int. J. Logist. Syst. Manag.* **2014**, *17*, 22–45. [[CrossRef](#)]
19. Clouthury, K.D.; Saha, S.; Das, M. An inventory model with Lot Size Dependent carrying/holding cost. *Assam Univ. J. Sci. Technol. Phys. Sci. Technol.* **2011**, *7*, 133–136. [[CrossRef](#)]
20. Asadabadi, M.R. A revision on cost elements of the EOQ model. *Stud. Bus. Econ.* **2016**, *11*, 5–14. [[CrossRef](#)]
21. Samak-Kulkarni, S.M.; Rajhans, N.R. Determination of Optimum Inventory Model for Minimizing Total Inventory Cost. *Procedia Eng.* **2013**, *51*, 803–809. [[CrossRef](#)]
22. Gambini, A.; Scarpello, G.M.; Ritelli, D. Mathematical properties of EOQ models with special cost structure. *Appl. Math. Model.* **2013**, *37*, 659–666. [[CrossRef](#)]
23. Ziuikov, S. A literature review on models of inventory management under uncertainty. *Bus. Syst. Econ.* **2015**, *5*, 26–35. [[CrossRef](#)]
24. Lesmono, D.; Limansyah, T. A multi item probabilistic inventory model. *IOP Conf. Ser. J. Phys. Conf. Ser.* **2017**, *893*, 012024. [[CrossRef](#)]
25. Devy, N.L.; Ai, T.J.; Astanti, R.D. A Joint Replenishment Inventory Model with Lost Sales. *IOP Conf. Ser. Mater. Sci. Eng.* **2018**, *337*, 012018. [[CrossRef](#)]
26. Bosnjakovic, M. Multicriteria inventory model for spare parts. *Tech. Gaz.* **2010**, *17*, 499–504.
27. Reddy, K.S. The state of case study approach in mergers and acquisitions literature: A bibliometric analysis. *Future Bus. J.* **2015**, *1*, 13–34. [[CrossRef](#)]
28. Yin, R.K. *Case Study Research and Applications: Design and Methods*, 6th ed.; Sage Publications: Thousand Oaks, CA, USA, 2018; pp. 6–39. ISBN 9781506336169.
29. Renishaw PLC Case Studies: Hydraulic Block Manifold Redesign for Additive Manufacturing. Available online: <http://www.renishaw.com/en/hydraulic-block-manifold-redesign-for-additive-manufacturing-38949> (accessed on 1 August 2018).
30. Shamvedi, D.; McCarthy, O.J.; O'Donoghue, E.; Danilenkoff, C.; O'Leary, P.; Raghavendra, R. 3D Metal printed heat sinks with longitudinally varying lattice structure sizes using direct metal laser sintering. *J. Virtual Phys. Prot.* **2018**. [[CrossRef](#)]



© 2018 by the authors. Licensee MDPI, Basel, Switzerland. This article is an open access article distributed under the terms and conditions of the Creative Commons Attribution (CC BY) license (<http://creativecommons.org/licenses/by/4.0/>).

Article

Analysis of Favorable Process Conditions for the Manufacturing of Thin-Wall Pieces of Mild Steel Obtained by Wire and Arc Additive Manufacturing (WAAM)

José Luis Prado-Cerqueira ¹, Ana María Camacho ^{1,*}, José Luis Diéguez ²,
Álvaro Rodríguez-Prieto ^{1,3}, Ana María Aragón ^{1,3}, Cinta Lorenzo-Martín ³
and Ángel Yanguas-Gil ³

¹ Department of Manufacturing Engineering, Universidad Nacional de Educación a Distancia (UNED), 28040 Madrid, Spain; jprado28@alumno.uned.es (J.L.P.-C.); alvaro.rodriguez@invi.uned.es (Á.R.-P.); amaragon@invi.uned.es (A.M.A.)

² Department of Design in Engineering, University of Vigo, C/Torrecedeira 86, 36208 Vigo (Pontevedra), Spain; jdieguez@uvigo.es

³ Applied Materials Division, Argonne National Laboratory, 9700 Cass Ave, Lemont, IL 60439, USA; lorenzo-martin@anl.gov (C.L.-M.); ayg@anl.gov (Á.Y.-G.)

* Correspondence: amcamacho@ind.uned.es; Tel.: +34-913-988-660

Received: 7 July 2018; Accepted: 13 August 2018; Published: 16 August 2018

Abstract: One of the challenges in additive manufacturing (AM) of metallic materials is to obtain workpieces free of defects with excellent physical, mechanical, and metallurgical properties. In wire and arc additive manufacturing (WAAM) the influences of process conditions on thermal history, microstructure and resultant mechanical and surface properties of parts must be analyzed. In this work, 3D metallic parts of mild steel wire (American Welding Society-AWS ER70S-6) are built with a WAAM process by depositing layers of material on a substrate of a S235 JR steel sheet of 3 mm thickness under different process conditions, using as welding process the gas metal arc welding (GMAW) with cold metal transfer (CMT) technology, combined with a positioning system such as a computer numerical controlled (CNC) milling machine. Considering the hardness profiles, the estimated ultimate tensile strengths (UTS) derived from the hardness measurements and the microstructure findings, it can be concluded that the most favorable process conditions are the ones provided by CMT, with homogeneous hardness profiles, good mechanical strengths in accordance to conditions defined by standard, and without formation of a decohesionated external layer; CMT Continuous is the optimal option as the mechanical properties are better than single CMT.

Keywords: additive manufacturing; WAAM; GMAW; cold metal transfer; hardness; mechanical properties; thermal input; microstructure

1. Introduction

One of the challenges in Additive Manufacturing (AM) of metallic materials is to obtain workpieces free of defects and with excellent physical, mechanical and metallurgical properties [1] to satisfy the strict requirements of engineering applications. Obtaining such mechanical requirements is a hard task, especially in parts fabricated as the result of layer by layer addition of the material. AM of metallic materials involves different techniques (powder bed fusion, binder jetting, sheet lamination, and directed energy deposition) and metals generally must be weldable and castable to be successfully processed in AM [2]. Till now, there have been only a limited number of commercial alloys used in AM [3], so there is a need to increase the number of alloys to be processed by AM techniques in order to

widen the application fields. Most of the current commercial metallic materials for AM are steels [4–7], aluminum [8], and titanium alloys [9,10].

Wire and arc additive manufacturing (WAAM) is a wire-feed AM process and one of the most promising techniques for producing larger components with moderate complexity and relative low costs compared to other AM techniques for metals [11]. WAAM processes have a promising future. Designs are already being made using this technique in different fields where WAAM is performing very well; some of them are lightweight aerospace components (landing gear parts, wing ribs or stiffeners) [12], wind tunnel models [13], bridges [14] and/or complex constructive features (such as the dragon bench in the manufacture of furniture), that could not be made with conventional processes such as casting, or computer numerical controlled (CNC) milling, among others [15].

WAAM processes generally involve high residual stresses due to high deposition rates and heat inputs [16]. The influences of process conditions (for example, energy input, wire-feed rate [17], welding speed and/or deposition pattern [18]) on thermal history, microstructure and resultant mechanical and surface properties of parts need to be analyzed [16] as there is not enough knowledge in the scientific community yet.

As explained in the work by Ge et al. [4], during WAAM processes, the added layers of material suffer a complicated thermal history that includes, among others, melting, fast cooling, solidification, and/or partial remelting, that greatly influence the final properties of the parts produced by these techniques.

A recent study about the microstructure is the one from Wang et al. [19], where mechanical properties of thin-walled parts of the die steel H13 were also analyzed, showing that the tensile properties were anisotropic but could become isotropic after 830 °C of heat treatment (annealing) for 4 h. Yan et al. [20] studied the effect of temperature gradient, solidification velocity, and alloy composition on grain morphology in AM of metallic materials. In the overview article of Herzog et al. [21], special attention was paid in analyzing AM specific grain structures, resulting from the complex thermal cycle and high cooling rates. Kok et al. [22] highlighted that anisotropy and heterogeneity in the mechanical properties of metallic AM parts are mainly due to the anisotropy and heterogeneity of the microstructure and material properties. Another work investigating the relationship between the microstructure and mechanical properties of the titanium alloy Ti-6Al-4V fabricated by the WAAM process is reported by Wang et al. [23].

On the other hand, in the work from Szost et al. [24], porosity, microstructure, and micro hardness of Al-6.3%Cu samples fabricated by WAAM were investigated considering cold metal transfer (CMT) variants, pulsed CMT, and advanced CMT. A very interesting paper from Cong et al. [25] explores in depth the influence of the arc mode for different CMT variants (CMT, CMT pulse, CMT advanced, and CMT pulse advanced) on the porosity of an aluminum alloy fabricated by WAAM. In this work, CMT pulse advanced showed excellent performance in controlling porosity, being the most suitable variant for depositing aluminum alloys. Other defects such as lack of fusion, have been also analyzed by the same authors in their work of 2018 [26] for maraging steel.

Mechanical properties obtained by WAAM, including hardness, are also a promising field of study as shown in works from Horgar et al. [27], where AA5183 aluminum alloy wire was deposited on an AA6082-T6 plate as substrate. Wu et al. [28] investigated the influence of the molten pool size on the microstructure and mechanical properties of pieces of Ti-6Al-4V alloy, whereas Lewandowski and Seifi [29] presented a review of mechanical properties for the most common alloys used in AM of metals (Ti-6Al-4V, TiAl, stainless steel, Inconel 625/718, and Al-Si-10Mg).

Micro-geometrical properties such as roughness are also being investigated, as in the case of manufacturing of multi-layer single-pass thin-walled parts [30] and in the work of Li et al. [31].

Arrizubieta et al. [32] presented a novel manufacturing technique combining laser metal deposition, laser beam machining, and laser polishing processes for the manufacturing of a complex Inconel 718 part, resulting in a cleaner technique as conventional machining operations were eliminated.

Another interesting work showing a suitable full-dimension sustainability life cycle assessment framework of parts produced by AM is the one presented by Ma et al. [33].

As we can see, due to the great variety of dimensions and parameters involved and their interdependencies [34], AM processes require multidisciplinary research, and many investigation lines are already open to reach a deeper knowledge about these technologies. In the present work, three-dimensional (3D) metallic parts of mild steel wire (AWS ER70S-6) are built with a WAAM process by depositing beads of weld metal layer by layer on a substrate of a S235 JR steel sheet of 3 mm thickness, using as the welding process gas metal arc welding (GMAW) [35] with Cold Metal Transfer technology [36], combined with a positioning system such as a CNC milling machine [37]. The paper will show some interesting results based on hardness measurements, along with complementary values of tensile strength at the working area and microstructure information.

2. Materials and Methods

2.1. Materials for WAAM process

Experiments have been carried out on a substrate of a S235JR steel sheet of 3 mm thickness, 150 mm long and 100 mm wide. This substrate has two main functions: as a support for the deposited metal and as a heat dissipation system for the heat generated during the process by conduction transfer through the aluminum work table.

The wire material (AWS ER70S-6) is a 0.8 mm diameter mild steel wire with a copper coating supplied on a 15 kg coil. This steel is commonly used in a lot of applications related to construction work, pipes, shafts, car bodies, tanks, steel castings or forgings, and general shop fabrications.

The properties of the base material (substrate) and the deposited material are shown in Table 1. The density of both materials is approximately the same, while the mechanical properties are better for the case of the deposited material.

Table 1. Properties of the substrate and the welding wire.

Mechanical Properties	S235 JR	AWS ER70S-6
Density (kg/m ³)	7800	7833
Yield point (MPa)	235	420
UTS (MPa)	370–510	500–640

Chemical composition of welding wire is shown in Table 2.

Table 2. Chemical composition of welding wire.

Element	C	Mn	S	Ni	V	Cr	Cu	Si	P	Mo
wt%	0.06–0.15	1.40–1.85	0.035 max	0.15 max	0.03 max	0.15	0.50	0.80–1.15	0.025	0.15 max

The results of the process depend on the protecting gas. It has been used a mixture composed of CO₂ (15%) and Argon (85%) that led to the stability of the process, improvement in the surface finishing quality, and a reduction of the splatters. It has been observed that the welding drops are smaller with the reduction of the amount of CO₂.

2.2. WAAM Equipment

The WAAM equipment is composed of two different systems (Figure 1), as described in detail in a previous work [38]:

- Welding system: cold metal transfer technology, patented by Fronius®, was used as welding process with a Fronius TPS 4000 CMT R machine (Fronius International GmbH, Wels, Austria).

In this technology the intensity and voltage control is made during the deposition. By virtue of this principle, the temperature of welding temperature is reduced and the wire movement is optimized. As a result of this, the quality of weld beads is better than using conventional GMAW welding [39].

- Positioning system. The control of the movement in an easy way was made by a BF 30 Vario Optimum CNC milling machine (Optimum Maschinen Germany GmbH, Hallstadt, Germany). It has been adapted by fixing the welding torch to the milling head in the Z axis, while the X-Y table of the CNC system enables the deposition of a layer in the fixed Z level. To deposit the next layer, the Z axis elevates the torch and makes the deposition in the next Z level.

As shown in Figure 1, an auxiliary working table has been developed in order to isolate electrically both systems as well as to cool the working area.

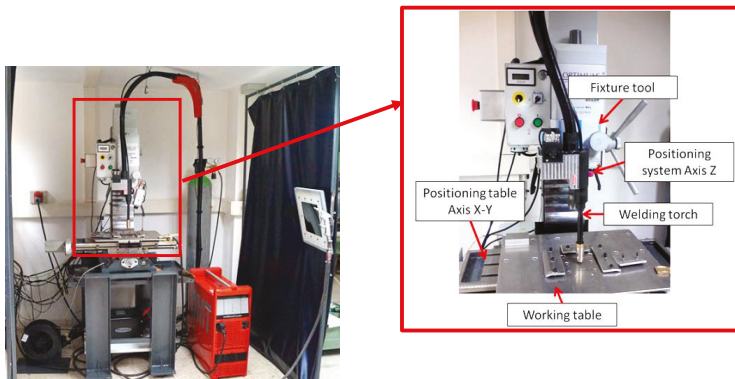


Figure 1. Setup of the integrated WAAM system in the positioning table.

2.3. Fabrication of Samples by WAAM

As explained in a previous work [38], in WAAM processes, the final product is manufactured by melting a wire using an electric arc (Figure 2). The deposition of the material rate is much higher with respect to other metallic additive manufacturing methods. In addition, higher working speeds allow higher workload and a significantly lower price than with other methods [40].



Figure 2. Examples of geometries obtained by WAAM: (a) Piece obtained by continuous trajectory and complex geometry in x-y direction; (b) Piece obtained by continuous trajectory and growing geometry in z direction.

In this work, a set of WAAM samples have been manufactured under different process conditions, considering the parameters with more influence in the mechanical properties of WAAM parts:

- WAAM process:
 - Metal inert gas (MIG)
 - CMT
 - CMT Advanced polarity −5 (CMT Adv. pol. −5)
 - CMT Advanced polarity 0 (CMT Adv. pol. 0)
 - CMT Advanced polarity (CMT Adv. pol. +5)
 - CMT continuous trajectory (CMT Cont.)
- Welding speed (constant = 400 mm/min)
- Deposition speed (constant = 2.5 m/min)
- Arc voltage (constant = 9.2 V)
- Current intensity (50 A, 66 A, 70 A, 78 A)
- Layer step (1.0 mm, 1.5 mm)

Different WAAM processes have been also applied to analyze the influence of using a conventional MIG process, a MIG process with CMT, and a MIG process with CMT advanced and different current polarities.

Cold metal transfer welding (CMT) is based on a MIG welding process but modified by a short-circuiting transfer process, firstly developed by Fronius Austria in 2004 [36]. CMT provides a controlled method of material deposition and low thermal input by incorporating an innovative wire feed system coupled with high-speed digital control [41]. With CMT, the arc only introduces any heat for a very brief period during the arc-burning phase and the arc remains stable, then CMT can be used everywhere and in every position [42].

The CMT advanced is an evolution of the previous process and it obtains a lower thermal input during welding with respect to the original CMT process thanks to the possibility of polarity change. This produces the reversal of the direction of the plasma jet several times per second leading to 35–40% lower thermal inputs [43]. The reversal of polarity takes place in the short-circuit phase so that this welding process guarantees the high stability expected from cold welding [44]. Thermal input is usually calculated based on the Equation (1):

$$TI = \frac{V \cdot I \cdot \mu}{\text{welding speed}} \quad (1)$$

where TI is the thermal input in J/mm, V is the arc voltage in volts (V), I is the process intensity in Amperes (A), μ is the thermal efficiency that is a constant coefficient based upon the welding process used; finally, the welding speed is provided in mm/s.

The samples and the definition of the parameters used are presented in Table 3, including the calculation of thermal input.

Table 3. Definition of parameters used for each sample and results.

Nº	Process	Intensity (A)	Thermal Input * 1 (J/mm)	Welding Speed (mm/min)	Deposition Speed (m/min)	Wall Thickness (mm)	Layer Step (mm)	Total Height (mm)	Layer Height (mm)
1	MIG	50	55.19	400	2.5	3.8	1.0	27.0	0.90
2	CMT	50	35.87	400	2.5	3.7	1.0	30.7	1.02
3	CMT Adv. pol. 0	70	50.22	400	2.5	4.2	1.0	20.2	1.44
4	CMT Adv. pol. 0	70	50.22	400	2.5	5.5	1.5	35.5	0.92
5	CMT Adv. pol. −5	66	47.36	400	2.5	4.5	1.5	41.2	1.07
6	CMT Adv. pol. +5	78	55.97	400	2.5	6.6	1.5	33.4	0.80
7	CMT Cont.	50	35.87	400	2.5	3.1	1.0	30.5	1.02

¹ Note 1*: thermal input has been calculated based on the power ($V \cdot I$) provided by the equipment, the welding speed and the thermal efficiency coefficients, typically μ (MIG) = 0.8, and μ (CMT) = 0.52 considering a 35% of lower thermal efficiency compared to MIG process [43].

Manufacturing of samples n° 1 to 6 is presented in Figure 3, where the substrate where they have been built is also shown.

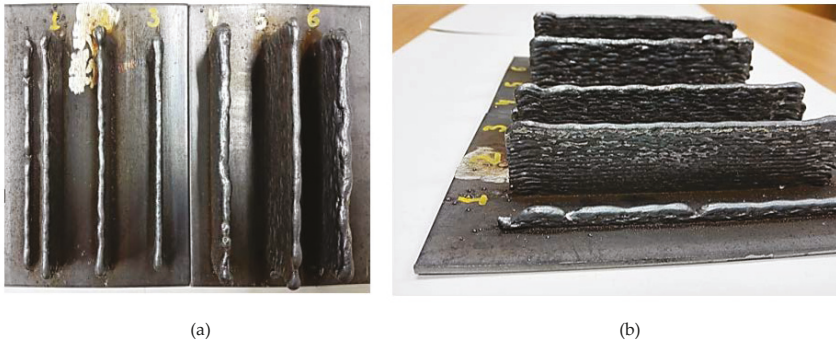


Figure 3. Manufacturing of samples n° 1 to 6: (a) Top view; (b) Lateral view.

Subsequently, the samples were removed from the substrate; an example of the final pieces obtained is shown in Figure 4a, with sample n° 4. Samples n° 2 and 7 share the same WAAM parameters; however, sample n° 7 differs from sample n° 2 in the way the wire is deposited. In order to provide a continuity during the deposition process, and to avoid edge effects, sample n° 7 has been obtained using a continuous tool path, as shown in Figure 4b (CMT continuous trajectory). Final sample after removing it from the substrate is also presented in this figure.

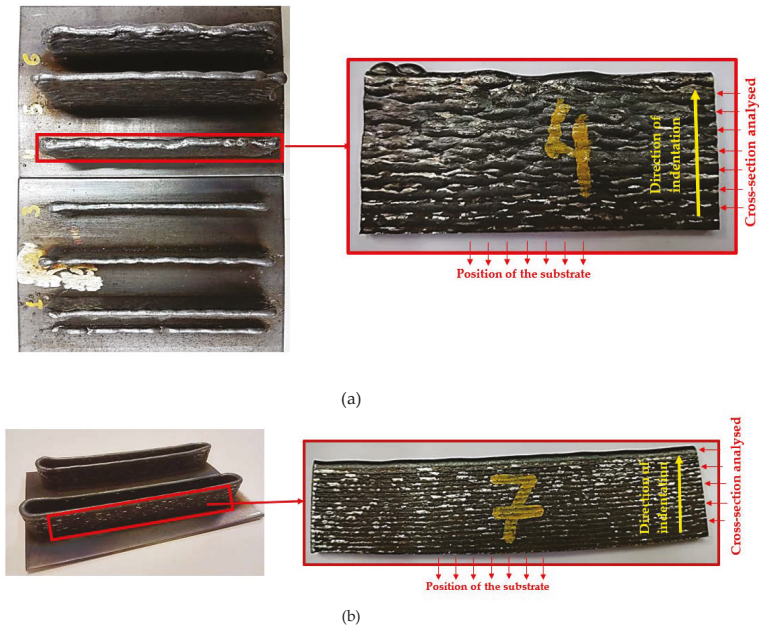


Figure 4. Location of the cross-section analyzed and the position of the substrate: (a) Samples n° 1 to 6, showing the location of the cross-section analyzed with sample n° 4; (b) Tool path during the deposition process in sample n° 7 and the final sample obtained.

2.4. Brinell Hardness Tests

Brinell Hardness Tests and Measurement of the Ball Prints

Brinell hardness tests have been developed [45] using a ball indenter of $\varphi 2.5$ mm and a test force of 612.9 N. The ball prints imprinted at the surface of the seven samples are presented in Figure 5. A set of 5 points have been imprinted at the cross-sections analyzed, as explained in Figure 4a,b. These surfaces have been previously polished to obtain a smooth condition and free from oxides and lubricants. The numbering of the points increases from the location of the substrate (see yellow arrow in Figure 4a,b). The aim is to obtain a hardness profile for each sample to compare the observed behavior depending on the manufacturing parameters used in each case.

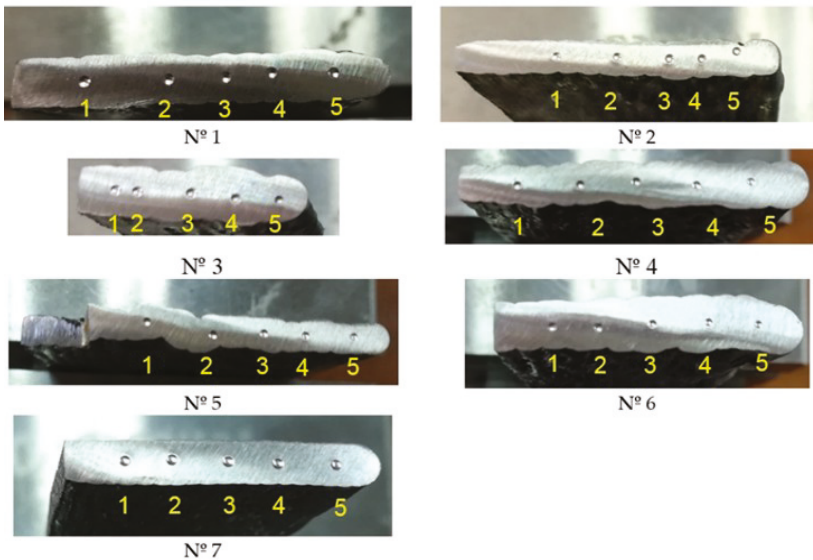


Figure 5. Brinell hardness tests applied to WAAM samples and identification of indentation points.

The measurement device to determine experimentally the print diameter is a profile projector TESA VISIO (TESA SA, Renens, Switzerland). Two indentation diameters measured at 90° have been obtained for each sample allowing to calculate a mean diameter of the indentation.

The Brinell hardness is proportional to the quotient obtained by dividing the test force by the surface area of the indentation left in the surface after removal of the test force.

The dispersion among measurements can be quantified using the reproducibility limit, R , which is calculated as shown in Equation (2) [46]:

$$R = \frac{d_{max} - d_{min}}{\langle d \rangle} \quad (2)$$

where d_{max} and d_{min} are the largest and smallest diameters and $\langle d \rangle$ is the mean of measured diameters.

2.5. Determination of Mechanical Strength

Hardness is usually defined as resistance to permanent indentation. This testing provides a measurement of the material strength through its resistance to scratching. Thus, the possibility to

predict tensile strength based on values of materials hardness is often used. Equation (3) provides the general relationship between hardness and tensile strength:

$$UTS = k \cdot H \quad (3)$$

where UTS is the ultimate tensile strength in MPa, H the hardness in a known scale and k is a coefficient. Several standards provide a correlation between hardness and tensile strength in steels using tables, charts, and coefficients of calculation, some of them are ASTM A370 [47], ISO 18265 [46], SAE J417 [48], being the ASTM standard the most consolidated and used.

2.6. Equipment and Measurement of Microstructure

Microstructural analysis has been performed using the following equipment from the center for nanoscale materials (CNM) of the Argonne National Laboratory: a high resolution and high vacuum, scanning electronic microscopy Hitachi S-4700-II (Hitachi, Krefeld, Germany)—equipped with electron dispersive spectroscopy (EDS) detector Bruker XFlash 6160 (Bruker, Billerica-MA, USA). The testing conditions were 10 keV and 10 mA.

3. Results

3.1. Evaluation of Hardness Profiles

As the WAAM process is layer-based, the most critical area is the one located at the overlapping of the two layers, or as close as possible to it. For this reason, we have chosen the positions of the indentations (ID), making sure that for each sample we have most of the points located at these critical areas. In Appendix A, the position of the points for every sample is shown. As we can see, most of the indentations are located following this criterion.

Table 4 provides the mean values of Brinell hardness along with the thermal input and the calculation of reproducibility limit (R) according to Equation (2), using the diameters of indentations.

Table 4. Process, Brinell hardness, and R values.

Sample n ^o	Process	Thermal Input (J/mm)	Brinell Hardness (Mean Value)	$\langle d \rangle$	d_{max}	d_{min}	R
1	MIG	55.19	172.89	0.729	0.731	0.7285	0.003
2	CMT	35.87	142.14	0.790	0.809	0.759	0.064
3	CMT Adv. pol. 0	50.22	159.03	0.761	0.790	0.725	0.086
4	CMT Adv. pol. 0	50.22	153.00	0.778	0.799	0.759	0.051
5	CMT Adv. pol. -5	47.36	154.49	0.773	0.789	0.759	0.038
6	CMT Adv. pol. +5	55.97	148.84	0.792	0.815	0.771	0.056
7	CMT Cont.	35.87	152.67	0.772	0.784	0.765	0.025

Conventional MIG (sample 1) process provides the biggest thermal input and hardness along with the minimum R value (0.003). The CMT process (samples 2 and 7) with the lowest thermal inputs, provides an adequate dispersion among values, exhibited by their R values (0.064 and 0.025, respectively). Hardness values in samples 3 to 6 (CMT advanced) do not seem to follow a pattern dependent on thermal input, but hardness and thermal inputs adopt intermediate values.

The hardness profiles are presented in Figure 6 along with the average values. A homogenous hardness profile is desirable as this means that the mechanical properties obtained by the WAAM process are appropriate and the in-service behavior of the parts is expected to be better than with the non-homogeneous ones.

As we can see in Figure 6h, according to the standard deviations of the hardness values, samples 3 and 6 present the least homogenous hardness profile, whereas samples 1 and 7 are the best ones.

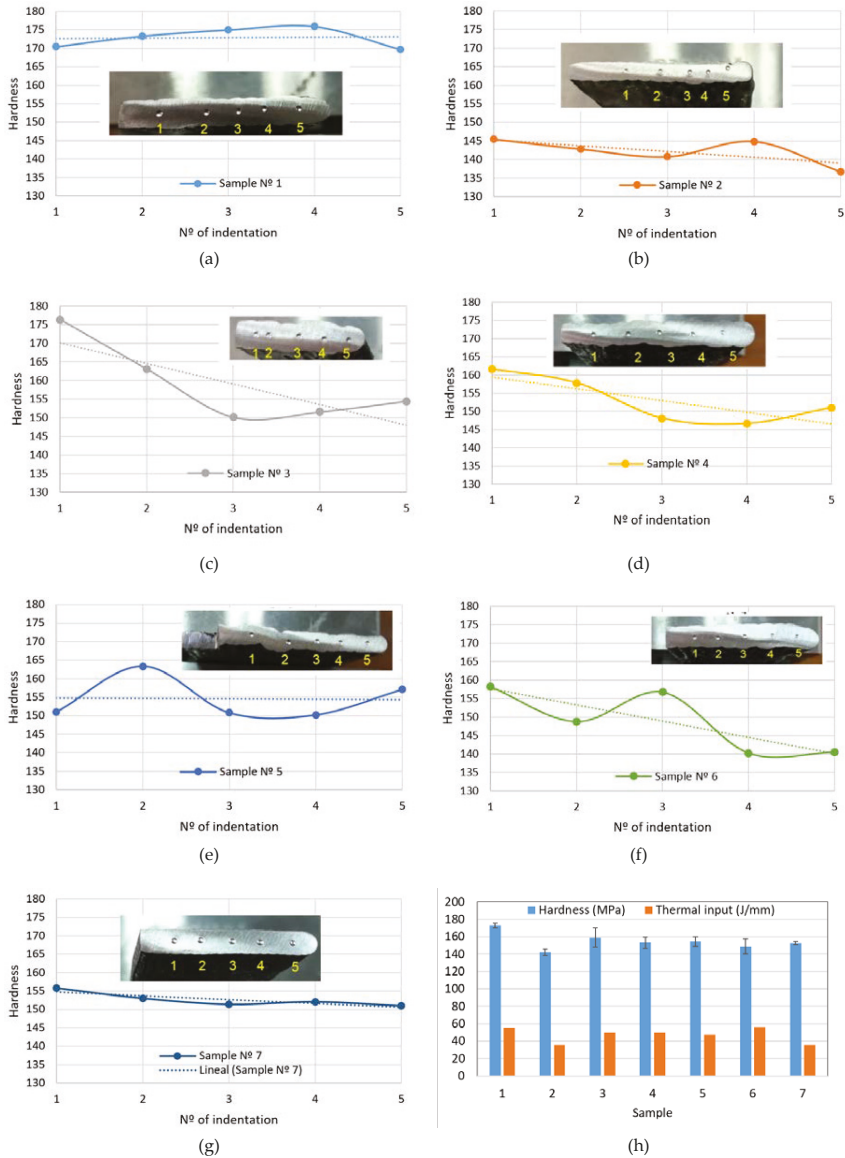


Figure 6. Brinell hardness profiles for the WAAM samples: (a) Sample n° 1, MIG (conventional); (b) Sample n° 2, CMT process; (c) Sample n° 3, CMT Adv. pol. 0; (d) Sample n° 4, CMT Adv. pol. 0; (e) Sample n° 5, CMT Adv. pol. -5; (f) Sample n° 6, CMT Adv. pol. +5; (g) Sample n° 7, CMT; (h) Mean hardness values with standard deviations and thermal inputs.

3.2. Evaluation of Mechanical Strength

Using the hardness measurements, estimated ultimate tensile strengths (UTS) have been calculated and provided in Table 5.

Table 5. Estimation of Ultimate Tensile Strength values based on ASTM A370 [47].

UTS (MPa) Correlation per Indentation (ID) According to Figure 6.							
ID	Process						
	MIG	CMT	CMT Adv. pol. 0	CMT Adv. pol. 0	CMT Adv. pol. -5	CMT Adv. pol. +5	CMT-Cont.
1	573.33	479.99	516.38	498.34	498.39	467.42	528.44
2	583.30	473.06	499.98	483.64	562.20	465.82	505.24
3	587.47	468.90	495.17	488.64	497.70	534.68	499.66
4	589.84	477.92	561.66	541.73	495.74	490.68	501.99
5	572.46	454.32	590.94	558.59	537.12	544.38	498.00
Mean	581.28	470.84	532.82	514.19	518.23	500.59	506.67

As it was previously mentioned, the welding wire is an ER70S-6 type, described by the american society of mechanical engineers ASME SFA 5.18 standard [49], which indicates some recommended base materials to be welded using this type of welding wire; these are SA-36 [50], equivalent to S235JR, SA-285 [51], SA-515 [52], and SA-516 [53]. Table 6 exhibits the specified range of UTS for these materials. These values are used to help analyze the ultimate tensile strength (UTS) calculated using the hardness measurement performed in the 7 samples.

Table 6. Ultimate Tensile Strength of typical base materials welded with ER70S-6 according to SFA 5.18 [49].

Base Material Specification	UTS (MPa)
SA-36 (equivalent to S235JR)	400–550
SA-285	310–515
SA-515	415–485
SA-516	380–485

3.3. Microstructure Findings

Microstructural analysis of each sample has been performed using a high-resolution scanning electronic microscopy at the center for nanoscale materials (CNM) of Argonne National Laboratory. Figure 7a provides an image of the surface along the deposition direction in Sample n° 1 (MIG conventional); a decohesionated layer in the upper edge is observed in this sample (a zoom of this area is presented in Figure 7b, showing the microstructure more in detail). Appendix B shows the surface of deposited material along the thickness for samples n° 2 to 7, where no decohesionated layer is found.

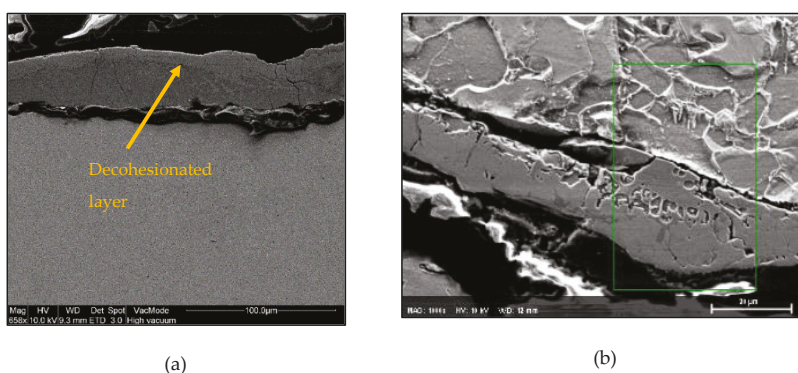


Figure 7. Scanning electronic microscopy (SEM) at the surface in Sample n° 1 (MIG conventional). (a) Decohesionated layer found; (b) Layer SEM image at 20 μm of scale.

Table 7 provides the compositional microanalysis of this layer observed in sample n° 1.

Table 7. Microanalysis of decohesionated external layer observed in Sample 1 (MIG conventional process).

Element	Mn	C	O	Si	Cu	Fe
wt%	1.58	7.59	1.79	0.83	0.44	87.77

The external layer of sample 1 (MIG process) seems to be formed by Fe_3C (6.67% C) and probably other complex carbides made up of some of the rest of the elements oxidized but present in the normal weight percentage according to the composition provided by the manufacturer (Mn 1.40–1.85%, Si 0.80–1.15%, Cu < 0.5%). In addition, in the process magnetite (Fe_3O_4) seems to be also present. Anyway, the external layer is a pernicious effect that could be avoided using the CMT process, as it is possible to see through the figure in Appendix B.

The presence of a decohesion layer implies poor surface properties; according to the analysis carried out, this layer comprises the formation of carbides (which are typically hard and brittle compounds) and oxides, which give the surface a poor surface finish and low resistance to external chemical and mechanical agents; therefore, these types of layers are not desirable and should be avoided.

Additionally, micrographs at the interface between layers have been obtained to zoom into this area at the microstructural level (Figure 8). No special findings are found at this level.

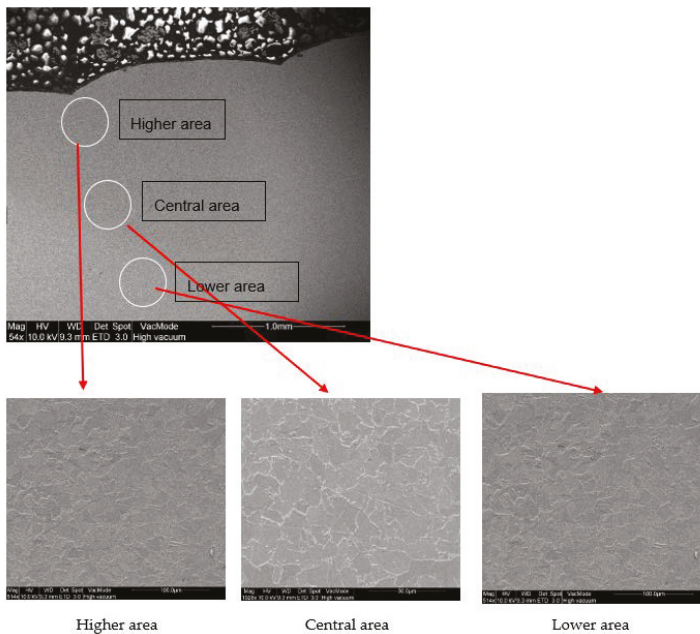


Figure 8. SEM Micrographs at interface between layers in Sample n° 1 (MIG conventional).

4. Discussion

As indicated, a homogenous hardness profile is desirable as this means that the mechanical properties obtained by the WAAM process lead to better in-service behavior of parts than with non-homogeneous ones.

The most homogeneous profiles are obtained in samples numbers 1, 2, and 7 (in sample 2 the measurement of point 5 has been obviated as the print is too close to the surface). Homogeneous profiles for MIG procedure (sample 1) were also obtained in the work by Wang et al. [19]. Samples 2 and 7 present lower values of hardness than sample 1 (Table 4); this can be explained as the CMT process applies lower thermal inputs compared to the conventional MIG process and therefore, the sample 1 experience greater sub-cooling from the melting state and then, a microstructure of finer grains is expected. Bigger grain sizes at the microstructure lead to lower hardness values as grains limits contribute to block the movement of material dislocations.

Slight differences between sample 2 (CMT) and 7 (CMT Cont.) are due to the effect of the continuous path applied in sample 7 that, for the same thermal input due to the same process parameters, implies an accumulation of heat at the zone due to lower heat transmission and consequently, induces a higher thermal input than the one computed and, as explained before, this leads to a higher hardness value in sample 7.

Samples fabricated by CMT Advanced processes have a pronounced decreasing trend of the hardness profile, showing the highest values closer to the substrate (see Figure 6c–f). This is due to the chilling effect of the substrate that generates a higher cooling rate and therefore, the sub-cooling effect from the melting state is higher in this zone [5]. The results are in good agreement with the ones presented by Liberini et al. in their work from 2017 [54]; where an increase of hardness is also found close to the free surface as a result of the thermal chilling due to contact with the air at room temperature. In this work [54], the authors also stated that the cooling curve is the factor that most influences the final microstructure and that no important differences between the samples are obtained from different process parameters. With CMT Advanced, the mean hardness values are very similar for samples 3 to 6, and the thermal inputs as well.

The most inhomogeneous profiles are obtained in samples 5 and 6, where some peaks are observed. In these two cases a polarity of 5 and +5, respectively, is applied during the process, and the intensity applied is also different in both cases (66 and 78 A, respectively). However, regardless the different conditions, the mean hardness values are close between them and to the ones obtained with polarity 0. In general, we can conclude that the CMT Advanced process does not show a better performance of the process regarding the homogeneity of the hardness profile of the parts and the mechanical properties.

Indentation points are located at the overlapping area (or as close as possible) of the two layers, the most critical area for an additive manufacturing process. No significant influence of the position of the indentation points on the hardness values is observed at this level of analysis, being these results in good agreement with those obtained by other authors using a similar methodology, such as Xu et al. [4]. Micrographs at the interface between layers did not show special findings at the microstructural level. Additional research will be conducted in future works in order to analyze locally the behavior between layers, combining higher resolution hardness tests and metallographic analysis in this area.

As WAAM is a layer-by-layer manufacturing process that uses a welding wire that melts on a previously welded substrate, it is important to ensure that the requirements of weldability, such as the mechanical properties of a material that are joined using the welding wire, are well suited. Using the recommendations provided by the Kobe Welding Handbook [55], the base material should present a minimum UTS between 400–480 MPa. Therefore, considering the requirements indicated in Table 6, in this evaluation, a range between 400 and 550 is considered suitable. Values higher than 550 MPa could lead to the appearance of hardness peaks between layers, which are not recommended as they do not guarantee the homogeneity of the mechanical behavior. This supposes that the estimated UTS at the surface of sample 1 (MIG conventional process), equal to 581.28 MPa, is greater than the upper limit that the new substrate should exhibit. The remaining mean values (samples 2 to 7) are between 400 and 550 MPa, nevertheless some specific values are above the upper limit (550 MPa) in samples 3 to 5. Thus, it can be concluded that CMT process (samples 2 and 7) and CMT Adv. pol. +5 (sample 6) provides the most adequate UTS values.

In addition, the microstructural analysis of each sample (1 to 7) has been performed using high-resolution scanning electronic microscopy. Homogeneity has been observed in the transition between layers in all samples. Nevertheless, a decohesionated layer in the upper edge is observed in sample 1 (MIG conventional). The external layer is a pernicious effect that can be avoided using the CMT process.

In agreement with other authors, there are no significant differences between the samples processed with different process parameters when using a particular WAAM process [16,54].

5. Conclusions and Future Work

After discussing the main results, Table 8 shows a summary of the best process conditions considered in this work.

Table 8. Summary of the best process conditions according to homogeneous hardness profiles and mean values, the estimated ultimate tensile strengths (UTS) derived from hardness measurements, and the absence of the decohesionated layer at the surface found at microstructural level.

Sample n ^o	Process	Most Homogeneous Hardness Profiles (Figure 6a–g)	Highest Values of Mean Hardness (Figure 6h)	Best Estimated UTS [55] (Table 5)	Absence of Decohesionated Layer at the Surface (Figure A2)
1	MIG	X	X		
2	CMT	X		X	X
3	CMT Adv pol. 0				X
4	CMT Adv pol. 0				X
5	CMT Adv pol. −5				X
6	CMT Adv pol. +5				X
7	CMT Cont.	X		X	X

Taking into account the hardness profiles and mean values, the estimated UTS derived from the hardness measurements and the microstructure findings, it can be concluded that the best process conditions are the ones provided by simple CMT, with homogeneous hardness profiles, good mechanical strengths in accordance to conditions defined by standard, and without formation of a decohesionated external layer; CMT Continuous is the optimal option as the mechanical properties are better than with single CMT (Figure 6h and Table 5).

In this study, we have been interested in defining global trends of the hardness at a macroscopic level for common values of manufacturing parameters to obtain results with a broad level of generality from an applicative point of view, of interest for users of these technologies. As there is still an important lack of information about the influence of the microstructure in the behavior of parts obtained by additive manufacturing processes in general, and in WAAM in particular, future work will be focused on developing an in-depth analysis about this promising topic, drawing special attention to the microstructure between layers, which is the most critical area in AM parts, and using higher resolution tests.

Author Contributions: Conceptualization, J.L.P.-C., A.M.C., J.L.D. and A.R.-P.; Formal analysis, J.L.P.-C., A.R.-P., A.M.A. and C.L.-M.; Funding acquisition, J.L.P.-C., A.M.C., J.L.D. and A.Y.-G.; Investigation, J.L.P.-C., A.M.C., J.L.D., A.R.-P., A.M.A. and C.L.-M.; Methodology, J.L.P.-C., A.M.C., and A.R.-P.; Project administration, A.M.C.; Resources, J.L.P.-C., J.L.D., and A.Y.-G.; Supervision, A.M.C.; Validation, J.L.P.-C.; Writing—original draft, J.L.P.-C.; Writing—review & editing, A.M.C., J.L.D., A.R.-P. and A.Y.-G.

Funding: This research was funded by the program “Innova” of the Galician Department of Education (Spain) and the APC was funded by the Annual Grants Call of the E.T.S.I.I. of UNED through the project of reference [2018-ICF04]. A mobility grant for junior researchers has been also granted by MES (Manufacturing Engineering Society) to Álvaro Rodríguez-Prieto.

Acknowledgments: This work has been developed within the framework of the doctorate program in Industrial Technologies of the UNED and in the context of the project DPI2016-81943-REDT of the Ministry of Economy, Industry and Competitiveness and the LDRD Project “Metal additive manufacturing modeling” with reference

2017-042-N0 of Argonne National Laboratory. We would like to extend our acknowledgement to the Department of Mechanical Manufacturing of the I.E.S. Politécnico de Vigo and the Manufacturing Engineering Department of the University of Vigo. The authors also acknowledge the Research Group of the UNED “Industrial Production and Manufacturing Engineering (IPME)”, Carlos Romano and Carlos Vicente for the given support during the development of this work and the Applied Materials Division of Argonne National Laboratory. We also acknowledge to Center for Nanoscale Materials (CNM), supported by the US Department of Energy, Office of Science and Office of Basic Energy Sciences under Contract N^o. DE-AC02-06CH11357.

Conflicts of Interest: The authors declare no conflict of interest. The funders had no role in the design of the study; in the collection, analyses, or interpretation of data; in the writing of the manuscript, and in the decision to publish the results.

Appendix A. Position of the Indentations

In Figure A1 the position of the indentation points for every sample is shown. Images of points located more clearly between layers are highlighted with red frame.

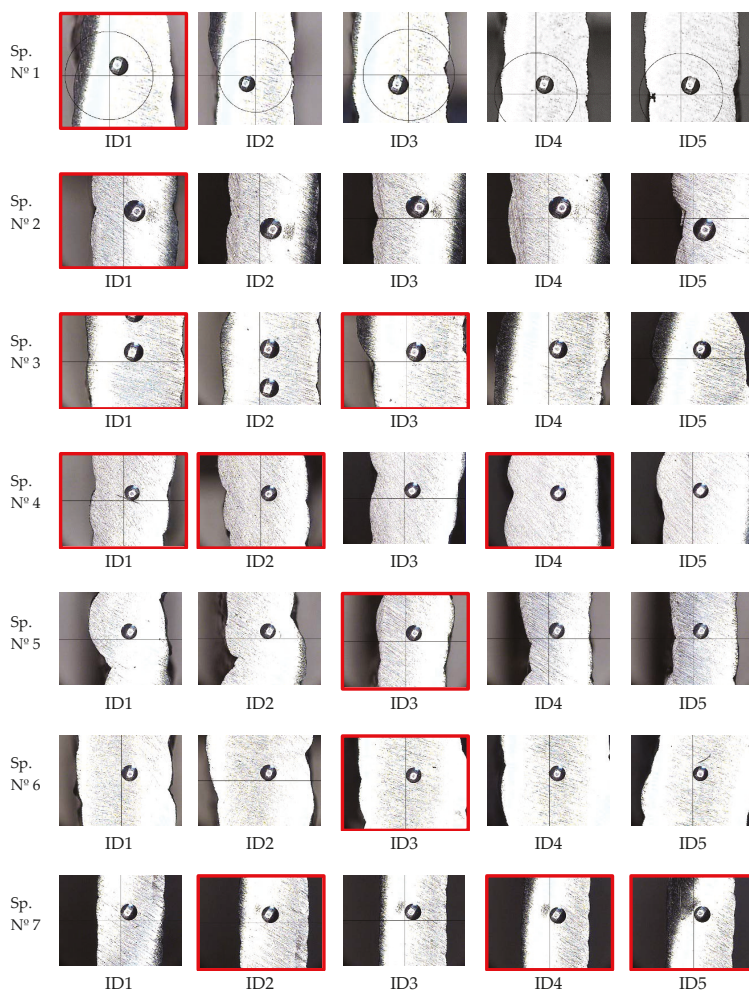
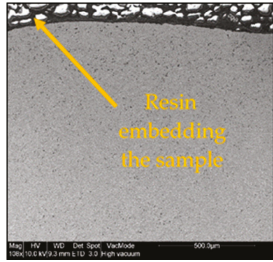


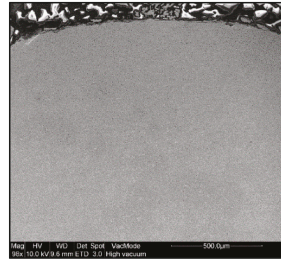
Figure A1. Brinell hardness tests applied to WAAM samples and identification of indentation points; images with red frame showing points located more clearly between layers.

Appendix B. Scanning Electronic Microscopy (SEM) to Detect Decohesiated Layer in the Upper Edge of the Surface

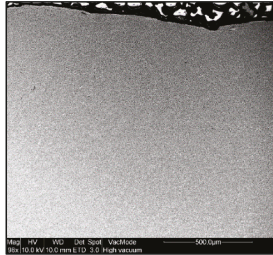
Figure A2 shows the surface of deposited material along the thickness for samples n° 2 to 7. The resin embedding the sample has not to be confused with the formation of the decohesionated layer that was only found in Sample n°1, using MIG conventional without CMT.



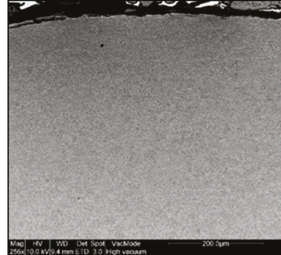
(a) Sample n° 2 (CMT)



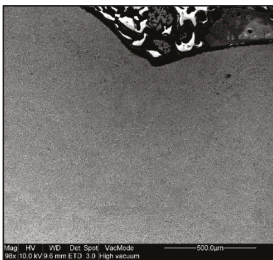
(b) Sample n° 3 (CMT Adv. pol. 0)



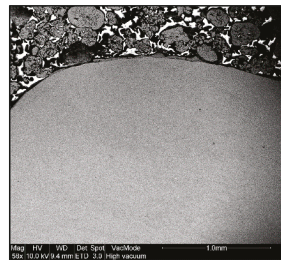
(c) Sample n° 4 (CMT Adv. pol. 0)



(d) Sample n° 5 (CMT Adv. pol. -5)



(e) Sample n° 6 (CMT Adv. pol. +5)



(f) Sample n° 7 (CMT)

Figure A2. SEM images showing no decohesionated layer formation in the upper edge of the surface.

(a) Sample n° 2, CMT process; (b) Sample n° 3, CMT Adv. pol. 0; (c) Sample n° 4, CMT Adv. pol. 0; (d) Sample n° 5, CMT Adv. pol. -5; (e) Sample n° 6, CMT Adv. pol. +5; (f) Sample n° 7, CMT Cont.

References

1. Singh, S.; Ramakrishna, S.; Singh, R. Material issues in additive manufacturing: A review. *J. Manuf. Process.* **2017**, *25*, 185–200. [[CrossRef](#)]
2. Bourell, D.; Kruth, J.P.; Leu, M.; Levy, G.; Rosen, D.; Beese, A.M.; Clare, A. Materials for additive manufacturing. *CIRP Ann.* **2017**, *66*, 659–681. [[CrossRef](#)]

3. Frazier, W.E. Metal additive manufacturing: A review. *J. Mater. Eng. Perform.* **2014**, *23*, 1917–1928. [[CrossRef](#)]
4. Xu, X.F.; Ganguly, S.; Ding, J.L.; Guo, S.; Williams, S.; Martina, F. Microstructural evolution and mechanical properties of maraging steel produced by wire + arc additive manufacture process. *Mater. Charact.* **2017**, in press.
5. Ge, J.G.; Lin, J.; Lei, Y.P.; Fu, H.G. Location-related thermal history, microstructure, and mechanical properties of arc additively manufactured 2Cr13 steel using cold metal transfer welding. *Mater. Sci. Eng. A* **2018**, *715*, 144–153. [[CrossRef](#)]
6. Hu, Z.Q.; Qin, X.P.; Shao, T. Welding thermal simulation and metallurgical characteristics analysis in waam for 5crnimo hot forging die remanufacturing. *Procedia Eng.* **2017**, *207*, 2203–2208. [[CrossRef](#)]
7. Artaza, T.; Alberdi, A.; Murua, M.; Gorrotxategi, J.; Frías, J.; Puertas, G.; Melchor, M.A.; Mugica, D.; Suárez, A. Design and integration of WAAM technology and in situ monitoring system in a gantry machine. *Procedia Manuf.* **2017**, *13*, 778–785. [[CrossRef](#)]
8. Luo, Y.; Li, J.L.; Xu, J.; Zhu, L.; Han, J.T.; Zhang, C.Y. Influence of pulsed arc on the metal droplet deposited by projected transfer mode in wire-arc additive manufacturing. *J. Mater. Process. Technol.* **2018**, *259*, 353–360. [[CrossRef](#)]
9. Wu, B.T.; Pan, Z.X.; Li, S.Y.; Cuiuri, D.; Ding, D.H.; Li, H.J. The anisotropic corrosion behaviour of wire arc additive manufactured Ti-6Al-4V alloy in 3.5% NaCl solution. *Corros. Sci.* **2018**, *137*, 176–183. [[CrossRef](#)]
10. Shi, X.Z.; Ma, S.Y.; Liu, C.M.; Wu, Q.R.; Lu, J.P.; Liu, Y.D.; Shi, W.T. Selective laser melting-wire arc additive manufacturing hybrid fabrication of Ti-6Al-4V alloy: Microstructure and mechanical properties. *Mater. Sci. Eng. A* **2017**, *684*, 196–204. [[CrossRef](#)]
11. Cunningham, C.R.; Wikshåland, S.; Xu, F.; Kemakolam, N.; Shokrani, A.; Dhokia, V.; Newman, S.T. Cost modelling and sensitivity analysis of wire and arc additive manufacturing. *Procedia Manuf.* **2017**, *11*, 650–657. [[CrossRef](#)]
12. Venturini, G.; Monteverchi, F.; Bandini, F.; Scippa, A.; Campatelli, G. Feature based three axes computer aided manufacturing software for wire arc additive manufacturing dedicated to thin walled components. *Addit. Manuf.* **2018**, *22*, 643–657. [[CrossRef](#)]
13. Williams, S.W.; Martina, F.; Addison, A.C.; Ding, J.; Pardal, G.; Colegrove, P. Wire + arc additive manufacturing. *Mater. Sci. Technol.* **2016**, *32*, 641–647. [[CrossRef](#)]
14. MX3D A smarter bridge. Available online: <http://mx3d.com/smart-bridge/> (accessed on 3 August 2018).
15. Bekker, A.C.M.; Verlinden, J.C. Life cycle assessment of wire + arc additive manufacturing compared to green sand casting and CNC milling in stainless steel. *J. Clean. Prod.* **2018**, *177*, 438–447. [[CrossRef](#)]
16. Ding, D.H.; Pan, Z.X.; Cuiuri, D.; Li, H.J. Wire-feed additive manufacturing of metal components: technologies, developments and future interests. *Int. J. Adv. Manuf. Technol.* **2015**, *81*, 465–481. [[CrossRef](#)]
17. Geng, H.B.; Li, J.L.; Xiong, J.T.; Lin, X.; Zhang, F.S. Optimization of wire feed for GTAW based additive manufacturing. *J. Mater. Process. Technol.* **2017**, *243*, 40–47. [[CrossRef](#)]
18. Venturini, G.; Monteverchi, F.; Scippa, A.; Campatelli, G. Optimization of WAAM Deposition Patterns for T-crossing Features. *Procedia CIRP* **2016**, *55*, 95–100. [[CrossRef](#)]
19. Wang, T.T.; Zhang, Y.B.; Wu, Z.H.; Shi, C.W. Microstructure and properties of die steel fabricated by WAAM using H13 wire. *Vacuum* **2018**, *149*, 185–189. [[CrossRef](#)]
20. Yan, F.Y.; Xiong, W.; Faierson, E.J. Grain structure control of additively manufactured metallic materials. *Materials* **2017**, *10*, 1260. [[CrossRef](#)]
21. Herzog, D.; Seyda, V.; Wycisk, E.; Emmelmann, C. Additive manufacturing of metals. *Acta Mater.* **2016**, *117*, 371–392. [[CrossRef](#)]
22. Kok, Y.; Tan, X.P.; Wang, P.; Nai, M.L.S.; Loh, N.H.; Liu, E.; Tor, S.B. Anisotropy and heterogeneity of microstructure and mechanical properties in metal additive manufacturing: A critical review. *Mater. Des.* **2018**, *139*, 565–586. [[CrossRef](#)]
23. Wang, F.D.; Williams, S.; Colegrove, P.; Antonysamy, A.A. Microstructure and mechanical properties of wire and arc additive manufactured Ti-6Al-4V. *Metall. Mater. Trans. A* **2013**, *44*, 968–977. [[CrossRef](#)]
24. Szost, B.A.; Terzi, S.; Martina, F.; Boisselier, D.; Prytuliak, A.; Pirling, T.; Hofmann, M.; Jarvis, D.J. A comparative study of additive manufacturing techniques: Residual stress and microstructural analysis of CLAD and WAAM printed Ti-6Al-4V components. *Mater. Des.* **2016**, *89*, 559–567. [[CrossRef](#)]
25. Cong, B.Q.; Ding, J.L.; Williams, S. Effect of arc mode in cold metal transfer process on porosity of additively manufactured Al-6.3%Cu alloy. *Int. J. Adv. Manuf. Technol.* **2015**, *76*, 1593–1606. [[CrossRef](#)]

26. Xu, X.F.; Ding, J.L.; Ganguly, S.; Diao, C.L.; Williams, S. Preliminary investigation of building strategies of maraging steel bulk material using wire + arc additive manufacture. *J. Mater. Eng. Perform.* **2018**, *1*–7. [[CrossRef](#)]
27. Horgar, A.; Fostervoll, H.; Nyhus, B.; Ren, X.; Eriksson, M.; Akselsen, O.M. Additive manufacturing using WAAM with AA5183 wire. *J. Mater. Process. Technol.* **2018**, *259*, 68–74. [[CrossRef](#)]
28. Wu, Q.R.; Lu, J.P.; Liu, C.M.; Fan, H.L.; Shi, X.Z.; Fu, J.; Ma, S.Y. Effect of molten pool size on microstructure and tensile properties of wire arc additive manufacturing of Ti-6Al-4V alloy. *Materials* **2017**, *10*, 749.
29. Lewandowski, J.J.; Seifi, M. Metal additive manufacturing: a review of mechanical properties. *Annu. Rev. Mater. Res.* **2016**, *46*, 151–186. [[CrossRef](#)]
30. Xiong, J.; Li, Y.J.; Li, R.; Yin, Z.Q. Influences of process parameters on surface roughness of multi-layer single-pass thin-walled parts in GMAW-based additive manufacturing. *J. Mater. Process. Technol.* **2018**, *252*, 128–136. [[CrossRef](#)]
31. Li, F.; Chen, S.J.; Shi, J.B.; Tian, H.Y.; Zhao, Y. Evaluation and optimization of a hybrid manufacturing process combining wire arc additive manufacturing with milling for the fabrication of stiffened panels. *Appl. Sci.* **2017**, *7*, 1233. [[CrossRef](#)]
32. Arrizubieta, J.I.; Cortina, M.; Ruiz, J.E.; Lamikiz, A. Combination of laser material deposition and laser surface processes for the holistic manufacture of inconel 718 components. *Materials* **2018**, *11*, 1247. [[CrossRef](#)] [[PubMed](#)]
33. Ma, J.F.; Harstvedt, J.D.; Dunaway, D.; Bian, L.; Jaradat, R. An exploratory investigation of additively manufactured product life cycle sustainability assessment. *J. Clean. Prod.* **2018**, *192*, 55–70. [[CrossRef](#)]
34. Rodríguez-Panes, A.; Claver, J.; Camacho, A.M. The influence of manufacturing parameters on the mechanical behaviour of pla and abs pieces manufactured by fdm: a comparative analysis. *Materials* **2018**, *11*, 1333. [[CrossRef](#)] [[PubMed](#)]
35. Taberero, I.; Paskual, A.; Álvarez, P.; Suárez, A. Study on arc welding processes for high deposition rate additive manufacturing. *Procedia CIRP* **2018**, *68*, 358–362.
36. Selvi, S.; Vishvaksean, A.; Rajasekar, E. Cold metal transfer (CMT) technology—An overview. *Def. Technol.* **2018**, *14*, 28–44. [[CrossRef](#)]
37. Ding, J.; Colegrove, P.; Mehnen, J.; Ganguly, S.; Almeida, P.M.S.; Wang, F.; Williams, S. Thermo-mechanical analysis of wire and arc additive layer manufacturing process on large multi-layer parts. *Comput. Mater. Sci.* **2011**, *50*, 3315–3322. [[CrossRef](#)]
38. Prado-Cerqueira, J.L.; Diéguez, J.L.; Camacho, A.M. Preliminary development of a wire and arc additive manufacturing system (WAAM). *Procedia Manuf.* **2017**, *13*, 895–902. [[CrossRef](#)]
39. González, J.; Rodríguez, I.; Prado-Cerqueira, J.L.; Diéguez, J.L.; Pereira, A. Additive manufacturing with GMAW welding and CMT technology. *Procedia Manuf.* **2017**, *13*, 840–847. [[CrossRef](#)]
40. Santos, E.C.; Shiomi, M.; Osakada, K.; Laoui, T. Rapid manufacturing of metal components by laser forming. *Int. J. Mach. Tools Manuf.* **2006**, *46*, 1459–1468. [[CrossRef](#)]
41. Pickin, C.G.; Williams, S.W.; Lunt, M. Characterisation of the cold metal transfer (CMT) process and its application for low dilution cladding. *J. Mater. Process. Technol.* **2010**, *211*, 496–502. [[CrossRef](#)]
42. Fronius CMT—Cold Metal Transfer: The Cold Welding Process for Premium Quality. Available online: <http://www.fronius.com/en/welding-technology/our-expertise/welding-processes/cmt> (accessed on 29 June 2018).
43. Anwar, M.S.; Untawale, S.P. Measuring the process efficiency of controlled welding processes. *Int. J. Instrum. Control Autom.* **2012**, *1*, 33–39.
44. Fronius CMT Advanced: A Higher Deposition Rate, Better Gap-Bridging Ability and Higher Stability. Available online: <http://www.fronius.com/en/welding-technology/our-expertise/welding-processes/cmt-advanced> (accessed on 29 June 2018).
45. *Metallic Materials—Brinell Hardness Test. Part 1—Test Method*; ISO 6506-1:2014; International Standards Organisation: Geneva, Switzerland, 2014.
46. *Metallic Materials—Conversion of Hardness Values*; ISO 18265:2013; International Standards Organisation: Geneva, Switzerland, 2013.
47. *Standard Test Methods and Definitions for Mechanical Testing of Steel Products*; ASTM A370-17a; American Society for Testings and Materials International: West Conshohocken, PA, USA, 2017.
48. *Hardness Tests and Hardness Number Conversions*; SAE J417:198312; SAE International: Troy, MI, USA, 1983.

49. *Guide to AWS Specification for Carbon Steel Electrodes and Rods for Gas Shielded Arc Welding*; ASME SFA 5.18; American Society of Mechanical Engineers: New York, NY, USA, 2017.
50. *Specification for Carbon Structural Steel*; ASME SA-36; American Society of Mechanical Engineers: New York, NY, USA, 2017.
51. *Specification for Pressure Vessels Plates, Carbon Steel, Low- and Intermediate- Tensile Strength*; ASME SA-285; ASTM International: West Conshohocken, PA, 2017.
52. *Specification for Pressure Vessels Plates, Carbon Steel, Low- and Intermediate- and Higher Temperature Service*; ASME SA-515; ASTM International: West Conshohocken, PA, USA, 2017.
53. *Specification for Pressure Vessels Plates, Carbon Steel, for Moderate- and Lower- Temperature Service*; ASME SA-516; ASTM International: West Conshohocken, PA, USA, 2017.
54. Liberini, M.; Astarita, A.; Campatelli, G.; Scippa, A.; Montevicchi, F.; Venturini, G.; Durante, M.; Boccarusso, L.; Minutolo, F.M.C.; Squillace, A. Selection of optimal process parameters for wire arc additive manufacturing. *Procedia CIRP* **2017**, *62*, 470–474. [[CrossRef](#)]
55. *Kobe Steel Welding Handbook*; Kobe steel Ltd.: Hyōgo, Japan, 2014.



© 2018 by the authors. Licensee MDPI, Basel, Switzerland. This article is an open access article distributed under the terms and conditions of the Creative Commons Attribution (CC BY) license (<http://creativecommons.org/licenses/by/4.0/>).

Article

Fabrication of Polymer Microstructures of Various Angles via Synchrotron X-Ray Lithography Using Simple Dimensional Transformation

Kyungjin Park ¹, Kanghyun Kim ², Seung Chul Lee ³, Geunbae Lim ^{1,2,*} and Jong Hyun Kim ^{2,3,*}

¹ School of Interdisciplinary Bioscience and Bioengineering, Pohang University of Science and Technology (POSTECH), 77 Cheongam-ro, Nam-gu, 37673 Pohang, Korea; kjpark@postech.ac.kr

² Department of Mechanical Engineering, Pohang University of Science and Technology (POSTECH), 77 Cheongam-ro, Nam-gu, 37673 Pohang, Korea; qwnerkang@postech.ac.kr

³ Pohang Accelerator Laboratory (PAL), Pohang University of Science and Technology (POSTECH), 77 Cheongam-ro, Nam-gu, 37673 Pohang, Korea; leesch00@postech.ac.kr

* Correspondence: limmems@postech.ac.kr (G.L.); kjh9818@postech.ac.kr (J.H.K.); Tel.: +82-54-279-2186 (G.L.); +82-54-279-1568 (J.H.K.)

Received: 7 July 2018; Accepted: 15 August 2018; Published: 17 August 2018

Abstract: In this paper, we developed a method of fabricating polymer microstructures at various angles on a single substrate via synchrotron X-ray lithography coupled with simple dimensional transformations. Earlier efforts to create various three-dimensional (3D) features on flat substrates focused on the exposure technology, material properties, and light sources. A few research groups have sought to create microstructures on curved substrates. We created tilted microstructures of various angles by simply deforming the substrate from 3D to two-dimensional (2D). The microstructural inclination angles changed depending on the angles of the support at particular positions. We used convex, concave, and S-shaped supports to fabricate microstructures with high aspect ratios (1:11) and high inclination angles (to 79°). The method is simple and can be extended to various 3D microstructural applications; for example, the fabrication of microarrays for optical components, and tilted micro/nanochannels for biological applications.

Keywords: Synchrotron X-rays; lithography; curved substrate; microstructures

1. Introduction

Synchrotron X-ray lithography (XRL) uses a hard X-ray source to fabricate nano/microstructures of various shapes [1,2]. Synchrotron XRL has been used to create high aspect ratio structures with good sidewall roughness; synchrotron X-rays are highly collimated, pass through thick polymers and other plastic materials, and exhibit high flux and intensity, the pattern accuracy of XRL is very high. Synchrotron XRL was first developed to fabricate uranium-separation nozzles, and several other applications have been found since. For example, synchrotron XRL has been used to fabricate high-density magnetic dot arrays [3], a vertical stepper [4], and micromechanical components [5].

Ultraviolet (UV) light is employed in conventional photolithography. The photomask pattern is copied to photoresist (PR) with various ratios, and a two-dimensional (2D) microstructure is formed on a flat substrate. Various techniques are used to create three-dimensional (3D) features on 2D substrates. Micro stereo lithography [6], 3D printing [7], oblique lithography [8], PR reflow [9], backside exposure lithography [10], grayscale lithography [11], nanoimprint lithography [12,13], nanosphere lithography [14], colloidal lithography [15], block copolymer lithography [16], and e-beam lithography [17] all allow extensive shaping. However, it is complicated to fabricate the desired structures using these techniques.

In 2011, Jongho et al. prepared copper microstructures on curved substrates via optical soft lithography and metal electroplating [18]. The microstructures had high aspect ratios, throughput was good, cost was low, and reproducibility was high.

Microcontact printing using cylindrical polydimethylsiloxane (PDMS) stamps has since been reported [19]. However, it was not possible to create various angles on a single substrate by flattening the curved substrates bearing the microstructures.

Here, we develop a method by which to fabricate tilted microstructures of various angles and shapes on a single substrate using synchrotron XRL. Synchrotron X-rays are highly collimated; they pass through polymers (because of their short wavelength). Such a unique feature of hard X-rays allows the fabrication of microstructures on curved substrates. The fabrication technique on curved substrates could be applied to the fabrication of precision optical elements [20] and the micromachining of ultraprecise molds on curved or cylindrical structures.

2. Materials and Methods

2.1. Experimental Setup

The experiment was conducted at the 9D (X-ray nano/micromachining [XNMM]) beamline [21] of the Pohang Light Source (PLS) using a polychromatic X-ray beam (Figure 1) emitted from an electron storage ring. Unlike conventional UV lithography, it is possible to impart dimensional changes to the X-ray mask to create gaps between the mask and the sample, thus improving technical performance.

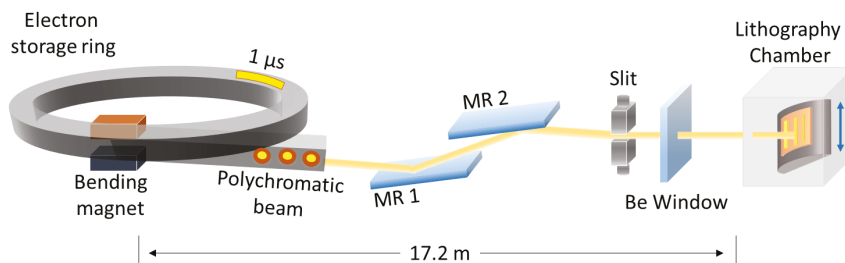


Figure 1. Schematic of synchrotron X-ray lithography. MR, mirror; Be, beryllium.

The energy of the linearly accelerated electrons is 3 GeV, and the current moving around the storage ring is 400 mA (Table 1). The 9D beamline uses a bending magnet to direct the X-rays into the lithography chamber. The horizontal divergence of the beam source from the bending magnet is about 8 mrad (Table 1). As the distance from the magnet to the sample is about 20 m, the beam width is about 16 cm, which is sufficient for a four-inch wafer process. X-rays emitted from the magnet pass through two mirrors and the Be windows before finally reaching the lithography chamber. The mirrors are inserted in the beam path to remove high-energy emissions [22]. The Be windows isolate the vacuum and experimental zones, and are surrounded by He (an inert, non-toxic noble gas). The He gas prevents Be window oxidation. The experimental chamber is also filled with He because the gas exhibits good X-ray transmittance, and flux degradation is minimal. Another effect of He atmosphere is that He atmosphere promotes heat dissipation by convection in the chamber, since He has high heat capacity. The sample stage of the experimental chamber moves vertically to provide homogeneous X-ray exposure distribution. The beam width covers the entire sample in the horizontal direction, but the vertical beam dimension is only about 1 cm; thus, the sample stage must move vertically to cover the entire sample (Figure S1).

Table 1. Specifications of the Pohang Light Source 9D nano/micromachining beamline.

Specification	9D Beamline
Electron energy	3 GeV ¹
Beam current	400 mA
Horizontal beam span	8 mrad
Vertical beam span	0.34 mrad
Beam size at sample	100 mm (H) × 10 mm (V)

¹ <http://pal.postech.ac.kr>.

2.2. Fabrication of a Flexible X-Ray Mask

Synchrotron XRL was used to create microstructures of various angles via simple dimensional transformations. Especially when using a curved substrate, the mask must be sufficiently flexible to adhere to the PR.

Figure 2 shows the fabrication of the flexible X-ray mask. The first step was the deposition of a gold layer on the polyimide (PI) film/silicon (Si) wafer (Figure 2a). The PI film was laminated onto the Si wafer using dry film resist (DFR) as adhesive. The PI film/Si wafer was chemically prepared and oxygen plasma-cleaned; the film was chemically resistant and thermostable. After cleaning and surface treatment, a 20-nm chrome layer and an 100-nm gold layer were then deposited. The chrome layer served to adhere the PI and the gold. A 100-nm gold seed layer for electroplating is then deposited. The second step in mask formation is shown in Figure 2b. The PR on the PI film is formed via UV photolithography. To create the PR, the PR (SU-8 3010; MicroChem, Westborough, MA, USA) was spin-coated onto the gold layer at 1,000 rpm for 30 s, and the sample was heated for 8 min at 95 °C (the soft bake). When all of the wrinkles had been removed, the PR was covered by the chrome mask and exposed to 15 mW of UV for 12 s (total energy: 175 mJ/cm²), followed by post-exposure baking (PEB) at 65 °C for 1 min and 95 °C for 23 min, rendering the latent PR pattern visible.

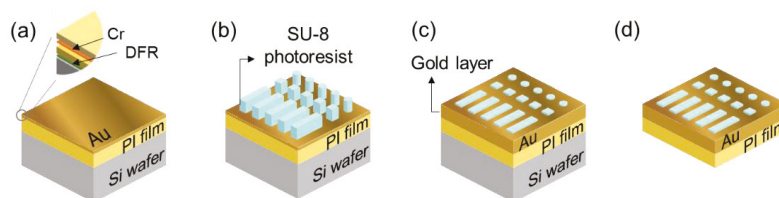


Figure 2. Fabrication of a flexible X-ray mask. (a) A gold layer on the polyimide (PI) film and silicon (Si) wafer; (b) Mask patterns on the gold layer after photolithography; (c) An electroplated gold (Au) layer between the mask patterns; (d) The completed flexible X-ray mask after separation from the Si wafer substrate. DFR, dry film resist.

The next step was the developmental process, after which only the pattern remains; other areas were chemically removed to expose the bottom gold surface, which acts as a seed layer for gold deposition during electroplating. Plasma ashing was used to remove residual PR. Electroplating (to form the masking pattern) was then performed (Figure 2c) using a customized electrochemical cell. The electrolyte solution was a gold preparation (SP Gold 2000; CNC Tech., Seoul, Korea). The gold substrate (the cathode) was covered with electroplating tape except in the patterned SU-8 area. DC current density of 1 mA/cm² was delivered to an area of 2600 mm² at 50 °C with mild agitation. The electroplating time was calculated using the experimental data, and was about 3 h at an electroplating rate of 4 μm/h, affording a final gold thickness of 12 μm. Then, the substrate was thoroughly rinsed with distilled water. Finally, the electroplated gold structures were detached (Figure 2d).

Optical microscopy confirmed that the SU-8 PR remained adherent to the substrate during mask fabrication. We created seven different patterns: four rows of lines with 20- μm , 50- μm , 100- μm , 200- μm , and 800- μm gaps between them; and rectangular, star, and circle patterns, as shown in Figure 3. Optical microscopy showed that the pattern edges were neatly formed, not only for relatively simple circles but also for (irregular) stars. We encountered no stress-induced gold peeling during electroplating.

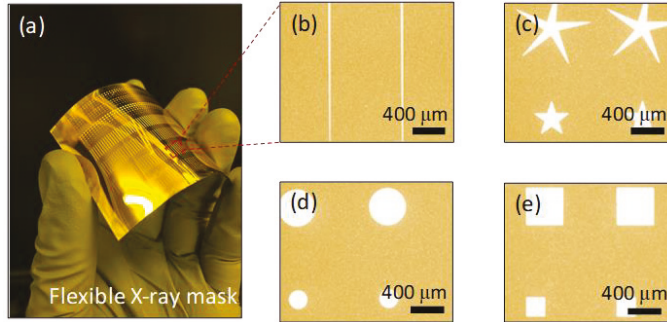


Figure 3. Flexible X-ray masks. (a) Picture of fabricated X-ray mask with various patterns including. (b) lines, (c) stars, (d) circles, (e) squares.

2.3. Fabrication of Microstructures of Various Angles

In this research, PR SU-8, the material used for the microstructures, was micropatterned onto a flexible substrate, forming structures $>100\ \mu\text{m}$ in height. In fact, the PR exhibited excellent substrate adhesion, even when forming structures of height $>3\ \text{mm}$ via dry-chip casting [23]. Therefore, SU-8 is optimal for producing tall structures with various angles and shapes.

2.3.1. Spin-Coating

After fabricating the mask, the SU-8 was first spin-coated onto a flat structure. Although spraying and roller-coating, dip-coating, and extrusion-coating methods are available, spin-coating is most commonly used to form flat PR layers. The height of the final structure was about 75% of the thickness of the PR. The micropatterned structure was supported by a flexible PI film. The PI film (5 cm \times 4 cm) was prepared via chemical and plasma cleaning, followed by surface treatment, as described for mask fabrication. PR (SU-8 2075; MicroChem) was spin-coated at 1000 rpm to a thickness of about 120 μm (Figure 4a), followed by heating (soft bake) to remove the solvent and cure the PR. The soft bake was performed at 65 $^{\circ}\text{C}$ for 8 min and 95 $^{\circ}\text{C}$ for 45 min. Wrinkles could have formed if the heating had been inadequate, resulting in surface distortion on contact with the mask, and thus the creation of dents on removal of the mask. In addition, the development time would have been extended. Then, the flexible X-ray mask was attached on top of the PR (Figure 4b) using an intermediate 30- μm PI film to prevent sticking.

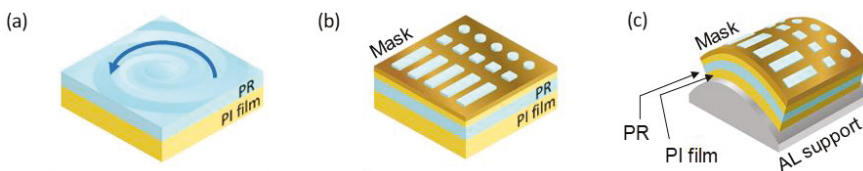


Figure 4. Cont.

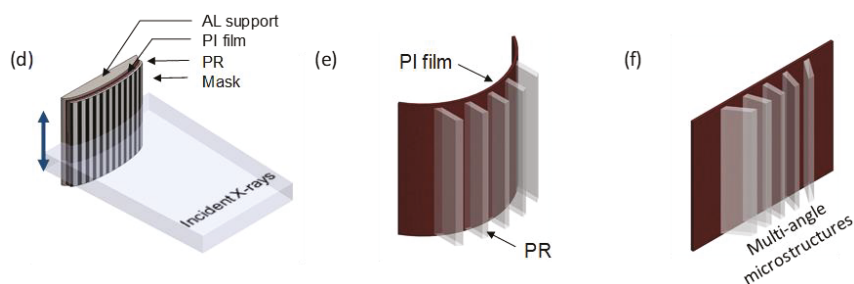


Figure 4. Fabrication of microstructures of various angles. (a) Spin-coating of photoresist (PR) onto a PI film. (b) The flexible PR X-ray mask. (c) The flexible structure wrapped on a curved substrate. (d) X-ray exposure of the curved structure. (e) Microstructures on a curved substrate. (f) Microstructures tilted at various angles.

2.3.2. X-Ray Exposure

The PR with the flexible X-ray mask was attached to a semicircular column by a lead sheet (Figure 4c), and then attached to a sample stage in the experimental chamber. Cooling lines were run under the sample stage. Heat control is important; heat generated by X-rays may deform the PR layer or create bubbles. After placing the sample in the stage, the chamber was evacuated and helium gas was injected. The X-ray beam dimensions were about 10 cm horizontally and 1 cm vertically. The stage had a reciprocating vertical motion to cover the entire field of view (FoV) of the sample (Figure 4d). The vertical scan speed was 2 cm/s and the total scan range was 7 cm. The dose delivered to the PR was about 90 J/cm^3 . After X-ray exposure, the PI/PR construct was removed from the curved support, and PEB was performed at 65°C for 5 min and 95°C for 10 min. Irradiated, negative X-ray PRs form strong acids, and the affected areas become cross-linked during PEB. The brittleness and ductility of the photopolymer during exposure and PEB are influenced by the sensitivity of the PR to X-rays, X-ray intensity, exposure time, temperature, and PEB time; all must be controlled to ensure appropriate microstructural stiffness and adhesion to the flexible substrate.

2.3.3. Development

After PEB, the PR/PI film was immersed in SU-8 developer for about 15 min. During development, the area exposed to the X-ray remains, and the area that is not exposed is removed (Figure 4e). As the substrate is flexible, it can be flattened, and the structures then exhibit various tilt angles depending on their distances from the center (Figure 4f).

3. Results

3.1. Fabricated Polymer Microstructures of Various Shapes on a Flexible Substrate.

Representative examples of the tilted microstructures are shown in Figure 5. Figure 5e–h are optical images acquired in top-down view; the shapes include lines, circles, stars, and squares. As the microstructural material is a polymer, the microstructures are transparent to visible light, allowing the morphology of the bottom substrate to be observed (red arrows in Figure 5a–d). The bottoms of the microstructures are dark (green arrows in Figure 5a–d). The four microstructures are shown from the side via scanning electron microscopy (SEM) in Figure 5e–h. The width of the line pattern microstructure is $50 \mu\text{m}$; the length is 5 mm, the height is about $200 \mu\text{m}$, the hypotenuse is about $560 \mu\text{m}$, and the tilt angle is about 69° . The aspect ratio of the tilted line structure is about 1:11. As the pattern is narrow, long, and highly tilted, the structure is vulnerable to external forces. Especially, during development, the developer solution must be circulated to remove non-crosslinked SU-8 PR. If stirring is too strong, the structure will collapse. If stirring is too weak, some polymer will remain

near the bottom, i.e., under the tilted structure (blue arrow in Figure 5e). In Figure 5a, residual polymer is present in the dark area (blue arrow). The radius of the smaller circular microstructure is $100\ \mu\text{m}$; the height is about $240\ \mu\text{m}$, the hypotenuse is $840\ \mu\text{m}$, and the tilt angle is about 73° . We also fabricated square-patterned microstructures with a tilting angle of 54° . The height of the structure was about $300\ \mu\text{m}$, the length of a side was about $200\ \mu\text{m}$, and the hypotenuse was $510\ \mu\text{m}$. Interestingly, we observed that star-patterned microstructures had the highest tilting angles, as shown in Figure 5h. The area of the star pattern was about $45\ \mu\text{m}^2$, the height of the microstructure was about $100\ \mu\text{m}$, the hypotenuse was $510\ \mu\text{m}$, and the tilting angle was about 79° .

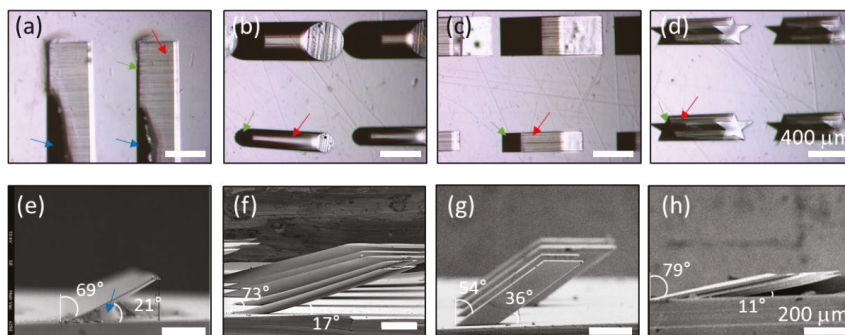


Figure 5. Fabricated polymer microstructures of various shapes on a flexible substrate. Optical microscopic images of various patterns (from the top) including (a) lines, (b) circles, (c) stars, (d) squares. Scanning electron microscopy (SEM) images of various patterns (side views): (e) lines, (f) circles, (g) stars, (h) squares. Scale bars, (a–d) $400\ \mu\text{m}$, (e–h) $200\ \mu\text{m}$.

3.2. Fabricated Polymer Microstructures of Various Angles on a Flexible Substrate

As shown in Figure 6, the polymer microstructure was fabricated on a single substrate with a single synchrotron X-ray exposure. The key to this development was that the tilt angle of the microstructures changed with the support structure. While the sample was irradiated with X-rays, the angle between the X-rays and the substrate of the microstructure determined the tilt angle of the microstructures. As shown in Figure 6a, when the exposure was performed with the PR attached to a convex support, the microstructures formed perpendicularly to the horizontal plane. When the substrate was flattened after separating the bent substrate from the convex support, the inclination angles of the microstructures were determined during exposure. For convex supports, the microstructures were inclined inwards at a greater angle as the position moved away from the center. Figure 6a shows a panoramic view of the tilted microstructures on a single substrate with tilt angles of 65° , 55° , and 45° as a representative data set. As shown in Figure 6a, the line, circle, and star microstructures had constant slopes at specific positions. For concave supports, the microstructures were inclined outwards at a greater angle as the position moved away from the center, as shown in Figure 6b. S-shaped supports were also used to fabricate microstructures on flexible substrates, as shown in Figure 6c. The S-shaped supports had two properties. The microstructures sloped inwards and outwards on the convex and concave supports, respectively.

One problem with the supports was that when a flexible X-ray mask was attached to the PR for exposure, some areas of the PR were pushed down when forces were applied to the flexible X-ray mask. In particular, it was difficult to attach the PR with a flexible X-ray mask on an S-shaped support because of its complicated structure. During the attachment, some deformation and damage occurred, and the height of the tilted microstructures varied at different positions. If slight deformation and damage occurred during attachment, the height of the tilted microstructures varied at different locations, as shown in Figure 6c.

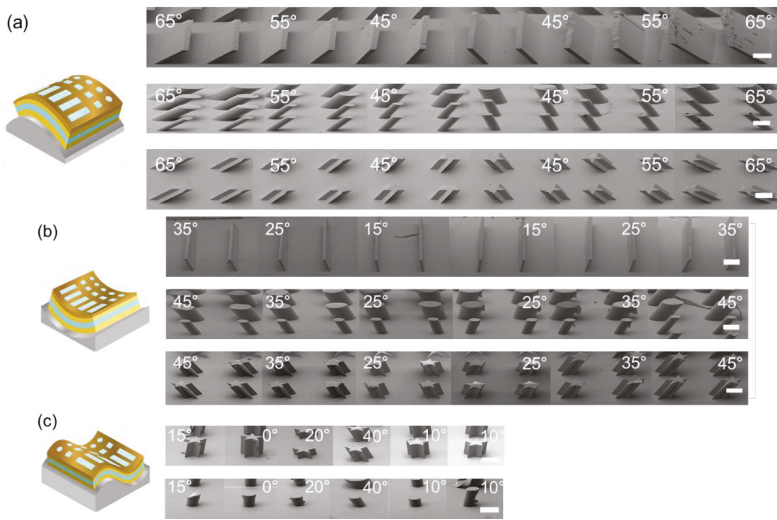


Figure 6. SEM images of microstructures fabricated on the (a) convex support, (b) concave support, (c) S-shaped support.

We selected the line structure on the convex support to compare between the structures on the mask and the actual structures after the last processing step. The substrate of the tilted microstructures was attached to an aluminum block (Figure 7a). The block was placed on the stage of the stereo microscope (Stemi 2000-C, Carl Zeiss, Jena, Germany) with the lateral side up. The side images of the structures were recorded using a charge-coupled device (CCD) camera (Retiga 4000R; QImaging, Surrey, BC, Canada). A total of 39 angles were observed along a single row. The slanted angles were measured using the angle tool in the ImageJ software package (NIH, Bethesda, MD, USA). The measured angle was proportional to the position of the structure (Figure 7b). However, the distance from the center and the angle of the micropattern did not coincide exactly. The slopes from the experimental results were slightly higher than the calculated values due to detachment between the aluminum (AL) support and PI substrate. According to the angle measurement (Table S1), there was a gap in the center part, between the PI substrate and the support (Figure S3). When we placed the RP with the PI and mask on the Al support by hand, there was a slight air gap between the PI film and the Al support at the center.

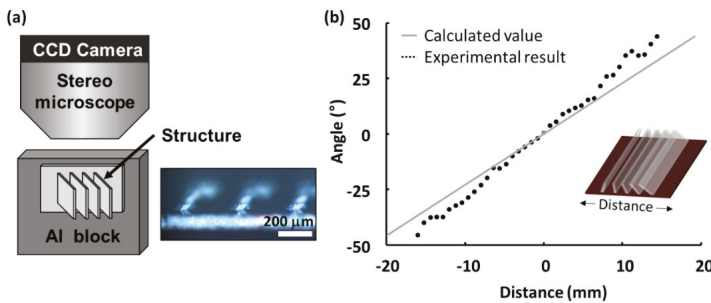


Figure 7. Angle measurement of the tiled microstructures. The structures were observed by a stereo microscope with a charge-coupled device (CCD) camera. (a) Experimental setup, (b) Calculated angle vs. measured angle.

4. Discussion

4.1. Interactions between the Beam Source and Materials

The mask on top of the PR layer blocked the X-rays selectively via gold patterned on a PI substrate; the PI film acted as a structural support that was transparent to X-rays.

The micropatterns on the mask were made of SU-8 PR, which is transparent to X-rays. The background was a thick gold layer that absorbs X-rays; the SU-8 micropatterned area was selectively excluded from electroplating. The ratios of X-rays passing through gold and PI are shown in Figure 8a.

The flux of the beam on the mask was calculated by reference to the characteristics of the beam source, as shown in Figure 8b. Such analysis reveals not only the interactions between the electrons and the surrounding materials, but also the required gold thickness. We obtained a wide range of X-ray energies from the bending magnet, i.e., from a few volts to tens of kilo-electron volts (thus of both high and low energy). However, high-energy photons are detrimental, penetrating to the bottom of the PR and then scattering inappropriately into adjacent areas during X-ray exposure [22]. The schematic of Figure 8c shows a cross-section of the X-ray exposure in the lithography chamber. Such backscattered photons compromise structural accuracy and pattern/substrate adhesion. Also, backscattered photons that strike the edges of the structure damage those edges. Another problem associated with high-energy photons is secondary radiation. As photons pass through the PR, electrons emitted after photon absorption hit the walls under the gold mask (Figure 8c), thus degrading the wall. Therefore, mirrors were used to eliminate the high-energy photons with energies over 7 keV.

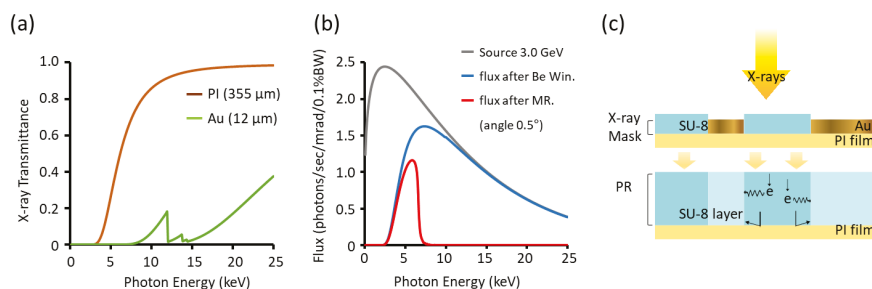


Figure 8. Experimental conditions for synchrotron X-ray lithography (XRL). (a) X-ray transmittance of the polyimide (PI) film and Au. (b) X-ray flux calculations before the beam entered the lithography chamber. (c) Schematic diagram of the exposure in the lithography chamber. PR, photoresist; MR, mirror; Be Win, beryllium window.

We calculated the thickness of the gold layer by calculating the X-ray flux and then estimating the dose incident on the PR numerically. The thickness of the gold was selected to minimize the transmission energy and was proportional to the product of the transmittance and the flux. The flux ejected from the linear accelerator fell by 66% after passing through the two Be windows (Figure 8b). The following equation [24] was used to calculate the number of transmitted X-rays (S_{TP}):

$$S_{TP} = S_M \times \exp(-\mu_P x_P) \quad (1)$$

where x_P is the depth, S_M is the X-ray energy spectrum of the PR, and μ_P is the absorption coefficient. The bottom doses should be about 90 J to promote cross-linking conditions. The thickness of the gold layer was calculated to be 10 μm. Thus, the SU-8 thickness must be >10 μm. The thickness was thus set to 12 μm, which was about 120% of the target thickness, with some margin.

4.2. The Utility of the Fabricated Structures in Real Applications

Again, we electroplated the microstructures with gold to make a mold for replicating the structure (Figure S4). We conducted a simple feasibility test to determine whether this mold can be used to fabricate microarrays for optical components, and tilted microchannels for many industrial applications. Further, the proposed development could also be applied to the manufacture of flexible electronics.

4.3. Limitations of the Fabrication Process

In the process described in Figure 4, both the substrate and the mask were bent. Due to the synchrotron beam being parallel across the entire FoV, there were deviations in the geometry over the whole FoV. There was a masking effect that resulted in a decreased structural width and increased structural height at the edge of the FoV. For 45° inclined structures, structures with a width of less than 12 μm were no longer illuminated by X-rays that did not partly pass through the gold absorber, thus reducing the dose absorbed by the resist. Theoretically, it is not possible to fabricate microstructures with critical dimensions less than the height of the mask pattern. The structures in this research were from tens of microns to a few hundred microns in height, so this effect was not obvious. This was not visible in the optical micrograph pictures of structures with a width of several 100 μm (Figure S2). However, it was of major relevance for the fabrication of structures smaller than the height of the mask pattern (12 μm).

The process can be modified to overcome this hindrance. For instance, the mask can be flat, and there can be a gap between the mask and the PR. In this case, the distance between the structures needs to be calculated exactly to achieve the desired pitch on the bending structure. In this research, we focused on providing a proof of concept and demonstrating the feasibility of using a simple dimensional transformation to produce polymer microstructures of various angles and shapes on a single substrate.

5. Conclusion

In this paper, we proposed a method of fabricating polymer microstructures with various angles on a single substrate by a simple dimensional transformation using synchrotron X-ray lithography. In the past, various techniques have been attempted to obtain various features on a 2D substrate, focusing on the exposure technology, material properties, and light source. Few research groups have attempted to create microstructures on 3D substrates. In this research, by the simple dimensional transformation of the substrate, we created tilted microstructures at various angles. Due to the high collimation of the synchrotron X-rays, microstructures with high aspect ratios could be realized simultaneously. The inclination angle of the microstructure changed depending on the support structure, which was at a constant inclination at each specific position. Three different-shaped supports: convex, concave, and S-shaped, were used to fabricate the microstructures. The microstructures had high aspect ratios of 1 to 11 for the line-shaped structures, and high inclination angles of 80° for the star-shaped structures. Further, the inclination angle of the microstructure can also be controlled by adjusting the degree of bending of the flexible substrate.

The developed method is simple, but can be extended to various microstructure applications. As a typical application, this technology can be applied to microarrays for optical components, and tilted micro/nanochannels for biological applications.

Supplementary Materials: The following are available online at <http://www.mdpi.com/1996-1944/11/8/1460/s1>, Figure S1: Experimental chamber, Figure S2: Photograph of the microstructure, Figure S3: Schematics of attachment of PI film on the Al support, Figure S4: Fabrication process of the electroplated mold. Table S1. Sampled measured angle, measured position of the microstructures, and the calculated position.

Author Contributions: For “Conceptualization, J.H.K.; Methodology, K.P., S.C.L. and K.K.; Validation, K.P. and K.K.; Formal Analysis, K.P. and K.K.; Investigation, J.H.K.; Resources, J.H.K.; Data Curation, K.P.; Writing-Original Draft Preparation, K.P.; Writing-Review & Editing, K.P. and J.H.K.; Visualization, K.P. and K.K.; Supervision, J.H.K. and G.L.; Project Administration, J.H.K.; Funding Acquisition, J.H.K.”

Acknowledgments: K.P. thanks Daeil Kim for the help with imaging the samples using a scanning electron microscope (SEM). This work was supported by the National Research Foundation of Korea (NRF) grant funded by the Korea government (No. 2015R1A2A1A14027903, No. 2017M3C1B2085309, and No. 2017R1D1A1B03032928), Innovation Program funded by the Ministry of Trade, Industry & Energy (MI, Korea) (No. 10048358). It was further supported by a Gumi Electronics & Information Technology Research Institute (GERI) (No. 40015088).

Conflicts of Interest: The authors declare no conflict of interest.

References

1. Becker, E.W. Fabrication of microstructures with high aspect ratios and great structural heights by synchrotron radiation lithography, galvanofarming, and plastic moulding (LIGA process). *Microelectron. Eng.* **1986**, *4*, 35–56. [[CrossRef](#)]
2. Backer, E.W. Production of separation-nozzle systems for uranium enrichment by a combination of X-ray lithography and galvanoplastics. *Naturwissenschaften* **1982**, *69*, 520–523. [[CrossRef](#)]
3. Rousseaux, F. Study of large area high density magnetic dot arrays fabricated using synchrotron radiation based x-ray lithography. *J. Vac. Sci. Technol. B Microelectron. Nanometer Struct. Process. Meas. Phenom.* **1995**, *13*, 2787–2791. [[CrossRef](#)]
4. Ishihara, S. A vertical stepper for synchrotron x-ray lithography. *J. Vac. Sci. Technol. B Microelectron. Process. Phenom.* **1989**, *7*, 1652–1656. [[CrossRef](#)]
5. Guckel, K. Fabrication of assembled micromechanical components via deep X-ray lithography. In Proceedings of the IEEE Micro Electro Mechanical Systems, Nara, Japan, 30 December 1990–2 January 1991.
6. Zhang, X.; Jiang, X.; Sun, C. Micro-stereolithography of polymeric and ceramic microstructures. *Sens. Actuators A Phys.* **1999**, *77*, 149–156. [[CrossRef](#)]
7. Cima, M. Three-dimensional printing techniques. US5387380A, 7 February 1995.
8. Jian, L.; Desta, Y.M.; Goettert, J. Multilevel microstructures and mold inserts fabricated with planar and oblique x-ray lithography of SU-8 negative photoresist. In Proceedings of the Micromachining and Microfabrication Process Technology VII, San Francisco, CA, USA, 28 September 2001.
9. O'Neill, F.T.; Sheridan, J.T. Photoresist reflow method of microlens production Part I: Background and experiments. *Optik Int. J. Light Electron Optics* **2002**, *113*, 391–404. [[CrossRef](#)]
10. Kim, K. A tapered hollow metallic microneedle array using backside exposure of SU-8. *J. Micromech. Microeng.* **2004**, *14*, 597. [[CrossRef](#)]
11. Rammohan, A. One-step maskless grayscale lithography for the fabrication of 3-dimensional structures in SU-8. *Sens. Actuators B Chem.* **2011**, *153*, 125–134. [[CrossRef](#)]
12. Chou, S.Y.; Krauss, P.R.; Renstrom, P.J. Nanoimprint lithography. *J. Vac. Sci. Technol. B* **1996**, *14*, 4129–4133. [[CrossRef](#)]
13. Guo, L.J. Nanoimprint lithography: Methods and material requirements. *Adv. Mater.* **2007**, *19*, 495–513. [[CrossRef](#)]
14. Hamdana, G. Towards fabrication of 3D isotopically modulated vertical silicon nanowires in selective areas by nanosphere lithography. *Microelectron. Eng.* **2017**, *179*, 74–82. [[CrossRef](#)]
15. Yang, S.M. Nanomachining by colloidal lithography. *Small* **2006**, *2*, 458–475. [[CrossRef](#)] [[PubMed](#)]
16. Gu, X.D. High Aspect Ratio Sub-15 nm Silicon Trenches From Block Copolymer Templates. *Adv. Mater.* **2012**, *24*, 5688–5694. [[CrossRef](#)] [[PubMed](#)]
17. Manfrinato, V.R. Resolution Limits of Electron-Beam Lithography toward the Atomic Scale. *Nano Lett.* **2013**, *13*, 1555–1558. [[CrossRef](#)] [[PubMed](#)]
18. Park, J.; Fujita, H.; Kim, B. Fabrication of metallic microstructure on curved substrate by optical soft lithography and copper electroplating. *Sens. Actuators Phys.* **2011**, *168*, 105–111. [[CrossRef](#)]
19. Park, J.; Kim, B. 3D micro patterning on a concave substrate for creating the replica of a cylindrical PDMS stamp. *Microelectron. Eng.* **2012**, *98*, 540–543. [[CrossRef](#)]
20. Jeong, K.H.; Kim, J.; Lee, L.P. Biologically inspired artificial compound eyes. *Science* **2006**, *312*, 557–561. [[CrossRef](#)] [[PubMed](#)]
21. Kim, J.H.; Chang, S.S.; Lim, G. Fabrication of multi-scale structures with multiple X-ray masks and synchrotron hard X-ray irradiations. *Curr. Appl. Phys.* **2014**, *14*, 833–837. [[CrossRef](#)]
22. Pantenburg, F.J.; Mohr, J. Influence of Secondary Effects on the Structure Quality in Deep X-Ray-Lithography. *Nucl. Instrum. Methods Phys. Res. Sect. B Beam Interact. Mater. Atoms* **1995**, *97*, 551–556. [[CrossRef](#)]

23. Becnel, C.; Desta, Y.; Kelly, K. Ultra-deep x-ray lithography of densely packed SU-8 features: II. Process performance as a function of dose, feature height and post exposure bake temperature. *J. Micromechan. Microeng.* **2005**, *15*, 1249–1259. [[CrossRef](#)]
24. Sugiyama, S.; Khumpuang, S.; Kawaguchi, G. Plain-pattern to cross-section transfer (PCT) technique for deep x-ray lithography and applications. *J. Micromechan. Microeng.* **2004**, *14*, 1399–1404. [[CrossRef](#)]



© 2018 by the authors. Licensee MDPI, Basel, Switzerland. This article is an open access article distributed under the terms and conditions of the Creative Commons Attribution (CC BY) license (<http://creativecommons.org/licenses/by/4.0/>).

Article

Delphi Prospection on Additive Manufacturing in 2030: Implications for Education and Employment in Spain

M. Puerto Pérez-Pérez ^{1,*}, Emilio Gómez ² and Miguel A. Sebastián ¹

¹ Manufacturing and Construction Engineering Department, ETS de Ingenieros Industriales, Universidad Nacional de Educación a Distancia, Calle Juan del Rosal, 12, 28040 Madrid, Spain; msebastian@ind.uned.es

² Mechanical Engineering, Chemistry and Industrial Design Department, ETS de Ingeniería y Diseño Industrial, Universidad Politécnica de Madrid, Calle Ronda de Valencia, 3, 28012 Madrid, Spain; emilio.gomez@upm.es

* Correspondence: mperez5467@alumno.uned.es; Tel.: +34-913-986-458

Received: 7 July 2018; Accepted: 14 August 2018; Published: 22 August 2018

Abstract: The term additive manufacturing (AM) groups together a set of technologies with similar characteristics forming part of the Fourth Industrial Revolution. AM is being developed globally, as evidenced by the standards published by and the agreements between the ISO and the ASTM in 2013. The purpose of this paper is to anticipate the main changes that will occur in AM by 2030 as forecast by more than 100 Spanish experts through Delphi prospection performed in 2018. In this way, the areas, aspects, and business models with the greatest probabilities of occurrence are obtained. The need for technical experts with specific knowledge and skills requires changes to current training syllabuses. Such changes will enable students to have the profiles foreseen in these job trends. The encouragement of STEAM (Science, Technology, Engineering, Arts, and Mathematics) training through the introduction of AM in study plans may be an appropriate alternative. Finally, the consequences of the Fourth Industrial Revolution for the employment market and on jobs, particularly in Spain, are set out and the latest Spanish Research, Development, and Innovation (R&D + I) plans are summarized as the framework for the possible implementation and development of AM.

Keywords: additive manufacturing; delphi prospection; 3D printing; education; employment

1. Introduction

“Additive Manufacturing is a process for joining materials to manufacture objects starting from 3D model data, generally layer by layer, as opposed to manufacturing methods based on the elimination of material and shaping” according to the definition given in the ISO/ASTM 52900: 2015 standard [1]; therefore, the term “additive manufacturing” (AM) groups together a set of technologies with similar characteristics in terms of manufacturing forms with the ability to generate parts starting from a digital design and without using additional tools, generally by applying material one layer after another [2]. What is currently known as additive manufacturing has been referred to by different names since the 1980s, such as Rapid Prototyping (RP), Rapid Manufacturing (RM), 3D Printing, Rapid Tooling, Generative Manufacturing, eManufacturing, Constructive Manufacturing, Additive Layer Manufacturing (ALM), Direct Manufacturing, Direct Digital Manufacture (DDM), Freeform Fabrication (FFF), and Solid Freeform Fabrication (SFF), among others.

AM is not a single technology but a multitude of different technologies [3–5] forming part of what has been called the Fourth Industrial Revolution [6] and currently undergoing great development, some in the research phase and others sufficiently mature to be used in the manufacturing of finished products, i.e., products ready to be used [7,8]. AM is being developed globally as attested to by the

standardization activities [9–12], the agreements between the ISO and the ASTM in 2013 [13], and the standards published by both the ISO [1,14–18] and by AENOR [19], indicating the importance of these technologies and the intention of standardization bodies to organize them in view of their tremendous potential. Current standards provide a classification of seven “process categories”. The ISO has still not published any specific standards on technologies and, although it is working on this, the difficulty is easy to understand, since some of the said technologies are still in the development phase and have not yet achieved maturity [20]. In different ways AM will transform manufacturing processes as we currently know them. Changes in supply chains and logistics [21], in business models [22], in the resulting products (embedded electronics, multiple materials simultaneously, one-off parts, short runs, previously impossible geometries). Also changes in the sustainability of manufacturing [21–23] and the behavior of the users (now converted into designers and producers or “prosumers”, i.e., a combination of both customer and supplier [5,24]), Will also change product warranties [25]. Finally AM may imply major changes for the economy [4], society, and industry of the future [26].

The purpose of this paper is to anticipate the main changes that will arise in AM by 2030 as forecast by more than 100 Spanish experts through a Delphi prospection [27–32] conducted in 2018. The conclusions of the survey enable a likely development situation for these technologies to be sketched in for 2030, obtaining conclusions about the aspects or areas with the greatest likelihood of growth and development. The results confirm that Spanish experts believe AM will be a reality in manufacturing settings, optimizing processes and improving the sustainability of manufacturing, but that it will also take place in homes. The predominance of certain groups of technologies over others is posited. The strengths of AM and the challenges—not only technical—to be overcome are classified. The need for competent personnel with specific skills and know-how within this timeframe and the track record of experiments performed regarding teaching combined with AM [5,33–39] enable the advantages of including AM in syllabuses to be set out from primary education through to university-level courses.

2. Methodology of the Study

AM is a suite of disruptive technologies [40,41] that are transforming or complementing the world of manufacturing. The speed of their development and their latest applications in the most innovative sectors (vehicle manufacturer, aeronautics, and medicine) in opposition to the different levels of development between the various technologies and how this may affect different marketing areas raise the underlying question of this paper: How do Spanish experts believe that AM will develop over the decade ahead?

In consequence, the year 2030 was chosen as the time horizon as this was understood to be a sufficiently close period of time to enable the experts to make projections with solid criteria and also sufficiently far away for them to be able to suggest and implement conclusions that could be inferred from the results of the Delphi study (for example, suggestions regarding training).

In order to carry out a prospection on the future, it was decided to use the Delphi method, a procedure backed by its use in numerous scientific prospections and particularly useful when no objective information is available or in the face of situations of uncertainty [32,42–45]. According to Landeta [46], the main features of this method are anonymity, controlled interaction and feedback, group response, and the heterogeneity of participants.

This methodology consists of drawing up a survey around the problem formulated and sending it to a group of selected experts (round one). The results of the prospection are obtained using the set of responses as a whole. The same survey is then sent out again to experts who participated in the first round so that they can respond for a second time, but they are informed on this occasion of the overall results obtained in round one. Thus, participants can evaluate how close/far away each of their assessments are with respect to the average assessment of the population consulted and reconsider the response in round two, either by sending in the same option that they chose in round one (confirmation of the initial opinion) or else accepting the option of the average of the population as

their own (changing their initial response to accept the group average) or bringing their initial response closer to the group response but without coinciding with it (influence of the group on individual response). The responses obtained generate a new set of consultation results with greater convergence in the responses. The Delphi methodology does not limit the number of iterations that could be applied but in the case we are concerned with, two rounds have been conducted, after which the results presented here were drawn up.

Once the methodology to be used in the consultation had been pinned down, the work on drafting the questionnaire and the choice of experts began according to the four main phases in the Delphi process [47] as shown in Figure 1.

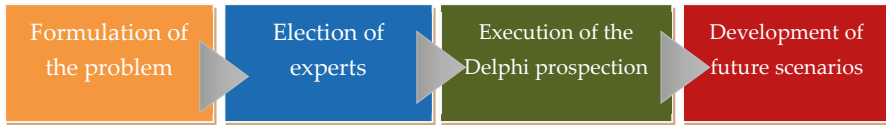


Figure 1. Main phases in the Delphi process.

The target population for the survey is made up of researchers and lecturers in areas related to manufacturing engineering and materials engineering. The heterogeneity required is achieved by bringing in experts from all over Spain, with different responsibilities in a variety of geographical areas.

In order to facilitate contributions and to be able to achieve a relevant level of response, it was decided to limit the form, format, and extension of the consultation. The conditions agreed by the authors were as follows:

Consultations must be brief, concise, and set out without any additional explanation or clarification notes. The drafting of the survey must be straightforward. Concision in responding to the form was considered a key factor in order to be able to obtain a good level of response. The form was designed in such a way that the responses could be given with a single action by participants, without the experts keying in any data or values, for example, by clicking with a mouse. In order to unify the responses, the evaluation of each question had to be qualitative, rather than quantitative (the transformation of qualitative results to quantitative values was done by the research team after compiling all the individual questionnaires). The options available to participants were always an even number, in order to prevent the existence of a central option that might provide comfort for an uncommitted choice. It was agreed that the number of possible answers would be four, giving the experts the option to choose how much they were in favor of the future projection presented: not at all, partly, mostly, or fully. The consultation had to be kept short, enabling an expert to complete it in less than five minutes. For this reason, it was agreed that the survey would present between 15 and 20 scenarios. In the end, the survey was sent out with 21 questions.

In the study, participants had to respond to the questionnaire individually, without knowing the answers given by the rest of the participants. Group data were shared with all experts only after round one was completed. The experts then decided whether or not the group response influenced them in their subsequent assessment. It was decided not to use the real-time application introduced by Gordon and Pease in 2006 [48] in which participants in a prospection could see the responses of the group of those who had responded previously, so that this information could influence their response (even in round one) [49]. Figure 2 provides a graphic outline of the steps in the process followed by the Delphi prospection.

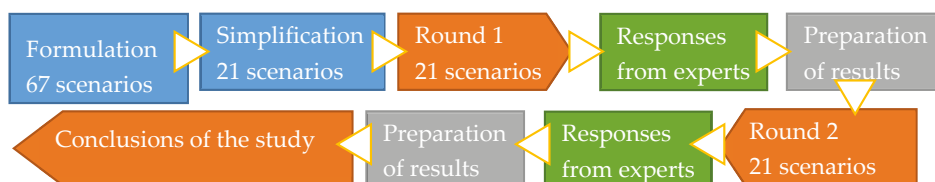


Figure 2. Main steps in the prospection process.

The tool selected for presenting and sending out the consultation was Google Forms [50] because, in addition to being free of charge, it enabled the results to be sent to Excel immediately, thus facilitating the subsequent processing of the results. Email was used for communicating information [51].

2.1. Progress of the Main Stages in the Study

2.1.1. Formulation of the Problem

As indicated above, the survey comprises 21 scenarios, the result of an effort in summarizing by the research team which initially started with 67 questions including various aspects and perspectives at first considered relevant [52]. The formulation of the survey covers the most significant aspects of the initial compilation and is divided into three distinct blocks: The first contains questions about the market, business models, supply chain, new products, services and applications, specific training, certification, intellectual property, and warranties. The second block attempts to view the process categories that will be used in 2030 depending on the manufacturing models. The third block focuses on the possible manufacturing technologies that will prevail, and on the strengths and weaknesses of AM.

These 21 scenarios were tested and adjusted by the research team as specified in detail in Tables 1–3.

Table 1. Delphi scenarios for 2030. Block 1 of questions.

No.	Block 1	Scope
1	In 2030, it will be possible to manufacture parts in more than 50% of homes in industrialized countries	Business model: Domestic/specialist store/large factory
2	In 2030, more than 50% of products will be manufactured in specialist stores with specialized personnel close to consumers (much like photocopiers in their day)	
3	In 2030, more than 50% of products will be manufactured in factories where AM is included among their manufacturing processes as just another group of technologies	
4	In 2030, more than 70% of prototypes will be manufactured using AM technologies	Development of real sectors in the market/changes in manufacturing
5	In 2030, more than 50% of tools will be manufactured using AM technologies	
6	In 2030, more than 50% of global production will be done using AM technologies	
7	In 2030, lathes will not be used for manufacturing	Quality assurance and part inspection
8	In 2030, AM processes will be monitored in real time Sensors and production control devices will be integrated and widespread in AM	
9	In 2030, there will be a new market niche for customized production runs that can only be manufactured using AM	

Table 1. Cont.

No.	Block 1	Scope
10	In 2030, users will obtain the digital formats of the parts to be manufactured from one (or more) databases	Supply chain and distribution
11	In 2030, digital formats will be free of charge and freely available	
12	In 2030, more than 50% of manufacturing will be delocalized or distributed. Production will take place at points close to the consumer and the distribution sector (supply chain) will have changed to service this new kind of manufacturing	
13	In 2030, more than 75% of AM processes and technologies will be classified, its production characteristics documented and standardized	Degree of AM maturity/qualification of personnel/legal
14	In 2030, specific training and qualification will be needed to produce using AM	
15	In 2030, there will be a procedure for issuing a warranty for unique parts (personalized) manufactured using AM technologies	
16	In 2030, AM will have contributed to the sustainability of manufacturing (manufacturing will be less polluting than at present)	Sustainability

Table 2. Delphi scenarios for 2030. Block 2 of questions.

No.	Block 2	Scope
17	In 2030, the techniques extensively used for “DOMESTIC Manufacturing” will be Photopolymerization in tanks or vats Material extrusion Material projection Powder bed fusion Agglutinant projection Localized energy deposition Sheet lamination Other	Process categories
18	In 2030, the techniques extensively used for “HYBRID Manufacturing” will be Photopolymerization in tanks or vats Material extrusion Material projection Powder bed fusion Agglutinant projection Localized energy deposition Sheet lamination Other	Process categories

Table 3. Delphi scenarios for 2030. Block 3 of questions.

No.	Block 3	Scope
19	Choose the 3 technologies that, in your opinion, will prevail over others on the market in 2030 (i.e., will be most used). Which 3 technologies will outlive the others? Stereolithography (SLA) Fused deposition modelling (FDM) Selective Laser Sintering (SLS) Selective Laser Modelling (SLM) Direct Metal Deposition (DMD) Laminated Object Manufacturing (LOM) Other	Technologies

Table 3. Cont.

No.	Block 3	Scope
20	Indicate the 3 factors you consider most relevant for AM to “impose itself” on other manufacturing methods in 2030 Democratization of manufacturing Freedom of designers. Flexibility for design changes Reduction in product development cycles and time to market Lower tooling costs Shorter production runs. Customized or one-off production Lower raw material costs (less waste) Reduction in transportation and distribution costs and times Reductions in storage: Of raw materials and finished products Contribution to environmental sustainability Other	Strengths
21	Indicate the 3 key factors you think must be resolved for AM to “take off” by 2030 The technical limitation for achieving the properties required in the end product The certification of parts and finished products Changes in the way of thinking when designing parts Industrial property rights, taxation, and the safety of the products manufactured The needs for training of AM equipment operators The cost of raw materials, machinery, and/or transportation Limitations on the volume and/or speed of manufacture The need for post-processing The integration of AM into current manufacturing methods Other	Weaknesses

2.1.2. Selection of Experts

The experts invited to take part in the study are mostly Spaniards and belong to universities, technological centers, or institutions related to manufacturing engineering and/or materials engineering, basically lecturers and researchers. The participation of the experts, classified according to their geographical location, is shown in Figure 3. A high concentration in Madrid is appreciated due to the large number of experts consulted in the universities of its geographical area.

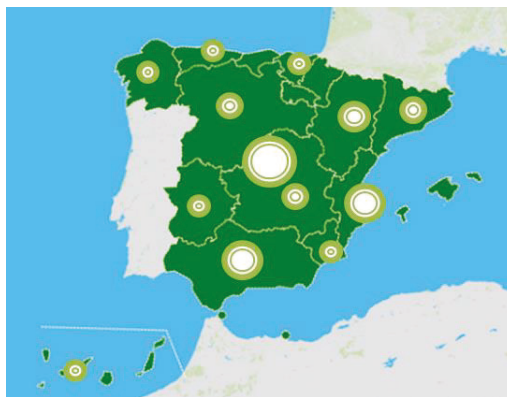


Figure 3. Participation of experts, graphic view based on the location of their centers or universities.

Of those who finally decided to complete both rounds of the survey, 21% are women. In total, they represent 31 centers and universities from 15 different regions of Spain.

2.1.3. Execution of the Delphi Prospection

The questions were posed following a different structure depending on the block that they belong to. In the first block it was possible to assess the position of the experts' proximity to the scenario proposed on a scale of 1 to 4 from "not at all" (total disagreement) to "fully" (total agreement). Only one of the four options could be chosen. In the second block, the questions were posed using a matrix, as it was intended to assess which AM process category (as defined in ISO standard 017296-2: 2015 [16]) will adapt more to the two different extreme types of manufacturing: home-based manufacturing and hybrid manufacturing. In the third block, it was necessary to choose three options from those proposed, with the expert being allowed to add another one if considered appropriate.

3. Results and Discussion

The results obtained are set out in the following three subsections. Comments and questions raised by the said results are also included.

3.1. Results of Block 1

In the first block of questions, a consensus of 50% or more was reached in 15 of the 16 scenarios proposed.

It should be highlighted that there was more than 70% of coincidence in the responses received, indicating clear agreement among participants. Of these, 77% felt that conventional lathe manufacturing will not cease to be used in the timeframe considered (2030). This question was intended to find out whether, in view of the developments and trends in AM, the experts felt that by this time a radical change would have taken place in manufacturing methods with respect to how items are manufactured at the moment, using the lathe-turning process as the most representative. A majority response in the affirmative would indicate the need for drastic changes in the training of students, so that those completing their studies in 2030 would be prepared for the radical transformation in manufacturing techniques suggested by the hypothetical response. Since the response has mostly been one of disagreement, it is inferred that current syllabuses must continue to include traditional manufacturing methods and that the changes necessary in view of the progress in manufacturing methods can be sequential.

It is also interesting that only 7% of survey interviewees felt that more than 50% of production would take place using AM technologies in 2030. In total, 94% believe that this situation will not arise or will occur only on an occasional basis, strengthening the idea that AM will end up being integrated into the current manufacturing systems without disruption (except perhaps in highly localized niches such as medicine where new and very advantageous opportunities arise with the personalization of prostheses and organs, for example [53,54]). The panorama set out is perfectly compatible with the manufacture of very short runs or single items, perhaps customized for the user. In fact, 63% of the experts felt that this niche of personalized items will be an inherent characteristic of AM technologies and that AM will be the exclusive means for their manufacture. AM techniques can, of course, be applied to personalized manufacture without any increases in cost (except in the design part), time, or effort, implying an immense differentiating advantage.

Of the participants, 54% fully agree with the statement that "In 2030, more than 50% of products will be manufactured at factories where AM is included among the manufacturing processes as just another group of technologies".

The responses mentioned above indicate that the future manufacturing model will include AM as another group of available technologies, for use whenever convenient or efficient for the processes, which will be combined and used by those responsible for manufacturing to produce as efficiently as possible. In this model, AM technologies will be integrated and used in factories just like any other current technology.

It is also indicative that 89% of experts believe that domestic manufacture of parts will be an occasional or majority reality by 2030, but there is dispersion regarding the opinion that more than 50% of households in the industrialized countries will own this technology (perhaps because of the technical requirements needed? Because of the lack of guarantee for the items manufactured? Due to the scant application they foresee? Because their use in households at the moment is mostly among amateurs?). According to the results obtained from the survey carried out to the experts, the least likely marketing model is that of a specialist store close to consumers, which may recall the model of high-street photocopying and printing centers that were so successful in the 1990s and where the work would be carried out, or at least advice provided, by a specialist technician.

One of the main challenges for the future development of a market for one-off or customized parts manufacturing is being able to give a warranty for their manufacture. How can a warranty be issued regarding a part with a unique design? Any design change with respect to a standard part may affect its aesthetics, functionality, features (its resistance or conductivity, for example), or any other aspect of the product. How can this problem be dealt with in a generalized manner? Responding to this question is key for the customized manufacturing niche to be able to grow. A 76% majority of participants believe that these issues will be resolved by 2030.

In addition, 71% of those surveyed state that AM technologies will for the most part be classified and standardized by 2030. For this to happen, the current panorama needs to be clarified: technologies need to be developed and documented prior to their subsequent standardization. The standardization of AM is currently underway, partly due to the dizzying advances in techniques, materials, uses, and other characteristics of these technologies. The current standardization status is advancing according to the work carried out by the ISO TC 261 Technical Committee [55].

How will the application of AM technologies affect the sustainability of manufacturing in 2030? Will it help to increase sustainability of made-to-order manufacturing by lowering levels of raw material and stocks in storage, or reducing the consumption of fuel for transportation because items are manufactured closer to their end users? On the other hand, will the manufacture of single parts or small runs mean that the energy synergies of serial manufacturing will be lost and more energy will be consumed? Of the responses, 78% indicate that AM will contribute mostly or fully to the sustainability of manufacturing. Obviously, this paper is not sufficiently extensive to be able to delve deeper into this issue, but this is a very interesting aspect for possible future research [56,57].

Each AM technology requires specific qualifications although, taken together, they all share a preparation in digital design techniques. If specific qualifications are going to be required in 2030 as almost 90% of participants believe either mostly (62%) or fully (27%), it is necessary for universities and technical training centers to apply changes to their syllabuses. These changes must begin as soon as possible so that the technical experts are ready by 2030. The definition of the changes required to current syllabuses is, of course, outside the scope of this study, although the skills that will be necessary in the new digital period are suggested in the last part of the document.

Of the experts, 69% believe that AM will be used occasionally to manufacture tools in contrast with 58% of them who believe that more than 70% of prototypes will be manufactured using AM technology 2030. This is an interesting differentiation from which it may be inferred that the immediacy of AM is seen as a clear advantage for prototyping, preliminary models, use in marketing, etc.

By 2030, the tools and control devices capable of monitoring and overseeing real-time production using AM techniques will have been developed. In total, 90% (61% + 29%) of interviewees believe mostly or fully that this will be a reality. Monitoring of processes simultaneously with manufacture rather than after manufacture is complete is one of the challenges currently facing AM for use as a standard manufacturing technique. Control is currently possible but it takes place after the part has been finished, requiring the post hoc rejection of any not meeting specifications (with the evident loss of resources). Real-time monitoring has the advantage of increasing the degree of specification-compliant manufacturing. The experts consulted mostly believe that this integration will arise in 2030, indicating

that the development of control techniques and sensors are fields with extensive future scope for development.

With respect to the supply chain, 60% of interviewees feel that the distribution of designs for AM will in general be done digitally, using one or more databases. Of the experts, 23% believe that this will be a reality. In other words, there is a consensus among the experts that designs will mostly be acquired from a digital market accessed by users. This confirms the theory in some publications stating that there will be two markets: one for the marketing of digital designs and another for the marketing of manufactured items. Some of these theories maintain that production values will become digital, as has already happened in other sectors (telephony and Internet). That is to say, the value of the product will lie more in its digital part (design, in this case) than in the physical manufacture of the product itself; therefore, the “value” of the design (the digital purchase) will be far higher than that of physical manufacture, which will end up being a “utility”. Another question arises in connection with this one: we wanted to know whether the experts felt that that digital market would be freely accessible (following the current trend for collaborative models) or whether payment would be required (thus monetising part of the supply chain). Most of the interviewees feel that the design market will be a pay-to-use market and will only occasionally be free of charge (or collaborative). The following questions arise immediately: Who will control this market? Large manufacturing corporations, the manufacturers of AM technology, or the users designing the models? Or perhaps it will be none of these and only large digital platforms such as Google or Amazon will be capable of reaching users?

Regarding the supply chain last questions, 61% responded that the distribution sector is going to undergo a transformation towards delocalization as confirmed in the work by Sray et al. [58]. Of the experts, 55% mostly feel that “more than 50% of manufacturing will be delocalized or distributed” and 6% believe that that scenario will be a reality. This question explores the possible changes that may arise in the distribution sector. A large part of centralized mass manufacturing models corresponds to product logistics and distribution. Manufacturing close to where assumption takes place would alter the weighting of the different segments in the production chain. Distribution, currently the key to mass production systems, may lose its relative importance in future, probably giving rise to a transformation in order to serve users differently than at present.

The numerical values for the results obtained are shown in Figure 4.

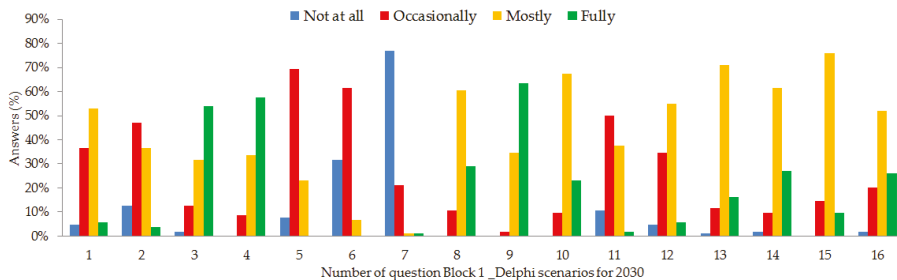


Figure 4. Results of Block 1 questions (%).

3.2. Results of Block 2

As mentioned above, the two questions included in this block tried to glimpse the process categories (according to the classification in the ISO 17296-2 standard [16]) that will apply in each of the two extreme manufacturing models: domestic manufacture and hybrid manufacture (in factories).

According to the participants consulted, domestic “printers” based on “material extrusion” AM technologies are most likely to be implemented in homes.

However, “material projection” and “localized energy deposition” technologies (76% including both “mostly” and “fully”) followed by extrusion technologies are those believed by experts to be in most widespread use in hybrid manufacture by 2030 (in use just like any other technology in factories). Sheet lamination and photopolymerization technologies will be used less in manufacturing centers, according to these results.

The numerical values for the results obtained are shown in Figure 5.

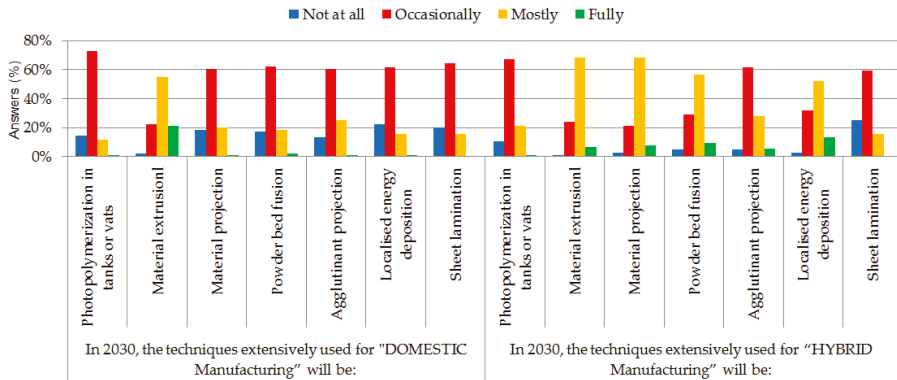


Figure 5. Results of Block 2 questions (%).

3.3. Results of Block 3

In this set of questions, we were trying to consult opinions about which technologies will lead the field in 2030, and also discover the three strengths of AM and the three most important challenges to be resolved.

According to the specialists, the technologies that will prevail over others in the market in 2030 are fused deposition modelling (FDM), selective laser sintering (SLS), and selective laser modelling (SLM), as shown in Table 4.

Table 4. Results on technologies. Block 3 (%).

AM Technologies	Prevalence
Fused Deposition Modelling (FDM)	29%
Selective Laser Sintering (SLS)	25%
Selective Laser Modelling (SLM)	25%
Direct Metal Deposition (DMD)	12%
Laminated Object Modelling (LOM)	2%
Stereolithography (SLA)	6%
Others	1%

The results indicate that the most relevant factors for the development of AM are related to the product itself and to production and market factors, as shown in Table 5. Design freedom gives the possibility to manufacture products with as-yet-impossible geometries. In addition, flexibility in design changes gives the ability to create different products with the same base, thus generating infinite possibilities for personalization, adaptation, etc. Secondly, the experts are of the opinion that being able to produce short manufacturing runs or one-off items (personalization) is a determining factor for AM to take off. Personalized manufacturing is a unique feature of AM technologies that does not make the process more expensive, except in the digital part, since each item requires its own design which will not be reused. Lastly, the reduction in development time and time to market is the

third most voted characteristic. This quality enables items produced with AM technologies to be used for the verification of a product's operation on the market with possible savings in terms of time and cost with respect to current procedures, a matter of great value for developers and promoters.

Table 5. Results on the strengths of AM. Block 3 (%).

Factors for the Development of AM	Prevalence
Freedom of designers. Flexibility for design changes	28%
Shorter production runs. Customized or one-off production	25%
Reduction in product development cycles and time to market	21%
Reduction in transportation and distribution costs and times	6%
Democratization of manufacturing	5%
Lower tooling costs	5%
Reductions in storage: of raw materials and finished products	5%
Lower raw material costs (less waste)	3%
Contribution to environmental sustainability	2%
Others	0%

The technical limitation for achieving the properties required in the end product stands out among the other challenges to be overcome. Anisotropy [59] and the control of physical properties (such as resistance to traction, size verification, or the surface finish), of chemical properties, or of any other kind of property required in the product are clearly an essential current limitation for the use of AM technologies beyond one-off developments or highly specific market niches. In addition to the improvement in the control of products' properties, the experts believe that there is currently a limitation on the manufacturing process (a limitation on manufacturing volume, mainly due to the manufacturing equipment, production speed, or a combination of both factors). The latest developments from equipment manufacturers try to resolve the speed limitation by placing multiple heads that work simultaneously. Lastly, the certification and warranty of parts and finished products is the third important challenge receiving the most votes from the participants interviewed, as shown in Table 6. It is useless to manufacture the desired part to the required specifications and at a suitable speed if, at the end of the day, it is impossible to certify what has been produced. Certification is one of the constraints currently found in sectors like aeronautics [60].

Table 6. Results on AM weaknesses. Block 3 (%).

AM Weaknesses	Prevalence
The technical limitation for achieving the properties required in the end product	28%
Limitations on the volume and/or speed of manufacture	21%
The certification of parts and finished products	19%
The integration of AM into current manufacturing methods	10%
The cost of raw materials, machinery, and/or transportation	7%
Changes in the way of thinking when designing parts	6%
The need for post-processing	4%
Industrial property rights, taxation, and the safety of the products manufactured	3%
The needs for training of AM equipment operators	1%
Others	1%

4. Implications for Education and Design of Training Programs

Several studies have been published on the development and/or implementation status of AM in different countries—USA (Minnesota) [61], Finland [62,63], South Africa [64,65], Germany [66], Mexico [67], India [68], UK [69], China and USA [70]—analyzing a number of aspects, an indication of the importance of these technologies.

The prospect of using information and communication technologies (ICTs) and massive automation (which might include, among others, the use of AM, smart software, robotics, drones, Artificial Intelligence (AI), or Big Data) ushers in the need for specialists to carry out the necessary research in order to overcome current challenges as well as technicians able to lead the technologies to a suitable level of maturity for them to be used on the market and, in particular, in the manufacturing industry.

In order to have human capital available with skills in these fields of optimization and ICTs, it is necessary to design a national-level training plan starting from basic education (primary schools) all the way up to university degrees, particularly in engineering [71]. The training needed is directly related to STEAM (Science, Technology, Engineering, Arts, and Mathematics) and ICTs.

The inclusion of the use of AM in current syllabuses is necessary if the opinions of Spanish experts turn out to be true and, in 2030, technicians with specific qualifications for AM manufacturing are going to be needed.

Education must provide the knowledge and skills for future professionals to be able to work in the future market, within the framework of the Fourth Industrial Revolution. Future technicians will be required to have cognitive competence in order to deal with a changing technological environment (mathematics, logic, data processing, project management). In addition, they will need to have noncognitive skills [72] (critical thinking, teamwork, achievement of goals, interpersonal relationship skills, or troubleshooting abilities [73]), bearing in mind that jobs requiring noncognitive skills will be the last to be replaced by automated processes and therefore will be among the most valued. The skills mentioned above should be transmitted through education, although some of these are difficult to measure and evaluate using conventional testing [74].

AM technologies require the use of different academic disciplines such as material sciences, machinery design, fluid mechanics, heat transfer, computing, statistics, graphic design, etc. These disciplines can be treated as and when practical manufacturing is developed, in order to help with their acquisition or a deeper understanding depending on the prior training of the students in question [34].

A number of different experiments have shown that the use of AM in educational processes speeds up the training and makes it more interesting, bringing education closer to the real world. Some experiments in the use of AM technologies in training at different levels of education and in multiple countries have provided an overview of their usefulness and the knowledge and skills developed through these practices.

There are several actions and experiments reported in the literature documenting the advantages of introducing AM into training, both for schools [33,75–78] and for universities [36,37,39,79], for teachers [38], national plans [69,80], and even in libraries [35]. These experiments have shown that, in addition to the disciplines mentioned inherent to manufacturing, participants also develop other nontechnical skills such as teamwork and collaboration, creativity, flexibility vis-à-vis changes, communication skills, handling of changing information, concentration, planning, perseverance, and self-control.

Although there is evidence that training through AM is very useful, the experiences documented to date have been carried out by professors or researchers using their own methodology. There is as yet no specific textbook or methodology for implementing this kind of training [5], yet, nonetheless, the conclusions of the practical activities documented show a positive result.

5. Implications and Consequences for Employment

The emergence of technologies in society, new consumer behavior, and the birth of new business models form the pillars of what is known as the Fourth Industrial Revolution [6,81,82].

AM is a group of technologies of great importance within the generic framework of the Fourth Industrial Revolution, since on the one hand it moves within the ICTs, but on the other it is clearly a productive resource that is largely alternative to the more traditional manufacturing processes (such as it emerges from the prospective study of the previous section), even to those processes with higher levels of automation. Therefore, in the field of future employment and its expectations, the increasing use of AM technologies will contribute to enhancing the strategic nature of ICTs and highly automated manufacturing, representing a niche for employment framed in both ICTs and in highly automated advanced manufacturing processes.

Technological transformation will affect employment and the welfare state in a manner that will not be homogeneous across industries, occupations, and countries [83–89]. Numerous authors defend the direct correlation between an increase in automation and the level of unemployment based on the idea that robots will increasingly be able to carry out tasks currently allocated to humans [88] as their dexterity increases, becoming more efficient and requiring no rest. The truth is that the Fourth Industrial Revolution is full of uncertainties; not only with regard to employment levels but also the quality and variety of the same, and also with respect to a variety of aspects such as business models, in-demand professions, displaced occupations, and those others that will emerge to offer new services, earned income, and legislation, to mention a few.

5.1. *New Professions and the Disappearance of Some Current Occupations*

Smart software, robotics, Big Data, Artificial Intelligence (AI), drones, and Additive Manufacturing (AM) will displace certain activities and professions and will lead to the development of other, new professions that do not currently exist [90,91]. The risk of job losses in Spain over the next 10–12 years as a result of automation (jobs with at least a 70% probability of being replaced by machines) is estimated at 12% according to the study *The Risk of Automation for Jobs in OECD Countries* [92], published in May 2018. According to BBVA Research published in March, 2018 [86], this figure is 36%. This result is based on a 2016 study by Frey and Osborne [88] which classified 702 different professions in the United States according to their chances of being substituted as a result of automation.

Several authors [92] put the results of the study by Frey and Osborne into context [88], arguing that although the rate of technological development is exponential (one of the characteristics of the Fourth Industrial Revolution), integration of such technology in society and industry does not depend exclusively on technological development factors but must be considered more holistically to take into account the political and social context of each country and must also consider the human factor; that is, new technologies that are developed will be taken on by society not upon their development but once society is ready for them.

Quantitative values help us understand the significance of this issue and which prevention measures are essential. By considering the automation probabilities obtained by Frey and Osborne [88] and applying them to the active population classified by economic activity in the first quarter of 2018 in Spain published by the National Statistics Institute [93], we find that 1,750,000 persons are employed in jobs with a high probability of automation (those with a probability above 70% of being replaced by machines), and only 1,550,000 are at a low risk of automation (with a lower than 30% probability of being ousted by machines). This information can be seen in Table 7 and is displayed graphically in Figure 6.

Table 7. Distribution of the occupied population in Spain by level of automation. Table prepared using figures from (***) the National Statistics Institute (INE) on population for the first quarter of 2018 [93] and (*) information on the probability of automation and the distribution of the occupied population by level of automation taken from BBVA Research [86]. Own production.

Sector of Activity	Occupied Population According to Industry.		Probability of the Distribution of the Occupied Population per Automation Level (%) (*)		Probability of the Distribution of the Occupied Population Per Automation Level (Absolute Value) (Thousands of Persons)		
	Both Genders.	Percentage (**)	Low	High	Low	Medium	High
Status	Absolute value (**) 2018T1 (thousands of persons)	2018T1 (%)	<0.3	>0.7	<0.3	>0.3 and <0.7	>0.7
A Agriculture, farming, forestry, and fisheries	833.8	4.4	0.5	10.3	4.2	743.7	85.9
B Extractive industries	34.3	0.2	0.1	0.2	0.0	34.2	0.1
C Manufacturing industry	2420.7	12.8	7.6	18.7	184.0	1784.1	452.7
D Energy supply (electricity, gas, steam, and air conditioning)	73.8	0.4	0.6	0.2	0.4	73.2	0.15
E Water supply and treatment, waste management	147.6	0.8	0.3	0.8	0.4	146.0	1.2
F Construction	1151.9	6.1	4.4	5.3	50.7	1040.2	61.1
G Wholesale and retail trade; motor industry	2934.2	15.5	16.2	21.3	475.3	1833.9	624.9
H Transport and storage	958.5	5.1	1.2	4.2	11.5	906.7	40.3
I Hotel and catering trade	1558.5	8.3	2.6	16.3	40.5	1263.9	254.0
J Information and communications	587.2	3.1	4.9	0.8	28.8	553.7	4.7
K Financial and insurance activities	453.1	2.4	2.1	2.5	9.5	432.3	11.3
L Real estate activities	136.0	0.7	0.3	0.4	0.4	135.0	0.5
M Professional, scientific, and technical activities	974.3	5.2	9.0	2.6	87.7	861.3	25.3
N Clerical activities and ancillary services	916.9	4.9	1.3	3.0	11.9	877.5	27.51
O Public Administration and defense; Social Security	1327.1	7.0	9.8	6.5	130.1	1110.8	86.3
P Education	1323.0	7.0	17.8	1.6	235.5	1066.3	21.2
Q Healthcare activities and social services	1571.3	8.3	16.5	2.6	259.3	1271.2	40.8
R Artistic, leisure, and entertainment activities	373.6	2.0	2.7	1.7	10.1	357.2	6.3
S Other services	459.0	2.4	1.3	1.0	6.0	448.4	4.6
T Domestic service activities in households	637.7	3.4	0.7	0.8	4.5	628.1	5.1
U Activities in organizations	1.8	0.0	-	-	-	-	-
Total	18,874.3	100.0	99.9	100.8	1550.7	15,567.7	1754.0

5.2. Digital Divide

One of the consequences of automation will be that new, as-yet-undefined jobs related to technology will emerge. These occupations will require specific training and skills that not all the population will have access to. Jobs with higher qualification requirements will be increasingly better paid and jobs with low qualification requirements will be increasingly worse paid. In all of these, routine tasks may be automated. This may give rise to the displacement in the outsourcing of routine tasks, which are currently outsourced to countries with lower wages and which, in the future, may be outsourced to machines and robots [6]. This situation gives rise to what is known as the “digital divide” between workers in the digital market and those outside it. We can think of it as a society with separate “castes” as a result of a highly polarized labor market (which is very dangerous for social stability).

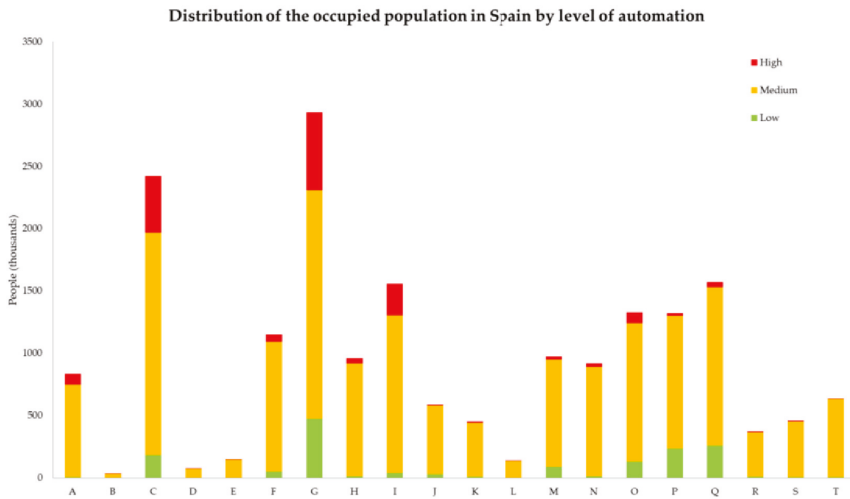


Figure 6. Probability of the distribution of the occupied population in Spain according to the level of automation. A Agriculture, farming, forestry, and fisheries; B Extractive industries; C Manufacturing industry; D Energy supply (electricity, gas, steam, and air conditioning); E Water supply and treatment, waste management; F Construction; G Wholesale and retail trade, motor industry; H Transport and storage; I Hotel and catering trade; J Information and communications; K Financial and insurance activities; L Real estate activities; M Professional, scientific, and technical activities; N Clerical activities and ancillary services; O Public Administration and defence, Social Security; P Education; Q Healthcare activities and social services; R Artistic, leisure, and entertainment activities; S Other services; T Domestic service activities in households.

As Frey and Osborne established [88], if we separate the labor market into three segments—highly paid, highly technological jobs (or with “human” requirements); average jobs (not very technological and not very routine work) with average pay; and highly routine work with very low wages—then those in the middle tier are the most prone to being replaced by automation as the cost/benefit ratio will be more profitable (sales, administration, transport, service, productive or manufacturing tasks). The first group requires high qualifications or characteristics that are difficult to automate and are related to human behavior (programmers, specialists in digital security, designers, psychologists, doctors, artists, teachers, judges, etc.); wages for the last group will be so low that the investment required in automation will not be worthwhile (maid services, delivery persons, farming harvesters).

Unlike previous industrial revolutions, even nonroutine jobs which are not currently considered as being open to being robotized will be open to being robotized in this so-called Fourth Industrial

Revolution. This change will take place as the skills required are developed, such as sensorization, artificial intelligence, and massive storage in a super-reduced space (for instance, self-driving vehicles).

In order to carry out this training at all levels, including at business level, policies must be put in place to foster research development in all areas (university, business, individual, institutes of technology) and to promote reindustrialization to compensate for the loss in relevance of industry in favor of services in developed economies [94–96]. In short, implementing an effective employment policy [97]. It seems necessary to generate a structure that suitably fosters labor reintegration and lifelong training and guarantees equal opportunities [98–101]. In particular, the reintegration into the labor market of workers who missed the technological train and whose “digital divide” widens every day will require specific support and training to return to paid employment.

5.3. Labor Market

The labor market will change (and is changing) both in geolocation and in regulation. Globalization allows companies not to have boundaries. This has an effect not only on multinationals with headquarters in different countries [102]. Small and medium enterprises will also be global—many already are—since their services may be hired over the Internet.

Employees will work in a global market, leading to labor and trade union regulations that are no longer national in scope. There will be no territorial limits. Industrial relations will be ultraflexible in regard to both jobs and competences, and highly diversified: new regulations will be required to regulate this added staff flexibility (workforce on demand). Our grandparents worked for one company all of their lives; it is now normal to work for 3 to 7 companies in the course of a career; our children will simultaneously work for 7 different companies, probably carrying out different tasks. Companies will try to hire talented staff (Digital Talent) regardless of their place of birth.

The ties to a job or to a single company will weaken until they disappear, there will be constant changes in activity and/or employment, and many employees will not be required to go to work in an office. Employment will be a mixture between a paid job and self-employment [103]. This model is called the gig economy, collaborative economy [104], or freelance economy, using the Internet as a platform [105]. By way of example, we may consider the Uber model; namely, short-lasting jobs for specific tasks. Highly qualified professionals will work independently for several companies, organize their own time, and develop the skills needed to participate in multiple work teams [106]. In the gig economy, everyone is their own boss, setting their own working times (earnings permitting); however, workers are neither paid employees nor self-employed workers. Social protection for these workers must be developed accordingly. Workers will adjust to market requirements and, similarly, legislation must change to follow these labor models [96]. One of the possibilities is evolving towards “flexicurity”, which considers “the protection of flexible employment contracts and training and reintegration policies” [6], a model that Scandinavian countries have already developed.

Flexibility to carry out different jobs will be a valued skill, which leads to the need for continuous and permanent training throughout a worker’s professional life, affording them the quality of adaptation in such a way that education in the 21st century should be “teaching to learn”. “Education is closely linked to technological change: it isn’t only shaping the inventors of the present and future but is providing the entire population with the tools required to adapt to and make the most of new technologies” [74,107].

In order to mitigate the effects that the Fourth Industrial Revolution may have, public administrations should draw up and publish in advance a plan to eliminate institutional barriers and foster infrastructures minimizing any negative impacts on the labor market.

Investment in human capital (a production factor that depends not only on quantity but also on quality, the level of training, and productivity of persons involved in a productive process) will be an increasingly determining factor for economic growth [108].

To this end, teaching centers and universities must foster a more extensive and tighter collaboration between University and Business, especially in Spain where university research is not easily transferred to companies, which in turn leads to a low impact of financing in private research.

5.4. Investment in Technological R&D + I (Research, Development, and Innovation) in Spain

The development of AM and its use in manufacturing depend on culminating several research, development, and innovation processes. R&D + I investment in each country is a benchmark for the support given by government policy to fostering economic growth and productivity, and is understood as the basis for progress and social wellbeing in that country.

Below is a summary of the main plans and policies related to R&D + I in Spain.

In response to the Europe 2020 Strategy [109], Spain amended its “National Science and Technology Strategy” (2007–2015) [110] by passing the “National Innovation Strategy” (E2i) in 2010, with five priority axes [111].

In 2012, the “National Strategy for Science and Technology and Innovation 2013–2020” [112] replaced the earlier plans in reaction to the fall in R&D financing in Spain (changing the upwards trend of previous decades), partly as a result of the economic crisis, and after verifying that the results obtained by the two former plans had not reached the objectives set out.

The “National Plan for Scientific and Technical Research and Innovation 2017–2020” [113] is the instrument used by the General State Administration to implement the scope of objectives set out by the Europe 2020 strategy and the Spanish Strategy. This Plan only includes financial aid allocated to R&D and is made up of four State Programs (similar to the “National Plan for Scientific and Technical Research and Innovation 2013–2016” [114].)

The trend seen in the main indicators reflects the state of R&D in Spain. These indicators can be consulted on the FECYT website (Indicators of the Spanish System for Science, Technology and Innovation. 2017 Edition) [115].

6. Conclusions

The term AM groups together a suite of technologies undergoing development and framed within the so-called Fourth Industrial Revolution. The results of a Delphi prospection carried out with over 100 Spanish experts have highlighted that AM will be included within existing manufacturing processes and will change various aspects of manufacturing: From the business models and the distribution chain to the concept of client and supplier. The likeliest panorama in 2030, according to the responses from experts, includes the integration of AM as more efficient and more sustainable processes in factories and the domestic use of these technologies. The predictions indicate that many processes will be developed and classified in AM, and that certification and standardization will be a reality. AM will grow most in the prototype market, occasionally in the tools market, and will be of practically exclusive use in customized manufacture. AM has certain features that will boost its take-off, such as the possibility of shorter production runs, the capacity to manufacture parts with geometries that are impossible using current methods, flexibility with respect to design changes, or the prospect of generating unique items. For this to happen, AM has to overcome certain challenges, such as ensuring the quality of each phase of the production process (so that the properties of the products obtained in this way can be certified), the lack of homogeneity in product properties, or the limitation of current AM machines with regard to manufacturing volume or production speed. The groups of AM technologies that will be in greatest use in domestic manufacturing models and in factory manufacturing are specified. The manufacturing business model may change. The designs for parts will be housed in digital databases that will mostly be available on a pay-for-use basis, according to our interviewees. The distribution chain will be changed as and when changes arise in the size and location of production centers.

The result of the study considers a future in which AM is developed and integrated into manufacturing processes. For this transformation to be successful, it will be necessary to have

competent technicians available and adequately trained to cope with the changes that will arise. The skills and know-how needed for this are still pending definition, development, and offering at universities and training centers. One of the possibilities is the use of AM itself as a training tool, through which not only is a knowledge of the many areas needed for the achievement of manufacturing communicated, but the students also develop noncognitive skills such as teamwork, change management, or the acceptance of errors, which will be highly appreciated in that new context. The use of AM also provides practical training that motivates and challenges students.

The use of AM, alongside other digital techniques such as smart software, robotics, Big Data, and Artificial Intelligence (AI), is part of the Fourth Industrial Revolution. This Revolution will entail a change in the job market, polarizing professions and occupations depending on whether or not they use these technologies. Some professions will disappear and others, as yet unknown, will become essential. Permanent training and the inclusion of STEAM as part of educational plans are presented as options to minimize these effects.

Author Contributions: Conceptualization, E.G. and M.A.S.; Investigation, M.P.P.-P.; Methodology, M.A.S.; Supervision, E.G. and M.A.S.; Validation, E.G.; Writing—original draft, M.P.P.-P.; Writing—review & editing, M.P.P.-P., E.G. and M.A.S.

Funding: This research was funded by the Annual Grants Call of the E.T.S.I.I. of UNED through the project of reference [2018-ICF10].

Acknowledgments: The present paper has been produced within the scope of the doctoral activities carried out by the lead author at the International Doctorate School of the Spanish National Distance-Learning University (EIDUNED_ Escuela Internacional de Doctorado de la Universidad Nacional de Educación a Distancia). The authors are grateful for the support provided by this institution. The authors of this work would also like to thank the more than 100 experts for their selfless participation in the Delphi prospecting process.

Conflicts of Interest: The authors declare no conflict of interest.

Acronyms

AENOR	Asociación Española de Normalización y Certificación; Spanish Association for Standardization and Certification
AI	Artificial Intelligence
ALM	Additive Layer Manufacturing
AM	Additive Manufacturing
ASTM	ASTM International “American Society for Testing and Materials”
DDM	Direct Manufacturing, Direct Digital Manufacture
DMD	Direct Metal Deposition
EIDUNED	Escuela Internacional de Doctorado de la Universidad Nacional de Educación a Distancia; International Doctorate School of the Spanish National Distance-Learning University
FDM	Fused deposition modelling
FECYT	Fundación Española para la Ciencia y Tecnología; Spanish System for Science, Technology and Innovation
FFF	Freeform Fabrication
ICTs	Information and Communication Technologies
INE	Instituto Nacional de Estadística; National Statistics Institute
ISO	International Organization for Standardization
TC 261	Technical Committee 261
LOM	Laminated Object Manufacturing
R&D + I	Research, Development, and Innovation
RM	Rapid Manufacturing
RP	Rapid Prototyping
SFF	Solid Freeform Fabrication
SLA	Stereolithography

SLM	Selective Laser Modelling
SLS	Selective Laser Sintering
STEAM	Science, Technology, Engineering, Arts, and Mathematics
UNED	Universidad Nacional de Educación a Distancia; Distance Learning University

References

1. ISO/ASTM 52900 2015 (ASTM F2792): *Additive Manufacturing-General Principles-Terminology*; International Organization for Standardization: Geneva, Switzerland, 2015.
2. Gibson, I.; Rosen, D.; Stucker, B. *Additive Manufacturing-3D Printing, Rapid Prototyping, and Direct Digital Manufacturing*; Springer: Berlin, Germany, 2015.
3. Mueller, B. Additive manufacturing technologies-Rapid prototyping to direct digital manufacturing. *Assem. Autom.* **2012**. [CrossRef]
4. Steenhuis, H.; Pretorius, L. Consumer additive manufacturing or 3D printing adoption: An exploratory study. *J. Manuf. Technol. Manag.* **2016**, *27*, 990–1012. [CrossRef]
5. Ford, S.; Minshall, T. 3D Printing in Teaching and Education: A Review of Where and How It is Used. Additive Manufacturing. Available online: https://www.researchgate.net/publication/308204531_3D_printing_in_education_a_literature_review (accessed on 14 August 2018).
6. González-Páramo, J. Cuarta Revolución Industrial, Empleo y Estado de Bienestar. Available online: <http://www.racmyp.es/R/racmyp/docs/anales/A95/A95-7.pdf> (accessed on 14 August 2018).
7. Gibson, I. The changing face of additive manufacturing. *J. Manuf. Technol. Manag.* **2017**, *28*, 10–17. [CrossRef]
8. Wohlers, T. Wohlers Report 2016; Wohlers Associates. Available online: <https://wohlersassociates.com/2016report.htm> (accessed on 14 August 2018).
9. Barkouskaya, N. Standardization of 3D Printing. Available online: <https://rep.bntu.by/bitstream/handle/data/14868/1.%20146-147.pdf?sequence=1> (accessed on 14 August 2018).
10. Pandian, A.; Belavek, C. A Review of Recent Trends and Challenges in 3D Printing. Available online: <https://pdfs.semanticscholar.org/e143/888b62e0720fe5560d131f462e0cd7737756.pdf> (accessed on 14 August 2018).
11. García, A.M.; Pérez, I.S.; Gisbert, J.G. Acción de soporte a la normalización en fabricación aditiva. Proyecto SASAM. *3C Technol.* **2013**, *2*, 1–8.
12. Monzón, M.; Ortega, Z.; Martínez, A.; Ortega, F. Standardization in additive manufacturing: Activities carried out by international organizations and projects. *Int. J. Adv. Manuf. Technol.* **2015**, *76*, 1111–1121. [CrossRef]
13. *ISO and ASTM International Unveil Framework for Creating Global Additive Manufacturing Standards*; International Organization for Standardization: Geneva, Switzerland, 2016.
14. ISO/ASTM 52921: 2013. *Standard Terminology for Additive Manufacturing-Coordinate Systems and Test Methodologies*; International Organization for Standardization: Geneva, Switzerland, 2013.
15. ISO 52915: 2013. *Standard Specification for Additive Manufacturing File Format (AMF) Version 1.1*; International Organization for Standardization: Geneva, Switzerland, 2013.
16. ISO 17296-2: 2015. *Additive Manufacturing-General Principles-Part 2: Overview of Process Categories and Feedstock*; International Organization for Standardization: Geneva, Switzerland, 2015.
17. ISO 17296-3: 2014. *Additive Manufacturing-General Principles-Part 3: Main Characteristics and Corresponding Test Methods*; International Organization for Standardization: Geneva, Switzerland, 2014.
18. ISO 17296-4: 2014. *Additive Manufacturing-General Principles-Part 4: Overview of Data Processing*; International Organization for Standardization: Geneva, Switzerland, 2014.
19. AENOR, Asociación Española de Normalización y Certificación. AENOR_Buscador de Normas. Available online: <http://www.aenor.es/aenor/normas/buscadornormas/resultadobuscnormas.asp> (accessed on 14 August 2018).
20. Pérez-Pérez, M.P.; Sebastián, M.A.; Gómez-García, E. Análisis y Propuesta Para la Utilización de Los Contenidos en Normas Técnicas Para la Enseñanza de la Fabricación Aditiva. In Proceedings of the Acta XXII Congreso Nacional de Ingeniería Mecánica, Madrid, Spain, 19–21 September 2018. Available online: <http://www.xxiicnim.es> (accessed on 16 August 2018).
21. Srari, J.S.; Gregory, M.J. A supply network configuration perspective on international supply chain development. *Int. J. Oper. Manag.* **2008**, *5*, 386–411. [CrossRef]

22. Despeisse, M.; Ford, S.; Viljakainen, A. Product Life Extension through Additive Manufacturing. Available online: https://www.researchgate.net/profile/Melanie_Despeisse/publication/289335537_Product_life_extension_through_additive_manufacturing_The_business_model_implications/links/568b945708ae1975839f58b9.pdf (accessed on 14 August 2018).
23. Rayna, T.; Striukova, L. From rapid prototyping to home fabrication: How 3D printing is changing business model innovation. *Technol. Forecast. Soc. Chang.* **2016**, *102*, 214–224. [CrossRef]
24. Benkler, Y. *The Wealth of Networks: How Social Production Transforms Markets and Freedom*; Yale University Press: London, UK, 2006.
25. Jiang, R.; Kleer, R.; Piller, F.T. Predicting the future of additive manufacturing: A Delphi study on economic and societal implications of 3D printing for 2030. *Technol. Forecast. Soc. Chang.* **2017**, *117*, 84–97. [CrossRef]
26. Birtchnell, T.; Urry, J. 3D, SF and the future. *Futures* **2013**, *50*, 25–34. [CrossRef]
27. Landeta, J. *El método Delphi. Una Técnica de Previsión del Futuro*; Ariel: Barcelona, Spain, 1999.
28. Christie, C.A.; Barela, E. The Delphi technique as a method for increasing inclusion in the evaluation process. *Can. J. Progr. Eval.* **2005**, *20*, 105.
29. Giannarou, L.; Zervas, E. Using Delphi technique to build consensus in practice. *Int. J. Bus. Sci. Appl. Manag.* **2014**, *9*, 65–82.
30. Julio, C.A.; Alfonso, I.M. Empleo del método Delphi y su empleo en la investigación en comunicación y educación. *Edutec* **2014**, *48*, 1–16.
31. Mercedes, R.A.; Merce, T.F. El método Delphi. *REIRE. Revista d'Innovació i Recerca en Educació* **2016**, *9*, 87–102.
32. Dalkey, N.C. *An Introduction to Technological Forecasting*; Routledge: London, UK, 2018; pp. 25–30.
33. Milić, M.; Maričić, S.; Radolović, D. Implementation of additive technologies in elementary education. *MATEC Web Conf.* **2017**, *137*, 02007. [CrossRef]
34. Go, J.; Hart, A.J. A framework for teaching the fundamentals of additive manufacturing and enabling rapid innovation. *Add. Manuf.* **2016**, *10*, 76–87. [CrossRef]
35. Elrod, R.E. Classroom innovation through 3D printing. *Libr. Hi. Tech. News.* **2016**, *33*, 5–7. [CrossRef]
36. Minetola, P.; Iuliano, L.; Bassoli, E.; Gatto, A. Impact of additive manufacturing on engineering education—evidence from Italy. *Rapid Prototyp. J.* **2015**, *21*, 535–555. [CrossRef]
37. Gatto, A.; Bassoli, E.; Denti, L.; Iuliano, L.; Minetola, P. Multi-disciplinary approach in engineering education: Learning with additive manufacturing and reverse engineering. *Rapid Prototyp. J.* **2015**, *21*, 598–603. [CrossRef]
38. Schelly, C.; Anzalone, G.; Wijnen, B.; Pearce, J.M. Open-source 3-D printing technologies for education: Bringing additive manufacturing to the classroom. *J. Vis. Lang. Comput.* **2015**, *28*, 226–237. [CrossRef]
39. Kostakis, V.; Niaros, V.; Giotitsas, C. Open source 3D printing as a means of learning: An educational experiment in two high schools in Greece. *Telemat. Inf.* **2015**, *32*, 118–128. [CrossRef]
40. Dawson, F. How Disruptive Is 3D Printing Really. Available online: <https://www.forbes.com/forbes/welcome/?toURL=https://www.forbes.com/sites/freddiedawson/2014/09/30/how-disruptive-is-3d-printing-really/&refURL> (accessed on 14 August 2018).
41. Potstada, M.; Parandian, A.; Robinson, D.K.; Zybura, J. An alignment approach for an industry in the making: DIGINOVA and the case of digital fabrication. *Technol. Forecast. Soc. Chang.* **2016**, *102*, 182–192. [CrossRef]
42. Rowe, G.; Wright, G. Expert opinions in forecasting: The role of the Delphi technique. In *Principles of Forecasting*; Springer: Berlin, Germany, 2001; pp. 125–144.
43. Dalkey, N.C. The Delphi Method: An Experimental Study of Group Opinion. Available online: https://www.rand.org/content/dam/rand/pubs/research_memoranda/2005/RM5888.pdf (accessed on 14 August 2018).
44. Okoli, C.; Pawlowski, S.D. The Delphi method as a research tool: An example, design considerations and applications. *Inf. Manag.* **2004**, *42*, 15–29. [CrossRef]
45. Nowack, M.; Endrikat, J.; Guenther, E. Review of Delphi-based scenario studies: Quality and design considerations. *Technol. Forecast. Soc. Chang.* **2011**, *78*, 1603–1615. [CrossRef]
46. Landeta, J. *El Método Delphi. Una Técnica de Previsión del Futuro*. Available online: http://prospectiva.eu/zaharra/Metodo_delphi.pdf (accessed on 14 August 2018).
47. Heiko, A.; Darkow, I. Scenarios for the logistics services industry: A Delphi-based analysis for 2025. *Int. J. Prod. Econ.* **2010**, *127*, 46–59.
48. Gordon, T.; Pease, A. RT Delphi: An efficient, “round-less” almost real time Delphi method. *Technol. Forecast. Soc. Chang.* **2006**, *73*, 321–333. [CrossRef]

49. Gnatzy, T.; Warth, J.; Vonder Gracht, H.; Darkow, I. Validating an innovative real-time Delphi approach-A methodological comparison between real-time and conventional Delphi studies. *Technol. Forecast. Soc. Chang.* **2011**, *78*, 1681–1694. [CrossRef]
50. How to Use Google Forms. Available online: <https://support.google.com/docs/answer/6281888?co=GENIE.Platform%3DDesktop&hl=en> (accessed on 14 August 2018).
51. Outlook Options (Advanced). Available online: <https://support.office.com/en-us/article/outlook-options-advanced-809f40dc-4c5e-43f7-95c4-d92a324ff8cb> (accessed on 14 August 2018).
52. Mitroff, I.I.; Linstone, H.A. *The Unbounded Mind: Breaking the Chains of Traditional Business Thinking*; Oxford University Press: Oxford, UK, 1995.
53. Sun, J.; Vijayavenkataraman, S.; Liu, H. An overview of scaffold design and fabrication technology for engineered knee meniscus. *Materials* **2017**, *10*, 29. [CrossRef] [PubMed]
54. Zhang, X.; Fang, G.; Zhou, J. Additively manufactured scaffolds for bone tissue engineering and the prediction of their mechanical behavior: A review. *Materials* **2017**, *10*, 50. [CrossRef] [PubMed]
55. *ISO/TC 261 Additive Manufacturing*; International Organization for Standardization: Geneva, Switzerland, 2011.
56. Paris, H. A life cycle assessment-based approach for evaluating the influence of total build height and batch size on the environmental performance of electron beam melting. *Int. J. Adv. Manuf. Technol.* **2018**. [CrossRef]
57. Le Bourhis, F.; Kerbrat, O.; Hascoët, J.; Mognol, P. Sustainable manufacturing: Evaluation and modeling of environmental impacts in additive manufacturing. *Int. J. Adv. Manuf. Technol.* **2013**, *69*, 1927–1939. [CrossRef]
58. Srari, J.S.; Kumar, M.; Graham, G. Distributed manufacturing: Scope, challenges and opportunities. *Int. J. Prod. Res.* **2016**, *54*, 6917–6935. [CrossRef]
59. Monzón, M.; Ortega, Z.; Hernández, A.; Paz, R.; Ortega, F. Anisotropy of photopolymer parts made by digital light processing. *Materials* **2017**, *10*, 64. [CrossRef] [PubMed]
60. Jornada, I.K. Impacto de la Fabricación Aditiva en la Industria: Visión Tecnológica y Últimas Tendencias. Available online: <https://www.madrimasd.org/notiweb/agenda/impacto-fabricacion-aditiva-en-industria-vision-tecnologica-ultimas-tendencias> (accessed on 14 August 2018).
61. Regional Center of Excellence, ATE. Additive Manufacturing: Recommendations for Northwest Minnesota. Available online: <http://michellelandsverk.com/wp-content/uploads/2017/03/Additive-Manufacturing-2014-Whitepaper.pdf> (accessed on 15 August 2018).
62. Lindqvist, M.; Piili, H.; Salminen, A. Benchmark study of industrial needs for additive manufacturing in Finland. *Phys. Proced.* **2016**, *83*, 854–863. [CrossRef]
63. Ituarte, I.F.; Salmi, M.; Ballardini, R.M.; Tuomi, J.; Partanen, J. Additive manufacturing in Finland: Recommendations for a renewed innovation policy. *Phys. Proced.* **2017**, *89*, 70–79. [CrossRef]
64. Kunniger, D.; Walwyn, D.R. Weaknesses in policy to support technology diffusion: A study of additive manufacturing in South Africa. *Int. J. Technol. Learn. Innov. Dev.* **2017**, *9*, 137–152. [CrossRef]
65. Du Preez, W.B.; De Beer, D.J. Implementing the South African additive manufacturing technology roadmap—the role of an additive manufacturing centre of competence. *S. Afr. J. Ind. Eng.* **2015**, *26*, 85–92. [CrossRef]
66. Baumann, F.W.; Roller, D. Overview of German additive manufacturing companies. *Data* **2017**, *2*, 23. [CrossRef]
67. Arcos-Novillo, D.A.; Güemes-Castorena, D. Development of an additive manufacturing technology scenario for opportunity identification—The case of Mexico. *Futures* **2017**, *90*, 1–15. [CrossRef]
68. Dwivedi, G.; Srivastava, S.K.; Srivastava, R.K. Analysis of barriers to implement additive manufacturing technology in the Indian automotive sector. *Int. J. Phys. Distrib. Logist. Manag.* **2017**, *47*, 972–991. [CrossRef]
69. Thomas-Seale, L.; Kirkman-Brown, J.; Attallah, M.; Espino, D.; Shepherd, D. The barriers to the progression of additive manufacture: Perspectives from UK industry. *Int. J. Prod. Econ.* **2018**, *198*, 104–118. [CrossRef]
70. Huang, H.; Wang, G. Comparison study on the industrial policies of additive manufacturing in US and China. In Proceedings of the 2016 International Conference on the Industrial Economics System and Industrial Security Engineering (IEIS), Sydney, Australia, 24–27 July 2016. [CrossRef]
71. Melton, J.Z. The Case for Adding Art in Technical Curriculums. Available online: <http://www.newequipment.com/industry-trends/case-adding-art-technical-curriculums> (accessed on 15 August 2018).

72. García Arenas, J. Los Pilares de La Educación: Una Visión Moderna. Available online: <http://www.caixabankresearch.com/los-pilares-de-la-educacion-una-vision-moderna> (accessed on 15 August 2018).
73. Fernandez, E. La Buena Educación. Available online: <http://www.caixabankresearch.com/en/node/31441> (accessed on 15 August 2018).
74. Morron, A. Enseñar a Aprender: La Educación Ante el Cambio Tecnológico. Available online: <http://www.caixabankresearch.com/ensenar-aprender-la-educacion-ante-el-cambio-tecnologico> (accessed on 15 August 2018).
75. Berman, A.; Deuermeyer, E.; Nam, B.; Chu, S.L.; Quek, F. Exploring the 3D printing process for young children in curriculum-aligned making in the classroom. In Proceedings of the 17th ACM Conference on Interaction Design and Children, Trondheim, Norway, 19–22 June 2018; ACM: New York, NY, USA, 2018.
76. Stickel, O.; Hornung, D.; Aal, K.; Rohde, M.; Wulf, V. 3D printing with marginalized children—an exploration in a Palestinian refugee camp. In Proceedings of the 14th European Conference on Computer Supported Cooperative Work, Oslo, Norway, 19–23 September 2015; Springer: Cham, Switzerland, 2015.
77. Thurn, L.K.; Balc, N.; Gebhardt, A.; Kessler, J. Education packed in technology to promote innovations: Teaching additive manufacturing based on a rolling lab. *MATEC Web Conf.* **2017**, *137*, 02013. [CrossRef]
78. Eisenberg, M. 3D printing for children: What to build next? *Int. J. Child Comput. Interact.* **2013**, *1*, 7–13. [CrossRef]
79. Bush, G.K. A Problem Based Learning Project Analyzing Rubrics Used to Evaluate Elementary STEM Immersion Programs. Available online: <https://search.proquest.com/openview/925f76de41ed8424f6f3b90a-7726bfb4/1?pq-origsite=gscholar&cbl=18750&diss=y> (accessed on 15 August 2018).
80. Ozfidan, B.; de Miranda, M.A. K12 teacher credentialing containing engineering content in the USA. *Eur. J. Mathemath. Sci. Technol. Educ.* **2017**, *14*, 3–13. [CrossRef]
81. Hobsbawm, E.J. *En Torno a Los Origenes de La Revolución Industrial*; Siglo XXI de España: Madrid, Spain, 1988.
82. Schwab, K. *La Cuarta Revolución Industrial*; Debate: Barcelona, Spain, 2016.
83. Dutta, S.; Geiger, T.; Lanvin, B. The global information technology report 2015. *World Econ. Forum* **2015**, *1*, 80–85.
84. Hemphill, T.A.; White, G.O., III. The World Economic Forum and Nike: Emerging ‘Shared responsibility’ and institutional control models for achieving a socially responsible global supply chain? *Bus. Hum. Rights J.* **2016**, *1*, 307–313. [CrossRef]
85. Corvalán, J.G. Desarrollo Tecnológico y Empleo: Avances Preliminares. Available online: <http://dpicuantico.com/sitio/wp-content/uploads/2017/05/Desarrollo-tecnologico-y-empleo.pdf> (accessed on 15 August 2018).
86. Doménech, R.; García, J.R.; Montañez, M.; Neut, A. Cuán Vulnerable es España a la Revolución Digital? Available online: <https://www.bbvaesearch.com/publicaciones/cuan-vulnerable-es-el-empleo-en-espana-a-la-revolucion-digital/> (accessed on 15 August 2018).
87. World Economic Forum. The New Production Workforce: Responding to Shifting Labor Demands. Available online: <https://www.weforum.org/whitepapers/the-new-production-workforce-responding-to-shifting-labour-demands> (accessed on 15 August 2018).
88. Frey, C.B.; Osborne, M.A. The future of employment: How susceptible are jobs to computerisation? *Technol. Forecast. Soc. Chang.* **2017**, *114*, 254–280. [CrossRef]
89. Sánchez, F.R. La Digitalización y el Empleo Decente en España Retos y Propuestas de Actuación. Available online: <http://docpublicos.ccoo.es/cendoc/049594DigitalizacionEmpleoDecente.pdf> (accessed on 15 August 2018).
90. The Future of Jobs Employment, Skills and Workforce Strategy for the Fourth Industrial Revolution. Available online: http://www3.weforum.org/docs/WEF_Future_of_Jobs.pdf (accessed on 15 August 2018).
91. Capgemini. The Digital Talent Gap-Are Companies Doing Enough? Available online: <https://www.capgemini.com/resources/digital-talent-gap/> (accessed on 15 August 2018).
92. Arntz, M.; Gregory, T.; Zierahn, U. The risk of automation for jobs in OECD countries. In *OECD Social, Employment and Migration Working Papers, No. 189*; OECD: Paris, France, 2016.
93. Ministerio de Economía, Industriay Competitividad, MINECO. INE, Instituto Nacional de Estadística. Available online: <http://www.ine.es> (accessed on 15 August 2018).
94. Bernard, A.B.; Fort, T.C. Factoryless goods producing firms. *Am. Econ. Rev.* **2015**, *105*, 518–523. [CrossRef]

95. Rodrik, D. Premature deindustrialization. *J. Econ. Growth* **2016**, *21*, 1–33. [CrossRef]
96. Crozet, M.D.; Milet, E. The Servitization of French Manufacturing Firms. Available online: http://www.cepii.fr/PDF_PUB/wp/2014/wp2014-10.pdf (accessed on 15 August 2018).
97. Fernandez, E. El Futuro de la Industria. Available online: <http://www.caixabankresearch.com/el-futuro-de-la-industria> (accessed on 15 August 2018).
98. Domènech, M.M.; Ruiz, À. Igualdad de Oportunidades: Nivelar el Terreno de Juego Para Todos. Available online: <http://www.caixabankresearch.com/igualdad-de-oportunidades-nivelar-el-terreno-de-juego-para-todos> (accessed on 15 August 2018).
99. Canals, C.; Eras, C. Medidas Para Favorecer la Igualdad de Oportunidades. Available online: <http://www.caixabankresearch.com/medidas-para-favorecer-la-igualdad-de-oportunidades> (accessed on 15 August 2018).
100. Montoriol-Garriga, J. La Calidad del Empleo en España. Available online: <http://www.caixabankresearch.com/la-calidad-del-empleo-en-espana> (accessed on 15 August 2018).
101. Schwab, K.; Salai-Martin, X. The Global Competitiveness Report 2016–2017. Available online: http://www3.weforum.org/docs/GCR2016-2017/05FullReport/TheGlobalCompetitivenessReport2016-2017_FINAL.pdf (accessed on 15 August 2018).
102. Aspachs, O. Cambio Tecnológico y Crecimiento Económico: A Nuevas Preguntas, Nuevas Respuestas. Available online: <http://www.caixabankresearch.com/cambio-tecnologico-y-crecimiento-economico-nuevas-preguntas-nuevas-respuestas> (accessed on 15 August 2018).
103. Tirole, J. La Economía del Bien Común. Available online: <https://www.megustaleer.com/libros/la-economia-del-bien-comn/MES-080926/fragmento/> (accessed on 15 August 2018).
104. Martínez, J.M.D. La Economía Colaborativa: La Sociedad Ante un Nuevo Paradigma Económico. Available online: <https://dialnet.unirioja.es/servlet/articulo?codigo=6108211> (accessed on 15 August 2018).
105. Katz, L.F.; Krueger, A.B. The Rise and Nature of Alternative Work Arrangements in the United States, 1995–2015. Available online: https://scholar.harvard.edu/files/lkatz/files/katz_krueger_cws_resubmit_clean.pdf (accessed on 15 August 2018).
106. News Mundo, B. Qué es la “Economía Gig”, Por Qué Está Creciendo tan Rápido y Cuáles Son Sus Riesgos. Available online: <http://www.elmostrador.cl/agenda-pais/2017/09/06/que-es-la-economia-gig-por-que-esta-creciendo-tan-rapido-y-cuales-son-sus-riesgos/> (accessed on 15 August 2018).
107. Elizabeth, G.S.; Garcés Suárez, E.; Alcívar Fajardo, O. Las Tecnologías de la Información en el Cambio de la Educación Superior en el Siglo XXI: Reflexiones Para la Práctica. *Rev. Univ. Soc.* **2016**, *8*, 171–177.
108. Galor, O. Inequality human capital formation and the process of development. *Handb. Econ. Edu.* **2011**, *4*, 441–493.
109. European Council. European Council Conclusions. Updated 2010. Spain. Available online: http://ec.europa.eu/eu2020/pdf/council_conclusion_17_june_en.pdf (accessed on 15 August 2018).
110. Comisión Ministerial de Ciencia y Tecnología, Spain. Estrategia Nacional de Ciencia y Tecnología (ENCYT 2007–2015). Available online: http://www.idi.mineco.gob.es/portal/site/MICINN/menuitem.7eeac5cd345b4f34f09dfd1001432ea0/?vgnextoid=a5c5c10fb468c310VgnVCM1000001d04140aRCRD&lang_chosen=gl (accessed on 15 August 2018).
111. State Innovation Strategy E21. General Secretariat for Innovation. Available online: <http://www.idi.mineco.gob.es/portal/site/MICINN/menuitem.7eeac5cd345b4f34f09dfd1001432ea0/?vgnextoid=33a5c10fb468c310VgnVCM1000001d04140aRCRD> (accessed on 15 August 2018).
112. Estrategia Española de Ciencia y Tecnología y de Innovación 2013–2020: Claves. Available online: http://www.ciencia.gob.es/stfls/MICINN/Investigacion/FICHEROS/Estrategia_espanola_ciencia_tecnologia_Innovacion.pdf (accessed on 15 August 2018).
113. Plan Estatal de Investigación Científica y Técnica y de Innovación 2017–2020. Available online: <http://www.idi.mineco.gob.es/portal/site/MICINN/menuitem.edc7f2029a2be27d7010721001432ea0/?vgnextoid=9af75ab2e7bb0610VgnVCM1000001d04140aRCRD> (accessed on 15 August 2018).

114. Plan Estatal de Investigación Científica y Técnica y de Innovación 2013–2016. Available online: <http://www.idi.mineco.gob.es/portal/site/MICINN/menuitem.7eeac5cd345b4f34f09dfd1001432ea0/?vgnnextoid=83b192b9036c2210VgnVCM1000001d04140aRCRD> (accessed on 15 August 2018).
115. FECYT, Spain. Indicadores del Sistema Español de Ciencia, Tecnología e Innovación. Edición 2017. Available online: <https://icono.fecyt.es/informes-y-publicaciones/analisis-estadisticas-de-id-e-innovacion> (accessed on 15 August 2018).



© 2018 by the authors. Licensee MDPI, Basel, Switzerland. This article is an open access article distributed under the terms and conditions of the Creative Commons Attribution (CC BY) license (<http://creativecommons.org/licenses/by/4.0/>).

Article

A Tangible Educative 3D Printed Atlas of the Rat Brain

Darío R. Quiñones ^{1,†}, Jorge Ferragud-Agulló ^{1,†}, Ricardo Pérez-Feito ²,
Juan A. García-Manrique ³, Santiago Canals ⁴ and David Moratal ^{1,*}

¹ Centre for Biomaterials and Tissue Engineering, Universitat Politècnica de València, 46022 Valencia, Spain; dariomrxpro2@hotmail.com (D.R.Q.); jorgeferragudagullo@gmail.com (J.F.-A.)

² Thermodynamics Department, Universitat Politècnica de València, 46022 Valencia, Spain; riperez@upvnet.upv.es

³ Institute of Design for Manufacturing and Automated Production, Universitat Politècnica de València, 46022 Valencia, Spain; jugarcia@mcm.upv.es

⁴ Instituto de Neurociencias, Consejo Superior de Investigaciones Científicas—Universidad Miguel Hernández, 03550 Sant Joan d'Alacant, Spain; scanals@umh.es

* Correspondence: dmoratal@eln.upv.es

† These authors contributed equally to this work.

Received: 29 June 2018; Accepted: 23 August 2018; Published: 25 August 2018

Abstract: In biology and neuroscience courses, brain anatomy is usually explained using Magnetic Resonance (MR) images or histological sections of different orientations. These can show the most important macroscopic areas in an animals' brain. However, this method is neither dynamic nor intuitive. In this work, an anatomical 3D printed rat brain with educative purposes is presented. Hand manipulation of the structure, facilitated by the scale up of its dimensions, and the ability to dismantle the “brain” into some of its constituent parts, facilitates the understanding of the 3D organization of the nervous system. This is an alternative method for teaching students in general and biologists in particular the rat brain anatomy. The 3D printed rat brain has been developed with eight parts, which correspond to the most important divisions of the brain. Each part has been fitted with interconnections, facilitating assembling and disassembling as required. These solid parts were smoothed out, modified and manufactured through 3D printing techniques with poly(lactic acid) (PLA). This work presents a methodology that could be expanded to almost any field of clinical and pre-clinical research, and moreover it avoids the need for dissecting animals to teach brain anatomy.

Keywords: brain; rapid prototyping; atlas; rat; magnetic resonance imaging; educative model

1. Introduction

The use of animals for scientific or educational purposes presents a great moral dilemma for current society. Although social progress leads to greater empathy towards animals, it is true that experimentation with them has allowed a large advance in the neuroscience field. This type of experimentation has helped the study of brain diseases and their causes, which would not have been possible otherwise according to current knowledge. However, nowadays, it is possible to study the brain without harming animals thanks to neuroimaging technologies.

Neuroimaging technologies, such as Computed Tomography (CT) and Magnetic Resonance Imaging (MRI), are indispensable tools for the diagnosis and treatment of central nervous system diseases [1–6]. Even though MRI and CT techniques collect three-dimensional (3D) data, clinicians typically view these data on two-dimensional (2D) screens. 2D representations limit our appreciation of complex structures, such as brain convolutions, and 2D displays of these models on computer screens prevent us from interacting with a model of the physical brain. Furthermore, appreciating complex

3D spatial relationships in a 2D screen requires a strong foundational understanding of anatomy and mental 3D visualization skills [7].

A tangible physical model based on MR images or digital templates would permit biologists, neuroscientists and students to complement information obtained by 2D and virtual 3D imaging. Furthermore, physical 3D models could be more advantageous for clinical education than computer-based 3D models [7–9]. Therefore, high-resolution multiscale and multimodal 3D models of the brain can be seen as essential tools to understand its complex structural and organization [10]. A commercial rat brain model called “C29 Rat Brain Comparative Anatomy” (3B Scientific GmbH, Hamburg, Germany) exists for educational purposes, but it is not detailed enough for scientific purposes.

The most widely used MRI template of a rat brain is that developed by Schwarz et al., [11]. It is co-registered with the stereotaxic co-ordinates of the Paxinos and Watson (1982) digital atlas [12]. The template set provides anatomical images as well as tissue class probability maps for brain parenchyma and CerebroSpinal Fluid (CSF). The use of this template paves the way for the use of standard fMRI software for tissue segmentation of rat brain data. This enables the atlas structure and the stereotaxic coordinates that correspond to a feature within a statistical map to be interactively reported, which facilitates the localization of functional effects. Furthermore, voxels, which are within selected brain structures, can be combined to define anatomically based 3D volumes of interest (VOIs) [11]. The use of standard functional Magnetic Resonance Imaging (fMRI) software for tissue segmentation of rat brain data is facilitated by the use of this template.

3D printing is rapidly becoming a source of novel biomedical applications, as well as a cost-effective mean of producing customized 3D objects [13–16], for example, printing organic tissue [17] or developing scaffolds for tissue engineering [18]. However, some of the most complex applications use high-end industrial printers that are too expensive for educative purposes or even for research centers with limited funds. Nonetheless, the progression of open source platforms has increased the capabilities and popularity of desktop 3D printers.

In this work, we describe a step-by-step, end-to-end easily replicable methodology to generate and scale a 3D printed model of a rat brain with the most important macroscopic regions. It is based on an MRI template of the rat brain co-localized with the Paxinos and Watson rat brain atlas, combined with 3D computer-aided design (CAD) tools and 3D prototyping technologies to obtain a didactic 3D printed brain. Furthermore, each 3D printed region of the brain is designed to be easily attached to or detached from the other parts. This model could have a big impact on the way biologists and neuroscientists teach in the future. It makes more “tangible” the understanding of the relevant areas of the brain for teaching, while reduces the use of experimental animals for these purposes. In addition, the methodology can be extrapolated to different regions of the brain or even to other body regions.

2. Materials and Methods

The methodology presented in this paper consists of the following steps to generate 3D objects from clinical or pre-clinical: (i) selection of the data; (ii) segmentation of the region of interest (ROI); (iii) transformation of the data from 2D ROIs to a 3D triangular mesh; (iv) editing the 3D mesh (to clean uneven areas, add support structures, etc.); (v) transferring the data to 3D printer software in order to create printing coordinates; and (vi) sending it to production (Figure 1).

2.1. Data Selection: The Eight Most Relevant Macroscopic Areas in the Rat Brain

The first step in creating 3D printed models from a digital atlas is the selection of the regions of interest. The image data choice is important; low-resolution images can result in a discrepancy between the generated model and actual anatomy. In this particular case, a stereotaxic MRI template set for the rat brain with tissue class distribution maps made by Schwarz et al., [11] and co-registered anatomical atlas “*The Rat Brain in Stereotaxic Coordinates*” from Paxinos and Watson (1982) [12], was chosen. This document shows sagittal and coronal cuts throughout the brain of a specimen rat. The atlas

partially contains all the encephalon of a rat, but the brain is the main part which appears in the MRI atlas. However, the whole cerebellum, the medulla and the olfactory bulb are not included in the atlas.

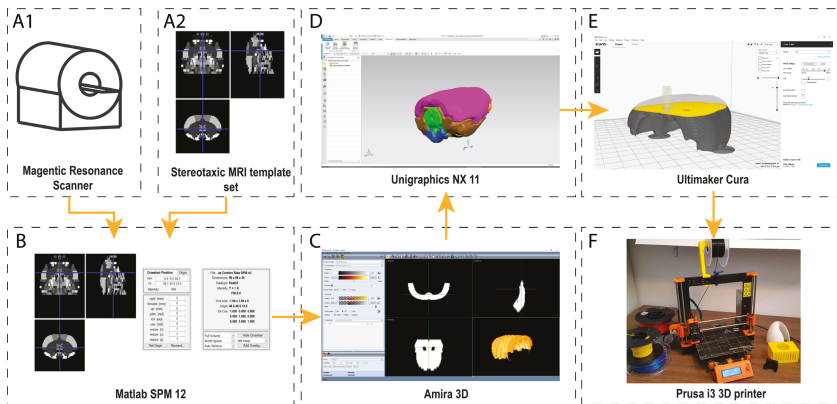


Figure 1. This figure shows the pipeline of the process from a CT or MRI set of images to a physical 3D printed model. First, images from a CT or MRI scanner (A1) are colocalized with a stereotaxic template (A2). Next, these images are clustered in Matlab SPM (B) to create the Voxels of Interest (VOI). With this set of images, a 3D reconstruction is created in Amira 3D software (C). Then, the 3D surface, which was created in Amira, is opened in a 3D design tool, e.g. Unigraphics NX, (D) where 3D surfaces are converted into 3D solid bodies. These solid bodies are provided with joins and connectors to add detachable properties to the 3D printed body. Once this process is complete, the manufacturing process starts (E). This consists of transforming the 3D body into a physical set of coordinates, which the 3D printer can interpret. In this case, a Prusa i3 MK2 3D printer with Cura software was used (F).

The MRI template that was used is the one presented in [11]. Briefly, this template was created from multi-slice T2-weighted images of a rat brain acquired using a RARE sequence on a Bruker Avance 4.7-T MR scanner (Billerica, MA, USA) with the following acquisition parameters: RARE factor 8, matrix 256×256 ; FOV 40 mm, slice thickness 1 mm, 32 contiguous coronal slices; $TR_{eff} = 5500$ ms; $TE_{eff} = 76$ ms. A 72-mm birdcage resonator was used for RF transmission and the Bruker quadrature FRat Brain_ coil was used for RF reception. The images were acquired in the coronal plane, centered 8 mm caudal from the posterior edge of the olfactory bulb [11]. Each region is marked with a different gray intensity. In total, 466 brain regions were clustered into 38 sub-regions and grouped into eight regions with the participation of an experienced neurobiologist. These parts correspond to the eight pieces of the printed rat brain that is presented in this paper (Table 1).

Table 1. Regions clustering.

Regions	Sub-Regions
Neocortex	Cortex Parietal Association, Cortex Retrosplenial, Cortex Temporal Association, Corpus Cortex Sensory, Cortex Motor, Cortex Insular, Cortex Frontal Association, Cortex Orbitofrontal, Cortex Medial Prefrontal, Cortex Cingulate, Collosum
Archicortex	Hippocampus, Cortex Entorhinal Piriform
Paleocortex	Olfactory Nuclei, Olfactory Tubercle
Basal Ganglia	Globus Pallidus, Amygdala, Diagonal Band, IPAC, BNST, Caudate Putamen, Ventral Pallidum, Substantia Innominata, Caudate Putamen
Basal telencephalon	Septum, Accumbens
Diencephalon	Hypothalamus, Thalamus, Medial Geniculate, Zona Incerta
Midbrain	Raphe, Mesencephalic Region, Substantia Nigra, Periaqueductal Grey, Superior Colliculus, Interpeduncular Nucleus, VTA (Ventral Tegmental Area)
Metencephalon	Pons

To visualize and choose the desired areas from the stereotaxic MRI template set, a specific software was needed. In this case, Statistical Parametric Mapping 12 (SPM12) [19], which is designed as a MATLAB (The Mathworks Inc., Natick, MA, USA) toolbox, was chosen (Figure 2), because it is the most suitable and open source software available for the this purpose [20,21]. SPM is an academic software toolkit for the analysis of functional imaging data for users familiar with the underlying statistical, mathematical and image processing concepts. SPM12 can be also executed on GNU/Octave [22], which is an Open-Source alternative to Matlab. Once the areas were chosen in the atlas and identified in the MRI template set, they were grouped in SPM and saved in different files in *NIFTI* format (.nii).

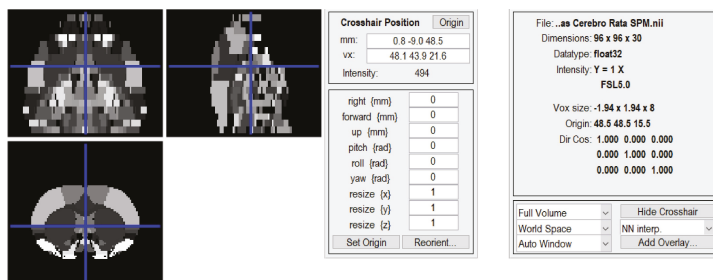


Figure 2. Statistical Parametrical Mapping toolbox. The image represents a slice of the employed digital atlas, whereas the specific coordinates are shown in SPM 12.

2.2. Three-Dimensional Reconstruction of the Desired Areas

Once all the macroscopic areas were chosen, a way to represent them in a 3D view was needed. Amira™ (Thermo Scientific™, Waltham, MA, USA) software was selected for 3D visualization and analysis. Amira is a powerful software tool capable of dealing with life science data from computed tomography, microscopy, MRI, and many other imaging modalities. Mango (UT Health, Houston, TX, USA) is an Open-Source alternative to Amira that can be use to the same purpose.

Figure 3 shows the chosen regions using Amira. Through the functionality “Labeling”, it was possible to group all the Regions of Interest (ROI) from each slice of the dataset. Once the labeling process was complete, and using the functionality “SurfaceGen”, all the labeled areas on each slice were transformed into a surfaced 3D body (facet body).

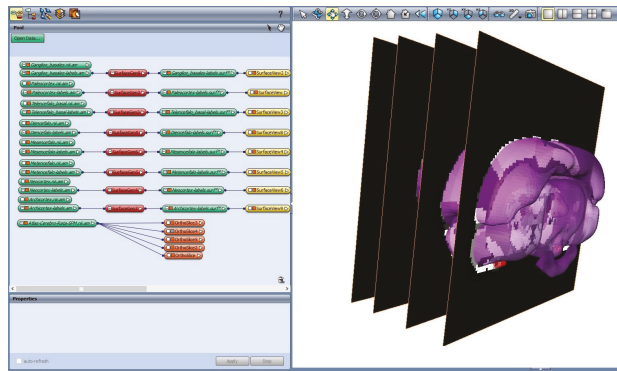


Figure 3. Data labeling in Amira 3D software. A set of slices is displayed, which belong to the Neocortex region, from the selected dataset. This functionality selects in each of the slices the regions with the same gray level.

This body was exported as an *OBJ* file, which is an extended open source format. The *OBJ* file format is a simple data-format that represents 3D geometry. It gives the position of each vertex, the vertex normals, and the faces that make each polygon defined as a list of vertices, and texture vertices. However, this format has a drawback: it is not easily editable because it only represents the surface of the 3D body with the necessary number of triangles. It does not represent the 3D object as 3D solid body. This means that Boolean 3D operations (e.g., add, subtract, and intersect) cannot be easily applied. In our specific case, it was necessary to edit the geometry of the resulting 3D faceted body, because the objective was to create an easily detachable 3D brain.

2.3. Transforming the Facet Body into an Editable Solid Body

To create a 3D brain with interlocking plastic parts, it was necessary to edit the facet bodies that were previously generated, and then to add fastener joins. This process was performed with Unigraphics NX 11 (Siemens, Munich, Germany). This software, widely used in the industry, enables design, structural analysis, simulations and image study, among other things. Through a program of this type, it is possible to create 2D and 3D designs from scratch, or to modify files from other sources. FreeCAD (Blender Foundation, Amsterdam, The Netherlands) can be used as Open-Source alternative to Unigraphics NX. Using these features, the *OBJ* files were imported and analyzed as a convergent body. Then, each analyzed part was converted into an editable 3D solid body. However, as shown in Figure 4A, the resulting shape is not as smooth as could be expected. These uneven surfaces are due to the low resolution of the template. To correct this, a constrained smoothing process was applied to each of the eight macroscopic regions. There are two methods of smoothing the surface of the 3D object. One, which is less computationally demanding, is using Amira 3D, but it has some drawbacks, as shown in Figure 4B. This method creates a well-smoothed body, but it suppresses relevant details of the region.

The other method is more computationally demanding and involves a tool of Unigraphics NX called “*surface smoothing*”, which allows smoothing of the surfaces without losing the relevant morphology of the region. This second method was chosen for all bodies that were extracted from the template.

To create the joins for each component, the ideal position of the join was studied for each part. According to the part dimension, the position of the join was determined as an extrusion (male) or a depression (female). Then, each join was added to the corresponding part in Unigraphics NX by converting the join and the part into a unique 3D solid body.

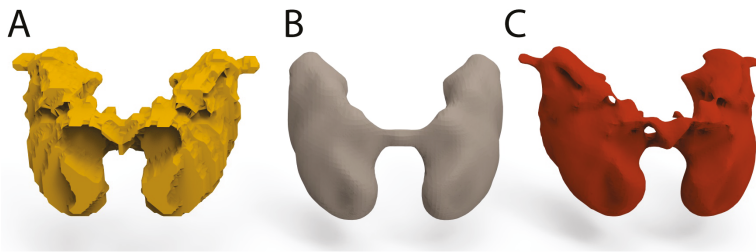


Figure 4. Smoothing process applied on the Basal Ganglia: (A) Basal ganglia before being smoothed; (B) smoothing process with Amira 3D software; and (C) smoothing process with Unigraphics NX.

The joints were added with a 5% tolerance to facilitate attach and detach parts after being 3D printed. As shown in Figure 5, each joint was created in a specific place and as specific shape to facilitate an interconnection between the parts. The Archicortex was further divided into two parts to make it easy to assemble and disassemble the inner parts of the brain.

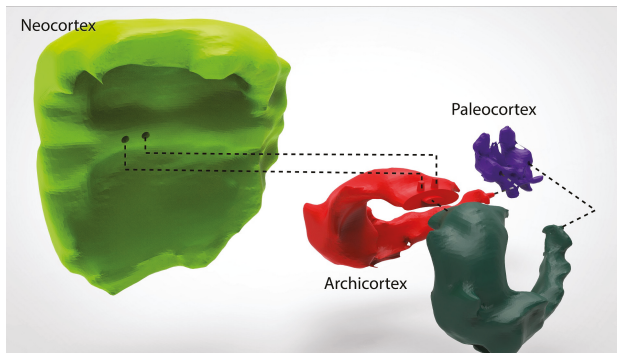


Figure 5. Interconnecting joints. Figure shows the interconnecting joints among three parts of the brain 3D model. It is possible to appreciate that the Neocortex, as well as the Paleocortex, has two depressions. These depressions fit perfectly with the protuberances on the top of the Archicortex.

2.4. Rapid Prototyping

Rapid prototyping can be defined as an approach or methodology used to quickly manufacture physical models using 3D CAD data. Rapid prototyping has also been referred to as solid free form, computer-automated or layered manufacturing. Rapid prototyping has its obvious use as a truly 3D method for visualization and better haptic interaction.

Nowadays, 3D home printers have become more accessible than industrial 3D printers, and this has increased the number of “Do It Yourself” (DIY) projects that are underway. The most affordable and common type of rapid prototyping is Fused Deposition Modelling (FDM) technology, also known as Fused Filament Fabrication (FFF). There are other types of rapid prototyping, such as Stereolithography (SLA) or Selective Laser Sintering (SLS) [23], which are more accurate and detailed but which cost more [24]. FDM technology prints an object one layer at a time by extruding heated plastic through a nozzle, while moving around a flat hot surface (hot bed).

A Prusa i3 MK2 with a precision of 50 microns per layer height, and a printing surface of 10,500 cm³ (25 × 21 × 20 cm or 9.84 × 8.3 × 8 in) was used to print all of the parts. With these manufacturing constraints and the modified solid models with the joints, a scale of four times the actual size (4:1) was chosen in the printing software Ultimaker Cura (Ultimaker B.V., Geldermalsen, The Netherlands).

3. Results

The final 3D printed model of the rat brain (Figure 6) is composed of the eight smoothed parts, all parts of which fit together perfectly. The scaled measures of each part are shown in Table 2. In addition, an external container was made to accommodate the eight regions.

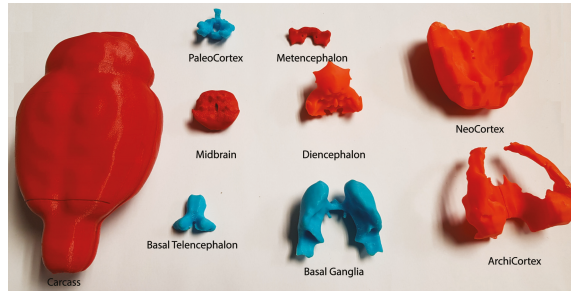


Figure 6. Final 3D model (disassembled) of the rat template.

This container was designed using the external contour of the brain in the template. It was then enlarged a little (4.2:1) to facilitate the accommodation of the other parts. In addition, the cover was divided in two to make it possible to open, as shown in Figure 7. Figure 6 shows the whole-brain model disassembled, all eight parts and the container that encloses them. Figure 7 shows that all of the parts fits perfectly together.

Table 2. Measurements on X, Y, and Z axes of each part, total assembly without container and total assembly with container.

Part	X (mm)	Y (mm)	Z (mm)	Part	X (mm)	Y (mm)	Z (mm)
Neocortex	59.60	28.94	54.40	Midbrain	26.72	24.90	15.10
Archicortex1	28.58	30.19	50.38	Metencephalon	26.43	12.48	6.02
Archicortex2	32.08	30.19	50.38	Bottom Cover	69.54	30.08	131.73
Paleocortex	24.00	17.94	18.69	Upper Cover	69.07	39.04	132.66
Basal ganglia	51.01	25.98	34.83	Small Cover	64.46	13.73	49.60
Basal Telencephalon	22.83	18.45	15.84	Total without cover	59.60	38.37	57.60
Diencephalon	33.02	24.35	30.35	Total with cover	69.54	52.34	132.66

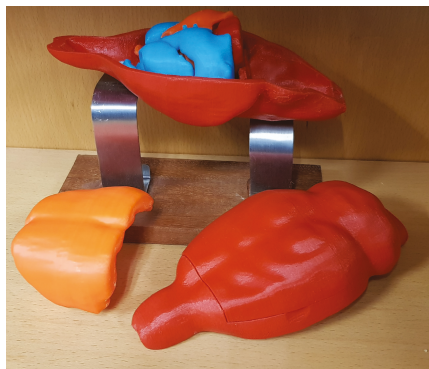


Figure 7. Final 3D model of the rat template.

In terms of material for the printing process, poly(lactic acid) (PLA) was chosen. This material is a thermoplastic polymer that is made from renewable resources. It melts at 160 degrees Celsius and it is less rigid than Acrylonitrile Butadiene Styrene (ABS), another commonly used material in 3D printing. This is important for the 3D model because it makes the printed parts more elastic and shock-resistant.

4. Discussion

Rapid prototyping has grown beyond its initial use in industrial sectors, e.g., the automobile industry, and today can be regarded as one of the most promising techniques for use in medical imaging. Although medical applications are relatively recent, their enormous potential has already been demonstrated in several studies [25–27]. Rapid prototyping objects are useful for training surgeons, as they allow surgical procedures to be simulated in a realistic manner. Even though medical research has already benefitted from rapid prototyping [28,29] and efforts have been made in the development of artificial organs and tissues [30,31], the traditional approach of teaching anatomy remains the same. This approach focuses mainly on MRI, CT and dissections of real animals, without taking into consideration any variations and pathological changes. Currently, there is a well-known rat brain model called “C29 Rat Brain Comparative Anatomy”, which aims for an educative point of view, but is not detailed enough for scientific purposes.

The 3D printed brain that is presented in this paper could serve as the medium for bringing anatomical variations to pre-clinical studies in order to improve the understanding of anatomy [7] while preserving animal lives. In addition, by using other materials to adapt transparency or rigidity, certain aspects can be emphasized for the trainee and the student.

In the scientific domain, adding the cranium of the subject to the 3D model, we envision applications of this approach in designing and probing brain implant prototypes, as recording chambers, electric and/or optogenetic stimulation holders, and designing coils for transcranial magnetic or direct current stimulation.

5. Conclusions

In this paper, a step-by-step, end-to-end easily replicable methodology to generate a 3D printed model of a rat brain has been presented. It is based on an MRI template of the rat brain co-localized with the Paxinos and Watson rat brain atlas, combined with 3D CAD tools and 3D prototyping technologies to obtain a tangible 3D printed atlas of the rat brain. In addition, each 3D printed region is designed to be easily attached or detached from the other parts. This model could have a big impact on the way biologists and neuroscientists teach in the future. It makes more “tangible” the understanding of the relevant areas of the rat brain for teaching, while reducing the use of experimental animals for these purposes. In addition, the methodology can be extrapolated to different regions of the brain or even to other body regions.

To obtain the necessary images to generate the 3D parts, a digital atlas, which was correlated with a stereotaxic anatomical atlas, was used. With the participation of an experienced biologist, 466 structures were extracted and clustered into eight different parts, which correspond to the eight pieces of the printed rat brain that is presented in this paper. These parts are the Neocortex, the Archicortex, the Paleocortex, the Basal Ganglia, the Basal Telencephalon, the Diencephalon, the Mesencephalon, and the Metencephalons. Each part has joins to fasten together the different parts. In addition, a housing formed by three additional pieces was created. This in turn performs the function of storing the rest of the pieces and serves as a spatial orientation for the assembly of the brain. In further research, a complete rat brain with 38 sub-regions will be developed.

This work presents a methodology that could be expanded to almost any field of clinical and pre-clinical research, and moreover it avoids the need to dissect animals to teach anatomy. In addition, all parts are available at <http://dmoratal.webs.upv.es/research.html>.

Author Contributions: Conceptualization, D.R.Q., S.C. and D.M.; Data curation, D.R.Q. and D.M.; Formal analysis, D.R.Q., J.F.-A., R.P.-F. and S.C.; Funding acquisition, J.A.G.-M. and D.M.; Investigation, D.R.Q.,

J.F.-A., S.C. and D.M.; Methodology, D.R.Q., R.P.-F., J.A.G.-M., S.C. and D.M.; Project administration, J.A.G.-M. and D.M.; Resources, J.A.G.-M., S.C. and D.M.; Software, D.R.Q., J.F.-A. and R.P.-F.; Supervision, J.A.G.-M., S.C. and D.M.; Validation, D.R.Q., S.C. and D.M.; Visualization, D.R.Q.; Writing—original draft, D.R.Q. and J.F.-A.; and Writing—review and editing, R.P.-F., J.A.G.-M., S.C. and D.M.

Funding: This work was supported in part by the Spanish Ministerio de Economía y Competitividad (MINECO) and FEDER funds under grants BFU2015-64380-C2-2-R (D.M.) and BFU2015-64380-C2-1-R and EU Horizon 2020 Program 668863-SyBil-AA grant (S.C.). S.C. acknowledges financial support from the Spanish State Research Agency, through the “Severo Ochoa” Programme for Centres of Excellence in R&D (ref. SEV- 2013-0317). D.R.Q. was supported by grant “Ayudas para la formación de personal investigador (FPI)” from the Vicerrectorado de Investigación, Innovación y Transferencia of the Universitat Politècnica de València.

Acknowledgments: The authors are grateful to Begoña Fernández for their technical support.

Conflicts of Interest: The authors declare no conflict of interest.

Abbreviations

The following abbreviations are used in this manuscript:

NIFTI	Neuroimaging Informatics Technology Initiative
OBJ	File format is a simple data-format that represents 3D geometry alone
CAD	Computer-Aided Design
FDM	Fused Deposit Modeling
FFF	Fused Filament Fabrication
SLS	Selective Laser Sintering
SLA	Stereolithography

References

1. Perrin, R.J.; Fagan, A.M.; Holtzman, D.M. Multimodal techniques for diagnosis and prognosis of Alzheimer’s disease. *Nature* **2009**, *461*, 916–922. [[CrossRef](#)] [[PubMed](#)]
2. Linden, D.E. The Challenges and Promise of Neuroimaging in Psychiatry. *Neuron* **2012**, *73*, 8–22. [[CrossRef](#)] [[PubMed](#)]
3. Teipel, S.; Drzezga, A.; Grothe, M.J.; Barthel, H.; Chételat, G.; Schuff, N.; Skudlarski, P.; Cavado, E.; Frisoni, G.B.; Hoffmann, W.; et al. Multimodal imaging in Alzheimer’s disease: Validity and usefulness for early detection. *Lancet Neurol.* **2015**, *14*, 1037–1053. [[CrossRef](#)]
4. Woo, C.W.; Chang, L.J.; Lindquist, M.A.; Wager, T.D. Building better biomarkers: Brain models in translational neuroimaging. *Nat. Neurosci.* **2017**, *20*, 365–377. [[CrossRef](#)] [[PubMed](#)]
5. Ivanov, I. The Neuroimaging Gap—Where do we go from Here? *Acta Psychopathol.* **2017**, *3*, 3, doi:10.4172/2469-6676.100090. [[CrossRef](#)]
6. Kastrup, O.; Wanke, I.; Maschke, M. Neuroimaging of infections. *NeuroRX* **2005**, *2*, 324–332. [[CrossRef](#)] [[PubMed](#)]
7. Preece, D.; Williams, S.B.; Lam, R.; Weller, R. “Let’s Get Physical”: Advantages of a physical model over 3D computer models and textbooks in learning imaging anatomy. *Anat. Sci. Educ.* **2013**, *6*, 216–224. [[CrossRef](#)] [[PubMed](#)]
8. Zheng, Y.X.; Yu, D.F.; Zhao, J.G.; Wu, Y.L.; Zheng, B. 3D Printout Models vs. 3D-Rendered Images: Which Is Better for Preoperative Planning? *J. Surg. Educ.* **2016**, *73*, 518–523. [[CrossRef](#)] [[PubMed](#)]
9. Li, Z.; Li, Z.; Xu, R.; Li, M.; Li, J.; Liu, Y.; Sui, D.; Zhang, W.; Chen, Z. Three-dimensional printing models improve understanding of spinal fracture—A randomized controlled study in China. *Sci. Rep.* **2015**, *5*, 11570, doi:10.1038/srep11570. [[CrossRef](#)] [[PubMed](#)]
10. Kettenbach, J.; Wong, T.; Kacher, D.; Hata, N.; Schwartz, R.B.; Black, P.M.L.; Kikinis, R.; Jolesz, F.A. Computer-based imaging and interventional MRI: Applications for neurosurgery. *Comput. Med. Imaging Gr.* **2008**, *23*, 76–80. [[CrossRef](#)]
11. Schwarz, A.J.; Danckaert, A.; Reese, T.; Gozzi, A.; Paxinos, G.; Watson, C.; Merlo-Pich, E.V.; Bifone, A. A stereotaxic MRI template set for the rat brain with tissue class distribution maps and co-registered anatomical atlas: Application to pharmacological MRI. *NeuroImage* **2006**, *32*, 538–550. [[CrossRef](#)] [[PubMed](#)]

12. Paxinos, G.; Watson, C. *The Rat Brain in Stereotaxic Coordinates/George Paxinos; Charles Watson, C., Ed.*; Academic Press: San Diego, CA, USA, 2007.
13. Marro, A.; Bandukwala, T.; Mak, W. Three-Dimensional Printing and Medical Imaging: A Review of the Methods and Applications. *Curr. Probl. Diagn. Radiol.* **2016**, *45*, 2–9. [[CrossRef](#)] [[PubMed](#)]
14. Michalski, M.H.; Ross, J.S. The Shape of Things to Come. *JAMA* **2014**, *312*, 2213, doi:10.1001/jama.2014.9542. [[CrossRef](#)] [[PubMed](#)]
15. Ratto, M.; Ree, R. Materializing information: 3D printing and social change. *First Monday* **2012**, *17*, doi:10.5210/fm.v17i7.3968. [[CrossRef](#)]
16. Rengier, F.; Mehndiratta, A.; von Tengg-Kobligk, H.; Zechmann, C.M.; Unterhinninghofen, R.; Kauczor, H.U.; Giesel, F.L. 3D printing based on imaging data: Review of medical applications. *Int. J. Comput. Assist. Radiol. Surg.* **2010**, *5*, 335–341. [[CrossRef](#)] [[PubMed](#)]
17. Mannoor, M.S.; Jiang, Z.; James, T.; Kong, Y.L.; Malatesta, K.A.; Soboyejo, W.O.; Verma, N.; Gracias, D.H.; McAlpine, M.C. 3D printed bionic ears. *Nano Lett.* **2013**, *13*, 2634–2639. [[CrossRef](#)] [[PubMed](#)]
18. Guy, J.R.; Sati, P.; Leibovitch, E.; Jacobson, S.; Silva, A.C.; Reich, D.S. Custom fit 3D-printed brain holders for comparison of histology with MRI in marmosets. *J. Neurosci. Methods* **2016**, *257*, 55–63. [[CrossRef](#)] [[PubMed](#)]
19. Friston, K.J.K.J.; Ashburner, J.; Kiebel, S.; Nichols, T.; Penny, W.D. *Statistical Parametric Mapping: The Analysis of Functional Brain Images*; Elsevier/Academic Press: New York, NY, USA, 2007; p. 647.
20. Friston, K.J.; Holmes, A.P.; Worsley, K.J.; Poline, J.P.; Frith, C.D.; Frackowiak, R.S. Statistical parametric maps in functional imaging: A general linear approach. *Human Brain Mapp.* **1994**, *2*, 189–210. [[CrossRef](#)]
21. Flandin, G.; Novak, M.J.U. fMRI data analysis using SPM. In *fMRI*; Springer: Berlin/Heidelberg, Germany, 2013; pp. 51–76. [[CrossRef](#)]
22. Eaton, J.W.; Bateman, D.; Hauberg, S. *GNU Octave Version 3.0.1 Manual: A High-Level Interactive Language for Numerical Computations*; SoHo Books: New York, NY, USA, 2007.
23. Mueller, B. Additive Manufacturing Technologies—Rapid Prototyping to Direct Digital Manufacturing. *Assembl. Autom.* **2012**, *32*, doi:10.1108/aa.2012.03332baa.010. [[CrossRef](#)]
24. Gulanova, J.; Kister, L.; Käer, N.; Gulan, L. A Comparative Study of various AM Technologies Based on Their Accuracy. *Procedia CIRP* **2018**, *67*, 238–243. [[CrossRef](#)]
25. D’Urso, P.S.; Barker, T.M.; Earwaker, W.J.; Bruce, L.J.; Atkinson, R.L.; Lanigan, M.W.; Arvier, J.F.; Effeney, D.J. Stereolithographic biomodelling in crano-maxillofacial surgery: A prospective trial. *J. Cranio-Maxillofac. Surg.* **1999**, *27*, 30–37. [[CrossRef](#)]
26. Müller, A.; Krishnan, K.G.; Uhl, E.; Mast, G. The Application of Rapid Prototyping Techniques in Cranial Reconstruction and Preoperative Planning in Neurosurgery. *J. Craniofac. Surg.* **2003**, *14*, 899–914. [[CrossRef](#)] [[PubMed](#)]
27. Guarino, J.; Tennyson, S.; McCain, G.; Bond, L.; Shea, K.; King, H. Rapid Prototyping Technology for Surgeries of the Pediatric Spine and Pelvis. *J. Pediatr. Orthop.* **2007**, *27*, 955–960. [[CrossRef](#)] [[PubMed](#)]
28. Canstein, C.; Cachot, P.; Faust, A.; Stalder, A.; Bock, J.; Frydrychowicz, A.; Küffer, J.; Hennig, J.; Markl, M. 3D MR flow analysis in realistic rapid-prototyping model systems of the thoracic aorta: Comparison with in vivo data and computational fluid dynamics in identical vessel geometries. *Magn. Reson. Med.* **2008**, *59*, 535–546. [[CrossRef](#)] [[PubMed](#)]
29. Giesel, F.L.; Mehndiratta, A.; von Tengg-Kobligk, H.; Schaeffer, A.; Teh, K.; Hoffman, E.; Kauczor, H.U.; van Beek, E.; Wild, J.M. Rapid Prototyping Raw Models on the Basis of High Resolution Computed Tomography Lung Data for Respiratory Flow Dynamics. *Acad. Radiol.* **2009**, *16*, 495–498. [[CrossRef](#)] [[PubMed](#)]
30. Malyala, S.K.; Ravi Kumar, Y.; Rao, C. Organ Printing With Life Cells: A Review. *Mater. Today Proc.* **2017**, *4*, 1074–1083. [[CrossRef](#)]
31. Foster, K.R. 3-Dimensional Printing in Medicine: Hype, Hope, and the Challenge of Personalized Medicine. In *Philosophy of Engineering and Technology*; Springer: Cham, Switzerland, 2017; pp. 211–228. [[CrossRef](#)]



© 2018 by the authors. Licensee MDPI, Basel, Switzerland. This article is an open access article distributed under the terms and conditions of the Creative Commons Attribution (CC BY) license (<http://creativecommons.org/licenses/by/4.0/>).

Article

3D Printing of Porous Scaffolds with Controlled Porosity and Pore Size Values

Irene Buj-Corral *, Ali Bagheri and Oriol Petit-Rojo

Department of Mechanical Engineering, Universitat Politècnica de Catalunya, Av. Diagonal, 647, 08028 Barcelona, Spain; ali.bagheri@upc.edu (A.B.); oriol.petit@hotmail.com (O.P.-R.)

* Correspondence: irene.buj@upc.edu; Tel.: +34-93-4054015

Received: 27 June 2018; Accepted: 22 August 2018; Published: 25 August 2018

Abstract: 3D printed scaffolds can be used, for example, in medical applications for simulating body tissues or for manufacturing prostheses. However, it is difficult to print porous structures of specific porosity and pore size values with fused deposition modelling (FDM) technology. The present paper provides a methodology to design porous structures to be printed. First, a model is defined with some theoretical parallel planes, which are bounded within a geometrical figure, for example a disk. Each plane has randomly distributed points on it. Then, the points are joined with lines. Finally, the lines are given a certain volume and the structure is obtained. The porosity of the structure depends on three geometrical variables: the distance between parallel layers, the number of columns on each layer and the radius of the columns. In order to obtain mathematical models to relate the variables with three responses, the porosity, the mean of pore diameter and the variance of pore diameter of the structures, design of experiments with three-level factorial analysis was used. Finally, multiobjective optimization was carried out by means of the desirability function method. In order to favour fixation of the structures by osseointegration, porosity range between 0.5 and 0.75, mean of pore size between 0.1 and 0.3 mm, and variance of pore size between 0.000 and 0.010 mm² were selected. Results showed that the optimal solution consists of a structure with a height between layers of 0.72 mm, 3.65 points per mm² and a radius of 0.15 mm. It was observed that, given fixed height and radius values, the three responses decrease with the number of points per surface unit. The increase of the radius of the columns implies the decrease of the porosity and of the mean of pore size. The decrease of the height between layers leads to a sharper decrease of both the porosity and the mean of pore size. In order to compare calculated and experimental values, scaffolds were printed in polylactic acid (PLA) with FDM technology. Porosity and pore size were measured with X-ray tomography. Average value of measured porosity was 0.594, while calculated porosity was 0.537. Average value of measured mean of pore size was 0.372 mm, while calculated value was 0.434 mm. Average value of variance of pore size was 0.048 mm², higher than the calculated one of 0.008 mm². In addition, both round and elongated pores were observed in the printed structures. The current methodology allows designing structures with different requirements for porosity and pore size. In addition, it can be applied to other responses. It will be very useful in medical applications such as the simulation of body tissues or the manufacture of prostheses.

Keywords: fused deposition modeling; 3D printing; scaffolds; porosity; pore size; multiobjective optimization

1. Introduction

Many new applications have arisen as a result of recent advances in 3D printing techniques. For example, printed parts are used for manufacturing space instrumentation, for both prototypes and flying parts [1], for manufacturing cost-effective parts in the sports industry or for developing new

protective structures for vehicles in the automotive industry [2]. 3D printing has many different medical applications, such as bioprinting tissues and organs, building vascularized organs, the manufacture of customized implants, prostheses and models for surgical preparation, among others [3]. Thus, 3D printed scaffolds can be employed as templates for initial cell attachment and tissue formation, for example in bone tissue engineering [4]. They can also be used for fixing prostheses by means of osseointegration. Scaffolds could be printed in different materials such as titanium, degradable polymers and degradable ceramics [5,6]. Specifically, in FDM or fused deposition modelling technique a material is melted through an extrusion head and deposited layer by layer [7]. Main advantages of FDM technology are its easiness of use and the fact that it allows printing a wide range of materials, as long as they can be extruded, for example plastic materials such as acrylonitrile butadiene styrene (ABS) or polylactic acid (PLA). It is also more cost-effective than other additive manufacturing techniques, and its lead times are short. However, it also has disadvantages. It does not provide high dimensional precision, layer steps are usually observed on the part's surface, causing the surfaces not to be smooth. Besides, the use of and the use of scaffolds with biocompatible materials is difficult, because the technology is limited to materials whose viscosity is sufficiently low that they can be extruded, but high enough so that their shape is maintained after extrusion [8–10].

Regarding the design of 3D printed porous scaffolds that simulate tissues, some properties to keep in mind are: surface area and interconnectivity, which are related to cell growth; permeability, which governs nutrient transport; and mechanical strength, which assures support and protection, among other properties.

One possibility to achieve required porosity is to use hierarchical scaffold design, creating libraries of unit cells that can be joined to obtain scaffold structures. Hollister observed that increasing the material volume of a certain structure increased elastic modulus and decreased permeability [11]. In the same line, Egan et al. defined four different types of scaffold structures, taking into account either beam-based unit cells or truss-based unit cells. In addition, each structure could be created by means of either continuous or hierarchical patterning. They found that, given a certain porosity value, truss-based scaffolds have higher surface areas and lower elastic moduli than beam-based ones [12]. On the other hand, Arabnejad et al. presented a visualization method that allows understanding the relationship among cell topology, pore size and porosity in stretch-dominated structures, such as tetrahedron and octet trusses [13].

Another possibility to create structures with required porosity is use of topology optimization, which consists of distributing material in regions having low and high material density respectively. This is achieved by periodically repeating a unit cell, which is composed of areas with and without material [14,15]. When applying topological optimization methods, several authors have carried out multiobjective optimization of different properties in scaffolds. Lin et al. used an objective function that assigned different weights to the two responses considered: porosity and stiffness. The function was then maximized or minimized by numerical methods [16]. In a similar way, Guest and Prévost [17], as well as Hollister and Lin [18] used topology optimization to maximize stiffness and fluid permeability. Kang et al. used a homogenization-based topology optimization method to achieve the required bulk modulus and isotropic diffusivity for a certain porosity value [19]. Other properties of the structures, such as thermal conductivity [20], have been addressed. On the other hand, although the increase in surface area of pores helps tissue growth, this growth is facilitated if concave surfaces are used. In this direction, Egan et al. modelled scaffolds with curvature. They first fixed required porosity to assure a certain permeability value, which is desirable for nutrient transport, and then addressed the problem of mechanical strength of structures [21].

Different authors have tested the properties of FDM printed porous scaffolds. Regarding mechanical properties, Habib et al. used finite element analysis and compressive strength tests [22]. Wang et al. printed scaffolds for vascularized bone tissues in different materials, in order to test both their biomimetics and their strength [23]. Aw et al. tested the effect of printing parameters on tensile strength of conductive acrylonitrile butadiene styrene/zinc oxide (CABS/ZnO) composites [24].

Helguero et al. modelled artificial bones and printed them in acrylonitrile butadiene styrene (ABS). They tested both anisotropy and compressive strength of the scaffolds [25]. As for porosity, Gregor et al. printed PLA scaffolds and measured their porosity by means of X-ray microtomography [26]. Regarding surface finish, Townsend et al. listed most usual methods for measuring roughness profiles (contact stylus), and surface topography (confocal microscopy, focus variation microscopy, coherence scanning interferometry, chromatic confocal microscopy, conoscopic holography, atomic force microscopy (AFM), and elastomeric sensors [27]). Krolczyk et al. compared the roughness obtained in turning processes with that obtained in FDM processes [28]. They observed that the machined surface had an anisotropic and periodic structure, while the printed surface had an undirected structure. With the manufacturing conditions employed, the FDM process showed higher roughness values than the turning process.

In the present paper, a model was developed to define the pore size and the porosity of porous structures. Unlike other methods that are based on truss structures, the present model allows obtaining irregular porous structures from random location of columns in the space, which leave voids among them. Specifically, the structure was modelled with parallel planes joined by columns, with a certain number of columns on each plane. The model was applied to a disk shape. Three variables were defined: the distance between parallel planes, the number of base points for columns on each plane, and the radius of each column. Next, dimensional analysis was used to reduce the number of process variables to 2. Then, the requirements were defined for a specific application case: the use of a porous structure in external layers of hemispherical hip prostheses. Subsequently, the design of experiments, with three-level factorial analysis, was used to obtain mathematical models for porosity, mean of pore size and variance of pore size as a function of dimensionless variables. They allowed multiobjective optimization in order to determine the optimal values for the process parameters.

In order to compare experimental results to computationally calculated ones, samples were printed with FDM technology, and total porosity, as well as pore size, was measured. X-ray tomography was used to determine the total porosity of the printed structures by means of computation of plastic volume and comparison with total volume of the printed shape.

The present study will help designing and manufacturing porous structures with specific requirements regarding the porosity and pore size that favour osseointegration. The same methodology can be used, however, to achieve other requirements of porous structures, such as mechanical strength and/or nutrient transport.

2. Materials and Methods

2.1. Model for the Porous Structure

2.1.1. Model Definition

The printing process of a random porous structure, such as a trabecular one, presents some difficulties: the walls in certain parts of the structure are too thin (Figure 1), there are some areas with burrs, some parts of the structure have a high inclination angle that leads to the use of printing structure supports, etc.

Such difficulties can be attributed to the fact that, when designing the structure, a completely random distribution of points in space is used. Since distribution is random, connections between different points in space can have any orientation. In the present paper, a proposed solution for modelling porous structures is presented. It involves defining some theoretical parallel planes, each one of them with several theoretical points that are randomly distributed. Once the points have been created on the surfaces, it is necessary to connect them by means of theoretical lines. For doing this, each point is connected to the three nearest points of the same plane or of the plane that is immediately below. Thus, almost vertical lines will be created that will have a correct inclination angle for printing. Figure 2 shows a scheme of the model applied to a disk shape.

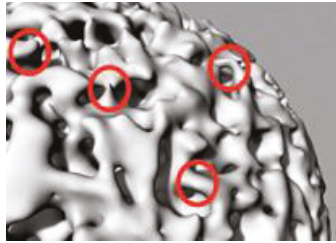


Figure 1. Trabecular structure with thin walls.

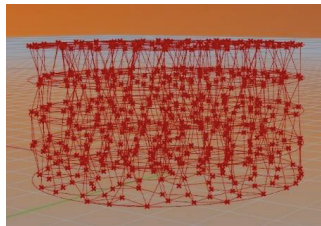


Figure 2. Structure obtained after applying the model to a disk shape.

The marching cubes algorithm allows lines and points to be given volume [29]. It is used in the present paper to create columns of the structure from the theoretical lines. The structure obtained after applying the model and the marching cubes algorithm to a disk shape is shown in Figure 3.

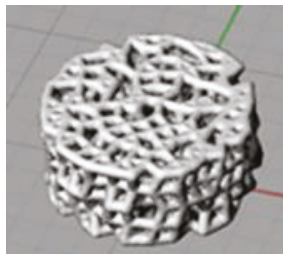


Figure 3. Structure obtained after applying the marching cubes algorithm to a disk shape.

Thus, there are three parameters to be controlled: distance between parallel planes H (mm), number of points per surface unit on a certain plane N (points/mm²) (Figure 4a), and radius r of columns that are created around the model lines (mm) (Figure 4b).

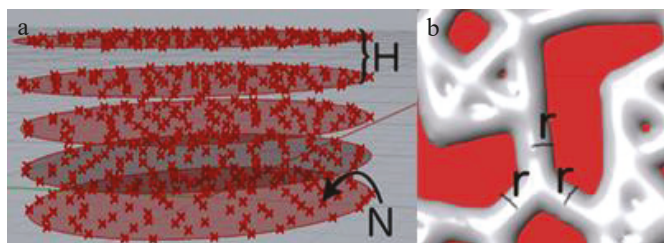


Figure 4. Parameters that define the porous structures: (a) parameters H and N , and (b) parameter r .

With the aim of determining optimum values for parameters, it is necessary to find the relationship between the three model parameters and the responses of porosity and pore size. To do so, a design of experiments was used to obtain mathematical models and perform multiobjective optimization. Before optimization, a reduction of the variables was applied so that each response considered depends on two dimensionless variables.

2.1.2. Reduction of Variables

Dimensional analysis allows reducing number of variables in a certain system [30]. If the problem depends on n dimensional variables, dimensional analysis reduces the problem to k dimensionless variables, where reduction is $n - k = 1, 2, 3,$ or 4 depending on the complexity of the system. One of the most used techniques for reducing the number of variables is the Buckingham Pi theorem. This allows obtaining dimensionless parameters that are a product of powers named $\Pi_1, \Pi_2, \Pi_3,$ etc. [31].

First part of the Pi theorem explains how to find reduction j Equation (1):

$$j = n - k \tag{1}$$

where n is the number of variables of the problem and k is the number of dependent variables. From n variables, k variables are chosen as basic and the rest are scale variables.

The second part of the Pi theorem shows that each dimensionless parameter is defined as the product of the rest of variables with a proper exponent different than zero. In this way, all dimensionless groups are independent. Each dimensionless parameter is related to the other ones by means of a function Equation (2):

$$\Pi_1 = g(\Pi_2, \Pi_3, \Pi_4, \dots) \tag{2}$$

where Π_1 is a dimensionless variable, and Π_2, Π_3, Π_4 are other variables.

In the present paper, three responses were analysed separately: porosity p (dimensionless), mean of pore size M (length) and variance of pore size V (length²), with process variables H (length), N (length⁻²) and r (length). Variable r was chosen as the scale variable.

For porosity, dimensionless parameters are described in Equations (3)–(5):

$$\Pi_1 = (H[\text{long}^1])^1 \cdot (r[\text{long}^1])^{-1} = \frac{H}{r} [\text{dimensionless}] \tag{3}$$

$$\Pi_2 = (N[\text{long}^{-2}])^1 \cdot (r[\text{long}^1])^2 = N \cdot r^2 [\text{dimensionless}] \tag{4}$$

$$\Pi_3 = p [\text{dimensionless}] \tag{5}$$

and the function to be found is presented in Equation (6):

$$\Pi_3 = g(\Pi_1, \Pi_2) \rightarrow p = g\left(\frac{H}{r}, N \cdot r^2\right) \tag{6}$$

Similar expressions were found for average value (M) and variance (V) of the probability density function and of the pore diameters Equations (7) and (8):

$$\frac{M}{r} = j\left(\frac{H}{r}, N \cdot r^2\right) \tag{7}$$

$$\frac{V}{r^2} = k\left(\frac{H}{r}, N \cdot r^2\right) \tag{8}$$

Thus, it was only necessary to perform experiments with two dimensionless factors, H/r and $N \cdot r^2$.

2.1.3. Requirements of the Structure

The kind of porous structure that is defined in the present paper can be used, for example, to replace or simulate bone trabecular tissue. At the macroscopic level, bones are formed by cortical and trabecular compartments. Bone tissues have several functions, for example, support, protection, mineral storage, and nutrient transport [32]. If a printed structure is to be fixed by means of osseointegration, a certain degree of porosity is required. Two main factors governing the porous external surface are the pore size and the porosity of the structure. According to Karageorgiou [33] and Bairo [34], optimum values of pore size were considered to range between 100 and 500 μm for a trabecular structure. The mean porosity value of scaffolds is recommended to be between 50 and 75% in volume. Although a certain variability of pore size, with small pores that improve cell attachment and large pores that favour nutrient transport could be desirable in some cases [35], in the present work only osseointegration was considered. For this reason, the variance of the pore size should take the lowest possible value, in order to assure that the maximum number of pores would lie within the interval. High connectivity between pores in the structures is also required, as porosity has to be accessible; an interconnecting channel structure is needed to allow tissue to grow on it.

2.2. Design of Experiments

In order to determine the required values for the two model variables considered and to optimize porosity, design of experiments was performed with simulated experiments. A full factorial design was employed with two dimensionless factors: H/r , the distance between surfaces where points are generated over a radius of generated volumes, and $N \cdot r^2$, the number of points per area unit. Three levels were defined for each factor and three replicates were performed for each experiment (since variability among replicates is high). In all, $3 \times 3^2 = 27$ runs were carried out. The radius of columns remained constant in all experiments.

Levels for variables were selected according to previous tests. A summary of levels is presented in Table 1.

Table 1. Levels of the factorial design.

	Level 1	Level 2	Level 3
H/r	3.2	4.0	4.8
$N \cdot r^2$	0.054	0.072	0.090

Responses considered were porosity, mean of pore diameters (mm), and variance of pore diameters (mm^2), in order to consider both the mean and dispersion of the probability function of porosity.

In order to calculate theoretical porosity and distribution of pore diameters, a program created by Dupuy et al. was used [36]. It is a MATLAB (MathWorks, Natick, MA, USA) script that, from a binary 3D image, returns the function of cumulated porosity vs. pore diameter. In the present study, a distribution of points in space was created with the program Rhinoceros 3D with the Grasshopper plug-in (Robert McNeel & Associates, Seattle, WA, USA).

2.3. Multiobjective Optimization

Once the mathematical models had been obtained, it was necessary to choose values for the parameters (N , H , r) that provided the required values for porosity, average pore size, and variance, taking into account the requirements of the responses.

The desirability function method was employed for the multiobjective optimization of responses [37]. It is based on defining desirability functions $d_i(x_i)$ for each response. The range for the desirability function is $[0, 1]$. Value 0 is assigned to a situation that is undesirable and value 1 is assigned to a completely desirable situation.

The objective function to maximize is the geometric average of the group of desirability functions. Taking into account different weights k_i for each objective Equation (9):

$$D = \sqrt[\sum_{i=1}^n k_i]{\prod_{i=1}^n (d_i(x_i))^{k_i}} \tag{9}$$

where n is number of responses to be optimized at the same time, and k_i defines the importance of each desirability function inside the objective function.

There are three kinds of desirability functions depending on the optimization goal: maximizing, minimizing, and target value desirability functions. As an example, in Equation (10) the maximization function is defined:

$$d_{i,max}(x_i) = \begin{cases} 0 & x_i \leq L \\ \left(\frac{x_i-L}{U-L}\right)^b & L < x_i < U \\ 1 & U \leq x_i \end{cases} \tag{10}$$

where L is a lower limit value from which the function becomes undesirable ($d_i = 0$) and U is an upper limit value from which the function is considered to be maximized ($d_i = 1$). Exponent b is a parameter that models the shape of the central part of the desirability function. It can take any value within $[0, \infty]$. If b takes values $[0, <1]$, the central part of the function will be concave, and a small increment of the response from the unacceptable point leads to a great increment of d_i . If b takes a value of 1, the central part of the function will be a straight line with constant slope. If b takes values $[>1, \infty]$, the central part of the curve will be convex, and, until a value that is very similar to the optimal one is obtained, the d_i value will be almost zero.

Table 2 shows the selected values of parameters for optimization.

Table 2. Selected values of parameters for optimization.

Response	Type of Desirability Function	Lower Value L	Target Value T	Upper Value U	b
Porosity	Of target value	0.500	0.625	0.750	1
Mean (mm)	Of target value	0.100	0.300	0.500	1
Variance (mm ²)	Minimization	0.000	*	0.010	1

* means that a certain parameter was not used.

For porosity and mean of pore size, lower (L) and upper (U) values were selected, defining an interval for each response. The average value of the interval was selected as target value (T).

For variance of pore size, lower value (L) was 0, since variance is to be minimized so that the maximum number of pores is contained within the required interval for the pore size. The upper value (U) was set at 0.01. It is supposed that pore size follows a normal distribution, in which 95.4% of the population is included within the $\mu \pm 2 \cdot \sigma$ interval. By equalling the range of pore diameters $[0.100, 0.500]$ with the a.m. interval Equation (11), the maximal standard deviation $\sigma_{max} = 0.100$ mm is found, according to Equation (12). Thus, the maximal variance $Variance_{max}$ is 0.010 mm² according to Equation (13):

$$[0.300 - 2 \cdot \sigma_{max}, 0.300 + 2 \cdot \sigma_{max}] \text{ mm} = [0.100, 0.500] \text{ mm} \tag{11}$$

$$\frac{0.300 - 0.100}{2} = 0.100 \text{ mm} = \sigma_{max} \tag{12}$$

$$Variance_{max} = \sigma_{max}^2 = 0.010 \text{ mm}^2 \tag{13}$$

A MATLAB program was implemented in a discrete optimization of the objective function by means of sweeping. The program generates m_i equispaced values within an interval for each variable ($H, N,$ and r). Then, it checks if each point (combination of values for the different variables), meets

the conditions defined in Table 1. Such conditions correspond to the space that is considered in the regression.

Table 3 corresponds to the intervals for variables and the m -values used for each variable. The value for m was selected so that the distance between contiguous values is lower than or equal to 0.005.

Table 3. Intervals for variables and m -values used for optimization.

	Interval	m
H (mm)	[0.48, 2.00]	300
N (points/mm ²)	[0.30, 4.00]	740
r (mm)	[0.15, 0.41]	200

Different solutions to be found will depend on the importance (k_i) of each response. Specifically, four different cases were analyzed:

- The first case involves giving the same importance to all responses.
- The second case consists in giving higher importance to porosity response over the rest of the responses ($k_{porosity} = 5$).
- The third case gives a higher importance to mean ($k_{mean} = 5$).
- The fourth case consists in giving higher importance to variance ($k_{variance} = 5$).

2.4. Experimental Tests

Printing experiments were performed in order to determine the experimental porosity of the samples. The techniques of fused filament fabrication (FFF) or fused deposition modelling (FDM) were selected. Cura software was used for generating the g-code for printing.

Disk-shaped samples of 6 mm diameter and 3 mm height were designed. Selected parameters for the structure were $H = 0.72$ mm, $r = 0.15$ mm, and $N = 3.65$ points/mm² (according to results of multiobjective optimization in Section 3.2).

Three specimens were printed in a dual-extruder Sigma printer from BCN3D. Due to the difficulty to print the required columns of diameter 0.3 mm, the geometry of the disks was rescaled by a scaling factor of five before printing (30 mm diameter and 15 mm height). The printing speed of the head was set to 37 mm/s. The nozzle diameter was 0.2 mm, the layer height was 0.1 mm, and the infill was 40%. The shell thickness was 0.4 mm.

The geometry of the samples was measured by means of X-ray tomography with Zeiss Metrotom 800 equipment. From the geometry, it was possible to calculate the percentage of air (porosity) and the percentage of plastic in the structure with VG Studio Max software. From the 3D geometry, a cross-section was obtained at half the height of each specimen, where the width of pores was measured.

3. Results

In the present section results about the design of the experiments, multiobjective optimization, and experimental tests are presented.

3.1. Design of Experiments

Table 4 shows the results for the 27 different runs performed. The levels for the two factors considered are presented in codified units. Results for porosity, the mean of the pore size, and the variance of the pore size were simulated with a MATLAB program. Since the results of experiments come from simulation, the order of the runs is indifferent, and a standard order was used for performing the experiments.

Table 4. Results of the porosity, the mean of the pore size, and the variance of the pore size.

Nr	H/r	N·r ²	Porosity	Mean (mm)	Variance (mm ²)
1	−1	−1	0.574	0.524	0.009
2	−1	0	0.491	0.439	0.009
3	−1	1	0.409	0.359	0.006
4	0	−1	0.599	0.549	0.012
5	0	0	0.537	0.450	0.011
6	0	1	0.472	0.378	0.005
7	1	−1	0.645	0.578	0.015
8	1	0	0.563	0.466	0.007
9	1	1	0.500	0.414	0.008
10	−1	−1	0.587	0.559	0.022
11	−1	0	0.473	0.414	0.008
12	−1	1	0.436	0.369	0.007
13	0	−1	0.635	0.547	0.008
14	0	0	0.552	0.482	0.012
15	0	1	0.484	0.401	0.008
16	1	−1	0.644	0.575	0.010
17	1	0	0.582	0.491	0.012
18	1	1	0.521	0.411	0.006
19	−1	−1	0.549	0.525	0.016
20	−1	0	0.477	0.447	0.010
21	−1	1	0.430	0.397	0.008
22	0	−1	0.621	0.542	0.009
23	0	0	0.516	0.439	0.006
24	0	1	0.462	0.376	0.006
25	1	−1	0.641	0.575	0.015
26	1	0	0.571	0.476	0.008
27	1	1	0.502	0.401	0.009

Data were analysed with Minitab 17 (Minitab, State College, PA, USA). Multiple linear regressions were used to examine the mathematical models for the porosity, the mean of pore size, and the variance of the pore size as a function of the two dimensionless factors considered. For all models, hypotheses were formulated for the linearity, constant variance, normality, and independence of errors. All terms having *p*-values higher than 5% were not included in the model.

Equation (14) corresponds to porosity in real units:

$$\text{Porosity} = 0.614 + 0.051 \left(\frac{H}{r} \right)_{\text{real}} - 3.948(N \cdot r^2)_{\text{real}} \tag{14}$$

The R-adj coefficient is 95.89%.

The function for the mean pore size in real units is shown in Equation (15):

$$\text{Mean} = 0.929 + 0.024 \left(\frac{H}{r} \right)_{\text{real}} - 11.336(N \cdot r^2)_{\text{real}} + 47.222(N \cdot r^2)_{\text{real}}^2 \tag{15}$$

The R-adj value is 96.29%.

Since variance does not follow a normal distribution pattern, the natural logarithm of variance was analysed, which shows a normal distribution. Equation (16) corresponds to real units for \ln variance, while Equation (17) refers to variance:

$$\ln(\text{Variance}) = -3.552 - 16.061(N \cdot r^2)_{\text{real}} \quad (16)$$

$$\text{Variance} = e^{-3.552 - 16.061(N \cdot r^2)_{\text{real}}} \quad (17)$$

The R-adj coefficient is 44.14%.

Porosity depends on both H/R and $N \cdot r^2$, the mean pore size depends on the same variables and on $(N \cdot r^2)^2$, while variance depends only on $N \cdot r^2$.

3.2. Multiobjective Optimization

Table 5 shows a comparison of all solutions found.

It was observed that radius $r = 0.15$ mm, which is the minimum value considered, is to be selected for all solutions. The recommended height found for all solutions is $H = 0.72$ mm. This value does not correspond to any limit for variable H . Finally, N varies depending on the solution considered.

Since porosity should be 0.625, with mean pore size 0.300 mm and minimal variance, it is not possible to achieve all objectives at the same time. As a result, depending on the importance given to any response, different N values are found.

In Figure 5, curves for porosity are presented vs. N for different values of H and r . As a starting point, the solution found in the multiobjective optimization for equivalent importance of all responses was taken into account. It corresponds to the blue continuous line ($H = 0.72$ mm, $r = 0.15$ mm). From this solution, either height H or radius r were varied.

Porosity decreases linearly with number of points per surface unit. A broad range of porosity values can be achieved between 0.5 and 0.9 for the different combinations of H and r . For radius $r = 0.15$ mm, the higher the distance between parallel layers H , the higher the porosity (continuous and dashed lines). For radius $r = 0.19$ mm (dashed-dotted line in brown colour), the line shows a similar slope than for radius $r = 0.15$ mm. However, for higher radius $r = 0.23$, a steeper slope is observed and porosity decreases more sharply (dashed-dotted line in purple colour).

In Figure 6, curves for the mean of the pore size are presented vs. N for different values of H and r .

The mean of the pore size decreases with the number of points with curves that exhibit asymptotic behaviour. Thus, the minimum achievable mean of the pore size ranges between 0.3 and 0.55 for the different conditions.

Figure 7 shows curves for the variance of the pore size (mm^2) vs. N (points/ mm^2).

The higher the number of points per unit area, the lower the variance of the pore size. The same variance values were calculated for all structures having $r = 0.15$ mm (the continuous curve is superimposed with the dashed ones). As the radius increases, the variance decreases. For $r = 0.23$ (dashed-dotted line in purple) and high N values, the variance values close to zero were obtained.

Table 5. Optimization results.

	H (mm)	N (Points/mm ²)	r (mm)	Porosity	Mean (mm)	Variance (mm ²)	k	Desirability
Equivalent importance	0.72	3.65	0.15	0.537	0.434	0.008	$k_{porosity} = k_{mean} = k_{variance} = 1$	0.283
Porosity more important	0.72	3.25	0.15	0.573	0.470	0.009	$k_{porosity} = 5$ $k_{mean} = k_{variance} = 1$	0.378
Mean more important	0.72	3.87	0.15	0.517	0.418	0.007	$k_{mean} = 5$ $k_{porosity} = k_{variance} = 1$	0.336
Variance more important	0.72	3.88	0.15	0.517	0.417	0.007	$k_{variance} = 5$ $k_{porosity} = k_{mean} = 1$	0.276

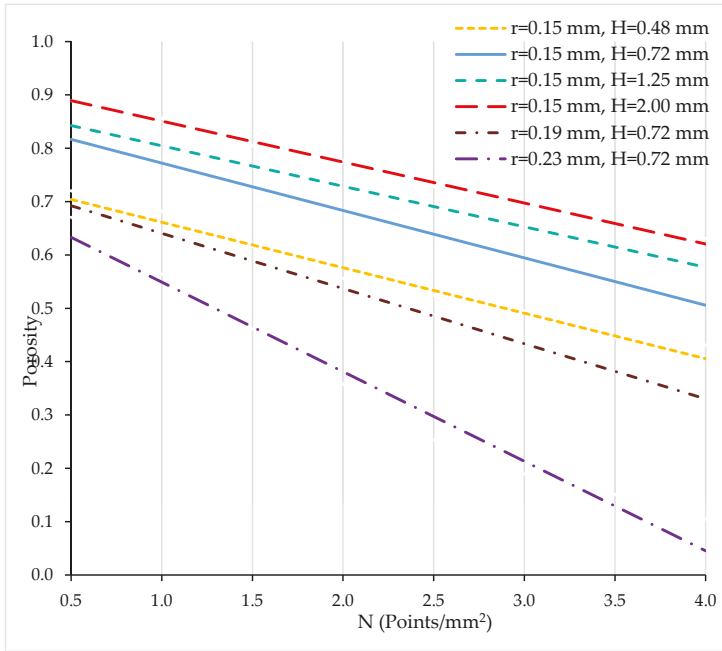


Figure 5. Porosity vs. N (points/mm²).

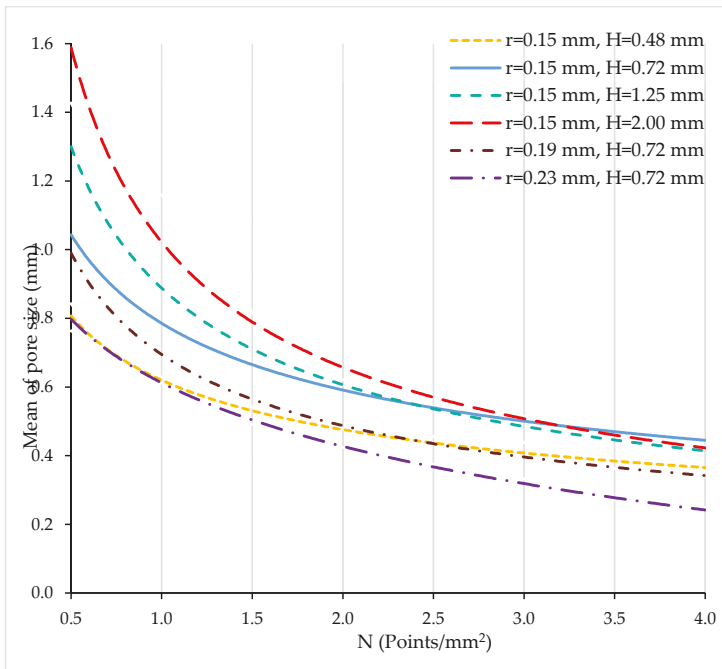


Figure 6. Mean of pore size (mm) vs. N (points/mm²).

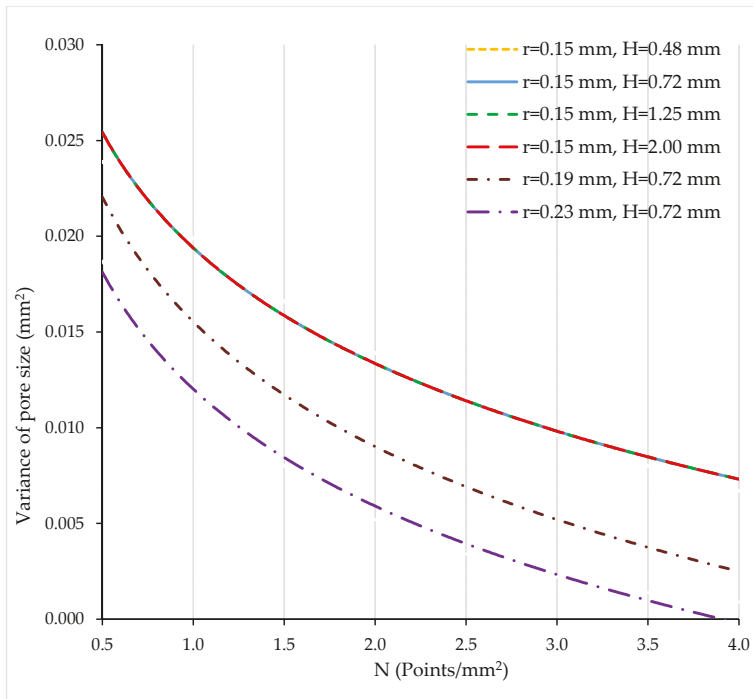


Figure 7. Variance of pore size (mm) vs. N (points/mm²).

3.3. Experimental Tests

A picture of the printed sample, which is a rescaling of the designed scaffold by a scaling factor of five, is presented in Figure 8. It corresponds to the optimal solution of multiobjective optimization, with $N = 3.65$ points/mm², $r = 0.15$ mm, and $H = 0.72$ mm.

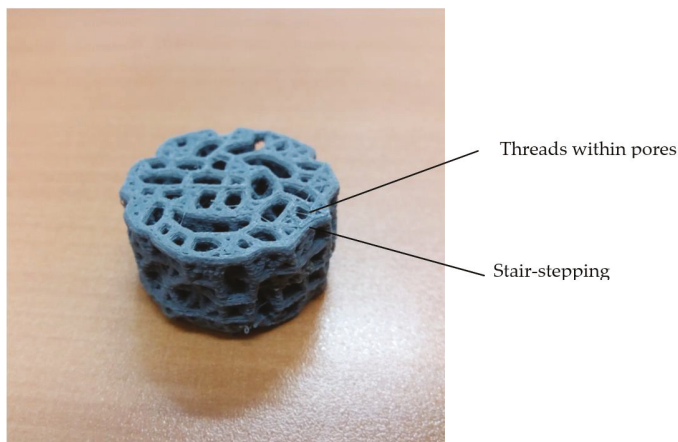


Figure 8. Printed porous structure (rescaling of the designed scaffold by scaling factor of five).

Some defects of the printed structure are observed. Small threads within pores are caused by the fact that retraction or recoil movement of the filament to prevent dipping when it is not printing did not work properly. In addition, surface finish shows stair-stepping defect due to layer-by-layer construction, which is more which is more patent the higher the layer height used. The printing process will be improved in further works.

As an example, Figure 9a depicts the measured geometry of specimen 1 with a cross-section at the half height of the disk. Figure 9b corresponds to the geometry of the cross-section of specimen 1. Both were obtained by means of X-ray tomography.

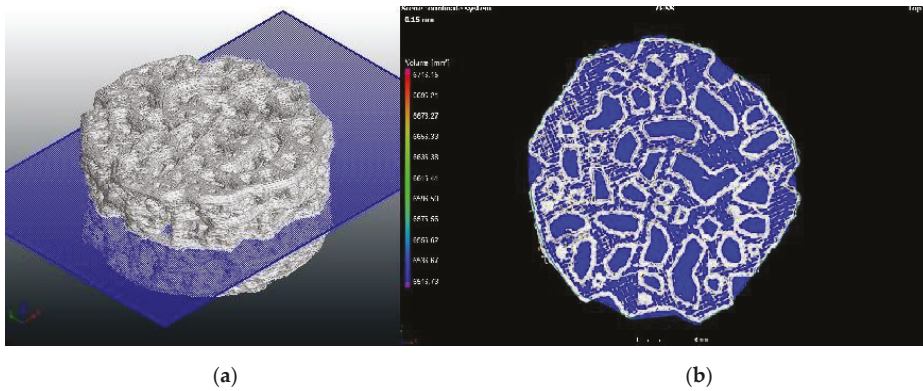


Figure 9. Cross-section of specimen 1: (a) 3D view, and (b) 2D view.

Both quite round pores and more elongated pores are observed, with a larger pore group and a smaller pore group. This fact could be useful when both nutrient transport and osseointegration are required [35]. The length of the largest elongated pore of rescaled printed specimen 1 is close to 5 mm (which corresponds to 1 mm in the designed specimen), which is a too high a value, and needs to be reduced in further works. However, the width of the same pore of the rescaled printed specimen is about 1.5 mm (0.3 mm in the designed specimen), which lies within the selected interval for the pore size.

Measured porosity, measured mean of the pore size, and measured variance of the three specimens are presented in Table 6.

Table 6. Measured porosity, mean of the pore size, and the variance of the pore size of the printed specimens.

Specimen	Measured Porosity	Measured Mean of Pore Size (mm)	Measured Variance of Pore Size (mm ²)
1	0.595	0.383	0.035
2	0.605	0.352	0.043
3	0.581	0.380	0.067
Average	0.594	0.372	0.048

The average value of the measured porosity for the three specimens was 0.594, showing good agreement with the result from multiobjective optimization, 0.537. The average value of the mean of the pore size was 0.372 mm, which is lower than the result from optimization, 0.434 mm. However, it is close to the centre of the considered interval, 0.300 mm. Variance ranges from 0.035 mm² to 0.067 mm², which is higher than target value of 0.010 mm². Nevertheless, this result could be desirable, since some variance of the pore size is required when both osseointegration and nutrient transport are

required [35]. Thus, printed PLA structures comply with the requirements for porosity and the mean of the pore size in trabecular structures.

4. Discussion

Unlike other methods for defining porous structures, which are based on truss structures, for example with hierarchical scaffold design [11,12] or with topology optimization [16,17], in the present paper a new method is presented that allows obtaining irregular porous structures from random location of columns, which leave voids of different sizes among them. The structure is defined with parallel planes having several points on each plane, and lines that join points from different planes or from the same plane. This theoretical structure, which would be infinite, must be bounded in a geometric figure, in this case a disk, although it could be applied to other types of figures such as prisms, cubes, cylinders, etc. Afterwards, the lines are converted into columns of a certain radius with help of the marching cubes algorithm [29]. Thus, the geometrical model is converted into a porous structure. The planes can be designated as layers and the lines as columns. From the correct selection of values for the independent variables of the system, it is possible to obtain structures with different porosity and pore size. In this case, three variables were chosen, namely the distance between parallel layers H , the number of points per area unit that generate columns on each layer, N , and the radius of columns, r . In order to reduce number of variables involved in the problem, dimensional analysis is applied [30]. In this case, radius of columns was used as the scale variable and two dimensionless variables were obtained: H/r and $N \cdot r^2$.

Once the model depends on $n-k$ dimensional variables (in this case $n-k = 3 - 1 = 2$ variables), it is possible to apply design of experiments in order to determine the influence of variables on selected responses. A full factorial design was selected, with three factors and three levels, with a total amount of 27 runs. In this work, responses were porosity, the mean of the pore size, and the variance of the pore size. Values for responses were calculated from simulated structures for each combination of variables. From results of design of experiments, by means of multiobjective optimization it is possible to select certain values for variables in order to achieve the required porosity and pore size values. Four different cases were taken into account, depending on importance given to each response. In this study, the desirability function method was employed, although other optimization methods are possible, either generating methods (no-preference, a posteriori, ...) or preference-based methods (a priori, interactive, ...) [38].

In the present work, main objective of optimization is to assure fixation of the structure by means of osseointegration. For this reason, target values were defined for both the porosity and the mean of the pore size according to the bibliography, while the mean of the pore size is to be minimized so that similar pores are obtained. However, in the future the methodology can be applied to other objectives, for example, the strength of the structure and/or nutrient transport. As a general trend, the lower the porosity, the higher the mechanical strength of a structure [39]. In case nutrient transport is considered as a goal, then a certain value for the variance of the pore size is recommended. Smaller pores are required with high surface/volume ratio in order to favour cell attachment before osseointegration and larger pores are needed to help nutrient transport [35].

In order to test if it was possible to print designed structures, three specimens were printed in PLA by means of FDM technology. Measured porosity of 0.594 was similar to the computationally-defined value of 0.537. Measured mean pore size of 0.372 mm was lower than the simulated value of 0.434 mm. Thus, the measured results for porosity and pore size are quite similar to the calculated ones, and agree with the requirements, although unlike the designed structure, which has round pores, in printed samples both round and elongated pores were observed. The experimental average value of the variance of the pore size was higher than the calculated one, and this will be addressed in further works.

Further research is required in order to improve the printing process of the scaffolds. Future trends include using FDM techniques with a lower nozzle diameter (below 0.1 mm) in order to reduce the

height of steps or controlling the flow in order to avoid filaments within the pores [40]. Other additive manufacturing technologies, such as stereolithography (STL), having higher dimensional accuracy than FDM, can also be employed [41].

5. Conclusions

In the present paper a new method for designing porous structures is presented. First, a geometric model is defined that is based on parallel layers with several columns of a certain radius that join them. The model can be applied to a certain shape, for example a disk. Then, by means of dimensional analysis, number of variables is reduced. In this case, two dimensionless variables are used: H/r and $N \cdot r^2$. Next, design of experiments allows obtaining mathematical models that relate process variables to responses, in this case the porosity (dimensionless), the mean of the pore size (mm) and the variance of the pore size (mm^2) of the structures. Then, multiobjective optimization provides the values of the variables that allow obtaining required values for the responses.

If the model is applied to a trabecular structure, in order to obtain target porosity of 0.625, target mean of pore size of 0.300 mm and low variance of pore size, recommended values were found for model variables: lowest radius of columns $r = 0.15$ mm and a medium value for height between parallel surfaces of $H = 0.72$. The number of points ranges from $N = 3.20$ to 3.90 points/ mm^2 depending on the importance given to each response. For example, if the three responses have the same importance, $N = 3.65$ points/ mm^2 are recommended. Higher number of points is recommended when mean or variance of pore size is more important than the rest of the variables. On the contrary, lower number of points is recommended when porosity is more important than the rest of the variables. The porosity and the mean of pore size obtained in experimental tests printed in polylactic acid (PLA), 0.594 and 0.372 mm respectively, were in good agreement with the simulated porosity and mean of pore size of 0.537 and 0.434 mm, respectively. Experimental variance of pore size is higher than the calculated one.

For fixed values of the distance between layers and of the radius of columns, the greater the number of points on layers, the lower the calculated porosity and the mean of pore size. A larger number of columns means there is less room for pores, leading to lower porosity, as well as shorter distance among columns, with lower pore size. The variance of pore size also decreases with number of points per surface unit. By varying the distance between layers, the radius of the columns and the number of columns per unit area, structures with different porosity and pore size can be achieved. The higher distance between layers is the higher porosity and mean of pore size. The higher the radius of columns is the lower porosity and mean of pore size. Thus, the model will be very useful in defining the required values for geometric variables, which will allow a certain degree of porosity and pore size in porous structures to be obtained.

The main limitation of the methodology is that it only takes into account the porosity of the structures that is required to achieve osseointegration, but not their mechanical properties (elastic modulus, compressive strength) or their ability to transport nutrients (permeability, diffusivity). Another limitation is that the structures are difficult to print with FDM technologies because of the low diameter of columns which is only slightly higher than nozzle diameter employed. For this reason, in the present work geometry was rescaled by a scaling factor of five prior to printing. Surface finish presents the stair-stepping defect due to layer-by-layer deposition.

In future work, other requirements for structures, related to either mechanical strength or mass transport, will be addressed. In addition, improvement of the FDM printing process is required in order to obtain more accurate and smooth parts. For example, nozzle diameter can be reduced and nozzle retraction can be controlled in order to minimise the stair-stepping effect and the presence of threads within pores respectively.

Author Contributions: I.B.-C. conceptualized the research, wrote the original draft and reviewed it, A.B. performed data analysis and calculated results, O.P.-R. defined the methodology.

Funding: This research was funded by Spanish Ministry of Economy, Industry, and Competitiveness grant number DPI2016-80345R.

Acknowledgments: The authors thank Ramón Casado-López and Sergi Aymerich for their support with experimental tests.

Conflicts of Interest: The authors declare no conflicts of interest.

References

1. Rochus, P.; Plessier, J.-Y.; Van Elsen, M.; Kruth, J.-P.; Carrus, R.; Dormal, T. New applications of rapid prototyping and rapid manufacturing (RP/RM) technologies for space instrumentation. *Acta Astronaut.* **2007**, *61*, 352–359. [[CrossRef](#)]
2. Ngo, T.D.; Kashani, A.; Imbalzano, G.; Nguyen, K.T.Q.; Hui, D. Additive manufacturing (3D printing): A review of materials, methods, applications and challenges. *Compos. Part B Eng.* **2018**, *143*, 172–196. [[CrossRef](#)]
3. Ventola, C.L. Medical Applications for 3D Printing: Current and Projected Uses. *Pharm. Ther.* **2014**, *39*, 704–711.
4. Leukers, B.; Güllkan, H.; Irsen, S.H.; Milz, S.; Tille, C.; Schieker, M.; Seitz, H. Hydroxyapatite scaffolds for bone tissue engineering made by 3D printing. *J. Mater. Sci. Mater. Med.* **2005**, *16*, 1121–1124. [[CrossRef](#)] [[PubMed](#)]
5. Hollister, S.J.; Lin, C.Y.; Saito, E.; Lin, C.Y.; Schek, R.D.; Taboas, J.M.; Williams, J.M.; Partee, B.; Flanagan, C.L.; Diggs, A.; et al. Engineering craniofacial scaffolds. *Orthod. Craniofac. Res.* **2005**, *8*, 162–173. [[CrossRef](#)] [[PubMed](#)]
6. Klammert, U.; Vorndran, E.; Reuther, T.; Müller, F.A.; Zorn, K.; Gbureck, U. Low temperature fabrication of magnesium phosphate cement scaffolds by 3D powder printing. *J. Mater. Sci. Mater. Med.* **2010**, *21*, 2947–2953. [[CrossRef](#)] [[PubMed](#)]
7. An, J.; Teoh, J.E.M.; Suntornnond, R.; Chua, C.K. Design and 3D Printing of Scaffolds and Tissues. *Engineering* **2015**, *1*, 261–268. [[CrossRef](#)]
8. Lipson, H.; Kurman, M. *Fabricated: The New World of 3D Printing*; Wiley and Sons: New York, NY, USA, 2013.
9. Gibson, I.; Rosen, D.; Stucker, B. *Additive Manufacturing Technologie*. Springer: New York, NY, USA, 2015.
10. Chia, H.N.; Wu, B.M. Recent advances in 3D printing of biomaterials. *J. Biol. Eng.* **2015**, *9*, 4. [[CrossRef](#)] [[PubMed](#)]
11. Hollister, S.J. Porous scaffold design for tissue engineering. *Nat. Mater.* **2005**, *4*, 518–524. [[CrossRef](#)] [[PubMed](#)]
12. Egan, P.F.; Ferguson, S.J.; Shea, K. Design of hierarchical three-dimensional printed scaffolds considering mechanical and biological factors for bone tissue engineering. *J. Mech. Des. N. Y.* **2017**, *139*, 061401-7. [[CrossRef](#)]
13. Arabnejad, S.; Burnett Johnston, R.; Pura, J.A.; Singh, B.; Tanzer, M.; Pasini, D. High-strength porous biomaterials for bone replacement: A strategy to assess the interplay between cell morphology, mechanical properties, bone ingrowth and manufacturing constraints. *Acta Biomater.* **2016**, *30*, 345–356. [[CrossRef](#)] [[PubMed](#)]
14. Bendsoe, M.P.; Kikuchi, N. Generating optimal topologies in structural design using a homogenization method. *Comput. Methods Appl. Mech. Eng.* **1988**, *71*, 197–224. [[CrossRef](#)]
15. Sigmund, O. Materials with prescribed constitutive parameters: An inverse homogenization problem. *Int. J. Solids Struct.* **1994**, *31*, 2313–2329. [[CrossRef](#)]
16. Lin, C.Y.; Kikuchi, N.; Hollister, S.J. A novel method for biomaterial scaffold internal architecture design to match bone elastic properties with desired porosity. *J. Biomech.* **2004**, *37*, 623–636. [[CrossRef](#)] [[PubMed](#)]
17. Guest, J.K.; Prevost, J.H. Optimizing multifunctional materials: Design of microstructures for maximized stiffness and fluid permeability. *Int. J. Solids Struct.* **2006**, *43*, 7028–7047. [[CrossRef](#)]
18. Hollister, S.J.; Lin, C.Y. Computational design of tissue engineering scaffolds. *Comput. Methods Appl. Mech. Eng.* **2007**, *196*, 2991–2998. [[CrossRef](#)]
19. Kang, H.; Lin, C.-Y.; Hollister, S.J. Topology optimization of three dimensional tissue engineering scaffold architectures for prescribed bulk modulus and diffusivity. *Struct. Multidiscip. Optim.* **2010**, *42*, 633–644. [[CrossRef](#)]
20. De Kruijf, N.; Zhou, S.; Li, Q.; Mai, Y.W. Topological design of structures and composite materials with multiobjectives. *Int. J. Solids Struct.* **2007**, *44*, 7092–7109. [[CrossRef](#)]

21. Egan, P.F.; Shea, K.A.; Ferguson, S.J. Simulated tissue growth for 3D printed scaffolds. *Biomech. Model. Mechanobiol.* **2018**. [[CrossRef](#)] [[PubMed](#)]
22. Habib, F.N.; Nikzad, M.; Masood, S.H.; Saifullah, A.B.M. Design and Development of Scaffolds for Tissue Engineering Using Three-Dimensional Printing for Bio-Based Applications. *3D Print. Addit. Manuf.* **2016**, *3*, 119–127. [[CrossRef](#)]
23. Wang, M.O.; Vorwald, C.E.; Dreher, M.L.; Mott, E.J.; Cheng, M.-H.; Cinar, A.; Mehdizadeh, H.; Somo, S.; Dean, D.; Brey, E.M.; et al. Evaluating 3D-Printed Biomaterials as Scaffolds for Vascularized Bone Tissue Engineering. *Adv Mater.* **2015**, *27*, 138–144. [[CrossRef](#)] [[PubMed](#)]
24. Aw, Y.Y.; Yeoh, Ch.K.; Idris, M.A.; Teh, P.L.; Hamzah, K.A. Effect of printing parameters on tensile, dynamic mechanical, and thermoelectric properties of FDM 3D printed CABS/ZnO composites. *Materials* **2018**, *11*, 466. [[CrossRef](#)] [[PubMed](#)]
25. Helguero, C.G.; Amaya, J.L.; Komatsu, D.E.; Pentyala, S.; Mustahsan, V.; Ramirez, E.A.; Kao, I. Trabecular Scaffolds' Mechanical Properties of Bone Reconstruction Using Biomimetic Implants. *Procedia CIRP* **2017**, *65*, 121–126. [[CrossRef](#)]
26. Gregor, A.; Filová, E.; Novák, M.; Kronek, J.; Chlup, H.; Buzgo, M.; Blahnová, V.; Lukášová, V.; Bartoš, M.; Nečas, A.; et al. Designing of PLA scaffolds for bone tissue replacement fabricated by ordinary commercial 3D printer. *J. Biol. Eng.* **2017**, *11*, 31. [[CrossRef](#)] [[PubMed](#)]
27. Townsend, A.; Senin, N.; Blunt, L.; Leach, R.K.; Taylor, J.S. Surface texture metrology for metal additive manufacturing: A review. *Precis. Eng.* **2016**, *46*, 34–47. [[CrossRef](#)]
28. Krolczyk, G.; Raos, P.; Legutko, S. Experimental Analysis of Surface Roughness and Surface Texture of Machined and Fused Deposition Modelled Parts. *Tehnički Vjesnik* **2014**, *21*, 217–221.
29. Lorensen, W.E.; Cline, H.E. Marching cubes: A high resolution 3D surface construction algorithm. In *Proceedings of the 14th Annual Conference on Computer Graphics and Interactive Techniques—SIGGRAPH '87*; ACM Press: New York, NY, USA, 1987; pp. 163–169. [[CrossRef](#)]
30. White, F.M. *Fluid Mechanics*; McGraw Hill: New York, NY, USA, 2011.
31. Buckingham, E. On Physically Similar Systems: Illustrations of the Use of Dimensional Equations. *Phys. Rev.* **1914**, *4*, 345–376. [[CrossRef](#)]
32. De Acevedo-Marques, P.M.; Mencattini, A.; Salmeri, M.; Rangayyan, R.M. *Medical Image Analysis and Informatics: Computer-Aided Diagnosis and Therapy*; CRC Press: Boca Raton, FL, USA, 2018.
33. Karageorgiou, V.; Kaplan, D. Porosity of 3D biomaterial scaffolds and osteogenesis. *Biomaterials* **2005**, *26*, 5474–5491. [[CrossRef](#)] [[PubMed](#)]
34. Baino, F.; Vitale-Brovarone, C. Mechanical properties and reliability of glass-ceramic foam scaffolds for, bone repair. *Mater. Lett.* **2014**, *118*, 27–30. [[CrossRef](#)]
35. Egan, P.F.; Gonella, V.C.; Engensperger, M.; Ferguson, S.J.; Shea, K. Computationally designed lattices with tuned properties for tissue engineering using 3D printing. *PLoS ONE* **2017**, *12*, 1–21. [[CrossRef](#)] [[PubMed](#)]
36. Dupuy, P.M.; Austin, P.; Delaney, G.W.; Schwarz, M.P. Pore scale definition and computation from tomography data. *Comput. Phys. Commun.* **2011**, *182*, 2249–2258. [[CrossRef](#)]
37. Derringer, G.C.; Suich, R. Simultaneous optimization of several response variables. *J. Qual. Technol.* **1980**, *12*, 214–219. [[CrossRef](#)]
38. Rangaiah, G.P. *Multi-Objective Optimization: Techniques and Applications in Chemical Engineering*; World Scientific: Singapore, 2009.
39. Zhao, H.; Li, L.; Ding, S.; Liu, C.; Ai, J. Effect of porous structure and pore size on mechanical strength of 3D-printed comby scaffolds. *Mater. Lett.* **2018**, *223*, 21–24. [[CrossRef](#)]
40. Popescu, D.; Zapciu, A.; Amza, C.; Baci, F.; Marinescu, R. FDM process parameters influence over the mechanical properties of polymer specimens: A review. *Polym. Test.* **2018**, *69*, 157–166. [[CrossRef](#)]
41. Melchels, F.P.W.; Feijen, J.; Grijpma, D.W. A review on stereolithography and its applications in biomedical engineering. *Biomaterials* **2010**, *31*, 6121–6130. [[CrossRef](#)] [[PubMed](#)]



Article

Application of Pin-On-Disc Techniques for the Study of Tribological Interferences in the Dry Machining of A92024-T3 (Al–Cu) Alloys

Jorge Salguero *, Juan Manuel Vazquez-Martinez, Irene Del Sol and Moises Batista

Mechanical Engineering & Industrial Design Department Faculty of Engineering, University of Cadiz, Av. Universidad de Cadiz 10, E-11519 Puerto Real-Cadiz, Spain; juanmanuel.vazquez@uca.es (J.M.V.-M.); irene.delsol@uca.es (I.D.S.); moises.batista@uca.es (M.B.)

* Correspondence: jorge.salguero@uca.es; Tel.: +34-956-483-413

Received: 28 June 2018; Accepted: 17 July 2018; Published: 18 July 2018

Abstract: One of the main criteria for the establishment of the performance of a forming process by material removal is based on cutting tool wear. Wear is usually caused by different mechanisms, however, only one is usually considered as predominant or the controller of the process. This experimental research is focused on the application of Pin-on-Disc wear tests, in which the tribological interference between UNS A92024-T3 Aluminum–Copper alloy and tungsten carbide (WC–Co) has been studied. The main objective of this study is focused on the determination of the predominant wear mechanisms involved in the process, as well as the characterization of the sliding and friction effects by using SEM and Energy Dispersion Spectroscopy (EDS) techniques, as applied to WC–Co (cutting tool material)/Al (workpiece material) which are widely used in the aerospace industry. Performed analysis prove the appearance of abrasive wear mechanisms prior to adhesion. This fact promotes adhesion mechanisms in several stages because of the surface quality deterioration, presenting different alloy composition in the form of a Built-Up Layer (BUL)/Built-Up Edge (BUE).

Keywords: UNS A92024; WC–Co; wear mechanism; tribology; adhesion

1. Introduction

Light alloys, mainly aluminum and titanium, are commonly used in different manufacturing fields especially because of their high performance—weight rate, their excellent physical-chemical properties and their advantageous economic cost. In this context, the aluminum market has greatly benefited thanks to its wide application in the aerospace industry, among others.

Continuous growth in the use of these alloys, and constant requirements to improve the performance of their manufacturing processes follow an important tendency to gradually increase the development of different research lines. The aim of these is to find the optimum conditions for the forming procedures of aluminum alloys.

Material removal, or machining, is among the main applications of aluminum alloy forming processes for aerospace applications. However, in the last decades machining processes have been characterized by a reorientation towards less aggressive environmental processes by means of the minimization or elimination of the use of cutting fluids in the cutting process. Under these conditions, cutting tools show an intensification of their wear mechanisms, causing deviations on the initial design specifications in the machined part [1,2]. For this reason, preserving the initial geometry of the cutting tool as long as possible is essential to ensure final tolerances [3]. In this context, a preliminary study of the tribological interference between the material being machined and tools is critical to maintain a precise control of process parameters, obtaining higher performance ranges.

In general terms, when aluminum alloys are machined by chip removal processes, the tool wear process is mainly characterized by the appearance of secondary or indirect adhesion mechanisms [4]. This wear mechanism is specifically based on the incorporation of the machined material over two well-localized areas of the cutting tool: at the edge, giving rise to the Built-Up Edge (BUE); and at the rake face, giving rise to a Built-Up Layer (BUL). Both types of material incorporation may modify the initial cutting geometry, affecting the surface quality of the machined parts [5], as is mentioned previously, and can be seen in the macrographs of Figure 1. In addition, the mechanical instability of the involved effects tends to cause a friction process promoted by the chip, resulting in the lost of particles of the tool surface, which constitutes the main wear effect [6].

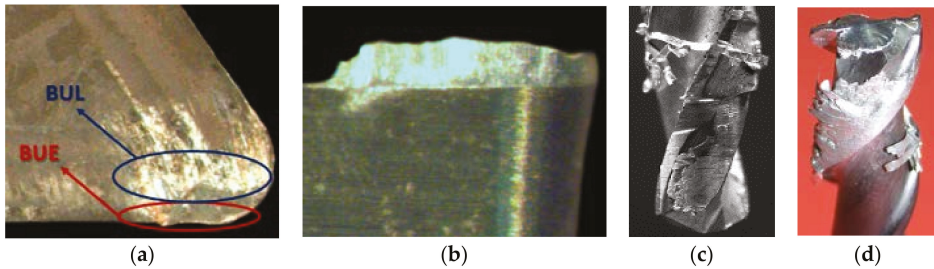


Figure 1. Cutting tools affected by adhesive wear mechanism in the machining of Al alloys: (a) turning insert tool; (b) detail of the adhered material thickness; (c) drilling tool; (d) milling tool for radial operations.

Tool wear mechanisms can be studied under lab conditions using Pin-on-Disk or Pin-on-Flat tests [7–10] reducing the material cost and improving the environmental sustainability of the process. However, only a few studies have been found which investigate the specific tribological pairing of aluminum and tungsten carbide [11]. For this reason, the present work is focused on the study of the wear mechanisms involved in the tribological friction and sliding conditions of the WC–Co (tool material) and UNS A92024-T3 aluminum alloy. Pin-on-Disc test techniques were performed and wear effects were analyzed by volume variation and SEM/Energy Dispersion Spectroscopy (EDS) microscopy in order to obtain a deeper understanding for the detected wear phenomena.

2. Materials and Methods

Pin-on-Disc tribological tests (PoD) were carried out under dry conditions, using a MT/60/NI Microtest Tribometer (Microtest S.A., Madrid, Spain) (motion diagram in Figure 2). The load (N) and linear speed (Ls), track radius (R) and turning speed (ω) were constant, while sliding distance varied, as is listed in Table 1. During the test development, the dynamometric response values, environmental conditions, and temperatures were measured.

Table 1. Test Conditions.

Load (N)	Sliding Speed (m/s)	Sliding Distance (m)												
		10	100	200	300	400	500	600	700	800	900	1000		
10	1.0													

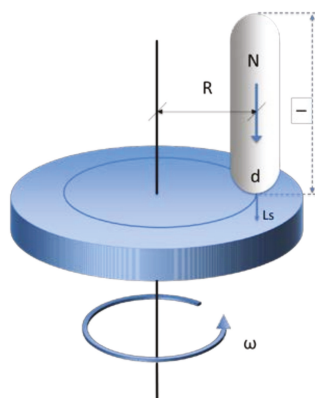


Figure 2. Pin-on-Disc tribometer motion diagram.

Firstly, Al–Cu UNS A92024-T3 ($R_a < 0.4 \mu\text{m}$) samples of $90 \times 90 \text{ mm}^2$ and thicknesses between 1.6 and 2.0 mm were selected as discs. Their composition is shown in Table 2.

Table 2. Composition of aluminum–copper alloy (Weight %).

Cu	Mg	Mn	Si	Fe	Zn	Ti	Cr	Al
4.00	1.50	0.60	0.50	0.50	0.25	0.15	0.10	rest

Then, (WC-6%Co) carbide metal bars with 30 mm length (l) and 4 mm diameter (d) hemispherical ends were used to simulate tool displacement (pins). The average and maximum Hertz contact pressure for the tribological pair were calculated as 0.91 and 1.37 GPa, respectively.

Wear evaluation was carried out following the guidelines of the ASTM G99-04 standard, expressing the friction effects in terms of material volume loss (mm^3) as a function of the sliding length. All samples were carefully cleaned using petroleum ether and alcohol (50%). The weight of the aluminum probes were evaluated by a precision scale (Ohaus Pioneer PA214, Parsippany, NJ, USA) before (P0) and after (PF) the development of the tribotests. The precision scale used in the weight evaluation of the samples have a 0.0001 g resolution. This scale resolution is the recommended by the ASTM G99 for the evaluation of results in Pin-on-Disc tribological tests.

In addition, visual inspection was carried out by optical microscopy techniques, using a stereoscopic microscopy device (Nikon SMZ-800, Tokyo, Japan) with the aim of analyzing the effects and consequences of the wear mechanisms involved in the process. The wear track was also measured by a profilometer Taylor Hobson Form Talysurf Series 2 (Leicester, UK).

Specific areas of the carbide pins and aluminum discs were established to perform deeper evaluation with a Scanning Electron Microscopy (SEM) and Energy Dispersion Spectroscopy (EDS) microcompositional characterization, by using a FEI Quanta 200 (ThermoFisher Scientific, Hillsboro, OR, USA) with EDAX Phoenix.

3. Results and Discussion

The friction coefficient behavior and wear mechanisms involved in the process were studied on the contact surface of the carbide pins. The tribological wear effects were evaluated through volume loss of aluminum discs as a function of sliding length. Additionally, a study on the tribological wear behavior between empirical and theoretical models was carried out taking the Archard coefficient as control parameter.

3.1. Friction Coefficient Evaluation

The friction coefficient (μ) of the specimens shows specific behavior for different sliding lengths. These phenomena may be mainly caused by the wear mechanisms involved in each stage of the friction process. In this way, through analyzing the obtained values for the friction coefficient, three stages were detected, with different behavior during the sliding course, Figure 3.

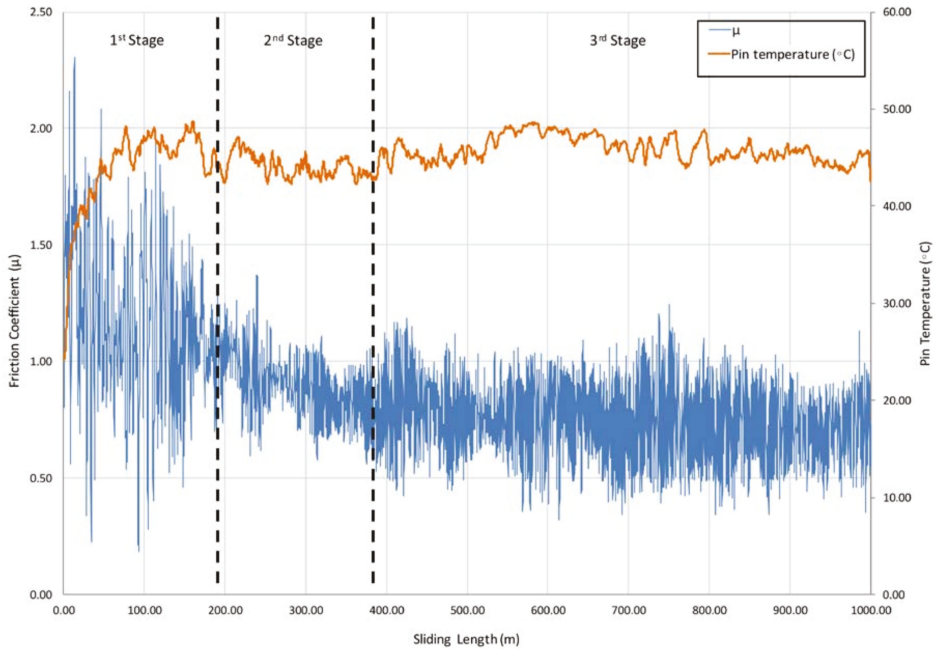


Figure 3. Friction coefficient and pin temperature as a function of sliding length for 1000 m.

The first stage is observed up to 200 m of sliding length, where the “stick-slip” phenomena takes place. This effect is developed in the dynamic contact between both surfaces, resulting in unstable movements along the sliding track. In the first friction instant, a significant increase in the contact force and μ were caused by the detachment of initial asperities which come from the surface material of the tribological pair. These asperities may cause specific roughness values, leading to a smaller contact surface between the pin and the disc, resulting in higher contact pressures. The action of high contact pressures on rough surfaces tend to remove soft asperities, favoring the detachment of wear debris on the sliding track, and giving place to high amplitude in the friction coefficient values and the appearance of the effects of abrasive wear mechanisms. In this aspect, an important increase of amplitude values implies a growth in the instability during the initial length of the process, especially because of the lack of uniformity of the circular trace, Figure 4.

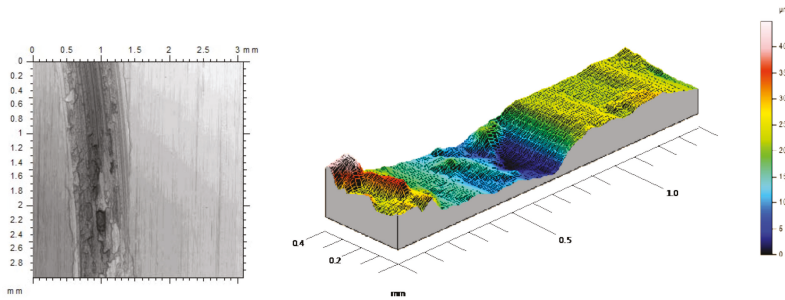


Figure 4. First stage sliding track with abrasive wear effects.

The increase in μ values is mainly caused by the movement of the pin over wear debris from initial aluminum asperities, involving a quick growth of the temperature in the contact area. A combination of friction and temperature conditions also favor adhesive phenomena from the aluminum particles to carbide surface.

The next stage starts with a decrease in μ values and a stabilization of the pin temperature. An important reduction in the oscillations amplitude of μ was also detected. This behavior is mainly due to a growth of the adhesion layer of aluminum alloy formed from the slip track over the pin in stratified sections. Under these conditions, adhesion of wear debris over the slip track and pin surface induces the modification towards softer topographies between contact elements, resulting in a sliding process where surfaces of the same material contact each other, Figure 5.

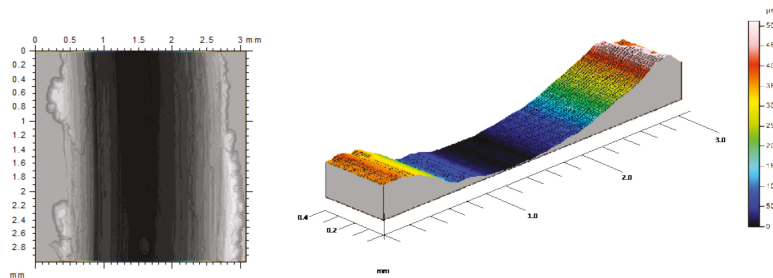


Figure 5. Second stage sliding track with abrasive wear effects.

In the last stage, the detachment is produced by aluminum adhered debris from the pin surface, as a result of reaching an excessive critical volume. Under these conditions, the adhered layer becomes unstable and may be removed as a consequence of the friction forces on the contact area. In this way, the carbide surface is subjected to wear from the adhered aluminum layer, promoting the loss of particles from the hemispheric surface. Because of this effect, wear debris of aluminum and carbide (harder than the disc) are deposited again over the sliding track. The material debris on the wear trace results in an increase of the μ values and the temperature of the pin, Figure 6. During this stage, the described effect is repeated as a continuous cyclic and dynamic behavior of adhesion wear mechanisms, as is described in previous works [12].

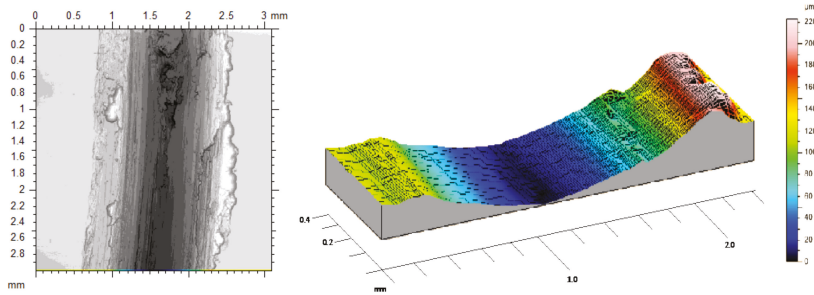


Figure 6. Third stage sliding track, with an adhered debris layer over the sliding way, and deposited material in the outer edges of the track.

When the carbide pin’s surface is analyzed, the existence of three different sections subjected to specific wear mechanisms are observed, Figure 7. In this aspect, similar wear effects are noticed from the morphological adhesion behavior over all of the tested specimens.

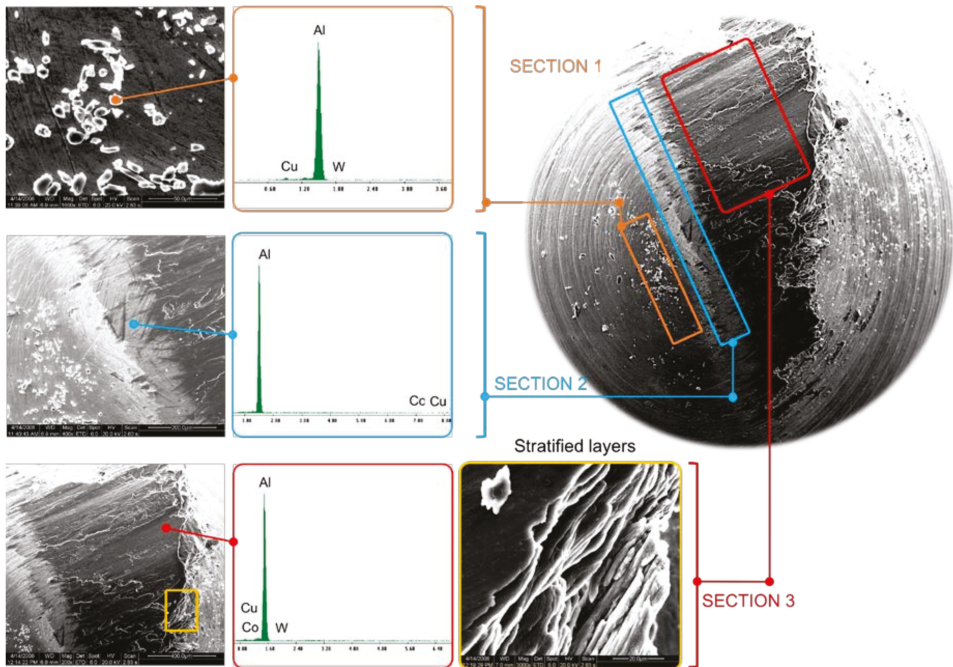


Figure 7. SEM (100×) micrograph of the Pin for test 500 m sliding distance. Detailed areas for the adhesion and punctual Energy Dispersion Spectroscopy (EDS) of the different wear phenomena.

Section 1 is especially characterized by the existence of Al–Cu alloy worn particles. These particles have been mechanically adhered to the hemispherical surface, giving place to abrasive wear phenomena in the first instants of the tribological tests.

Section 2 is formed by the primary layer developed in the first instants of the tribological test. EDS analysis shows that the composition of this layer is close to pure Al. According to previous research [13], this adhesive mechanism is mainly associated with a thermomechanical effect.

Section 3 is composed of the secondary layer, specifically described by a stratification of wear debris which is adhered over the primary layer through mechanical effects due to thermomechanical phenomena. Cu composition percentages near to 2.65% were observed.

3.2. Wear Effects Evaluation

The material volume loss was selected as the control parameter in order to study the sliding wear effects on the aluminum specimens. In this way, we might variations caused by the Pin-on-Disc test were measured on test probes with different sliding length configurations. The material volume loss was obtained by using the aluminum alloy density:

$$\Delta V = \frac{\Delta w}{\rho_A} = \frac{w_F - w_0}{\rho_A} \tag{1}$$

where w_F is the weight of the tested samples, w_0 is the weight of the samples before the sliding test, and ρ_A is the UNSA92024 aluminum alloy density.

In order to simplify analysis considerations and following the indications of the ASTM G99 Standard [6], the wear volume loss was considered negligible for the harder material (WC–Co). However, adhesive wear phenomena from the aluminum discs to carbide hemispherical pins have been evaluated

Figure 8 shows the analysis of the volume variation for different samples as a function of sliding length (L_d).

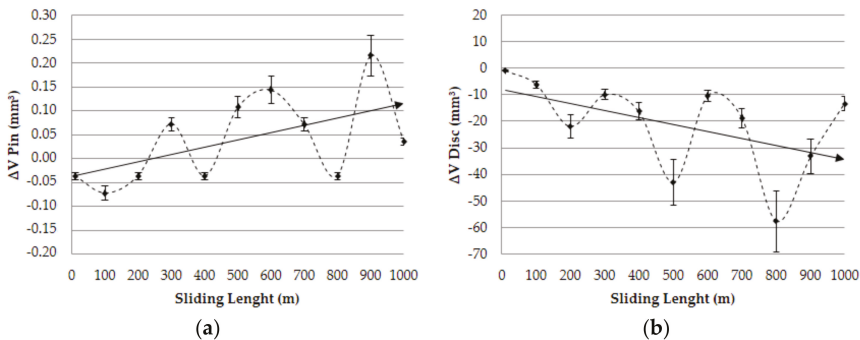


Figure 8. Volume variation vs. sliding length: (a) pin; (b) disc.

As was expected, a relevant increase in the values of volume lost for the aluminum discs was detected as a function of sliding length, fitting to a linear behavior and confirming previous research findings [7]. Regarding the pins, an estimation of the main wear mechanism was proposed. On the basis of the results indicated in the Figure 3, an important growth tendency was detected for the adhered material volume on the pins contact surface as a function of the sliding length. This fact may corroborate the raised hypothesis about the importance of secondary adhesion mechanisms in the analyzed tribological pair, detecting a progressive increase of the wear effects regarding the interaction time.

The appearance in the first instants of several negative values in the variation of volume of the pins should be noticed; this indicates the existence of a slight abrasive wear process prior to the adhesive phenomena. In this respect, SEM confirmed this behavior (Figure 9).

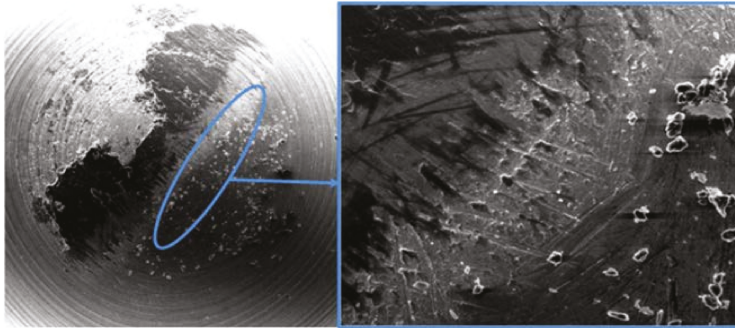


Figure 9. SEM (90×) micrography of the pin for test condition 900 m sliding distance. Detail of the abrasion produced by particles drag (600×).

This wear effect was observed in the first instant of sliding tests, as has been commented previously, in which the stick-slip phenomena takes place. The abrasive wear effect finishes when the surface tension of the material breaks, stabilizing the forces involved in the process and allowing the appearance of the first stage of adhesive mechanisms [14]. Furthermore, from the registered data in the tests, the Archard wear ratio [15] was determined, using the following expression:

$$K_s = a \cdot L_d^{-1} \quad (2)$$

where K_s is the Archard coefficient, L_d is the sliding distance and:

$$a = \frac{\Delta V \cdot H}{10^3 \cdot N} \quad (3)$$

where ΔV is the volume variation, and H is the softer material hardness [16].

The coefficient exposed in Equation (2) allowed us to carry out the marginal analysis of Archard ratio as a function of the sliding length, taking special care of the fact that the proportionality coefficient is not a constant value, where direct [ΔV , L_d] and indirect variables [H , N] are involved. In fact, the initial hardness of the material may vary as the sliding distance increases, mainly because of a superficial softening effect on the material, favored by the temperature increase in the contact area.

These considerations can differentiate the theoretical model from the real conditions. For this reason, marginal studies can be carried out by the approximation of the experimental results to an empirical model. In this way, a potential model has been selected, following the research lines with a specific interest in material removal [17–20].

$$K'_s = a' \times L_d^b \quad (4)$$

This equation can be linearity expressed by logarithmic expression:

$$\log K'_s = \log a' + b \times \log L_d \leftrightarrow y = m \times x + n \quad (5)$$

The potential model is shown in Figure 10 as a function of sliding distance for the different K_s coefficients obtained from empirical and theoretical models.

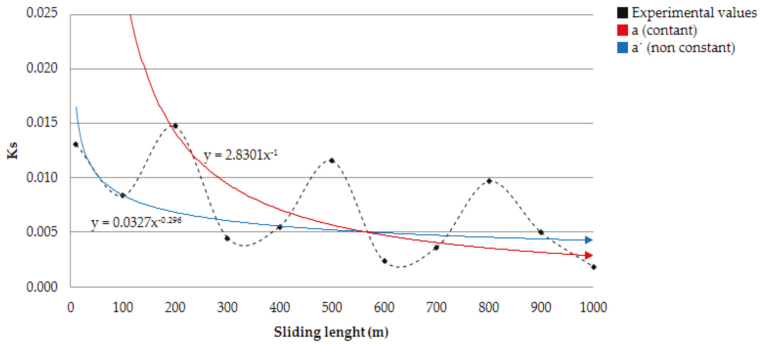


Figure 10. Archard wear coefficient vs. sliding distance.

Comparing the Archard theoretical model (K_s) and empirical model (K_s'), a relevant difference can be observed in the exponent which govern the sliding length. This disparity may be justified by the existence of specific wear mechanisms that are not taken into account in the theoretical model.

Material hardness (H), normal load (N), and wear volume (ΔV) are considered constant in this model. However, these components are direct or indirect variables of the process, making a coefficient not constant.

In this way, the K_s values tendency obtained are located in the Archard range for compatible and/or similar materials subjected to adhesive phenomena [21]. The first consideration may be justified by the friction behavior between the aluminum disc and adhered particles from the alloy to the carbide pins surface. The second one may be justified by the compatibility between Wolfram (W) with Aluminum (Al). This compatibility can be evaluated by the Rabinowicz relation [22], showing higher solubility values (>1%) and a high tendency towards adhesive mechanisms, Figure 11.

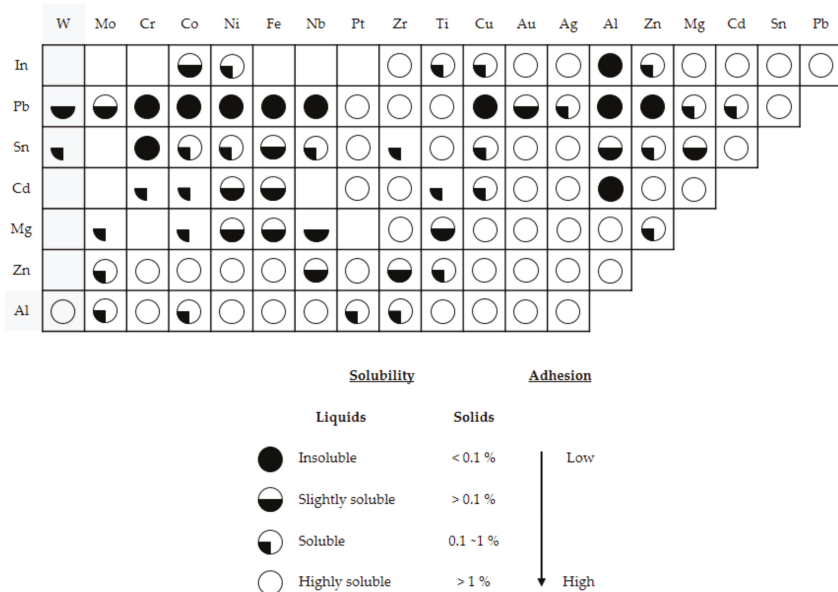


Figure 11. Partial reproduction of the Rabinowicz's table (adapted from [22]).

4. Conclusions

Wear mechanisms are the main responsible factors of cutting tool wear, being present on a wide temperature range. The main mechanism for the tribological pair Al–Cu and WC/Co is secondary adhesion, where the part material is removed and added to the cutting tool surface in the first step. After that, it brings with it the cutting tool's own particles, increasing the wear effects.

This work studied the tribological interference, simplifying to lab conditions (Pin-on-Disk) of a machining process. This allowed us to isolate the wear due to continuous friction between the contact pair, making it easy to characterize and to verify wear behavior.

The obtained results show an initial abrasion mechanism in the WC/Co pin, which is followed by the secondary adhesion of the aluminum alloy.

This adhesion takes place in two different stages. Firstly, thermomechanical effects (pre-fusion/adhesion) lead to the generation of a thin layer of pure aluminum, which comes from the aluminum matrix. After that, other layers with a similar composition to the Al–Cu alloy are adhered in a stratified way over the first one. This adhesion is due to mechanical effects. With the PoD tests it has been verified that, for pressures close to the ones achieved in finishing machining, the Built-Up Edge and Built-Up Layer effect can be studied for UNS A92024 alloy and WC–Co tribology pair. They are the main wear mechanisms for this pair against abrasion or erosion.

Furthermore, the classical model for the evaluation of Archard wear coefficient do not provide solid results, not taking into account variation of the process as it happens with the superficial hardness of the disc or the orientation of the pin.

Author Contributions: J.S. and M.B. conceived and designed the experiments; J.M.V.-M., I.D.S and J.S. performed the experiments; M.B. and J.M V.-M. analyzed the data; J.S. and J.M V.-M. wrote the paper.

Funding: This research was funded by the Spanish Government (MINECO/AEI/FEDER, UE), grant number [DPI2017-84935-R] and the Andalusian Government (PAIDI).

Conflicts of Interest: The authors declare no conflict of interest.

References

1. Kishawy, H.A.; Dumitrescu, M.; Ng, E.-G.; Elbestawi, M.A. Effect of Coolant Strategy on Tool Performance, Chip Morphology and Surface Quality during High-Speed Machining of A356 Aluminum Alloy. *Int. J. Mach. Tools Manuf.* **2005**, *45*, 219–227. [[CrossRef](#)]
2. Totten, G.E.; Liang, H. *Mechanical Tribology. Materials, Characterization and Applications*; Marcel Dekker: New York, NY, USA, 2004; ISBN 9780824748739.
3. Gómez-Parra, A.; Álvarez-Alcón, M.; Salguero, J.; Batista, M.; Marcos, M. Analysis of the evolution of the Built-Up Edge and Built-Up Layer formation mechanisms in the dry turning of aeronautical aluminium alloys. *Wear* **2013**, *302*, 1209–1218. [[CrossRef](#)]
4. List, G.; Nouari, M.; Géhin, D.; Gomez, S.; Manaud, J.P.; Le Petitcorps, Y.; Girot, F. Wear behaviour of cemented carbide tools in dry machining of aluminium alloy. *Wear* **2005**, *259*, 1177–1189. [[CrossRef](#)]
5. Veldhuis, S.C.; Dosbaeva, G.K.; Yamamoto, K. Tribological compatibility and improvement of machining productivity and surface integrity. *Tribol. Int.* **2009**, *42*, 1004–1010. [[CrossRef](#)]
6. Gokkaya, H.; Taskesen, A. The effects of cutting speed and feed rate on BUE-BUL formation, cutting forces and surface roughness when machining Aa6351 (T6) alloy. *J. Mech. Eng.* **2008**, *54*, 524–530.
7. Gharam, A.A.; Lukitsch, M.J.; Balogh, M.P.; Irish, N.; Alpas, A.T. High temperature tribological behavior of W-DLC against aluminum. *Surf. Coat. Technol.* **2011**, *206*, 1905–1912. [[CrossRef](#)]
8. Islam, M.A.; Farhat, Z. Wear of A380M Aluminum Alloy under Reciprocating Load. *J. Mater. Eng. Perform.* **2010**, *19*, 1208–1213. [[CrossRef](#)]
9. Ismail, O. Abrasive wear behavior of various reinforced AA6061 matrix composites produced with hot pressing process: A comparative study. *Materialwiss. Werksttech.* **2017**, *48*, 589–599. [[CrossRef](#)]
10. Strahin, B.L.; Doll, G.L. Tribological coatings for improving cutting tool performance. *Surf. Coat. Technol.* **2018**, *336*, 117–122. [[CrossRef](#)]

11. Xie, H.; Cheng, Y.; Li, S.; Cao, J.; Cao, L. Wear and corrosion resistant coatings on surface of cast A356 aluminum alloy by plasma electrolytic oxidation in moderately concentrated aluminate electrolytes. *Trans. Nonferrous Met. Soc. China* **2017**, *27*, 336–351. [[CrossRef](#)]
12. Sánchez, J.M.; Rubio, E.; Álvarez, M.; Sebastián, M.A.; Marcos, M. Microstructural characterisation of material adhered over cutting tool in the dry machining of aerospace aluminium alloys. *J. Mater. Process. Technol.* **2005**, *164–165*, 911–918. [[CrossRef](#)]
13. Carrilero, M.S.; Bienvenido, R.; Sánchez, J.M.; Álvarez, M.; González, A.; Marcos, M. A SEM and EDS insight into the BUL and BUE differences in the turning processes of AA2024 Al–Cu alloy. *Int. J. Mach. Tools Manuf.* **2002**, *42*, 215–220. [[CrossRef](#)]
14. Menezes, P.L.; Kishore; Kailas, S.V. On the effect of surface texture on friction and transfer layer formation—A study using Al and steel pair. *Wear* **2008**, *265*, 1655–1669. [[CrossRef](#)]
15. Liu, R.; Li, D. Modification of Archard’s equation by taking account of elastic/pseudoelastic properties of materials. *Wear* **2001**, *251*, 956–964. [[CrossRef](#)]
16. UNE-38314 *Aluminio y Aleaciones de Aluminio Para Forja, Serie 2000, AICu-AENOR 2000*; AENOR: Madrid, Spain, 2000.
17. Rubio, E.M.; Camacho, A.M.; Sánchez-Sola, J.M.; Marcos, M. Surface roughness of AA7050 alloy turned bars: Analysis of the influence of the length of machining. *J. Mater. Process. Technol.* **2005**, *162–163*, 682–689. [[CrossRef](#)]
18. Choudhury, I.A.; El-Baradie, M.A. Machinability assessment of inconel 718 by factorial design of experiment coupled with response surface methodology. *J. Mater. Process. Technol.* **1999**, *95*, 30–39. [[CrossRef](#)]
19. Chan, K.; Cheung, C.; Ramesh, M.; Lee, W.; To, S. A theoretical and experimental investigation of surface generation in diamond turning of an Al6061/SiCp metal matrix composite. *Int. J. Mech. Sci.* **2001**, *43*, 2047–2068. [[CrossRef](#)]
20. Abouelatta, O.B.; Mádl, J. Surface roughness prediction based on cutting parameters and tool vibrations in turning operations. *J. Mater. Process. Technol.* **2001**, *118*, 269–277. [[CrossRef](#)]
21. Archard, J.F. Contact and Rubbing of Flat Surfaces. *J. Appl. Phys.* **1953**, *24*, 981–988. [[CrossRef](#)]
22. Rabinowicz, E. *Friction and Wear of Materials*; Wiley: Hoboken, NJ, USA, 1995; ISBN 9780471830849.



© 2018 by the authors. Licensee MDPI, Basel, Switzerland. This article is an open access article distributed under the terms and conditions of the Creative Commons Attribution (CC BY) license (<http://creativecommons.org/licenses/by/4.0/>).

Article

Experimental Parametric Relationships for Chip Geometry in Dry Machining of the Ti6Al4V Alloy

Yezika Sánchez Hernández, Francisco Javier Trujillo Vilches *, Carolina Bermudo Gamboa and Lorenzo Sevilla Hurtado

Department of Manufacturing Engineering, EII, Universidad de Málaga, E-29071 Málaga, Spain; yezika.sanchez@uma.es (Y.S.H.); bgamboa@uma.es (C.B.G.); lsevilla@uma.es (L.S.H.)

* Correspondence: trujillov@uma.es; Tel.: +34-951-952-245

Received: 27 June 2018; Accepted: 18 July 2018; Published: 23 July 2018

Abstract: The Ti6Al4V alloy is included in the group of difficult-to-cut materials. Segmented chips are generated for a wide range of cutting parameters. This kind of chip geometry leads to the periodic variation of machining forces, tool vibrations, and work part-tolerance inaccuracies. Therefore, the analysis of chip morphology and geometry becomes a fundamental machinability criterion. However, few studies propose experimental parametric relationships that allow predicting chip-geometry evolution as a function of cutting parameters. In this work, an experimental analysis of the influence of cutting speed and feed rate on various chip-geometric parameters in dry machining of the Ti6Al4V alloy was carried out. In addition, the chip morphology and chip microstructure were studied. A clear dependence of certain chip-geometric parameters on the cutting parameters studied was found. From the experimental data, several parametric relationships were developed. These relationships were able to predict the evolution of different geometric parameters as a function of cutting speed and feed, within the tested range of values. The differences between the proposed models and the experimental data were also highlighted. These parametric equations allowed quantifying the value of parameters in which the trend was clear.

Keywords: Ti6Al4V alloy; chip geometry; dry machining; parametric models

1. Introduction

Titanium alloys exhibit exceptional properties that make them a good choice for many industrial applications, such as aeronautic, power-generation, or biomedical industries. Due to their low density, very high strength-to-weight ratio (even higher than wrought aluminum alloys), and excellent corrosion resistance at high temperatures, these alloys are widely used in structural parts of aircrafts and components which work under extreme environmental conditions (turbine blades, combustion chambers, etc.). In addition, their chemical inertness at room temperature is highly appreciated in the manufacture of medical implants [1–3].

Depending on their crystalline structure, titanium alloys can be classified into two large groups: (a) corrosion-resistant alloys (α), and (b) structural alloys (close α , $\alpha + \beta$, and β alloys). Regarding the aeronautical industry, structural alloys are the most common [4,5]. In particular, the Ti6Al4V ($\alpha + \beta$) alloy is within this last group, and represents 60% of the titanium used in this industry [6]. It is mainly used in the construction of components for engines and structures, either alone or hybridized with other materials such as carbon fiber reinforced polymer (CFRP) to form fiber metal laminate (FML) structures (CFRP/Ti) [7].

Machining (mainly turning, milling, and drilling) is one of the most common formation processes used in the manufacture of these structures [8]. Despite the good properties of the Ti6Al4V alloy, it is included in the group of difficult-to-cut materials, due to several problems not yet solved [9]. On one

hand, its low thermal conductivity avoids a fast evacuation of the heat generated in the cutting area. As a result, the cutting temperature increases, so tool wear and tool life are negatively affected. On the other hand, it shows high chemical reactivity above 500 °C. So, most tool materials are not suitable for machining this alloy because of their chemical affinity, which results in fast tool wear [10,11]. Furthermore, this alloy exhibits a low elastic modulus, which results in higher workpiece deformation and springback, inducing chattering and dimensional accuracy problems [12]. Finally, when machining this alloy, segmented chips (saw-tooth chips or serrated chips) are generated at relatively low cutting speeds. This chip geometry leads to the periodic variation of machining forces and tool vibrations, which may cause tool fatigue, breakage, and workpiece tolerance inaccuracies [13–15].

Traditionally, Ti alloys are cut at low cutting speeds, using cutting fluids in order to reduce the cutting temperature and to prevent tool wear. However, the use of these substances results in environmental pollution and fluid-saving problems. Thereby, new alternative methods to replace cutting fluids were developed [16]. Among them, dry machining minimizes the negative environmental effects, thermal shock in discontinuous machining operations, and health risks for workers [17–19]. However, the total absence of cutting fluids causes quick tool wear and the degradation of workpiece surface integrity [20,21]. Under these extreme conditions, the correct selection of cutting parameters (feed, cutting speed, and cutting depth) is of crucial importance to improving the machining performance from different points of view (environmental, economic, energy, and functional) [22].

Within this context, the analysis of chip morphology becomes a fundamental machinability criterion. The chip morphology provides information about the cutting operation's stability and the material response (thermal, mechanical, etc.) [23,24]. As previously commented, the segmented chip obtained while machining the Ti6Al4V alloy directly affects cutting forces, cutting temperature, tool wear, and workpiece surface quality. In addition, machining this alloy produces a large amount of continuous chips that must be evacuated and handled efficiently. This fact becomes a transcendental problem in the one-shot dry drilling of cutting materials (composite–metal assemblies) [25]. Hence, a correct understanding of cutting conditions, giving rise to an easier-to-handle chip, minimizing tool wear, and improving the surface integrity of machined parts, is highly important [26].

A large number of studies can be found in the literature devoted to the analysis of chip morphology and the chip-formation mechanism of the Ti6Al4V alloy. Nevertheless, this mechanism is not completely understood [27]. There are two main theories which explain the formation of segmented chips in this alloy: (a) thermoplastic deformation, and (b) fracture [8,28]. The first one supports that segmented chips are the result of the formation of adiabatic shear bands within the primary shear zone, caused by the predominance of thermal softening over strain hardening. The second theory explains chip segmentation through crack initiation and propagation from the outer chip surface toward the primary shear zone. Both theories are not mutually exclusive. Some authors suggest that the adiabatic shear band is the precursor of crack initiation [29–32].

The study of chip geometry provides valuable information about the energy consumption involved during machining, tool wear, and tool life, and the effect of machining on machined parts (surface quality, geometric deviations, residual stress, etc.). Because of this, a significant amount of research focuses on the analysis of several chip-geometric parameters (segment ratio, chip thickness, segment width, shear angle, shrinkage factor, chip segment frequency, etc.) of the Ti6Al4V alloy, and their evolution with cutting parameters [33,34].

Some studies analyzed chip geometry from an analytical point of view. Thus, several theoretical models were formulated [35–37]. Notwithstanding, there are many interacting variables involved in machining, and therefore, in the chip generation process. As a result, analytical studies are complex, and they require the application of a set of simplifications which usually lead to inaccurate predictions of various chip-geometric parameters [8,33,34]. Other studies used numerical models (finite element method, FEM) to simulate the chip generation process [8,23,27,38–41]. These models can be interesting as long as the constitutive laws of the material (tool and workpiece) are well defined. Regrettably, these

constitutive laws are often incomplete. As a consequence, these models frequently overestimate or underestimate certain chip-geometric parameters [27,33].

Longitudinal and transverse chip sections can also be experimentally observed using metallographic techniques (hot mounting, polishing, and etching) combined with stereoscopic optical microscopy (SOM) or scanning electron microscopy (SEM). The measurement of chip-geometric parameters can be carried out using a digital-image-capture system and image-processing software. In this regard, a lot of research that analyzes the influence of cutting parameters on chip geometry can be found in the literature [3,10,31]. However, few studies propose experimental parametric models that allow predicting the evolution of geometric parameters as a function of cutting parameters [20,22,42].

In this work, an experimental analysis of the influence of cutting speed and feed rate on various chip-geometric parameters was carried out in dry machining of the Ti6Al4V alloy. In addition, the chip morphology and chip microstructure were studied. From the experimental data, several parametric models were developed. These models were able to predict the evolution of different geometric parameters as a function of cutting speed and feed, within the range of values tested.

2. Materials and Methods

Table 1 shows the composition of the tested Ti6Al4V alloy. This composition was obtained using arc atomic emission spectroscopy (AES).

Table 1. Composition of the machined alloy (wt.%).

Alloy	C	Fe	N	O	Al	V	Ti
Part	0.08	0.164	0.05	0.05	5.47	4.09	Balance

Stereoscopic optical microscopy (SOM) techniques were used to observe the alloy microstructure (Figure 1a). A bimodal structure ($\alpha/\alpha + \beta$), which is typical in this alloy, can be observed. The structure was formed by a globular primary α phase (light color in the image) where aluminum was concentrated, and a transformed β phase containing an acicular α phase (lamellar structure, dark color in the image), where vanadium was concentrated (Figure 1b) [43,44]. The samples were polished prior to carrying out SOM.

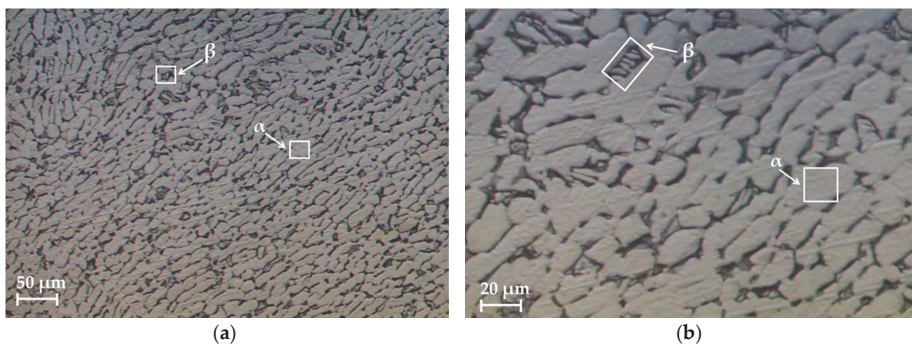


Figure 1. (a) Stereoscopic optical microscopy (SOM) images of the microstructure of the tested Ti6Al4V alloy and (b) amplification and identification of α and β .

The experimental study was designed to evaluate the influence of cutting parameters on the chip geometry of the Ti6Al4V alloy. For this purpose, a set of machining tests was carried out. Various combinations of cutting parameters (cutting speed (v_c), feed rate (f), and cutting depth (a_p)) were selected. A factor-by-factor study was applied, and their values are shown in Table 2. The range

of values was chosen based on industrial requirements. It is necessary to point out that low values of cutting speed were selected to prevent quick tool wear [4,9].

Table 2. Cutting parameters.

Feed Rate, f (mm/r)	Cutting Speed, v_c (m/min)	Cutting Depth, a_p (mm)
0.05	30	1
0.10	65	
0.20	125	
0.30		

In order to guarantee the repeatability of the tests, 10 specimens were machined for each combination of cutting parameters. Thereby, a total of 120 specimens were tested. All tests were conducted in a parallel lathe, and were performed dry, with the aim of using techniques with a low environmental impact.

Turning tests were carried out in an orthogonal configuration to minimize the influence of geometric variables, which could make the process more difficult to characterize (Figure 2) [27].

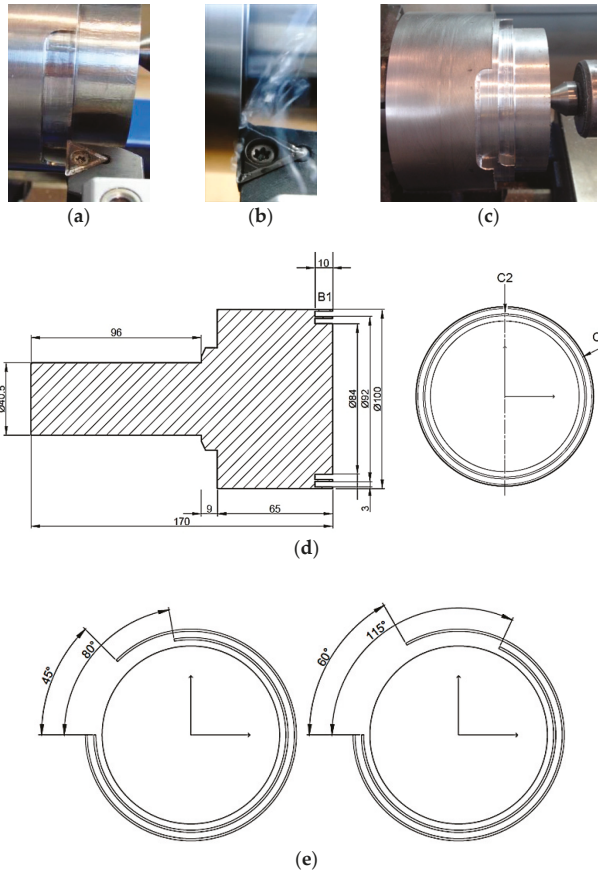


Figure 2. (a) Orthogonal cutting disposition; (b) initial machining instance; (c) sample for several cutting tests; (d) test sample design (mm); (e) relief zone design.

A combination of the tool insert, TCMT 16T308-F1, and the tool holder, STGCL 2020K16, provided geometrical features very close to an orthogonal configuration (Figure 2a,b). The tool used had WC-Co inserts coated with TiCN/Al₂O₃ [2,3]. A new tool was used for each cutting test in order to maintain the same initial conditions.

Specimens were designed with a tailored geometry to maintain orthogonal conditions across the tests, and to achieve different ranges of cutting speed and feed rate. Different grooving operations were carried out on a billet ($L = 170$ mm, $D = 105$ mm) to achieve a tubular geometry (Figure 2c). Specimens were formed by two crowns, corresponding to the two diameters machined previously (C1 and C2, Figure 2d). Each crown was machined with a specific thickness equal to a_p . B1 represents the work section at a 10-mm distance, equivalent to the total cut magnitude that corresponds to a certain combination of cutting parameters. Additionally, a relief zone was established, eliminating a sector of the crowns (Figure 2e), to ensure that the spindle reached a permanent regime. A 96-mm-long cylinder (on the left) was implemented to ensure correct fastening.

The chip generation process was monitored online using a digital camera. The chip samples were collected, photographed, stored, and codified after machining for further observations. Metallographic techniques were used to prepare the chip samples for observation (offline). The chip samples (longitudinal and transverse sections) were embedded in epoxy resin, before being polished and chemically etched (Kroll's reagent, 50 mL of H₂O + 2 mL of HF + 5 mL of HNO₃) to facilitate the observation.

An inverted metallurgical microscope (EPIHOT 280 NIKON, Tokyo, Japan) was used to observe the chip specimens. The SOM images were obtained using a CF Infinity Optical System (1.5× to 400×). Chip measurements were carried out using a digital-image-processing software (Omnimet BUEHLER, Lake Bluff, IL, USA).

Figure 3 shows the geometric parameters measured on the longitudinal and transverse chip sections, where h_p is the height of the peaks, h_v is the height of the valleys, S is the segment width, θ' is the complementary shear angle on the longitudinal section, and b and A are the chip width and area, respectively, on the transverse section (measured along the adiabatic shear band). To obtain b , a perpendicular line was drawn to the farthest point, starting from the base of a line approximately parallel to the chip edge.

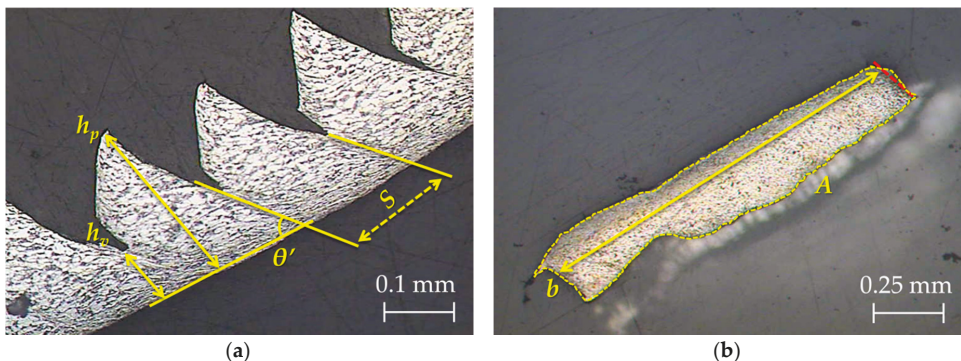


Figure 3. (a) Longitudinal and (b) transverse chip section measurements.

The shear angle, θ , can be indirectly obtained through its complementary angle, θ' (Figure 3), as presented in Equation (1).

$$\theta = \frac{\pi}{2} - \theta' \quad (1)$$

Likewise, the shrinkage factor (ζ), the segment ratio (G_s), and the equivalent chip thickness (t_c) can be calculated with Equations (2)–(4), respectively, where γ is the rake angle on the tool, assuming a constant volume and plane-strain hypothesis [22,33,34].

$$\zeta = \frac{\sin \theta}{\cos(\theta - \gamma)} \tag{2}$$

$$G_s = \frac{h_p - h_v}{h_p} \tag{3}$$

$$t_c = h_v + \frac{h_p - h_v}{2} \tag{4}$$

A total of five samples were analyzed, measuring each parameter three times, resulting in a total of 15 measurements for each combination of cutting parameters. The results for the various geometric parameters analyzed were expressed as the average value of these measurements.

3. Results and Discussion

3.1. Chip Morphology and Microstructure

Figure 4 shows the evolution of the chip morphology as a function of the cutting parameters, v_c and f . In general, the chip morphology is segmented and remains continuous across a wide range of v_c and f studied. Thus, the obtained chip is very difficult to evacuate and handle. This is a consequence, on one hand, of the high plasticity levels of this alloy, which makes it difficult to attain its shear limit. On the other hand, its low thermal conductivity results in thermal softening, which compensates for strain hardening and makes the chip more difficult to break [10,28,30,31].



Figure 4. Cont.

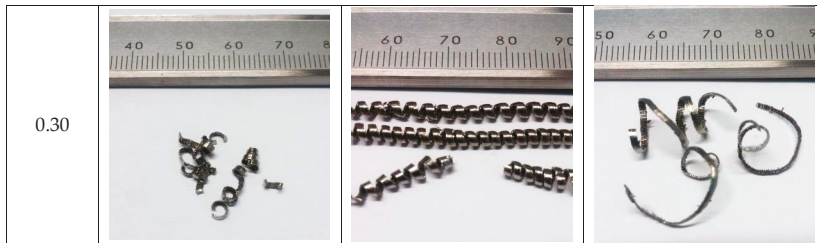


Figure 4. Evolution of the chip morphology as a function of cutting speed (v_c) and feed rate (f).

This fact becomes more noticeable when v_c was increased and f was reduced. In the lowest feed-rate range (0.05–0.10 mm/r), the chip morphology was continuously helical (Figure 5a) and showed a strong tendency toward forming chip nests for 0.05 mm/r. However, the chips tended to be tubular and more fragmented for the highest feed-rate range (0.20–0.30 mm/r) combined with low cutting speeds (30–65 m/min) (Figure 5b). For these values, the cutting forces were higher and the thermal-softening effects were lower; therefore, chip breaking was easier to achieve. From a machinability point of view based on chip control, the best results came from the highest values of feed rate and cutting speed. However, if other machinability criteria are taken into account, such as tool wear, cutting forces, superficial quality of parts, or temperature (not analyzed in this study), the results may present the opposite trend.

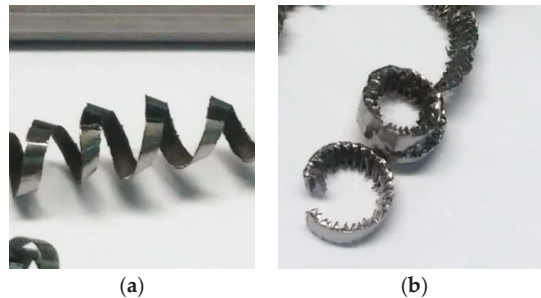


Figure 5. Chip morphology for (a) $v_c = 30$ m/min, $f = 0.05$ mm/r, and (b) $v_c = 30$ m/min, $f = 0.30$ mm/r.

Figure 6 shows the SOM images of the longitudinal and transverse chip sections as a function of v_c and f . From a qualitative point of view, a higher segmentation level was observed in the longitudinal section when v_c was increased. This increment was enhanced by the feed-rate action. A higher v_c results in an increase in cutting temperature; thus, the aforementioned thermal-softening effect is increased, and the chip is easier to deform. An increase in feed rate implies higher removal rates and cutting forces. As a consequence, the effect of cutting speed is maximized [33]. Therefore, this fact was less noticeable in the low range of feed rates used (0.05–0.10 mm/r). These observations were later quantified using measurements of the chip segment ratio (G_s). Regarding the transverse chip section, no significant changes were observed in the chip width (b) as a function of v_c or f . Obviously, the transverse section's area (A) increased proportionally to the feed rate.

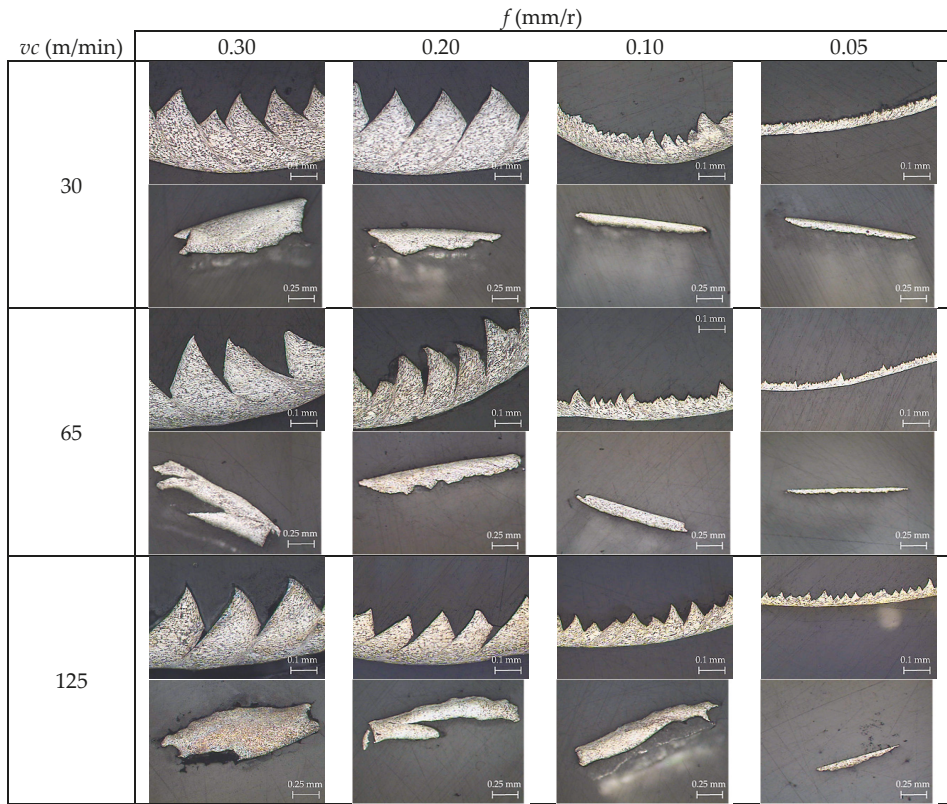


Figure 6. SOM images of the longitudinal (20 \times , 0.1 mm of each segment) and transverse (10 \times , 0.25 mm of each segment) chip sections.

When the chip microstructure (Figure 7) was compared with the stock microstructure before machining (Figure 1), grain deformation can be observed in the whole section [4,9]. In addition, two different grain alignments can be noted.

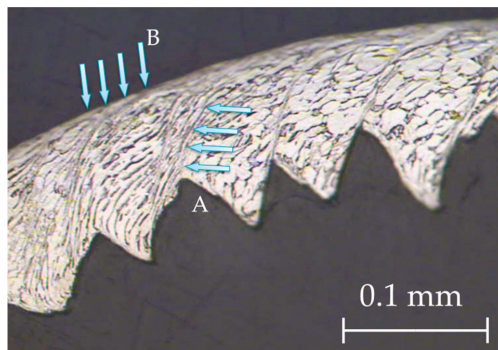


Figure 7. Grain deformation within the chip microstructure ($v_c = 125$ m/min, $f = 0.10$ mm/r).

Firstly, there was an alignment in the direction of the adiabatic shear band (primary deformation area, A in Figure 7), due to an intense plastic deformation in this narrow zone [4,45]. This fact was more noticeable when v_c increased, and a more refined grain structure was obtained (Figure 8). The influence of feed rate was more apparent at higher values of cutting speed. The phenomenon of crack initiation and propagation could be observed for high feed rates (0.20–0.30 mm/r), even when high values of cutting speed were applied (Figure 9).

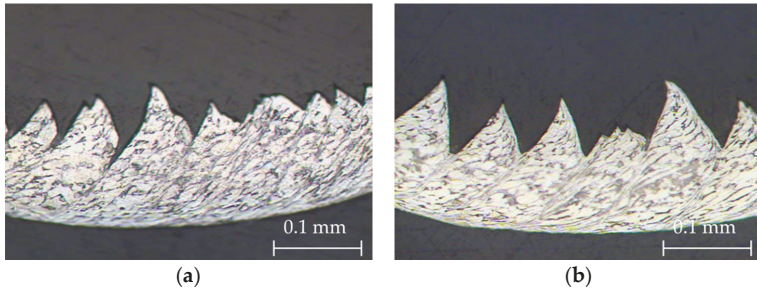


Figure 8. Chip microstructure (40 \times) for $f = 0.10$ mm/r: (a) $v_c = 30$ m/min, and (b) $v_c = 125$ m/min.

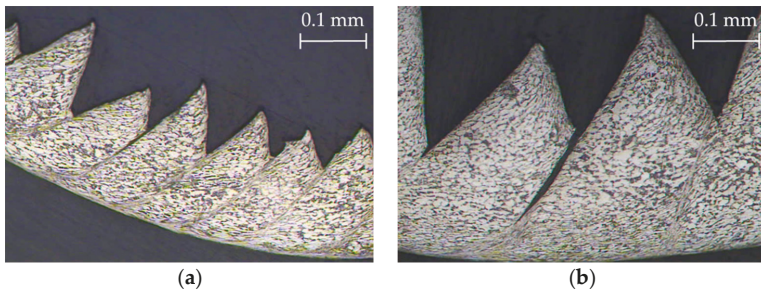


Figure 9. Chip microstructure (20 \times) at $v_c = 125$ m/min: (a) $f = 0.20$ mm/r, and (b) $f = 0.30$ mm/r.

Secondly, an alignment of the grain structure with the main cutting direction was observed, along a very thin layer on the contact surface between the chip and the face of the tool rake (B in Figure 7). This layer, the so-called white layer, was also present in the sub-machined surface of the part, and gave rise to a strain hardening of the machined surface, potentially reducing the alloy's machinability [2]. This effect was more intense when v_c and f were increased.

3.2. Geometric Parameters

Figure 10 shows the experimental mean values obtained for h_p and h_v as a function of the cutting parameters, v_c and f . An almost linear increase with feed rate could be observed for both parameters. This general trend was normal due to the direct proportionality between chip thickness and feed rate. Regarding v_c , a higher influence on h_p was shown for the lowest range of f considered. Specifically, for $f = 0.10$ mm/r, h_p showed an increasing trend with v_c (Figure 11). However, for the higher range of f (0.20–0.30 mm/r), the highest values of h_p were observed at $v_c = 30$ m/min. Moreover, no significant changes in h_v were noted as a function of v_c , except for $f = 0.05$ mm/r, where slightly higher values were observed when v_c decreased. An opposite trend was obtained for $f = 0.30$ mm/r.

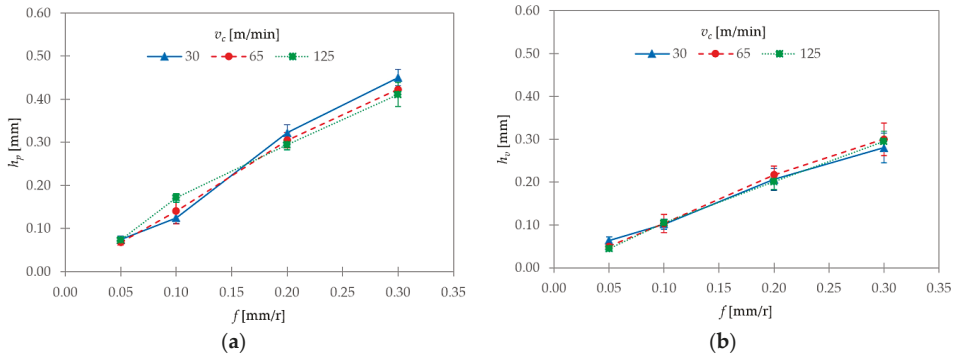


Figure 10. (a) Heights of peaks (h_p) and (b) valleys (h_v) as a function of v_c and f .

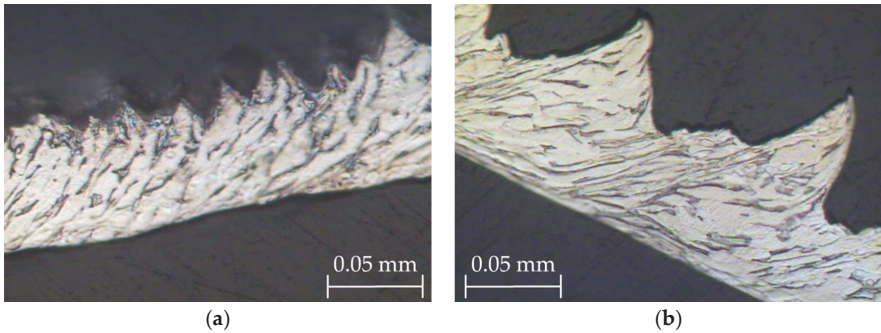


Figure 11. Chip SOM images (100 \times) for $f = 0.05$ mm/r: (a) $v_c = 30$ m/min, and (b) $v_c = 125$ m/min.

These observations were complemented by the calculations of the segment ratio (G_s , Equation (3)) and the equivalent chip thickness (t_c , Equation (4)). Their evolutions with v_c and f are shown in Figure 12.

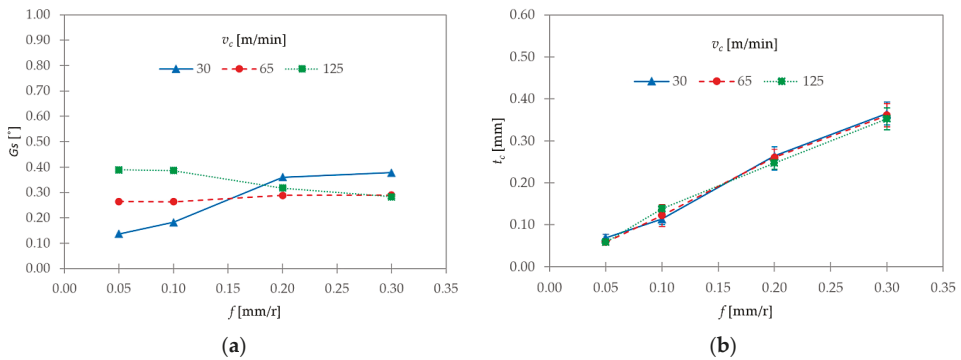


Figure 12. (a) Segment ratio (G_s) and (b) equivalent chip thickness (t_c) as a function of v_c and f .

Obviously, t_c showed the same trend as that observed for h_p (Figure 12b) as a consequence of the fact that h_v tended to remain more or less constant with cutting parameters. With regards to G_s ,

the influence of cutting speed was higher for the lowest range of feed rate considered, 0.05–0.10 mm/r (Figure 12a). In this range, the segment ratio tended to increase with v_c . Notwithstanding, G_s tended to remain constant with f , except at $v_c = 30$ m/min, where G_s increased when f varied from 0.05 to 0.10 mm/r. A different trend was observed for the highest range of f analyzed (0.20–0.30 mm/r). In this case, G_s tended to remain approximately constant with f . In addition, the influence of v_c was less noticeable at 65 and 125 m/min, and the highest G_s values corresponded to $v_c = 30$ m/min. In fact, G_s strongly increased at $v_c = 30$ m/min, and decreased at $v_c = 125$ m/min when f varied from 0.10 to 0.20 mm/r.

These observations may indicate that v_c was the most influential parameter when a low f was used. As a result, thermal softening was the segmentation mechanism that prevailed within this range. By contrast, f became more relevant at higher values (0.20–0.30 mm/r). As a result, the mechanism of crack initiation and propagation was more noticeable. Therefore, this mechanism was enhanced by the combination of a low cutting speed and a high feed rate. These observations are in good agreement with previous works [3,4,8,10,33].

Figure 13 shows the evolutions of the shear angle (θ) and the segment width (S) with cutting parameters. The shear angle oscillated from 35° to 44°; as such, it complied with Stabler’s theory for orthogonal cutting [46]. Notwithstanding, no clear trends with v_c and f could be observed in the analyzed interval. Some authors found a general trend of increasing θ for low ranges of cutting speed (0–40 m/min). However, scattered results were found between 40 and 140 m/min [33], in good agreement with the results exposed in this work. Thus, these results are within the normal variation of the measurement process.

Regarding segment width (S), this parameter showed a general trend of increase with f . On the other hand, S decreased with v_c . This trend was more noticeable for the highest values of f used (0.20–0.30 mm/r). This fact can be explained taking into account that an increase in cutting speed results in an increase in cutting temperature. Because of the low thermal conductivity of the Ti6Al4V alloy, the primary shear zone becomes more adiabatic, and the appearance of adiabatic shear bands is favored. Thus, the segmentation frequency is increased [4,9,33].

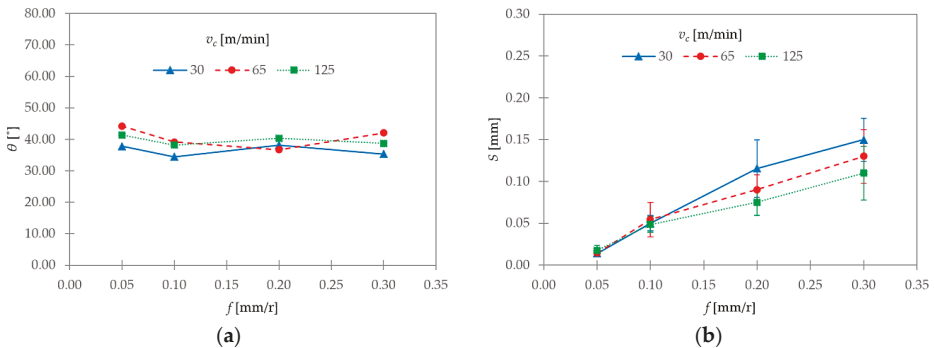


Figure 13. (a) Shear angle (θ) and (b) segment width (S) as a function of v_c and f .

Figure 14 shows two different geometric parameters of the transverse chip section and their evolutions with v_c and f : the chip width (b ; Figure 14a) and the chip transverse area (A ; Figure 14b). A general trend of remaining constant was observed for b , regardless of changes in v_c and f . Its value was very close to the theoretical value ($a_p = 1$ mm). As a result, the hypothesis of constant volume and plain strain during machining could be assumed.

As seen in Figure 14b, the chip transverse area (A) tended to increase with f , and it was independent of v_c . Its value was measured along the adiabatic shear band. Therefore, A was very close to the product of h_v and b . Its value only showed more dispersion for $f = 0.30$ mm/r. A possible

explanation is that the transverse area was less homogenous for 0.30 mm/r, and, as a result, more difficult to measure (Figure 6).

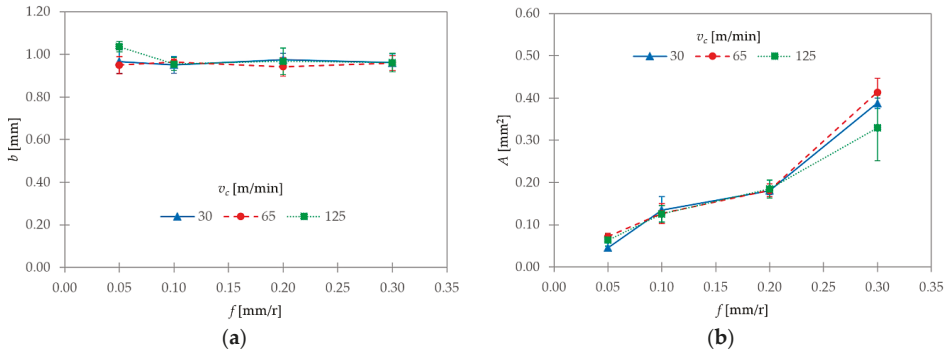


Figure 14. (a) Chip width (b_c) and (b) chip transverse area (A) as a function of v_c and f .

The shrinkage factor (ζ) provides important information about the chip’s total strain, the chip’s springback, and the consumed energy in the chip’s plastic deformation, among others [20,42]. The hypothesis of plain strain and constant volume allows calculating the shrinkage factor (ζ) via Equation (2), where $\gamma = 7^\circ$ and θ is the experimentally obtained shear angle. In addition, ζ can be calculated with Equation (5), using the theoretical chip thickness before machining (t_0) and the equivalent chip thickness (t_c). For the selected machining configuration ($\kappa_r = 90^\circ$, main cutting edge angle), t_0 was equal to f . Figure 15a,b show the evolution of ζ , as a function of v_c and f , calculated with Equations (2) and (5), respectively.

$$\zeta = \frac{t_0}{t_c} \tag{5}$$

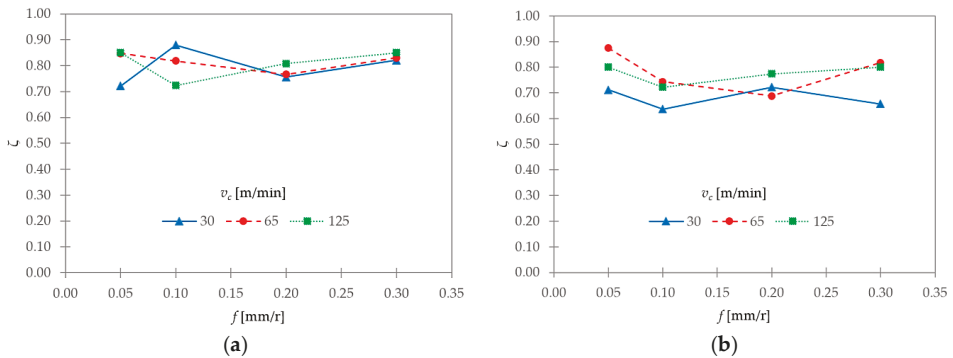


Figure 15. Shrinkage factor (ζ) as a function of v_c and f , calculated via (a) Equation (5), and (b) via Equation (2).

In the first case (Figure 15a) ζ varied from 0.72 to 0.88. In the second case (Figure 15b) ζ varied from 0.64 to 0.87. In both cases, there was no clear trend of increase or decrease with v_c or f . In general, the lowest values were obtained at $v_c = 30$ m/min, although some singularities could be observed for $f = 0.10$ mm/r (Figure 15a). Thus, low cutting speeds resulted in higher deformation rates.

3.3. Parametric Relationships

As mentioned in the introduction, the prediction of chip morphology before machining is of crucial importance [2,8]. In this research, various parametric relationships were developed from the experimental data. These relationships allow predicting the evolution of chip-geometric parameters as a function of the cutting parameters analyzed, v_c and f . To establish a global model was not intended, due to the large number of variables which influence the process, in addition to the cutting parameters. However, obtaining simpler models for a direct industrial application was interesting [42].

These relationships were obtained for the parameters with a strong dependence on cutting parameters (h_p , h_v , t_c , G_s , S , and A), and for those that showed a weaker dependence (θ and ζ). Obviously, no relationship was obtained for b , given its strong trend of remaining practically constant.

To achieve this objective, various mathematical models were tested. Among them, a potential model, as shown in Equation (6), exhibited the best fit to the experimental data for all geometric parameters (GP) studied.

$$GP = K \cdot v_c^x \cdot f^y \quad (6)$$

In Equation (6), K , x , and y are constants. Table 3 provides the results for the constants for each geometric parameter (GP) after fitting this model to the experimental data. An additional column was added, with the adjusted coefficient of determination (R^2).

Table 3. Model coefficients.

Geometric Parameter (GP)	K	x	y	R^2
Height of peak (h_p)	1.38	0.02	1.01	0.98
Height of valley (h_v)	1.20	−0.05	0.98	0.97
Chip thickness (t_c)	1.29	−0.01	0.99	0.98
Segment ratio (G_s)	0.15	0.24	0.17	0.52
Segment width (S)	0.87	−0.10	1.16	0.94
Transverse area (A)	0.94	0.02	0.95	0.92
Shear angle (θ)	28.43	0.06	−0.03	0.67
Shrinkage factor (ζ)	0.77	0.15	0.02	0.61

As can be seen in Table 3, h_p , h_v , t_c , S , and A showed a good fit to the proposed model (R^2 values between 0.92 and 0.98). The model coefficients for these geometric parameters indicated a strong influence of f , with the y coefficient almost linear. Because of the lower value of x , the influence of v_c was almost negligible. This fact is in good agreement with the experimental observations.

With regards to G_s , θ , and ζ , the model exhibited a lower fit (R^2 values between 0.52 and 0.67). Figure 16 contrasts the experimental data and the proposed model for these parameters.

As observed in Figure 16a, the G_s model showed a good fit at $v_c = 65$ m/min, regardless of changes in f . However, this model underestimated G_s at $v_c = 30$ m/min, and overestimated it at $v_c = 125$ m/min in the lower range of f studied (0.05–0.10 mm/r). An opposite trend was observed for higher f (0.10–0.20 mm/r). Regarding θ (Figure 16b) the model showed, in general, a good adjustment at $v_c = 30$ and 125 m/min. At $v_c = 65$ m/min, it seemed to overestimate it for $f = 0.05$ and 0.30 mm/r. Finally, because there was no clear tendency of ζ with cutting parameters, the model was only useful to show an average trend (very close to $\zeta = 0.8$, and almost equal to $K = 0.77$ in the model) within the studied v_c and f intervals (Figure 16c).

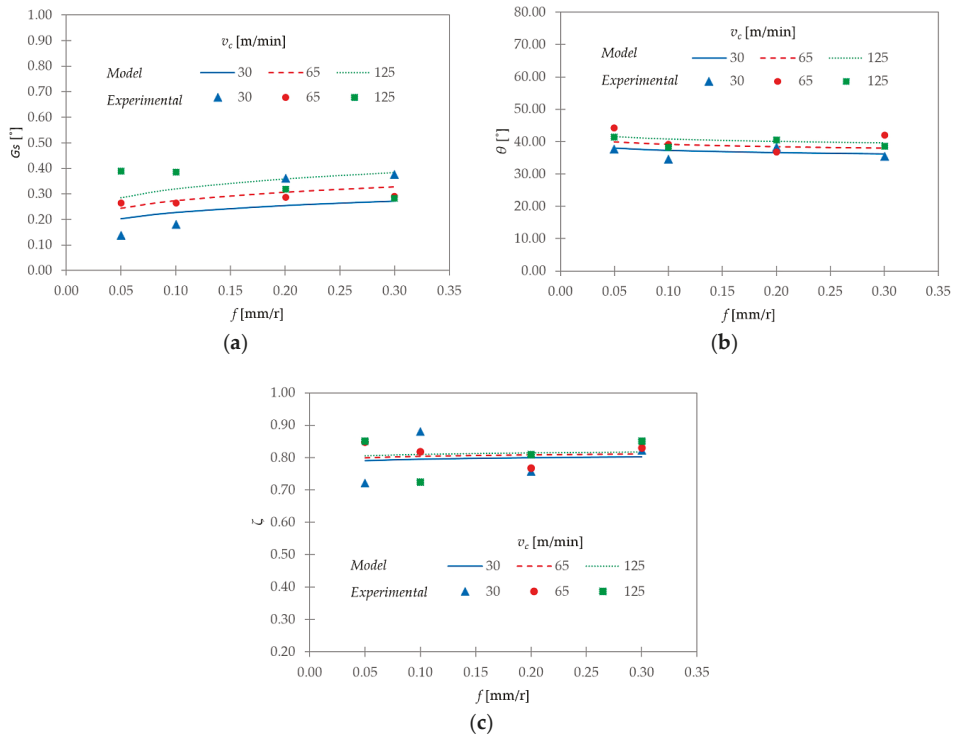


Figure 16. Comparisons between the experimental data and the proposed model for (a) G_s , (b) θ , and (c) ζ .

4. Conclusions

In this work, an experimental analysis of the influence of cutting speed and feed rate on chip morphology and geometry was carried out, during the dry machining of a Ti6Al4V alloy.

In general, the chip morphology was segmented, and it remained continuous across wide ranges of v_c and f . This was a consequence of the high plasticity levels of this alloy and its low thermal conductivity. This fact became more noticeable when v_c was increased and f was reduced. From a qualitative point of view, a higher segmentation level was observed in the chip’s longitudinal section when v_c was increased. This increase was enhanced by f .

Regarding chip microstructure, a grain deformation was observed in the whole section. In addition, two different grain alignments were noticed within two different areas: the adiabatic shear band and the contact surface between the chip and the face of the tool rake. Both alignments were more noticeable when v_c was increased.

Various chip-geometric parameters (longitudinal and transverse chip sections) were measured, and their evolutions with v_c and f were studied.

An almost linear increase with f was observed in the height of peaks (h_p), the height of valleys (h_v), the equivalent chip thickness (t_c), and the area on the transverse section (A). This general trend was expected, due to the direct proportionality between chip thickness and f . Regarding v_c , a higher influence on h_p was observed in the lowest range of f considered. No significant changes in h_v were noted as a function of v_c . The equivalent chip thickness (t_c) showed a similar trend to that observed for h_p , because h_v tended to remain more or less constant with cutting parameters.

The segment ratio (G_s) showed a general trend of increasing with v_c . This trend was stronger for the lowest range of f . The feed rate showed a lesser influence on this parameter. The segment width (S) exhibited a general trend of increasing with f , and of decreasing with v_c . This trend was more noticeable for the highest values of f . The shear angle (θ) oscillated from 35° to 44° . Notwithstanding, no clear trends with v_c and f were found. A general trend of remaining constant was observed for chip width (b), regardless of changes in v_c and f . As a result, the hypothesis of constant volume and plain strain during machining could be assumed. The shrinkage factor (ζ) varied from 0.64 to 0.88. No clear trends for this parameter were found as a function of v_c or f . Notwithstanding, the lowest values were obtained, in general, at the lowest value of v_c . Thus, low cutting speeds resulted in higher deformation rates.

Various parametric relationships were developed from the experimental data. These relationships allowed predicting the evolution of the chip-geometric parameters as a function of the cutting parameters. Several mathematical models were tested, and the potential model exhibited the best fit. The geometric parameters, h_p , h_v , t_c , S , and A , showed a good fit to the proposed model. This model exhibited a weaker fit for G_s , θ , and ζ .

It is necessary to point out that all these observations are only valid within the tested range of cutting parameters.

Author Contributions: Conceptualization, Y.S.H., F.J.T.V., C.B.G. and L.S.H. Methodology, Y.S.H. and L.S.H. Validation, Y.S.H. Formal analysis, Y.S.H. Investigation, Y.S.H. Resources, Y.S.H., F.J.T.V., C.B.G. and L.S.H. Data curation, Y.S.H. Writing—original draft preparation, Y.S.H., F.J.T.V. and C.B.G. Writing—review and editing, F.J.T.V., C.B.G. and L.S.H. Supervision, L.S.H.

Funding: This research received no external funding.

Acknowledgments: The Authors thank the University of Malaga—Andalucia Tech Campus of International Excellence for its contribution on this paper

Conflicts of Interest: The authors declare no conflict of interest.

References

1. Ezugwu, E.; Bonney, J.; Yamane, Y. An overview of the machinability of aeroengine alloys. *J. Mater. Process. Technol.* **2003**, *134*, 233–253. [[CrossRef](#)]
2. Niknam, S.A.; Khettabi, R.; Songmene, V. Machinability and Machining of Titanium Alloys: A Review. In *Machining of Titanium Alloys*; Springer: Berlin, Germany, 2014; Chapter 1; pp. 1–30, ISBN 978-3-662-43901-2.
3. Veiga, C.; Davim, J.P.; Loureiro, A.J.R. Review on machinability of titanium alloys: The process perspective. *Rev. Adv. Mater. Sci.* **2013**, *34*, 148–164.
4. Arrazola, P.-J.; Garay, A.; Iriarte, L.-M.; Armendia, M.; Marya, S.; Le Maître, F. Machinability of titanium alloys (Ti6Al4V and Ti555.3). *J. Mater. Process. Technol.* **2009**, *209*, 2223–2230. [[CrossRef](#)]
5. López de lacalle, L.; Pérez, J.; Llorente, J.; Sánchez, J. Advanced cutting conditions for the milling of aeronautical alloys. *J. Mater. Process. Technol.* **2000**, *100*, 1–11. [[CrossRef](#)]
6. Boyer, R.R.; Briggs, R.D. The use of β titanium alloys in the aerospace industry. *J. Mater. Eng. Perform.* **2013**, *22*, 2916–2920. [[CrossRef](#)]
7. Li, X.; Zhang, X.; Zhang, H.; Yang, J.; Nia, A.B.; Chai, G.B. Mechanical behaviors of Ti/CFRP/Ti laminates with different surface treatments of titanium sheets. *Compos. Struct.* **2017**, *163*, 21–31. [[CrossRef](#)]
8. Calamaz, M.; Coupard, D.; Girod, F. A new material model for 2D numerical simulation of serrated chip formation when machining titanium alloy Ti-6Al-4V. *Int. J. Mach. Tools Manuf.* **2009**, *48*, 275–288. [[CrossRef](#)]
9. Nouari, M.; Makich, H. Analysis of Physical Cutting Mechanisms and Their Effects on the Tool Wear and Chip Formation Process When Machining Aeronautical Titanium Alloys: Ti-6Al-4V and Ti-55531. In *Machining of Titanium Alloys*; Springer: Berlin, Germany, 2014; pp. 79–111, ISBN 978-3-662-43901-2.
10. Nouari, M.; Makich, H. On the Physics of Machining Titanium Alloys: Interactions between Cutting Parameters, Microstructure and Tool Wear. *Metals* **2014**, *4*, 335–358. [[CrossRef](#)]
11. Cotterell, M.; Byrne, G. Dynamics of chip formation during orthogonal cutting of titanium alloy Ti-6Al-4V. *CIRP Ann. Manuf. Technol.* **2008**, *57*, 93–96. [[CrossRef](#)]

12. Pramanik, A. Problems and solutions in machining of titanium alloys. *Int. J. Adv. Manuf. Technol.* **2014**, *70*, 919–928. [[CrossRef](#)]
13. Komanduri, R.; Hou, Z.-B. On thermoplastic shear instability in the machining of a titanium alloy (Ti-6Al-4V). *Metall. Mater. Trans. A* **2002**, *33*, 2995–3010. [[CrossRef](#)]
14. Wan, Z.P.; Zhu, Y.E.; Liu, H.W.; Tang, Y. Microstructure evolution of adiabatic shear bands and mechanisms of saw-tooth chip formation in machining Ti6Al4V. *Mater. Sci. Eng. A* **2012**, *531*, 155–163. [[CrossRef](#)]
15. Sima, M.; Özel, T. Modified material constitutive models for serrated chip formation simulations and experimental validation in machining of titanium alloy Ti-6Al-4V. *Int. J. Mach. Tools Manuf.* **2010**, *50*, 943–960. [[CrossRef](#)]
16. Shokrani, A.; Dhokia, V.; Newman, S.T. Environmentally conscious machining of difficult-to-machine materials with regard to cutting fluids. *Int. J. Mach. Tools Manuf.* **2012**, *57*, 83–101. [[CrossRef](#)]
17. Kelly, J.F.; Cotterell, M.G. Minimal lubrication machining of aluminium alloys. *J. Mater. Process. Technol.* **2002**, *120*, 327–334. [[CrossRef](#)]
18. Yoshimura, H.; Toda, Y.; Moriwaki, T.; Shibasaki, T.; Okida, J. Study on near dry cutting of aluminum alloys. *Mach. Sci. Technol.* **2006**, *10*, 289–299. [[CrossRef](#)]
19. Vinayagamorthy, R.; Xavier, M.A. Dry machining of Ti-6Al-4V using PVD coated tools. *Int. J. Appl. Eng. Res.* **2013**, *8*, 1373–1381.
20. Salguero, J.; Gerez, J.; Batista, M.; Garófano, J.E.; Marcos Bárcena, M. A Study of Macrogeometrical Deviations in the Dry Turning of UNS R56400 Ti Alloy. *Appl. Mech. Mater.* **2012**, *152–154*, 613–617. [[CrossRef](#)]
21. Ginting, A.; Nouari, M. Surface integrity of dry machined titanium alloys. *Int. J. Mach. Tools Manuf.* **2009**, *49*, 325–332. [[CrossRef](#)]
22. Trujillo, F.J.; Sevilla, L.; Marcos, M. Experimental Parametric Model for Indirect Adhesion Wear Measurement in the Dry Turning of UNS A97075 (Al-Zn) Alloy. *Materials* **2017**, *10*, 152. [[CrossRef](#)] [[PubMed](#)]
23. Hua, J.; Shivpuri, R. Prediction of chip morphology and segmentation during the machining of titanium alloys. *J. Mater. Process. Technol.* **2004**, *150*, 124–133. [[CrossRef](#)]
24. Molinari, A.; Soldani, X.; Miguélez, M.H. Adiabatic shear banding and scaling laws in chip formation with application to cutting of Ti–6Al–4V. *J. Mech. Phys. Solids* **2013**, *61*, 2331–2359. [[CrossRef](#)]
25. Liang, J.; Bi, S.S. Experimental Studies for Burrs in Dry Drilling of Stacked Metal Materials. *Adv. Mater. Res.* **2010**, *129–131*, 959–963. [[CrossRef](#)]
26. Yang, X.; Richard Liu, C. Machining Titanium and its Alloys. *Mach. Sci. Technol.* **1999**, *3*, 107–139. [[CrossRef](#)]
27. Calamaz, M.; Coupard, D.; Girof, F. Numerical simulation of titanium alloy dry machining with a strain softening constitutive law. *Mach. Sci. Technol.* **2010**, *14*, 244–257. [[CrossRef](#)]
28. Yameogo, D.; Haddag, B.; Makich, H.; Nouari, M. Prediction of the Cutting Forces and Chip Morphology When Machining the Ti6Al4V Alloy Using a Microstructural Coupled Model. *Procedia CIRP* **2017**, *58*, 335–340. [[CrossRef](#)]
29. Vyas, A.; Shaw, M.C. Mechanics of saw-tooth chip formation in metal cutting. *J. Manuf. Sci. Eng.* **1999**, *121*, 163–172. [[CrossRef](#)]
30. Barry, J.; Byrne, G.; Lennon, D. Observations on chip formation and acoustic emission in machining Ti-6Al-4V alloy. *Int. J. Mach. Tools Manuf.* **2001**, *41*, 1055–1070. [[CrossRef](#)]
31. Komanduri, R.; Von Turkovich, B.F. New observations on the mechanism of chip formation when machining titanium alloys. *Wear* **1981**, *69*, 179–188. [[CrossRef](#)]
32. Obikawa, T.; Usui, E. Computational machining of titanium alloy—Finite element modeling and a few results. *J. Manuf. Sci. Eng. Trans. ASME* **1996**, *118*, 208–215. [[CrossRef](#)]
33. Bai, W.; Sun, R.; Roy, A.; Silberschmidt, V.V. Improved analytical prediction of chip formation in orthogonal cutting of titanium alloy Ti6Al4V. *Int. J. Mech. Sci.* **2017**, *133*, 357–367. [[CrossRef](#)]
34. Joshi, S. Dimensional inequalities in chip segments of titanium alloys. *Eng. Sci. Technol. Int. J.* **2018**, *21*, 238–244. [[CrossRef](#)]
35. Turley, D.M.; Doyle, E.D.; Ramalingam, S. Calculation of shear strains in chip formation in titanium. *Mater. Sci. Eng.* **1982**, *55*, 45–48. [[CrossRef](#)]
36. Sutter, G.; List, G. Very high speed cutting of Ti-6Al-4V titanium alloy—Change in morphology and mechanism of chip formation. *Int. J. Mach. Tools Manuf.* **2013**, *66*, 37–43. [[CrossRef](#)]

37. Joshi, S.; Tewari, A.; Joshi, S.S. Microstructural Characterization of Chip Segmentation under Different Machining Environments in Orthogonal Machining of Ti6Al4V. *J. Eng. Mater. Technol.* **2015**, *137*, 011055. [[CrossRef](#)]
38. Baker, M.; Rosler, J.; Siemers, C. Finite Element Simulation of Segmented Chip Formation of Ti6Al4V. *J. Manuf. Sci. Eng.* **2002**, *124*, 485–488. [[CrossRef](#)]
39. Zhang, Y.; Outeiro, J.C.; Mabrouki, T. On the selection of Johnson-Cook constitutive model parameters for Ti-6Al-4V using three types of numerical models of orthogonal cutting. *Procedia CIRP* **2015**, *31*, 112–117. [[CrossRef](#)]
40. Wang, B.; Liu, Z. Shear localization sensitivity analysis for Johnson-Cook constitutive parameters on serrated chips in high speed machining of Ti6Al4V. *Simul. Model. Pract. Theory* **2015**, *55*, 63–76. [[CrossRef](#)]
41. Ducobu, F.; Rivière-Lorphèvre, E.; Filippi, E. Material constitutive model and chip separation criterion influence on the modeling of Ti6Al4V machining with experimental validation in strictly orthogonal cutting condition. *Int. J. Mech. Sci.* **2016**, *107*, 136–149. [[CrossRef](#)]
42. Batista, M.; Calamaz, M.; Girod, F.; Salguero, J.; Marcos, M. Using image analysis techniques for single evaluation of the chip shrinkage factor in orthogonal cutting process. *Key Eng. Mater.* **2012**, *504–506*, 1329–1334. [[CrossRef](#)]
43. Dye, D.; Hu, F.; Jones, N.G. Microstructure Formation in Alpha-Beta Titanium Alloys. In *Titanium*; Springer: Berlin, Germany, 2011.
44. Lütjering, G.; Williams, J.C. Alpha + Beta Alloys. In *Titanium*; Springer: Berlin, Germany, 2007; ISBN 978-3-540-73036-1.
45. Molinari, A.; Musquar, C.; Sutter, G. Adiabatic shear banding in high speed machining of Ti-6Al-4V: Experiments and modeling. *Int. J. Plast.* **2002**, *18*, 443–459. [[CrossRef](#)]
46. Grzesik, W. *Advanced Machining Processes of Metallic Materials: Theory, Modelling and Applications*; Elsevier: New York, NY, USA, 2008; ISBN 9780444637208.



© 2018 by the authors. Licensee MDPI, Basel, Switzerland. This article is an open access article distributed under the terms and conditions of the Creative Commons Attribution (CC BY) license (<http://creativecommons.org/licenses/by/4.0/>).

Article

Evaluation of the Functional Performance in Turned Workpieces: Methodology and Application to UNS A92024-T3

Álvaro Gómez-Parra ^{1,*}, Alfredo Sanz ² and Antonio J. Gámez ¹

¹ Department of Mechanical Engineering and Industrial Design, Faculty of Engineering, University of Cadiz, Avenida de la Universidad de Cadiz, 10, Puerto Real, E-11519 Cadiz, Spain; antoniojuan.gamez@uca.es

² Department of Aerospace Materials and Manufacturing, Polytechnic University of Madrid, Plaza del Cardenal Cisneros, 3, E-28040 Madrid, Spain; asl@aero.upm.es

* Correspondence: alvaro.gomez@uca.es; Tel.: +34-956-483-493

Received: 29 June 2018; Accepted: 20 July 2018; Published: 24 July 2018

Abstract: Turning of light alloys as aluminum-based UNS A92024-T3 is broadly implemented in the manufacture of critical aircraft parts, so ensuring a good functional performance of these pieces is essential. Moreover, operational conditions of these pieces include saline environments where corrosion processes are present. In this paper, a methodology for the evaluation of the functional performance in turned pieces is proposed. Specimens affected and not affected by corrosion are compared. In addition, performance in service through tensile stress tests of these parts is considered. The results show that turning improves the functional performance of UNS A92024-T3 alloy and that corrosion can enhance the mechanical properties of this alloy.

Keywords: turning; UNS A92024-T3; corrosion; surface integrity; Ra; residual stress; functional performance; ultimate tensile strength

1. Introduction

The evaluation of the performance of a manufacturing process is a complex task that can be better approached when four fundamental and complementary points of view are recognized: economical, energetic, environmental, and functional. In this context, the global process performance has been defined as the center of gravity of a tetrahedron defined by setting these four elements in its apexes [1].

In particular, the aeronautical industry considers high-performance manufacturing, even at the cost of a loss in economic performance, provided the process is enhanced from the energetic, environmental and especially, functional points of view [2–4]. Functionality can be understood as the state of health of the workpiece [5]. Therefore, the workpiece functionality is described as its ability to meet quality standards in order to fulfill the required performance in service.

For example, the critical components of an aircraft must be manufactured under high specifications of dimensional accuracy, surface finishing, and mechanical properties. In particular, the turning of aluminum alloy pieces by removing cutting fluids increases its environmental performance. This implies a loss of surface integrity that compromises safety and therefore functionality [1,6–8], as dry turning is a very aggressive process that enables tool wear or more specifically, secondary adhesion. This kind of wear involves the addition of machined material to the edge and to the rake face of the tool, giving rise to the so-called built-up edge (BUE) and built-up layer (BUL), respectively [9].

Additionally, functional properties of manufactured elements can be changed by the action of its environment. This action can be more or less intense depending on the surface state of the manufactured element. Therefore, in the case of saline environments, corrosion depends on the surface finishing of the worked elements [10] and, consequently, on the manufacturing process. In these cases,

the influence of the corrosion damage on the surface properties of the workpieces must be taken into account [11]. This is the case of different structural elements of aircrafts, especially transoceanic ones. All considered, in order to approach conditions of the actual service, it is necessary to research the influence of manufacturing process on mechanicals properties in conjunction with a corrosion environment. However, to our knowledge, there are no studies in the current literature that consider the salinity effect and its relationship with the machining process and the functional performance of the workpiece. For this reason, this paper analyses the influence of turning processes in the surface integrity of UNS A92024-T3 alloys, before and after corrosion by a saline atmosphere. More specifically, the ultimate tensile strength (UTS) is measured as a reference parameter to assess the functional performance of the material under corrosion.

2. Materials and Methods

An experimental methodology was designed to achieve the proposed goal (Figure 1).

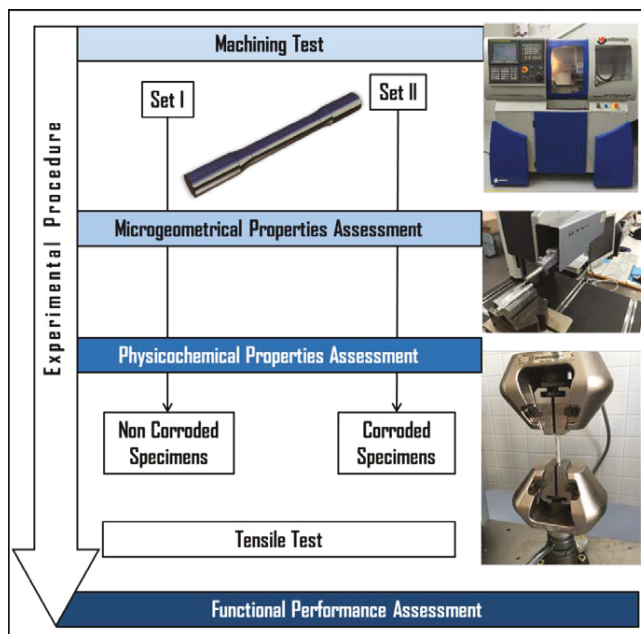


Figure 1. Experimental methodology scheme.

Al-Cu alloy UNS A92024-T3 specimens (composition in Table 1 [12]) were machined using a CNC lathe Eclipse from Alecop (Mondragón, Spain) (Figure 1). Specimens were designed according to ISO 6892-1:2016 (Figure 2a) [13]. The entire machining process was performed in absence of cooling fluids, therefore improving environmental performances.

Table 1. Composition of aluminum-copper alloy UNS A92024 (% weight).

Cu	Mg	Mn	Si	Fe	Zn	Ti	Cr	Al
4.0	1.5	0.6	0.5	0.5	0.25	0.15	0.10	Rest

Blocks of 32 specimens—divided in two equal sets of 16 pieces—were dry machined for this study. Workpieces for Set I were only dry turned before being tensile tested, while samples for Set II were exposed to corrosion after being dry turned and before being tensile tested.

Machining procedure of all specimens involved a roughing process using a cutting speed (V_c) of 80 m/min, a feed rate (f) of 0.03 mm/r and a cutting depth (d) of 0.50 mm as cutting parameters. The finishing pass of the sample surfaces were carried out in dry conditions and using a new tool for each machined specimen with the cutting parameters shown in Table 2.

The cutting tools used were neutral interchangeable insert (WC-Co) with commercial reference SECO, ref. DCMT 070208-F2 HX (Seco Tools AB, Fagersta, Sweden).

The surface microgeometry of the samples was evaluated through the average surface roughness parameter (R_a) according to the standard ISO 4288:1996 [14]. Four profiles were acquired in four equidistant generatrices for each sample using a Mahr Perthometer M1 profilometer (Mahr GmbH, Göttingen, Germany). Each specimen R_a was calculated as the mean value of the four R_a of the measured profiles.

Table 2. Cutting parameters performed in machining test for a total of 16 experiments.

V_c (m/min)	f (mm/r)	d (mm)
40	0.02	0.50
60	0.05	0.50
80	0.10	0.50
100	0.20	0.50

Next, Set II was exposed to corrosion by immersion in a 10-L solution of distilled and deionized water and NaCl (3.5%) for 72 h at 296.15 K (Figure 2b) following standard ASTM NACE/ASTMG31-12a [15]. Water evaporation was controlled every day.

After each corrosive treatment, the workpieces were cleaned with distilled water in a similar way to overseas aircrafts.

Finally, in order to obtain the UTS, both sets underwent a tensile test with a Shimadzu Autograph AG-X (50 kN) tensile-compression machine (Shimadzu, Kyoto, Japan) for a precision within 1%. The crosshead velocity was $u = 14.5$ mm/min for all tests and the standard ISO 6892-1:2016 was used.

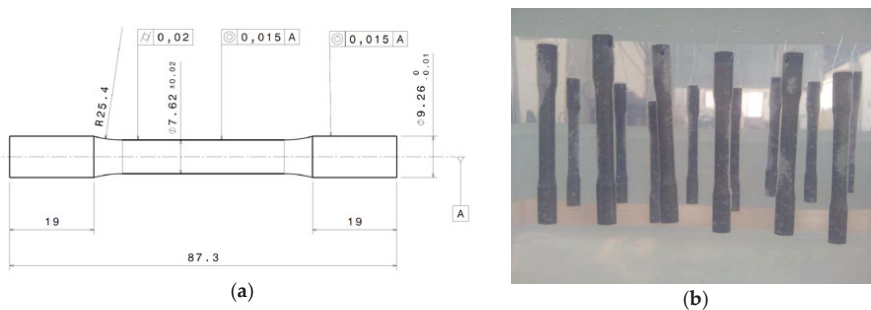


Figure 2. (a) Specimen dimensions according to standard UNE-EN ISO 6892-1:2016. (b) Set II samples during a corrosion test by immersion.

On the other hand, residual stress measurements were carried out by blind hole drilling, following the ASTM E837-13a standard [16], using a RS-200 equipment from Vishay (Raleigh, North Carolina, USA) (Figure 3) [17,18]. For this purpose, CEA-13-062UM strain gages (Vishay Precision Group—Micro-Measurements, Raleigh, NC, USA) were used in this study. This method was conducted

on bigger specimens with a radius of 50 mm as demonstrator, as blind hole drilling is not suitable for the 3.81 mm radii of curvature specimens. These samples followed the same turning and corrosion procedures as the original set of 32 specimens for reproducibility.

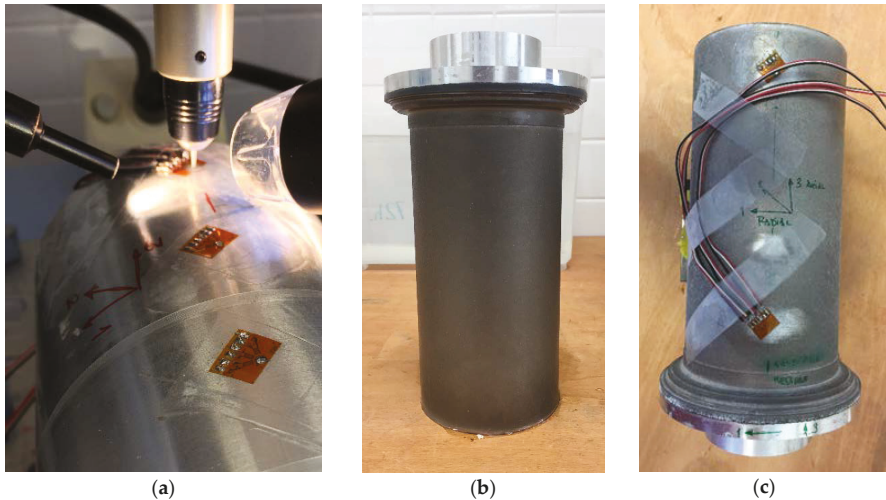


Figure 3. (a) Residual stress measurement of noncorroded specimen. (b) Specimen corroded after 72 h in solution of distilled and deionized water and NaCl (3.5%). (c) Set up of measures in corroded specimen.

Because residual stress in machined workpieces varies with depth from the specimen surface, the integral method was used to transform strains into stresses. Measurements had a probability bound of 90%.

3. Results and Discussion

As the time of machining is very short—ranging from 8.51 s for the shortest combination of cutting speed and feed rate to 212.74 s for the largest—no microstructural changes on the tool were expected [9,19–21]. However, the temperature can be high enough for softening the Al matrix and developing primary BUL. Figure 4 shows Stereoscopic Optical Microscopy (SOM) images of tools after machining under two different cutting parameters and a scheme of tool wear by secondary adhesion.

BUL was developed onto the rake face of the tool and its size was bigger when cutting speed increased (Figure 4a,c). Primary BUL was formed in the first 5 to 10 s of machining, and it was formed by pure aluminum (Figure 4e (1)) [9]. Tool changes facilitated the mechanical adhesion of the machined alloy, giving rise to BUE (Figure 4b,d). BUE was formed by the alloy material and it grew to a critical size (Figure 4e (2)) [1,9]. When the temperature was sufficiently high, BUE softened and extruded onto the rake face, giving rise to a secondary BUL (Figure 4e (3)) [1,9]. The temperature in the cutting region was higher for increasing cutting speeds [7]. This explains the aforementioned BUL thickness. According to that, a lower BUE thickness was detected when lower cutting speed was applied. On the other hand, a higher feed involved a higher lateral chip compression, facilitating BUL through the increase of temperature caused by the relaxation process after deformation [22].

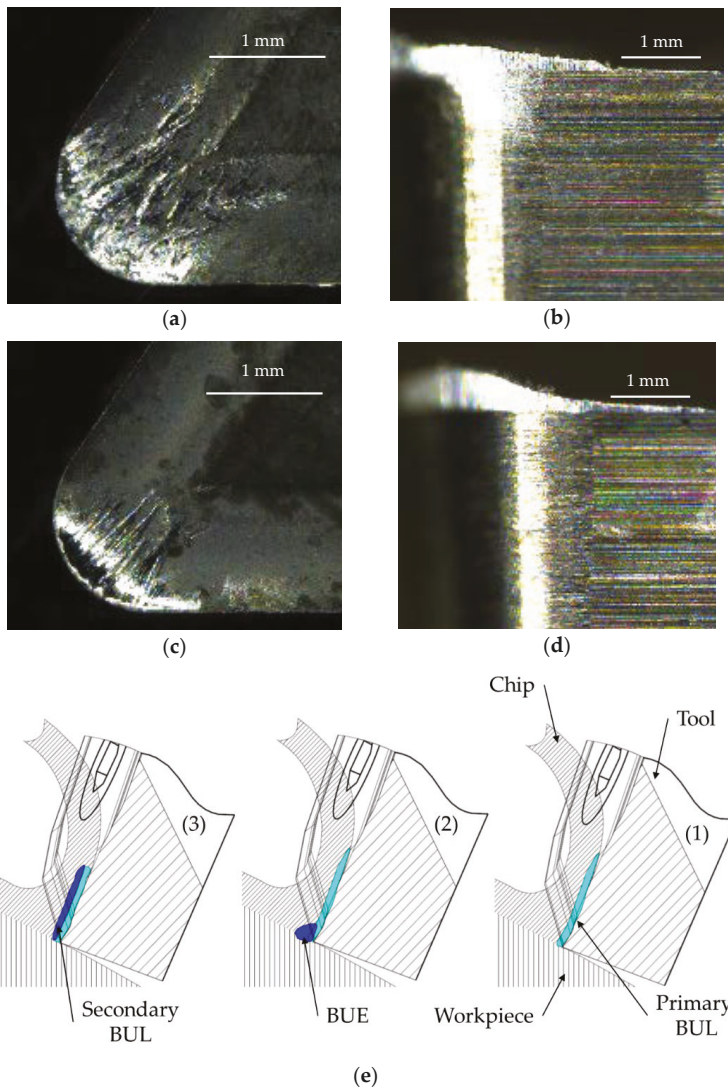


Figure 4. Comparison of built-up layer (BUL) and built-up edge (BUE) for different cases. (a,b) $V_c = 100$ m/min, $f = 0.2$ mm/r. (c,d) $V_c = 40$ m/min, $f = 0.05$ mm/r. (e) Scheme of the BUL and BUE formation.

From geometric considerations, R_a depends directly on f and the edge position angle of the tool for horizontal turning processes [1,9]. The BUE development diminished this angle and, consequently, the height of the peaks in the profile reduced and smoothed, thereby decreasing R_a (Figure 5a). This shows that the effect of the tool wear seems to be responsible for a decrease in R_a in certain sets of parameters. Secondary adhesion is a dynamic process, that is to say, the morphology of the tool can change at any time (Figure 5a). In this sense, when BUE was extruded, the height of peaks increased and so did R_a (Figure 5b) [1,9].

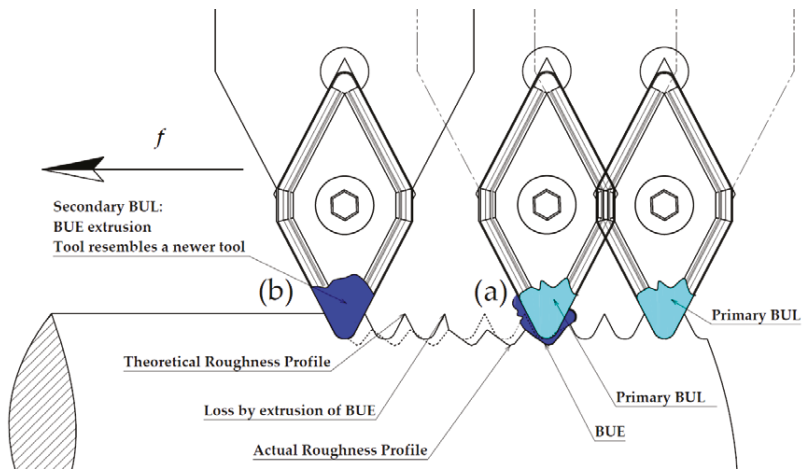


Figure 5. Effect of tool wear by secondary adhesion in the workpiece roughness profile for a horizontal dry turning process.

According to this, the extreme value of Ra found in $(Vc, f) = (60, 0.05)$ can be explained (Figure 6). On the other hand, despite dry turning significantly shortening the tool life, it may have a positive effect on the microgeometrical properties of the specimen, at least in a controlled length of machining [23]. In fact, surface integrity got worse as feed increased for every tested cutting speed, as expected (Figure 6). These results are in good agreement with previous studies [19,24].

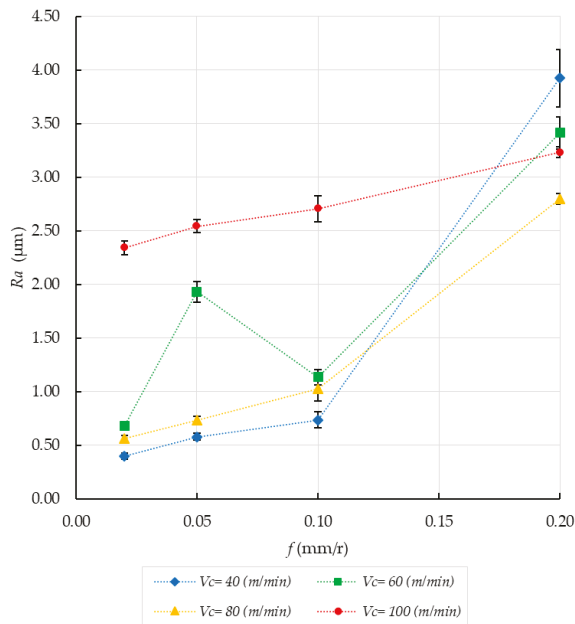


Figure 6. Evolution of Ra/f for all the cutting speeds studied. Error bars show the statistical standard deviation.

Figure 7 shows how the UTS increased with the feed rate for each tested specimen.

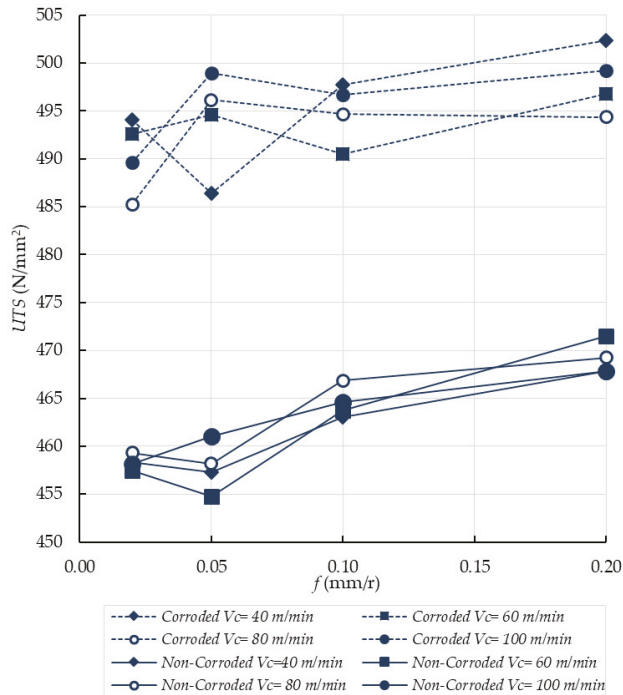


Figure 7. Changes in UTS/ f for all the analyzed cutting speeds. Set I, noncorroded specimens (continuous lines). Set II, corroded specimens (dotted lines).

We can observe that the machining process enhanced the tensile strength for all the studied cases. In fact, the standardized value of UTS for UNS A92024-T3 lies between 440 and 450 N/mm² [12,25,26]. Although the UTS variation is less than 4% of the reference value for this alloy, it is worth noting that the best results are achieved for higher feed conditions. Our findings show that higher Ra results in higher UTS. This can suggest that physicochemical properties of the material prevail over microgeometrical properties for surface integrity functional performance [27–29].

As expected, higher feed rates resulted in higher compressive stresses in the surface of the specimens (Figure 8) [29–32]. However, the stress distribution was not homogeneous. The region between 0.1 to 0.9 mm was under compression, while tensile stresses were located in the first 0.1 mm of the surface where the corrosion process took place. In fact, corrosion of Al-Cu alloys in aerated NaCl solutions is complex. As a first step, the Cu of anodic intermetallics is dissolved, changing their character to a cathodic behavior. The rest of intermetallics are cathodic to the Al matrix and therefore OH⁻ is produced in the surrounding of those intermetallics. As a result, the metal matrix is dissolved by alkaline action, provoking them to fall. This process is known as Localized Alkaline Corrosion (LAC), and it does not promote the presence of cracks onto the alloy surface [11,33]. At macroscopic scale, a preferential attack cannot be seen. Moreover, different mechanisms are responsible for the deterioration [33], although the final results are homogeneously distributed onto the surface. Therefore, no pitting is developed on the specimen surfaces (Figure 9). For this reason, corrosion only affects the first layers of material, removing the tensile stress region and therefore enhancing the functional performance by a significant increase in the UTS for each workpiece, (Figure 7).

Figure 8 shows the behavior of the axial residual stress with depth in the material surface. Axial residual stresses must be taken into account because they contribute to the stress carried out by the tensile tests. Furthermore, microgeometrical defects are disposed perpendicularly to the tensile strength, so any compressive stress will tend to close surface defects, improving the functional performance [29,34]. In addition, the level of compressive residual stress increases with feed for noncorroded specimens, strengthening the compressive residual stress that the unmachined material originally supports [30–32]. By contrast, for decreasing feeds, compressive residual stresses are lower than that of the unmachined specimens. This is to say, functional performance is improved at higher feeds.

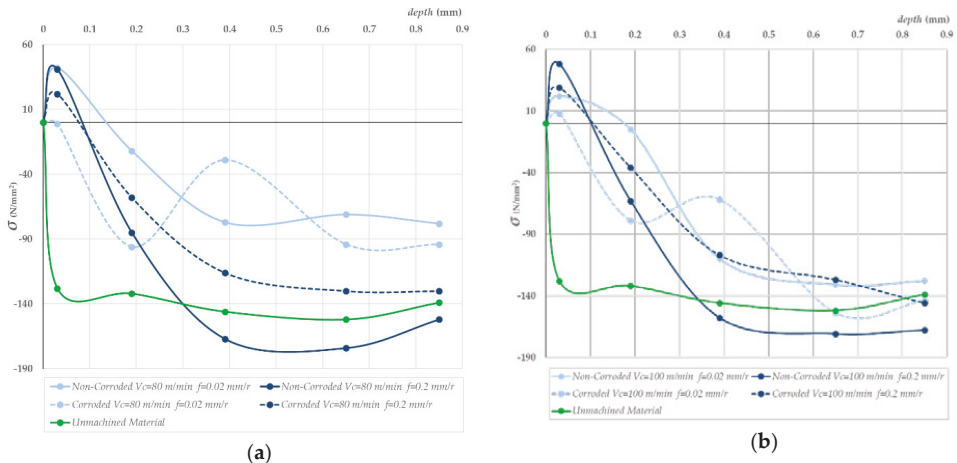


Figure 8. Evolution of axial residual stress/depth after machining for the cutting parameters indicated in noncorroded and corroded specimens. (a) $V_c = 80$ mm/min, (b) $V_c = 100$ mm/min. Two feed rates shown in both cases, $f = 0.02$ mm/r and $f = 0.2$ mm/r.

In summary, corrosion removed the tensile stress region at the surface of the workpieces, improving the functional performance. However, an accurate control of the corrosion process is needed because the corrosive process can have an impact in the intermetallic loss, these particles being responsible for the alloy strength [33].



Figure 9. (a) General image of corroded specimen ($V_c = 60$ m/min, $f = 0.2$ mm/r). (b) Detail ($\times 72$) of the corroded surface.

4. Conclusions

A novel approach to study the influence of turning processes in the UTS performance after corrosion of the UNS A92024-T3 alloy has been carried out. From analysis of the results, the conclusions can be summarized as follows:

1. Machining process can improve the tensile strength of horizontal dry turned samples of aeronautical alloy UNS A92024-T3. In this limited context, functional performance is favored by machining. Physicochemical properties are responsible for improving the mechanical properties and hence the functional performance.
2. Generally speaking, the UTS increases with the feed. Thus, there is no predominant influence of the microgeometrical properties acquired after machining over the UTS. In this sense, tensile residual stress taking place on the surface after machining is not large enough to generate a decrease of UTS value.
3. The compressive residual stress after machining is responsible for the best results of UTS. Furthermore, as the feed increases, the compressive residual stress increases too, thereby improving the value of compressive residual stress of the unmachined material. Thus, the higher the compressive residual stress, the higher the UTS value.
4. The results of the test of tensile stress after corrosion show a generalized improvement of the UTS value. The corrosion process removes the first layers of material. These layers, as shown in the results, carry a tensile residual stress and are softer than the unmachined material.

Author Contributions: Á.G.-P. and A.S. designed the methodology. Á.G.-P. performed the experiments. A.J.G. and Á.G.-P. discussed the results and wrote the manuscript.

Funding: This work has been funded by the University of Cadiz: Program for development and promotion of research and transfer activities.

Acknowledgments: In memoriam of Mariano Marcos.

Conflicts of Interest: The authors declare no conflict of interest.

References

1. Gómez-Parra, A.; Álvarez-Alcón, M.; Salguero, J.; Batista, M.; Marcos, M. Analysis of the evolution of the Built-Up Edge and Built-Up Layer formation mechanisms in the dry turning of aeronautical aluminium alloys. *Wear Mater.* **2013**, *302*, 1209–1218. [[CrossRef](#)]
2. Jayal, A.D.; Badurdeen, F.; Dillon, O.W., Jr.; Jawahir, I.S. Sustainable manufacturing: Modeling and optimization challenges at the product, process and system levels. *Sustain. Dev. Manuf. Syst.* **2010**, *2*, 144–152. [[CrossRef](#)]
3. Pusavec, F.; Krajnik, P.; Kopac, J. Transitioning to sustainable production—Part I: Application on machining technologies. *J. Clean. Prod.* **2010**, *18*, 174–184. [[CrossRef](#)]
4. Pusavec, F.; Kramar, D.; Krajnik, P.; Kopac, J. Transitioning to sustainable production—Part II: Evaluation of sustainable machining technologies. *J. Clean. Prod.* **2010**, *18*, 1211–1221. [[CrossRef](#)]
5. Akhavan Niaki, F.; Mears, L. A comprehensive study on the effects of tool wear on surface roughness, dimensional integrity and residual stress in turning IN718 hard-to-machine alloy. *J. Manuf. Process.* **2017**, *30*, 268–280. [[CrossRef](#)]
6. Salguero, J.; Batista, M.; Carrilero, M.S.; Álvarez, M.; Marcos, M. Sustainable manufacturing in aerospace industry. Analysis of the viability of intermediate stages elimination in sheet processing. *Adv. Mater. Res.* **2010**, *107*, 9–14. [[CrossRef](#)]
7. Marksberry, P.W.; Jawahir, I.S. A comprehensive tool-wear/tool-life performance model in the evaluation of NDM (near dry machining) for sustainable manufacturing. *Int. J. Mach. Tools Manuf.* **2008**, *48*, 878–886. [[CrossRef](#)]

8. M'Saoubi, R.; Outeiro, J.C.; Chandrasekaran, H.; Dillon Jr, O.W.; Jawahir, I.S. A review of surface integrity in machining and its impact on functional performance and life of machined products. *Int. J. Sustain. Manuf.* **2008**, *1*, 203–236. [[CrossRef](#)]
9. Carrilero, M.S.; Bienvenido, R.; Sánchez, J.M.; Álvarez, M.; González, A.; Marcos, M. A SEM and EDS insight into the BUL and BUE differences in the turning processes of AA2024 Al–Cu alloy. *Int. J. Mach. Tools Manuf.* **2002**, *42*, 215–220. [[CrossRef](#)]
10. Fullen, W.J.; Deheck, J. Aluminum Surface Finishing Corrosion Causes and Troubleshooting. *NASf Surf. Technol. White Pap.* **2014**, *79*, 1–15.
11. Bienvenido, R.; Díaz Vázquez, J.E.; Botana, J.; Cano, M.J.; Marcos, M.; Díaz-Vázquez, J.E.; Botana, J.; Cano-Iglesias, M.J.; Marcos, M. Preliminary Study of the Influence of Machining Conditions in the Response to Corrosion of UNS-A92024 Alloy. *Adv. Mater. Res.* **2010**, *107*, 117–121. [[CrossRef](#)]
12. UNE-EN 573-3:2014. *Aluminium and Aluminium Alloys—Chemical Composition and Form of Wrought Products—Part 1: Numerical Designation System*; AENOR: Madrid, Spain, 2014.
13. ISO 6892-1:2016. *Metallic Materials—Tensile Testing—Part 1: Method of Test at Room Temperature*; ISO: Geneva, Switzerland, 2016.
14. ISO 4288:1996. *Geometrical Product Specifications (GPS)—Surface Texture: Profile Method—Rules and Procedures for the Assessment of Surface Texture*; ISO: Geneva, Switzerland, 1996.
15. ASTM ASTM NACE/ASTMG31-12a. *Standard Guide for Laboratory Immersion Corrosion Testing of Metals*; ASTM International: West Conshohocken, PA, USA, 2012.
16. ASTM ASTM E837-13a. *Standard Test Method for Determining Residual Stresses by the Hole-Drilling Strain-Gage Method*; ASTM International: West Conshohocken, PA, USA, 2013.
17. Schajer, G.S. *Practical Residual Stress Measurement Methods*; John Wiley & Sons: West Sussex, UK, 2013; ISBN 978-1-11-834237-4.
18. H-DRILL Hole-Drilling Residual Stress Calculation Program 2009. Available online: <http://www.schajer.org/index.htm> (accessed on 20 June 2018).
19. Sánchez, J.M.; Rubio, E.; Álvarez, M.; Sebastián, M.A.; Marcos, M. Microstructural characterisation of material adhered over cutting tool in the dry machining of aerospace aluminium alloys. *J. Mater. Process. Technol.* **2005**, *164*, 911–918. [[CrossRef](#)]
20. Sánchez, J.M.; Sebastián Pérez, M.A.; González, J.M.; Carrilero, M.S.; Marcos Bárcena, M. Microstructural Differences of Adhered Material in the Tool Edge and Tool Rake Face. Application to the Machining of Al Alloys. *Mater. Sci. Forum* **2005**, *480–481*, 181–186. [[CrossRef](#)]
21. Salguero, J.; Carrilero, M.S.; Batista, M.; Álvarez, M.; Marcos, M.; Segui, V.J. Analysis of the Influence of Thermal Treatment on the Dry Turning of Al–Cu Alloys. *AIP Conf. Proc.* **2009**, *1181*, 594–602.
22. Iskra, P.; Tanaka, C.; Ohtani, T. Energy balance of the orthogonal cutting process. *Holz als roh-und Werkstoff* **2005**, *63*, 358–364. [[CrossRef](#)]
23. Rubio, E.M.; Camacho, A.M.; Sánchez-Sola, J.M.; Marcos, M. Surface roughness of AA7050 alloy turned bars: Analysis of the influence of the length of machining. *J. Mater. Process. Technol.* **2005**, *162–163*, 682–689. [[CrossRef](#)]
24. Trujillo Vilches, F.J. *Análisis Paramétrico del Mecanizado en Seco de la Aleación UNS A97075*. Ph.D. Thesis, University of Malaga, Málaga, Spain, 2013.
25. UNE 38314:2000. *Wrought Aluminium and Aluminium Alloys. 2000 Series. AlCu. Alloy EN AW-2024, EN AW-AlCu4Mg1*; AENOR: Madrid, Spain, 2000.
26. ASTM ASTM B211—03. *Standard Specification for Aluminum and Aluminum-Alloy Bar, Rod, and Wire*; ASTM International: West Conshohocken, PA, USA, 2003.
27. Gómez-Parra, A.; Puerta, F.J.; Rosales, E.I.; González-Madrugal, J.M.; Marcos, M. Study of the Influence of Cutting Parameters on the Ultimate Tensile Strength (UTS) of UNS A92024 Alloy Dry Turned Bars. *Procedia Eng.* **2013**, *63*, 796–803. [[CrossRef](#)]
28. Gómez-Parra, Á.; Puerta, F.J.; Rosales, E.I.; García-Jurado, D.; Mainé, J.M.; Marcos, M. Influence of the Dry Turning Parameters on the Ultimate Tensile Strength (UTS) of UNS A92024 Samples. *Mater. Sci. Forum* **2014**, *797*, 65–70. [[CrossRef](#)]
29. Novovic, D.; Dewes, R.C.C.; Aspinwall, D.K.K.; Voice, W.; Bowen, P. The effect of machined topography and integrity on fatigue life. *Int. J. Mach. Tools Manuf.* **2004**, *44*, 125–134. [[CrossRef](#)]

30. Dahlman, P.; Gunnberg, F.; Jacobson, M. The influence of rake angle, cutting feed and cutting depth on residual stresses in hard turning. *J. Mater. Process. Technol.* **2004**, *147*, 181–184. [[CrossRef](#)]
31. Choi, Y. Influence of feed rate on surface integrity and fatigue performance of machined surfaces. *Int. J. Fatigue* **2015**, *78*, 46–52. [[CrossRef](#)]
32. Hua, J.; Shivpuri, R.; Cheng, X.; Bedekar, V.; Matsumoto, Y.; Hashimoto, F.; Watkins, T.R. Effect of feed rate, workpiece hardness and cutting edge on subsurface residual stress in the hard turning of bearing steel using chamfer + hone cutting edge geometry. *Mater. Sci. Eng. A* **2005**, *394*, 238–248. [[CrossRef](#)]
33. Bethencourt, M.; Botana, F.J.; Cano, M.J.; Marcos, M.; Sánchez-Amaya, J.M.; González-Rovira, L. Behaviour of the alloy AA2017 in aqueous solutions of NaCl. Part I: Corrosion mechanisms. *Corros. Sci.* **2009**, *51*, 518–524. [[CrossRef](#)]
34. Jeelani, S.; Musial, M. Effect of cutting speed and tool rake angle on the fatigue life of 2024-T351 aluminium alloy. *Int. J. Fatigue* **1984**, *6*, 169–172. [[CrossRef](#)]



© 2018 by the authors. Licensee MDPI, Basel, Switzerland. This article is an open access article distributed under the terms and conditions of the Creative Commons Attribution (CC BY) license (<http://creativecommons.org/licenses/by/4.0/>).

Article

Tool Wear Mechanism in Cutting of Stack CFRP/UNS A97075

Severo Raul Fernandez-Vidal *, Sergio Fernandez-Vidal, Moises Batista and Jorge Salguero

Industrial Design Department, Faculty of Engineering, Mechanical Engineering, University of Cadiz, Av. Universidad de Cádiz 10, E-11519 Puerto Real-Cádiz, Spain; sergio.fernandezvidal@mail.uca.es (S.F.-V.); moises.batista@uca.es (M.B.); jorge.salguero@uca.es (J.S.)

* Correspondence: raul.fernandez@uca.es; Tel.: +34-956-48-3460

Received: 1 July 2018; Accepted: 23 July 2018; Published: 25 July 2018

Abstract: The aeronautics industry's competitiveness has led to the need to increase productivity with one shot drilling (OSD) systems capable of drilling stacks of dissimilar materials (fibre/metal laminates, FML) in order to reduce riveting times. Among the materials that constitute the current aeronautical models, composite materials and aluminium (Al) and titanium (Ti) alloys stand out. These one-pass machining techniques produce high-quality holes, especially when all the elements that have to be joined are made of the same material. This work has followed a conventional OSD strategy and the same cutting conditions applied to CFRP (carbo-fibre-reinforced polymer), Al and CFRP/Al stacked sheets to know the wear mechanisms produced. With this purpose, results were obtained by using current specific techniques, such as microstructural analysis, monitoring of the shear forces and analysis of macrogeometric deviations. It has been determined that when these drilling techniques are applied under the same cutting conditions to stacks of materials of a different nature, the results of the wear mechanisms acting on the tool differ from those obtained when machining each material separately. This article presents a comparison between the effects of tool wear during dry drilling of CFRP and UNS A97075 plates separately and when machined as stacks.

Keywords: wear; drilling; machining; dry drilling; stack; FML; CFRP; UNS A97075

1. Introduction

The aeronautical sector has always been a benchmark in research, development and innovation. This has been motivated by the intense competitiveness that exists within the sector, generating a continuous need to improve functional, environmental and energetic efficiency in the processes, guaranteeing quality and seeking a direct impact on economic performance [1].

The first challenge the aerospace industry faces in its fourth revolution is to automate processes that nowadays include the extensive use of manual labour, especially in relevant operations such as assembly operations [2].

Among the different joining methods available in the industry, riveting is still most often used, regardless of the materials involved in the assembly. This joining process requires a previous drilling operation. OSD techniques can produce high-quality holes, especially in cases where all the elements to be joined are made of the same material [3,4].

In the construction of the latest aircraft models, the excellent characteristics of the carbon-fibre-reinforced thermoset matrix composites (CFRP) have formed a balance with the current light metal alloys (aluminium alloys 2XXX and 7XXX and titanium alloys Ti6Al4V) [3–6]. These structures are known as fibre/metal laminates (FML). The present study focuses on comparisons when facing drilling stacks of diverse types of material, resulting in a very different situation from machining them separately [7].

This case requires us to study the wear mechanisms that affect the tool during the drilling process of composite material stacks with metal alloys, relating them to the final quality of the drill in order to improve the performance of the process. Although some authors use optical techniques to quantify wear, these techniques do not offer a continuous record of wear and tear, and are difficult to integrate into the company's intelligent systems. It has become necessary to monitor continuous variables directly related to tool wear during drilling, such as axial force [7]. This will favour the virtual integration of the company, being one of the main paradigms pursued in industry 4.0. The techniques used to carry out the analysis include microstructural analysis, monitoring of the shear forces and analysis of macrogeometric deviations.

1.1. Tool Wear Mechanisms in CFRP Drilling

The conventional drilling process of CFRP involves continuous interaction between the tool and two types of materials. One is more plastic (matrix) and easily meltable at low temperatures, which can cause its thermal fixation to the tool. The other one, of higher hardness, is discontinuous in the matrix such as carbon fibre (CF); it is easily breakable and its particles (interacting with the edge, the release face and the evacuation channel of the drill bit) act in an abrasive way (Figure 1).



Figure 1. Evacuation of the composite material by dry OSD.

The abrasive action occurs in two different ways:

1. Direct. The particles of CF impact at high speed on the tool, producing a microblasting effect that reduces the cutting angle and the rigidity of the tool. When this action is combined with the cutting effect at the closest areas to the edge, dents can occur in the tool material, resulting in chipping or in a loss of sharpness of the tool material, also known as rounding [8–10].
2. Indirect. Once impacted over the tool, the dragged material causes its own removal in the direction of evacuation, which may develop longitudinal traces that accumulate tensile stresses. These reduce the tool resistance to compression and may cause its premature failure [11–13].

1.2. Tool Wear Mechanisms in Aluminium Drilling

The main wear mechanism during the machining of aluminium alloys is adhesion. When the material that has to be machined comes into contact with the tool surface, it creates bonding forces much stronger than the mechanical strength of the materials in contact, resulting in the transfer of particles from one surface to another [14]. This type of wear can occur in two ways:

1. Primary or direct adhesion. The particles of the tool are adhered to the chip being welded by the action of the forces developed in the tool–material interchange. In this case, when the yield stress of the chip is higher than the breakage limit of the adhered particles, these are pulled out of the tool and transported by the chip. This event can also promote abrasion on the release side due to the friction caused by these particles [15–17].

2. Secondary or indirect adhesion. This occurs when the machined material is incorporated into the tool, modifying its initial conditions. Depending on where it is located in the cutting tool, it is called [17]:
 - Adhesion on the cutting edge or raised edge (BUE—built-up edge).
 - Adhesion on the release side (BUL—built-up layer).

This phenomenon involves modifications in the properties of the cutting edge, with successive layers of machined, welded and hardened material becoming part of the edge. As mentioned before, wear is a dynamic mechanism, so the filler edge or BUE can be detached and regenerated, slowly removing material from the tool and causing primary or direct adhesion [17].

The friction of the chip with the tool within a certain temperature range increases the affinity between the materials of the tool and the piece, which promotes wear by adhesion. This situation is usually mitigated by high cutting temperatures [16].

Continuous action of primary and secondary adhesion causes premature wear of the cutting tool, causing geometrical variations that affect both surface finishing and dimensional and geometrical tolerances (Figure 2).

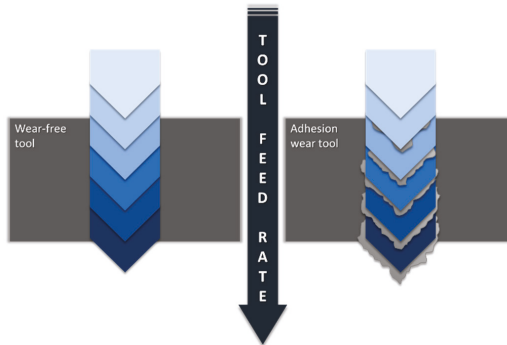


Figure 2. Influence of adhesive wear on the surface, dimensional and geometric quality of the borehole.

2. Materials and Methods

2.1. Materials

The materials used were presented in $210 \times 210 \text{ mm}^2$ sheets with thicknesses of 4.5 mm for CFRP and 4.86 mm for UNS A97075-T6 (UNS A97075). Figure 3 shows the different configurations. These materials have been selected for their importance in commercial airships.

The CFRP composite was made using unidirectional prepregs supplied by Hexcel Composite Company (Stamford, Connecticut, United States) referenced under HEXPLY M21/34%/194/T800S-24K (resin/resin content by weight (%)/fibre weight (gsm)/fibre type). The mechanical properties of the prepregs are density 1.28 g/cc, flexural yield strength 147 MPa, flexural modulus 3.50 GPa, flexural strain at yield 5%, glass transition temperature 185 °C. The lay-up sequence of the CFRP was (0/90/45/-45/45/-45)S so as to get a quasi-isotropic laminate. Aluminium alloy UNS A97075-T6 (composition Al 88.78%, Cu 1.87%, Mg 2.62%, Mn 0.08%, Zn 6.03%, Ti 0.11%, other 0.02%) was used on the other sheet. The properties of the aluminium alloy are: density 2.81 g/cc, ultimate tensile strength 524 MPa, yield tensile strength 462 MPa, elongation at break 11%, modulus of elasticity 71.7 GPa.

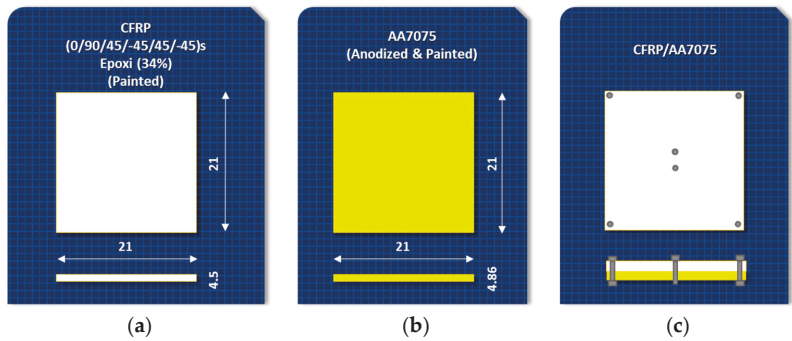


Figure 3. Characteristics and configuration of test materials: (a) CFRP; (b) UNS A97075 and (c) stacked CFRP/UNS A97075.

2.2. Tools

The chosen tool was a helical model from WC-Co without coating, being selected considering the materials that compose the stacks to be drilled, their thickness, the required qualities and cutting conditions. It has a double-angled tip; the section closest to the centre corresponds to the largest tip angle (140°) and the projection of the outer edges provides a tighter angle (118°) (Figure 4).

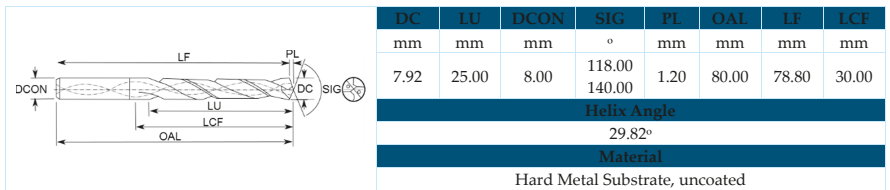


Figure 4. Characteristics of the drill bit used.

2.3. Equipment Used for the Operation and Evaluation of Drills

The selected OSD strategy has been the conventional dry type, applied separately to the CFRP and Al plank and the CFRP/Al stack. The stack configuration was CFRP/Al as it is the established machining sequence in the aerospace industry. This sequence aims to minimize the defects produced in the internal faces during the application of one-way assembly (OWA) techniques. The use of lubrication has not been considered, as we are looking to develop an environmentally friendly drilling process. The joining method has been defined in order to avoid possible failures caused by displacements of the plates that compose the stack.

The set values for the cutting parameters have been defined on the basis of other studies and real application cases, and are indicated in Table 1. Two tests were carried out using a Kondia Five 400 5-axis machining centre (Elgoibar, Guipuzcoa, Spain), controlled by a Heidenhain iTNC530 control system (Traunreut, Bavaria, Germany).

Table 1. Tested cutting conditions.

Diameter (mm)	Cutting Speed (m/min)	Feed Speed (mm/min)	Holes (n)	Lubrication
7.92	145	250	25	Dry

Microstructural analysis has been developed using scanning electron microscopy (SEM,) techniques. The compositional analysis of the materials and the cutting tool were carried out by means of EDS (energy-dispersive spectrometry) techniques with analytical capacity. The equipment used for the application of SEM and EDS techniques was the EDAX EDS System (Mahwah, NJ, USA).

For monitoring the shear forces, a dynamometer table model KITSLER© 9255B (Fx, Fy, Fz and Mz) (Kistler Holding AG, Winterthur, Zürich, Switzerland) was used. This instrument is connected to a computer that transfers the obtained data to the computer using Labview software (National Instruments, 2014, Austin, TX, USA) for processing. The sampling rate is 1000 Hz.

One of the analysis parameters studied within the macrogeometric deviations was the dimensional tolerance of the hole diameters. This measurement was carried out with a Mitutoyo three-contact internal micrometre (Mitutoyo Corporation, Kawasaki-shi, Kanagawa, Japan) with a measuring range of 6–8 mm, an accuracy of 0.001 mm and a measurement uncertainty of 2 μm . A total of three were measured sizes at different heights and angles per hole in each material.

3. Results and Discussion

3.1. Tool Wear during CFRP Drilling

Through the observation of different images obtained by SEM, abrasion was ratified as the main wear mechanism as a consequence of the continuous cutting action of carbon fibre (CF) [11–13]. Its geometric effects along the tool were visible when the tool surface's own marks disappear (Figure 5a). Other consequences found were erosion of the cutting edges (Figure 5b) and the tool tip (Figure 5c), and the appearance of marks along the periphery of the drill bit (Figure 5d).

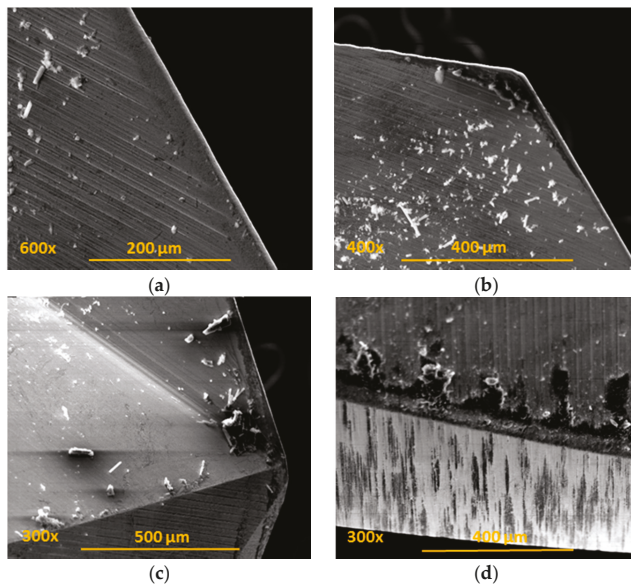


Figure 5. Location of drill wear by the abrasive action of carbon fibres: (a) main edge; (b) primary and secondary edge union; (c) tool tip; (d) peripheral face.

The continuous action of the carbon fibre on the cutting edge of the tool caused its irregularity as a consequence of abrasion [8–10] (Figure 6).

The incipient fusion of the epoxy matrix may cause its dispersed adhesion over the tool. Adhered elements in the tool can incorporate particles or small pieces of CF that interfere with machining,

especially when located in chip evacuation channels. A considerable amount of adhered material (Figure 7) was observed, which could be a signal of further deterioration of the matrix in the walls of the drilled material. The absence of resin is the cause of the problematic loss of the fibres junction, with a consequent decrease in the quality of the hole.

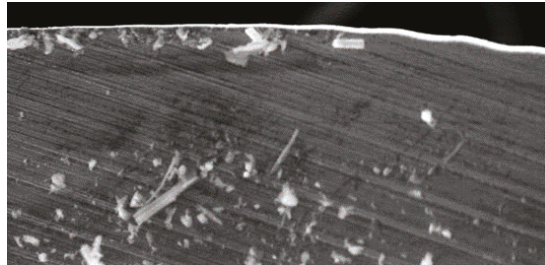


Figure 6. Detail of irregularities in the cutting edge of the tool.

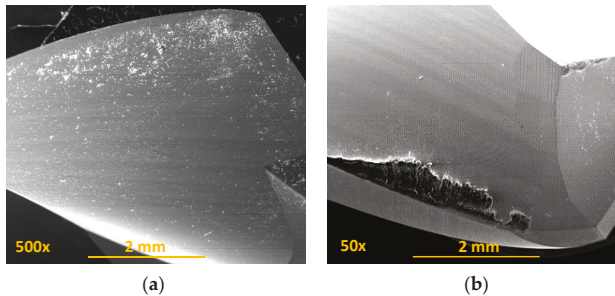


Figure 7. Accumulation of carbon fibre adhered to the tool: (a) face rake; (b) the area next to the guide surface of the tool.

3.2. Tool Wear in Conventional Drilling UNS A97075

During conventional drilling of the aluminium alloy UNS A97075, the interaction between the workpiece and the tool caused a large helical chip (Figure 8), which makes machining difficult [2]. The zinc (Zn) contained in the UNS A97075 alloy provides a high degree of plasticity, making breakage difficult due to its ductility [3].

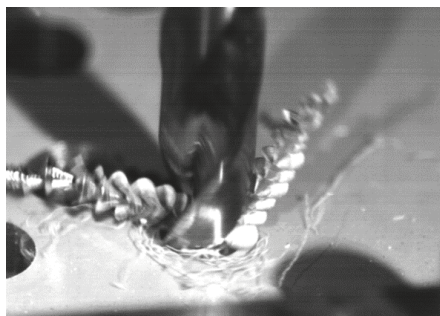


Figure 8. Chip evacuation during dry drilling of alloy UNS A97075.

The secondary adhesion of the aluminium alloy on the tool was the main wear mechanism detected. This was favoured by the absence of refrigeration and lubrication, as happened in this case. Thus, in the first stage, the aluminium matrix was melted down and welded onto the tool surface, forming a pure Al layer and giving rise to the primary BUL (Figure 9a). This circumstance provided the conditions for the mechanical adhesion of the alloy, mainly in the areas of the edge, resulting in a built-up edge (BUE) that grew to a critical size at which it began to extrude, giving rise to a secondary BUL that was deposited as a second layer over the primary BUL [4–6,17].

The location of the BUE is usually over boundary edge zones, but the BUL, during the drilling, may extend to areas outside the rake face, such as the chip evacuation channel, seriously hampering the quality of the process (Figure 9b).

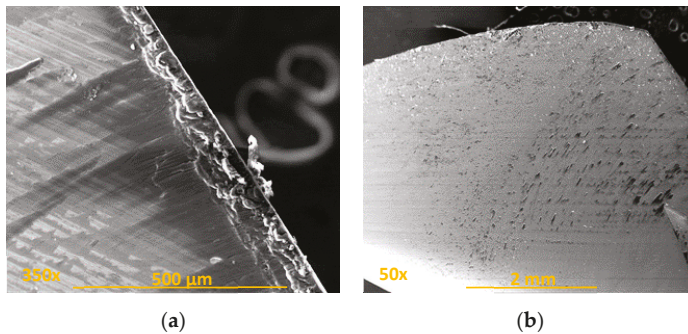


Figure 9. Wear by bonding mechanisms (BUL–BUE) on the tool after conventional drilling of the aluminium alloy UNS A97075: (a) Main cutting edge; (b) evacuation channel.

The raised friction in the piece–tool–chip interactions during cutting resulted in an elevation of the process temperature, increasing the affinity between the tool material and the aluminium, and intensifying the plasticity of the alloy, which facilitated this type of wear [7–9]. This process caused higher adhesion of the aluminium over the rake face, as in the regrowth of the cutting edges (Figure 10).

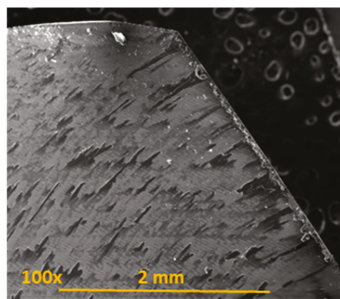


Figure 10. Increased bond wear with the number of holes.

The analysis of the cutting edges showed irregularities. These were produced by the dynamic phenomenon of primary adhesion, which, with the detachment of the BUE and its new generation, slowly removes material from the tool (Figure 11a). At the same time, this action can cause abrasive wear on the tool surface or affect the quality of the surface generated on the workpiece itself (Figure 11b).

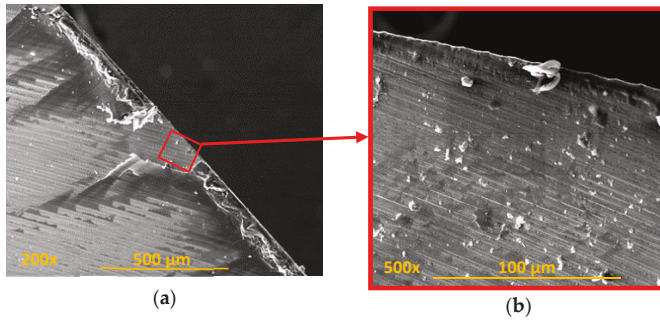


Figure 11. (a) Primary adhesion mechanism; (b) geometric irregularities observed in the cutting edges.

3.3. Tool Wear in Conventional Stack Drilling CFRP/UNS A97075

When drilling stacks of CFRP/UNS A97075, the drill bit comes into contact with two materials at the same time and acts on them with similar parameters.

Observation of the tools showed how adhesion was the main type of wear in the conventional drilling of this stack. During machining, the rake face was subjected to increased pressure and temperature [18,19], hence helping in the formation of an adhesive layer in the contact zone between the tool and the workpiece [14,20]. Adhesion wear was caused by the mechanical removal of the tool material when the adhesive junctions were broken. The effects of the abrasion wear mechanism were attenuated by the adhered material (Figure 12).

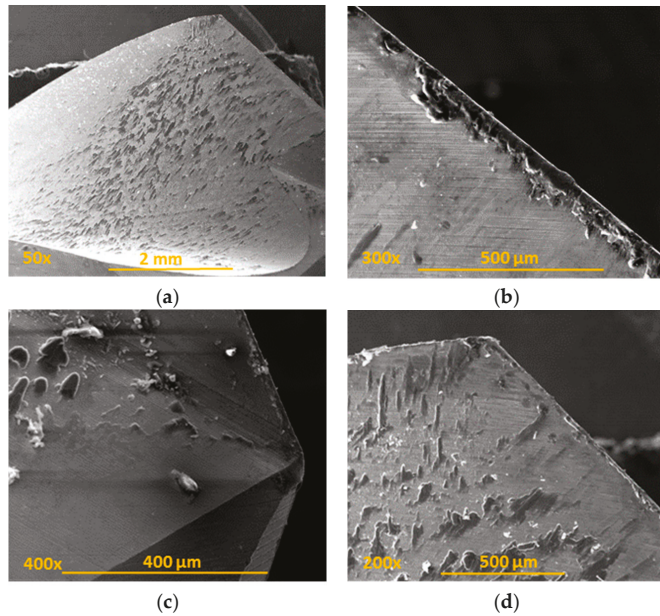


Figure 12. Wear located on the tool after conventional drilling of the CFRP/UNS A97075 stack: (a) Flute (BUL); (b) cutting lip (BUE y BUL); (c) tool tip; (d) joining of primary and secondary cutting edges (BUL).

It was seen how the adhered material was composed of both aluminium alloy and carbon fibre particles. This caused a geometric change in the tool, affecting the final quality of the hole [20–22] but

also its mechanical characteristics, since the incorporation of the Al-CFRP mixture was abrasive to the material that had to be machined (Figure 13).

This blend of aluminium and CF seemed to facilitate chip adhesion along the tool during dry drilling of CFRP/ UNS A97075, as shown in Figure 14.

One method to decrease wear during the drilling process is to reduce the temperature. This can be done by the use of lower cutting speeds and higher feed rates and the use of advanced techniques (vibration-assisted drilling, strategies with minimum quantity lubricant (MQL) and cryogenic machining, for instance).

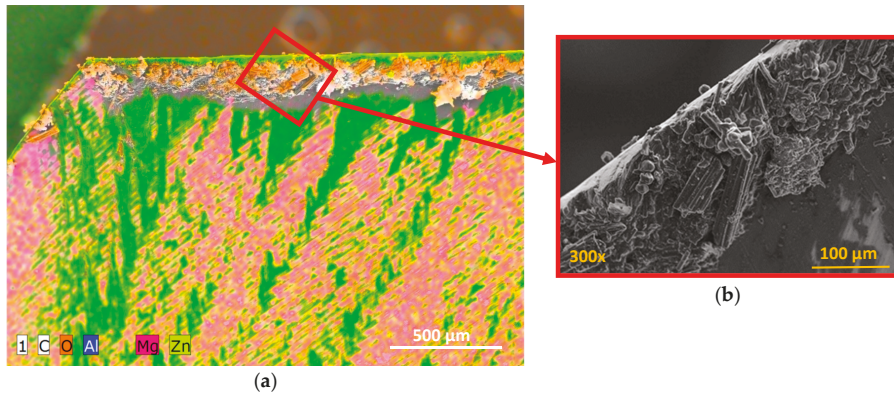


Figure 13. (a) Composition analysis of the BUE and release side after dry drilling of the stack CFRP/UNS A97075; (b) details of the BUE with carbon nanotube adhered to aluminium.

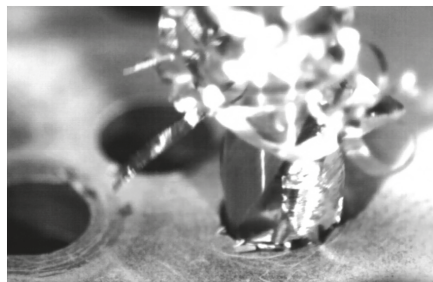


Figure 14. Chip removal during stacking drilling CFRP/UNS A97075 using conventional technology.

3.4. Driven Force in CFRP, UNS A97075 and CFRP/UNS A97075 Stacks

Figure 15a shows the values of the thrust force with regard to the height of the tool in CFRP plate, while Figure 15b shows the results obtained in UNS A97075 plate. In the first case (CFRP), the force when the tool is fully embedded in the material was increased by the number of holes drilled, from approximately 40 N to 100 N. This might be due to the rounding of the cutting edge by the abrasive action of the fibre. The force level remained significantly lower than the aluminium alloy with the same number of holes drilled. In this second case, the force remains almost constant after 25 holes. Adhesion wear does not appear to be significant.

Evolution of the values of thrust forces regarding to the feed rate of the tool in the stack is shown in Figure 16. The axial load values were increased in both materials with the number of holes.

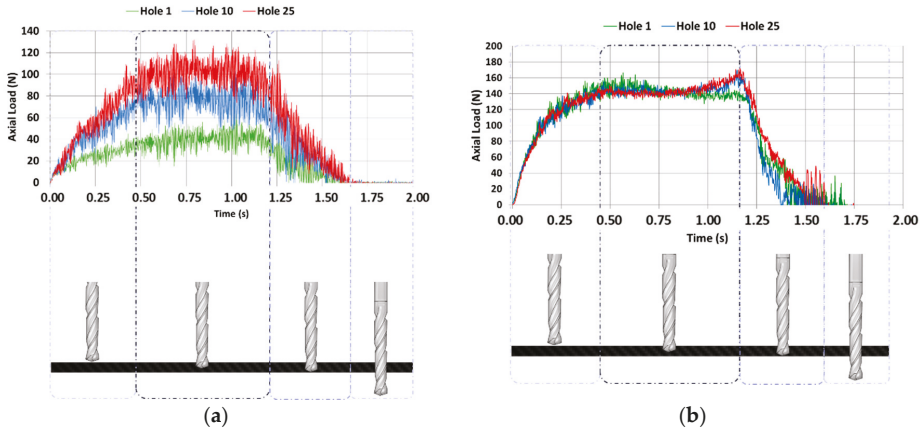


Figure 15. (a) Axial force with respect to the time applied to the drilling of CFRP plate; (b) axial force with respect to the time applied to the drilling of UNS A97075 plate.

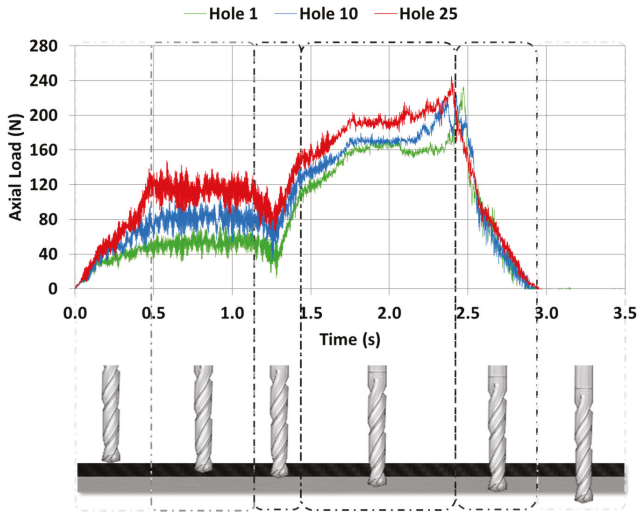


Figure 16. Axial force respecting the time applied to the drilling of CFRP/UNS A97075 stack.

A potential model was used to represent tool wear, as suggested by different studies [4,7,23]:

$$F_z = KN^m \tag{1}$$

where F_z is the axial force, K is a constant depending on the geometry of the tool and the properties of the material being machined, N is the number of holes, and m measures the degree of wear of the tool.

The axial force values and their models for the same number of holes are shown in Figure 17. The mean axial drilling forces in CFRP separately go from 39.44 N to 106.72 N, with deviations from 7.5 N to 12.78 N. The mean axial drilling forces in Al separately go from 136.96 N to 141.44 N, with deviations from 8.12 N to 11.36 N. The mean axial drilling forces in CFRP in stack go from 44.94 N to 111.15 N, with deviations from 7.26 N to 11.44 N. The mean axial drilling forces in Al stack drilling

range from 148.95 N to 197 N, with deviations from 7.2 N to 11.59 N. The force values during stack machining were similar to those for CFRP plank separately, but were highly increased by the number of holes in comparison to the Al plank. This might be caused by the increased friction due to the adhesion of Al and CF, which resulted in an elevation of the process temperature. This increased the affinity between the tool material and the aluminium and intensified the plasticity of the alloy, favouring the generation of BUE [7–9]. The wear of the drill bit seems to be more influenced by the adhesion wear of the Al than by the abrasion of the CFRP.

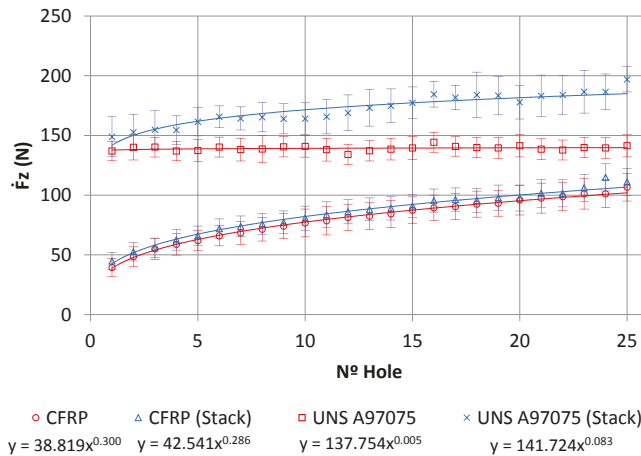


Figure 17. Axial load versus number of holes for CFRP and Al alloy plates alone and CFRP/UNS A97075 stack.

3.5. Hole Quality in Drilling: Diameter

Figure 18 shows the evolution of the hole diameter with the number of holes measured on both materials when machined separately or in a stack. The mean diameters in the separate CFRP drilling range from 7.95 to 7.94 mm, with deviations from 0.001 to 0.002 mm. The mean diameters in the separate Al drilling range from 7.98 to 7.99 mm, with deviations from 0.002 to 0.014 mm. The average diameters in the drilling of CFRP in stack go from 7.93 to 7.97 mm, with deviations from 0.001 to 0.003 mm. The average diameters in the Al stack drilling range from 7.95 to 7.97 mm, with deviations from 0.001 to 0.012 mm. There were discrepancies in the diameter between the CFRP and UNS A97075 plates, with the lowest and most stable values being the CFRP ones. The general trend of CFRP drilling is that the diameter decreases with the number of holes, which can be attributed to the progressive loss of material in the tool due to the abrasion effect of CF, while the diameter of the hole in the plate of UNS A97075 is the opposite, attributed to the adhesion effect of the cut material produced.

When machining the stack, there was a variation in the diameter of the holes compared to machining the same material separately. The CFRP inlet could cause a deterioration in the hole in this material in the evacuation of Al that can be attributed mainly to the abrasion on the surface of the hole caused by the rotation of the aluminium chip next to the drill bit. On the contrary, in UNS A97075 the variation in the diameter of the holes was reduced, possibly as a result of the negative synergies produced by the CFRP and the UNS A97075 on the tool. The discrepancy between the diameters could also be related to the different temperatures developed during drilling. As a result, thermal deformations in the planks may vary and lead to different diameters.

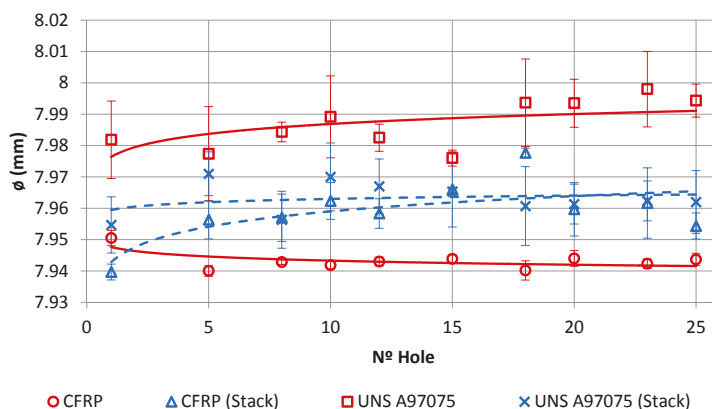


Figure 18. Evolution of hole diameter with number of holes.

4. Conclusions

This paper reports a comparison of the wear mechanisms produced during the dry drilling of CFRP and UNS A97075 planks separately and when machined as stacks.

Tool wear combines the effects of CFRP and UNS A97075 alloy machining. In CFRP drilling, the fundamental wear is the abrasion by impact and/or drag of the carbon fibre particles removed during the process. However, adhesion is detected by incipient fusion of the epoxy matrix, which in turn incorporates CF particles. This makes chip evacuation difficult, especially when combined with drilling of the metal alloy.

In the drilling of alloy UNS A97075, the wear mechanism includes different stages. The secondary adhesion of the aluminium alloy on the tool is the main wear mechanism detected. In the first stage, the aluminium matrix is melted and welded onto the tool surface, forming a pure Al layer. This creates the primary BUL, which facilitates the mechanical adhesion of the alloy, mainly in the areas of the edge and making up a BUE that grows to a critical size, from which it begins to extrude. This leads to a secondary BUL, deposited as a second layer over the primary BUL.

The interaction of CFRP and Al materials when drilled together is reflected by the comparison of wear when drilled separately. Bond wear seems to predominate over abrasion of the tool surface. The BUE generated on the edge of the tool contains CF fragments that seem to facilitate the adhesion of aluminium and reduce the diameter differences in the drilling of materials.

Author Contributions: J.S., M.B. and S.R.F.-V. developed drilling tests and data treatment. S.F.-V., M.B. and S.R.F.-V. analysed the influence of the parameters involved. S.F.-V. collaborated in preparing figures and tables and S.R.F.-V. and S.F.-V. wrote the paper.

Funding: This research was funded by the Spanish Government via the Ministry of Economy, Industry and Competitiveness, the European Union (FEDER/FSE) and the Andalusian Government (PAIDI), project MINERVA.

Acknowledgments: The authors acknowledge the financial support for the work. A special mention for a passionate engineer with a tireless capacity for work, whose academic contributions have left a legacy and shown us the way forward due to his determination to continue progressing and developing not just engineering professionals, but good people overall. His great research contributions and his memory are a stimulus for us to try to be at his level, day by day, without disappointing him. Mariano Marcos-Barcelona, in memoriam.

Conflicts of Interest: The authors declare no conflict of interest.

References

1. Cirillo, P.; Marino, A.; Natale, C.; Di Marino, E.; Chiacchio, P.; De Maria, G. A low-cost and flexible solution for one-shot cooperative robotic drilling of aeronautic stack materials. *IFAC-PapersOnLine* **2017**, *50*, 4602–4609. [[CrossRef](#)]

2. Caggiano, A.; Rimpault, X.; Teti, R.; Balazinski, M.; Chatelain, J.-F.; Nele, L. Machine learning approach based on fractal analysis for optimal tool life exploitation in CFRP composite drilling for aeronautical assembly. *CIRP Ann.* **2018**. [[CrossRef](#)]
3. Fernández-Vidal, S.R.; Mayuet, P.; Rivero, A.; Salguero, J.; del Sol, I.; Marcos, M. Analysis of the Effects of Tool Wear on Dry Helical Milling of Ti6Al4V Alloy. *Procedia Eng.* **2015**, *132*, 593–599. [[CrossRef](#)]
4. Tsao, C.C.; Hocheng, H. Effect of tool wear on delamination in drilling composite materials. *Int. J. Mech. Sci.* **2007**, *49*, 983–988. [[CrossRef](#)]
5. Huang, X. Fabrication and Properties of Carbon Fibers. *Materials* **2009**, *2*, 2369–2403. [[CrossRef](#)]
6. Brinksmeier, E.; Janssen, R. Drilling of Multi-Layer Composite Materials consisting of Carbon Fiber Reinforced Plastics (CFRP), Titanium and Aluminum Alloys. *CIRP Ann.* **2002**, *51*, 87–90. [[CrossRef](#)]
7. Liu, D.; Tang, Y.; Cong, W.L. A review of mechanical drilling for composite laminates. *Compos. Struct.* **2012**, *94*, 1265–1279. [[CrossRef](#)]
8. Feito, N.; Díaz-Álvarez, J.; Díaz-Álvarez, A.; Cantero, J.L.; Miguélez, M.H. Experimental Analysis of the Influence of Drill Point Angle and Wear on the Drilling of Woven CFRPs. *Materials* **2014**, *7*, 4258–4271. [[CrossRef](#)] [[PubMed](#)]
9. Wang, X.; Kwon, P.Y.; Sturtevant, C.; Kim, D.; Lantrip, J. Tool wear of coated drills in drilling CFRP. *J. Manuf. Proc.* **2013**, *15*, 127–135. [[CrossRef](#)]
10. Poulachon, G.; Outeiro, J.; Ramirez, C.; André, V.; Abrivard, G. Hole Surface Topography and Tool Wear in CFRP Drilling. *Procedia CIRP* **2016**, *45*, 35–38. [[CrossRef](#)]
11. Raj, D.S.; Karunamoorthy, L. A new and comprehensive characterisation of tool wear in CFRP drilling using micro-geometry and topography studies on the cutting edge. *J. Manuf. Proc.* **2018**, *32*, 839–856. [[CrossRef](#)]
12. Faraz, A.; Biermann, D.; Weinert, K. Cutting edge rounding: An innovative tool wear criterion in drilling CFRP composite laminates. *Int. J. Mach. Tools Manuf.* **2009**, *49*, 1185–1196. [[CrossRef](#)]
13. Wang, F.; Qian, B.; Jia, Z.; Fu, R.; Cheng, D. Secondary cutting edge wear of one-shot drill bit in drilling CFRP and its impact on hole quality. *Compos. Struct.* **2017**, *178*, 341–352. [[CrossRef](#)]
14. Nouari, M.; List, G.; Giroit, F.; Géhin, D. Effect of machining parameters and coating on wear mechanisms in dry drilling of aluminium alloys. *Int. J. Mach. Tools Manuf.* **2005**, *45*, 1436–1442. [[CrossRef](#)]
15. Naerheim, Y.; Trent, E.M. Diffusion wear of cemented carbide tools when cutting steel at high speeds. *Met. Technol.* **1977**, *4*, 548–556. [[CrossRef](#)]
16. Trent, E.M.; Wright, P.K. Chapter 12—Modeling of metal cutting. In *Metal Cutting (Fourth Edition)*; Butterworth-Heinemann: Woburn, MA, USA, 2000; pp. 371–409. ISBN 978-0-7506-7069-2.
17. Gómez-Parra, A.; Álvarez-Alcón, M.; Salguero, J.; Batista, M.; Marcos, M. Analysis of the evolution of the Built-Up Edge and Built-Up Layer formation mechanisms in the dry turning of aeronautical aluminium alloys. *Wear* **2013**, *302*, 1209–1218. [[CrossRef](#)]
18. Sorrentino, L.; Turchetta, S.; Bellini, C. In process monitoring of cutting temperature during the drilling of FRP laminate. *Compos. Struct.* **2017**, *168*, 549–561. [[CrossRef](#)]
19. Zitoune, R.; Cadorin, N.; Collombet, F.; Šíma, M. Temperature and wear analysis in function of the cutting tool coating when drilling of composite structure: In situ measurement by optical fiber. *Wear* **2017**, *376–377*, 1849–1858. [[CrossRef](#)]
20. Zitoune, R.; Krishnaraj, V.; Collombet, F.; Le Roux, S. Experimental and numerical analysis on drilling of carbon fibre reinforced plastic and aluminium stacks. *Compos. Struct.* **2016**, *146*, 148–158. [[CrossRef](#)]
21. Sorrentino, L.; Turchetta, S.; Bellini, C. A new method to reduce delaminations during drilling of FRP laminates by feed rate control. *Compos. Struct.* **2018**, *186*, 154–164. [[CrossRef](#)]
22. Zitoune, R.; Krishnaraj, V.; Collombet, F. Study of drilling of composite material and aluminium stack. *Compos. Struct.* **2010**, *92*, 1246–1255. [[CrossRef](#)]
23. Iliescu, D.; Gehin, D.; Gutierrez, M.E.; Giroit, F. Modeling and tool wear in drilling of CFRP. *Int. J. Mach. Tools Manuf.* **2010**, *50*, 204–213. [[CrossRef](#)]



Article

Spiral Bevel Gears Face Roughness Prediction Produced by CNC End Milling Centers

Álvaro Álvarez ¹, Amaia Calleja ^{2,*}, Mikel Arizmendi ³, Haizea González ⁴
and Luis Norberto Lopez de Lacalle ⁵

¹ Ibarria, Polígono Industrial Etxesaga, s/n, 20720 Azkoitia, Gipuzkoa, Spain; alvaro.alvarez@ibarmia.com

² Department of Mechanical Engineering, University of the Basque Country (UPV/EHU), Nieves Cano 12, 01006 Vitoria, Spain

³ Department of Mechanical Engineering, TECNUN-Universidad de Navarra, Paseo de Manuel Lardizabal 13, 20018 Donostia-San Sebastián, Spain; marizmendi@tecnun.es

⁴ Department of Mechanical Engineering, University of the Basque Country (UPV/EHU), Plaza Ingeniero Torres Quevedo 1, 48013 Bilbao, Spain; haizea.gonzalez@ehu.es

⁵ CFAA—University of the Basque Country (UPV/EHU), Parque Tecnológico de Zamudio 202, 48170 Bilbao, Spain; norberto.lzlacalle@ehu.es

* Correspondence: amaia.calleja@ehu.es; Tel.: +34-946-017-347

Received: 6 June 2018; Accepted: 25 July 2018; Published: 27 July 2018

Abstract: The emergence of multitasking machines in the machine tool sector presents new opportunities for the machining of large size gears and short production series in these machines. However, the possibility of using standard tools in conventional machines for gears machining represents a technological challenge from the point of view of workpiece quality. Machining conditions in order to achieve both dimensional and surface quality requirements need to be determined. With these considerations in mind, computer numerical control (CNC) methods to provide useful tools for gear processing are studied. Thus, a model for the prediction of surface roughness obtained on the teeth surface of a machined spiral bevel gear in a multiprocess machine is presented. Machining strategies and optimal machining parameters were studied, and the roughness model is validated for 3 + 2 axes and 5 continuous axes machining strategies.

Keywords: gear manufacturing; roughness model; multitasking machines/multiprocess machines

1. Introduction

Large size spiral bevel gears are frequently used in applications [1,2] that require smooth and silent high-power transmission. This is the case for equipment dedicated to thermal energy generation, ship propulsion systems, wind turbines or power transmission in the aeronautical sector, among many others. Nowadays, there is a continuous demand for energy, and consequently, there has been an increase in the amount of equipment dedicated to energy generation and its components, such as large sized spiral gear. Traditionally, these types of gears have been manufactured with specific gear cutting machines. There are different methods for traditional gear cutting, for example, some of the most commonly used are: (1) gear hobbing with perimeter cut (Gleason) [3]; (2) continuous generation by spiral hobbing with perimeter cut (Cyclo-Paloid from Klingelnberg and Oerlikon) [4]; and (3) continuous generation by spiral hobbing with conic type cut (Palloid from Klingelnberg) [5].

However, the eruption in the market of multitasking or multiprocess machines [6], and the continuous improvement experienced in the area of numerical controls and CAM software, has led to the appearance of a suitable medium for the manufacturing of these complex geometric elements in general purpose machines and with standard tools [7,8]. This type of technology is especially interesting for the manufacture of high module gears (4–12 mm), where it is not so common to find

specific gear cutting machines as in the case of lower value modules. The use of standard tools is also an advantage given the reduction in both cost and delivery times, which are parameters of vital importance in production. Special tools for gear manufacturing are also available [9], thus providing flexible alternatives for producing small or medium batches of large bevel gears using a five-axis machine and a disk tool cutting method. This methodology also allows the manufacture of gears of varied geometries, for example, straight gears, helical gears, double helical gear, bevel gears and hypoid gears. The manufacture of gears in multitasking machines [10–17] is seen as an increasingly widespread solution, especially given their high flexibility [18]. Four-axis [19] and 5-axis [20,21] CNC machining can be performed for spiral bevel gears manufacturing. Some of the advantages of this method include an increase in the versatility of the manufacturing process, both in terms of typology and size, allowing the realization of arbitrary modifications of the different gear teeth. Surface quality and the structure of the materials are also important for gear life, as studied in [21]. In order to guarantee the quality of the manufactured components and gear contact [22–26], the machining process of the gear surfaces requires special attention. Surface morphology [27] will determine machining strategies, making it possible to machine gear sculptured surfaces [9], classified as developable ruled surfaces [28], with flank milling strategies [29,30].

On the other hand, gears, and more specifically spiral bevel gears (bevel gears with helical teeth), are geometrically complex components. Once the feasibility of manufacturing these components in multi-axis general-purpose machines has been demonstrated, it is necessary to evaluate whether the number of the machines axes involved in the machining strategy influence the resulting gear surface quality. Since the transmission of movement and power between different axes is the main function of this type of gears, there is a greater contact surface between the pinion and gear compared to a pair of straight bevel gears. Due to the helix angle, spiral gears work in a gradual way, operating with greater smoothness and more silently, allowing work at higher speed ranges. However, this type of gear presents a greater sensitivity to contact errors than other types of gears.

Therefore, in order to ensure good gear contact, the surface roughness parameter is a parameter to be considered and studied in the manufacture of spiral bevel gears by multi-process machines. Optimal surface roughness values ensure good contact [31], which is translated into the correct transmission of both movement and power, increasing the useful life of the element. It is worth mentioning that both excessive surface roughness and polished surfaces are harmful for gear contact. On one hand, gear rough surfaces influence component life, and, on the other hand, gear polished surfaces hinder proper lubrication.

In this work, a predictive model of surface roughness for spiral bevel gears manufactured by multiprocess machines with ball end mills was developed and validated. The model estimates surface topography for each gear surface based on parameters such as tool inclination and orientation, the geometrical cutting parameters, and mill feed and speed values. The gear machining finishing process is optimized by the simulation of different machining conditions. Thus, it is not necessary to perform trial and error tests, which results in cost and time savings. This optimized process also adjusts cutting parameters depending on the required surface quality, without having to machine a greater number of passes than strictly necessary. This also reduces machining time and tool life.

2. Spiral Bevel Gears Manufacturing Process in Multitasking Machines

The gear manufacturing process consists of several stages. First, the geometry of the component, which directly influences the subsequent manufacturing stages, is defined.

2.1. Design

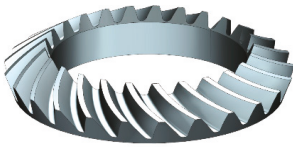
There are different options for the design of gear geometry [32–34]: Standard CAD/CAM software (CatiaV5, Siemens NX12), specific gear design module inside standard CAD/CAM software (GearTrax module for Solid Edge, SolidWorks and Inventor), specific CAD/CAM software (EUKLID),

software developed by machine tool manufacturers (gear MILL from DMG-MORI, GearPro from Mag), and, software developed by tool manufacturers (InvoMilling and Up-Gear Technology from Sandvik).

In this particular case, the “3d spiral bevel gear software” was used for the design of the gear geometry. The main reason for choosing this software was the reduced cost of the license in comparison to other software. Specifically, this program allows the design of the spiral bevel geometry, with the option to choose between Gleason and Klingelberg manufacturing methods.

A spiral bevel gear geometry was selected (Table 1) according to the Gleason method, since it is the most used method. The objective was to choose a complex and large dimension geometry to validate the capacity of general purpose multiprocessing machines for gear manufacturing.

Table 1. Spiral bevel gear geometry and parameters.

Spiral Bevel Gearing Design and Parameters		
	Gear heel pitch diameter (D_p)	200 mm
	Gear outside diameter (D_e)	207.6 mm
	Teeth number (Z)	25
	Spiral angle (β)	35°
	Face angle	59.5°
	Pressure angle (α)	20°

The selected material is a commonly used steel for manufacturing gears, F-1550 (18CrMo4) (C 0.186%, Si 0.259%, Mn 0.805%, P 0.011%, S 0.028%, Cr 1.071%, Mo 0.155%), and it reaches values up to 47 HRC (Rockwell Scale of Hardness, part C).

First, geometric parameters were introduced into the design software (module, gear ratio, gear direction, teeth number, pressure angle, etc.). With this information, the software generated the geometry of one of the teeth, from which the three-dimensional gear was generated.

2.2. Manufacturing

Once the geometry was obtained and analyzed, the machining strategies were designed. In this case, the CAM software used was NX10 from Siemens.

2.3. Equipment—Multiprocess Machine

A multi-process machine ZVH38/L1600 (Figure 1) from Ibarria (Azkoitia, Spain) was used for gear manufacturing. The machine includes turning and milling capabilities by the integration of 3 linear axes (X, Y, Z) in a mobile column and 2 rotary axes, one of them in a rotating head (B) and the other in a rotary table (C). The main advantage of multitasking machines is that the number of machines and setups required for workpiece manufacturing are reduced and often limited to one.



Figure 1. Ibarria ZVH45/L1600 ADD + PROCESS kinematic.

2.4. Machining Strategies

Machining strategies were programmed with Siemens® NX manufacturing module. First of all, the roughing operation was programmed with the aim of reducing machining time, chip thickness and

cutting forces [18] as much as possible and obtaining a near to net shape geometry. As can be seen in Table 2, the roughing operation (Figure 2) consisted of two different steps. First, a cavity mill strategy was performed, and then, a variable contour strategy was used in order to obtain a near to net shape geometry for finishing strategies. In R-I a frontal mill was used and in R-II a conical mill.

Table 2. Roughing strategy.

	Roughing Strategy	Teeth Number	Tool
R-I	Cavity mill (3 + 1-axis) Follow periphery	1–25	Frontal mill Ø4 mm
R-II	Variable contour (5-axis) Stream line	1–25	Conical mill Ø3 mm

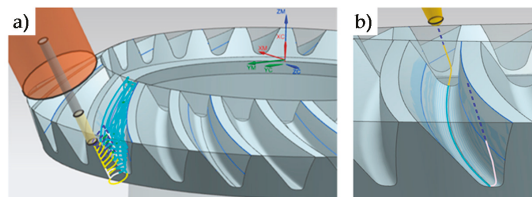


Figure 2. R-I (a) and R-II (b) roughing strategies.

For finishing operations (Table 3), different strategies and conditions were tested for the gear teeth. Different radial depths and cut patterns (zig and zig-zag) were evaluated, for both 5 continuous axes (F-II) machining operations and 3 + 2 axes (F-I) machining. In the latter machining operation (3 + 2), the tool axis is fixed and perpendicular to the head of each tooth, as can be seen in Figure 3. Machining conditions were S = 11,900 rpm and F = 400 mm/min.

Table 3. Finishing strategies.

	Finishing Strategy	Teeth Number	Tool
F-I	Surface area + Relative vector (3 + 2 axes) Cut pattern: ZIG (1–6) ZIG/ZAG(7–12) (Scallop 0.01–0.02–0.03 mm)	1–12	Conical mill Ø3 mm
F-II	Surface area + Relative vector (5 axes) Cut pattern: ZIG (13–18) ZIG/ZAG(19–25) (Scallop 0.01–0.02–0.03 mm)	13–25	8° Taper Ball nose TiAlN Number of flutes3 Helix angle 45°

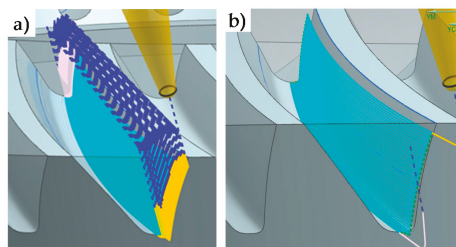


Figure 3. Finishing strategies. F-I (a) 3 + 2 finishing strategy. F-II (b) 5 continuous axes finishing strategy.

2.5. Machining

Finally, the gear was machined. After the roughing and finishing operations, the resultant gear is shown in Figure 4. Machined strategies were R-I (cavity mill) for teeth 1–25 and R-II (variable contour) after R-I and for teeth 1–25. For the finishing strategies: F-I for teeth 1–12, and F-II for teeth 13–25.

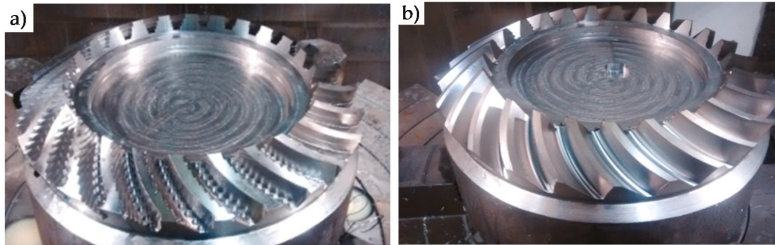


Figure 4. Roughing strategies result (a); Finishing strategies result (b).

3. Predictive Model of Topography on Gear Flank

The developed model estimates the gear teeth surface topography depending on machining parameters such as tool inclination and orientation, cutting geometric parameters and tool feed and speed values. The model was tested for two different finishing operations; a 5 continuous axes machining operation and a 3 + 2 axes machining operation in order to determine the influence of the machining number of axes on the surface finish.

The model follows the following steps:

1. **Interdental gap points and trajectories representation (Figure 5).** In this first step, for each interpolation point the model obtains from the machining program (CL data): the tool tip point position (x_j, y_j, z_j) and the tool axis orientation defined by a direction vector (u_j, v_j, w_j) in the workpiece reference system XYZ.

Milling trajectories can be obtained by means of the coordinates of successive tool tip points. Figure 5a shows the tool tip point positions obtained from the machining program of an interdental gap. In Figure 5b, the milling trajectories are represented. In the next steps, milling trajectories are evaluated after the elimination of initial and final noncutting movements, as shown in Figure 6a.

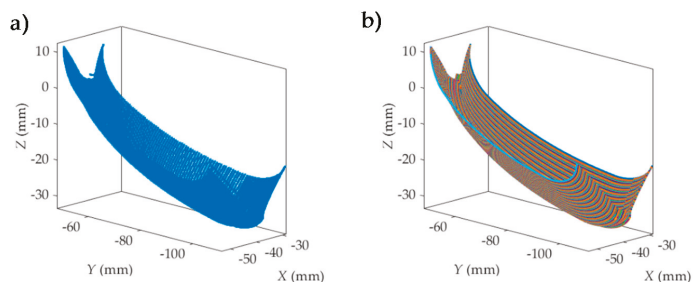


Figure 5. Interdental gap points (a) and trajectories (b) representation.

2. **Simulation area definition (Figure 6).** Secondly, as can be seen in Figure 6a, five simulation areas are defined (in black) in the feed direction. Each of these simulation areas is defined by 6 points in the feed direction and about 30 points in the direction perpendicular to the feed direction.

The dimension of the simulation area depends on the programmer’s criteria. The reference trajectory for the study is defined in magenta, corresponding to the one located in the middle of the simulation area. As an example, Figure 6b shows the milling trajectories followed by the tool tip in one of the simulation areas considered in Figure 6a. Black points in each milling trajectory represent the interpolation points given by the machining program for the selected simulation area. Next, the surface topography generated in each simulation area is predicted. In order to achieve this, a local reference system $O_W X_W Y_W Z_W$ is defined for each simulation area (Step 4). First, the positions of the tool center point (C) in the selected simulation area are deduced in Step 3.

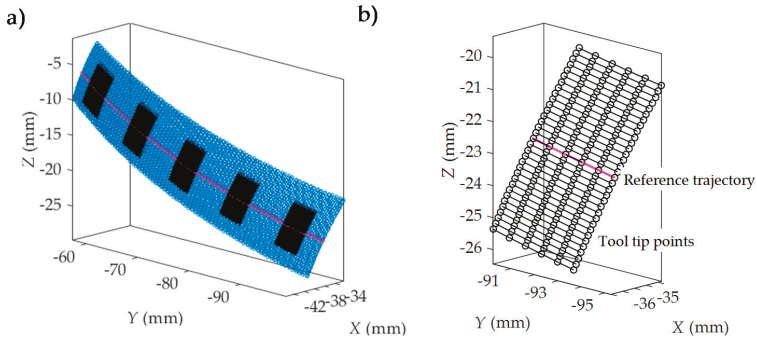


Figure 6. Simulation area (a) and reference trajectory points (b) for the study definition.

3. **Tool center position determination (Figure 7).** In order to obtain the coordinates of the tool center point (C) (Figure 7f), tool tip point coordinates (x_j, y_j, z_j) and tool axis direction vector (u_j, v_j, w_j) given in the machining program and the ball end mill, radius R needs to be taken into account. First, the line passing through the point (x_j, y_j, z_j) and parallel to the vector (u_j, v_j, w_j) is considered by means of the following equation:

$$\frac{x - x_j}{u_j} = \frac{y - y_j}{v_j} = \frac{z - z_j}{w_j} \tag{1}$$

Next, taking into account that the tool center point (C) is located at a distance equal to the tool radius R from the tool tip point of coordinates (x_j, y_j, z_j) , the coordinates (x, y, z) of the tool center point must fulfill this equation:

$$\sqrt{(x - x_j)^2 + (y - y_j)^2 + (z - z_j)^2} = R \tag{2}$$

Therefore, in order to obtain the coordinates (x, y, z) of the tool center point when the tool tip point is located at a point of coordinates (x_j, y_j, z_j) and tool axis vector is (u_j, v_j, w_j) , Equations (1) and (2) must be solved for x, y and z .

The red points shown in Figure 7a represent the positions of the tool center point (C) for the simulation area shown in Figure 6b. The surface generated by the positions of the tool center point approximates to a surface parallel to the tool tip point positions.

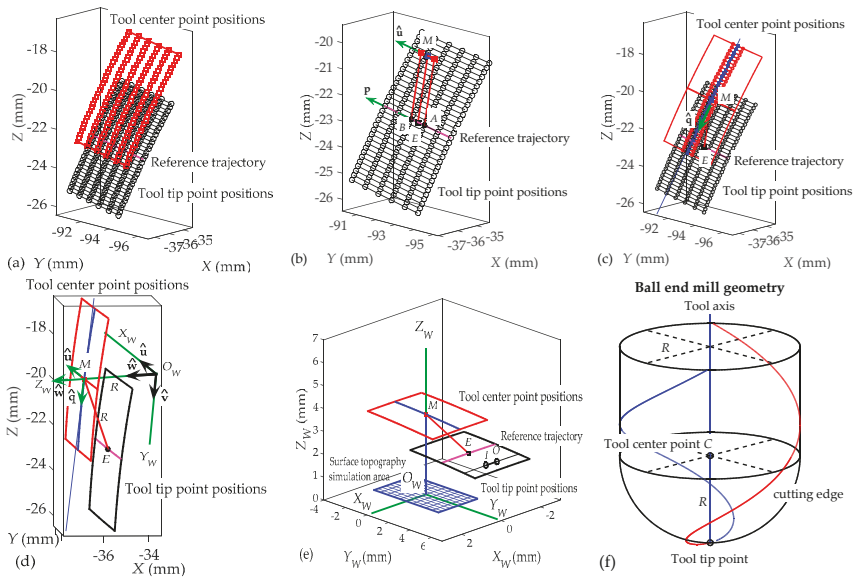


Figure 7. Tool center points (red) in relation to tool tip points (black) and to tool axis orientation and local reference system $O_W X_W Y_W Z_W$ attached to workpiece (gear tooth). (a) Tool center points position; (b) M point definition; (c) Reference trajectory; (d) Tool tip and center point positions; (e) Reference for the prediction of the topography generated in the surface of gear teeth; (f) Ball end mill geometry.

4. **Definition of workpiece local coordinate system.** In order to predict the surface topography generated in each simulation area, a local coordinate system $O_W X_W Y_W Z_W$ attached to the workpiece (gear tooth surface) is defined. The definition of this local coordinate system for each simulation area is based on the tool tip point positions and the tool axis orientations given in the machining program for the reference milling trajectory shown in magenta in Figures 6 and 7. The origin O_W and the axis Z_W are the elements of this system that are obtained first. In order to achieve this, a set of auxiliary elements (a point M and two unit vectors \hat{u} and \hat{q}) is considered. Firstly, two interpolation points, named A and B , which are located in the center of the reference trajectory (Figure 7b) are selected. The middle point D of the linear interpolation between points A and B is considered. The coordinates (x_D, y_D, z_D) of point D are calculated as a function of the coordinates (x_A, y_A, z_A) and (x_B, y_B, z_B) of points A and B :

$$x_D = \frac{x_A + x_B}{2}; y_D = \frac{y_A + y_B}{2}; z_D = \frac{z_A + z_B}{2} \quad (3)$$

Taking into account the tool axis orientation when the tool tip goes from point A to point B , the position of the tool center point when the tool tip point is located at point D can be calculated through Equations (1) and (2). Therefore, this position defined in this paper as point M (Figure 7b), with coordinates (x_M, y_M, z_M) , can be obtained from the resolution of the following equations:

$$\frac{x_M - x_D}{u_{AB}} = \frac{y_M - y_D}{v_{AB}} = \frac{z_M - z_D}{w_{AB}} \quad (4)$$

$$\sqrt{(x_M - x_D)^2 + (y_M - y_D)^2 + (z_M - z_D)^2} = R \quad (5)$$

where (u_{AB}, v_{AB}, w_{AB}) is the direction vector of tool axis, given by the machining program, when the tool tip goes from point A to point B. The point M is calculated for each simulation area and employed for the definition of the local system attached to each simulation area. In this paper, it is assumed that axis Z_W of the local system passes through this point M.

Next, the vector defining the direction of axis Z_W is calculated by considering two unit vectors. A unit vector $\hat{u} = (u_x, u_y, u_z)$ parallel to the tool linear motion direction between points A and B is defined as:

$$\hat{u} = \frac{\mathbf{p}}{|\mathbf{p}|} \text{ where } \mathbf{p} = (x_B - x_A, y_B - y_A, z_B - z_A) \tag{6}$$

A second unit vector $\hat{q} = (q_x, q_y, q_z)$ that takes into account the direction at point M of the middle points of the milling trajectories selected in the simulation area is also defined (Figure 7c). Once the unit vectors \hat{u} and \hat{q} are obtained, a unit vector $\hat{w} = (w_x, w_y, w_z)$ perpendicular to \hat{u} and \hat{q} is defined as follows:

$$\hat{w} = \hat{u} \times \hat{q} \tag{7}$$

This vector \hat{w} is assumed to coincide with the direction of axis Z_W (Figure 7d). In addition, in order to define the position of the origin O_W , it is assumed that this point is located at a distance R from the point M. Therefore, taking into account that point O_W is also located on a line passing through point M and parallel to vector \hat{w} , the coordinates (x_{Ow}, y_{Ow}, z_{Ow}) of point O_W are obtained by solving these equations:

$$\frac{x_{Ow} - x_M}{w_x} = \frac{y_{Ow} - y_M}{w_y} = \frac{z_{Ow} - z_M}{w_z} \tag{8}$$

$$\sqrt{(x_{Ow} - x_M)^2 + (y_{Ow} - y_M)^2 + (z_{Ow} - z_M)^2} = R \tag{9}$$

Once the origin O_W and the axis Z_W have been obtained, axes X_W and Y_W are defined. The axis X_W is assumed to have the same direction as the unit vector \hat{u} (Figure 7d). Therefore, the axis X_W coincides with the feed direction of the tool between points A and B. Finally, the axis Y_W is perpendicular to axes X_W and Z_W . The direction of axis Y_W is defined by a unit vector $\hat{v} = (v_x, v_y, v_z)$ calculated as the cross product between vectors \hat{w} and \hat{u} :

$$\hat{v} = \hat{w} \times \hat{u} \tag{10}$$

Figure 7e shows an equivalent representation of Figure 7d. In Figure 7e, the local system $O_W X_W Y_W Z_W$ is taken as a reference for the prediction of the topography generated in the surface of gear teeth. The surface topography will be simulated in a rectangular area defined along axes X_W and Y_W , as shown in Figure 7e. In order to model the surface roughness, the equations expressing the trajectories of tool cutting edges in this local system are deduced in Step 6 as a function of the ball end mill geometry (Step 5), the tool axis orientation and the milling trajectories followed by the tool in the simulation area. Firstly, the coordinates of points defining the milling trajectories and the direction vector of tool axis orientations expressed in the workpiece system XYZ (given by the machining program and obtained in Step 1) must be transformed into the local system $O_W X_W Y_W Z_W$.

In order to express the coordinates of a point in the local system $O_W X_W Y_W Z_W$ from its coordinates in the workpiece system XYZ, a homogeneous transformation matrix **T** is defined as a function of the unit vectors \hat{u} , \hat{v} and \hat{w} and the coordinates of the origin O_W in the system XYZ. The coordinates (x_j, y_j, z_j) of the tool tip point positions given in the machining program can be expressed in the local system $O_W X_W Y_W Z_W$, (x_j^W, y_j^W, z_j^W) , as:

$$\begin{bmatrix} x_j \\ y_j \\ z_j \\ 1 \end{bmatrix} = \begin{bmatrix} u_x & v_x & w_x & x_{Ow} \\ u_y & v_y & w_y & y_{Ow} \\ u_z & v_z & w_z & z_{Ow} \\ 0 & 0 & 0 & 1 \end{bmatrix} \begin{bmatrix} x_j^W \\ y_j^W \\ z_j^W \\ 1 \end{bmatrix} = \mathbf{T} \begin{bmatrix} x_j^W \\ y_j^W \\ z_j^W \\ 1 \end{bmatrix} \rightarrow \begin{bmatrix} x_j^W \\ y_j^W \\ z_j^W \\ 1 \end{bmatrix} = \mathbf{T}^{-1} \begin{bmatrix} x_j \\ y_j \\ z_j \\ 1 \end{bmatrix} \tag{11}$$

Similarly, a direction vector (u_j, v_j, w_j) given in the machining program can be expressed in the local system $O_W X_W Y_W Z_W$, (u_j^W, v_j^W, w_j^W) by means of a matrix T_1 depending on the unit vectors \hat{u} , \hat{v} and \hat{w}

$$\begin{bmatrix} u_j \\ v_j \\ w_j \\ 1 \end{bmatrix} = \begin{bmatrix} u_x & v_x & w_x & 0 \\ u_y & v_y & w_y & 0 \\ u_z & v_z & w_z & 0 \\ 0 & 0 & 0 & 1 \end{bmatrix} \begin{bmatrix} u_j^W \\ v_j^W \\ w_j^W \\ 1 \end{bmatrix} = T_1 \begin{bmatrix} u_j^W \\ v_j^W \\ w_j^W \\ 1 \end{bmatrix} \rightarrow \begin{bmatrix} u_j^W \\ v_j^W \\ w_j^W \\ 1 \end{bmatrix} = T_1^{-1} \begin{bmatrix} u_j \\ v_j \\ w_j \\ 1 \end{bmatrix} \quad (12)$$

Once the tool tip point positions and the tool axis orientations are expressed in the local system $O_W X_W Y_W Z_W$, the equations for the cutting edge trajectory are deduced. In order to achieve this, the geometry of the tool cutting edges is first modeled.

5. **Tool geometric modelization (Figure 8).** The roughness model is developed for a ball end mill geometry, whose behavior resembles that of a conical tool that only cuts with the spherical area of the tool tip for gear teeth finishing trajectories. Figure 8a shows schematically the 3D geometry of a ball end mill of radius R and helix angle i_0 . For simplicity, only one of the edges is represented in the figure (Figure 8b), but the developed model is generalized for a N_t edge mill. It is assumed that the cutting edge represented in this figure represents one of the edges of the milling cutter, which is referred to as a k edge, where $k = 1, 2, \dots, N_t$. To define the position of a point located on the edge k , a reference system $O_T X_T Y_T Z_T$ attached to the ball end mill is defined:

- The reference system origin O_T is located on the tool tip being coincident with the tool axis
- The axis Z_T corresponds to the tool axis
- The axis X_T is radial and tangent to edge 1 projection in the plane containing point O_T and perpendicular to Z_T axis
- The axis Y_T is perpendicular to axes X_T and Z_T forming a right-handed system.

The position angle φ_k of cutting edge k with respect to axis X_T can be expressed as:

$$\varphi_k = \frac{2\pi}{N_t}(k - 1) \quad (13)$$

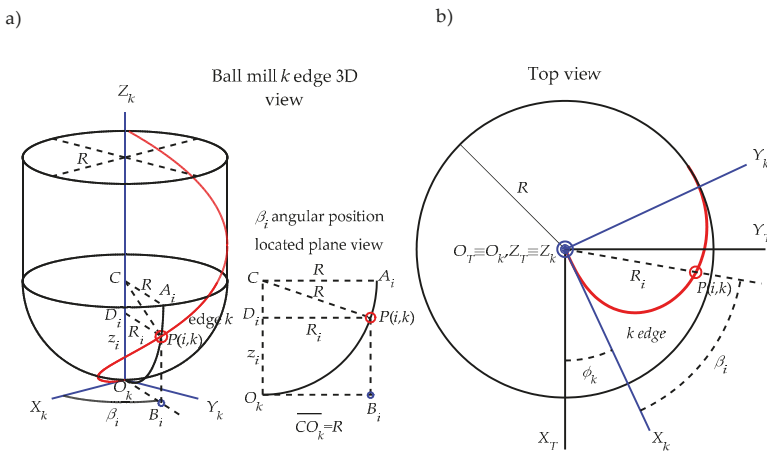


Figure 8. Ball end mill geometry (a) and k edge geometry definition (b).

The position of a cutting edge point $P(i, k)$, located at a height z_i on the edge k , can be written in the tool reference system $O_T X_T Y_T Z_T$ as a function of (a) the radius R_i and the position angle β_i of cutting edge point at height z_i and (b) the position angle φ_k of edge k as follows:

$$x_{P(i,k)}^T = R_i \cdot \cos(\beta_i + \varphi_k) \tag{14}$$

$$y_{P(i,k)}^T = R_i \cdot \sin(\beta_i + \varphi_k) \tag{15}$$

$$z_{P(i,k)}^T = z_i \tag{16}$$

where, from ball end mill geometry, the radius R_i and the position angle β_i are:

$$R_i = \sqrt{2Rz_i - (z_i)^2} \tag{17}$$

$$\beta_i = z_i \cdot \tan(i_0) / R \tag{18}$$

Next, the equations of trajectories followed by cutting edge points are deduced.

- 6. Tool axis orientation and points trajectories determination (Figures 9 and 10).** In this step, the trajectory followed by any cutting edge point in a five-axis milling operation is expressed as a function of cutting parameters, tool axis orientation and milling trajectories defined in the machining program. The cutting parameters are the feed value (F) in mm/min and the spindle speed (S) in rpm. Therefore, the tool feed in mm per revolution can be calculated as:

$$f \left(\frac{\text{mm}}{\text{rev}} \right) = \frac{F(\text{mm/min})}{S(\text{rpm})} \tag{19}$$

In order to define the cutting trajectories, as an example, the linear motion shown in Figure 7e, when the tool tip point goes from a point O to a point I in a milling trajectory of the simulation area, is considered. The procedure presented below is carried out in every section of the milling trajectories located inside the simulation area.

From the machining program, the coordinates (x_O, y_O, z_O) and (x_I, y_I, z_I) of points O and I and the direction vector (u_{OI}, v_{OI}, w_{OI}) of tool axis orientation during this linear motion can be known. By means of the matrices given by Equations (11) and (12), the coordinates (x_O^W, y_O^W, z_O^W) and (x_I^W, y_I^W, z_I^W) of these points and the direction vector $(u_{OI}^W, v_{OI}^W, w_{OI}^W)$ can be expressed in the local system $O_W X_W Y_W Z_W$ attached to each simulation area.

Taking into account the feed direction of the ball end mill along the linear motion between points O and I , feed values f_x, f_y and f_z along axes X_W, Y_W and Z_W can be defined. In order to achieve this, a unit vector $\hat{r} = (r_x, r_y, r_z)$ that considers the tool feed direction between points O and I , is defined as a function of their coordinates:

$$\hat{r} = \frac{\mathbf{q}}{|\mathbf{q}|} \text{ where } \mathbf{q} = \left(x_I^W - x_O^W, y_I^W - y_O^W, z_I^W - z_O^W \right) \tag{20}$$

The components f_x, f_y and f_z of the tool feed can be expressed as:

$$f_x = f r_x \tag{21}$$

$$f_y = f r_y \tag{22}$$

$$f_z = f r_z \tag{23}$$

By means of feed values f_x, f_y and f_z , the position of the tool tip point along the linear displacement between points O and I is expressed as a function of the tool rotation angle α in radians. In Figure 9, it is assumed that the tool tip point is located at a point O_1 whose coordinates are:

$$x_{O_1}^W = x_O^W + f_x \frac{\alpha}{2\pi} \tag{24}$$

$$y_{O_1}^W = y_O^W + f_y \frac{\alpha}{2\pi} \tag{25}$$

$$z_{O_1}^W = z_O^W + f_z \frac{\alpha}{2\pi} \tag{26}$$

where the tool rotation angle α goes from 0 to $\alpha_I - \alpha_O$, being α_I and α_O , the tool rotation angles when the tool tip point is located at points I and O , respectively.

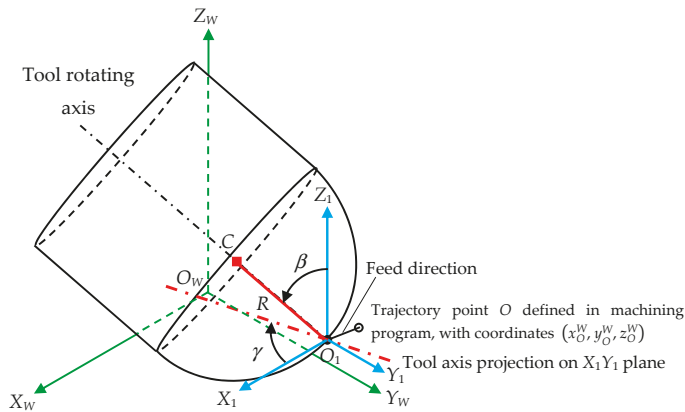


Figure 9. 5-axis milling scheme with tool tilt angle β and lead angle γ .

In order to simplify the deduction of cutting edge trajectories, the tool axis orientation is defined in this step by means of two angles, which are represented in Figure 9: a tilt angle β and a lead angle γ .

- The tilt angle β is defined as the angle between the tool rotating axis and the axis Z_1 , which is parallel to axis Z_W .
- The lead angle γ is the angle between the projection of the tool rotating axis into plane $X_1 Y_1$ (which is parallel to plane $X_W Y_W$) with respect to axis X_W direction.

These angles β and γ can be written as function of the tool axis direction vector $(u_{O_1}^W, v_{O_1}^W, w_{O_1}^W)$:

$$\beta = \text{acos}(w_{O_1}^W) \tag{27}$$

$$\gamma = \text{atan}\left(-\frac{v_{O_1}^W}{u_{O_1}^W}\right) \tag{28}$$

In order to obtain the equations expressing the trajectory of cutting edge points in the local system $O_W X_W Y_W Z_W$ from their coordinates in the tool system $O_T X_T Y_T Z_T$, three auxiliary systems $O_1 X_1 Y_1 Z_1$, $O_2 X_2 Y_2 Z_2$ and $O_3 X_3 Y_3 Z_3$, shown in Figure 10, are defined as a function of:

- The current position of the tool tip point given by the coordinates of point O_1 (Figure 9). A translation of system $O_1 X_1 Y_1 Z_1$ with respect to system $O_W X_W Y_W Z_W$ (Figure 10a) is considered.

The system $O_1X_1Y_1Z_1$ is shifted in X_W, Y_W and Z_W by distances x_{O1}^W, y_{O1}^W and z_{O1}^W respectively. The homogeneous transformation matrix $\mathbf{T}_{W1}(f_x, f_y, f_z, \alpha)$ of this translation in X_W, Y_W and Z_W is:

$$\mathbf{T}_{W1}(f_x, f_y, f_z, \alpha) = \begin{bmatrix} 1 & 0 & 0 & x_{O1}^W \\ 0 & 1 & 0 & y_{O1}^W \\ 0 & 0 & 1 & z_{O1}^W \\ 0 & 0 & 0 & 1 \end{bmatrix} = \begin{bmatrix} 1 & 0 & 0 & x_O^W + f_x \alpha / (2\pi) \\ 0 & 1 & 0 & y_O^W + f_y \alpha / (2\pi) \\ 0 & 0 & 1 & z_O^W + f_z \alpha / (2\pi) \\ 0 & 0 & 0 & 1 \end{bmatrix} \quad (29)$$

- The lead angle γ (Figure 10b). The system $O_2X_2Y_2Z_2$ is rotated by an angle γ about axis Z_1 in clockwise direction. The homogeneous transformation matrix $\mathbf{T}_{12}(\gamma)$ of this rotation about Z_1 -axis is:

$$\mathbf{T}_{12}(\gamma) = \begin{bmatrix} \cos(\gamma) & \sin(\gamma) & 0 & 0 \\ -\sin(\gamma) & \cos(\gamma) & 0 & 0 \\ 0 & 0 & 1 & 0 \\ 0 & 0 & 0 & 1 \end{bmatrix} \quad (30)$$

- The tilt angle β (Figure 10c). The system $O_3X_3Y_3Z_3$ is rotated by an angle β about axis Y_2 in a clockwise direction. The homogeneous transformation matrix $\mathbf{T}_{23}(\beta)$ of this rotation about Y_2 -axis is:

$$\mathbf{T}_{23}(\beta) = \begin{bmatrix} \cos(\beta) & 0 & \sin(\beta) & 0 \\ 0 & 1 & 0 & 0 \\ -\sin(\beta) & 0 & \cos(\beta) & 0 \\ 0 & 0 & 0 & 1 \end{bmatrix} \quad (31)$$

- The rotation angle α (Figure 10d). The tool system $O_TX_TY_TZ_T$ is rotated by an angle α about axis Z_3 in clockwise direction. The homogeneous transformation matrix $\mathbf{T}_{3T}(\alpha)$ of this rotation about Z_3 -axis is:

$$\mathbf{T}_{3T}(\alpha) = \begin{bmatrix} \cos(\alpha + \alpha_O) & \sin(\alpha + \alpha_O) & 0 & 0 \\ -\sin(\alpha + \alpha_O) & \cos(\alpha + \alpha_O) & 0 & 0 \\ 0 & 0 & 1 & 0 \\ 0 & 0 & 0 & 1 \end{bmatrix} \quad (32)$$

where α_O is the tool rotation angle when the tool tip point is located at point O .

Finally, the trajectory of any cutting edge point $P(i, k)$ located at a height z_i on the edge k , as shown in Figure 8, is expressed in the system $O_WX_WY_WZ_W$ of the gear tooth (Figure 9) as a function of the previous transformation matrices $\mathbf{T}_{W1}(f_x, f_y, f_z, \alpha)$, $\mathbf{T}_{12}(\gamma)$, $\mathbf{T}_{23}(\beta)$ and $\mathbf{T}_{3T}(\alpha)$ and the coordinates of the cutting edge point $P(i, k)$ in the tool system $O_TX_TY_TZ_T$ (Equations (14)–(16) in Step 5):

$$\begin{bmatrix} x_{P(i,k)}^W \\ y_{P(i,k)}^W \\ z_{P(i,k)}^W \\ 1 \end{bmatrix} = \mathbf{T}_{W1}(f_x, f_y, f_z, \alpha) \cdot \mathbf{T}_{12}(\gamma) \cdot \mathbf{T}_{23}(\beta) \cdot \mathbf{T}_{3T}(\alpha) \cdot \begin{bmatrix} x_{P(i,k)}^T \\ y_{P(i,k)}^T \\ z_{P(i,k)}^T \\ 1 \end{bmatrix} \quad (33)$$

Once the cutting edge trajectories are obtained, surface topographies generated in each simulation area are obtained through the procedure described in Step 7.

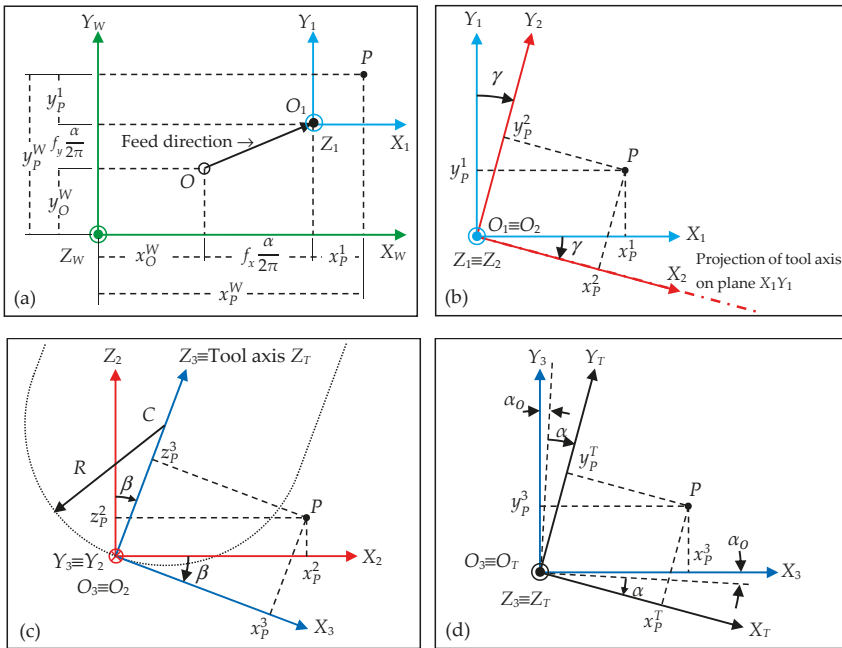


Figure 10. Definition of auxiliary systems $O_1X_1Y_1Z_1$ (a,b); $O_2X_2Y_2Z_2$ (c) and $O_3X_3Y_3Z_3$ (d).

7. **Surface topographies determination (Figure 11).** The surface topography in the gear teeth is obtained from successive point positions of cutting edge points located on the N_i edges with the tool rotating movement. The surface topography is simulated in a rectangular area defined along axes X_W and Y_W , as shown in Figure 7e. This area is divided into a discrete number of planes perpendicular to axes X_W and Y_W . For each plane, taking into account the trajectories of cutting edge points given by Equation (33), the model predicts the area swept by the tool cutting edges during the tool rotation and feed motion. The profile generated at each plane is obtained from the lowest positions of marks left by cutting edge points. By considering the profiles generated in those planes, the 3D surface topography in the rectangular area can be predicted. This allows the profiles generated along axes X_W and Y_W to be analyzed. As an example, Figure 11 shows the surface topography predicted for the simulation area selected in Figure 6b. In Figure 11a, a 3D representation of the predicted surface topography is shown. When the 2D profiles generated at two planes ($Y_W = 0$ and $X_W = 0$) are considered (Figure 11b,c), it can be observed that profiles are not only composed of roughness marks left by tool cutting edges. In Figure 11b, the straight sections defining the tool trajectory (red line) can be observed. In Figure 11c, the form of the gear tooth surface can also be observed. In order to analyze the surface roughness, the effect of tool trajectory in each milling pass is removed for each profile predicted along Y_W -axis. As a consequence, roughness profiles (in black) are obtained. In Figure 11c, the form of the gear surface is also removed from the predicted profile and the roughness profile in black is obtained. In Figure 11d, the predicted surface roughness without the influence of the milling trajectory is shown. It can be observed that the step over between milling passes has a significant influence on the topography and the roughness peak-to-valley values. However, for this case, the effect of tool feed on roughness is less.

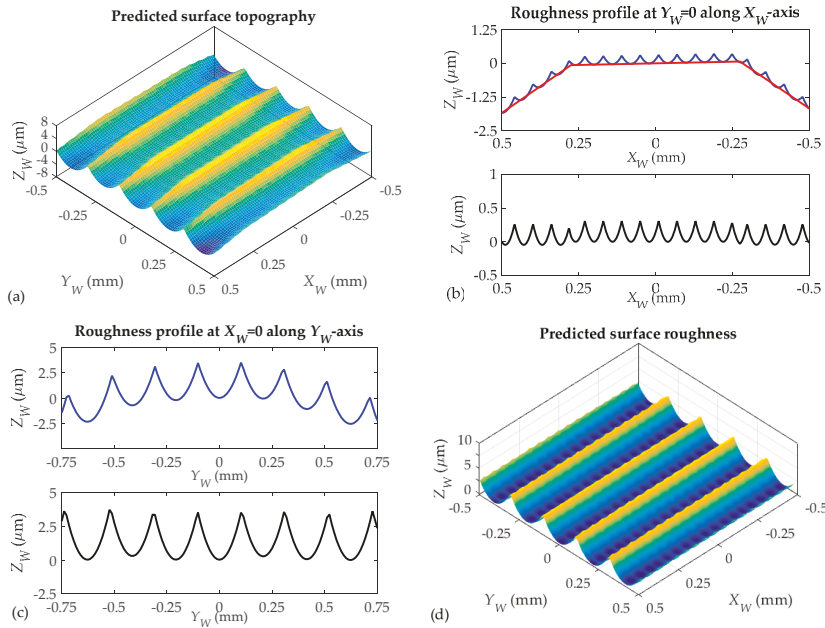


Figure 11. 3D simulated surface topography (a); roughness profiles (b,c) and surface roughness (d): ball end mill with 3 mm diameter and $N_t = 3$ cutting edges and feed value $f = 0.18$ mm/rev.

4. Model Validation Results

In order to validate the surface roughness predictive model explained in the previous section, measured roughness after gear machining, and model predicted roughness, were compared.

4.1. Gear Roughness Measurement

For measuring gear surface roughness (R_a and R_z) (Table 4), confocal tridimensional Leica® DMC 3D and contact profilometer Taylor Hobson® Form Taylorsurf were used for the 3D and 2D roughness measurement, respectively.

Table 4. Roughness measured results for gear teeth after finishing strategies.

Teeth Number	Machining	Strategy	Scallops (mm)	Measured Roughness Values	
				R_a (μm)	R_z (μm)
1	3 + 2 AXES	ZIG	0.01		
2	3 + 2 AXES	ZIG	0.01	1.68	8.64
3	3 + 2 AXES	ZIG	0.02		
4	3 + 2 AXES	ZIG	0.02	2.72	13.03
5	3 + 2 AXES	ZIG	0.03		
6	3 + 2 AXES	ZIG	0.03	4.66	20.83
7	3 + 2 AXES	ZIG-ZAG	0.01		
8	3 + 2 AXES	ZIG-ZAG	0.01	1.91	10.12
9	3 + 2 AXES	ZIG-ZAG	0.02		
10	3 + 2 AXES	ZIG-ZAG	0.02	2.71	15.43
11	3 + 2 AXES	ZIG-ZAG	0.03		
12	3 + 2 AXES	ZIG-ZAG	0.03	4.83	22.20

Table 4. Cont.

Teeth Number	Machining	Strategy	Scallops (mm)	Measured Roughness Values	
				R_a (μm)	R_z (μm)
13	5 AXES	ZIG	0.01	1.34	7.78
14	5 AXES	ZIG	0.01		
15	5 AXES	ZIG	0.02	2.62	13.44
16	5 AXES	ZIG	0.02		
17	5 AXES	ZIG	0.03	4.58	19.63
18	5 AXES	ZIG	0.03		
19	5 AXES	ZIG-ZAG	0.01	4.24	20.03
20	5 AXES	ZIG-ZAG	0.01		
21	5 AXES	ZIG-ZAG	0.02	6.86	31.62
22	5 AXES	ZIG-ZAG	0.02		
23	5 AXES	ZIG-ZAG	0.02	7.68	35.63
24	5 AXES	ZIG-ZAG	0.03		
25	5 AXES	ZIG-ZAG	0.03		

As it is mentioned in Section 3, the developed model predicts surface roughness in 5 different gear tooth zones. Nevertheless, surface roughness is only measured in two zones, always avoiding tooth edges (zones 1 and 5) and coinciding with the intermediate tooth zone. This fact must be taken into consideration when comparing predicted and measured roughness values. Therefore, for model validation, measured roughness values were compared to predicted values from zones 2–4.

4.2. Gear Roughness Prediction

The developed roughness model analyses 5 gear tooth zones and predicts surface roughness and generates surface topography and roughness profiles in each of these 5 zones. Thanks to this, different roughness profiles are predicted along tool feed direction X_W . They are simulated for different tool edges number (N_t) and feed values (f) as can be seen in Figures 10 and 11.

In Table 5, roughness values for each gear tooth flank depending on machining type, cutting patterns and programmed scallop height are shown. These values also depend on tooth flank (concave or convex), and on the analyzed zone (1–5). In Table 5, the first of the rows corresponds to the concave flanks and the second to convex ones.

In this case, taking into account that the selected gear design method corresponds to the Gleason method, the roughness values (R_a and R_z) are slightly different in the 5 analyzed zones. This is a consequence of the Gleason method, which generates a gear with a variable gearing height. For this reason, in the areas closest to the outer diameter, the obtained roughness values are higher.

The shape of the roughness profiles is a consequence of the straight sections between two points of the machining program (interpolation points) that define tool trajectory. The distance between the different interpolation points within the same path is approximately 0.56 mm.

In the left-side figures (Figures 12 and 13), the straight sections defined by machining G1 (linear movement) are represented by a red line. The blue color represents the roughness profile. As can be seen, the roughness profile depends on the tool edge number (N_t) and programmed tool feed value (f). In the right-side figures (Figures 12 and 13), the form associated to workpiece component is eliminated, and for each roughness profile, both the arithmetic mean roughness parameter (R_a) and the average roughness parameter (R_z) are obtained.

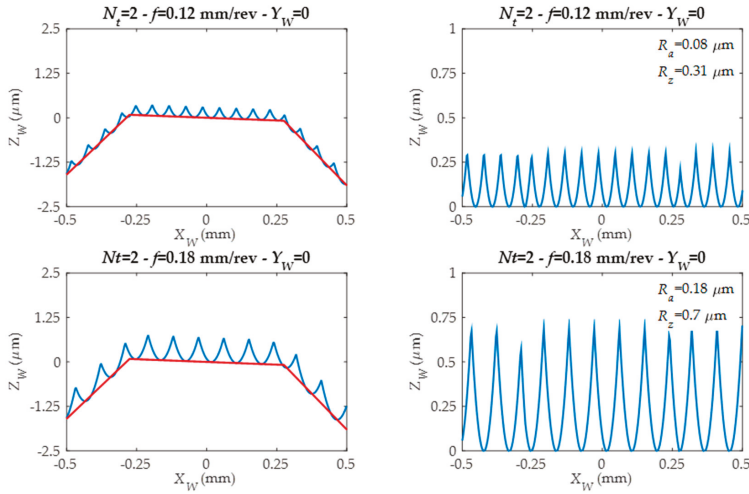


Figure 12. Predicted roughness profiles for different feed values and for the same tool.

Table 5. Roughness predicted results for gear teeth.

Teeth N°	Machining Strategy	Scallop (mm)	Zone 1		Zone 2		Zone 3		Zone 4		Zone 5		
			R _a (μm)	R _z (μm)	R _a (μm)	R _z (μm)	R _a (μm)	R _z (μm)	R _a (μm)	R _z (μm)	R _a (μm)	R _z (μm)	
1, 2	3+2 AXES	ZIG	0.01	1.2	5.19	1.39	5.74	1.56	6.6	1.73	7.31	1.85	7.66
				2.1	9	1.89	8.68	1.65	7.92	1.41	6.92	1.18	6.72
3, 4	3+2 AXES	ZIG	0.02	2.44	10.43	2.8	11.75	3.27	13.5	3.49	15.38	3.89	16.42
				4.33	18.71	3.82	16.37	3.39	14.47	2.88	13.15	2.36	11.1
5, 6	3+2 AXES	ZIG	0.03	3.72	16.39	4.31	18.6	4.93	20.16	5.42	22.35	5.7	24.45
				5.96	26.13	5.57	23.29	4.71	20.94	3.97	17.4	3.28	14.62
7, 8	3+2 AXES	ZIG-ZAG	0.01	1.19	5.16	1.35	5.77	1.65	9.29	1.66	7.07	1.83	7.75
				2.2	9.58	1.93	8.63	8.63	7.89	1.46	7.3	1.19	6.2
9, 10	3+2 AXES	ZIG-ZAG	0.02	2.28	9.8	2.63	11.44	11.44	14.38	3.34	17.21	3.47	15.01
				4.32	18.36	3.86	16.5	16.5	14.43	2.9	12.7	2.36	10.53
11, 12	3+2 AXES	ZIG-ZAG	0.03	3.41	14.75	3.96	16.95	16.95	19.71	5.07	20.07	5.35	19.98
				6.17	27.68	5.58	24.67	24.67	21.78	4.15	18.08	3.32	14.68
13, 14	5 AXES	ZIG	0.01	1.11	4.63	1.3	5.35	1.48	5.97	1.62	6.67	1.82	7.34
				2.3	9.68	2.19	8.93	1.93	8.21	1.68	7.42	1.46	6.52
15, 16	5 AXES	ZIG	0.02	2.25	9.2	2.59	10.52	2.95	11.93	3.32	13.39	3.6	14.66
				4.92	19.95	4.51	18.28	4.06	16.59	3.54	15.13	3.15	13.45
17, 18	5 AXES	ZIG	0.03	3.43	14.42	4.05	16.66	4.6	18.75	5.3	21.1	5.49	22.9
				7.16	29.17	6.56	26.78	5.84	25.04	1.58	23.39	4.89	20.33
19, 20	5 AXES	ZIG-ZAG	0.01	1.06	4.61	1.24	5.5	1.41	6.23	1.58	6.59	1.72	7.12
				2.5	9.61	2.22	8.63	2.02	7.67	1.92	7.35	1.59	6.37
21, 22, 23	5 AXES	ZIG-ZAG	0.02	2.22	8.34	2.47	9.59	2.86	11.05	3.25	12.44	3.43	13.34
				5.16	20.07	4.61	17.6	4.25	16.78	3.77	15.46	3.36	13.91
24, 25	5 AXES	ZIG-ZAG	0.03	3.2	11.76	3.71	13.62	4.27	16.91	4.87	19.54	5.37	20.01
				7.35	30.22	6.72	27.63	5.91	25.06	5.5	22.63	4.76	19.97

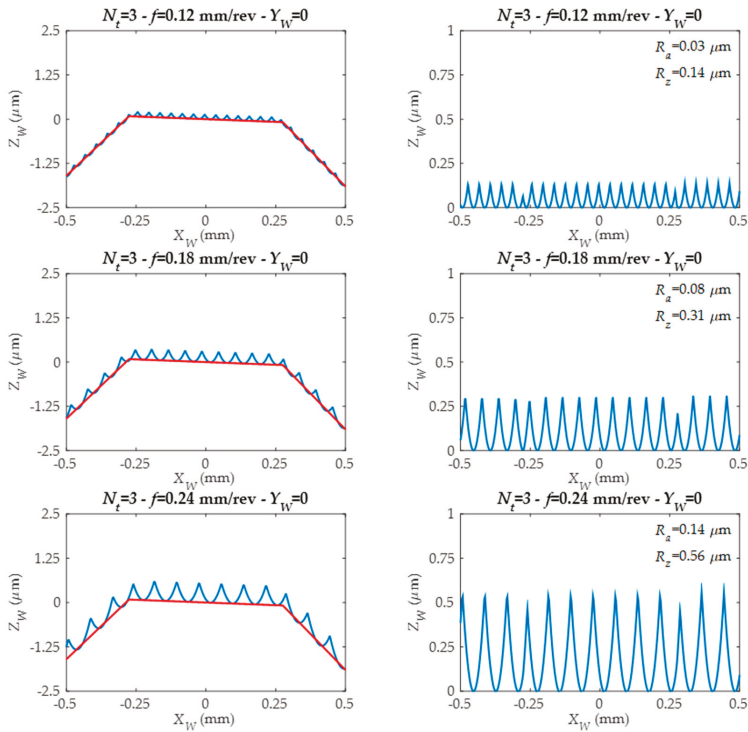


Figure 13. Predicted roughness profiles for tools with different edge numbers and working with different feed values.

4.3. Gear Roughness Predictive Model Validation

Figure 14 shows a comparison, for the same gear tooth, between the profile generated after gear measurement (after the machining process) and the profile generated by the developed roughness predictive model. The variations shown in some roughness profiles peaks correspond to the trajectory when interpolating between the different interpolation points that make up the same machining path.

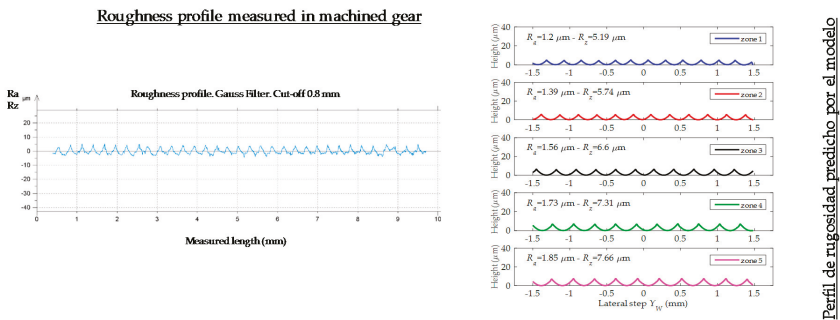


Figure 14. Roughness comparison of predictive model vs. measured roughness.

5. Discussion

The obtained roughness results, which determine gear quality, agree with cited works related to gear manufacturing in CNC machines, and, indicate improved surface quality and process versatility. Moreover, more detailed results are added in this work for optimal machining strategies and predicting roughness.

There are several aspects to mention in relation to machining strategies, cutting parameters and roughness results. On one hand, for 3 + 2 axis machining, for both zig and zig-zag strategies, the obtained R_a and R_z values are slightly different for the zig strategy. The tool works down milling and machining time is increased due to non-cutting movements. Machining time is almost doubled. For 5 continuous axis machining, obtained results show differences that need to be taken into account. For zig cutting patterns, obtained roughness values for R_a and R_z are considerably lower than the ones obtained for zig-zag cutting patterns, about 50% lower. If both, 3 + 2 axis and 5 continuous axis machining are compared, better surface roughness values were obtained for 5 continuous axis machining with zig cutting pattern. On the contrary, the worst surface roughness results are obtained for 5 continuous axis machining with zig-zag cutting pattern. In relation to programmed stepovers, when programmed stepovers are reduced and the tool works up milling, the tool tends to go back to already machined path increasing roughness values. This is called 'rail effect' and is a consequence of tool deflection, which could explain why surface roughness values are higher for those machining trajectories with zig-zag cutting patterns.

The surface roughness prediction model was also used to analyze 5 axes and 3 + 2 axes machining strategies behavior. In the 3 + 2 axes machining case, the roughness values obtained from concave and convex gear flanks were similar. Instead, in the 5 continuous axis machining case, obtained surface roughness values were higher in convex gear flanks. Thanks to the developed roughness model, this problem can be corrected by changing the tool axis attack angle in the machining surface in order to improve surface roughness. Indirectly, the model also detects the so-called 'rail effect' previously mentioned, that is, the obtained roughness values almost doubled. The presented model also determined the influence of cutting parameters such as tool feed values (mm/rev) and tool edge number. Thus, it can be concluded, that for a higher tool edge number (maintaining tool feed values), the obtained roughness results were significantly lower. Clearly there is a direct link between programmed feed values and obtained roughness results. The results showed that a small increase in the feed value has a significant effect on the final surface quality obtained. After roughness values analysis in the tool feed direction and comparing these with those generated in the direction perpendicular to it, it is clear that the roughness due to the application of the different stepovers, for the same feed value programmed, is always higher. This makes it a more restrictive parameter, which is why it is measured in each of the different machined flanks.

6. Conclusions

In recent years, technological advances have enabled gear manufacturing in general purpose machines. This is a feasible process that is less limited to gear size and geometry than traditional technologies. The machining of gears in multitasking machines is presented here as a real application for this type of technology due to its flexibility, size and the variety of geometries that can be machined in this type of machine. It can be concluded that the presented roughness predictive model fulfills its function, making it possible to predict and control the cutting strategies and parameters to obtain the required surface finish. The use of standard tools for the machining of gears requires less time for tool supply, provides a greater variety range and competitive time and costs. In addition, it is possible to exchange tools between different machines. Specific gear manufacturing machines require 'blank' material for gear manufacturing. On the contrary, general purpose machines with multitasking technology enable the entire gear machining in a single machine and take a single reference in the workpiece. This ensures tight execution times and the required quality consecution. Therefore, the presented study has demonstrated that although spiral bevel gears geometry is a complex geometry,

it is possible to machine it with 3 + 2 machining axes kinematics. The rotary axis can be positioned and fixed from the beginning for a more robust process. The obtained surface roughness values are acceptable in this case. Moreover, 3 + 2 machining is cheaper because less interpolated axes are required. Also, 3 + 2 axes programming is not as challenging as 5 axes programming. This work validates the developed surface topography model for a ball mill. There is concordance between experimentally obtained values and theoretical values obtained by the model. Moreover, the obtained values for different programmed stepovers maintain the same tendency. Topographical simulation becomes an essential tool after the programming of each of the finishing strategies because it optimizes machining results without resorting to the trial and error method. Thus, costs and time is reduced, which is desirable under current market conditions.

Author Contributions: Á.Á. and A.C. designed and performed the experiments. Additionally, M.A. developed roughness model. A.C. wrote the paper. H.G. analyzed roughness measurements. Finally, L.N.L.d.L. contributed to the resources (machine, tools, material, etc.) and supervised all of the work carried out in this research.

Funding: This research received no external funding.

Acknowledgments: Thank you to the Department of Education, and to the Universities and Research program of the Basque Government for their financial support, by means of the ZABALDUZ program. We also thank the UFI in Mechanical Engineering department of the UPV/EHU for its support of this project.

Conflicts of Interest: The authors declare no conflict of interest. The founding sponsors had no role in the design of the study; in the collection, analyses, or interpretation of data; in the writing of the manuscript; and in the decision to publish the results.

References

1. Qin, Z.; Luo, Y.; Li, K.; Peng, H. Optimal design of a novel hybrid Electric powertrain for tracked vehicles. *Energies* **2017**, *10*, 2141. [[CrossRef](#)]
2. Xu, G.; Hua, D.; Dai, W.; Zhang, X. Design and performance analysis of a coal bed gas drainage machine based on incomplete non-circular gears. *Energies* **2017**, *10*, 1933. [[CrossRef](#)]
3. Stadtfeld, H.J. *Gleason Bevel Gear Technology: The Science of Gear Engineering and Modern Manufacturing Methods for Angular Transmissions*; Gleason Works: Rochester, NY, USA, 2014; ISBN 9780615964928.
4. Watson, H.J. Gear Milling. In *Modern Gear Production*; Elsevier: New York, NY, USA, 1970; Chapter 8; pp. 146–158. ISBN 9780080158358.
5. Lechner, G. Klingelnberg spiral bevel gears. *J. Mech.* **1968**, *3*, 217–218. [[CrossRef](#)]
6. Calleja, A.; Gonzalez, H.; Polvorosa, R.; Ortega, N.; Lopez-de-Lacalle, L.N. Multitasking machines: Evolution, resources, processes and scheduling. *DYNA* **2017**, *92*, 637–642. [[CrossRef](#)]
7. Klocke, F.; Brumm, M.; Staudt, J. Quality and surface of gears manufactured by free form milling with standard tools. In Proceedings of the International Gear Conference, Lyon, France, 26–28 August 2014; pp. 26–28.
8. Shih, Y.P.; Sun, Z.H.; Wu, F.C. A disk tool cutting method for bevel gear manufacture on a five-axis machine. *Int. J. Adv. Manuf. Technol.* **2018**, *94*, 855–865. [[CrossRef](#)]
9. Suh, S.H.; Jih, W.S.; Hong, H.D.; Chung, D.H. Sculptured surface machining of spiral bevel gears with CNC milling. *Int. J. Mach. Tools Manuf.* **2001**, *41*, 833–850. [[CrossRef](#)]
10. Uzun, M. The investigation on manufacturing time of a new type concave-convex gear by a CNC milling machine. *Int. J. Adv. Manuf. Technol.* **2015**, *77*, 1275–1280. [[CrossRef](#)]
11. Dudás, I.; Bodzás, S.; Dudás, I.S.; Mándy, Z. Development of spiroid worm gear drive having arched profile in axial section and a new technology of spiroid worm manufacturing with lathe center displacement. *Int. J. Adv. Manuf. Technol.* **2015**, *79*, 1881–1892. [[CrossRef](#)]
12. Li, J.B.; Ma, H.J.; Deng, X.Z. An approach to realize the networked closed-loop manufacturing of spiral bevel gears. *Int. J. Adv. Manuf. Technol.* **2017**, *89*, 1469. [[CrossRef](#)]
13. Lin, C.; Fan, Y.; Zhang, Z. Additive manufacturing with secondary processing of curve-face gears. *Int. J. Adv. Manuf. Technol.* **2016**, *86*, 9–20. [[CrossRef](#)]
14. Li, Z.; Wang, B.; Ma, W. Comparison of ironing finishing and compressing finishing as post-forging for net-shape manufacturing. *Int. J. Adv. Manuf. Technol.* **2016**, *86*, 3333–3343. [[CrossRef](#)]

15. Hyatt, G.; Piber, M.A.; Chaphalkar, N.; Kleinhenz, O.; Mori, M. Review of New Strategies for Gear Production. *Procedia CIRP* **2014**, *14*, 72–76. [[CrossRef](#)]
16. Kawasaki, K.; Tsuji, I.; Abe, Y.; Gunbara, H. Manufacturing method of large sized spiral bevel gears in cyclo palloid system using multi axis control and multitasking machine tool. In Proceedings of the International Conference on Gears, Garching, Germany, 4–6 October 2012; Volume 1, pp. 337–348.
17. Bouquet, J.; Hensgen, L.; Klink, A.; Jacobs, T.; Klocke, F.; Lauwers, B. Fast production of gear prototypes—A comparison of technologies. *Procedia CIRP* **2014**, *14*, 77–82. [[CrossRef](#)]
18. Tang, J.; Yang, X. Research on manufacturing method of planning for spur face-gear with 4-axis CNC planer. *Int. J. Adv. Manuf. Technol.* **2016**, *82*, 847–858. [[CrossRef](#)]
19. Deng, X.; Li, G.; Wei, B.; Deng, J. Face-milling spiral bevel gear tooth surfaces by application of 5-axis CNC machine tool. *Int. J. Adv. Manuf. Technol.* **2014**, *71*, 1049–1057. [[CrossRef](#)]
20. Álvarez, A.; Calleja, A.; Ortega, N.; López de Lacalle, L.N. Five-Axis Milling of Large Spiral Bevel Gears: Toolpath Definition, Finishing, and Shape Errors. *Metals* **2018**, *8*, 353. [[CrossRef](#)]
21. Fuentes, A.A.; Ruiz-Orzaez, R.; Gonzalez-Perez, I. Numerical approach for determination of rough-cutting machine-tool settings for fixed setting face-milled spiral bevel gears. *Mech. Mach. Theory* **2017**, *112*, 22–42. [[CrossRef](#)]
22. Litvin, F.L.; Wang, A.G.; Handschu, R.F. Computerized generation and simulation of meshing and contact of spiral bevel gears. *Comput. Methods Appl. Mech. Eng.* **1998**, *158*, 35–64. [[CrossRef](#)]
23. Artoni, A.; Gabiccini, M.; Guiggiani, M. Optimization of the loaded contact pattern in hypoid gears by automatic topography modification. *ASME J. Mech. Des.* **2010**, *131*, 011008. [[CrossRef](#)]
24. Stadtfeld, H.J.; Gaiser, U. The ultimate motion graph. *ASME J. Mech. Des.* **2000**, *122*, 317–322. [[CrossRef](#)]
25. Ding, H.; Tang, J.; Zhou, Y.; Zhong, J.; Wan, G. A multi-objective design for machine setting correction correlating to high tooth contact performance in spiral bevel gears based on nonlinear interval number optimization. *Mech. Mach. Theory* **2017**, *113*, 85–108. [[CrossRef](#)]
26. Ding, H.; Tang, J.; Zhong, J.; Zhou, Y. A hybrid modification approach of machine-tool setting considering high tooth contact performance in spiral bevel and hypoid gears. *J. Manuf. Syst.* **2016**, *41*, 228–238. [[CrossRef](#)]
27. Bae, I.; Schirru, V. An Approach to Find Optimal Topological Modification to Duplicate Tooth Flank Form of the Existing Gear. In Proceedings of the International Gear Conference, Lyon, France, 26–28 August 2014; pp. 34–43.
28. Zhou, Y.; Zezhong, C.C.; Tang, J. A New Method of Designing the Tooth Surfaces of Spiral Bevel Gears With Ruled Surface for Their Accurate Five-Axis Flank Milling. *J. Manuf. Sci. Eng.* **2017**, *139*, 061004. [[CrossRef](#)]
29. Zhou, Y.; Zezhong, C.C.; Tang, J.; Liu, S. An innovative approach to NC programming for accurate five-axis flank milling of spiral bevel or hypoid gears. *Comput. Aided Des.* **2017**, *84*, 15–24. [[CrossRef](#)]
30. Calleja, A.; Bo, P.; González, H.; Bartoñ, M.; López de Lacalle, L.N. Highly accurate 5-axis flank CNC machining with conical tools. *Int. J. Adv. Manuf. Technol.* **2018**, *97*, 1605–1615. [[CrossRef](#)]
31. Litvin, F.L.; Fuentes, A. *Gear Geometry and Applied Theory*; PTR Prentice Hall: Englewood Cliffs, NJ, USA, 2004.
32. Artetxe, E.; Olvera, D.; López de Lacalle, L.N.; Campa, F.J.; Olvera, D.; Lamikiz, A. Solid subtraction model for the surface topography prediction in flank milling of thin-walled integral blade rotors (IBRs). *Int. J. Adv. Manuf. Technol.* **2016**, *90*, 741–752. [[CrossRef](#)]
33. Xing, Y.; Qin, S.; Wang, T. Study of Subdivision Surface Modelling for Spiral Bevel Gear Manufacturing. In *Proceedings of the 6th CIRP-Sponsored International Conference on Digital Enterprise Technology*; Springer: Berlin, Germany, 2010; Volume 66. [[CrossRef](#)]
34. Teixeira, J.; Guingand, M.; de Vaujany, J.P. Designing and Manufacturing Spiral Bevel Gears Using 5-Axis Computer Numerical Control (CNC) Milling Machines. *J. Mech. Des.* **2013**, *135*, 024502. [[CrossRef](#)]



Article

Cutting Parameter Selection for Efficient and Sustainable Repair of Holes Made in Hybrid Mg–Ti–Mg Component Stacks by Dry Drilling Operations

Eva María Rubio ^{1,*}, María Villeta ², José Luis Valencia ² and José Manuel Sáenz de Pipaón ¹

¹ Department of Manufacturing Engineering, Industrial Engineering School, Universidad Nacional de Educación a Distancia (UNED), St/Juan del Rosal 12, E28040 Madrid, Spain; jm@saenzdepipaon.com

² Department of Statistics and Data Science, Faculty of Statistical Studies, Complutense University of Madrid (UCM), Ave. Puerta de Hierro 1, E28040 Madrid, Spain; mvilleta@estad.ucm.es (M.V.); joseval@estad.ucm.es (J.L.V.)

* Correspondence: erubio@ind.uned.es; Tel.: +34-913-988-226

Received: 7 July 2018; Accepted: 3 August 2018; Published: 7 August 2018

Abstract: Drilling is one of the most common machining operations in the aeronautic and aerospace industries. For assembling parts, a large number of holes are usually drilled into the parts so that they can be joined later by rivets. As these holes are subjected to fatigue cycles, they have to be checked regularly for maintenance or repair, since small cracks or damage in its contour can quickly cause breakage of the part, which can have dangerous consequences. This paper focuses on finding the best combinations of cutting parameters to perform repair and maintenance operations of holes in stacked hybrid magnesium–titanium–magnesium components in an efficient, timely, and sustainable (without lubricants or coolants) manner, under dry drilling conditions. For the machining trials, experiments were designed and completed. A product of a full factorial 2^3 and a block of two factors (3×2) was used with surface roughness as the response variable measured as the mean roughness average. Analysis of variance (ANOVA) was used to examine the results. A set of optimized tool and cutting conditions is presented for performing dry drilling repair operations.

Keywords: hybrid components stack; titanium; magnesium; repair and maintenance operations; drilling; dry machining; roughness average (*Ra*); ANOVA

1. Introduction

Reduction in energy consumption is a constant demand in various industries, such as aeronautic, aerospace, and automotive, due to economic and environmental reasons. However, as energy consumption is closely linked to weight, one method to reduce energy consumption is to use lighter components composed of light alloys, such as titanium (Ti), aluminium (Al), and/or magnesium (Mg), all of which have an excellent weight/mechanical properties ratio.

The parts used in the aforementioned industries have to be rigid, strong, and light. In addition, they have to meet high precision and quality standards. As such, the production of these light alloys has been extensively studied [1–33]. Their repair and maintenance has also been thoroughly studied. Given their uniqueness and high cost, replacement parts are often not available when they have to be maintained or repaired [34–49].

The development of new alloys or polymers that increase the number of applications may be expensive but not always achievable. Sometimes, even when a material exists, it struggles to simultaneously satisfy all the necessary properties for concrete application using the material alone. Then, the combination of two or more materials is an alternative for producing hybrid components

whose properties satisfy the requirements in areas not covered by the individual components separately [50–58]. Different combinations of materials and technologies have been studied in order to improve their properties [50–70], so the use of hybrid structures is becoming more common.

The complexity of aeronautic and aerospace parts means that most have to be mechanized until achieving their final geometry. Then, using hybrid components, machining together several materials simultaneously is necessary. Drilling is one of the most usual machining operations in these industrial sectors, since it is used to create a large number of holes for assembling the parts. As these holes are subjected to fatigue cycles, every so often they must be checked for their maintenance since small cracks or damage in its contour can quickly degenerate into the breakage of the piece. Given the nature of these environments, breakages can have serious consequences. Due to the cost and complexity of these types of pieces, replacement parts are not maintained in stock to be used for repair or maintenance [3,36,49].

Performing machining operations in complex geometries of hybrid components or stacks is a significant challenge in terms of accuracy and quality, especially when the combined materials are magnesium and titanium. Magnesium is the lighter metal and has good mechanical properties that make magnesium alloys attractive for applications in industries where weight is crucial. Titanium is in demand due to its physical, chemical, and thermal properties. However, both materials present some problems. Magnesium is easily ignited by the heat generated during the machining process. The low thermal conductivity of titanium increases risk of tool wear, its low modulus means that parts move away from the cutting tool during machining, and its high chemical reactivity and low hardness tend to produce cracks in the cutting tools [71–73].

For solving these problems, different compatible and environmentally sustainable lubricants and coolants have been developed [26,38–40,45,74]. However, more research is needed because machining hybrid components causes an increase in the instability of the process due to the different cutting characteristics of the different materials. Many investigations have been reported for the simultaneous machining of materials in the search for optimal combinations of cutting conditions, tools, and cooling systems [56,57,75–89].

This paper focuses on drilling processes, and especially on finding the best combinations of cutting conditions and type of tools to perform hole repair and maintenance operations with dry machining on hybrid stacks of Mg–Ti–Mg in the shortest time and most sustainable method possible.

The magnesium–titanium–magnesium stack (Figure 1) was predrilled to simulate repair operations in hybrid components that are assembled with rivets. The two parts of magnesium were considered the base of the stack and the titanium was considered the insert.

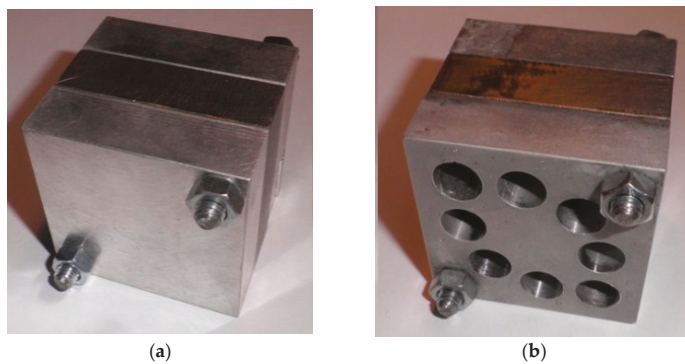


Figure 1. Hybrid magnesium–titanium–magnesium stack for (a) drilling and (b) hole repair trials [56,57].

When a rivet hole is damaged, it has to be drilled to a larger diameter and an oversized rivet has to be assembled. This repair process is widely used in aeronautics and has to be performed with care as cracks in the structure can produce catastrophic consequences.

In this work, the surface roughness on the inside the holes was obtained by drilling the hybrid stacks. The stacks were composed of a magnesium alloy and titanium alloy to determine if it is possible to efficiently and sustainably repair or maintain aeronautic and aerospace industry parts with very strict surface finish requirements. To achieve this goal, a design of experiments (DOE) was defined for the drilling trials and the surface roughness measurements. The design selected was the product of a full factorial 2^3 and a block of two factors (3×2), whose possible influential cutting parameter factors were feed rate, f , cutting speed, V , and tool coating type, T . The location factors in terms of measuring the surface roughness included location on the specimen, LRS , and location on the insert, LRI . The obtained results were analyzed via analysis of variance (ANOVA), which helped establish a ranking of the parameter combinations based on the surface roughness achieved in the machining trials and helped determine the optimum combination of factors for performing these types of operations.

2. Materials and Methods

We followed the guidelines provided by Montgomery [87]. First, in the planning stage, factors, levels, ranges, and response variables were determined (Table 1). Then, the design of experiments (DOE) was performed. The design was elected according to the fixed resources and objectives. In this case, the goal was to analyze the variability in the surface roughness inside the holes obtained by drilling of hybrid stacks composed of UNS M11917 magnesium alloy and UNS R56400 titanium alloy (Table 2). The design selected was the product of a full factorial 2^3 and a block of two factors (3×2 ; $LRI \times LRS$) with a total of 48 experimental runs, as can be observed in Table 2. In this table, each line represents two experimental runs, one for each level of the LRI factor.

Next, the machining trials were completed. To execute the drilling trials, it was first necessary to establish the protocols both for the cutting conditions to be used and for registering the obtained data. Then, it was necessary to prepare the workpieces with the specimens of the hybrid stacks, the tools, and the machine tool, introducing the cutting conditions selected. Next, the machining operations were performed, and finally, we photographed and recorded videos of all the trials for further analysis once the process was finished.

Then, we measured the response variable. Surface roughness was selected as the response variable, measured as the roughness average (Ra) [88]. Once the data were obtained, we performed a statistical analysis. The variability of the average roughness values, Ra , was modelled using ANOVA, identifying both the influential factors and interactions among them on surface roughness. In addition, an exploratory data analysis was performed to obtain a clear graphical view of the key aspects in terms of the distribution of the influential factors on the surface finish of hybrid magnesium–titanium–magnesium stacks. The relationships between pairs of influential factors were illustrated and analyzed. After the statistical analysis of the results, some conclusions were established.

Table 1. Factors and levels.

Factor	Level
Feed rate, f (mm/min)	$f1, f2$
Cutting speed, V (m/min)	$V1, V2$
Tool coating type, T	$T1, T2$
Location with respect to the specimen, LRS	$LRS1, LRS2$
Location with respect to the insert, LRI	$LRI1, LRI2, LRI3$

Table 2. Experimental design: product of a full factorial 2³ and a block of two factors 3 × 2.

<i>T</i>	<i>V</i> (m/min)	<i>f</i> (mm/min)	<i>LRI</i>	<i>LRS</i>	
<i>T1</i>	<i>V1</i>	<i>f2</i>	<i>LRI2</i>	<i>LRS1</i>	<i>LRS2</i>
<i>T1</i>	<i>V1</i>	<i>f2</i>	<i>LRI1</i>	<i>LRS1</i>	<i>LRS2</i>
<i>T1</i>	<i>V1</i>	<i>f2</i>	<i>LRI3</i>	<i>LRS1</i>	<i>LRS2</i>
<i>T1</i>	<i>V1</i>	<i>f1</i>	<i>LRI3</i>	<i>LRS1</i>	<i>LRS2</i>
<i>T1</i>	<i>V1</i>	<i>f1</i>	<i>LRI2</i>	<i>LRS1</i>	<i>LRS2</i>
<i>T1</i>	<i>V1</i>	<i>f1</i>	<i>LRI1</i>	<i>LRS1</i>	<i>LRS2</i>
<i>T1</i>	<i>V2</i>	<i>f1</i>	<i>LRI2</i>	<i>LRS1</i>	<i>LRS2</i>
<i>T1</i>	<i>V2</i>	<i>f1</i>	<i>LRI1</i>	<i>LRS1</i>	<i>LRS2</i>
<i>T1</i>	<i>V2</i>	<i>f1</i>	<i>LRI3</i>	<i>LRS1</i>	<i>LRS2</i>
<i>T2</i>	<i>V1</i>	<i>f1</i>	<i>LRI3</i>	<i>LRS1</i>	<i>LRS2</i>
<i>T2</i>	<i>V1</i>	<i>f1</i>	<i>LRI2</i>	<i>LRS1</i>	<i>LRS2</i>
<i>T2</i>	<i>V1</i>	<i>f1</i>	<i>LRI1</i>	<i>LRS1</i>	<i>LRS2</i>
<i>T2</i>	<i>V2</i>	<i>f2</i>	<i>LRI3</i>	<i>LRS1</i>	<i>LRS2</i>
<i>T2</i>	<i>V2</i>	<i>f2</i>	<i>LRI2</i>	<i>LRS1</i>	<i>LRS2</i>
<i>T2</i>	<i>V2</i>	<i>f2</i>	<i>LRI1</i>	<i>LRS1</i>	<i>LRS2</i>
<i>T1</i>	<i>V2</i>	<i>f2</i>	<i>LRI3</i>	<i>LRS1</i>	<i>LRS2</i>
<i>T1</i>	<i>V2</i>	<i>f2</i>	<i>LRI1</i>	<i>LRS1</i>	<i>LRS2</i>
<i>T1</i>	<i>V2</i>	<i>f2</i>	<i>LRI2</i>	<i>LRS1</i>	<i>LRS2</i>
<i>T2</i>	<i>V1</i>	<i>f2</i>	<i>LRI1</i>	<i>LRS1</i>	<i>LRS2</i>
<i>T2</i>	<i>V1</i>	<i>f2</i>	<i>LRI2</i>	<i>LRS1</i>	<i>LRS2</i>
<i>T2</i>	<i>V1</i>	<i>f2</i>	<i>LRI3</i>	<i>LRS1</i>	<i>LRS2</i>
<i>T2</i>	<i>V2</i>	<i>f1</i>	<i>LRI1</i>	<i>LRS1</i>	<i>LRS2</i>
<i>T2</i>	<i>V2</i>	<i>f1</i>	<i>LRI2</i>	<i>LRS1</i>	<i>LRS2</i>
<i>T2</i>	<i>V2</i>	<i>f1</i>	<i>LRI3</i>	<i>LRS1</i>	<i>LRS2</i>

3. Trials

This work focused on the manufacturing process of drilling and on repair operations of holes used to join parts of different materials by means of rivets. Materials, cutting tools, cutting conditions, and measurement locations were established as influential factors on the variability in surface roughness.

3.1. Specimens: Materials and Geometries

The materials used in the manufacture of the workpieces for hole repair drilling operations included magnesium alloy UNS M11917 and titanium alloy UNS R56400, whose compositions are outlined in Table 3. In the absence of standards, national or international, in relation to the design and manufacture of test pieces, we decided to use 50 × 50 × 15 mm parallelepipeds (Figure 2) [57]. The hybrid component stacks were composed of a total of three pieces or parallelepipeds called specimens: two of magnesium alloy and one of titanium alloy. The two UNS M11917 magnesium alloy specimens were called the base and the UNS R56400 titanium alloy specimen, located between the two magnesium pieces, was called the insert; this is similar to previous works involving other processes and other materials analyzed. The specimens were positioned one above the other to differentiate the measurements when collecting data. The three parallelepipeds or specimens were mechanically fixed together so that it was possible to disassemble and measure the surface roughness inside the machined holes with relative ease. In order to simulate repair and maintenance operations, a test piece was predrilled with a number of holes in accordance with the requirements for the planned experiments.

Table 3. Chemical compositions of materials used for manufacturing specimens.

UNS M11917 (AZ91D)	UNS R56400 (Ti-6Al-4V)
Al 8.30–9.70%	Al 5.5–6.75%
Cu ≤ 0.03%	C ≤ 0.08%
Fe ≤ 0.005%	H ≤ 0.015%
Mg 90%	Fe ≤ 0.4%
Mn ≥ 0.13%	N ≤ 0.03%
Ni ≤ 0.002%	O ≤ 0.2%
Si ≤ 0.1%	Ti 87.725–91%
Zn 0.35–1%	Zn 3.5–4.5%

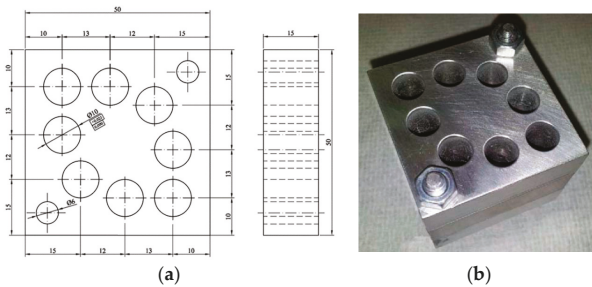


Figure 2. (a) Design of the geometry of each of the three parts of the workpiece; (b) Predrilled workpiece used during the trials to simulate hole repair operations on hybrid stacks [56,57].

3.2. Tools

Two types of tools were selected for drilling operations with the same geometry (Figure 3a) but with different coatings (Figure 3b) (GARANT, Hoffmann Iberia Quality Tools S.L., San Fernando de Henares, Madrid, Spain). We selected tools made of High-Speed Steel (HSS CO): two-flute twist drills with 130° point angle and in two different qualities, A11240 and A11253. A11240 is recommended for titanium, steel, and stainless steel, whereas A11253 is coated with titanium nitride (TiN) and recommended for steel, stainless steel, titanium, aluminium alloys, and copper alloys. This selection allows us to use the tools in the largest number of trials involving different material combinations, considering that this work is inside a wider project that involves different machining processes (turning, milling, drilling), materials (steel, aluminium, titanium, and magnesium), tools, and workpieces of several types, shapes, and sizes.

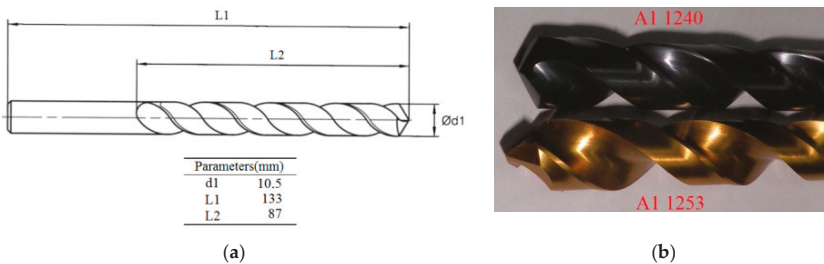


Figure 3. (a) Drill tool geometry and dimensions; (b) Materials and uses of the tools: A11240 is composed of High-Speed Steel and recommended for titanium, steel, and stainless steel and A11253 is composed of High-Speed Steel coated with titanium nitride and recommended for steel, stainless steel, titanium, aluminium alloys, and copper alloys [64].

3.3. Cutting Parameters

The trials were carried out in a Tongtai TMV510 machining center (Tongtai Machine & Tool Co., Luzhu Dist, Kaohsiung City, Taiwan) equipped with a Fanuc Control Numeric Computer (CNC) (FANUC Iberia, Castelldefels, Barcelona, Spain) (Figure 4) under dry conditions. The values usually used during repair and maintenance operations were selected for the factor levels of feed rate, f : 50 mm/min and 100 mm/min; cutting speed, V : 20 m/min and 25 m/min; and depth of cut, d : 0.25 mm.



Figure 4. Tongtai TMV510 machining center equipped with a Fanuc Control Numeric Computer (CNC).

3.4. Measurement Locations

The measurements of the surface roughness were recorded using a Mitutoyo Surftest SJ 401 roughness tester (Mitutoyo America Corporation, Aurora, IL, USA) (Figure 5a). From Table 1, the measurement locations along with the specimen and the insert were used as influential factors (Figure 5b). These factors are *LRS* for the specimen and *LRI* for the insert. For the *LRS*, two values were chosen: *LRS1*, the roughness at the beginning of the hole, and *LRS2*, the roughness at the end of the hole along the feeding direction. Specifically, *LRS1* was recorded within the first 7 mm of the hole and *LRS2* was recorded within the last 7 mm of the hole (Figure 5c). For the *LRI*, three levels were established according to the drilling direction: *LRI1*, the roughness before the insert (first specimen), which is the roughness inside the holes of the first magnesium piece; *LRI2*, the roughness on the insert (second specimen), which is the roughness inside the holes of the titanium piece; and *LRI3*, the roughness after the insert, which is the roughness inside the holes of the second magnesium piece (third specimen).

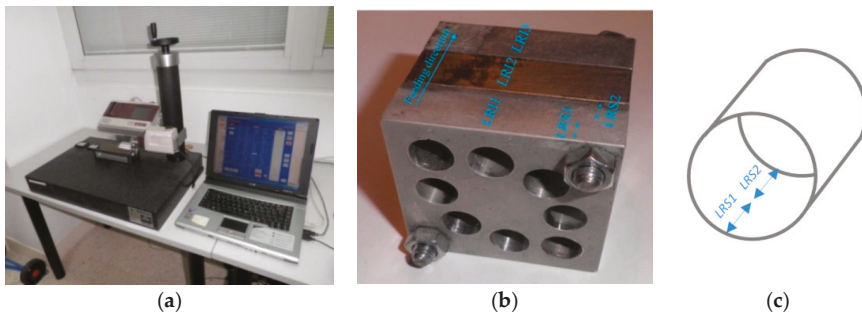


Figure 5. (a) Mitutoyo Surftest SJ 401 roughness tester; (b) location of the measurements of LRS and LRI along the feeding direction, inside each hole; and (c) detail of the specific measurement locations in the holes of each specimen.

3.5. Factors and Levels Selected

The values selected for the levels of factors analyzed in this study are shown in Table 4. The depth of cut, d , was recorded at 25 mm and was equal in all tests. This value was selected to simulate repair and maintenance operations in which it is necessary to adhere to the tolerance dimensions established during the design of the parts.

Table 4. Factor and level values.

Factor	Level Value
Feed rate, f , (mm/min)	50/100
Cutting speed, V , (m/min)	20/25
Type of tool, T	A1 1253/A1 1240
Location with respect to the specimen, LRS	Beginning of the specimen, end of the specimen
Location with respect to the insert, LRI	Before the insert, on the insert, after the insert

4. Results, Analysis, and Discussion

4.1. Results

The surface roughness in terms of the roughness average, Ra , was measured after performing all the drilling trials inside all the holes and in the different locations established in Table 4, following the direction and locations shown in Figure 5b,c for each hole. The results obtained for the 48 Ra experimental values are outlined in the last two columns of Table 5.

We firstly assessed the initial obtained results to determine any trend and to compare the findings with those obtained in previous works in which the materials were studied separately or along with other materials. The Ra mean values in the three measured zones are provided in Table 6.

The values obtained in this work aligned with those in other previous works about titanium using a similar feed rate, cutting speed, or point angle [81,89–91], as well as with those obtained when drilling magnesium matrix composites [83]. For optimizing magnesium alloys during drilling operations, other point angles are suitable; however, similar surface roughness values were obtained in this work [92].

Table 5. Roughness average Ra (μm) obtained during the experiments.

T	V (m/mnin)	f (mm/min)	LRI	Ra (μm)	
				$LRS1$	$LRS2$
A11253	20	100	$LRI2$	1.28	3.09
A11253	20	100	$LRI1$	0.36	1.73
A11253	20	100	$LRI3$	1.52	2.28
A11253	20	50	$LRI3$	1.91	6.28
A11253	20	50	$LRI2$	0.74	1.46
A11253	20	50	$LRI1$	1.23	0.31
A11253	25	50	$LRI2$	0.86	0.89
A11253	25	50	$LRI1$	0.10	0.87
A11253	25	50	$LRI3$	0.78	1.09
A11240	20	50	$LRI3$	0.64	1.94
A11240	20	50	$LRI2$	0.86	1.13
A11240	20	50	$LRI1$	1.73	1.54
A11240	25	100	$LRI3$	0.83	1.43
A11240	25	100	$LRI2$	0.80	0.85
A11240	25	100	$LRI1$	1.59	0.77
A11253	25	100	$LRI3$	1.81	1.79
A11253	25	100	$LRI1$	1.73	0.37
A11253	25	100	$LRI2$	1.60	1.03
A11240	20	100	$LRI1$	0.68	0.45
A11240	20	100	$LRI2$	1.11	0.87
A11240	20	100	$LRI3$	0.61	1.28
A11240	25	50	$LRI1$	2.62	1.65
A11240	25	50	$LRI2$	1.19	1.34
A11240	25	50	$LRI3$	1.63	1.78

Table 6. Ra (μm) mean values in the three measured zones versus the feed rate, f , and the cutting speed, V .

Ra (μm)	f (mm/min)		V (m/min)	
	50	100	20	25
Ra_{LRI1}	1.26	0.96	1.00	1.21
Ra_{LRI2}	1.06	1.33	1.32	1.08
Ra_{LRI3}	2.01	1.44	2.06	1.39

4.2. Analysis and Discussion

In order to statistically analyze the experimental Ra data collected (Table 5), a fixed effects ANOVA was performed to examine the interactions up to second order and excluding an effect each time. The selection criteria of the significant effects in the ANOVA after each iteration were as follows [93]: in each new ANOVA, the effect with a higher p -value (which was therefore less statistically significant) was excluded; the backward algorithm finishes when all the effects that remain in the ANOVA have a p -value lower than 0.05.

The final outcome of this iterative ANOVA algorithm over the experimental Ra data did not lead to any conclusive result. For that reason, a logarithmic transformation of the experimental Ra data was performed. Such a transformation allows maintaining the order of the original Ra data while smoothing the impact of the outliers. The outcome of the first iteration of the ANOVA over the transformed Ra data—over the Ra Naperian logarithm $\ln Ra$ —is provided in Table 7. A second iteration for the ANOVA was then completed for the effects contained in the table, excluding the LRI^*V effect which had a maximum p -value of 0.828.

Table 7. Outcome of the first iteration for the ANOVA over *Ra* Napierian logarithm.

Effect	DF	Sum of Squares	Mean Square	F-Value	Pr > F
<i>LRI</i>	2	2.426	1.213	3.77	0.036
<i>T</i>	1	0.007	0.007	0.02	0.823
<i>T*LRI</i>	2	3.041	1.521	4.73	0.017
<i>f</i>	1	0.021	0.021	0.06	0.802
<i>LRI*f</i>	2	0.225	0.112	0.35	0.708
<i>T*f</i>	1	2.206	2.206	6.86	0.014
<i>LRS</i>	1	0.492	0.492	1.53	0.227
<i>LRI*LRS</i>	2	0.886	0.443	1.38	0.270
<i>T*LRS</i>	1	0.177	0.177	0.55	0.465
<i>f*LRS</i>	1	0.214	0.214	0.67	0.422
<i>V</i>	1	0.092	0.092	0.29	0.597
<i>LRI*V</i>	2	0.122	0.061	0.19	0.828
<i>T*V</i>	1	1.565	1.565	4.86	0.036
<i>f*V</i>	1	0.211	0.211	0.65	0.425
<i>V*LRS</i>	1	0.429	0.429	1.33	0.259
Error	27	8.686	0.322		
Total	47	20.800			

DF: Degrees of Freedom.

The final result of the backward algorithm for the last iteration is displayed in Table 8. In this table, all the *p*-values are lower than 0.05, so the three effects in the first column of this table can be considered statistically significant. Therefore, as a consequence of the ANOVA, we concluded that the interaction between type of tool and the location with respect to the insert *T*LRI*, the location with respect to the insert *LRI*, and the interaction between type of tool and feed rate *T*f* are the three effects among the 15 analyzed with a significant statistical influence on the surface finish of the machining on the dry drilling stack, composed of magnesium alloy UNS M11917 and titanium alloy UNS R56400. For example, the *LRS* effect, which measures the roughness differences between the beginning and end of the specimen along the feeding direction, did not have a statistically significant influence on the surface finish because this effect was not included in the outcome of the last iteration for the ANOVA summarized in Table 8.

Table 8. Outcome of the last iteration for the ANOVA over *Ra* Napierian logarithm.

Effect	DF	Sum of Squares	Mean Square	F-Value	Pr > F
<i>T*f</i>	1	2.206	2.206	7.06	0.011
<i>LRI</i>	2	2.426	1.213	3.88	0.028
<i>T*LRI</i>	2	3.041	1.521	4.87	0.013
Error	42	13.127	0.313		
Total	47	20.800			

DF: Degrees of Freedom.

Considering the variability in the surface roughness of the magnesium–titanium–magnesium drilling stacks explained by the statistically significant effects obtained from the ANOVA, the percentage of variability attributed to each effect is shown in the pictogram in Figure 6. The contribution of each effect was obtained as the ratio of the sum of squares of the effect to the sum of squares due to the model. For example, the percentage of variability attributed to the *T*f* effect is the ratio of 2.206 to 7.673 (%). That is, 39.63% of the variability is due to the *T*LRI* effect, 31.63% of the variability is due to the *LRI* effect, and the remaining 28.73% of the variability is due to the *T*f* effect.

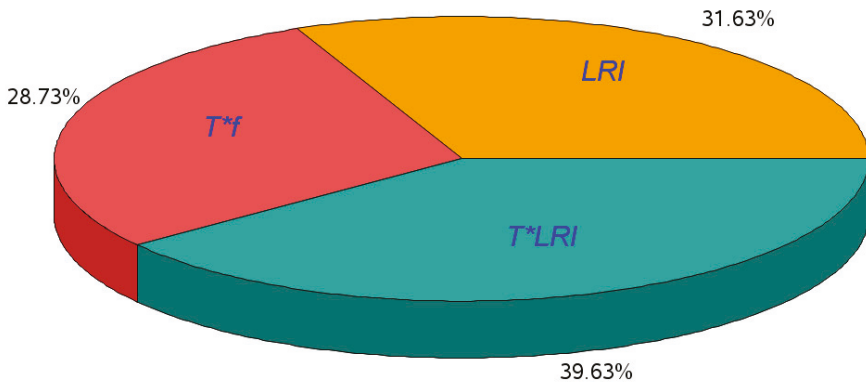


Figure 6. Distribution of the percentage of variability attributed to each effect over the variability explained by the ANOVA model.

The distribution of the Naperian logarithm of the surface roughness of the drilling process ($\ln Ra$) with respect to the three levels of the measurement location on the insert (LRI) is depicted in Figure 7. As shown in the figure, small differences existed between $\ln Ra$ before and after the insert. The dispersion is observably greater for small values before the insert.

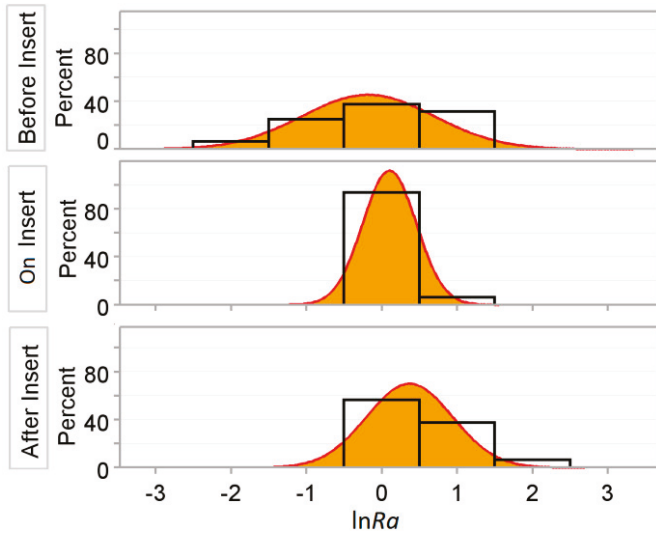


Figure 7. Distribution of the Naperian logarithm of the surface roughness ($\ln Ra$) for each of the three levels of measurement location on the insert (LRI).

On the other hand, when assessing statistically significant interactions, considering the behavior of the interaction between type of tool and the location with respect to the insert T^*LRI , the A1 1253 tool produced better results in terms of roughness before the insert and worse after the insert. This did not occur with the A1 1240 tool, which had a few differences. This behavior is illustrated in Figure 8.

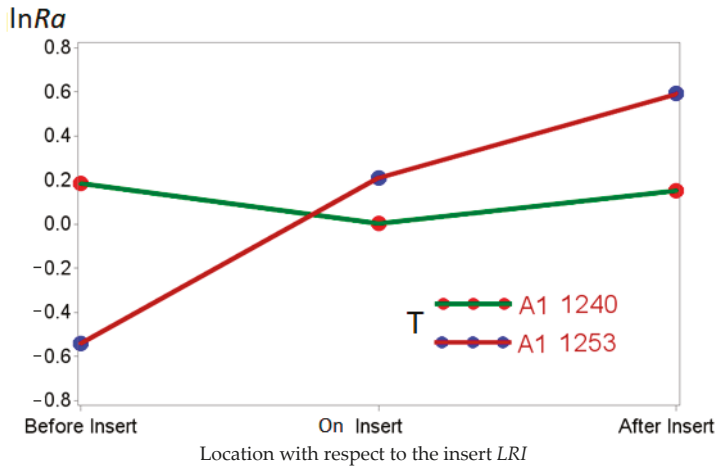


Figure 8. lnRa interaction between type of tool and the location with respect to the insert T^*LRI .

With respect to the interaction between type of tool and feed rate T^*f (Figure 9), an increase in the advance of f generated a reduction in the roughness for the A1 1240 tool, whereas for the A1 1253 tool, the opposite occurred. The figure clearly demonstrates the T^*f interaction.

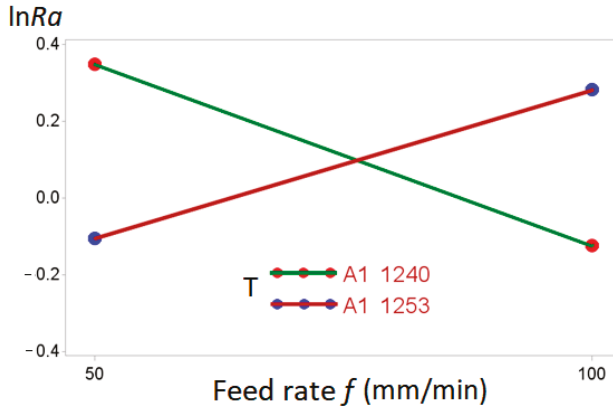


Figure 9. lnRa interaction between type of tool and feed rate T^*f .

The variability in the logarithm of the surface roughness lnRa of dry drilling magnesium–titanium–magnesium stacks was modelled from the ANOVA using Equation (1). In this equation, μ is a constant term to adjust the mean; α_i , $\beta\alpha_{ji}$, and $\beta\gamma_{jk}$ represent the effects of the levels of the location with respect to the insert, the interaction of the type of tool with the measurement location with respect to the insert, and the interaction of the type of tool with the feed rate, respectively; and ε_{ijk} is the error term.

$$\ln Ra_{ijk} = \mu + \alpha_i + \beta\alpha_{ji} + \beta\gamma_{jk} + \varepsilon_{ijk} \tag{1}$$

The estimations of the parameters of the model in Equation (1) are listed in the third column of Table 9. The table also includes an indicator of the parameter estimation errors (the standard deviation)

in the fourth column. The fifth column collects the *t*-statistic values, and the sixth column provides the statistical significances of the parameter estimations.

Table 9. Parameter estimations of the model in Equation (1).

Parameter	Designation	Estimation	Standard Error	<i>t</i> -Value	Pr > <i>t</i>
Intercept	μ	0.7862	0.2336	3.37	0.0017
A1 1253*50 (mm/min)	$\beta\gamma_{11}$	-0.3873	0.2336	-1.66	0.1052
A1 1253*100 (mm/min)	$\beta\gamma_{12}$	0	.	.	.
A1 1240*50 (mm/min)	$\beta\gamma_{21}$	-0.4004	0.3304	-1.21	0.2326
A1 1240*100 (mm/min)	$\beta\gamma_{22}$	-0.8706	0.3304	-2.64	0.0119
Before the insert	α_1	-1.1333	0.2861	-3.96	0.0003
On the insert	α_2	-0.3820	0.2861	-1.34	0.1894
After the insert	α_3	0	.	.	.
A1 1253*Before the insert	$\beta\alpha_{11}$	0	.	.	.
A1 1253*On the insert	$\beta\alpha_{12}$	0	.	.	.
A1 1253*After the insert	$\beta\alpha_{13}$	0	.	.	.
A1 1240*Before the insert	$\beta\alpha_{21}$	1.1654	0.4046	2.88	0.0064
A1 1240*On the insert	$\beta\alpha_{22}$	0.2335	0.4046	0.58	0.5671
A1 1240*After the insert	$\beta\alpha_{23}$	0	.	.	.

The parameter estimations included in Table 9 allowed us to obtain the residuals of the model in Equation (2), which provides the differences between the observed values and the estimated values of $\ln Ra$. Analyzing these residuals, the model hypotheses were checked. Figure 10 shows that the residuals follow a normal law, so the hypothesis is supported. This hypothesis can be contrasted by different tests, such as normality on residuals, as shown in Table 10.

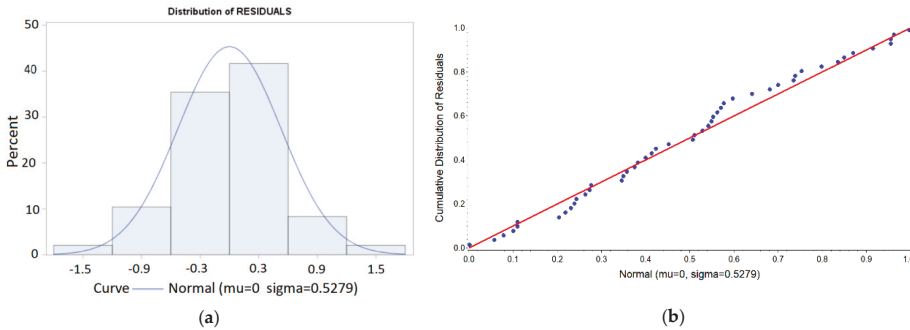


Figure 10. Checking the hypothesis of normality for the residuals: (a) histogram of residuals and (b) Probability–Probability plot for residuals.

Table 10. Tests for normality on residuals.

Test for Normality	Statistic	<i>p</i> -Value
Shapiro–Wilk	W 0.977919	Pr < W 0.4952
Kolmogorov–Smirnov	D 0.0900	Pr > D >0.150

Figure 11a shows that the residuals satisfy the homoscedasticity hypothesis and Figure 11b shows that the existence of nonrandomized patterns in the residuals was not observed.

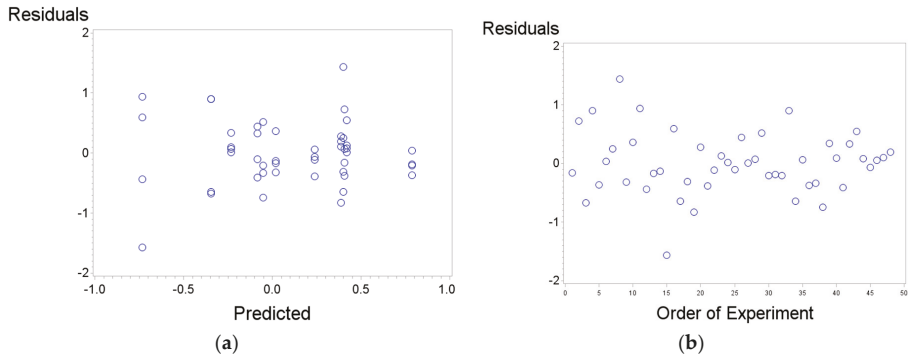


Figure 11. (a) Checking the homoscedasticity hypothesis for residuals; (b) Checking the nonexistence of special patterns on residuals.

Once the hypotheses of the model in Equation (1) were checked, we confirmed that the variability in the surface roughness *Ra* of dry drilling stacks composed of magnesium alloy UNS M11917 and titanium alloy UNS R56400 could be statistically modelled by Equation (2).

$$Ra_{ijk} = \exp (\mu + \alpha_i + \beta\alpha_{ji} + \beta\gamma_{jk} + \varepsilon_{ijk}) \tag{2}$$

From modelling the surface roughness *Ra* described in Equation (2), and considering the parameter estimations in Table 9, the predicted values for surface roughness of the drilling machining were computed for the various combinations of the levels of the statistically significant effects in the surface finish of the dry drilling stacks. The values of the predicted roughness of these combinations are listed in increasing order in Table 11. The second predicted roughness, denoted with an asterisk (*) and included in the last column of the table, contains the predicted *Ra* values using only the parameters with a statistical significance at the $p < 0.05$ level. Considering this second roughness prediction (*), the combinations of the levels of statistically significant effects were classified into four roughness classes, as shown in the last column of Table 11.

Table 11. Predicted roughness of the level combinations of significant effects on dry drilling.

<i>LRI</i>	<i>T</i>	<i>f</i> (mm/min)	ln <i>Ra</i> Predicted $\alpha_i + \beta\alpha_{ji} + \beta\gamma_{jk}$	<i>Ra</i> Predicted (μm) $\exp (\alpha_i + \beta\alpha_{ji} + \beta\gamma_{jk})$	<i>Ra</i> Predicted* (μm) $\exp (\alpha_i^* + \beta\alpha_{ji}^* + \beta\gamma_{jk}^*)$
Before insert	A1 1253	50	−0.734	0.48	
Before insert	A1 1253	100	−0.347	0.71	0.71 (Class I)
On insert	A1 1240	100	−0.233	0.79	
After insert	A1 1240	100	−0.084	0.92	0.92 (Class II)
Before insert	A1 1240	100	−0.052	0.95	0.95 (Class III)
On insert	A1 1253	50	0.017	1.02	
On insert	A1 1240	50	0.237	1.27	
After insert	A1 1240	50	0.386	1.47	
After insert	A1 1253	50	0.399	1.49	
On insert	A1 1253	100	0.404	1.50	2.20 (Class IV)
Before insert	A1 1240	50	0.418	1.52	
After insert	A1 1253	100	0.786	2.20	

Focusing on this classification, the best combinations of the levels of parameters that achieved a lower predicted roughness value (a better surface finish) during the dry drilling process on a stack composed of magnesium alloy UNS M11917 and titanium alloy UNS R56400 included the A1 1240 cutting tool with a feed rate of 100 mm/min. Appropriate levels of surface finish should be

achieved by these drilling conditions: a predicted roughness of 0.92 μm on the insert and after the insert (in the second class), and a predicted roughness of 0.95 μm before the insert (in the third class). A mean roughness Ra under 1 μm could be achieved in all the stack superficial areas.

These types of light alloys are usually employed in the aeronautical industry and in this industrial sector, the values for the surface roughness specifications of Ra usually lie between 0.8 μm and 1.6 μm [91]. As such, roughness values Ra under 1 μm clearly satisfy the surface finish requirements. Notably, the quality improvement in the surface finish was achieved with higher feed rates, which promoted a decrease in machining time and, consequently, a decrease in costs, enabling the efficient optimization of the surface quality.

4.3. Technological Point of View

To apply the results obtained in this study, analyzing them from a technological point of view was necessary. Thus, as most components in the aeronautical and aerospace sectors are complex and have strict dimensional and surface quality requirements (within the range of $0.8 \mu < Ra < 1.6 \mu\text{m}$ [94]), their manufacturing is usually expensive and pieces are not stocked for repair or maintenance purposes. Therefore, parts have to be repaired or maintained as soon as possible to restore the plane or the aircraft to its functional conditions.

In this study, the best results were obtained for the following combinations of cutting parameters: $f = 100 \text{ mm/min}$, $V = 25$, and $T = A1 \ 1240 \text{ m/min}$; and $f = 50 \text{ mm/min}$, $V = 25$, and $T = A1 \ 1253 \text{ m/min}$. The surface roughness achieved in the holes of the different materials and locations in the stack were all within the range usually required in the aeronautical industry [94]. Between the two combinations, the first was better due to the feed rate value being higher so the repair operation can be finished in a shorter time, thereby reducing costs associated with the operation. Additionally, these real results are in accordance with the results of the ranking of the cutting condition combinations based on the estimated values of Ra .

Performing all tests under dry conditions is important not only from an economic point of view but an environmental viewpoint as well. Not using any additional lubricant or coolant provides cost savings and allows for more sustainable repair and maintenance operations.

5. Conclusions

In this paper, we examined a drilling process on a stack formed by two UNS M11917 magnesium alloy bases and one UNS R56400 titanium alloy insert in an experimental study. The interaction between the type of tool and the measurement location on the insert influences the inner surface of the holes. The best type of tool for the drilling repair operations was determined to be the A1 1240, which was especially efficient for higher values of feed rate (100 mm/min) and cutting speed (25 m/min). The surface roughness obtained in the inner of the holes was independent of material and location considered, and the values fell within the usual acceptable range in the aeronautical sector. The surface roughness increased as the tool advanced through the stack, especially after the insert. However, the differences observed along each component in the stack, at both the beginning and the end of the component, were not statistically significant. The repair operations performed with drilling can be sustainably completed, as was proven in this study, which was completed under dry conditions.

Author Contributions: Conceptualization, E.M.R., M.V., J.L.V. and J.M.S.d.P.; Data curation, E.M.R. and J.M.S.d.P.; Formal analysis, E.M.R., M.V., J.L.V. and J.M.S.d.P.; Funding acquisition, E.M.R., M.V. and J.L.V.; Investigation, E.M.R., M.V., J.L.V. and J.M.S.d.P.; Methodology, E.M.R., M.V. and J.L.V.; Project administration, E.M.R.; Resources, E.M.R.; Software, M.V. and J.L.V.; Supervision, E.M.R., M.V. and J.L.V.; Validation, E.M.R., M.V., J.L.V. and J.M.S.d.P.; Visualization, E.M.R., M.V., J.L.V. and J.M.S.d.P.; Writing—original draft, E.M.R., M.V., J.L.V. and J.M.S.d.P.; Writing—review & editing, E.M.R., M.V., J.L.V. and J.M.S.d.P.

Funding: This work has been funded, in part, by five grants from Ministerio de Ciencia e Innovación, Ministerio de Economía y Competitividad, Agencia Estatal de Investigación (AEI), Fondo Europeo de Desarrollo Regional (FEDER), and Industrial Engineering School-UNED (DPI2014-58007-R, CGL2014-58322-R MTM2016-78227-C2-1-P, MTM2017-90584-REDT and REF2018-ICF05), Spain.

Acknowledgments: The authors thank the Research Group of the UNED “Industrial Production and Manufacturing Engineering (IPME)” for the support given during the development of this work and they also thank the Antolín Group for the material provided.

Conflicts of Interest: The authors declare no conflict of interest.

References

1. Pervaiz, S.; Deiab, I.; Darras, B. Power consumption and tool wear assessment when machining titanium alloys. *Int. J. Precis. Eng. Manuf.* **2013**, *14*, 925–936. [[CrossRef](#)]
2. Calamaz, M.; Dominique, C.; Franck, G. A new material model for 2D numerical simulation of serrated chip formation when machining titanium alloy Ti-6Al-4V. *Int. J. Mach. Tools Manuf.* **2008**, *48*, 275–288. [[CrossRef](#)]
3. Khanna, N.; Davim, J.P. Design-of-Experiments application in machining titanium alloys for aerospace structural components. *Measurement* **2015**, *61*, 280–290. [[CrossRef](#)]
4. Wyen, C.F.; Wegener, K. Influence of cutting edge radius on cutting forces in machining titanium. *CIRP Ann.* **2010**, *59*, 93–96. [[CrossRef](#)]
5. Kuttolamadom, M.; Joshua, J.; Laine, M.; Von Oehsen, J.; Kurfess, T.; Ziegert, J. High performance computing simulations to identify process parameter designs for profitable titanium machining. *J. Manuf. Syst.* **2017**, *43*, 235–247. [[CrossRef](#)]
6. Jackson, M.J.; Novakov, T.; Whitfield, M.; Robinson, G.; Handy, R.; Sein, H.; Ahmed, W. VFCVD Diamond-Coated cutting tools for micro-machining titanium alloy Ti6Al4V. *Int. J. Adv. Manuf. Technol.* **2017**, *92*, 2881–2918. [[CrossRef](#)]
7. Pervaiz, S.; Amir, R.; Ibrahim, D.; Cornel, M.N. An experimental investigation on effect of minimum quantity cooling lubrication (MQCL) in machining titanium alloy (Ti6Al4V). *Int. J. Adv. Manuf. Technol.* **2016**, *87*, 1371–1386. [[CrossRef](#)]
8. Yang, X.P.; Liu, C.R. Machining titanium and its alloys. *Mach. Sci. Technol.* **1999**, *3*, 107–139. [[CrossRef](#)]
9. Hoyne, A.C.; Nath, C.; Kapoor, S.G. On cutting temperature measurement during titanium machining with an atomization-based cutting fluid spray system. *J. Manuf. Sci. Eng.* **2015**, *137*, 024502. [[CrossRef](#)]
10. Liu, Z.Q.; Xu, J.Y.; Han, S.; Chen, M. A coupling method of response surfaces (CRSM) for cutting parameters optimization in machining titanium alloy under minimum quantity lubrication (MQL) condition. *Int. J. Precis. Eng. Manuf.* **2013**, *14*, 693–702. [[CrossRef](#)]
11. Ramesh, S.; Karunamoorthy, L.; Palanikumar, K. Fuzzy modeling and analysis of machining parameters in machining titanium alloy. *Mater. Manuf. Process.* **2008**, *23*, 439–447. [[CrossRef](#)]
12. Revuru, R.S.; Zhang, J.Z.; Posinasetti, N.R.; Kidd, T. Optimization of titanium alloys turning operation in varied cutting fluid conditions with multiple machining performance characteristics. *Int. J. Adv. Manuf. Technol.* **2018**, *95*, 1451–1463. [[CrossRef](#)]
13. Sun, J.; Guo, Y.B. Material flow stress and failure in multiscale machining titanium alloy Ti-6Al-4V. *Int. J. Adv. Manuf. Technol.* **2009**, *41*, 651–659. [[CrossRef](#)]
14. Sun, S.; Brandt, M.; Dargusch, M.S. Characteristics of cutting forces and chip formation in machining of titanium alloys. *Int. J. Mach. Tools Manuf.* **2009**, *49*, 561–568. [[CrossRef](#)]
15. Sima, M.; Tuğrul, Ö. Modified material constitutive models for serrated chip formation simulations and experimental validation in machining of titanium alloy Ti-6Al-4V. *Int. J. Mach. Tools Manuf.* **2010**, *50*, 943–960. [[CrossRef](#)]
16. Liu, Z.; Qinglong, A.; Jinyang, X.; Ming, C.; Shu, H. Wear performance of (Nc-AlTiN)/(a-Si₃N₄) coating and (Nc-AlCrN)/(a-Si₃N₄) coating in high-speed machining of titanium alloys under dry and minimum quantity lubrication (MQL) conditions. *Wear* **2013**, *305*, 249–259. [[CrossRef](#)]
17. Kannan, S.; Kishawy, H.A. Tribological aspects of machining aluminium metal matrix composites. *J. Mater. Process. Technol.* **2008**, *198*, 399–406. [[CrossRef](#)]
18. Sreejith, P.S. Machining of 6061 aluminium alloy with MQL, dry and flooded lubricant conditions. *Mater. Lett.* **2008**, *62*, 276–278. [[CrossRef](#)]
19. Nouari, M.; List, G.; Girot, F.; Coupard, D. Experimental analysis and optimisation of tool wear in dry machining of aluminium alloys. *Wear* **2003**, *255*, 1359–1368. [[CrossRef](#)]
20. Kelly, J.F.; Cotterell, M.G. Minimal lubrication machining of aluminium alloys. *J. Mater. Process. Technol.* **2002**, *120*, 327–334. [[CrossRef](#)]

21. Davoodi, B.; Tazehkandi, A.H. Experimental investigation and optimization of cutting parameters in dry and wet machining of aluminum alloy 5083 in order to remove cutting fluid. *J. Clean. Prod.* **2014**, *68*, 234–242. [[CrossRef](#)]
22. Kouadri, S.; Necib, K.; Atlati, S.; Haddag, B.; Nouari, M. Quantification of the chip segmentation in metal machining: Application to machining the aeronautical aluminium alloy AA2024-T351 with cemented carbide tools WC-Co. *Int. J. Mach. Tools Manuf.* **2013**, *64*, 102–113. [[CrossRef](#)]
23. Hovsepian, P.E.; Luo, Q.; Robinson, G.; Pittman, M.; Howarth, M.; Doerwald, D.; Tietema, R.; Sim, W.M.; Deeming, A.; Zeus, T. TiAlN/VN superlattice structured PVD coatings: A new alternative in machining of aluminium alloys for aerospace and automotive components. *Surf. Coat. Technol.* **2006**, *201*, 265–272. [[CrossRef](#)]
24. Arumugam, P.U.; Malshe, A.P.; Batzer, S.A. Dry machining of aluminum–silicon alloy using polished CVD diamond-coated cutting tools inserts. *Surf. Coat. Technol.* **2006**, *200*, 3399–3403. [[CrossRef](#)]
25. Nouari, M.; List, G.; Giro, F.; Géhin, D. Effect of machining parameters and coating on wear mechanisms in dry drilling of aluminium alloys. *Int. J. Mach. Tools Manuf.* **2005**, *45*, 1436–1442. [[CrossRef](#)]
26. Sánchez, J.M.; Rubio, E.; Álvarez, M.; Sebastián, M.A.; Marcos, M. Microstructural characterisation of material adhered over cutting tool in the dry machining of aerospace aluminium alloys. *J. Mater. Process. Technol.* **2005**, *164*, 911–918. [[CrossRef](#)]
27. Pu, Z.; Umbrello, D.; Dillon, O.W.; Lu, T.; Puleo, D.A.; Jawahir, I.S. Finite element modeling of microstructural changes in dry and cryogenic machining of AZ31B magnesium alloy. *J. Manuf. Process.* **2014**, *16*, 335–343. [[CrossRef](#)]
28. Denkena, B.; Lucas, A. Biocompatible magnesium alloys as absorbable implant materials—Adjusted surface and subsurface properties by machining processes. *CIRP Ann.* **2007**, *56*, 113–116. [[CrossRef](#)]
29. Gariboldi, E. Drilling a magnesium alloy using PVD coated twist drills. *J. Mater. Process. Technol.* **2003**, *134*, 287–295. [[CrossRef](#)]
30. Dinesh, S.; Senthilkumar, V.; Asokan, P.; Arulkirubakaran, D. Effect of cryogenic cooling on machinability and surface quality of bio-degradable ZK60 mg alloy. *Mater. Des.* **2015**, *87*, 1030–1036. [[CrossRef](#)]
31. Menezes, P.L.; Kailas, K.S.V. Influence of roughness parameters on coefficient of friction under lubricated conditions. *Sadhana* **2008**, *33*, 181–190. [[CrossRef](#)]
32. Pu, Z.; Outeiro, J.C.; Batista, A.C.; Dillon, O.W.; Puleo, D.A.; Jawahir, I.S. Enhanced surface integrity of AZ31B mg alloy by cryogenic machining towards improved functional performance of machined components. *Int. J. Mach. Tools Manuf.* **2012**, *56*, 17–27. [[CrossRef](#)]
33. Shokrani, A.; Dhokia, V.; Newman, S.T. Environmentally conscious machining of difficult-to-machine materials with regard to cutting fluids. *Int. J. Mach. Tools Manuf.* **2012**, *57*, 83–101. [[CrossRef](#)]
34. Shaharun, M.A.; Ahmad, R.Y. Effects of irregular tool geometry and machining process parameters on the wavelength performance of process damping in machining titanium alloy at low cutting speed. *Int. J. Adv. Manuf. Technol.* **2016**, *85*, 1019–1033. [[CrossRef](#)]
35. Rubio, E.M.; Sáenz de Pipaón, J.M.; Villeta, M.; Sebastián, M.A. Experimental study for improving repair operations of pieces of magnesium UNS M11311 obtained by dry turning. In Proceedings of the 12th CIRP Conference on Modelling of Machining, San Sebastian, Spain, 7–8 May 2009; pp. 819–826.
36. Villeta, M.; Agustina, B.; Sáenz de Pipaón, J.M.; Rubio, E.M. Efficient optimisation of machining processes based on technical specifications for surface roughness: Application to magnesium pieces in the aerospace industry. *Int. J. Adv. Manuf. Technol.* **2011**, *60*, 1237–1246. [[CrossRef](#)]
37. Villeta, M.; Rubio, E.M.; Sáenz de Pipaón, J.M.; Sebastián, M.A. Surface finish optimization of magnesium pieces obtained by dry turning based on Taguchi techniques and statistical tests. *Mater. Manuf. Process.* **2011**, *26*, 1503–1510. [[CrossRef](#)]
38. Rubio, E.M.; Valencia, J.L.; Saá, A.J.; Carou, D. Experimental study of the dry facing of magnesium pieces based on the surface roughness. *Int. J. Precis. Eng. Manuf.* **2013**, *14*, 995–1001. [[CrossRef](#)]
39. Rubio, E.M.; Villeta, M.; Carou, D.; Saá, A.J. Comparative analysis of sustainable cooling systems in intermittent turning of magnesium pieces. *Int. J. Precis. Eng. Manuf.* **2014**, *15*, 929–940. [[CrossRef](#)]
40. Rubio, E.M.; Valencia, J.L.; Agustina, B.; Saá, A.J. Tool selection based on surface roughness in dry facing repair operations of magnesium pieces. *Int. J. Mater. Prod. Technol.* **2014**, *48*, 116–134. [[CrossRef](#)]
41. Carou, D.; Rubio, E.M.; Davim, J.P. Discontinuous cutting: Failure mechanisms, tool materials and temperature study—A review. *Rev. Adv. Mater. Sci.* **2014**, *38*, 110–124.

42. Carou, D.; Rubio, E.M.; Lauro, C.H.; Davim, J.P. Experimental investigation on surface finish during intermittent turning of UNS M11917 magnesium alloy under dry and near dry machining conditions. *Measurement* **2014**, *56*, 136–154. [CrossRef]
43. Bureau of Labor Statistics, Productivity and Costs by Industry: Manufacturing and Mining Industries-2017, Economic New Release, 2018. Available online: www.bls.gov/news.release/pdf/prin.pdf (accessed on 3 July 2018).
44. Rubio, E.M.; de Agustina, B.; Marín, M.M.; Bericua, A. Cooling systems based on cold compressed air: A review of the applications in machining processes. *Proc. Eng.* **2015**, *132*, 413–418. [CrossRef]
45. Carou, D.; Rubio, E.M.; Davim, J.P. A note on the use of the minimum quantity lubrication (MQL) system in turning. *Ind. Lubr. Tribol.* **2015**, *67*, 256–261. [CrossRef]
46. Carou, D.; Rubio, E.M.; Davim, J.P. Analysis of ignition risk in intermittent turning of UNS M11917 magnesium alloy at low cutting speeds based on the chip morphology. *Proc. Inst. Mech. Eng. Part B J. Eng. Manuf.* **2015**, *229*, 365–371. [CrossRef]
47. Carou, D.; Rubio, E.M.; Lauro, C.H.; Davim, J.P. Experimental investigation on finish intermittent turning of UNS M11917 magnesium alloy under dry machining. *Int. J. Adv. Manuf. Technol.* **2015**, *75*, 1417–1429. [CrossRef]
48. Carou, D.; Rubio, E.M.; Lauro, C.H.; Davim, J.P. The effect of minimum quantity lubrication in the intermittent turning of magnesium based on vibration signals. *Measurement* **2016**, *94*, 338–343. [CrossRef]
49. Carou, D.; Rubio, E.M.; Agustina, B.; Marín, M.M. Experimental study for effective and sustainable repair and maintenance of bars made of Ti-6Al-4V alloy application to the aeronautic industry. *J. Clean. Prod.* **2017**, *164*, 465–475. [CrossRef]
50. Ben Artzy, A.; Munitz, A.; Kohn, G.; Bronfin, B.; Shtechman, A. Joining of light hybrid constructions made of magnesium and aluminum alloys. *TMS Ann. Meet.* **2002**, *1*, 295–302.
51. Ashby, M.F.; Brécht, Y.J.M. Designing hybrid materials. *Acta Mater.* **2003**, *51*, 5801–5821. [CrossRef]
52. Amancio, S. *Innovative Solid-State Spot Joining Methods for Fiber Composites and Metal-Polymer Hybrid Structures; Joining in Car Body*; Helmholtz-ZentrumGeesthacht: Geesthacht, Germany, 2012; pp. 1–47.
53. Gururaja, M.N.; Rao, A.N.H. A review on recent applications and future prospectus of hybrid composites. *Int. J. Soft Comput. Eng.* **2012**, *1*, 352–355.
54. Suryawanshi, B.K.; Prajitsen, G.D. Review of design of hybrid aluminum/composite drive shaft for automobile. *Int. J. Innov. Technol. Explor. Eng.* **2013**, *2*, 259–266.
55. Lee, D.; Morillo, C.; Oller, S.; Bugada, G.; Oñate, E. Robust design optimization of advance hybrid (fiber-metal) composite structures. *Compos. Struct.* **2013**, *99*, 181–192. [CrossRef]
56. Rubio, E.M.; Villeta, M.; Valencia, J.L.; Sáenz de Pipaón, J.M. Experimental study for improving repair of magnesium-aluminium hybrid parts by turning processes. *Metals* **2018**, *8*, 59. [CrossRef]
57. Rubio, E.M.; Sáenz de Pipaón, J.M.; Valencia, J.L.; Villeta, M. *Design, Manufacturing and Machining Trials of Magnesium Based Hybrid Parts, Machining of Light Alloys: Aluminium, Titanium and Magnesium*; CRC-Press: Boca Raton, FL, USA, 2018; in press.
58. Zakaria, B.; Yazid, H. Friction stir welding of dissimilar materials Aluminum Al6061-T6 to ultra low carbon steel. *Metals* **2017**, *7*, 42.
59. Casalino, G. Advances in welding metal alloys, Dissimilar metals and additively manufactured parts. *Metals* **2017**, *7*, 32. [CrossRef]
60. Casalino, G.; Guglielmi, P.; Lorusso, V.D.; Mortello, M.; Peyre, P.; Sorgente, D. Laser offset welding of AZ31B magnesium alloy to 316 stainless steel. *J. Mater. Process. Technol.* **2017**, *242*, 49–59. [CrossRef]
61. Li, Y.; Liu, C.; Yu, H.; Zhao, F.; Wu, Z. Numerical simulation of Ti/Al bimetal composite fabricated by explosive welding. *Metals* **2017**, *7*, 407. [CrossRef]
62. Wagner, F.; Zerner, I.; Kreimeyer, M.; Seefeld, T.; Sepold, G. Characterization and properties of dissimilar metal combinations of Fe/Al and Ti/Al sheet materials. In Proceedings of the ICALEO'01, Orlando, FL, USA, 15–18 October 2001.
63. Luo, J.G.; Acoff, V.L. Interfacial reactions of titanium and aluminum during diffusion welding. *Weld. J.* **2000**, *79*, 239–243.
64. Sáenz de Pipaón, M.J. *Diseño y Fabricación de Probetas de Componentes Híbridos con Aleaciones de Magnesio para Ensayos de Mecanizado*. Ph.D. Thesis, UNED (Universidad Nacional de Educación a Distancia), Madrid, Spain, 2013.

65. Qi, X.; Song, G. Interfacial structure of the joints between magnesium alloy and mild steel with nickel as interlayer laser-TIG welding. *Mater. Des.* **2010**, *31*, 605–609. [[CrossRef](#)]
66. Nasiri, A.M.; Li, L.; Kim, S.H.; Zhou, Y.; Weckman, D.C.; Nguyen, T.C. Microstructure and properties of laser brazed magnesium to coated steel. *Weld. J.* **2011**, *90*, 211–219.
67. Nasiri, A.M.; Weckman, D.C.; Zhou, Y. Interfacial microstructure of diode laser brazed AZ31B magnesium to steel sheet using a nickel interlayer. *Weld. J.* **2013**, *92*, 1S–10S.
68. Dau, J.; Lauter, C.; Damerow, U.; Homberg, W.; Tröster, T. Multi-material systems for tailored automotive structural components. In Proceedings of the 18th International Conference on Composite Materials, Jeju Island, Korea, 21–26 August 2011.
69. Frantz, M.; Lauter, C.; Tröster, T. Advanced manufacturing technologies for automotive structures in multi-material design consisting of high-strength steels and CFRP. In Proceedings of the 56th International Scientific Colloquium, Ilmenau, Germany, 12–16 September 2011.
70. DRL. *Innovation Report 2011*; Institute of Composites Structures and Adaptive Systems: Braunschweig, Germany, 2011.
71. Amin, N. Titanium Alloys—Towards Achieving Enhanced Properties for Diversified Applications. Edited by A.K.M. Nurul Amin, 2012. Available online: www.intechopen.com (accessed on 1 July 2018).
72. Bisker, J.; Christman, T.; Allison, T.; Goranson, H.; Landmesser, J.; Minister, A.; Plonski, R. *DOE Handbook, Primer on Spontaneous Heating and Pyrophoricity*; U.S. Department of Energy: Washington, DC, USA, 1994; pp. 1–68.
73. NanoMAG. *Hydro Magnesium's Machining Magnesium*; Technical Document; NanoMAG: Livonia, MI, USA, 2009; Available online: <http://nanomag.us> (accessed on 22 November 2017).
74. Layens, C.; Peters, M. *Titanium and Titanium Alloys. Fundamentals and Applications*; Wiley-VCH Verlag GmbH & Co.: Weinheim, Germany, 2003.
75. Sáenz de Pipaón, J.M.; Rubio, E.M.; Villeta, M.; Sebastián, M.A. Analysis of the chips obtained by dry turning of UNS M11311 magnesium. In Proceedings of the 3rd Manufacturing Engineering Society International Conference 2009, Alcoy, Spain, 17–19 June 2009; pp. 33–38.
76. Sáenz de Pipaón, J.M.; Rubio, E.M.; Villeta, M.; Sebastián, M.A. Selection of the cutting tools and conditions for the low speed turning of bars of magnesium UNS M11311 based on the surface roughness. In *Innovative Production Machines and Systems*; Whittles Publishing: Scotland, UK, 2010; pp. 174–179, ISBN 978-184995-006-0.
77. El-CGizawy, A.S.; Khasawneh, F.A.; Bogis, H. Drilling process design for hybrid structures of polymer composites over titanium alloy. *J. Mater. Sci. Eng.* **2016**, *5*, 243. [[CrossRef](#)]
78. Matsumara, T.; Tamura, S. Cutting simulation of titanium alloy drilling with energy analysis and FEM. In Proceedings of the 15th CIRP Conference on Modelling of Machining Operations, Karlsruhe, Germany, 11–12 June 2015; pp. 252–257.
79. Poutord, A.; Rossi, F.; Paulachon, G.; M'Saoubi, R.; Abrivard, G. Local approach of wear in drilling Ti6Al4V/CFRP for stack modelling. In Proceedings of the 14th CIRP Conference on Modelling of Machining Operations, Turin, Italy, 13–14 June 2013; pp. 316–321.
80. Shetty, P.K.; Shetty, R.; Shetty, D.; Rehaman, F. Machinability study on dry drilling of titanium alloy Ti-6Al-4V using L₉ orthogonal array. *Procedia Mater. Sci.* **2014**, *5*, 2605–2614. [[CrossRef](#)]
81. Ramulu, M.; Spaulding, M. Drilling of hybrid titanium composite laminate (HTCL) with electrical discharge machining. *Materials* **2016**, *9*, 746. [[CrossRef](#)] [[PubMed](#)]
82. Grasin, K.; Ayvar-Soberanis, S. Evaluation of workpiece temperature during drilling of GLARE fiber metal laminates using infrared techniques: Effect of cutting parameters, fiber orientation and spray mist application. *Materials* **2016**, *9*, 622. [[CrossRef](#)]
83. Abdulgadir, M.; Demir, B.; Emre Turam, M. Hybrid reinforced magnesium matrix composites (Mg/Sic/GNPs): Drilling investigation. *Metals* **2018**, *8*, 215. [[CrossRef](#)]
84. Li, M.; Huang, M.; Jiang, X. Study on burr occurrence and surface integrity during slot milling of multidirectional and plain woven CFRPs. *Int. J. Adv. Manuf. Technol.* **2018**, *97*, 163–173. [[CrossRef](#)]
85. Bellini, C.; Polini, W.; Sorrentino, L. A new class of thin composite parts for small batch productions. *Adv. Compos. Lett.* **2014**, *23*, 115–120.
86. Liao, B.B.; Liu, P.F. Finite element analysis of dynamic progressive failure properties of GLARE hybrid laminates under low-velocity impact. *J. Compos. Mater.* **2018**, *52*, 1317–1330. [[CrossRef](#)]

87. Montgomery, D.C. *Design and Analysis of Experiments*; John Wiley & Sons, Inc.: Hoboken, NJ, USA, 2017.
88. ISO. *Geometrical Product Specifications (GPS) Surface Texture: Profile Method. Rules and Procedures for the Assessment of Surface Texture*; International Organization for Standardization: Geneva, Switzerland, 1998.
89. Zhang, P.F.; Churi, N.J.; Treadwell, C. Mechanical drilling processes for titanium alloys: A literature review. *Mach. Sci. Technol.* **2008**, *12*, 417–444. [[CrossRef](#)]
90. Celik, Y.M. Investigating the effects of cutting parameters on the hole quality in drilling the Ti-6Al-4V alloy. *Mater. Technol.* **2014**, *48*, 653–659.
91. Rahim, E.A.; Sharif, S.; Sasahara, H. Machinability of titanium alloys in drilling. Chapter 6. In *Titanium Alloys-Towards Achieving Enhanced Properties for Diversified Applications*; Edited by A.K.M. Nurul Amin; 2012; Available online: www.intechopen.com (accessed on 1 July 2018).
92. Chong, K.Z.; Shih, T.S. Optimizing drilling conditions for AZ61A magnesium alloy. *Mater. Trans.* **2002**, *43*, 2148–2156. [[CrossRef](#)]
93. Taguchi, G. *System of Experimental Design: Engineering Methods to Optimize Quality and Mimimize Costs*, 1st ed.; Kraus International Publications: New York, NY, USA, 1987; Volume 1.
94. The American Society of Mechanical Engineers. *Surface Texture: Surface Roughness, Waviness and Lay*; ANSI/ASME B46.1-2009; ASME: New York, NY, USA, 2010.



© 2018 by the authors. Licensee MDPI, Basel, Switzerland. This article is an open access article distributed under the terms and conditions of the Creative Commons Attribution (CC BY) license (<http://creativecommons.org/licenses/by/4.0/>).

Article

Delamination Study in Edge Trimming of Basalt Fiber Reinforced Plastics (BFRP)

Maria Dolores Navarro-Mas ^{1,*}, Juan Antonio García-Manrique ¹,
Maria Desamparados Meseguer ¹, Isabel Ordeig ¹ and Ana Isabel Sánchez ²

¹ Department of Mechanical Engineering and Materials, Universitat Politècnica de València, Camino de Vera s/n 46022 Valencia, 46022 València, Spain; jugarcia@mcm.upv.es (J.A.G.-M.); amesegue@mcm.upv.es (M.D.M.); iordeig@mcm.upv.es (I.O.)

² Department of Statistics and Operational Research, Universitat Politècnica de València, Camino de Vera s/n 46022 Valencia, 46022 València, Spain; aisanche@eio.upv.es

* Correspondence: lnavarro@mcm.upv.es; Tel.: +34-963-877-622

Received: 29 June 2018; Accepted: 27 July 2018; Published: 13 August 2018



Abstract: Although there are many machining studies of carbon and glass fiber reinforced plastics, delamination and tool wear of basalt fiber reinforced plastics (BFRP) in edge trimming has not yet studied. This paper presents an end milling study of BFRP fabricated by resin transfer molding (RTM), to evaluate delamination types at the top layer of the machined edge with different cutting conditions (cutting speed, feed rate and depth of cut) and fiber volume fraction (40% and 60%). This work quantifies delamination types, using a parameter S_d/L , that evaluates the delamination area (S_d) and the length (L), taking into account tool position in the yarn and movement of yarns during RTM process, which show the random nature of delamination. Delamination was present in all materials with 60% of fiber volume. High values of tool wear did not permit to machine the material due to an excessive delamination. Type II delamination was the most usual delamination type and depth of cut has influence on this type of delamination.

Keywords: basalt fiber reinforced plastic (BFRP); delamination; edge trimming; tool wear

1. Introduction

Nowadays, aeronautical and automotive manufacturers use fiber reinforced composites, because of their properties of light weight and high strength [1]. In many cases, these composites are manufactured using processes such as resin transfer molding (RTM), vacuum infusion, prepegs, etc. Nevertheless, a machining process step is necessary after curing to meet the required tolerances and final shape of the part [2] or to allow the union of different components. Edge trimming and drilling are the most extended machining processes [3].

Machining damage is unavoidable due to the high mechanical resistance of the fibers, which causes excessive tool wear and poor surface finish [4]. In edge trimming, delamination of the top and/or the bottom layer of the composite, due to the axial tool force generated by the helix inclination angle of the milling tool is another important factor that affects dimensional precision and mechanical performance of parts. Delamination occurs because the fiber is not restrained by the outside in the top layer, and the tool bends the fibers outward and deflect them away from the plane of the laminate. Types of delamination can be classified into three groups (I, II and III) [5]. Type I delamination characterizes areas where the surface fibers have been broken some distance inward from the trimmed edge. Type II delamination takes into account uncut fibers that protrude from the trimmed edge. Type I/II is a combination of the two previous types. Type III delamination describes fibers parallel to the machining surface.

Studies on delamination are focused on drilling and milling (slot milling and edge trimming). Main factors that affect delamination are the tool wear, determined by the machining conditions, tool geometry, and volume and orientation of fiber in the composite material [6,7].

In drilling, a study based on digital image analysis defines different factors to evaluate delamination [8]. Firstly, delamination factor ($F_d = D_{max}/D_o$) is calculated as the ratio of the maximum diameter of the delamination zone (D_{max}) to the drill diameter (D_o). Secondly, the adjusted delamination factor (F_d) represents the conventional delamination factor (F_d) plus the damage area contribution. Some authors have used this delamination factor to evaluate spindle speed, feed rate and the point angle in delamination of carbon fiber reinforced plastics (CFRP) with response surface methodology [9] generating a second order regression model. With high spindle speed and low feed rate, delamination reduces at the entrance of the hole.

In milling works, there are mainly two different processes studied: slot milling and edge trimming. In slot milling, recent studies evaluate the occurrence and propagation of delamination in CFRP [10] concluding that delamination is influenced by fiber orientation and tool wear. On the other hand, the undulation of the woven yarn provokes different types of delamination: fiber protrusion and surface damage [11]. Cutting conditions (spindle speed, feed rate and depth of cut) and number of end milling flutes are evaluated to minimize delamination (delamination factor F_d) and surface roughness using neural network and genetic algorithm in glass fiber reinforced plastics (GFRP). As conclusion, F_d increases with feed rate and decreases with spindle speed [12].

In edge trimming, surface delamination is random [13]. Damage caused by delamination in edge trimming of CFRP using burr tools can be quantified in terms of delamination depth and frequency of occurrence per length, taking into account feed rate, cutting speed and tool wear [13]. Delamination increases when feed rate and machining length increase and the spindle speed decrease [14].

Most studies that approach fiber reinforced composites machining are focalized in glass and carbon fibers, however, there are almost no studies with basalt fiber reinforced plastic (BFRP) [15]. Basalt is a natural mineral with good properties, with a similar mechanical behavior that carbon fiber [16]. BFRP process manufacturing is similar to GFRP, without additives and with a lower amount of energy [17,18].

In this paper, a plain weave basalt fiber reinforced plastic is milled with edge trimming in order to study delamination. Cutting conditions (cutting speed, feed per tooth and depth of cut) and fiber volume fraction are varying, as tool wear is evaluated. Tool selection takes into account a commercial tool suitable for edge trimming, with a high productivity due to a long tool life for chosen cutting parameters and with a high cutting length. This work studies and quantifies delamination types depending on the position that the tool hits the yarn, and establishes parameters to compare different experiments.

2. Materials and Methods

Basalt fiber reinforced plastic (BFRP) laminates used in this study were manufactured using RTM process. The material was a rectangular (420 mm × 260 mm) bidirectional panel with plies of plain weave basalt fibers impregnated with an epoxy resin (Prime 20 LV Gurit, Switzerland). Fiber orientation was 90°. Figure 1 shows the laminate and its top layer. In the top layer, it is possible to see different zones, depending on the quantity of resin and the position of the fibers. The thickness of the material was 3.4 mm. Step between yarns was 3 mm, which represents a limit for X_d (Figure 2), X_d being the distance of the warp yarn from the trimmed edge until the next dip below the crossing fill yarn [11].

Edge trimming operation (down milling) was conducted using a Kondia B-500 milling machine (Kondia, Elgoibar, Spain), with a spindle power of 6 KW and a maximum rotation speed of 6000 rpm. A Mitsubishi Materials milling tool holder of diameter 25 mm (AXD4000R252SA25SA Mitsubishi Materials, Japan), with two exchangeable uncoated carbide cutting inserts (XDGX175008PDR-GL TF15 Mitsubishi Materials, Japan) was used for machining.

Clamps were used in the milling machine to avoid vibrations and displacement of the laminate, leaving the minimum cantilevered possible. A film bag involving machining zone was used to avoid dust (Figure 3).

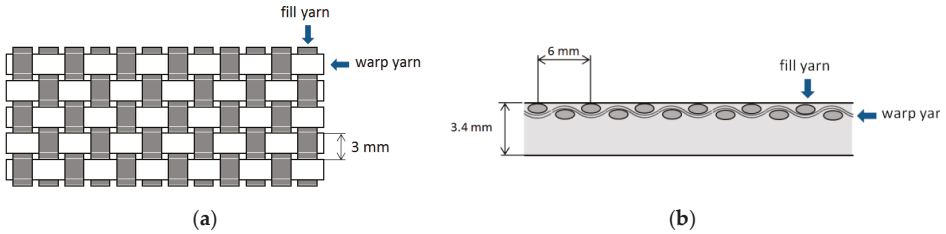


Figure 1. (a) Bidirectional panel; (b) Top layer laminate.

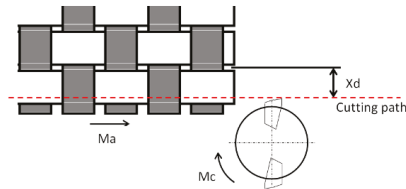


Figure 2. Xd Schema.

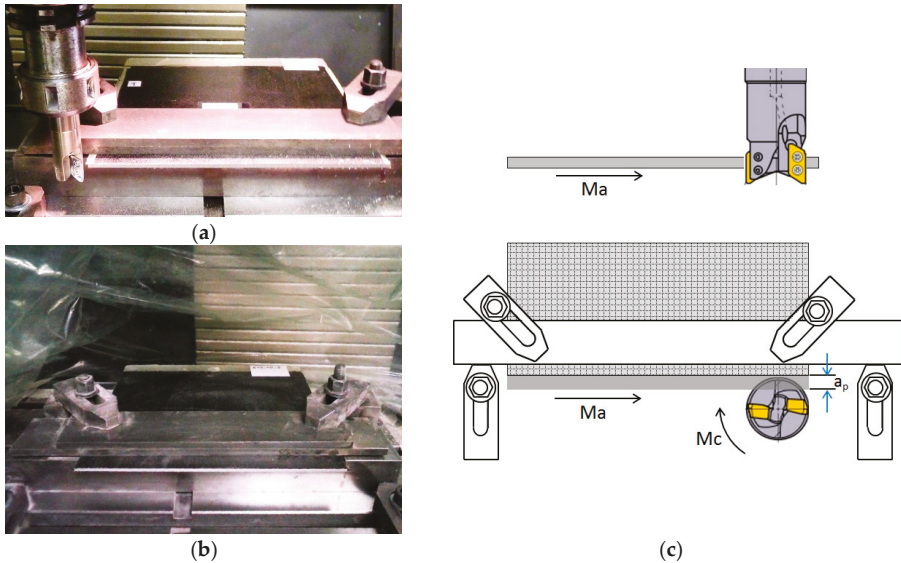


Figure 3. (a) Fixture with clamps; (b) Film bag; (c) Down milling schema.

Cutting conditions (cutting speed, feed per tooth and depth of cut) and material characteristics (fiber volume fraction) were considered to study delamination, taking into account the flank wear of the tool. The Taguchi’s method for four variables at two-levels was used to elaborate the design of experiments. Table 1 shows the variables studied and their levels.

Table 1. Variables and levels.

Level	Cutting Speed Vc (m/min)	Feed per Tooth Fz (mm)	Depth of Cut ap (mm)	Fiber Volume Fv (%)
1	300	0.1	0.5	40
2	470	0.4	1.5	60

In this paper, a L_8 orthogonal array was selected for determining combinations of factor levels to use for each experimental case. Table 2 shows the values of the parameters for each experiment using an L_8 orthogonal array. Due to the time consumed for each experiment, a full factorial design was not used, in order to reduce the number of experiments. No replicas were done, because of the random nature of delamination.

Table 2. Experimental parameters.

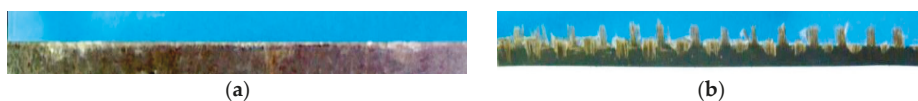
Test	Cutting Speed Vc (m/min)	Feed per Tooth Fz (mm)	Depth of Cut ap (mm)	Fiber Volume Fv (%)
1	470	0.1	0.5	60
2	470	0.4	1.5	60
3	300	0.1	1.5	60
4	300	0.4	0.5	60
5	470	0.1	1.5	40
6	470	0.4	0.5	40
7	300	0.1	0.5	40
8	300	0.4	1.5	40

In every experiment, a tool with new inserts machined without coolant for 80 min. Different stopping times (30, 55, and 80 min), or cutting times (T_c), were made to measure delamination and flank wear (V_b) in both cutting inserts. Measuring of delamination and flank wear are carried out recording and analyzing images of the laminate material and the clearance face of the tool, respectively. An Olympus SZ61 microscope (Olympus, Japan) and image processing software (Olympus stream software, GIMP 2.8) with pixel calibration was used to measure delamination and flank wear. In flank wear, measurements were repeated two times in every insert and a maximum value was chosen for every experiment.

3. Results and Discussion

3.1. Types of Delamination

In the experimental results obtained in this study, laminates with a 40% of fiber in volume do not present delamination (Figure 4a), because the resin restrains the fiber in the top layer. Laminate with a 60% of fiber in volume presents delamination (Figure 4b) at the top surface.

**Figure 4.** (a) Fv 40% without delamination; (b) Fv 60% with high delamination.

Delamination can be classified in three Types (I, II and III) [5], as shown in Figure 5.

For each delamination type, the maximum value (V_{max}) and the surface occupied (S_d) were measured (Figure 6). Only V_{max} has been measured by some authors [11,13], but not S_d (surface damage or surface protrusion).

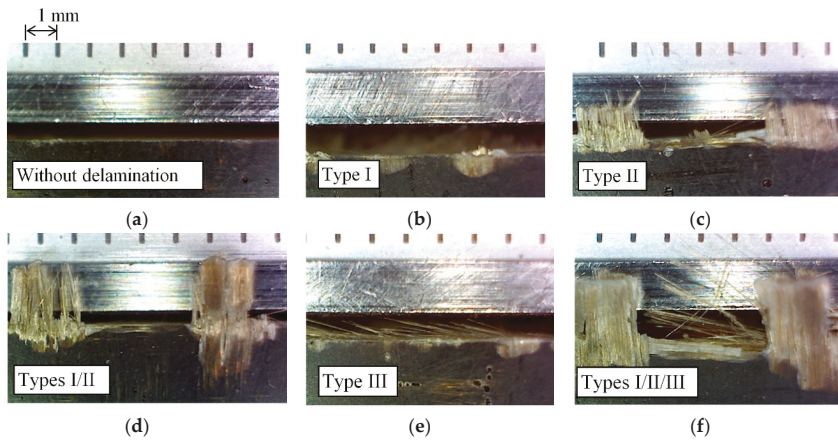


Figure 5. (a) Top layer without delamination (Fv 40%); (b) Surface damage (Type I); (c) Fiber protrusion (Type II); (d) Types I and II delamination; (e) Type III delamination; (f) All delamination Types.

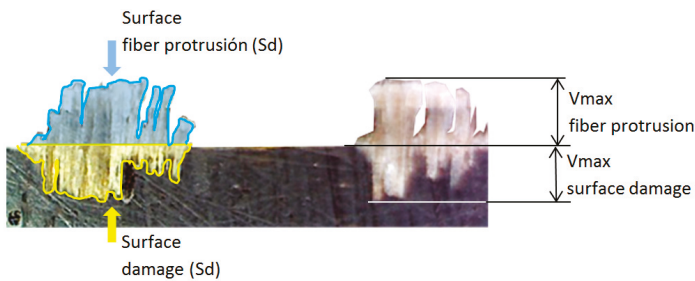


Figure 6. Surface damage and fiber protrusion measurement.

Table 3 shows values of tool wear and surface damage (Type I) for each step. Table 4 shows values of tool wear and fiber protrusion (Types II and III) for each step. A length of 80 mm was measured and the value of “% L” represents the percentage of this length with delamination. In most experiments “% L” occupied for delamination is important, but values of Sd are maintained low, so they are acceptable. Values for Sd and Vmax were expected to increase as cutting time and tool wear increase as well. Nevertheless, some values decrease instead of increase. It is due to the random nature of delamination and the tool position when it hits the yarn. This will be explained in more detail in Section 3.3.

In Experiment 2, cutting conditions were the worst (high cutting speed, high feed rate and high depth of cut) and flank wear increased very highly and no cutting was possible after 30 min. This experiment only shows values at 5, 10 and 30 min. High tool wear depends on high cutting speed and high feed per tooth [13].

In Type I delamination, Vmax value is less than yarn size, and the highest values are with large feed per tooth. In Type II delamination, in most cases, Vmax values are larger than depth of cut (ap). This can be explained because, originally, the fill yarn has a sine wave form and after cutting the yarn is stretched (Figure 7), according to other studies [14].

Table 3. Surface damage values (Type I).

Test	Vc	Fz	ap	Fv %	Tc (min)	Vb (mm)	Type I		
							Sd (mm ²)	% L	Vmax (mm)
1	470	0.1	0.5	60	30	0.049	3.80	41%	0.30
					55	0.057	7.48	69%	0.61
					80	0.072	6.43	58%	0.74
2	470	0.4	1.5	60	5	0.211	21.68	95%	0.96
					10	0.232	30.11	99%	2.29
					30	0.247	30.79	94%	2.28
3	300	0.1	1.5	60	30	0.032	6.46	45%	0.68
					55	0.047	9.26	73%	0.81
					80	0.073	9.36	95%	0.49
4	300	0.4	0.5	60	30	0.041	13.65	65%	1.83
					55	0.048	10.03	53%	1.43
					80	0.063	11.14	81%	1.14

Table 4. Fiber protrusion values (Types II and III).

Test	Vc	Fz	ap	Fv %	Tc (min)	Vb (mm)	Type II			Type III			Total	II and III
							Sd (mm ²)	% L	Vmax	Sd (mm ²)	% L	Vmax	Sd (mm ²)	% L
1	470	0.1	0.5	60	30	0.049	6.35	41%	0.614	0	0%	6.35	41%	
					55	0.057	10.44	42%	0.611	5.89	43%	16.33	85%	
					80	0.072	4.12	35%	0.655	4.94	38%	9.06	73%	
2	470	0.4	1.5	60	5	0.211	92.17	48%	2.110	14.29	52%	106.46	100%	
					10	0.232	43.04	45%	2.584	29.41	54%	72.45	99%	
					30	0.247	41.21	39%	2.468	17.77	55%	58.98	94%	
3	300	0.1	1.5	60	30	0.032	10.64	72%	1.487	0	0%	10.64	72%	
					55	0.047	10.66	70%	0.993	5.00	22%	15.66	92%	
					80	0.073	25.07	68%	2.104	2.59	30%	27.66	98%	
4	300	0.4	0.5	60	30	0.041	14.34	55%	1.201	6.01	20%	20.35	75%	
					55	0.048	5.35	40%	0.715	1.84	16%	7.19	56%	
					80	0.063	10.66	55%	0.634	6.85	32%	17.51	87%	

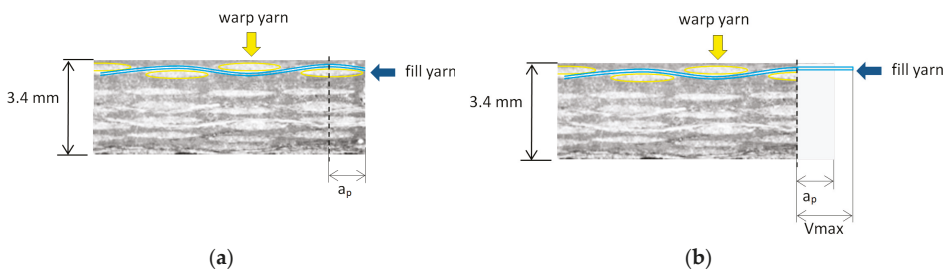


Figure 7. (a) Depth of cut (ap) before machining; (b) Vmax and ap after machining.

When ap is less than yarn size, Type I delamination can be larger than Type II.

In Experiment 3 at 80 min and in Experiment 4 at 30 min, values of Vmax were very high because Type II and III delamination were superimposed. In these experiments, Types I and III were lower than Type II, being Type II the most critical delamination.

3.2. Relation between Fiber Orientation and Fiber Position in Laminate Respect to Machining Direction

Delamination measurement is needed to justify the phenomenon that occurs when machining a plain weave sample. Relation between fiber orientation and position in the laminate to machining direction is an important parameter. Position fiber refers to the point where tool hits the width of the

yarn. Two different kinds of delamination can be found: uniform and sine wave form. On the trimmed edge, delamination is uniform if the machining direction is aligned with fiber orientation. Delamination can be low or high, depending on the position the tool hits the yarn (Figure 8). Low delamination occurs when tool trajectory is into the space between yarns, while higher delamination occurs if the tool trajectory passes in the center of the yarn.

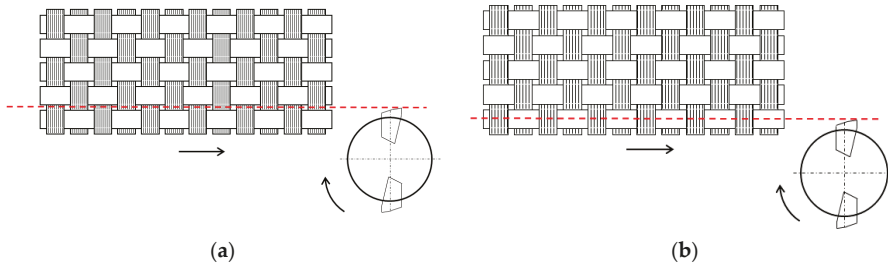


Figure 8. (a) Low uniform delamination; (b) High uniform delamination.

Sine wave form is appreciated when machining direction is slightly inclined (α°) in respect to the fiber orientation (Figure 9), due to movement in the yarns during RTM process or tool position during machining.

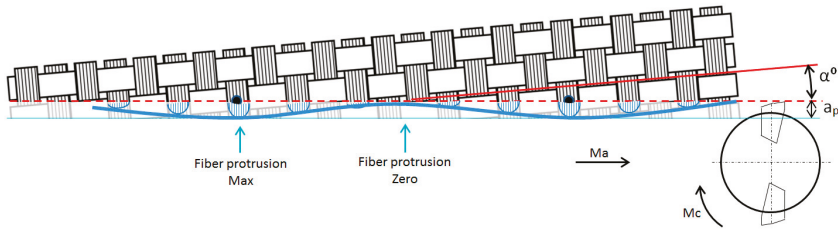


Figure 9. Sine wave effect.

Figure 10 shows values of Sd for every fill yarn, and the wave effect described previously can be appreciated. Red numbers show deformation in the plain weave and yellow maximums and minimums. Depending on the inclination of the cutting path to the yarn, the amplitude of the sine wave varies.

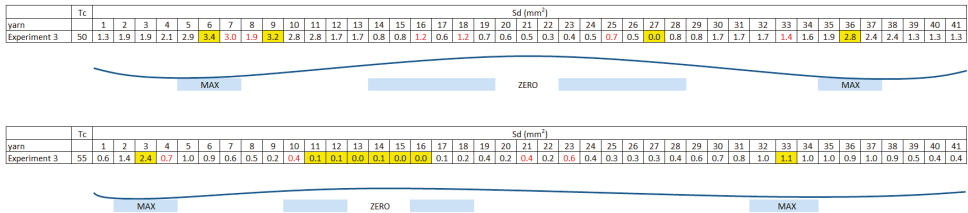


Figure 10. Sine wave effect.

3.3. Definition of Sd/L Parameter to Compare Delamination Values

To compare delamination types among experiments a delamination parameter (Sd/L) is needed. In this parameter, a length (L) of 80 mm is evaluated, as well as the measured area of each type of delamination (as shown in Tables 3 and 4). This parameter is similar to the one used to measure Ra in surface roughness. Table 5 shows Sd/L parameter, with cutting length (CL) and Xd measured.

Table 5. Sd/L parameter.

Test	Vc	Fz	ap	Tc	Vb	CL (m)	Sd/L (mm)				Xd (mm)		Trend Type II
							Type I	II	III	II + III	Left	Right	
1	470	0.1	0.5	30	0.049	35.9	0.05	0.08	0.00	0.08	1.88	1.8	Sd ↓
				55	0.057	65.8	0.09	0.13	0.07	0.20	0.91	0.94	uniform
				80	0.072	95.7	0.08	0.05	0.06	0.11	1.17	2.74	Sd ↓
2	470	0.4	1.5	5	0.211	23.9	0.27	1.15	0.18	1.33	-	-	-
				10	0.232	47.9	0.38	0.54	0.37	0.91	-	-	-
				30	0.247	143.6	0.38	0.52	0.22	0.74	-	-	-
3	300	0.1	1.5	30	0.032	22.9	0.08	0.13	0.00	0.13	0.9	0.95	uniform
				55	0.047	42.0	0.12	0.13	0.06	0.20	1.1	1.16	Sd ↓
				80	0.073	61.1	0.12	0.31	0.03	0.35	2.1	1.5	Sd ↑
4	300	0.4	0.5	30	0.041	91.7	0.17	0.18	0.08	0.25	2.11	2.3	uniform
				55	0.048	168.1	0.13	0.07	0.02	0.09	2.35	1.57	Sd ↓
				80	0.063	244.5	0.14	0.13	0.09	0.22	2.71	1.93	Sd ↓

Xd measurement is difficult. It can only be measured in the edges of the laminate (left Xd and right Xd). These values allow the calculation of the machining path of the tool on the yarn. Theoretical values of Xd did not coincide with observed values in every fill yarn along the length of the laminate, because plain weave form fibers move and deform in the mold during the RTM process because of injection pressure and plain weave manipulation. Due to this, expected area (Sd) value in Type II delamination did not coincide with the measured value.

A qualitative trend can be observed, distinguished between, if the cutting tool path was inclined or not. If machining cutting (edge trimmed) advances to a yarn crossing, Sd decreases, and a value lower than expected is obtained (Sd ↓). If machining cutting path advances to a yarn center Sd increases, and a value higher than expected is obtained (Sd ↑). In every experiment, it can be explained why Sd is different than expected (Figure 11).

If the yarn direction and cutting path are coincident, Sd values in Type II of delamination are uniform (Figure 12) along the length, for instance Test 1 at 55 min, Test 3 at 30 min and Test 4 at 30 min.

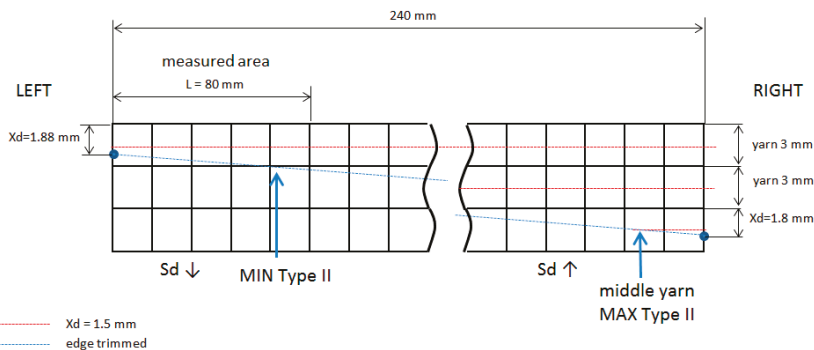


Figure 11. Xd values and cutting path in Test 1 at 30 min.

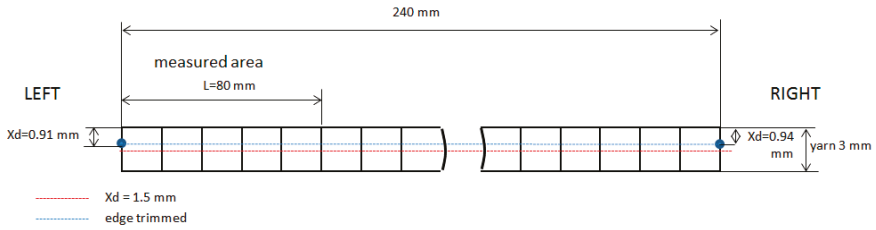


Figure 12. X_d values and cutting path in Test 1 at 55 min.

Figures 13 and 14 show experiments to appreciate movements of the weave plain during resin transfer molding (RTM) process.

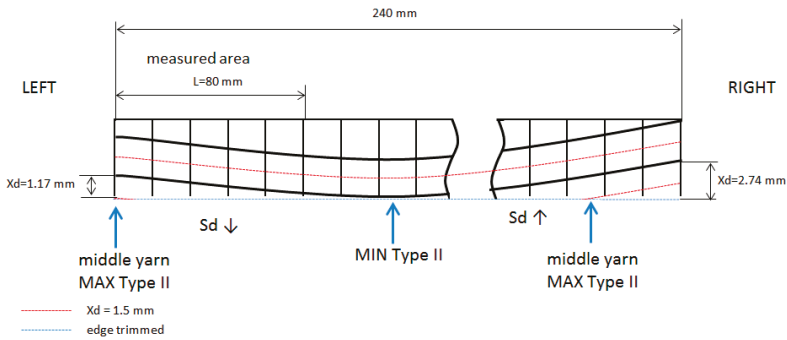


Figure 13. X_d values and cutting path in Test 1 at 80 min.

In every experiment, parameter S_d/L is represented by each delamination type (Figure 15). Values of these parameters are similar in all experiments, except Experiment 2, because of the high flank wear of the tool.

Results of S_d/L , taking into account values of X_d , are shown in Figure 16. For instance, in Experiment 1 at 30 min and 80 min, trend for S_d is lower ($S_d \downarrow$) than the real value. For this reason, the points of the graph are not increasing.

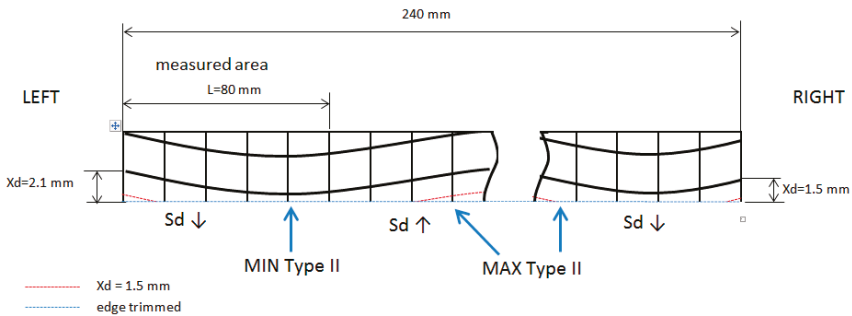


Figure 14. X_d values and cutting path in Test 3 at 80 min.

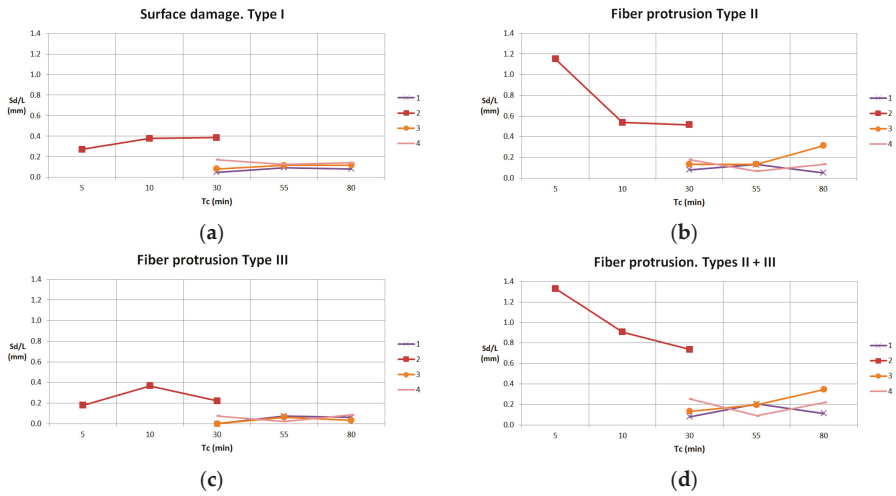


Figure 15. (a) Sd/L values for Type I delamination; (b) Sd/L values for Type II delamination; (c) Sd/L values for Type III delamination; (d) Sd/L values for Types II and III delamination.

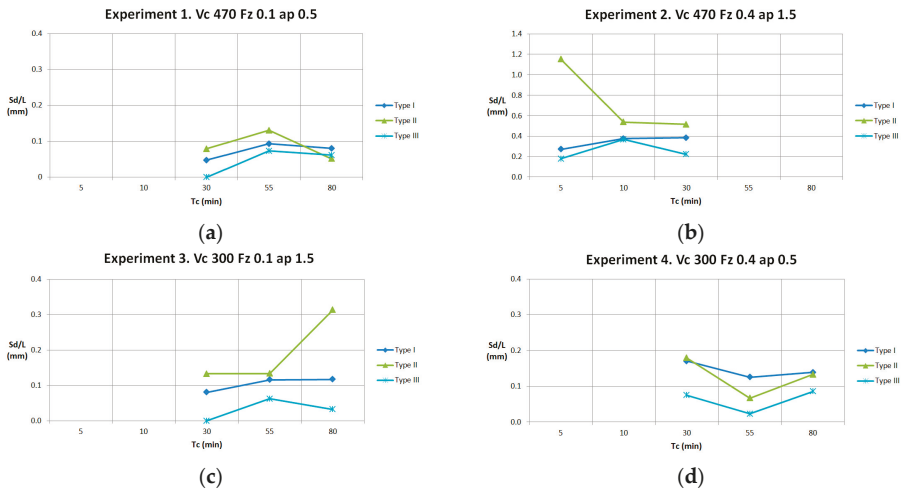


Figure 16. (a) Sd/L in Experiment 1; (b) Sd/L in Experiment 2; (c) Sd/L in Experiment 3; (d) Sd/L in Experiment 4.

3.4. Relation between Tool Wear and Delamination Parameters

High cutting conditions provokes high delamination and, in consequence, high tool wear, avoiding machining. In Figure 17, flank wear is shown at Experiments 2 and 3, with Vb values of 0.247 and 0.073 mm respectively.

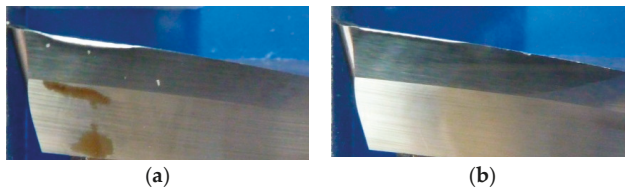


Figure 17. (a) Flank wear in Experiment 2; (b) Flank wear in Experiment 3.

In Experiments 1, 3 and 4, after machining 80 min, flank wear does not reach the maximum tool wear to avoid machining, having a linear behavior and maintaining a low value (maximum flank wear tool is 0.073 mm), allowing machining until 240 m. For this reason, delamination is low and very similar in all experiments (Figures 18 and 19).

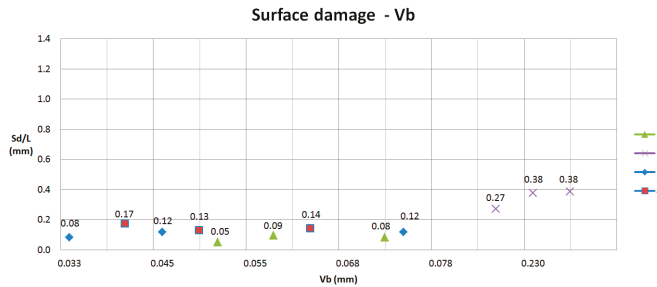


Figure 18. Sd/L respect Vb for surface damage (Type I).

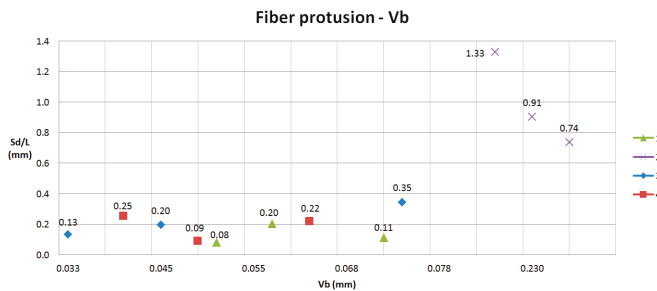


Figure 19. Sd/L respect Vb for fiber protrusion (Types II and III).

4. Conclusions

This paper evaluates delamination in edge trimming of basalt fiber reinforced plastics (BFRP), manufactured by resin transfer molding (RTM), varying cutting conditions (cutting speed, feed rate and depth of cut) and fiber volume fraction. Cutting tool selection has been an important issue, allowing machining large cutting lengths and maintaining a low flank wear.

Delamination appears in the top layer of the laminate with a high fiber volume fraction (60%). If fiber volume is lower, resin layer at the top prevent delamination defect. In plain weave sample machining, relation between fiber orientation and position in the laminate to machining direction generate two different kinds of delamination: uniform and sine wave form.

Three types of delamination (I, II and III) have been evaluated, increasing their values as cutting speed and feed rate increases. Delamination values are maintaining in low values, allowing cutting lengths until 240 m, except with high cutting conditions. In this case, cutting is not possible for a high tool wear, which provokes high delamination.

Delamination prediction is not an easy task, because of its random nature. This is due to the movement of fibers during the RTM process and the position of the trimmed edge to the yarns. To explain delamination values of each type, a parameter relating surface areas and length (S_d/L) has been evaluated, together with the distance of the warp yarn from the trimmed edge until the next dip below the crossing fill yarn (X_d).

Type II delamination is the most usual. In Type II delamination the maximum value of fiber protrusion is higher than depth of cut, because originally the fill yarn has a sine wave form and after cutting the yarn is stretched. For this reason, depth of cut is an important variable in delamination values.

Author Contributions: M.D.N.-M., M.D.M. and J.A.G.-M. proposed the topic of this study and designed the process; M.D.N.-M. and I.O. performed the experiments and analyses; M.D.N.-M., M.D.M. and A.I.S. performed the analysis and wrote the paper.

Funding: The authors gratefully acknowledge the funding by the Ministerio de Educación y Ciencia of the Spanish government under grant DPI2013-44903-R-AR.

Acknowledgments: The authors acknowledge collaboration and cutting tools provided by Mitsubishi Materials.

Conflicts of Interest: The authors declare no conflicts of interest.

References

1. Teti, R. Machining of composite materials. *CIRP Ann. Manuf. Technol.* **2002**, *51*, 611–634. [[CrossRef](#)]
2. Voss, R.; Seeholzer, L.; Kuster, F.; Wegener, K. Influence of fibre orientation, tool geometry and process parameters on surface quality in milling of CFRP. *CIRP J. Manuf. Sci. Technol.* **2017**, *18*, 75–91. [[CrossRef](#)]
3. Lopresto, V.; Caggiano, A.; Teti, R. High Performance Cutting of Fiber Reinforced Plastic Composite Materials. *Proc. CIRP* **2016**, *46*, 71–82. [[CrossRef](#)]
4. König, W.; Grass, P. Quality definition and assessment in drilling of fibre reinforced thermosets. *CIRP Ann. Manuf. Technol.* **1989**, *38*, 119–124. [[CrossRef](#)]
5. Colligan, K.; Ramulu, M. The effect of edge trimming on composite surface plies. *Manuf. Rev. (USA)* **1992**, *5*, 274–283.
6. Azmi, A.I.; Lin, R.J.T.; Bhattacharyya, D. Machinability study of glass fibre-reinforced polymer composites during end milling. *Int. J. Adv. Manuf. Technol.* **2013**, *64*, 247–261. [[CrossRef](#)]
7. Davim, J.P.; Reis, P. Damage and dimensional precision on milling carbon fiber-reinforced plastic using design experiments. *J. Mater. Process. Technol.* **2005**, *160*, 160–167. [[CrossRef](#)]
8. Davim, J.P.; Campos Rubio, J.; Abrao, A. A novel approach based on digital image analysis to evaluate the delamination factor after drilling composite laminate. *Compos. Sci. Technol.* **2007**, *67*, 1939–1945. [[CrossRef](#)]
9. Gaitonde, V.N.; Karnik, S.R.; Campos Rubio, J.; Esteves Correia, A.; Abrão, A.M.; Davime, J.P. Analysis of parametric influence on delamination in high-speed drilling of carbon fiber reinforced plastic composites. *J. Mater. Process. Technol.* **2008**, *1–3*, 431–438. [[CrossRef](#)]
10. Hintze, W.; Hartmann, D.; Schütte, C. Occurrence and propagation of delamination during the machining of carbon fibre reinforced plastics (CFRPs)—An experimental study. *Compos. Sci. Technol.* **2011**, *71*, 1719–1726. [[CrossRef](#)]
11. Hintze, W.; Cordes, M.; Koerkel, G. Influence of wear structure on delamination when milling CFRP. *J. Mater. Process. Technol.* **2015**, *216*, 199–205. [[CrossRef](#)]
12. Razfar, M.R.; Zanjani Zadeh, M.R. Optimum damage and surface roughness prediction in end milling glass fibre-reinforced plastics, using neural network and genetic algorithm. *Proc. Inst. Mech. Eng. Part B J. Eng. Manuf.* **2009**, *223*, 653–664. [[CrossRef](#)]
13. Sheikh-Ahmad, J.Y.; Dhuttargaon, M.; Cheraghi, H. New tool life criterion for delamination free milling of CFRP. *Int. J. Adv. Manuf. Technol.* **2017**, *92*, 2131–2143. [[CrossRef](#)]

14. Sheikh-Ahmad, J.Y.; Urban, N.; Cheraghi, H. Machining Damage in Edge Trimming of CFRP. *Mater. Manuf. Process.* **2012**, *27*, 802–808. [[CrossRef](#)]
15. Navarro, M.D.; Meseguer, M.D.; Sánchez, A.I.; Gutiérrez, S.C. Tool wear study in edge trimming on basalt fibres reinforced plastics. *Proced. Manuf.* **2017**, *13*, 259–266. [[CrossRef](#)]
16. Lopresto, V.; Leone, C.; De Iorio, I. Mechanical characterisation of basalt fibre reinforced plastic. *Compos. Part B* **2011**, *42*, 717–723. [[CrossRef](#)]
17. Fiore, V.; Scalici, T.; Di Bella, G.; Valenza, A. A review on basalt fibre and its composites. *Compos. Part B* **2015**, *74*, 74–94. [[CrossRef](#)]
18. Fiore, V.; Di Bella, G.; Valenza, A. Glass-basalt/epoxy hybrid composites for marine applications. *Mater. Des.* **2011**, *32*, 2091–2099. [[CrossRef](#)]



© 2018 by the authors. Licensee MDPI, Basel, Switzerland. This article is an open access article distributed under the terms and conditions of the Creative Commons Attribution (CC BY) license (<http://creativecommons.org/licenses/by/4.0/>).

Article

Analysis of Force Signals for the Estimation of Surface Roughness during Robot-Assisted Polishing

Beatriz de Agustina ^{1,*}, Marta María Marín ¹, Roberto Teti ² and Eva María Rubio ¹

¹ Department of Manufacturing Engineering, Universidad Nacional de Educación a Distancia (UNED), C/Juan del Rosal 12, E28040 Madrid, Spain; mmarin@ind.uned.es (M.M.M.); erubio@ind.uned.es (E.M.R.)

² Department of Chemical, Materials and Industrial Production Engineering, University of Naples Federico II, Piazzale Tecchio, 80, 80125 Naples, Italy; roberto.teti@unina.it

* Correspondence: bdeagustina@ind.uned.es; Tel.: +34-91-398-6448

Received: 11 July 2018; Accepted: 13 August 2018; Published: 15 August 2018

Abstract: In this study feature extraction of force signals detected during robot-assisted polishing processes was carried out to estimate the surface roughness during the process. The purpose was to collect significant features from the signal that allow the determination of the end point of the polishing process based on surface roughness. For this objective, dry polishing turning tests were performed on a Robot-Assisted Polishing (RAP) machine (STRECON NanoRAP 200) during three polishing sessions, using the same polishing conditions. Along the tests, force signals were acquired and offline surface roughness measurements were taken at the end of each polishing session. As a main conclusion, it can be affirmed, regarding the force signal, that features extracted from both time and frequency domains are valuable data for the estimation of surface roughness.

Keywords: robot-assisted polishing; force signal; surface roughness; end point detection

1. Introduction

These days, finishing processes such as polishing are not yet fully automated in manufacturing industries. Traditionally, polishing has largely been a manual operation that is very labor-intensive, highly skill-dependent, inefficient due to long processing times, high-cost, error-prone, and hazardous due to abrasive dust [1]. For this reason, a considerable percent of the total time required for manufacturing products such as dies, molds, machine tools, and optical components is spent on the finishing operations, which account for approximately 30% to 50% of the manufacturing time [2,3].

Due to the fact that polishing is not performed by position control but by pressure control, efforts towards automated polishing have mainly focused on the identification and the execution of the motions involved in manual polishing techniques, performing under a desired contact force exerted on the tool [4]. This is an important challenge in die polishing, especially for the manufacturing of components with complex shapes and machine tools that contain freeform surfaces and functional relevant edges.

The automated polishing systems developed until now can employ a conventional machine tool structure or an articulated robot arm to hold the finishing tool. For both configurations, force control methods have been designed and can be broadly classified as active and passive force controls. Active force control systems measure and correct the force applied on the workpiece, independently of the tool path, and passive control systems rely on compliance in the tool itself to maintain a nominal contact force or rely on magnetic force to achieve this [1,5–7].

Also, the polishing tool-path has been controlled by the integration of intelligent network systems, using multiple vision sensors to capture images of the polished surface as input collected data [8]. Furthermore, tool-path planning methods based on contact mechanics have been designed for automated polishing [9–11].

Apart from the approaches made towards the tool-path planning for automated polishing processes, there are other studies focused on endpoint detection; this occurs when a certain target surface roughness value is reached, or it is required to replace the tool with another one with finer grain size and/or implement other polishing conditions. As a result, the polishing sequence can be improved. For this purpose, signals from different sensors have been employed to monitor the surface roughness obtained by polishing. In this scheme, signals from AE, motor current, and light sensors have been employed for the development of expert systems integrated with the data collected during the polishing process [2,6,12].

In this study, feature extraction of force signals detected during robot-assisted polishing processes was carried out to estimate the surface roughness during the process. The purpose was to collect significant features from the signal that allow the determination of the end point of the polishing process based on surface roughness. For this objective, dry polishing turning tests were performed on a Robot-Assisted Polishing (RAP) machine (STRECON NanoRAP 200) during three polishing sessions, using the same polishing conditions. During the tests, force signals were acquired and offline surface roughness measurements were taken at the end of each polishing session.

2. Experimental Procedure

The experimental procedure of this study as follows.

2.1. Polishing Tests

The polishing tests were performed by a Robot-Assisted Polishing (RAP) system (STRECON NanoRAP 200, Sønderborg, Denmark) fitted with a robotic arm in which interchangeable polishing tools are mounted. Four cutting parameters can be set up by the integration of a control module in the robotic arm: cutting speed, feed rate, the contact force between the tool and workpiece, and the tool pulsation in the feed direction. Three sessions of polishing tests (60 polishing passes each one) were carried out on a cylindrical probe of alloy steel (UNS G52986) with a length of 75 mm and diameter of 30 mm (Figure 1). The same cutting parameters were employed for all polishing sessions: spindle speed of 300 rpm, feed rate of 5 mm/s, tool pulsation in the feed direction of 500 pulses/min on a length of 1 mm and a contact force of 9.8 N (movement indicated in Figure 1). The abrasive tool selected has a grit number of 800, which corresponds to a grain size of approximately 11 μm from Gesswein (MP800) according to the Commercial Standard CS271-65 [13].



Figure 1. Robot-Assisted Polishing (RAP) machine.

2.2. Acquisition of Force Signal during Polishing Tests

A gauge was employed to detect the force signal during the polishing tests. First of all, a calibration process was made to establish a relationship between the voltage signal generated on the gauge device and the corresponding force. Table 1 shows the different forces (N) used and the voltage signal recorded. For the polishing tests, signal samples were taken with an interval time

between acquisitions of, approximately, 0.93 s. That is, across the three polishing sessions (180 passes), there was a total of 2790 acquisitions, with 16,384 data points for each acquisition. The sample rate was set up for 50 kHz.

Table 1. Values of forces and the corresponding voltage signal generated during the calibration.

Forces (N)	Voltage Signals (V)
0.0	0.00025
0.98	0.0035
1.96	0.0071
2.94	0.011
4.9	0.0185
6.86	0.0263

At this point, it is important to remark that the signal force plotted on the different figures along the present paper is expressed in volts; the objective is to show a trend of the values of forces rather than calculating their absolute values.

2.3. Surface Roughness Measurements

Five offline surface roughness measurements were taken on the workpiece (on one of its generatrix) at the end of the each polishing session, using a roughness MahrSurf XD1 (Mahr, Göttingen, Germany) tester equipped with a radius tip of 2 μm . The cut-off selected was 0.25 mm and the evaluation length was 1.25 mm. In the measurement process, data (x_i, z_i) of the surface geometry workpiece were registered for the determination of the arithmetical average roughness parameter, R_a . According to ISO 4288 (ISO 4288, 1996) [14] standards, such a parameter is defined as the arithmetical average of the absolute values of the deviations of the roughness profile, R , and is expressed mathematically by means of Equation (1):

$$R_a = \frac{1}{l_m} \int_0^{l_m} |z(x)| dx. \quad (1)$$

2.4. Analysis of Force Data

Row force signal data arrays, each with 16,384 values, are stored and analyzed by Matlab software (R2011b, Mathworks, Natick, MA, USA). Different features were calculated from both the time and frequency domains. In the time domain, a preliminary analysis was made. Different statistical features were calculated from the 2790 signal acquisitions and plotted for each feature. For those feature plots in which a trend can be clearly observed, the average and variance were also determined for each polishing session at the last three passes.

In the frequency domain, *FFT* (Fast Fourier Transform) power spectral graphics at different polishing time were plotted. The objective is to select a range or ranges of frequencies in which the amplitudes of certain peaks shown in their corresponding *FFT* power spectral plots may change over time, just as the AE (Acoustic Emission) signal detected during polishing has been processed in previous studies [15–17].

Once the range of frequencies was selected, the maximum amplitude was calculated from all the force signal acquisitions registered. Afterwards, the average and variance were also calculated for each polishing session at the last three passes.

Finally, an analysis of the features extracted from the time and frequency was carried out to identify a possible trend and a correlation with the surface roughness.

3. Results and Discussion

The resultant R_a calculated for each polishing session, together with the surface roughness measured before polishing, is represented in the Figure 2.

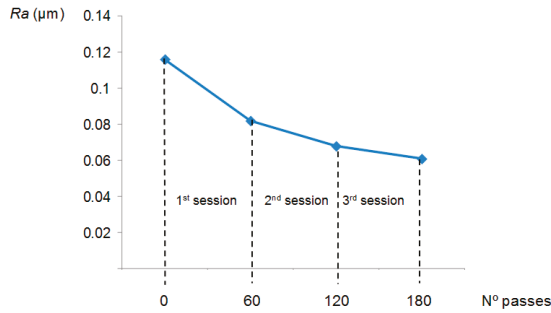


Figure 2. Ra versus polishing passes obtained at the end of each polishing session.

As was expected, Ra decreased with the number of passes. In a first step (1st polishing session) the decrease is more accentuated due to the higher quantity of material removed in the first stage of polishing. Hereafter, the analysis of the different features extracted from the force signal is shown and discussed. At time domain, among all the statistical features calculated from the row force signal, only average and variance follow a trend with polishing time, designated in this study as $F_{average}$ and $F_{variance}$. This can be observed in Figures 3 and 4.

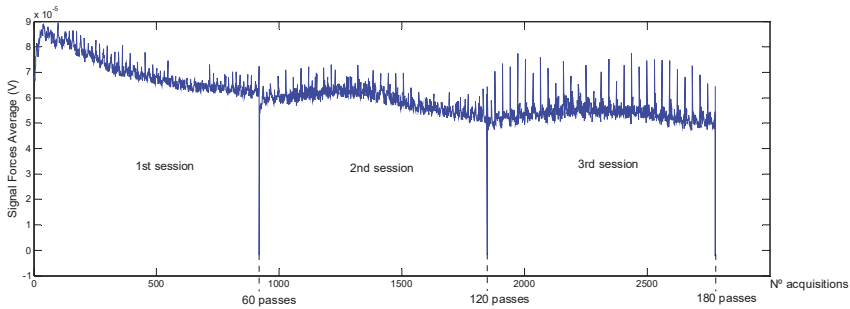


Figure 3. Signal forces average ($F_{average}$) during the three polishing sessions.

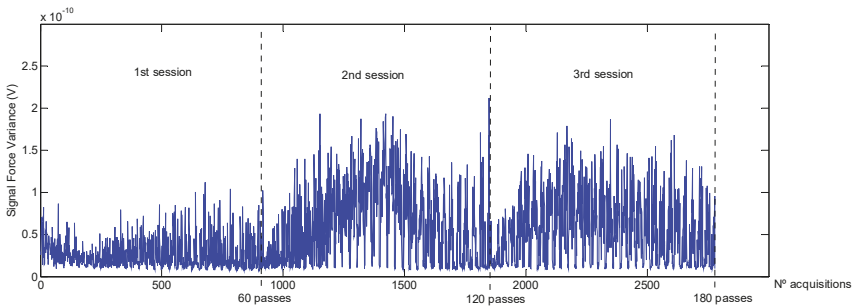


Figure 4. Signal forces variance ($F_{variance}$) during the three polishing sessions.

Moreover, the fact that Ra hardly decreased during the last session (3rd polishing session), from 0.068 to 0.061 µm, indicates that endpoint detection was almost reached. Also, this can be expected as the force signal in the last session presents a periodical form that does not vary with time (Figure 3).

The trend followed by $F_{average,a}$ (Figure 5a) is the same as Ra ; it decreases with the number of passes, to a major extent, at the beginning of the process, which indicates that this parameter extracted from the force signal could be used for the estimation of Ra during the polishing process. In addition, as was previously pointed out, the quantity of material removed or metal removal rate (MRR) decreases with the polishing passes. This parameter also has a direct relationship with the contact force according to the following expression [18]:

$$MRR = \frac{2kr_{avg}Fs}{H_w f A}, \tag{2}$$

where k is a constant r_{avg} , the average size of the grain tool, F the contact force, s , the rotational speed, f , the feed rate, H_w , the workpiece hardness, and A the contact area between the tool and the workpiece. In spite of the fact that, for all the polishing tests, a constant contact force was applied, contact force and its variations detected along the tests, represented by the parameter $F_{average,a}$, follow the same trend that the Ra values obtained. Regarding the rest of the parameters calculated, $F_{average,v}$, $F_{variance,a}$ and $F_{variance,v}$, it can be seen that their tendency is inversely proportional to Ra (Figures 5 and 6).

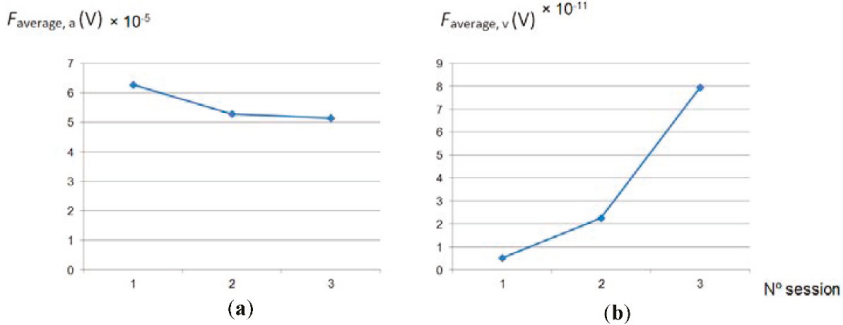


Figure 5. Signal: (a) arithmetical average and (b) variance, calculated from signal forces average versus number polishing session.

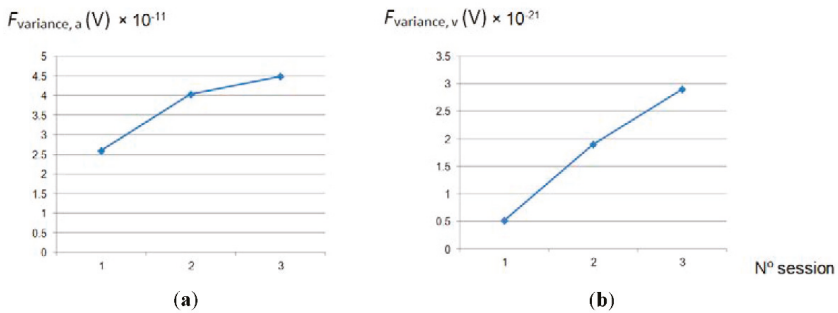


Figure 6. (a) Arithmetical average and (b) variance, calculated from signal forces variance versus number polishing session.

From the analysis on frequency domain, according to the peaks shown in the FFT power spectral representations, the range selected was between 100 and 1000 Hz. Maximum amplitudes calculated from each acquisition along the three polishing sessions are plotted in Figure 7.

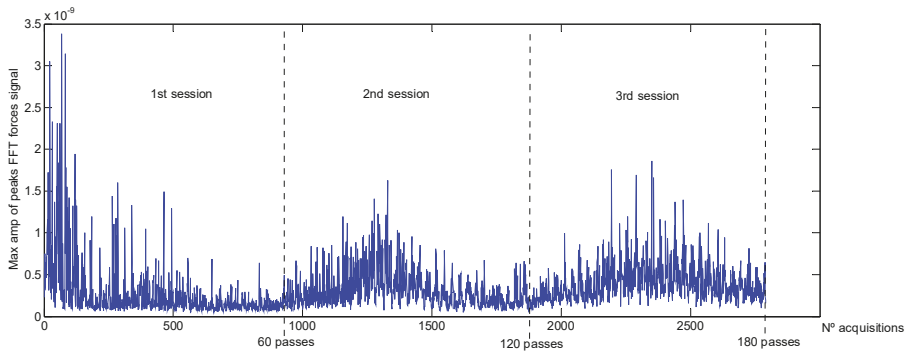


Figure 7. Maximum amplitudes of FFT power spectral of forces signal (100–1000 Hz).

Finally, the average of the amplitudes FFT power spectral was calculated for each polishing session and shown in Figure 8. It can be seen that the relationship with *Ra* is inverse (see Figure 2) and therefore, it can be considered a valuable parameter for the monitoring of the surface roughness. Nevertheless, this dependency varied within the polishing session: during the 1st polishing session, the parameter decreased with the number of passes and, during the other two sessions, the graphic exhibits a maximum around the middle of the polishing session (Figure 7). Taking this into account, the implementation of this parameter as input data to predict the surface roughness must be considered, together with the number polishing passes.

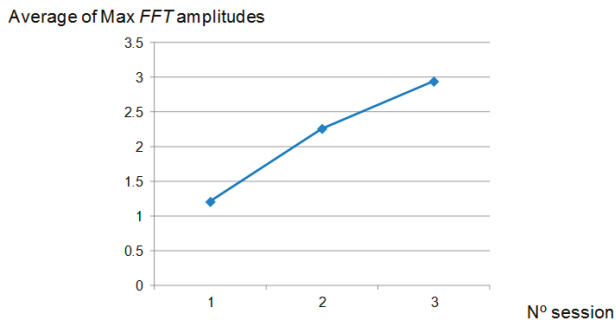


Figure 8. Arithmetical average calculated from maximum amplitudes of FFT power spectral of forces signal versus number of polishing session.

4. Conclusions

In this work, an evaluation of the signal forces detected during Robot-Assisted Polishing (RAP) by a STRECON NanoRAP 200 machine was studied. Dry polishing turning tests, under the same cutting conditions, were performed on a cylindrical probe of alloy (UNS G52986) using a tool with a grit number of 800. This semiautomatic polishing system allows the setting of not only conventional polishing parameters such as cutting speed and feed rate, but also the contact force between the tool and workpiece and the tool pulsation in the feed direction. It obtained the trends of different features from the force signal and the surface roughness along the polishing processes to evaluate whether the mentioned features are valuable data for the estimation of *Ra*. For this purpose, an analysis of the force signal, in both the time and frequency domains, detected during the process was made with the objective of finding a feature or features sensitive to the variations of the surface roughness (*Ra*)

measured at the end of three polishing sessions. The main conclusions extracted from the results obtained in this study can be summarized as follows:

- After 180 polishing passes under the polishing conditions used in this study, the endpoint detection is almost reached; this is after 45 min of polishing under the cutting conditions employed in this study.
- In spite of the fact that for the all the polishing tests a constant contact force between the tool and the workpiece was applied, different features extracted from the signal force detected during the process can be considered valuable data for the indirect evaluation of surface roughness.
- In the time domain, average and variance were calculated for each acquisition of force signal and from these signals a feature per polishing session (average and variance) was extracted to compare with the surface roughness, designated in this study by $F_{average,a}$, $F_{average,v}$, $F_{variance,a}$ and $F_{variance,v}$. This makes their relationship with the surface roughness, in the case of $F_{average,a}$, proportional, and in the case of $F_{average,v}$, $F_{variance,a}$ and $F_{variance,v}$, inversely proportional.
- In the frequency domain, within the range of frequencies between 100 and 1000 Hz a feature was calculated. This is the maximum amplitude of the peak reached in the range of frequencies for each acquisition of force signal. The average calculated per polishing session is inversely proportional to the surface roughness, so it is a valuable feature for the estimation of Ra in polishing processes.
- Finally, for future research it is proposed to collect valuable data from the force signal (concretely average feature according to this study) during polishing processes, together with features extracted from other sensors, to further develop polishing systems.

Author Contributions: Conceptualization R.T.; Methodology, B.d.A. and R.T.; Software, B.d.A. and R.T.; Validation, B.d.A., M.M.M., R.T. and E.M.R.; Formal Analysis, B.d.A., M.M.M., R.T. and E.M.R.; Investigation, B.d.A., M.M.M., R.T. and E.M.R.; Resources, B.d.A., M.M.M., R.T. and E.M.R.; Data Curation, B.d.A., M.M.M., R.T. and E.M.R.; Writing—Original Draft Preparation, B.d.A.; Writing—Review & Editing, B.d.A., M.M.M., R.T. and E.M.R.; Visualization, B.d.A., M.M.M., R.T. and E.M.R.; Supervision, R.T. and E.M.R.; Funding Acquisition, B.d.A., M.M.M., R.T. and E.M.R.

Funding: This research was funded by the European project (FP7 IFaCOM reference: 285489), the Spanish Ministry of Science and Innovation (Project DPI2011-27135), and the Industrial Engineering School—UNED (Projects (Ref: 2018-ICF03, Ref: 2018-IFC09 and Ref: 2018-ICF05)).

Acknowledgments: The authors thank the “Industrial Production and Manufacturing Engineering (IPME)” research group of the UNED for support during the development of this work.

Conflicts of Interest: The authors declare no conflict of interest.

References

1. Liao, L.; Xi, F.; Liu, K. Modeling and control of automated polishing/deburring process using a dual-purpose compliant tool head. *Int. J. Mach. Tools Manuf.* **2008**, *48*, 1454–1463. [[CrossRef](#)]
2. Ahn, J.H.; Shen, Y.F.; Kim, H.Y.; Jeong, H.D.; Cho, K.K. Development of a sensor information integrated expert system for optimizing die polishing. *Robot. Comput. Integr. Manuf.* **2001**, *17*, 269–276. [[CrossRef](#)]
3. Yin, Y.H.; Hu, H.; Xia, Y.C. Active tracking unknown surface using force sensing and control technique for robot. *Sens. Actuators A Phys.* **2004**, *112*, 313–319. [[CrossRef](#)]
4. Güvenç, L. An overview of robot-assisted die and mold polishing with emphasis on process modeling. *J. Manuf. Syst.* **1997**, *16*, 48–58. [[CrossRef](#)]
5. Yoshikawa, T. Dynamic hybrid position/force control of robot manipulators—description of hand constraints and calculations of joint driving force. *J. Robot. Autom.* **1987**, *3*, 386–392. [[CrossRef](#)]
6. Huissoon, J.P.; Ismail, F.; Jafari, A.; Bedi, S. Automated polishing of die steel surfaces. *Int. J. Adv. Manuf. Technol.* **2002**, *19*, 285–290. [[CrossRef](#)]
7. Kakinuma, Y.; Igarashi, K.; Katsura, S.; Aoyama, T. Development of 5-axis polishing machine capable of simultaneous trajectory, posture, and force control. *CIRP Ann. Manuf. Technol.* **2013**, *62*, 379–382. [[CrossRef](#)]
8. Kuo, R.Y.; Cohen, P.H. Manufacturing process control through integration of neural network and fuzzy model. *Fuzzy Sets Syst.* **1998**, *98*, 15–31. [[CrossRef](#)]

9. Rososhansky, M.; Xi, F. Coverage based tool-path planning for automated polishing using contact mechanics theory. *J. Manuf. Syst.* **2011**, *30*, 144–153. [[CrossRef](#)]
10. Warkentin, A.; Ismail, S.; Bedi, F. Intersection approach to multi-point machining of sculptured surfaces. *Comput. Aided Geom. Des.* **1998**, *15*, 567–584. [[CrossRef](#)]
11. Klocke, F.; Dambon, O.; Schneider, U.; Zunke, R.; Waechter, D. Computer-based monitoring of the polishing processes using LabView. *J. Mater. Process. Technol.* **2009**, *209*, 6039–6047. [[CrossRef](#)]
12. Kim, S.Y.; Park, C.J.; Seo, Y.J. Signal analysis of the end point detection method based on motor current. *Microelectron. Eng.* **2003**, *66*, 472–479. [[CrossRef](#)]
13. *Commercial Standard CS 271-65. Grading of Abrasive Grain for Grinding Wheels*; U.S. Department of Commerce: Washington, DC, USA, 12 April 1965.
14. *ISO 4288:1996 Geometrical Product Specifications (gps). Surface Texture: Profile Method. Rules and Procedures for the Assessment of Surface Texture*; ISO: Genève, Switzerland, 1996.
15. Chang, Y.P.; Hashimura, M.M.; Dornfeld, D.A. An investigation of the AE Signals in the lapping process. *CIRP Ann. Manuf. Technol.* **1996**, *45*, 331–334. [[CrossRef](#)]
16. Lazarev, R. Monitoring and Control of Fine Abrasive Polishing Processes. Ph.D. Thesis, University of Southern Denmark, Sønderborg, Denmark, 2012.
17. Agustina, B.; Marin, M.M.; Teti, R.; Rubio, E.M. Surface roughness evaluation based on acoustic emission signals in Robot Assisted Polishing. *Sens. Actuators A Phys.* **2014**, *14*, 21514–21522. [[CrossRef](#)] [[PubMed](#)]
18. Ahn, J.H.; Lee, M.C.; Jeong, H.D.; Kim, S.R.; Cho, K.K. Intelligently automated polishing for high quality surface formation of sculptured die. *J. Mater. Process. Technol.* **2002**, *133–134*, 339–344. [[CrossRef](#)]



© 2018 by the authors. Licensee MDPI, Basel, Switzerland. This article is an open access article distributed under the terms and conditions of the Creative Commons Attribution (CC BY) license (<http://creativecommons.org/licenses/by/4.0/>).

Article

Characterization of a New Dry Drill-Milling Process of Carbon Fibre Reinforced Polymer Laminates

Alessandra Caggiano ^{1,2}, Ilaria Improta ³ and Luigi Nele ^{3,*}

¹ Fraunhofer Joint Laboratory of Excellence on Advanced Production Technology (Fh-J_LEAPT UniNaples), 80125 Naples, Italy; alessandra.caggiano@unina.it

² Department of Industrial Engineering, University of Naples Federico II, 80125 Naples, Italy

³ Department of Chemical, Materials and Industrial Production Engineering, University of Naples Federico II, 80125 Naples, Italy; ilaria.improta@unina.it

* Correspondence: luigi.nele@unina.it; Tel.: +39-0817682376

Received: 2 July 2018; Accepted: 13 August 2018; Published: 18 August 2018

Abstract: Carbon Fibre Reinforced Polymer (CFRP) composites are widely used in aerospace applications that require severe quality parameters. To simplify the assembly operations and reduce the associated costs, the current trend in industry is to optimize the drilling processes. However, the machining of CFRP composites is very challenging compared with metals, and several defect types can be generated by drilling. The emerging process of orbital drilling can greatly reduce the defects associated with the traditional drilling of CFRP, but it is a more complex process requiring careful process parameters selection and it does not allow for the complete elimination of the thrust force responsible for delamination damage. As an alternative to traditional and orbital drilling, this work presents a new hole making process, where the hole is realized by a combination of drilling and peripheral milling performed using the same cutting tool following a novel tool path strategy. An original tool design principle is proposed to realize a new drill-milling tool, made of a first drilling and a subsequent milling portion. Two different tool configurations are experimentally tested to evaluate the performance of the newly-conceived combined drill-milling process. This process is quick and easy, and the experimental results show an improvement in the drilled hole quality.

Keywords: CFRP; hole making; dry machining; roughness

1. Introduction

Carbon fibre reinforced polymer (CFRP) composites are widely used in the aerospace industry. In this sector, the prevalent machining process performed on CFRP components is drilling, as mechanical joining by means of rivets or bolts represents the most common joining technique for aircraft components. However, the drilling of CFRP is very challenging in comparison with the drilling of metals, as the phenomena underlying the material removal for composite materials are substantially different from those characteristic of metal machining [1]. The different properties of the reinforcement and matrix phases make the material removal mechanism highly complex, because of the heterogeneity and anisotropic behaviour of composites [1–3]. König [4] highlighted how the machining of composite materials depends on the specific properties and relative content of the reinforcement and matrix. Moreover, when machining fibre reinforced composite materials, fibre orientation plays a fundamental role, affecting the mechanism of chip formation and the cut surface quality. During the drilling process, because of the heterogeneous and anisotropic behaviour of the fibre reinforced composites, different kinds of damage can be generated in the workpiece, such as delamination, fibre pull-out, fibre breakage, matrix cracking, and thermal damage [5,6], which can affect the drilled component service life. The most relevant damage induced during CFRP drilling is delamination [7,8], which has been considered as the principal cause of notable reduction in the fatigue strength of

composite components, cutting down the long-term performance of the CFRP parts. In particular, delamination onset at the hole exit, also known as push-out delamination, is generated if the axial load exerted on the workpiece during drilling exceeds a threshold value [9]. As demonstrated by Davim and Reis [10], the delamination damage grows with increasing cutting speed and feed values. As a matter of fact, a feed rate increase raises the thrust force, with consequent delamination damage enlargement at the hole exit [11].

Moreover, tool geometry significantly affects the drilling induced damage [10,12]. Designing new tools with a better performance in terms of cost, damage reduction, and hole quality is a key factor for drilling process optimisation [12]. Piquet et al. [13] analysed the effects of drilling tool geometry, comparing the results obtained with a traditional tool and a specially designed cutting tool. Feito et al. [14] and Gaitonde et al. [15] demonstrated how the delamination increases with increasing the point angle of the twist drill bit for high speed drilling of CFRP laminates. Saudi et al. [16] developed a model to predict the critical thrust force responsible for exit-ply delamination during the drilling of multi-directional carbon fibre-reinforced plastic laminates with core drills made of diamond grits. Cadornin et al. [17] studied the mechanisms of damage and tool wear in the drilling of three-dimensional (3D) woven composite materials using diamond-coated carbide three lips twist drills. Zitoune et al. [18] investigated the influence of the tool coating on temperature and tool wear when drilling 3D woven composite materials using three types of cutting tools, one coated with a diamond layer and the other two coated with different nano-composite multi-layers, showing that the nature of the coating is a key factor affecting the temperature of machining.

To reduce the delamination and thermal damage defects generated when drilling composites, a new process called orbital drilling (OD) has been proposed in the literature. This process is more versatile than traditional drilling, as it allows for obtaining holes with different diameters without replacing the tool. OD is a circular ramp machining process, consisting of milling with a discontinuous peripheral cut and drilling with a continuous cut along the cutting-edge axis at the same time. Hence, this technology involves the simultaneous movement along a circular path (X , Y) and an axial advancement (Z) with a pre-determined step [19].

In OD, the orthogonal thrust exerted on the surface is very low, resulting in a superior hole quality, especially in the case of the composite materials subject to delamination damage. This type of machining process is particularly suitable for applications in the aeronautical field, as it allows for a decrease of cutting forces and temperatures, which results in a reduction of polymer matrix damage [20]. On the other hand, the main drawbacks related to OD concern the difficulties in selecting the proper process parameters and the need to employ a three-axis machining centre to avoid vibration problems. OD operations are carried out by portable and highly flexible machines, which tend to exhibit severe chatter and forced vibrations that lead to a poor hole quality. Moreover, the thrust force responsible for delamination is reduced but still not eliminated with OD [21]. As a matter of fact, while in traditional drilling, the axial loading consists of a concentrated load at the centre of the last ply of the laminate, in orbital drilling, the axial loading is determined by an eccentric distributed load, which acts along the cutting-edge of the mill [20].

As an alternative to both traditional drilling and orbital drilling processes, this research work proposes an innovative hole making process for CFRP components, where the hole is realised by a combination of drilling and peripheral milling, carried out using the same cutting tool. The objective is to further reduce the process-induced delamination damage in comparison with traditional and orbital drilling. To perform the new combined drill-milling process, an innovative drill-milling tool was developed. The main results of the experimental drill-milling tests on the CFRP composite laminates are reported in this paper, showing encouraging results in terms of the hole surface finish. The new drill-milling process is performed under dry conditions in a green technology perspective, offering advantages because of the absence of cutting fluids and a lower environmental impact.

2. Proposed Drill-Milling Process

In conventional drilling of fibre reinforced composite materials, in accordance with the model of linear elastic fracture mechanics, the delamination onset at the hole exit, also known as push-out, occurs if the axial load acting on the workpiece exceeds a threshold value [9,22]. The axial load performs a work equal to the sum of the energy necessary to deform the last ply of the laminate and the energy required to generate a new fracture surface [23].

For traditional drilling, the axial load evaluation generally refers to a concentrated load at the centre of the last ply of the laminate, as studied in the delamination analysis by Hocheng et al. [9,24]. Instead, for orbital drilling, an energy criterion characterized by the application of an eccentric distributed load, which acts along the cutting-edge of the mill, is adopted. This means that the thrust force causing delamination is reduced but not eliminated, as reported in Figure 1a,b [20].

To fully eliminate the drilling-induced delamination, a different original technique for CFRP hole making is proposed in this work, where the hole is realised by means of a combination of drilling and peripheral milling processes. In Figure 1c, the two phases of the process are illustrated, namely: in the first phase traditional drilling is employed to produce a hole with a smaller diameter than the final hole, and then, in the second phase, the material around the first hole is removed by peripheral milling until the final diameter is achieved. These two phases are sequentially combined in a single process carried out using the same cutting tool.

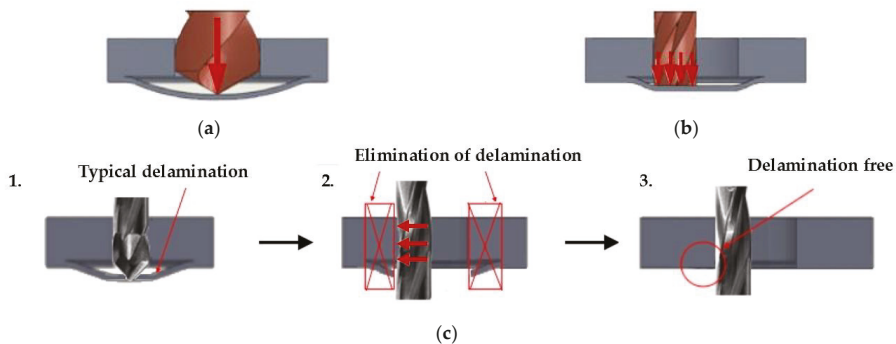


Figure 1. Representation of (a) traditional drilling; (b) orbital drilling [20] and (c) drill-milling processes. The red arrows indicate the load.

To develop this technique, an innovative drill-milling tool was designed and realized, and experimental cutting tests on CFRP laminates were performed to characterize the process. During the machining tests, the thrust force and radial force signals were detected through a sensor system to allow for the analysis of the cutting forces occurring during the process. Moreover, the produced holes were characterised via metrological and roughness measurement procedures to evaluate the hole quality in terms of size, roundness, and internal surface finish.

3. Materials and Methods

3.1. Preparation of the Specimen

The work-material employed for the drill-milling tests consisted of CFRP laminates composed of 26 prepreg plies, made of CYCOM 977-2, Cytec Industries Inc., Woodland Park, NJ, USA epoxy matrix, and Toray T300 unidirectional carbon fibres (Toray Industries, Inc., Tokyo, Japan), with stacking sequence $[\pm 45/0/\pm 45/90/\pm 45/0/-45/90/45/90]_s$. The main mechanical properties of the single unidirectional plies are reported in Table 1.

Table 1. Main mechanical properties of the unidirectional plies.

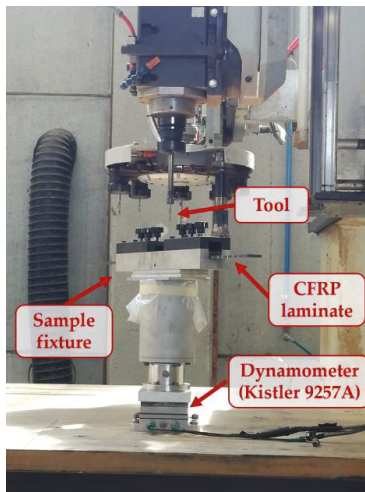
Property	Value
Young Modulus 0°	145 GPa
Tensile strength 0°	220 MPa
Young Modulus 90°	8.50 GPa
Tensile strength 90°	75 MPa

The nominal thickness of each CFRP laminate was 5 mm, and a thin fiberglass/epoxy ply reinforced with 0°/90° fabric was laid on the laminate front and back surfaces. In the aeronautical sector, it is common practice to apply one or more lightweight fiberglass fabric plies on the front and back surfaces of the laminate in order to limit the corrosion occurring as a result of the connection of materials of a different nature. The laminates were fabricated according to the procedure employed in the aeronautical industry, consisting of hand lay-up of prepreg plies, vacuum bag moulding, and curing cycle in autoclave. The curing cycle was controlled through the use of sensors within the autoclave, and it was performed according to the cycle suggested by the CYCOM 977–2 resin matrix producer. Heating was carried out up to 177 °C with speed equal to 2 °C/min, then, the laminate was held at 177 °C for 2 h, and eventually, a natural cooling in autoclave was accomplished.

Because of the fabrication process, the bag side laminate surface was irregular compared to the smooth mould side surface. To perform the drill-milling tests, specimens of 30 mm × 400 mm were cut from the original CFRP laminates.

3.2. Equipment

The drill-milling tests were performed under dry conditions on a five-axis Cosmec Conquest 3200 NC machining centre (Poggibonsi, Siena, Italy), equipped with a sensor system to detect the cutting force signals generated during the process (Figure 2). The signals of the thrust force, F_z , and radial force, F_x , were detected by a Kistler (Kistler Group, Winterthur, Switzerland) three-axis stationary dynamometer model 9257A, positioned under the workpiece fixture. The sensor system included a Kistler charge amplifier model 5007, and a National Instruments data acquisition board model 9239 (Austin, TX, USA) that digitized the F_x and F_z signals at 10 kS/s.

**Figure 2.** Equipment employed for the experimental drill-milling tests.

The radial force can be resolved into two components acting along the X and Y dynamometer directions, respectively. As the process is symmetrical in the CFRP laminate plane, the values of the radial forces were similar, so that it was decided to report only the values recorded along the X direction.

All of the tests were carried out using ISO CNC programming. According to the new drill-milling process, the first operation is the drilling of a pilot hole with a nominal diameter of 6 mm, followed by a peripheral milling operation. Specifically, once the pilot hole is realised, the tool follows a spiral milling path to increase the hole diameter by 0.10 mm per revolution, up to a hole diameter of 6.9 mm. Finally, three boring revolutions at constant diameter are executed. The process phases are shown in Figure 3.

In the experimental tests, the parameters selected for the drilling phase were chosen so as to limit the drilling-induced delamination damage to an extent that is lower than the radius of the material to be removed by the peripheral milling. In particular, the drilling speed was set to 10,000 rpm and the axial feed to 375 mm/min, while the milling speed was set to 14,000 rpm and the axial feed to 375 mm/min.

The drill-milling tests were conducted on 60 consecutive holes to analyse the process behaviour with a tool wear increase.

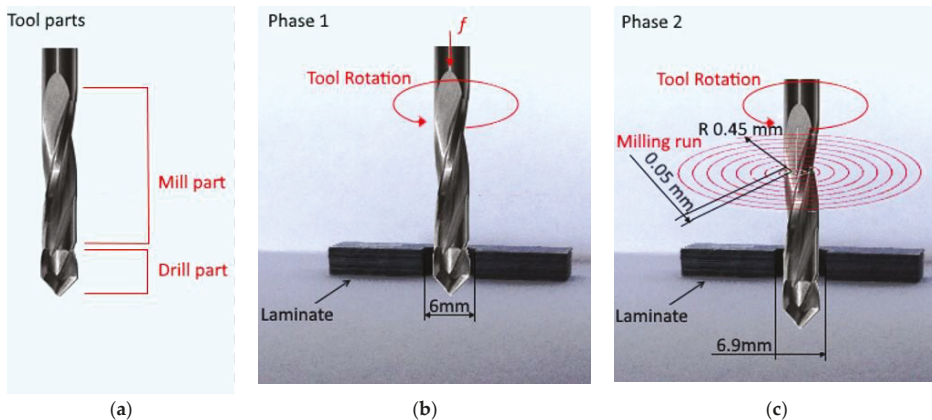


Figure 3. Representation of the following (a) tool parts and process phases; (b) drilling and (c) milling.

3.3. Tool

Two drill-milling tools characterised by different geometries were developed and employed for the experimental tests, to compare their performance. The characteristics and geometry of the two tools are shown in Figure 4. The first tool, T1, is made of tungsten carbide (WC) and has a 6 mm diameter and 100 mm length; the drilling portion is 8 mm long, with two cutting-edges, a 120° point angle, and a 20° helix angle; and the milling portion is 18 mm long, with three flutes, a 15° helix angle, a 10° rake angle, and a 7° clearance angle. The second tool, T2, is made of tungsten carbide (WC) and has a 6 mm diameter and 100 mm length; the drilling portion is 8 mm long, with two cutting-edges, a 120° point angle, and a 20° helix angle; and the milling portion is 18 mm long, with five flutes, a 20° helix angle, a 10° rake angle, and a 7° clearance angle.



Tool	Milling Portion Geometry	Diameter [mm]	Picture
T1	ha15ra10ca7 Z3	6	
T2	ha20ra10ca7 Z5	6	

Figure 4. Comparison of the two newly developed drill-milling tools and milling portion geometry parameters (ha—helix angle; ra—rake angle; ca—clearance angle; Z—flutes number).

3.4. Dimensional Analysis

In the aeronautical sector, very tight tolerance ranges are applied to the hole diameters [25]. In order to characterize the new drill-milling process, the produced hole diameters were measured with a digital calliper. The inner size of each hole was measured at a half laminate thickness along four directions (0° , $\pm 45^\circ$, and 90°). The diameters were calculated as the arithmetic average of the measured values.

3.5. Surface Finish

To characterize the hole surface finish, roughness measurements were carried out using a stylus profilometer with tri-axial movement (Taylor–Hobson Form Talysurf-50, Taylor-Hobson, Leicester, UK) by dragging it along the x-axis a probe with a diamond tip radius of $2\ \mu\text{m}$. The roughness evaluations were performed through software code Ultra ver. 4.6.8, which allows for viewing and processing the data.

To perform the measurements, the holes were sectioned; this was done every ten holes (number 1-10-20-30-40-50-60). The measurement length was 4 mm, with a probe travel speed of 0.5 mm/s, and the roughness tests were carried out according to standard UNI ISO 4288-2000 [26], a Gaussian filter with a 0.8 mm cut off was selected.

The roughness tests were performed three times for each hole, along three separate lines spaced by 0.05 mm.

The drilling of the CFRP laminates results in a series of micro-fibre fractures, fibre pull-outs, and matrix cracking; for this reason, the roughness parameter Ra (average) alone was not considered sufficient, and roughness parameters Rz (maximum peak to valley height) and R_{Pc} (peaks per mm count) were also evaluated [27].

4. Results and Discussion

4.1. Cutting Forces

The values and trends of the F_x and F_z cutting force signals were studied to analyse the cutting forces that develop during the drill-milling process. It was observed that F_z is predominant in the first phase (drilling process), while F_x is predominant in the second phase, where it is possible to observe the characteristic sinusoidal pattern of the peripheral milling process. To perform signal smoothing, the moving average method (with a window length of 200 samples, corresponding to 0.02 s) was applied to the F_x and F_z signals, as reported in Figures 5 and 6, respectively. The goal of smoothing is to facilitate the extraction of the maximum values of the force signals, without taking into consideration high-frequency oscillations.

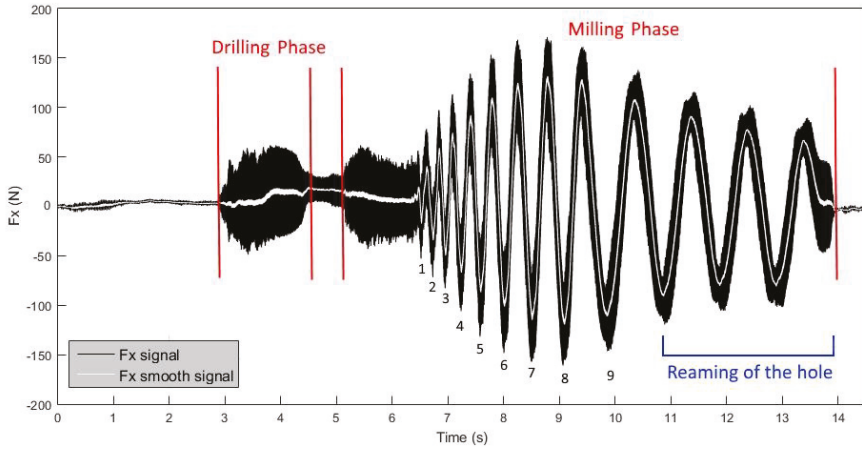


Figure 5. Signal of radial force, F_x , in the drill-milling process for tool T2.

The F_x signals during the milling phase show a sinusoidal trajectory, where each sine wave represents a complete revolution of the tool inside the work-material. The size increase of the hole after each revolution is constant. The sine wave period increases, as the peripheral speed of the tool is constant, while the path to complete the whole revolution increases, as the radius becomes greater after each revolution. The volume of material removed also grows after, and during, each revolution as the radius of curvature increases (Figure 7). Because the work-material thickness is constant, the volume of material removed grows proportionally to the area increase, that is, with the square of the radius, according to a non-linear correlation. Moreover, the same considerations allow for stating that the amplitude of the sine wave also increases.

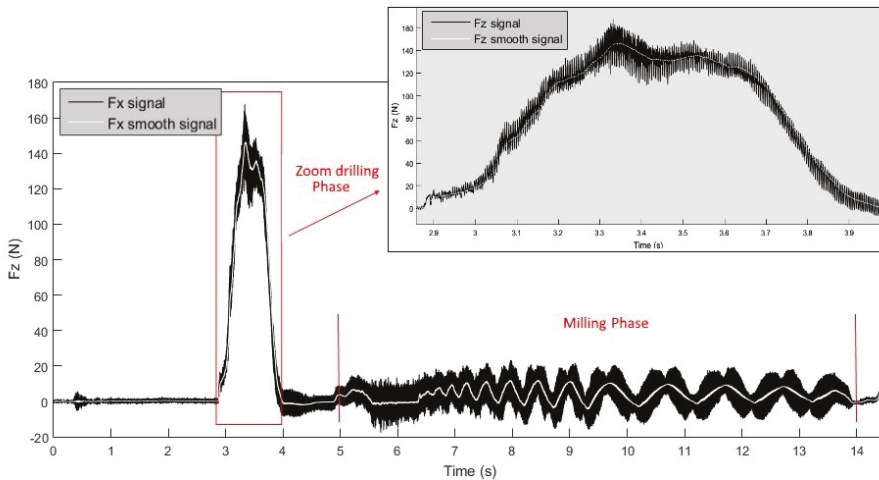


Figure 6. Signal of axial force, F_z , in the drill-milling process for tool T2.

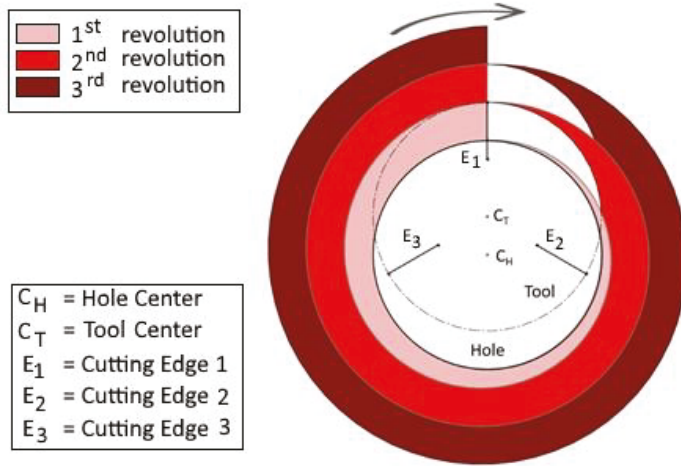


Figure 7. Scheme of the tool path during the drill-milling process. The removed material area increases at each revolution.

From Figure 7, it can be observed that, after a complete revolution, at the same polar coordinate of the previous revolution, the volume of material that the tool faces at the front cutting-edge is greater than for the previous revolution. Table 2 shows the values of the area of material removed after each revolution, calculated by means of a CAD software (Autocad 2017 version) tool.

Table 2. Area of material removed after each revolution.

Revolution	Area of Material Removed (mm ²)
1	0.46
2	0.86
3	0.88
4	0.90
5	0.93
6	0.96
7	1.00
8	1.04

The growth of the area that the tool must cut leads to an increase of forces during the milling phase up to the eighth revolution, while the last revolution is characterized by a path that leads to the closure of the spiral and to a decrease of the cutting forces.

Then, there are three boring revolutions during which the sinusoidal waves display a decreasing amplitude, as shown in Figure 5, because the tool will follow the same path three times, removing less material at each revolution.

Using the Pearson’s correlation coefficient, a strong correlation (>0.7) was found between the area of the material removed and the maximum value of the force in the X direction achieved after each spiral revolution. Specifically, a strong correlation was found for both tool T1 (0.86) and tool T2 (0.93).

Figures 8 and 9 show the maximum Fx and Fz cutting force values measured for all of the 60 holes made during the experimental testing campaign with tools T1 and T2. In all of the cases, an increase of both the Fx and Fz cutting forces with an increasing hole number, that is, with tool wear progression, is visible. Moreover, it can be observed that, during the tests with tool T2, the recorded forces in both the X and Z directions are higher than the ones recorded with tool T1. Using tool T1, the maximum

thrust force, $F_{z_{max}}$, during the drilling phase is 201.27 N and the maximum radial force, $F_{x_{max}}$, during the milling phase is 134.05 N (hole number 60). Using tool T2, the maximum thrust force, $F_{z_{max}}$, during drilling is 188.41 N and the maximum radial force, $F_{x_{max}}$, during milling is 179.57 N (hole number 60). It was verified that the values of $F_{z_{max}}$ are quite similar to those found in the literature [8,12] for a traditional drilling process.

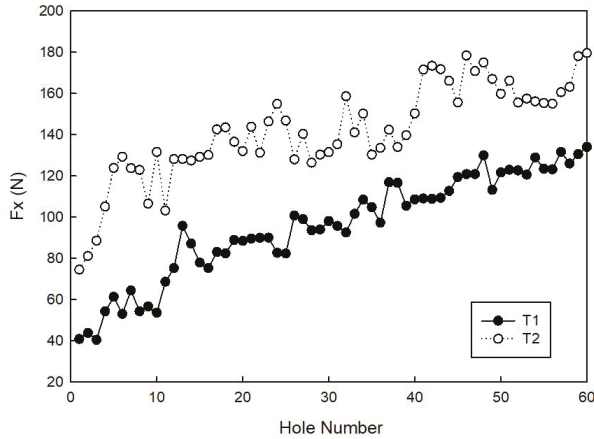


Figure 8. Maximum cutting force in the X direction, $F_{x_{max}}$, measured for tools T1 and T2.

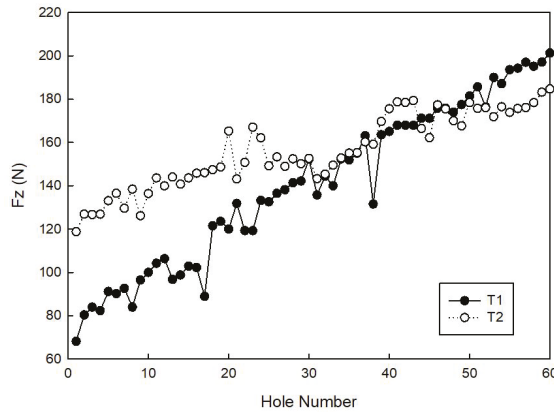


Figure 9. Maximum cutting force in the Z direction, $F_{z_{max}}$, measured for tools T1 and T2.

4.2. Metrological Analysis

With regards to the hole size, generally, hole diameter decreases with an increasing number of holes as a result of tool wear. Furthermore, this gradual decrease can be attributed also to the increase of tool deflection due to the growth of radial cutting force [9].

This behaviour is confirmed by the measurements of the hole diameters, which always show a decreasing trend of the measured values for 60 consecutive holes made with the same parameters and tools, as shown in Figure 10. Diameter reduction is due to heavy tool wear during the drilling process, which is also caused by the decision to employ uncoated WC tools. This decision was made to verify the tool geometry and the cutting parameters independently of the tool material.

As shown in Figure 10, up until hole number 48, the tool T1 has a lower size reduction, whereas from hole number 48, both tools behave in a similar way.

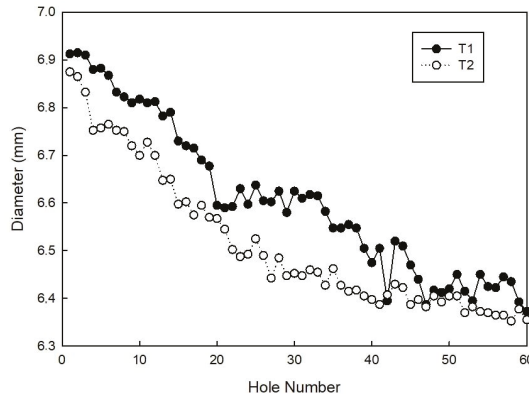


Figure 10. Hole diameter as a function of the number of holes.

With regards to the roundness of the CFRP holes, Figure 11 shows that the holes made by tool T1 keep their roundness up to hole number 30, and lose their roundness in one direction at hole number 60, whereas the holes made by tool T2 do not display any loss of roundness. Figures 12 and 13 show holes number 1, number 30, and number 60 realized with tools T1 and T2, respectively. No presence of uncut fibers was verified in the holes, even in the case of high tool wear, contrarily to what often happens for traditional drilling [14,25]. This was true for both the T1 and T2 tools, as it can be observed in Figures 12c and 13c.

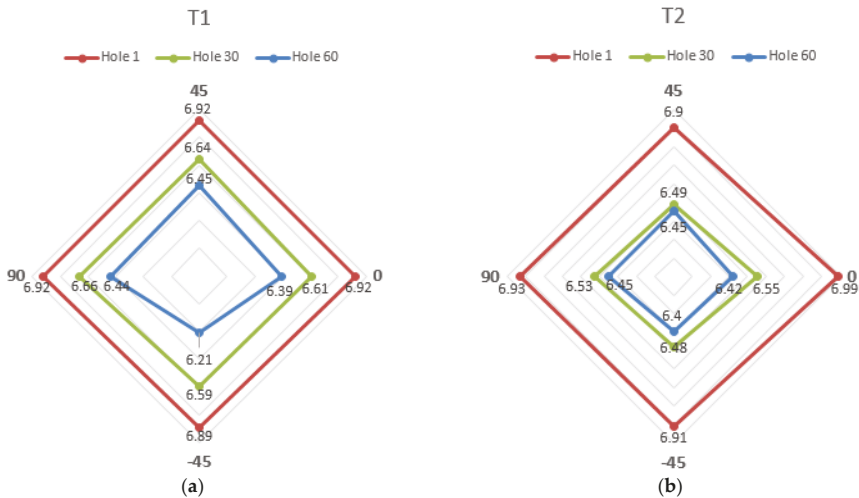


Figure 11. Hole diameter (mm) measured in four directions for holes number 1, number 30, and number 60, made by (a) tools T1 and (b) tool T2.

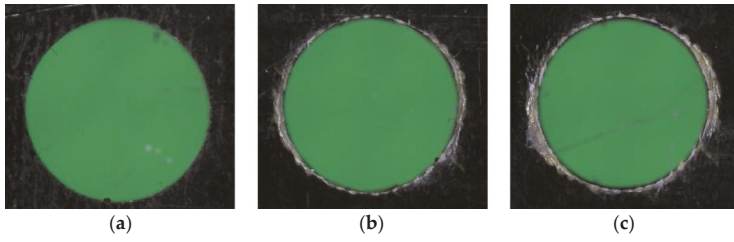


Figure 12. Pictures of (a) hole number 1, (b) hole number 30, and (c) hole number 60, made by tool T1.

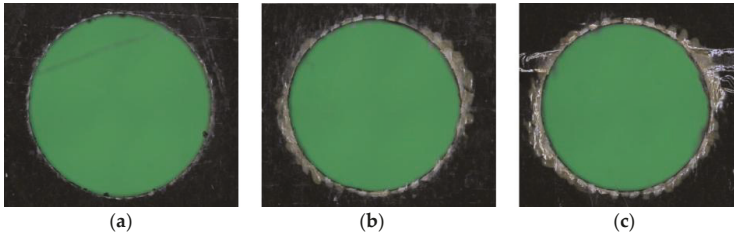


Figure 13. Pictures of (a) hole number 1, (b) hole number 30, and (c) hole number 60, made by tool T2.

4.3. Surface Roughness

Figure 14 reports the Ra values for tools T1 and T2, showing in both cases an increase with the increasing hole number. The holes made with tool T2 have internal surface Ra values greater than those made with tool T1. For the holes made with tool T1, the difference of Ra values between hole number 60 and number 1 is 2.96 μm , whereas for the holes made with tool T2, the difference of Ra values between hole number 60 and number 1 is 4.62 μm . As identical cutting conditions were employed with both tools, the Ra difference can be related to the different wear level of the tool cutting-edge [28,29].

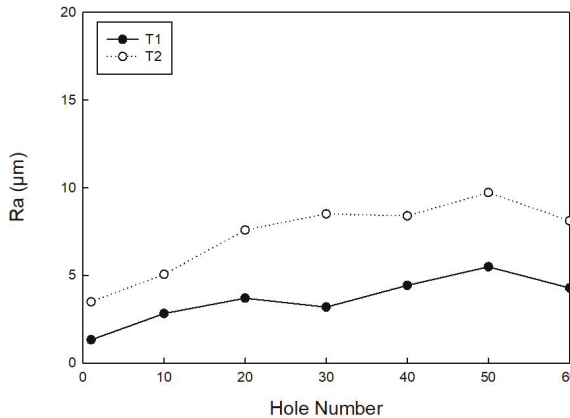


Figure 14. Ra measured for every ten holes made by tool T1 and tool T2.

Figure 15 reports the Rz values measured for every ten holes made by both tool T1 and tool T2. This roughness parameter demonstrates that, although the Ra values are slightly different, tool T1 responds with a better cut of the fibres. Taking into consideration hole number 1, the Rz values for the

two tools differ by 13.92 μm , whereas for hole number 60, they differ by 21.07 μm , showing that tool T2 generates a severer fibre pull-out phenomenon.

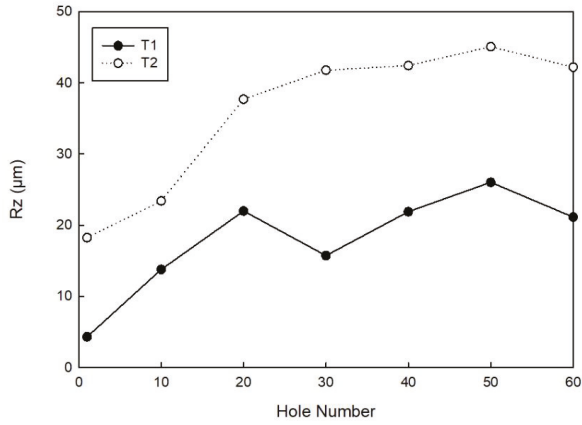


Figure 15. Rz measured for every ten holes made by tool T1 and tool T2.

Figure 16 reports the trend of the RPc parameter measured for every 10 holes. It can be observed that the number of peaks per mm is not high for both tools (only peaks exceeding $\pm 0.5 \mu\text{m}$ were considered). This roughness parameter indicates that the surface finish of the hole is good, but there are gaps due to the fibre pull-out phenomenon, as observed in the literature on CFRP drilling [30,31].

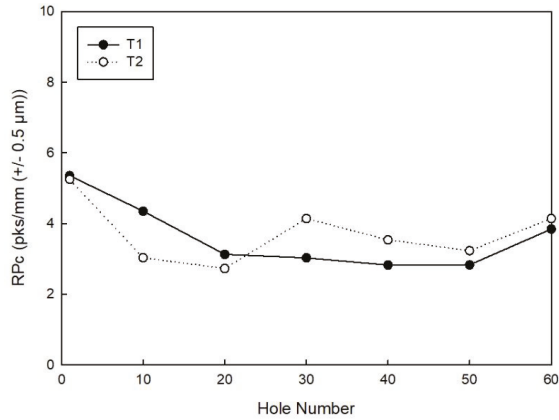


Figure 16. RPc measured for every ten holes made by tool T1 and tool T2.

5. Conclusions

This study presented an innovative hole-making process for CFRP laminates, where the hole is generated by a combination of drilling and peripheral milling processes. To develop this technique, innovative drill-milling tools were designed and realized, and experimental machining tests on CFRP laminates were performed using two different tool configurations, T1 and T2. During the drill-milling process, the thrust cutting force and the radial cutting force were detected through a sensor system to analyse the cutting force behaviour. The holes made with the two cutting tool configurations

employing identical cutting conditions were characterized in terms of size, roundness, and surface finish. The following conclusions can be drawn from the obtained results:

- The maximum values of the thrust cutting force, $F_{z_{max}}$, occurring during the drilling phase are consistent with those obtained in the experimental testing campaigns of traditional drilling.
- In terms of the cutting forces, the results obtained with tool T1 are better than those obtained with tool T2, as lower forces were recorded.
- In both tools, a rapid reduction in the diameter of the hole was observed, due to speedy tool wear growth, and also because the selected WC tools were uncoated.
- Tool T1 responded better in terms of a decrease in the hole diameter, and the use of a coated WC tool could lead to further improvement; it was also observed that the roundness of the hole is maintained with the increasing hole number.
- By comparing the measured roughness parameter values, the trends display a growing tendency with an increasing hole number in all of the cases. Moreover, the Ra roughness values are similar for both tools.
- The Rz roughness parameter values are better for tool T1. From this result, it can be inferred that tool T1 induces a lower fibre pull-out phenomenon in the CFRP.
- The R_pc roughness parameter values indicate that the number of peaks per mm inside the CFRP is low, suggesting that the surface finish is good, except for the points where the voids caused by the pull-out phenomenon appear.

Overall, this process represents an interesting opportunity to reduce the delamination damage produced by traditional drilling and, although to a minor extent, by orbital drilling. The advantages of this new hole-making process are represented by the ease of programming, the absence of coolants, with benefits in terms of green technology, and the good surface finish, as shown by the roughness measurements, with particular reference to the R_pc parameter. As a future development, the use of coated WC tools will be tested to further improve the surface finish in terms of all of the measured roughness parameters. Moreover, different path strategies will be tested in order to verify the potential benefits in terms of the hole quality and tool wear improvement.

Author Contributions: Conceptualization and Methodology, L.N.; Investigation, L.N. and I.I.; Data Curation, A.C. and L.N.; Writing-Original Draft Preparation, A.C., I.I. and L.N.; Writing-Review & Editing, A.C., I.I., L.N.; Project Administration, L.N.; Funding Acquisition, L.N.

Funding: This research was funded by MISE, Ministry of Economic Development, Italy, PON03PE_00129_1 B56D12000520007.

Acknowledgments: The authors gratefully acknowledge LAER Srl, Acerra (Naples) facility, for providing access to the five-axis CNC machine tool used for the drill-milling tests.

Conflicts of Interest: The authors declare no conflict of interest.

References

1. Caprino, G.; Santo, L.; Nele, L. On the origin of cutting forces in machining unidirectional composite materials. *Am. Soc. Mech. Eng. Pet. Div.* **1996**, *75*, 83–87.
2. Caggiano, A. Machining of fibre reinforced plastic composite materials. *Materials* **2018**, *11*, 442. [[CrossRef](#)] [[PubMed](#)]
3. Teti, R. Machining of composite materials. *CIRP Ann. Manuf. Technol.* **2002**, *51*, 611–634. [[CrossRef](#)]
4. König, W.; Wulf, C.; Grass, P.; Willerscheid, H. Machining of fibre reinforced plastics. *CIRP Ann. Manuf. Technol.* **1985**, *34*, 537–548. [[CrossRef](#)]
5. Chen, W.C. Some experimental investigations in the drilling of carbon fiber-reinforced plastic (CFRP) composite laminates. *Int. J. Mach. Tools Manuf.* **1997**, *37*, 1097–1108. [[CrossRef](#)]
6. Kumar, D.; Singh, K.K.; Zitoune, R. Experimental investigation of delamination and surface roughness in the drilling of GFRP composite material with different drills. *Adv. Manuf. Polym. Compos. Sci.* **2016**, *2*, 47–56. [[CrossRef](#)]

7. Jain, S.; Yang, D.C.H. Delamination-free drilling of composite laminates. *J. Eng. Ind.* **1994**, *116*, 475–481. [[CrossRef](#)]
8. Lin, S.C.; Chen, I.K. Drilling carbon fiber-reinforced composite material at high speed. *Wear* **1996**, *194*, 156–162. [[CrossRef](#)]
9. Ho-Cheng, H.; Dharan, C.H.K. Delamination during drilling in composite laminates. *J. Eng. Ind.* **1990**, *112*, 236–239. [[CrossRef](#)]
10. Davim, J.P.; Reis, P. Study of delamination in drilling carbon fiber reinforced plastics (CFRP) using design experiments. *Compos. Struct.* **2003**, *59*, 481–487. [[CrossRef](#)]
11. Hocheng, H.; Tsao, C.C. The path towards delamination-free drilling of composite materials. *J. Mater. Process. Technol.* **2005**, *167*, 251–264. [[CrossRef](#)]
12. Durão, L.M.P.; Gonçalves, D.J.S.; Tavares, J.M.R.S.; de Albuquerque, V.H.C.; Aguiar Vieira, A.; Torres Marques, A. Drilling tool geometry evaluation for reinforced composite laminates. *Compos. Struct.* **2010**, *92*, 1545–1550. [[CrossRef](#)]
13. Piquet, R.; Ferret, B.; Lachaud, F.; Swider, P. Experimental analysis of drilling damage in thin carbon/epoxy plate using special drills. *Compos. Part A Appl. Sci. Manuf.* **2000**, *31*, 1107–1115. [[CrossRef](#)]
14. Feito, N.; Díaz-Álvarez, J.; Díaz-Álvarez, A.; Cantero, J.L.; Miguélez, M.H. Experimental analysis of the influence of drill point angle and wear on the drilling of woven CFRPs. *Materials* **2014**, *7*, 4258–4271. [[CrossRef](#)] [[PubMed](#)]
15. Gaitonde, V.N.; Karnik, S.R.; Rubio, J.C.; Correia, A.E.; Abrão, A.M.; Davim, J.P. Analysis of parametric influence on delamination in high-speed drilling of carbon fiber reinforced plastic composites. *J. Mater. Process. Technol.* **2008**, *203*, 431–438. [[CrossRef](#)]
16. Saoudi, J.; Zitoune, R.; Gururaja, S.; Salem, M.; Mezleni, S. Analytical and experimental investigation of the delamination during drilling of composite structures with core drill made of diamond grits: X-ray tomography analysis. *J. Compos. Mater.* **2018**, *52*. [[CrossRef](#)]
17. Cadorin, N.; Zitoune, R.; Seitier, P.; Collombet, F. Analysis of damage mechanism and tool wear while drilling of 3D woven composite materials using internal and external cutting fluid. *J. Compos. Mater.* **2015**, *49*, 2687–2703. [[CrossRef](#)]
18. Zitoune, R.; Cadorin, N.; Collombet, F.; Šíma, M. Temperature and wear analysis in function of the cutting tool coating when drilling of composite structure: In situ measurement by optical fiber. *Wear* **2017**, *376–377*, 1849–1858. [[CrossRef](#)]
19. Lindqvist, R.; Eriksson, I.; Wolf, M. Orbital drilling of sandwich constructions for space applications. In *SAE Technical Paper 2001-01-2571*; SAE: Warrendale, PA, USA, 2001; p. 10.
20. Sadek, A.; Meshreki, M.; Attia, M.H. Characterization and optimization of orbital drilling of woven carbon fiber reinforced epoxy laminates. *CIRP Ann. Manuf. Technol.* **2012**, *61*, 123–126. [[CrossRef](#)]
21. Ozturk, O.M.; Kilic, Z.M.; Altintas, Y. Mechanics and dynamics of orbital drilling operations. *Int. J. Mach. Tools Manuf.* **2018**, *129*, 37–47. [[CrossRef](#)]
22. Babu, P.R.; Pradhan, B. Effect of damage levels and curing stresses on delamination growth behaviour emanating from circular holes in laminated FRP composites. *Compos. Part A Appl. Sci. Manuf.* **2007**, *38*, 2412–2421. [[CrossRef](#)]
23. Durão, L.; Tavares, J.; de Albuquerque, V.; Marques, J.; Andrade, O. Drilling damage in composite material. *Materials* **2014**, *7*, 3802–3819. [[CrossRef](#)] [[PubMed](#)]
24. Hocheng, H.; Tsao, C.C. Comprehensive analysis of delamination in drilling of composite materials with various drill bits. *J. Mater. Process. Technol.* **2003**, *140*, 335–339. [[CrossRef](#)]
25. Caggiano, A.; Angelone, R.; Teti, R. Image analysis for CFRP drilled hole quality assessment. *Procedia CIRP* **2017**, *62*, 440–445. [[CrossRef](#)]
26. UNI ISO EN 4288–2000. *Geometrical Product Specifications (gps)-Surface Texture: Profile Method-Rules and Procedures for the Assessment of Surface Texture*; International Organization for Standardization: Geneva, Switzerland, 2000.
27. Gaitonde, V.N.; Karnik, S.R.; Rubio, J.C.; Abrão, A.M.; Correia, A.E.; Davim, J.P. Surface roughness analysis in high-speed drilling of unreinforced and reinforced polyamides. *J. Compos. Mater.* **2012**, *46*, 2659–2673. [[CrossRef](#)]

28. Li, S.; Qin, X.; Jin, Y.; Sun, D.; Li, Y. A comparative study of hole-making performance by coated and uncoated WC/Co cutters in helical milling of Ti/CFRP stacks. *Int. J. Adv. Manuf. Technol.* **2018**, *94*, 2645–2658. [[CrossRef](#)]
29. Park, K.-H.; Beal, A.; (Dae-Wook) Kim, D.; Kwon, P.; Lantrip, J. A comparative study of carbide tools in drilling of CFRP and CFRP-Ti stacks. *J. Manuf. Sci. Eng.* **2013**, *136*, 014501. [[CrossRef](#)]
30. Ramirez, C.; Poulachon, G.; Rossi, F.; Saoubi, R.M. Tool wear monitoring and hole surface quality during CFRP drilling. *Procedia CIRP* **2014**, *13*, 163–168. [[CrossRef](#)]
31. Eneyew, E.D.; Ramulu, M. Experimental study of surface quality and damage when drilling unidirectional CFRP composites. *J. Mater. Res. Technol.* **2014**, *3*, 354–362. [[CrossRef](#)]



© 2018 by the authors. Licensee MDPI, Basel, Switzerland. This article is an open access article distributed under the terms and conditions of the Creative Commons Attribution (CC BY) license (<http://creativecommons.org/licenses/by/4.0/>).

Article

Influence of Milling Parameters on Mechanical Properties of AA7075 Aluminum under Corrosion Conditions

María Jesús Martín *, María José Cano, Germán Castillo, Manuel José Herrera and Francisco Martín

Civil, Material and Manufacturing Engineering Department, EIL, University of Málaga, 29071 Málaga, Spain; mjcano@uma.es (M.J.C.); gcastillo@uma.es (G.C.); mherrera@uma.es (M.J.H.); fdmartin@uma.es (F.M.)

* Correspondence: mjmartin@uma.es (M.J.M.); Tel.: +34-951-952-243

Received: 1 July 2018; Accepted: 14 September 2018; Published: 17 September 2018

Abstract: The paper describes an experimental study developed on the AA7075 T651, which is an aluminum alloy extensively used in the aeronautical industry. This work presents a double approach of investigation where there is no literature about previous research. This includes the analysis of the results obtained by the combination of mechanical and chemical actions on the mechanical properties of this material. On the one hand, the combinations of relevant milling parameters (feed rate, cutting speed) on flat samples (flat specimens have been selected by attempting to reproduce with the most accurate way the geometry and the type of machining process known as face milling is usually used in this manufacturing field). On the other hand, the stimulating effect of the corrosion by salt spray on selected batches of specimens was machined in the previous stage. Results from tensile tests performed on the whole of specimens allowed us to evaluate how the main mechanical properties (yield strength, tensile strength, and elongation at break) have been affected by the processes applied. Elongation at the break presents a reduction in an inverse order to feed a rate increase (up to 24.5%) and this reduction is extended (additional 19.17%) in specimens under corrosion conditions, which results in a greater fragility of the material.

Keywords: machining; mechanical properties; corrosion; aluminum; flat specimen; AA7075

1. Introduction

The aerospace industry requires materials with exceptional performance and long-term reliability. In this sense, aluminum and its alloys is one of the materials used most commonly in this field. This is thanks to some of its unique characteristics such as a high strength-to-weight, ease of fabrication, or its relative low cost. There are several different types of aluminum used but the 7075 Al alloy remains the baseline [1–3]. Part of this is due to its good balance of properties required for aerospace applications. Additionally, it is possible to apply sequences of mechanical and thermal treatments to produce annealed states as well as major combinations of characteristics through variations in treatment conditions. Taking into account that AA7075 T651 is widely used in aeronautics, this alloy will be the focus of this research.

Nowadays, advanced composites consisting of a combination of high-strength stiff fibers embedded in a common matrix material [4] or titanium alloys are also widely being used in the aerospace industry. Both compete with aluminum [5,6] but present manufacturing difficulties especially in machining processes. Aluminum alloys can be machined rapidly and economically because of their micro-constituents that have important effects on machining characteristics [7–9]. In this way, numerous conventional machining processes can be performed on these materials (milling, drilling, and turning) by taking into account the different geometric characteristics required in each process [10].

Concretely, manufacturing of lightened plates of aluminum by face milling or profile milling is one of the most applied machining processes. Therefore, in this project, this type of machining process will be performed on the flat specimen to study in the attempt to reproduce as accurately as possible the way in which aircraft structures are made of. We studied the influence of different dominant parameters of this type of machining such as cutting speed, feed per tooth or cutting depth, fixing values of cutting speed and depth of cut, and taking the feed rate as the parameter to establish a degree of freedom in this experiment due to its significant influence on the roughness surface of the parts machined [11–15]. For this variable, a range of three values will be applied.

Traditionally, cutting fluids have been widely used in metalworking processes by providing cooling and lubrication while also preventing corrosion and facilitating the ejection of cut metal. However, their composition, usage, and disposal can negatively impact the environment and the health of exposed individuals by making necessary their reduction and even their elimination [16–18]. Specifically, in aluminum machining, the mixture of chip and cutting fluid make more difficult a correct recycling [19]. Other times, aluminum alloys are machined jointly with different types of materials such as composites or polymers reinforced with carbon fiber, which do not have a satisfactory performance with cutting fluids. Because of this, dry cutting is presented as an alternative to minimize or avoid the use of cutting fluid [20–23]. However, dry machining demands more rigorous requirements in machining operations and affects largely the surface finish [24].

Taking as a starting point the previous machining conditions, it is needed to define combinations of cutting parameter values to improve the mechanical behavior of the material studied [25]. This premise will define the first of the three stages of the present project.

Studies about AA7075 alloy hardly exists in literature, which is remarkable when considering that this material is widely used in aeronautic components.

On the other hand, it is widely known that corrosion is a universal enemy whose presence is inevitable in a productive process or any other. Corrosion can be defined as the chemical or electrochemical reaction of a metal or alloy with its surrounding environment and with the consequent deterioration of its properties [26,27]. One of the most obvious manifestations of corrosion is its direct effect on the surface of the metal subject. This allows us to establish that this relationship provokes a stimulant effect on the surface geometric imposed [28] and, therefore, has a greater influence on the variation of the mechanical properties of the material subjected to a corrosive environment.

It is possible to distinguish between corrosion by oxidation of the metal with the formation of metal cations and the dissolution of a metal in other metals or molten salts. There is a form of corrosion in which two effects are superimposed: the first one is chemical or electrochemical, which constitutes the corrosion itself, and the other one is mechanical. For example, the process of corrosion-erosion or corrosion under tension. The basic corrosion reaction is defined by the transit of the metal or alloy from its elementary form to the ionic or combined form (Equation (1)).



n being the number of free electrons.

To complete the process, electrons must be fixed by affinity (an oxidant) by some substances that are present in the medium in contact such as oxygen. The elemental metal through the corrosion mechanism returns to the combined form by making oxides, sulfides, and more including the state in which metals are usually found in nature and are thermodynamically more stable.

It is possible to classify corrosion processes using different criteria. For example, considering the morphology of the attack, it could be described as uniform or localized (selective corrosion, intergranular attacks, among others) [29,30]. However, the most interesting scientific classification is based on the mechanism that produces this phenomenon. From this point of view, corrosion will be produced electrochemically by electrochemical battery cells on the metallic surface and, therefore, does not produce the same effect on the whole metallic surface due to the cathodic regions not being attacked. This type of corrosion appears when metal materials are in contact with electrolytic

conductivity media specifically with water, salt solutions, or the simple humidity of the atmosphere and soils. The other fundamental type of corrosion occurs in conditions of absence of humidity on the complete metal surface at high temperatures.

The phenomenon of stress corrosion cracking is typical of alloys including passive ones. This phenomenon is characterized by the appearance of cracks that advance in an approximately normal direction with respect to the application of tension [31,32]. Stress corrosion cracking results from the conjoint action of three components.

- (a) Material under tensions higher than a defined threshold, whether applied or residual.
- (b) Material susceptible to cracking, determined by the composition of the alloy, its microstructure or its grain size.
- (c) Material in contact with a specific aggressive environment for it.

Regarding the first condition, it is important to emphasize that tension cannot only be applied when the alloy is part of a structural element but can be a residual tension arising from its forming process or its thermal history.

Previously described in this project, electrochemical corrosion under wet and saline environment has mainly been reproduced. Nevertheless, it also is possible to consider the stress corrosion cracking phenomenon, which could be implicated because of the notch effect. In our study, the notch effect in the sample will depend on the different levels of machining obtained by means of the variation of the milling parameters.

Machining conditions imposed on specimen batches and the corrosive environment subsequently applied to them allow us to analyze the influence of the ones on the mechanical properties of the material studied. Sometimes corrosion and machining working jointly can cause weakness and fragility of the material, which are able to result in a reduction of its tensile strength [33,34] and yield strength as well as a decrease in its percentage of elongation.

2. Materials and Methods

Because of the high interest within the aeronautic scope in the use of light alloys especially aluminum ones, this work is focused on the mechanical behavior analysis of one of the most important alloys used in this field including the AA7075 T651 alloy (thermal treatment and tensile controlled of 1.5% to 3% (according to the manufacturer). It starts from the aluminum sheet 8 mm thick, EN AW7075 (AlZn5, 5MgCu) (Table 1). The choice of this thickness is conditioned by the fact that both faces of the sheet are going to be machined under different cutting parameters by following the purpose of doing the analysis of the influence of these machining conditions on samples subject to a corrosive environment. Vibration effects from the machine operation on the work held to the table can produce warps and waves. This situation obliges it to choose a particular initial thickness, according to the last 4 mm thick. Samples are created by the top face and edge machining. Because the main goal of this work is the study of the influence of the milling parameters on the corrosion effect on the samples and the effect on their mechanical behavior, it is absolutely necessary to perform a controlled material-removal process [8,12].

Table 1. AA7075 alloy composition.

%	Si	Fe	Cu	Mn	Mg	Cr	Zn	Ti	Others Elements	Al
Minimum	-	-	1.20	-	2.10	0.18	5.10	-	Zr + Ti	Total
Maximum	0.40	0.50	2.00	0.30	2.90	0.28	6.10	0.20	0.25	0.15 rest

It has been used with the three axes milling machine Kondia K600 with CNC control FAGOR 8050. The rotating face milling cutter is a face mill STD B0 0302 of 63 mm external diameter with a major cutting edge angle (or Entering angle) of 90° that holds six inserts STD ISO APKT 160408 B0

0138 of K10/20 quality. The rotating edge milling cutter is an edge mill STD FP07 of ASP material (high performance steel from the powder metallurgy process) and cutting length of 19 mm and an 8 mm external diameter with 4 teeth or cutting edges.

Due to the requirements in standard UNE-EN ISO 6892-1:2017 (ISO 6892-1:2016) [35], which regulates tensile tests, it has been considered the typical tensile flat specimen shown in Figure 1.

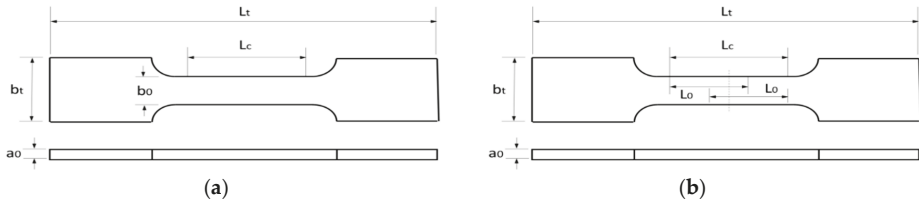


Figure 1. (a) Tensile specimen dimension; (b) Gage section and measurement distances.

Flat specimens will be used with dimensions as specified below by considering a proportional flat specimen.

$$a_0 = 4 \text{ mm}, b_0 = 20 \text{ mm}, S_0 = a_0 \cdot b_0$$

S_0 = original cross sectional area

L_0 = original gauge length

$$L_0 = K \cdot \sqrt{S_0}, K = 5.65$$

$L_0 = 50 \text{ mm}$

L_c = parallel length

$$L_c \geq L_0 + 1.5 \cdot \sqrt{S_0}$$

$L_c = 80 \text{ mm}$

L_t = total length

Transition radius of 12 mm are defined between gauge and gripping sections.

This study analyzes the influence of machining parameters on the specimens subjected to corrosion conditions. Milling machining has been selected as the machining operation to be carried out because it is said to be an essential process in the aeronautical industry. The next step consists of establishing the machining conditions that will be applied. The three primary input control parameters that will be taken into account are: cutting speed (V_c), depth of cut (a_p), and feed rate (F). The first two variable values will be in accordance with the cutter tool geometry and they will remain constant. The feed rate (F) will be the parameter to be modified. Three values chosen from the values range provided by the manufacturer will be given. Consequently, three different study batches of specimens will be generated. Following the supplier recommendations and the milling tool characteristics, the depth of cut must be less than 7 mm in face milling and less than 19 mm in profile or edge milling. In this experience, it is established that there will be 2 mm of the depth of cut in the face milling and 4 mm in the other. Referring to cutting speed (V_c), due to the milling tools selected, the reference interval will be a 200 to 700 m/mm range for face milling and a 100 to 150 m/mm range for edge milling (manufacturer’s information). Then, by taking the lowest value of cutting speed from each range, the spindle speed is determined (Equation (2)).

$$s \left(\frac{\text{rev}}{\text{min}} \right) = \frac{V_c \left(\frac{\text{m}}{\text{min}} \right) \cdot 1000 \left(\frac{\text{mm}}{\text{m}} \right)}{\pi \cdot D \text{ (mm)}} \tag{2}$$

Spindle speed in face milling (Equation (3)).

$$s = \frac{200 \cdot 1000}{\pi \cdot 63} = 1010.50 \tag{3}$$

Spindle speed in edge milling (Equation (4)).

$$s = \frac{100 \cdot 1000}{\pi \cdot 8} = 3978.86 \tag{4}$$

where

- s = revolution per minute of the cutter,
- V_c = lineal cutting speed of the material in m/mm,
- D = diameter of the cutter in mm

Feed rate comes from the next equation (Equation (5)).

$$F \left(\frac{\text{mm}}{\text{min}} \right) = s \left(\frac{\text{rev}}{\text{min}} \right) \cdot Z \text{ (teeth)} \cdot fz \left(\frac{\text{mm}}{\text{tooth}} \right) \tag{5}$$

with

- fz = movement per tooth of cutter in mm
- Z = number of teeth of cutter

For feed per tooth, manufacturer recommendations indicate a range of 0.1 to 0.31 mm using the face milling tool. Experiments will be conducted taking three feed per tooth levels: 0.1 mm, 0.2 mm, and 0.3 mm. Therefore, considering these values on face machining, F_{1F} , F_{2F} , and F_{3F} , identify the feed rate established for batch 1, batch 2, and batch 3, respectively (Equations (6)–(8)).

$$F_{1F} = 1010.50 \cdot 6 \cdot 0.1 = 606.30 \tag{6}$$

$$F_{2F} = 1010.50 \cdot 6 \cdot 0.2 = 1212.60 \tag{7}$$

$$F_{3F} = 1010.50 \cdot 6 \cdot 0.3 = 1818.90 \tag{8}$$

By taking the previous three feed rate levels on profile or edge machining, F_{1E} , F_{2E} , and F_{3E} are defined below (Equations (9)–(11)).

$$F_{1E} = 3978.86 \cdot 4 \cdot 0.06 = 954.93 \tag{9}$$

$$F_{2E} = 3978.86 \cdot 4 \cdot 0.065 = 1034.50 \tag{10}$$

$$F_{3E} = 3978.86 \cdot 4 \cdot 0.07 = 1114.08 \tag{11}$$

Machining conditions are included in Table 2.

Table 2. Machining conditions.

Batch	Face Milling V_c (m/min)	Face Milling a_p (mm)	Face Milling F_f (mm/min)	Edge Milling V_c (m/min)	Edge Milling a_p (mm)	Edge Milling F_E (mm/min)
1	200	2	606.30	100	4	954.93
2	200	2	1212.60	100	4	1034.50
3	200	2	1818.90	100	4	1114.08

Figure 2 shows different finish surface levels depending on the cutting conditions, which includes sample numbers 3, 8, and 12 from the batches 1, 2, and 3, respectively.

Once specimens have been machined under the cutting conditions defined in Table 2 from each batch, one sample is defined as a “control sample” and the three others will be subjected to a salt spray testing. It is widely used as a rapid method for evaluating material performance under highly corrosive conditions.



Figure 2. Machined samples from batches 1, 2, and 3 (scale bar in mm).

The aim of this experience is the evaluation of the influence of cutting parameters by using corrosion as an enhancer medium on the mechanical behavior of aluminum alloys AA7075 T651.

Previously, the application of the corrosion test, the thickness, and width of each of the specimens was measured at different points of the gauge length by calculating the average section of each specimen in that zone.

Afterward, samples are exposed to salt fog or spray that is even distributed among the samples inside a testing chamber. The salt spray (salt fog) chamber consists of a fog chamber, which is a salt solution reservoir, a supply of suitably conditioned compressed air, one or more atomizing nozzles, specimen supports, provision for heating the chamber, and necessary means of control. In this case, the apparatus is HSN400 Heraeus Votsch. Samples have been suspended between 15° and 30° from the vertical parallel to the principal direction of the flow of fog.

This practice provides a controlled corrosive environment by chloride solution to produce relative corrosion in the specimens exposed in the test chamber. The salt fog testing conditions applied are:

- The salt solution is a solution of sodium chloride dissolved in distilled water with (50 ± 5) g/L concentration
- The exposure zone of the salt spray chamber has been maintained at $35 \text{ }^\circ\text{C} \pm 2 \text{ }^\circ\text{C}$
- The pH of the salt solution is such that, when atomized to $35 \text{ }^\circ\text{C}$, the collected solution will be in a pH range between 6.5 to 7.2. The registered pH values have approached 6.5 and were measured by pH test paper.
- Spraying has been controlled by the average collected speed of atomized solution in minimum periods of 24 h. The spraying range in a horizontal manifold of 80 cm^2 must be 1 to 2.5 mL/h. The volumes collected every 24 h have come close to 50 mL. Lastly, the period of exposure reached 168 h.

At the end of the test, specimens have been carefully removed and dipped in distilled water to remove salt and deposits from their surface and then they are immediately dried.

Once dried, they are wrapped in cellulose with desiccants. They will be kept in a watertight compartment until the next step. Figure 3a–c show the effect of the corrosive process on the samples tested.

Along with finished previous stages, the machined process, and the salt spray test, specimens will be subjected to tensile tests. They will provide information about the strength or their mechanical behavior.

The equipment used is a universal testing machine for tensile/compression/flexure 1 to 500 kN, ME 405 SERVOSIS, controlled by PCD2K test software (version 1.2) [36] that will give a test report with the required calculations and test results, data, and graphics. This testing machine works with two load cells of which the 100 kN one will be used in this experiment.

Tensile tests are performed at a room temperature range between $10 \text{ }^\circ\text{C}$ and $35 \text{ }^\circ\text{C}$ (Figure 4). The sample dimensions have been described before. They are proportional with gage length, rectangular cross-sectional area, and soft transition radius connecting gage and gripping sections. Elongation at the break will be evaluated by measuring the length increase between the initial marks of the samples. The displacement speed of wedge grips is fixed in 1 mm/min [35].

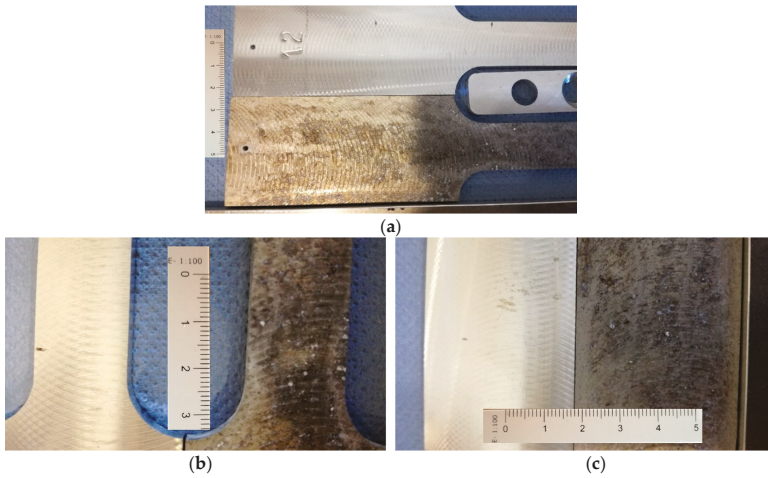


Figure 3. (a–c) Subject and no subject to corrosion specimens (scale bar in mm).

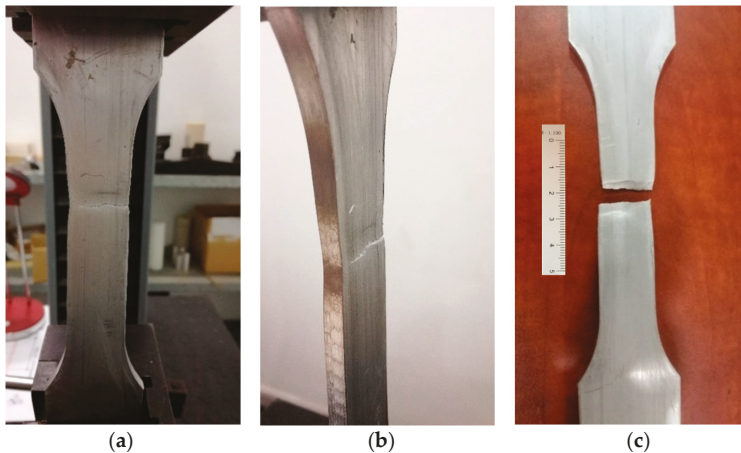


Figure 4. (a,b) Sample during the test; (c) Sample after the test (scale bar in mm).

The tensile force is recorded as a function of the increase in gage length. Such plots of the tensile force versus tensile elongation would be normalized to the Stress-Strain curve.

- Engineering stress: $\sigma = \frac{F}{S_0}$ where F is the tensile force and S_0 is the initial cross-sectional area of the gage section.
- Nominal engineering strain: $\epsilon_n = \frac{(L_u - L_0)}{L_0}$ where L_0 is the initial gage length and L_u is the final one.

Taking this curve as a starting point, the value of the conventional elastic limit is determined by applying a linear regression method to the registers of the proportional elastic zone of the curve. Due to the need of a high goodness of fit of the data to the mathematical relationship, the correlation coefficient, R^2 , will not be less than 0.999. Once this curve has been adjusted again to the estimated deformation of 0.2%, the cut point of this new curve with the initial curve adjusted will provide the value of the elastic limit corresponding to the material tested (σ_e) (Figure 5). Last instant of the tensile test is delimited by tensile strength σ_R .

Regarding the elongation at break, A , it will be calculated from the next expression.

$$A = \frac{L_u - L_0}{L_0} \cdot 100$$

with L_0 = initial length and L_u = length after a break. Measuring L_u is especially critical because it requires a careful approach to ensure the best contact between both parts. This distance has been measured using a digital Vernier caliper of precision 0.01 mm.

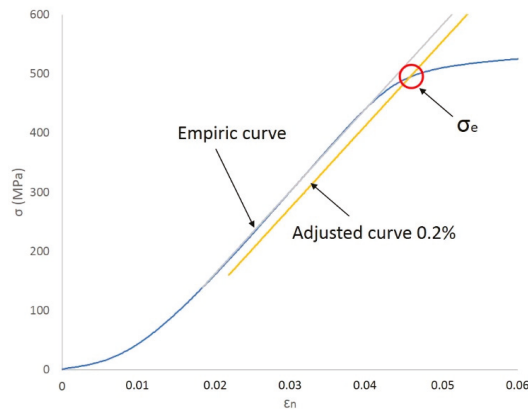


Figure 5. Elastic limit in an adjusted curve.

3. Results and Discussion

Once the tensile tests have been done on both types of flat specimens considered, the denominated “control samples” and ones that have been previously subjected to a corrosive environment (specifically identified with the letter “C”) as well as the parameter values that characterize their mechanical behavior, yield strength, tensile strength, and elongation are analyzed.

Table 3 presents the set of results obtained.

Table 3. Testing and measurement results.

Specimen	Section (mm ²)	Yield Strength 0.2% σ_e (MPa)	Tensile Strength σ_R (MPa)	Elongation at Break A (%)
1C	80.80	498.50	557.75	11.18
2C	79.41	495.11	554.36	13.06
3	79.69	497.90	557.90	14.32
4C	82.16	481.94	548.30	8.18
5C	79.35	487.87	553.37	10.04
6C	80.72	492.02	553.73	9.72
7C	81.48	480.32	546.70	10.40
8	80.34	486.37	547.49	12.80
9C	82.76	481.65	542.09	10.74
10C	82.92	486.11	554.46	12.76
11C	80.81	483.39	536.72	11.12
12	80.24	488.20	556.63	11.50

From these results, it is possible to do comparative evaluations between the controlled parameters on each specimen by considering the different variables on influence.

- Kind of specimen
- Corrosive action
- Milling machining conditions

Due to the specimens' dimensions, it is necessary to calculate not only the absolute values of the mechanical parameters (elastic limit, tensile strength, and elongation at break) but the relative values of these three parameters, according to each specimen cross section (S_0). Thus, the next tables and graphics show results from the evaluation of yield strength and yield strength/section relation (Table 4, Figure 6), tensile strength and tensile strength/section relation (Table 5, Figure 7), elongation to break and elongation at break/section relation (Table 6, Figure 8), and relation tensile strength/elongation at break (Table 7, Figure 9).

Table 4. Yield strength and yield strength/section relation values per specimen and Medium values.

Specimen	Yield Strength	Yield Strength/Section
	(MPa)	(MPa/mm ²)
3	497.90	6.25
8	486.37	6.05
12	488.20	6.08
Medium value a (3, 8, 12)	490.82	6.13
Standard deviation	6.20	0.11
1C	498.50	6.17
2C	495.11	6.23
4C	481.94	5.87
Medium value b (1C, 2C, 4C)	491.85	6.09
Standard deviation	8.75	0.19
5C	487.87	6.15
6C	492.02	6.09
7C	480.32	5.89
Medium value c (5C, 6C, 7C)	486.74	6.05
Standard deviation	5.93	0.14
9C	481.65	5.82
10C	486.11	5.86
11C	483.39	5.98
Medium value d (9C, 10C, 11C)	483.72	5.89
Standard deviation	2.25	0.08
Corrosion total medium value (MVt = (MVb + MVc + MVd)/3)	487.43	6.01
Standard deviation	4.11	0.11

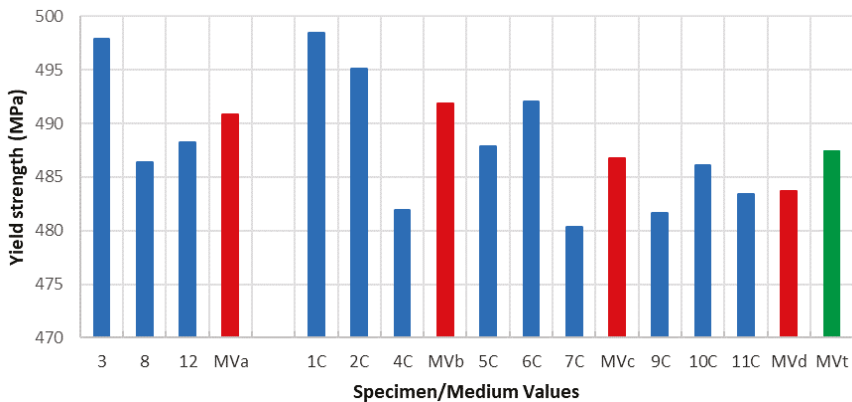


Figure 6. Yield strength vs. specimen and medium values.

Table 5. Tensile strength and tensile strength/section relation values per specimen and medium values.

Specimen	Tensile Strength	Tensile Strength/Section
	(MPa)	(MPa/mm ²)
3	557.90	7.00
8	547.49	6.81
12	556.63	6.94
Medium Value a (3, 8, 12)	554.01	6.92
Standard deviation	5.68	0.10
1C	557.75	6.90
2C	554.36	6.98
4C	548.30	6.67
Medium value b (1C, 2C, 4C)	553.47	6.85
Standard deviation	4.79	0.16
5C	553.37	6.97
6C	553.73	6.86
7C	546.70	6.71
Medium value c (5C, 6C, 7C)	551.27	6.81
Standard deviation	3.96	0.13
9C	542.09	6.55
10C	554.46	6.67
11C	536.72	6.64
Medium value d (9C, 10C, 11C)	544.42	6.94
Standard deviation	9.10	0.06
Corrosion total medium value (MVt = (MVb + MVc + MVd)/3)	549.72	6.77
Standard deviation	4.72	0.07

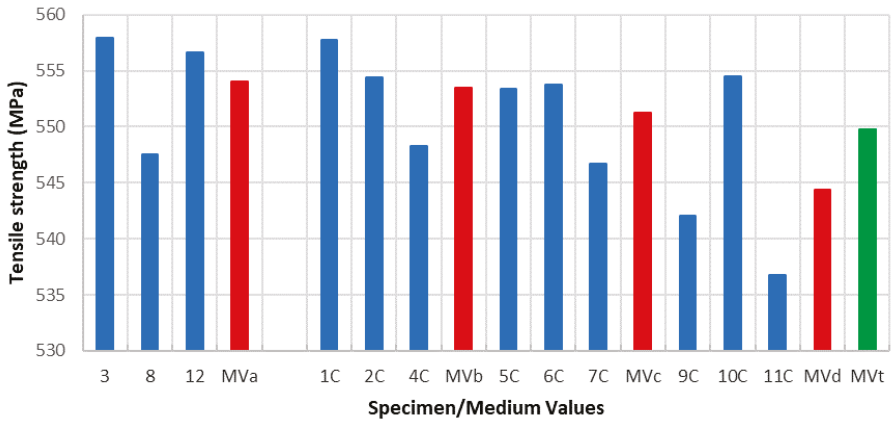


Figure 7. Tensile strength vs. specimen and medium values.

Table 6. Elongation at break and elongation at break/section relation values per specimen and medium values.

Specimen	Elongation	Elongation/Section
	(%)	(%/mm ²)
3	14.32	0.18
8	12.80	0.16
12	11.50	0.14
Medium value a (3, 8, 12)	12.87	0.16
Standard deviation	1.41	0.02
1C	11.18	0.14
2C	13.06	0.16
4C	8.18	0.10
Medium value b (1C, 2C, 4C)	10.81	0.13
Standard deviation	2.46	0.03
5C	10.04	0.13
6C	9.72	0.12
7C	10.40	0.13
Medium value c (5C, 6C, 7C)	10.05	0.12
Standard deviation	0.34	0.01
9C	10.74	0.13
10C	12.76	0.15
11C	11.12	0.14
Medium value d (9C, 10C, 11C)	11.54	0.14
Standard deviation	1.07	0.01
Corrosion total medium value (MVt = (MVb + MVc + MVd)/3)	10.80	0.13
Standard deviation	0.75	0.01

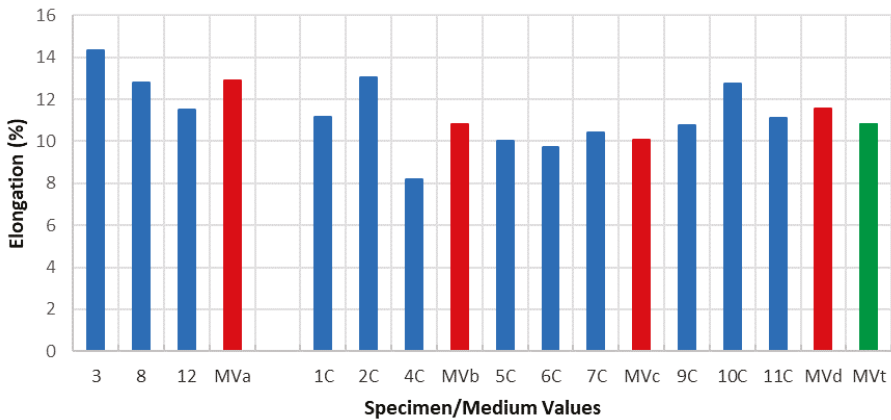


Figure 8. Elongation vs. specimen and medium values.

Table 7. Tensile strength/elongation relation values per specimen and medium values.

Specimen	Tensile Strength/Elongation (MPa/%)
3	38.96
8	42.77
12	48.40
Medium value a (3, 8, 12)	43.38
Standard deviation	4.75
1C	49.89
2C	42.45
4C	67.03
Medium value b (1C, 2C, 4C)	53.12
Standard deviation	12.60
5C	55.12
6C	56.97
7C	52.57
Medium value c (5C, 6C, 7C)	54.88
Standard deviation	2.21
9C	50.47
10C	43.45
11C	48.27
Medium value d (9C, 10C, 11C)	47.40
Standard deviation	3.59
Corrosion total medium value (MVt = (MVb + MVc + MVd)/3)	51.80
Standard deviation	3.91

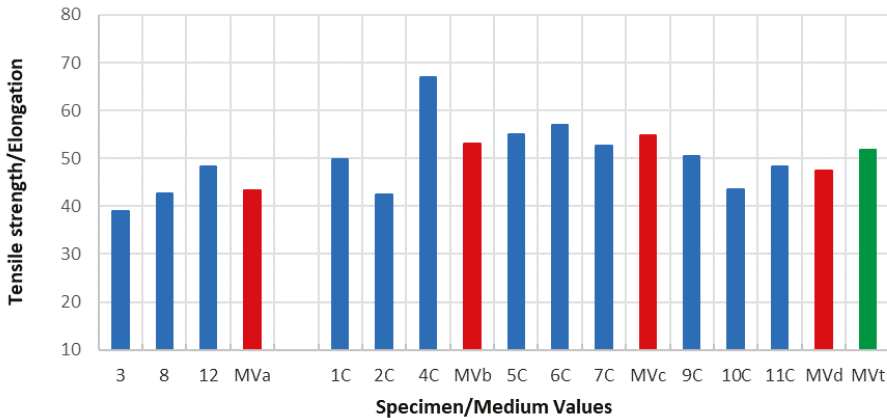


Figure 9. Tensile strength/elongation relation values and medium values.

Data shown in Tables 4–7 and Figures 6–9 express those results relative to specimens not subjected to a corrosive environment (“control specimens”) and the three milling machined conditions (specimens 3, 8, and 12). In addition, medium values have been calculated and identified as MVa (medium value a). On the other side, Specimens 1C, 2C, and 4C belongs to batch 1 and they have been exposed to salt fog. Its corresponding medium value is MVb. Specimens from batch 2 including 5C, 6C, and 7C have suffered a corrosive attack. In this case, it is assigned the medium value MVc. The three next specimens include 9C, 10C, and 11C from batch 3 and under corrosive action present a medium value identified by MVd. Eventually, the last column shows the medium value of the three previous medium values from the batches of samples subjected to corrosion conditions that include MVb, MVc, and MVd. This parameter, MVt, represents the total medium value corresponding to the behavior of the studied variable.

Establishing relations between the samples areas and the machining parameters considered allows us to make a more accurate evaluation of how their mechanical behavior is affected by the machining conditions. According to standard deviations included in Tables 4–7, the results show a reduced dispersion when cross sections are taken into account. Tables 8 and 9 and Figures 10 and 11 show the percentage variations of the elastic limit and the tensile strength. As shown, both percentages do not exceed the 4.6% between extreme values from each batch. Concretely, the reduced difference that both parameters present in batch 2 may indicate that, for this combination of machining parameters, the variation of the micro-geometry does not significantly affect the mechanical properties considered (tensile strength and elastic limit).

Table 8. Yield strength/section values per specimen and medium values vs. batch.

Batch	Yield Strength/Section Specimen without Corrosion (1) (MPa/mm ²)	Yield Strength/Section Medium Values with Corrosion (2) (MPa/mm ²)	(1)/(2) (%)
1	6.25 (specimen 3)	6.09 (MVb)	2.59
2	6.05 (specimen 8)	6.04 (MVc)	0.13
3	6.08 (specimen 12)	5.89 (MVd)	3.33
Extreme values variation (%)	3.21	3.43	

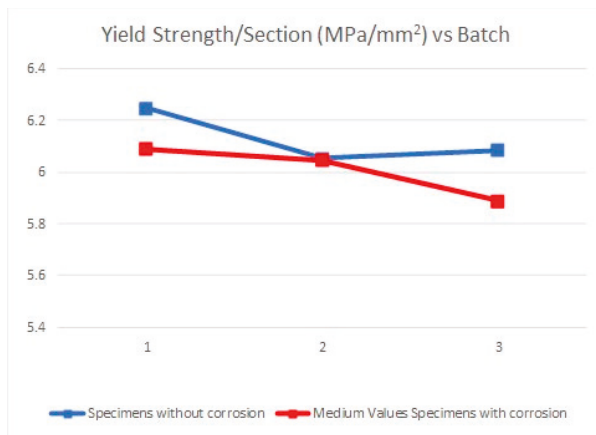


Figure 10. Yield strength/Section vs. Batch.

Table 9. Tensile strength/Section values per specimen and Medium values vs. Batch.

Batch	Tensile Strength/Section Specimen without Corrosion (1) (MPa/mm ²)	Tensile Strength/Section Medium Values with Corrosion (2) (MPa/mm ²)	(1)/(2) (%)
1	7.00 (specimen 3)	6.85 (MVb)	2.17
2	6.81 (specimen 8)	6.85 (MVc)	−0.48
3	6.94 (specimen 12)	6.63 (MVd)	4.69
Extreme values variation (%)	2.73	3.41	

In the opposite, the elongation at break is strongly influenced by the machining process and the activator effect of the corrosion on the surface roughness of each specimen (Table 10, Figure 12). In this sense, the increasing roughness level dependent on the machining conditions ($R_{a1} < R_{a2} < R_{a3}$) prompts a fragility increase and consequently a lesser percentage elongation. Likewise, a similar situation is presented in specimens exposed to a corrosive environment and machined under cutting conditions

identified as batch 1 and batch 2. In this case, not only is there a decrease on the percentage elongation but that decrease is very significant. Furthermore, an important difference appears with the percentage elongation of the “control specimen” being 33.97% in batch 1 and 27.60% in batch 2. These results show how the Aluminum 7075 ductility can be affected by the machining conditions applied.

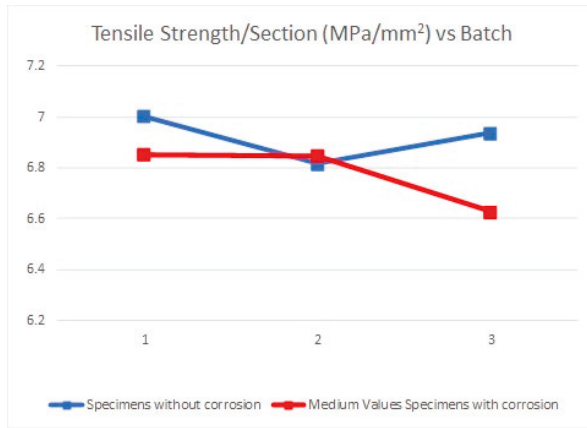


Figure 11. Tensile strength/Section vs. Batch.

Table 10. Elongation/Section values per specimen and Medium values vs. Batch.

Batch	Elongation/Section Specimen without Corrosion (1) (%/mm²)	Elongation/Section Medium Values with Corrosion (2) (%/mm²)	(1)/(2) (%)
1	0.18 (specimen 3)	0.13 MVb	33.97
2	0.16 (specimen 8)	0.12 MVc	27.60
3	0.14 (specimen 12)	0.14 MVd	2.06
Extreme values variation (%)	25.38	12.46	

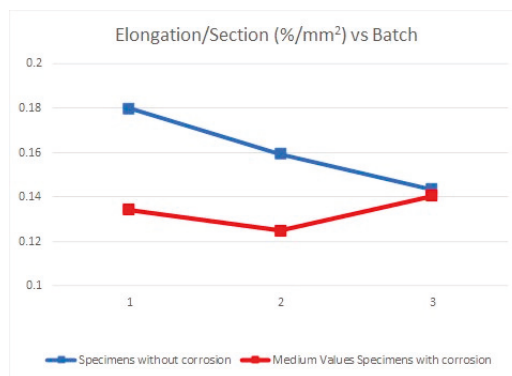


Figure 12. Elongation/Section vs. Batch.

However, batch 3 does not present the same behavior than batches described before. A similar comparison between values from the “control specimen” and specimens under corrosion conditions produces a result of 2.06%. The amount is especially insignificant compared to the results obtained with batches 1 and 2. Analyzing these results, it can be deduced that the combination of cutting

depth, feed per teeth, and cutting speed in batch 3 reduces strongly the stimulator effect of the corrosion in relation to its fragility. These are not, nevertheless, the suitable machining conditions because the higher increase of the feed per tooth produces a rise in surface roughness and a fall in the percentage elongation.

Taking absolute values (without relation to cross sections), the conclusions deduced from the study of each one of the parameters contemplated in the different conditions of the test reveals that, in the case of the elastic limit, the similar behavior under different machining conditions and the average value obtained from the specimens without a corrosive action is 490.82 MPa. Therefore, we can establish this value as the elastic limit value of the material under study. For the samples subjected to a corrosive attack, the evolution of the average values of the yield strength is such that the result from batch 1, 491.85 MPa, is insignificant while it is demonstrated that a higher influence on the value of the elastic limit for the samples from batches 2 and 3. It can be observed as a downward trend of this evolution. The result is 486.74 MPa, which is the value of batch 2, and 483.72 MPa, which is the value for batch 3. This tendency is evident in the total average from the set of specimens under corrosion. This parameter (MVt) offers the value of 487.43 MPa.

Regarding the tensile strength, the evolution presents a similar aspect than the previous case. The average value of samples 3, 8, and 12 is 554.01 MPa while those one from the batches 1, 2, and 3 are 553.47 MPa, 551.27 MPa, and 554.42 MPa, respectively, which offers an average value of 549.72 MPa. It can be seen that a similar downward trend of the tensile strength occurs, according to the three different machined conditions.

Referring to elongation at break, results evidence a greater difference of the behavior of the samples subjected to corrosion tests. The summarized results according to the medium values obtained are: Average value of elongation at break for, without corrosion, 12.87% (similar to usual values in alloys of this type), specimens from corrosion tests and batch 1, 10.81%, batch 2, 10.05%, and batch 3, 11.54%, resulting in a total medium value of 10.80%. Overall, the decrease in the value of the percentage of elongation is even greater than in the two previous parameters contemplated.

Due to the tensile strength and elongation at break having been obtained by procedures of different empirical nature, mechanical testing in the first case and geometrical measurements in the second one establish the level of reliability offered by the two methods employed based on a relation that has been established between them with an eminently qualitative character. Since the reduction of the values of elongation is greater than that presented by the tensile strength values about the set of specimens subjected to corrosion, the medium values obtained for the considered relationship must be higher in the three series studied under these conditions (43.38 of MVa, against values of 53.12 of MVb, 54.88 of MVc, 47.40 of MVd and, therefore, 51.80 of MVt).

4. Conclusions

This work is supposed to present a new approach in the study of the response of the AA7075 T651 alloy, which is widely used in the aeronautic industry, to different mechanical and chemical actions such as milling machining and the corrosion process. In this sense, this work deals with a study field where it hardly exists in the literature.

Considering typical processes used in aeronautics, dry face milling has been selected as the machining operation to perform on the flat samples (different combinations by fixing cutting speed and depth of cut and modifying the feed rate). The corrosive environment has been obtained by means of a salt fog chamber.

Different specific combinations of geometrical and technological cutting parameters are applied on flat specimens, which have been divided in two study groups. Samples belong to the second group and have been additionally exposed to a corrosive environment.

Based on the results obtained, it can be clearly seen as a relevant influence of both processes. On the one hand, whatever combination of milling parameters is applied, samples without a corrosion effect show an insignificant variation of their mechanical property values (2.37% in tensile strength

and 1.90% in yield strength). However, the elongation at break presents a great reduction (24.5%) that varies inversely with the feed rate increase. Consequently, a higher feed rate results in a greater fragility of the material.

On the other hand, analyzing specimens machined and subjected to corrosion, results reveal that this phenomenon provokes a strong influence on the elongation at break. The elongation reduction follows a similar tendency with respect to samples without corrosion, but these samples present an evident greater fragility with an average elongation of 10.80% in comparison to the 12.87% of the first ones. Therefore, it produced an additional significant reduction of the 19.17%.

It is necessary to point out that all these observations are only valid within the tested range of milling parameters.

Author Contributions: Conceptualization and Investigation, M.J.M., F.M. and M.J.C. Methodology, M.J.M., F.M., M.J.C. and G.C. Resources, M.J.H. Formal Analysis and Writing—Review & Editing, M.J.M. Writing—Original Draft Preparation, M.J.M. and F.M. Visualization and Supervision, F.M.

Funding: This research received no external funding.

Acknowledgments: The authors want to thank the University of Malaga-Andalucia Tech, International Campus of Excellence, for its financial support of this paper.

Conflicts of Interest: The authors declare no conflict of interest.

References

1. Ezugwu, E.; Bonney, J.; Yamane, Y. An overview of the machinability of aeroengine alloys. *J. Mater. Process. Technol.* **2003**, *134*, 233–253. [[CrossRef](#)]
2. Dursun, T.; Soutis, C. Recent developments in advanced aircraft aluminum alloys. *Mater. Des.* **2014**, *56*, 862–871. [[CrossRef](#)]
3. UNE-EN 573-3:2014. *Aluminium and Aluminium Alloys—Chemical Composition and Form of Wrought Products—Part 1: Numerical Designation System*; AENOR: Madrid, Spain, 2014.
4. Sahoo, A.K.; Pradhan, S.; Rout, A.K. Development and machinability assessment in turning Al/SiCp-metal matrix composite with multilayer coated carbide insert using Taguchi and statistical techniques. *Arch. Civ. Mech. Eng.* **2013**, *13*, 27–35. [[CrossRef](#)]
5. Charles, J.A.; Crane, F.A.A.; Furness, J.A.G. 15-Materials for airframes. In *Selection and Use of Engineering Materials*, 3rd ed.; Butterworth-Heinemann: Oxford, UK, 1997; pp. 227–255.
6. Hinrichsen, J.; Bautista, C. The challenge of reducing both airframe weight and manufacturing cost. *Air Space Eur.* **2001**, *3*, 119–121. [[CrossRef](#)]
7. De Agustina, B.; Bernal, C.; Camacho, A.M.; Rubio, E.M. Experimental analysis of the cutting forces obtained in dry turning processes of UNS A97075 Aluminum alloys. *Procedia Eng.* **2013**, *63*, 694–699. [[CrossRef](#)]
8. Gokkaya, H. The effects of machining parameters on cutting forces, surface roughness, built-up edge (BUE) and built-up layer (BUL) during machining AA2014 (T4) alloy. *J. Mech. Eng.* **2010**, *56*, 584–593.
9. De Agustina, B.; Rubio, E.M.; Sebastián, M.A. Surface roughness predictive model of UNS A97075 aluminum pieces obtained by dry turning tests based on the cutting forces. *Appl. Mech. Mater.* **2012**, *217–219*, 1628–1635. [[CrossRef](#)]
10. Trujillo, F.J.; Sevilla, L.; Marcos, M. Cutting speed-feed coupled experimental model for geometric deviations in the dry turning of UNS A97075 Al-Zn alloys. *Adv. Mech. Eng.* **2014**, *1*, 1–11. [[CrossRef](#)]
11. Salguero, J.; Batista, M.; Calamaz, M.; Giro, F.; Marcos, M. Cutting forces parametric model for the dry highspeed contour milling of aerospace aluminum alloys. *Procedia Eng.* **2013**, *63*, 735–742. [[CrossRef](#)]
12. Baek, D.K.; Ko, T.J.; Kim, H.S. Optimization of feedrate in a face milling operation using a surface roughness model. *Int. J. Mach. Tools Manuf.* **2001**, *41*, 451–462. [[CrossRef](#)]
13. Salguero Gómez, J. Analysis, Evaluation and Proposals for Performance Enhancing in Highspeed Machining of Aeronautical Aluminum Alloys. Ph.D. Thesis, University of Cadiz, Cadiz, Spain, 2013.
14. Cai, X.J.; Ming, W.W.; Chen, M. Surface integrity analysis on high speed end milling of 7075 aluminium alloy. *Adv. Mater. Res.* **2012**, *426*, 321–324. [[CrossRef](#)]
15. Ammula, S.C.; Guo, Y.B. Surface integrity of Al 7050-T7451 and Al 6061-T651 induced by high speed milling. *J. Aerosp.* **2005**. [[CrossRef](#)]

16. Sreejith, P.S. Machining of 6061 aluminium alloy with MQL, dry and flooded lubricant conditions. *Mater. Lett.* **2008**, *62*, 276–278. [CrossRef]
17. Shokrani, A.; Dhokia, V.; Newman, S.T. Environmentally conscious machining of difficult-to-machine materials with regard to cutting fluids. *Int. J. Mach. Tools Manuf.* **2012**, *57*, 83–101. [CrossRef]
18. Itoigawa, F.; Childs, T.H.C.; Nakamura, T.; Belluco, W. Effects and mechanisms in minimal quantity lubrication machining of an aluminum alloy. *Wear* **2006**, *260*, 339–344. [CrossRef]
19. Chen, L.; Hsieh, C.-C.; Wetherbee, J.; Yang, C.-L. Characteristics and treatability of oil-bearing wastes from aluminum alloy machining operations. *J. Hazard. Mater.* **2008**, *152*, 1220–1228. [CrossRef] [PubMed]
20. Haddag, B.; Atlati, S.; Nouari, M.; Moufki, A. Dry machining aeronautical aluminum alloy AA2024-T351: Analysis of cutting forces, chip segmentation and built-up edge formation. *Metals* **2016**, *6*, 197. [CrossRef]
21. Rubio, E.M.; Camacho, A.M.; Sánchez-Sola, J.M.; Marcos, M. Chip arrangement in the dry cutting of aluminum alloys. *J. Achiev. Mater. Manuf. Eng.* **2006**, *16*, 164–170.
22. López de la Calle, L.N.; Pérez, J.; Llorente, J.J.; Sánchez, J.A. Advanced cutting conditions for the milling of aeronautical alloys. *J. Mater. Process. Technol.* **2000**, *100*, 1–11. [CrossRef]
23. Trujillo, F.J. Parametric Analysis in the Dry Machining of UNSA97075 Alloy. Ph.D. Thesis, University of Malaga, Malaga, Spain, 2013.
24. Korkut, I.; Donertas, M.A. The influence of feed rate and cutting speed on the cutting forces, surface roughness and tool chip contact length during face milling. *Mater. Des.* **2007**, *28*, 308–312. [CrossRef]
25. Sánchez-Sola, J.M.; Batista, M.; Salguero, J.; Gómez, A.; Marcos, M. Cutting speed-feed based parametric model for macro-geometrical deviations in the dry turning of UNS A92024 al-cu alloys. *Key Eng. Mater.* **2012**, *504–506*, 1311–1316. [CrossRef]
26. Otero Huerta, E. *Corrosión y Degradación de Materiales*, 2nd ed.; Editorial Síntesis, S. A.: Madrid, Spain, 2012; ISBN 978-84-773851-8-9.
27. Huang, I.-W.; Hurley, B.L.; Yang, F.; Buchheit, R.G. Dependence on Temperature, pH, and Cl in the uniform corrosion of aluminum alloys 2024-T3, 6061-T6, and 7075-T6. *Electrochim. Acta* **2016**, *199*, 242–253. [CrossRef]
28. Bienvenido, R.; Díaz Vázquez, J.E.; Botana, J.; Cano, M.J.; Marcos, M.; Díaz-Vázquez, J.E.; Botana, J.; Cano-Iglesias, M.J.; Marcos, M. Preliminary study of the influence of machining conditions in the response to corrosion of UNS-A92024 alloy. *Adv. Mater. Res.* **2010**, *107*, 117–121. [CrossRef]
29. Aballe, A.; Bethencourt, M.; Botana, F.J.; Cano, M.J.; Marcos, M. Localized alkaline corrosion of alloy AA5083 in neutral 3.5% NaCl solution. *Corros. Sci.* **2001**, *43*, 1657–1674. [CrossRef]
30. Kamoutsi, H.; Haidemenopoulos, G.N.; Bontozoglou, V.; Pantelakis, S. Corrosion-induced hydrogen embrittlement in aluminum alloy 2024. *Corros. Sci.* **2006**, *48*, 1209–1224. [CrossRef]
31. Rout, P.K.; Ghosh, K.S. Effect of microstructural features on stress corrosion cracking behaviour of 7017 and 7150 aluminum alloy. *Mater. Today Proc.* **2018**, *5*, 2391–2400. [CrossRef]
32. Song, R.G.; Dietzel, W.; Zhang, B.J.; Liu, W.J.; Tseng, M.K.; Atrens, A. Stress corrosion cracking and hydrogen embrittlement of an Al–Zn–Mg–Cu alloy. *Acta Mater.* **2004**, *52*, 4727–4743. [CrossRef]
33. Gómez-Parra, A.; Puerta, F.J.; Rosales, E.I.; González-Madrigal, J.M.; Marcos, M. Study of the influence of cutting parameters on the Ultimate Tensile Strength (UTS) of UNS A92024 alloy dry turned bars. *Procedia Eng.* **2013**, *63*, 796–803. [CrossRef]
34. Gómez-Parra, Á.; Puerta, F.J.; Rosales, E.I.; García-Jurado, D.; Mainé, J.M.; Marcos, M. Influence of the dry turning parameters on the Ultimate Tensile Strength (UTS) of UNS A92024 samples. *Mater. Sci. Forum* **2014**, *797*, 65–70. [CrossRef]
35. UNE EN ISO 6892-1:2017. *Materiales Metálicos. Ensayo de Tracción. Parte 1: Método de Ensayo a Temperatura Ambiente*; AENOR: Madrid, Spain, 2017.
36. Servosis SL Serie ME-405. 2012. pp. 1–8. Available online: <https://www.servosis.com/fileuploads/products/sv-sl-me-405.pdf> (accessed on 29 June 2018).



Article

On the Performance of Thin-Walled Crash Boxes Joined by Forming

Diogo F. M. Silva ¹, Carlos M. A. Silva ¹, Ivo M. F. Bragança ², Chris V. Nielsen ³, Luis M. Alves ¹ and Paulo A. F. Martins ^{1,*}

¹ Instituto de Engenharia Mecânica, Instituto Superior Técnico, Universidade de Lisboa, Av. Rovisco Pais, 1049-001 Lisboa, Portugal; diogogmsilva@tecnico.ulisboa.pt (D.F.M.S.); carlos.alves.silva@tecnico.ulisboa.pt (C.M.A.S.); luisalves@tecnico.ulisboa.pt (L.M.A.)

² Instituto Superior de Engenharia de Lisboa, Rua Conselheiro Emídio Navarro, 1959-007 Lisboa, Portugal; ibraganca@dem.isel.pt

³ Department of Mechanical Engineering, Technical University of Denmark, 2800 Kgs. Lyngby, Denmark; cvni@mek.dtu.dk

* Correspondence: pmartins@tecnico.ulisboa.pt; Tel.: +351-21-8419006

Received: 7 June 2018; Accepted: 28 June 2018; Published: 29 June 2018

Abstract: A new joining by forming process that combines lancing and shearing with sheet-bulk compression is utilized to assemble thin-walled crash boxes utilized as energy absorbers. Process design and fabrication of the new crash boxes are analyzed by finite elements and experimentation. Axial crush tests were performed to compare the overall crashworthiness performance of the new crash boxes against that of conventional crash boxes assembled by resistance spot-welding. Results show that the joining process is a good alternative to resistance spot-welding because the new crash boxes can absorb the same crushing energy, and because the new process helps to overcome typical manufacturing problems of welding.

Keywords: crash boxes; joining by forming; resistance spot-welding; crashworthiness

1. Introduction

An energy absorber is an important element of a vehicle because it protects the lives of passengers by managing the absorption of energy and collapse of its structure during an accident. One of the strategies currently employed by vehicle manufacturers to meet the increasing requirements on safety and the diminishing weight targets is the utilization of energy absorbers made of high-strength materials in lightweight body structures. However, the search for more effective energy absorbers is wider and includes new geometries and materials with the potential to enhance the crashworthiness performance of the structures under different types of loading. These trends are comprehensively discussed in two recently published state-of-the-art reviews on energy absorbers [1,2].

The search for new processes to manufacture energy absorbers has so far received little attention. Most of the publications in the field make use of energy absorbers produced by conventional extrusion [3,4] or by combination of forming and welding [5,6] (or, adhesive bonding) with or without hydroforming [7]. However, the design of energy absorbers with higher performance and wider applicability than the existing ones requires the development of new fabrication processes that allows for a combination of dissimilar materials with different thicknesses and types of surface coatings, as well as a combination of adhesives.

Joining by forming [8] can also be successfully utilized to fabricate efficient, low-cost, energy absorbers. Lee et al. [9], for example, made use of self-piercing riveting to assemble thin-walled crash boxes with double hat-shaped sections made from steel and aluminum formed panels. They analyzed the overall crashworthiness performance and concluded that the energy absorbed by the self-piercing

riveted crash boxes is higher than that of the adhesive-bonded. Gronostajski and Polak [10] utilized two different clinching processes to assemble thin-walled crash boxes with double hat-shaped sections made of steel formed panels and concluded that clinching can be successfully applied to fabricate energy absorbers.

Table 1 summarizes the main advantages and disadvantages of the fabrication processes that are commonly utilized to assemble crash boxes with top-hat and double-hat shaped sections made from individual formed panels.

Table 1. Main characteristics of the fabrication processes that are commonly utilized to assemble thin-walled crash boxes with top-hat or double-hat shaped sections.

Process	Resistance Spot Welding	Adhesive Bonding	Self-Piercing Riveting	Clinching
Materials	Mostly steels. Metallurgical compatibility necessary for dissimilar metals	Engineering materials	Engineering materials with reasonable ductility and fracture toughness	Engineering materials with reasonable ductility and fracture toughness
Coatings	Thick metal and organic coatings are difficult	Coatings and lubricants must be cleaned	Organic coatings and lubricants can affect the properties of the joints	Organic coatings and lubricants can affect the properties of the joints
Surface preparation	None	Caution preparation	None	None
Consumables	Electrodes	Adhesives	Rivets (coatings needed for steel rivets)	None
Environmental impact	Sparks, fumes, and noise	Chemicals	Noise	Noise
Aesthetics and geometry	Indentation on both sides. Damage of coatings. Distortion and residual stresses due to thermal cycle	None	Flush in one side and protrusion on the other side	Hole in one side and large protrusion on the other side
Performance	High shear strength and medium peel strength	Low shear and peel strengths	High shear strength and medium peel strength	Medium shear strength and low peel strength
Productivity	High	Low (long curing time)	Intermediate	High (no pre-working required)

This paper is focused on the assembly of thin-walled crash boxes with double-hat shaped sections made from individual formed panels. The aim and objective is to present a new fabrication process that combines lancing of the tenons, in which specific areas of the panels are sheared and bent in a single press operation (Figure 1a), shearing of the mortises, in which holes are cut out of the opposite panels (Figure 1b), and sheet-bulk compression of the tenons during which the two panels are assembled by means of “mortise-and-tenon” joints placed along the flanges (Figure 1c,d).

The new fabrication process draws from two previous investigations on joining by forming in which “mortise-and-tenon” joints were successfully utilized to fix two sheets longitudinally in position by sheet-bulk compression. The two sheets were joined either perpendicular [11] or parallel [12] to each other. The reason behind the utilization of “mortise-and-tenon” joints as an alternative to resistance spot-welded or adhesive bonded joints is because they offer the same advantages of self-piercing riveted and clinched joints (refer to Table 1) without having the constraints related to organic coatings

and lubricants. Moreover, the “mortise-and-tenon” joints have the ability to be easily combined with adhesives in order to increase stiffness and are also capable of ensuring higher-peel strength than self-piercing riveted and clinched joints due to the protrusion of the flat-shaped surface heads of the tenons above the adjacent sheet panels, after compression.

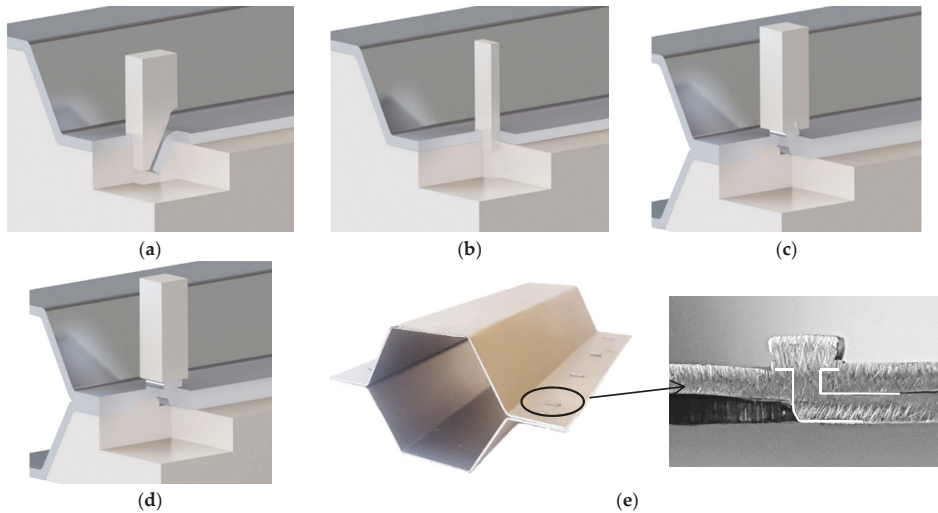


Figure 1. New fabrication process to assemble the individual formed panels of thin-walled crash boxes with double-hat shaped sections: (a) lancing (shearing and bending) of the tenon; (b) shearing of the mortise; (c) sheet-bulk compression of the tenon with a tapered punch; (d) mechanical locking by sheet-bulk compression of the tenon with a flat punch; (e) cross-section of a “mortise-and-tenon” joint. Note: the lancing in (a) is upside-down in order to replicate the press movement.

The main challenge of applying the “mortise-and-tenon” joint concept in the assembly of crash boxes (Figure 1e) derives from the need to compress thin-walled formed panels in the direction perpendicular to thickness. However, the authors solved the problem by introducing a novel two-stage variant of the sheet-bulk compression process that makes use of a tapered heading punch in the first stage (Figure 1c), and a flat heading punch in the second stage (Figure 1d). The tapered heading punch ensures a better balance of material displacement and diminishes the risk of buckling during the initial compression of the panels. The flat heading punch ensures the mechanical locking of the two individual panels.

The crash boxes assembled with the new proposed “mortise-and-tenon” joint concept are subjected to static and dynamic axial crushing and its overall crashworthiness performance is compared against that of resistance spot-welded. Results show that the new crash boxes are a good alternative to those assembled by resistance spot-welding.

2. Materials and Methods

2.1. Mechanical Characterization

The new proposed joining by forming process can easily assemble thin-walled crash boxes with individual panels made from dissimilar materials with different thicknesses. However, it was decided to select a single high-strength low alloy steel (HSLA 340) with 1 mm thickness and 7 μm thickness galvanized coating to ensure a fair comparison of the crashworthiness performance of the new crash boxes against those assembled by resistance spot-welding.

The mechanical characterization of the HSLA 340 steel was performed by means of stack compression tests [13] due to its capability to characterize the material stress response up to the large strains that were found in the compression of the flat-shaped surface heads of the tenons. The stack compression tests were carried out at room temperature in a hydraulic testing machine (Instron SATEC 1200 kN, Norwood, MA, USA) with a cross-head velocity of 10 mm/min and made use of multi-layer cylinder test specimens that were assembled by piling up 10 circular disks with 10 mm diameter cut out from the supplied sheets by wire-electro discharge machining (wire-EDM).

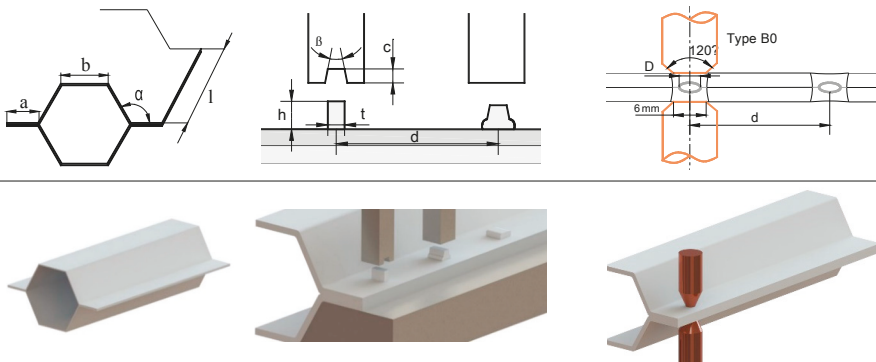
2.2. Fabrication of the Crash Boxes

The thin-walled crash boxes with double hat-shaped sections were made from two individual formed panels that were assembled by sheet-bulk compression with “mortise-and-tenon” joints placed every 40 mm along their flanges. Table 2 provides the geometry of the crash boxes and a schematic detail of the new proposed joining by forming process.

Conventional thin-walled crash boxes assembled by resistance spot welding were included in the experimental work plan for reference purposes. The welding parameters were selected by finite element modelling (refer to Section 3.2) and the joints consisted of around 5.4 mm diameter spots, positioned similarly along the flange as the “mortise-and-tenon” joints.

Table 2. Geometry and parameters of the thin-wall crash boxes assembled by sheet-bulk compression with “mortise-and-tenon” joints and by conventional resistance spot-welding.

Geometry		Sheet-Bulk Compression		Resistance Spot-Welding	
Thickness t	1 mm	Tenon width w	5 mm	Electric current	7.8 kA
Flange a	24 mm	Tenon length h	3.5–6 mm	Time (distributed in two pulses)	320 ms
Top section b	36.6 mm	Distance between joints d	40 mm	Force	3.3 kN
Angle α	120 degrees	Tapered punch angle β	$\sim 4^\circ$	Resulting nugget diameter D	5.4 mm
Length l	160 mm	Tapered punch length c	1.5 mm	Distance between welds d	40 mm



2.3. Axial Crush Tests

The crash boxes were tested for quasi-static and dynamic axial crushing at room temperature. The quasi-static crush tests were performed in the hydraulic testing machine (Instron SATEC 1200 kN) that had been used in the mechanical characterization of the material. A cross-head velocity $v = 10$ mm/min was utilized, and the tests were stopped after reaching a prescribed crushing distance of 55 mm (approximately 1/3 of the initial length of the crash boxes).

The dynamic crush tests were performed in a drop weight testing machine that was designed and fabricated by the authors. The machine and its main components are schematically shown in Figure 2a.

The mass M and drop height H of the falling ram can be adjusted up to maximum values of 250 kg and 5 m, respectively.

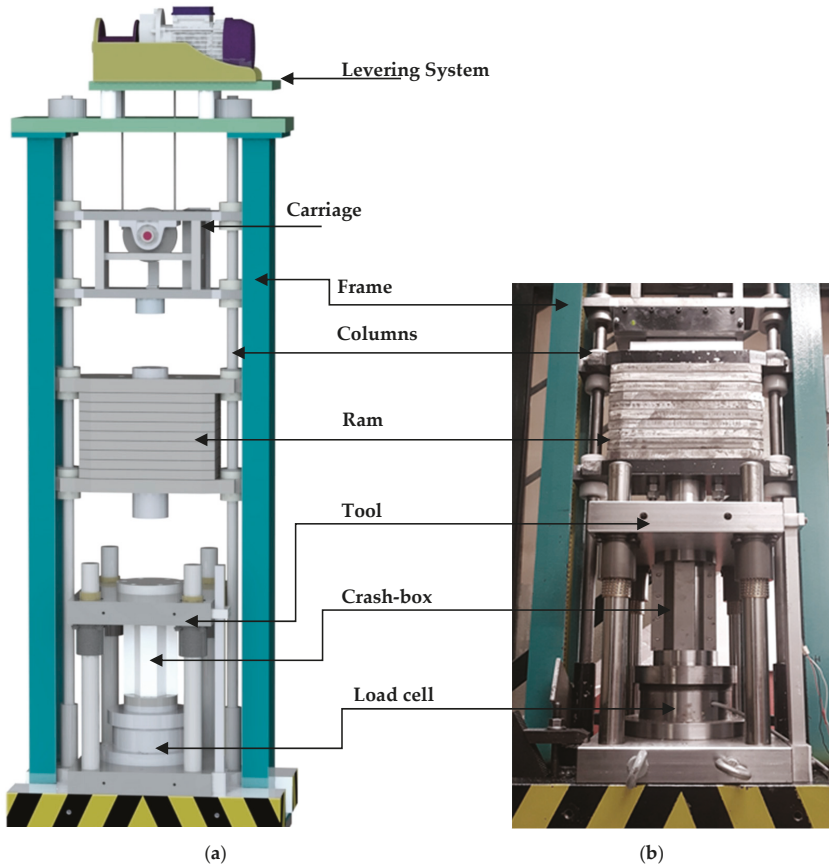


Figure 2. The drop weight testing machine: (a) schematic representation and identification of its main components; (b) photograph of the tool utilized in the crush tests.

The tool utilized in the quasi-static and dynamic crush tests is shown in Figure 2b. The crash boxes were placed centrally in the tool, without any further support and were subsequently compressed between the top and bottom flat platens. The tool was instrumented with a load cell based on traditional strain gauge technology in full wheatstone bridge with a capacity of 500 kN, a nominal sensitivity of 1 mV/V, and an accuracy class of 0.7. The load cell was connected to a signal amplifier unit (Vishay 2310B) and a personal computer data logging system based on a DAQ card (National Instruments, PCI-6115, Austin, TX, USA). The displacement transducer is a commercial linear variable differential transformer (Solartron LVDT AC15, Farnborough, UK). A special purpose LabView based software was designed to acquire and store the experimental data from both the load cell and the displacer.

Table 3 gives a summary of the main operating conditions utilized in the quasi-static and the dynamic axial crush tests.

Table 3. Summary of the quasi-static and dynamic axial crush testing conditions.

Quasi-Static Axial Crush Tests	
Equipment	Hydraulic testing machine
Velocity v	10 mm/min (1.7×10^{-4} m/s)
Dynamic Axial Crush Tests	
Equipment	Drop weight testing machine
Ram mass M	82 kg
Upper tool moving mass M_t	45 kg
Height of the fall H	4 m
Efficiency η	~60%
Velocity v_i	9.5 m/s

2.4. Finite Element Modelling

The assembly of the individual panels of the thin-walled crash boxes by means of sheet-bulk compression with “mortise-and-tenon” joints was simulated with the finite element computer program I-form. The computer program was developed by the authors and is based on the irreducible finite element formulation,

$$\Pi = \int_V \bar{\sigma} \dot{\bar{\epsilon}} dV + \frac{1}{2} K \int_V \dot{\epsilon}_V^2 dV - \int_{S_T} T_i u_i dS + \int_{S_f} \left(\int_0^{|u_r|} \tau_f du_r \right) dS, \tag{1}$$

where, the symbol $\bar{\sigma}$ is the effective stress, $\dot{\bar{\epsilon}}$ is the effective strain rate, $\dot{\epsilon}_V$ is the volumetric strain rate, K is a large positive constant imposing the incompressibility of volume V , S is the surface under consideration, T_i and u_i are the surface tractions and velocities on surface S_T , τ_f and u_r are the friction shear stress and the relative velocity on the contact interface S_f between the material and tooling. Further details on the computer program with special emphasis to contact and frictional sliding between rigid and deformable objects are available in Reference [14].

The numerical simulation made use of two-dimensional plane strain deformation models and the cross section of the tenons and mortises were discretized by means of approximately 1000 quadrilateral elements. The tools were modelled as rigid objects and their geometries were discretized by means of linear contact-friction elements.

The assembly of the individual panels of the thin-walled crash boxes by means of resistance spot-welding was simulated with the commercial finite element computer program SORPAS [15], which is based on an electro-thermo-mechanical formulation as described in details in [14]. The mechanical formulation follows Equation (1). Solution of the electrical potential Φ is based on integration of Laplace’s equation, which in variational form can be written as

$$\int_V \Phi_{,i} \delta \Phi_{,i} dV = 0, \tag{2}$$

where subscripts indicate spatial derivatives. The current density, calculated from the derivative of the potential and electrical resistivity, is used in the calculation of Joule heating during the welding process. The following variational equation governs the thermal solution for the temperature field T ,

$$\int_V k T_{,i} \delta T_{,i} dV + \int_V \rho c \dot{T} \delta T dV - \int_V \dot{q} \delta T dV - \int_S k T_{,n} \delta S = 0 \tag{3}$$

The first term is related to heat conduction through the conductivity k , and the second term is related to the temperature rate \dot{T} with material properties being mass density ρ and heat capacity c .

Joule heating and heating from plastic work are included in the heat generation rate per volume \dot{q} in the third term. Finally, the last term includes heat generation and loss along surfaces stemming from frictional heating, convection and radiation. The subscript in the last term refers to spatial derivative along a surface normal. Further details like treatment of contact conditions are available in Reference [14].

3. Results

3.1. Mechanical Characterization

The stress-strain curve of the HSLA 340 steel obtained from the stack compression tests is shown in Figure 3. The enclosed photograph shows the multi-layer cylinder test specimens that were assembled by piling up 10 circular disks before and after compression. The stress-strain curve is utilized in the finite element simulation of the assembly of thin-walled crash boxes by sheet-bulk compression with “mortise-and-tenon” joints.

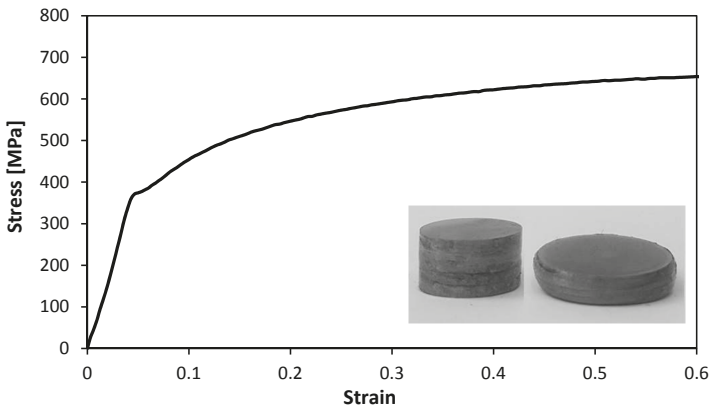


Figure 3. Stress-strain curve of the high-strength low alloy (HSLA) 340 steel obtained from stack compression tests.

3.2. Finite Element Modelling and Experimentation of the Fabrication Process

The reference joining process was simulated by the commercial software SORPAS [15]. The simulation result is shown in Figure 4 in terms of process peak temperature and identification of weld nugget. The simulation was based on the parameters given in Table 2. The simulation reveals a weld nugget with a diameter of 5.4 mm across the interface and a proper penetration into both of the two HSLA 340 sheets.

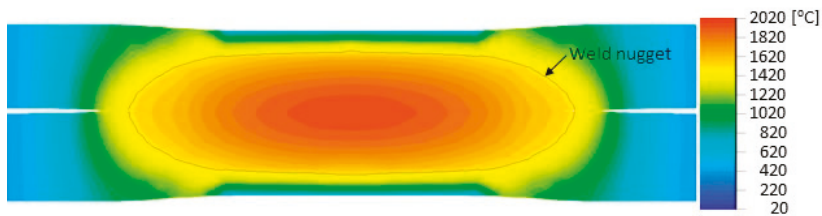


Figure 4. Distribution of simulated peak temperature in resistance spot-welding together with identification of the weld nugget.

The assembly of the thin-walled crash boxes by the novel sheet-bulk compression process with “mortise-and-tenon” joints required the tenons to be cut and bent out of the panels by lancing (Figure 1a), and subsequently compressed in the direction perpendicular to thickness (Figure 1c,d). Figure 5a,b show the finite element computed distribution of effective strain in the tenons at the end of the first sheet-bulk compression stage. Two different process operating conditions (Table 2) are shown: a tenon with a free length $h = 4.5$ mm that is successfully compressed by a tapered heading punch (Figure 5a) and a tenon with a free length $h = 6$ mm that fails by buckling (Figure 5b).

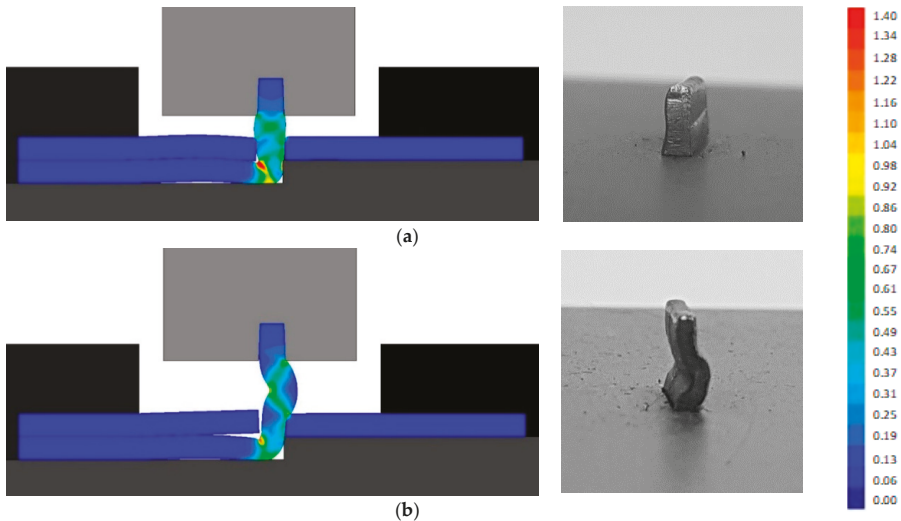


Figure 5. Assembling the individual formed panels of the thin-walled crash boxes: (a) effective strain distribution at the end of the first stage of the sheet-bulk compression of a tenon with a free length $h = 4.5$ mm; (b) effective strain distribution at the end of the first stage of the sheet-bulk compression of a tenon with a free length $h = 6$ mm.

Successfully compressed tenons are needed for the second stage of the sheet-bulk compression, during which a flat heading punch assembles the crash boxes by mechanically locking the individual formed panels to each other.

Figure 6 shows finite element deformed meshes at different instants of the crash box assembly by means of sheet-bulk compression with “mortise-and-tenon” joints. The case included in the figure consists of a bent tenon with a free length $h = 4.5$ mm and corresponds to the working conditions that were utilized to fabricate all the crash boxes with “mortise-and-tenon” joints that were subjected to the axial crush tests.

As seen in Figure 6a,b, the tapered heading punch prevents the collapse by buckling at the early stages of deformation. The flat heading punch (Figure 6c,d) produces the flat-shaped surface heads (Figure 6e) that will lock the panels to each other and assemble the crash box.

Figure 7 shows the experimental and finite element computed evolution of the force with displacement for the first and second stages of the sheet-bulk compression with “mortise-and-tenon” joints. The agreement is good and allows estimating the energy required to perform the first and second stages of the new proposed joining by forming process.

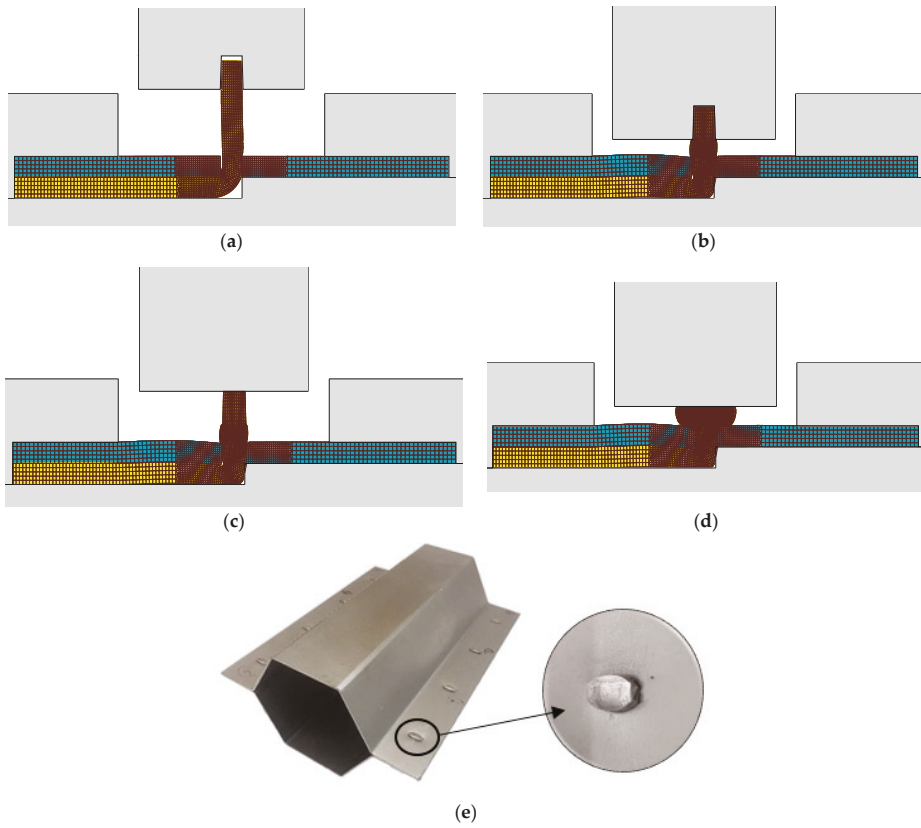


Figure 6. Fabrication of the crash boxes by sheet-bulk compression with “mortise-and-tenon” joints ($h = 4.5$ mm): (a) finite element mesh at the beginning of the first stage; (b) computed finite element mesh at the end of the first stage; (c) computed finite element mesh at the beginning of the second stage; (d) computed finite element mesh at the end of the second stage; (e) crash box with a detail showing the flat-shaped surface head of a compressed tenon.

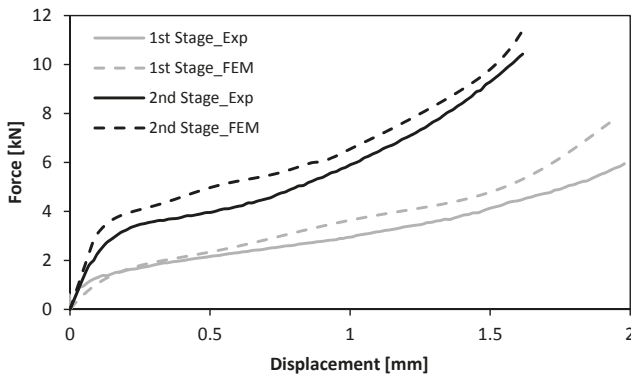


Figure 7. Experimental and numerical evolution of the force with displacement for the first and second stages of the sheet-bulk compression of tenons with $h = 4.5$ mm.

3.3. Axial Crush Tests

Figure 8a shows the force-displacement curves for the quasi-static axial crush tests of the thin-walled crash boxes with double-hat section assembled by sheet-bulk compression with “mortise-and-tenon” joints and by resistance spot-welding. As seen, the force increases steeply up to a peak value where the first fold is formed (initiation of collapse). Then, the force decreases and the subsequent folds, corresponding to the oscillations of the force-displacement curve, are triggered for smaller local force peaks.

Figure 8b shows the force-displacement curves for the dynamic axial crush tests of the two types of crash boxes. The tests were performed in the drop weight testing machine (Figure 2), which converts the potential energy E_p at the beginning of the fall,

$$E_p = MgH, \tag{4}$$

into an axial crush velocity v_i at the impact by conservation of linear momentum between the mass M of the falling ram and the mass M_t of the upper tool part containing the compression platen,

$$v_i = \eta M \sqrt{2gH} / M_t, \tag{5}$$

In the above equation, g is the gravity acceleration and η is the efficiency, which accounts for the air resistance, friction sliding along the columns and type of collision between the falling ram and the upper tool part (Figure 2a). The mass M and the drop height H of the falling ram were adjusted to deform the crash boxes by approximately 1/3 of their initial length with an impact velocity $v_i \simeq 16$ m/s. Finally, it is worth noting that the impact velocity v_i is progressively reduced to zero by the absorption of energy.

As seen, the overall trend of the dynamic force-displacement curves is similar to that of the quasi-static tests (Figure 8a) but the peak force to trigger collapse increases from 89 kN to 115 kN, in case of the crash boxes assembled with “mortise-and-tenon” joints. Similar increase in the peak force is obtained for the resistance spot-welding joints.

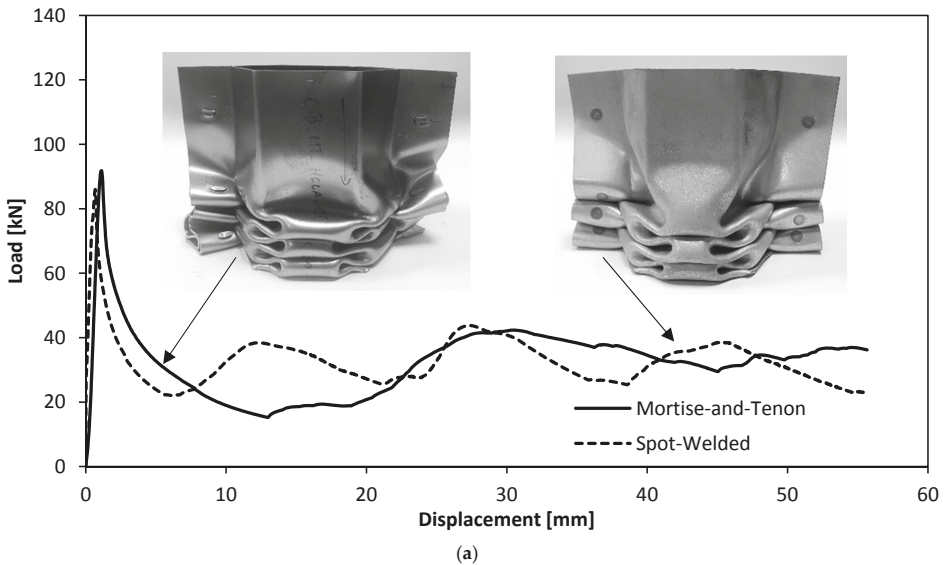


Figure 8. Cont.

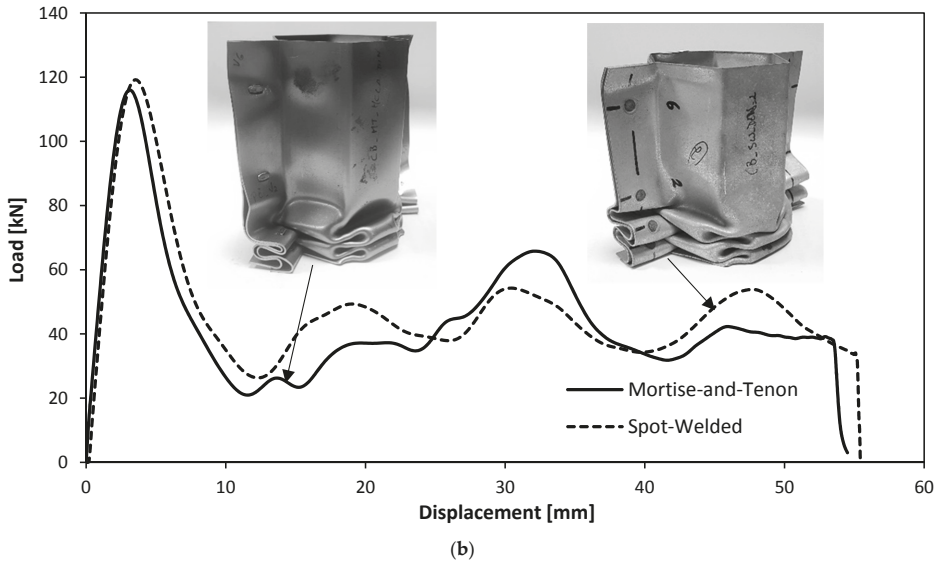


Figure 8. Experimental evolution of the force with displacement for the axial crush tests of thin-walled crash boxes with double-hat section assembled by sheet-bulk compression with “mortise-and-tenon” joints and by resistance spot-welding: (a) quasi-static tests; (b) dynamic tests.

3.4. Alignment of the “Mortise-And-Tenon” Joints

The crashworthiness performance of the new crash boxes with “mortise-and-tenon” joints raises the question of the alignment of the protrusions of the flat-shaped surface heads of the tenons above the adjacent sheet panel, after compression. Should the flat-shaped surface heads be collinear or perpendicular to the longitudinal axis of the crash box?

Experiments performed by the authors revealed that the flat-shaped surface heads must be perpendicular to the longitudinal axis of the crash boxes because if they are collinear, they are easily pulled-out during axial crushing, diminishing the overall performance of the crash box (Figure 9).

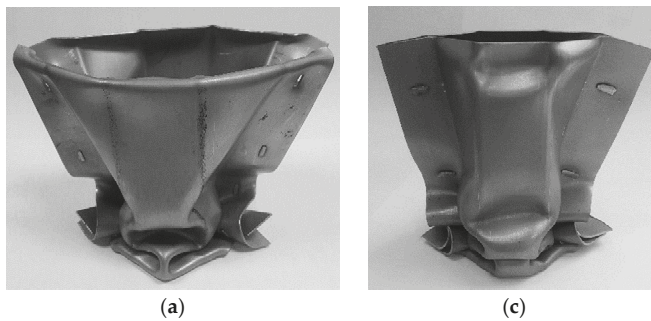


Figure 9. Cont.

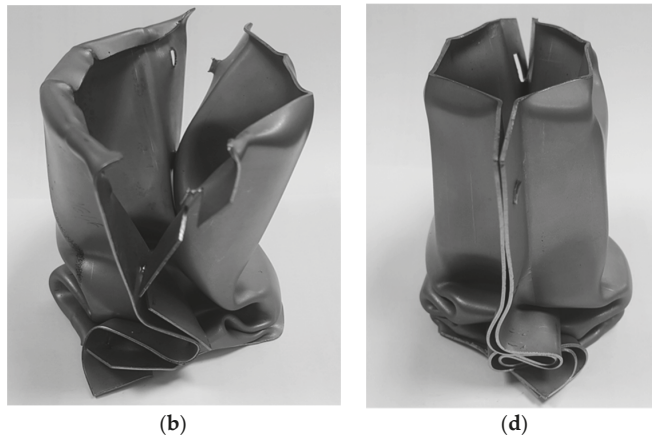


Figure 9. Thin-walled crash boxes with double-hat section assembled by sheet-bulk compression with “mortise-and-tenon” joints after axial crushing: The flat-shaped surface heads of the tenons are (a) collinear (front view), (b) collinear (side view), (c) perpendicular (front view), and (d) perpendicular (side view) to the longitudinal axis of the crash box.

4. Discussion

The evolution of the force with displacement for the quasi-static and dynamic axial crush tests performed with the two different types of crash boxes allow concluding that the new proposed “mortise-and-tenon” joints can successfully replace resistance spot-welds. In fact, Figure 8 shows that the overall trend of the force-displacement curves is similar with peak forces to trigger collapse being higher in the dynamic crush tests. In case of the crash boxes assembled with “mortise-and-tenon” joints, for example, the peak values increase from 89 kN to 115 kN when dynamic conditions are applied.

The energy E absorbed by the crash boxes during the axial crush tests are obtained from the areas below the experimental force-displacement curves of Figure 8,

$$E = \int_0^{\delta_{\max}} F d\delta, \quad (6)$$

where $\delta_{\max} = 55$ mm is the maximum specified testing distance (refer to Figure 8).

The results are shown in Figure 10 and allow concluding that the new type of crash box can absorb an overall level of energy similar to that of the resistance spot-welded crash boxes.

The maximum absorbed energy in the dynamic tests, is approximately 30% higher than in the quasi-static tests. This increase of crashworthiness performance with velocity is attributed to the strain-rate sensitivity of the HSLA 340 steel [16]. However, it is worth noting that the maximum absorbed energy in the dynamic tests is approximately 25% smaller than the total energy provided by the drop weight machine (3.2 kJ) because part of this energy is lost in the conversion of linear momentum between the mass M of the falling ram and the mass M_t of the tool, in the elastic deformation of the tool and of the drop weight testing machine, and in the vibration of its different components.

Another result that is relevant from a manufacturing point of view is the total energy required to fabricate a “mortise-and-tenon” joint and a resistance spot-welded joint. From the experimental and numerical evolution of the force with displacement for the first and second stages of the sheet-bulk compression of the tenons it may be concluded that approximately 7 J and 10 J will be needed to accomplish both stages. Thus, by considering these values of energy as well as that required to perform

the lancing operation, it is concluded that the total amount of energy to fabricate a “mortise-and-tenon” joint is a very small fraction of that required by a resistance spot-welded joint (Figure 11). This is an important advantage of the new proposed type of crash boxes regarding environmental friendliness.

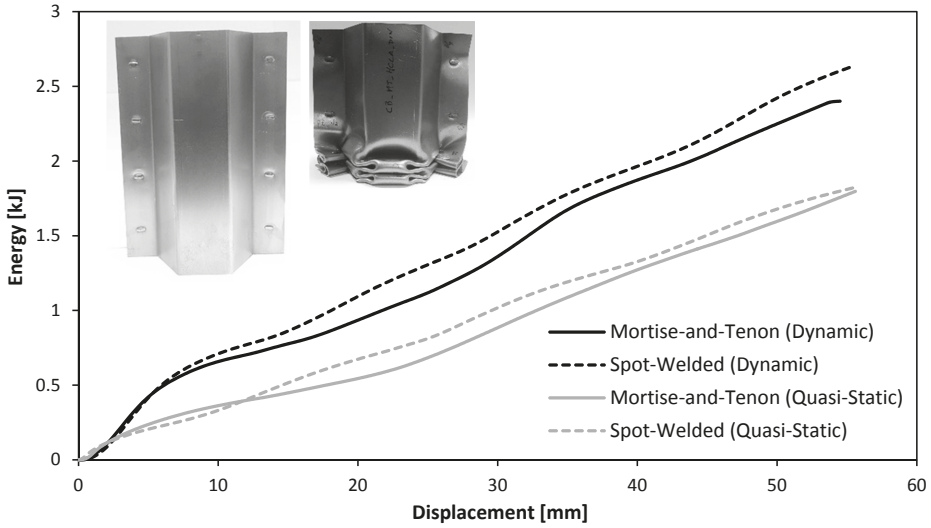


Figure 10. Experimental evolution of the absorbed energy with displacement for the axial crush tests of thin-walled crash boxes with double-hat section assembled by sheet-bulk compression with “mortise-and-tenon” joints and by resistance spot-welding: (a) quasi-static tests; (b) dynamic tests.

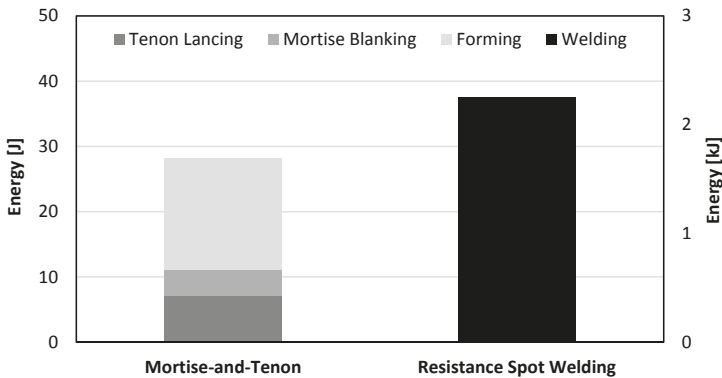


Figure 11. Energy required to produce “mortise-and-tenon” and resistance spot-welded joints. The energy required by the mortise-and-tenon joint is referred to the vertical left axis whereas that of the resistance spot-welded joint is referred to the vertical right axis.

5. Conclusions

The fabrication of crash boxes by sheet-bulk compression with “mortise-and-tenon” joints can successfully replace conventional production processes based on resistance spot-welding. The crash boxes with “mortise-and-tenon” joints can absorb the same amount of energy as those with resistance spot-welding joints in quasi-static and dynamic axial crush tests. They can also avoid the problems

caused by residual stresses in the resistance spot-welding of panels made from dissimilar materials with different thicknesses.

The greater applicability of the new crash boxes comes with a disadvantage regarding productivity due to the multi-stage characteristics of the proposed joining by forming process. However, this disadvantage can be offset by the environmental friendliness resulting from the total required energy to assemble a crash box by sheet-bulk compression with “mortise-and-tenon” joints being a very small fraction (1.3%) of that required by resistance spot-welding.

Author Contributions: D.F.M.S., C.M.A.S., and I.M.F.B. designed and fabricated the crash boxes with “mortise-and-tenon” joints. C.V.N. and C.M.A.S. designed and fabricated the crash boxes with resistance spot-welded joints. D.F.M.S., C.M.A.S., and I.M.F.B. performed the quasi-static and dynamic axial crush tests. D.F.M.S. and C.V.N. performed the finite element simulations. C.M.A.S. and I.M.F.B. analyzed the results. L.M.A. and P.A.F.M. contributed as advisors and proposed the subject. P.A.F.M. supervised the overall research work and wrote the article with the collaboration of all the other authors.

Funding: This research was funded by Fundação para a Ciência e a Tecnologia of Portugal under LAETA—UID/EMS/50022/2013 and PDTC/EMS-TEC/0626/2014.

Acknowledgments: The authors would like the technical support of Mahsa Seyyedian Choobi in the resistance spot-welding experiments.

Conflicts of Interest: The authors declare no conflict of interest. The funders had no role in the design of the study; in the collection, analyses, or interpretation of data; in the writing of the manuscript, and in the decision to publish the results.

References

1. Baroutaji, A.; Sajjia, M.; Olabi, A.-G. On the crashworthiness performance of thin-walled energy absorbers: Recent advances and future developments. *Thin-Walled Struct.* **2017**, *118*, 137–163. [[CrossRef](#)]
2. Yusof, N.S.B.; Sapuan, S.M.; Sultan, M.T.H.; Jawaid, M.; Maleque, M.A. Design and materials development of automotive crash box: A review. *Ciência Tecnol. Mater.* **2017**, *29*, 129–144. [[CrossRef](#)]
3. Reyes, A.; Langseth, M.; Hopperstad, O.S. Crashworthiness of aluminum extrusions subjected to oblique loading: Experiments and numerical analyses. *Int. J. Mech. Sci.* **2002**, *44*, 1965–1984. [[CrossRef](#)]
4. Jin, S.Y.; Altenhof, W.; Kapoor, T. An experimental investigation into the cutting deformation mode of AA6061-T6 round extrusions. *Thin-Walled Struct.* **2006**, *44*, 773–786. [[CrossRef](#)]
5. Schneider, F.; Jones, N. Influence of spot-weld failure on crushing of thin-walled structural sections. *Int. J. Mech. Sci.* **2003**, *45*, 2061–2081. [[CrossRef](#)]
6. Pan, C.-L.; Yu, W.-W. Bending strength of hybrid cold-formed steel beams. *Thin-Walled Struct.* **2002**, *40*, 399–414. [[CrossRef](#)]
7. Abedrabbo, N.; Mayer, R.; Thompson, A.; Salisbury, C.; Worswick, M.; Riemsdijk, I. Crash response of advanced high-strength steel tubes: Experiment and model. *Int. J. Impact Eng.* **2009**, *36*, 1044–1057. [[CrossRef](#)]
8. Mori, K.; Bay, N.; Fratini, L.; Micari, F.; Tekkaya, A.E. Joining by plastic deformation. *CIRP Ann. Manuf. Technol.* **2013**, *62*, 673–694. [[CrossRef](#)]
9. Lee, M.-H.; Kim, H.-Y.; Oh, S.-I. Crushing test of double hat-shaped members of dissimilar materials with adhesively bonded and self-piercing riveted joining methods. *Thin-Walled Struct.* **2006**, *44*, 381–386. [[CrossRef](#)]
10. Gronostajski, Z.; Polak, S. Quasi-static and dynamic deformation of double-hat thin-walled elements of vehicle controlled body crushing zones joined by clinching. *Arch. Civ. Mech. Eng.* **2008**, *VIII*, 57–65. [[CrossRef](#)]
11. Bragança, I.M.F.; Silva, C.M.A.; Alves, L.M.; Martins, P.A.F. Joining sheets perpendicular to one other by sheet-bulk metal forming. *Int. J. Adv. Manuf. Technol.* **2017**, *89*, 77–86. [[CrossRef](#)]
12. Pragana, J.P.M.; Silva, C.M.A.; Bragança, I.M.F.; Alves, L.M.; Martins, P.A.F. A new joining by forming process to produce lap joints in metal sheets. *CIRP Ann. Manuf. Technol.* **2018**. [[CrossRef](#)]
13. Alves, L.M.; Nielsen, C.V.; Martins, P.A.F. Revisiting the fundamentals and capabilities of the stack compression test. *Exp. Mech.* **2011**, *51*, 1565–1572. [[CrossRef](#)]

14. Nielsen, C.V.; Zhang, W.; Alves, L.M.; Bay, N.; Martins, P.A.F. *Modelling of Thermo-Electro-Mechanical Manufacturing Processes with Applications in Metal Forming and Resistance Welding*; Springer: London, UK, 2013; ISBN 978-1-4471-4643-8.
15. SWANTEC Software and Engineering ApS. SORPAS®2D Hybrid-Version 12.92. Available online: www.swantec.com (accessed on 25 May 2018).
16. Strain Rate Sensitivity and Crash Modelling of High Strength Steels. Available online: https://thyme.ornl.gov/ASP_Main/matdata/matdata.cgi (accessed on 6 June 2018).



© 2018 by the authors. Licensee MDPI, Basel, Switzerland. This article is an open access article distributed under the terms and conditions of the Creative Commons Attribution (CC BY) license (<http://creativecommons.org/licenses/by/4.0/>).

MDPI
St. Alban-Anlage 66
4052 Basel
Switzerland
Tel. +41 61 683 77 34
Fax +41 61 302 89 18
www.mdpi.com

Materials Editorial Office
E-mail: materials@mdpi.com
www.mdpi.com/journal/materials



MDPI
St. Alban-Anlage 66
4052 Basel
Switzerland

Tel: +41 61 683 77 34
Fax: +41 61 302 89 18

www.mdpi.com



ISBN 978-3-03936-743-6